

**LAHAR DYNAMICS IN THE BELHAM RIVER VALLEY,
MONTSERRAT: APPLICATION OF REMOTE CAMERA-
BASED MONITORING FOR IMPROVED
SEDIMENTOLOGICAL INTERPRETATION OF POST-
EVENT DEPOSITS**

MELANIE J. FROUDE

A thesis submitted for the degree of Doctor of Philosophy

University of East Anglia, Norwich

School of Environmental Sciences

May 2015

© This copy of the thesis has been supplied on condition that anyone who consults it is understood to recognise that its copyright rests with the author and that use of any information derived there from must be in accordance with current UK Copyright Law. In addition, any quotation or extract must include full attribution.

Abstract

In active volcanic regions, the sedimentology of lahar deposits combined with available flow observations informs the choice of numerical models used to calculate lahar inundation risk maps and applied in the design of engineering structures to retard flow. Critically, field monitoring of lahars has focused on capturing the initiation conditions of flow and downstream transitions in bulk flow dynamics, but very few studies have directly linked inter-event observations of sediment-laden flow with depositional processes and sedimentary structures, in natural settings.

A remote camera was installed to monitor a channel section in the lahar prone Belham River Valley, 4.7 km from the active Soufrière Hills volcano, Montserrat, Caribbean, and captured images (1 fps) of a large lahar on 13th-14th October 2012. In combination with seismic and rainfall data, repeat topographic surveys and sedimentological observations, camera images were analysed to improve understanding of intra-flow variability and sediment transport during a single lahar. Flow was rapidly varying, unsteady and sediment-laden changing in character downstream. Seven peaks in seismic signal corresponded with observations of increased discharge, apparent turbulence, cobble-boulder transport and bore incidence. The bores (roll-waves) occurred at irregular intervals and increased flow depth and sediment transport; formation was driven by inherent flow instability caused by hydraulic geometry and flow Froude number.

Trains of water-surface-waves were common in flow; systematic measurements of wavelength provided estimates of flow velocity, depth and discharge. Deposits from flows between 2010 and 2013 were dominated by sedimentary structures indicative of upper-flow-regime bedforms including cyclic shifts from upper-planar-beds to antidunes. Although $\sim 4.4 \times 10^6 \text{ m}^3$ of sediment remained in storage in the Belham River Valley, preservation of channel deposits over decadal timescales is low because with time from volcanic sedimentation, sediment supply decreases and channels incise. Further research should aim to link distal debris fan successions with proximal flow dynamics.

Contents

ABSTRACT.....	III
LIST OF FIGURES.....	VIII
LIST OF TABLES.....	XXII
ACKNOWLEDGEMENTS.....	XXV
CHAPTER 1: INTRODUCTION.....	1
1.1. INTRODUCTION AND RESEARCH RATIONALE	1
1.2. RESEARCH QUESTIONS, AIMS AND OBJECTIVES	9
1.3. CLIMATIC SETTING	12
1.4. GEOLOGICAL SETTING	15
1.4.1. Tectonic setting and volcanic terrain	15
1.4.2. Sub-surface geology and hydrogeology	21
1.5. LAND SURFACE COVER: SOIL AND VEGETATION	26
1.6. VOLCANIC ACTIVITY	28
1.7. HAZARD ZONATION AND LAHAR MANAGEMENT	31
CHAPTER 2: A MULTI-METHOD APPROACH TO MONITORING LAHARS: FROM INTRA-FLOW VARIABILITY TO DECADAL GEOMORPHIC CHANGE.....	35
2.1. INTRODUCTION	35
2.2. MONITORING DECADAL GEOMORPHIC CHANGE IN THE BELHAM CATCHMENT	39
2.2.1. Catchment-change	39
2.2.2. Estimating tephra fall volume	42
2.2.2.1. Data availability	42
2.2.2.2. Valley-fills	42
2.2.2.3. Tephra fall	47
2.2.3. Belham River Valley change	48
2.2.3.1. Elevation	48
2.2.3.2. Lahar database	52
2.2.3.3. Rainfall data	55
2.3. IN-SITU INSTRUMENTATION TO MEASURE INTRA-FLOW LAHAR DYNAMICS	57
2.3.1. Existing volcano monitoring network	57
2.3.2. Development of a bespoke remote camera unit	58

2.3.2.1. Choice of site	58
2.3.2.2. Instrument set-up	60
2.3.3. Image processing for flow measurement	62
2.4. Additional measurements collected during 13th-14th October 2012 lahar	65
2.4.1. Event rainfall time series	66
2.4.2. Suspended sediment	73
2.4.3. Ground photographs and video	77
2.5. Sedimentology	78
2.5.1. Sediment logging	81
2.5.1.1. Log sites	81
2.5.1.2. Logging method	84
2.5.1.3. Sediment sampling	85
2.5.1.4. Architectural diagrams	86
2.5.2. Bed surface grain size and geomorphological mapping of the valley-floor at the camera site	86
CHAPTER 3: RESPONSE OF THE BELHAM CATCHMENT AND CHANNEL TO 18 YEARS OF VOLCANIC PERTURBATION.....	89
3.1. INTRODUCTION	89
3.2. MODIFICATIONS TO THE BELHAM CATCHMENT	91
3.2.1. Contributions of sediment by Farrell's Plain and Tyre's Ghaut- Dyer's River	93
3.2.2. Development of Gage's Valley Fan	104
3.3. TEPHRA FALL AND RUNOFF DYNAMICS	116
3.4. RAINFALL AND LAHAR RECORD	120
3.4.1. Daily rainfall and lahar occurrence	124
3.4.2. Lahar magnitude and antecedent, triggering and sustaining rainfall	127
3.5. IMPACTS OF LAHAR ACTIVITY ON THE BELHAM RIVER VALLEY	134
3.5.1. 1995- 2010	134
3.5.2. 2010- 2013	148
3.6. DISCUSSION	155
3.7. CONCLUSIONS	163
CHAPTER 4: CHARACTERISTICS OF MULTI-ORDER DISCHARGE FLUCTUATIONS OBSERVED IN LAHARS TRIGGERED BY TROPICAL STORM RAFAEL, 13-14TH OCTOBER 2012, AND IMPACTS ON SEDIMENT TRANSPORT.....	165
4.1. INTRODUCTION	165

4.2. LAHARS 2010 TO 2013	166
4.3. TROPICAL STORM RAFAEL	169
4.3.1. Rainfall	171
4.4. OBSERVATIONS 11TH -15TH OCTOBER 2012	172
4.4.1. Bed surface and flow prior to the onset of the lahar on 13th October 2012	174
4.4.1.1 Discussion	179
4.4.2. Rapidly varying unsteady flow during 13th-14th October 2012 interpreted from monitoring data	181
4.4.2.1. Bores	182
4.4.2.2. Water-surface-waves and flow unsteadiness	191
4.4.3. Waning flow	201
4.4.3.1. Bed surface change	202
4.5. THE IMPLICATIONS OF OBSERVATIONS BETWEEN 11TH AND 15TH OCTOBER 2012 ON OTHER LAHARS IN THE BELHAM RIVER VALLEY	203
4.6. CONCLUSIONS	205
CHAPTER 5: SEDIMENTARY STRUCTURES FORMED BY LAHARS IN THE BELHAM RIVER VALLEY.....	207
5.1. INTRODUCTION	207
5.2. ANTIDUNES	209
5.2.1. Formation and flow dynamics	209
5.2.2. Deposit characteristics	211
5.3. LOCATION OF LOGGED VERTICAL EXPOSURES IN THE DEPOSITIONAL RECORD	217
5.4. DEPOSIT DESCRIPTION	218
5.5. FACIES ASSOCIATIONS (FA)	229
5.5.1. FA1: Dipping sand and pebble beds with pumice clasts	229
5.5.2. FA2: Massive sand beds containing matrix-supported gravel lenses	235
5.5.3. FA3: Inter-bedded planar sands and pebbles	240
5.5.4. FA4: Dipping sand and pebble beds in planar and trough bedsets	243
5.5.5. FA5: Clast-supported gravel beds with lens patterns	247
5.6 OTHER STRUCTURES	251
5.7. DISCUSSION	252
5.7.1. Variations in structures interpreted as antidune origin	253
5.7.2. Preservation of structures interpreted as transitions between different upper flow regime bedforms during the same flow	254
5.7.3. Preservation of deposits from the 2012 flow	256

5.8 Conclusions	257
CHAPTER 6: DISCUSSION.....	261
6.1. IN-SITU MONITORING FOR LAHAR DETECTION AND SCIENTIFIC ANALYSIS	261
6.2. PRESERVATION OF FLOW VARIABILITY IN THE SEDIMENT RECORD	264
CHAPTER 7: CONCLUSIONS	273
APPENDIX (with digital material)	285
Appendix 1	286
Appendix 2	289
Appendix 3	310
Appendix 4	315
Appendix 5	322
Appendix 6	323
REFERENCES	325

List of Figures

- Figure 1.1** Global lahar incidence (green circles) and volcanic eruptions (red triangles) since 2000. Lahar prone volcanoes that have caused a large human impact (fatalities, permanent loss of home/livelihood and temporary evacuation) are labelled. Data compiled from GVP, 2014, Siebert *et al.*, 2010 and World Bank, 2014 see Appendix 1.1). 6
- Figure 1.2** (a) Location of Montserrat. Base map: GEBCO bathymetry data (GEBCO, 2014). (b) Location of the Belham Catchment (shown in green) within Montserrat (insert). Main map shows the Belham River Valley within the Belham Catchment. The topographic base map shows contours ascending from 0 m above sea level in 100 m intervals. Contours and drainage routes were calculated from the a merged DEM from 1999 (north of island) and 2010 (south of island), WGS84 20N orthometric heights. 10
- Figure 1.3** Storm track map for large-scale synoptic weather systems passing within 300 km of Montserrat between January 1995 and May 2014. Track data from NOAA (2014), redrawn in ESRI ArcGIS. Storm details (numbered) correspond to numbered tracks in the map. The storm date is the period during which a storm warning was issued for Montserrat. 14
- Figure 1.4** Regional tectonic context of the Lesser Antilles arc, reproduced from (Kenedi *et al.*, 2010; Cassidy *et al.*, 2012). Faults and extension directions described in (Feuillet *et al.*, 2002). Motion of the North American plate (NAM) and the South American plate (SAM) from DeMets *et al.* (2000) and Weber *et al.* (2001). Half arrows show the sinistral and dextral motion along the arc (Kenedi *et al.*, 2010). Base map: GEBCO bathymetry data (GEBCO, 2014). 17
- Figure 1.5** Map showing local tectonic structures offshore and onshore of Montserrat showing the Redonda Fault, Montserrat-Havers Fault, and the Bouillante-Montserrat Fault systems. Major active normal faults are indicated. Minor active normal faults are shown by a plain black line. Arrow size reflects the relative dominance of fault extension. Reproduced from Feuillet *et al.* (2010) and Cassidy *et al.* (2012). Base maps: GEBCO bathymetry data (GEBCO, 2014) and Montserrat merged Digital Elevation Model (DEM) from 1999 (north of island) and 2010 (south of the island). 18

- Figure 1.6** Map of Montserrat showing key locations and topographic features relevant to the study. Topographic base map: merged DEM from 1999 (north of island) and 2010 (south of the island), WGS84 20N orthometric heights. Drainage routes calculated from the topographic base map. Elevation highs calculated from the topographic base map and the observed dome height of SHV, 1088 m, after the 10th February 2010 collapse (Wadge *et al.*, 2014). The volcanic complexes are delineated into three zones (based on Harford *et al.*, 2002). The Belham Valley Catchment is shown. 19
- Figure 1.7** Map showing the tectonic and volcanological features in the area local to the Belham Valley catchment. Several surveys have contributed to the fault line map (EGS, 2010; Feuillet *et al.*, 2010; Ryan *et al.*, 2013) and it is noted that the surveys did not always agree. The main faults included: BVF, Richmond Hill Fault (RHF), Kinsale-St Patrick Fault (KSPF) and MHFS. Other faults are labelled arbitrarily. Local extension direction is shown (based on Feuillet *et al.*, 2010). The location of English's Crater, the Soufrière Hills domes and uplifted areas are reproduced from Harford *et al.* (2002). 100 m contour interval from 0 m at sea level. 22
- Figure 1.8** (a) Resistivity map at sea level (0 m a.s.l.). Black lines indicate fault zones. Reproduced from EGS (2010, p.36). Location of Hydrosource, 2004 survey shown by purple rectangle. (b) Location of Belham River Valley boreholes, MBV-P1, MBV-P2, MBV-T1 (red markers) and one of the ten CSAMT/microgravity survey lines (green). Base map: 1 m resolution shaded relief model (azimuth= 315, altitude= 45) of merged DEM from 1999 (north of island) and 2010 (south of island). (c) Example of CSAMT survey, line 0. Blue indicates areas of high resistivity. Survey line ranges from -130 m to 150 m and corresponds to the survey line marked in (b). 23
- Figure 1.9** 2D EQ resistivity transects from EGS (2010) survey. (a) Top transect corresponds to the blue line in (c). (b) Bottom transect corresponds to the purple line in (c). (c) The location of the Belham Catchment is shown by the red catchment outline. Key survey stations relevant to the Belham Catchment are indicated by numbered arrows in (a) and (b), corresponding to points in (c) 25
- Figure 1.10** Vegetation maps of Montserrat showing the distribution of different forest types before human inhabitation (left) and after 27

13 years of volcanic activity (right). The left map provides some indication of vegetation lost to volcanic inundation (orange, right), although coastal areas to the south west were densely populated prior to volcanic activity. Photographs correspond to dominant vegetation types on island. Maps reproduced from Young, 2008, p. 19 and 31. Source MANSAT Arnaud, Kew, June 2007

Figure 1.11	The main drainage routes from the Soufrière Hills Volcano, Montserrat. Topographic base map: 100 m contour from 0 m at sea level. Merged DEM from 1999 (north of island) and 2010 (south of the island), WGS84 20N orthometric heights. Drainage routes calculated from the topographic base map.	29
Figure 1.12	Montserrat Hazard Level System modified to include key locations in the Belham River Valley (yellow labels) and the location of the valley is labelled. (MVO, 2014)	33
Figure 2.1	Calculation of Pyroclastic Density Current (PDC) volumes in Tyres Ghaut using vertical aerial/satellite photographs.	44
Figure 2.2	Calculation of Pyroclastic Density Current (PDC) volumes in Tyres Ghaut using oblique photographs and including measurements of channel incision.	46
Figure 2.3	Post-processed GPS tracks from 2011-2013 surveys. The sea-level (-38 m) and top of Garibaldi Hill (162 m) are ellipsoid heights.	51
Figure 2.4	(a) Example of lahar 13/4/2010 (19:30 UTC onwards) on digital helicorder plot generated automatically by the MVO seismic network. (b) Example of lahar 13/4/2010 (19:30 UTC onwards) on spectrogram plot automatically generated by the MVO seismic network. Digital records were available from 1999.	53
Figure 2.5	Map showing the location of the monitoring camera installed in March 2012, weather stations and seismometers operational during the period of study, and rain gauges that were operational prior to the study but provided data for analysis of rainfall on lahar days. The Belham Catchment is shaded in green. The topographic base map shows contours ascending from 0 m above sea level in 100 m intervals. Contours and drainage routes were calculated from a merged DEM from 1999 (north of island) and 2010 (south of island).	56

Figure 2.6	(a) Photograph looking from north to south across the valley-floor at the camera site (March 2012). (b) Camera location 12 m above valley floor and set-up on pole. (c) Example of camera image of valley floor (annotated). Multiple scale bars are included in several images showing the change in scale between the foreground and background.	59
Figure 2.7	Field computer (components inside the peli-case)	61
Figure 2.8	Calculation of point: metre scaling law. Red circles show the location of measured boulders used to test Equation 2.2. Multiple scale bars are included in several images showing the change in scale between the foreground and background.	64
Figure 2.9	Rainfall rate calculated from 15-minute rainfall accumulation at the SGH AWS tipping-bucket rain gauge between 00:00:00 UTC on 13 th October 2012 to 00:00:00 UTC on 15 th October 2012. Error range shaded red is based on manufacturers guidance that instrument measurement is to within 4% accuracy (Davis Instruments, 2010).	67
Figure 2.10	(a) Wind speed at the SGH AWS tip bucket rain gauge between 00:00:00 UTC on 13 th October 2012 to 00:00:00 UTC on 14 th October 2012. Error range shaded red is based on manufacturers guidance that instrument measurement is to within 5% accuracy (Davis Instruments, 2010). (b) Rainfall (mm) measured by the SGH AWS tip bucket rain gauge every minute between 00:00:00 UTC on 13 th October 2012 to 00:00:00 UTC on 14 th October 2012 (blue). Adjusted rainfall (mm) using the (Kru) correction factor is shown in light-blue. Errors (not displayed) were 4% for rainfall (described in Figure 4.3). Adjusted rainfall error 11% equates from the manufacture's guidance for rain gauge and anemometer measurement accuracy (Davis Instruments, 2010), and the performance accuracy of (Yang et al., 1998)'s model, reported at 2% (Yang et al., 1995b).	69
Figure 2.11	Rainfall rate calculated from adjusted rainfall over 15-minute intervals between 00:00:00 UTC on 13 th October 2012 to 00:00:00 UTC on 14 th October 2012 (blue). See Figure 4.5 for adjusted rainfall error (red) description. Also shown, original rainfall rate (green) calculated from 15-minute rainfall accumulation at the SGH AWS tip bucket rain gauge between 00:00:00 UTC on 13 th October 2012 to 00:00:00 UTC on 14 th October 2012. See Figure 2.9 for rainfall error (green) description.	70

Figure 2.12	(a) Example of MFG radar image. Montserrat is located in the red box to the north-west. (b) Location of the Belham Catchment in Montserrat, on the radar image. Pixels were extracted from the radar image within (and inclusive) of the red catchment boundary	71
Figure 2.13	Rainfall rate calculated over 15 minute intervals from adjusted rainfall (black), the maximum value of the Catchment radar subsection (red). Error range shaded in grey, 11%.	72
Figure 2.14	[left] Location of commercial aggregate extraction during 2012 (shown in red). The Belham Catchment is shaded in green. The topographic base map shows contours ascending from 0 m above sea level in 100 m intervals. Contours and drainage routes were calculated from a merged DEM from 1999 (north of island) and 2010 (south of island). [right] Sketch map of the channel structure within the area of commercial aggregate extraction (October 2012).	74
Figure 2.15	Illustration for method of collecting a suspended sediment sample with a 500 ml bottle at Site B2 during the 13th-14th October 2012 lahar. The bottle was inserted (with lid on) to 0.3 m above the bed surface. The lid was removed and water (and sediment) filled the container until full as it was lifted at a uniform rate upwards for 0.2 m.	76
Figure 2.16	Lahar facies types, reproduced from Scott (1988, p.A19). igb = Inversely graded bedding	81
Figure 2.17	(A) Photomontage of 1918 jökulhlaup deposits in the area of Mýrdalssandur, to the south of the Mýrdalsjökull ice cap and Katla Volcanic System. (B) Line drawing highlighting the main architectural features of interest within the middle vertical section (unit 2) of the deposit. Figure reproduced from Figure 9 in Duller <i>et al.</i> (2009), p.949.	82
Figure 2.18	Location of logged exposures in the Belham River Valley. Line shows division between two areas of aggregate extraction in the valley, Area 1 was more intensively worked prior to November 2011, however when the volcanic hazard level was reduced at this time, commercial activities moved upstream to Area 2; extraction in Area 1 also continued. Base map: March 2011, Quickbird Image.	83
Figure 2.19	(a) Pole-aerial-photography (PAP) set-up. The pole was kept at a consistent angle using a waist pole mount, neck strap and clinometer. The camera (not shown in photograph) was secured	87

to a self-levelling camera mount. (b) Example photograph from PAP. Tape measure is shown within the image.

- Figure 3.1** (a) Change to surface extent of the Belham Catchment between 1995 and June 2010, in response to sediment deposition from multi-phases of volcanic activity. Catchment extent based on DEM analysis using Arc Hydro tools in Arc GIS software. Change in coastline between 1995 and 2010, from sediment mobilisation downstream by lahars is shown by grey shading. Contour intervals of 50 m displayed from 0 m at the coast; orthometric heights used. (b) Sub-basins within the catchment were defined using the June 2010 LiDAR DEM. These surface divisions represented drainage area contributing runoff to the Belham River Valley at different locations along the channel. 92
- Figure 3.2** The timing of volcanic inputs to the Belham Catchment. Tephra fall represents periods of repeat dome collapses and explosions resulting in multiple fall deposits (see Section 3.3) and single significant events. The record of events was compiled from Cole *et al.*, 1998, Young *et al.*, 1998, Cole *et al.*, 2002, Loughlin *et al.*, 2002, Druitt *et al.*, 2002a, Druitt *et al.*, 2002b, Norton *et al.*, 2002, Carn *et al.*, 2004, Herd *et al.*, 2005, Edmonds *et al.*, 2006, Barclay *et al.*, 2007, Wadge *et al.*, 2009, Alexander *et al.*, 2010, Komorowski *et al.*, 2010, MVO, 2010, Wadge *et al.*, 2014, Stinton *et al.*, 2014. While it does not represent a complete record of activity, it is complete based on available published observations. 94
- Figure 3.3** Chanel cross-sections of Tyres Ghaut and Dyers River. Apparent erosion to the pre-eruption bed surface may be in part representing the loss of vegetation; the pre-eruption DEM was not strictly bare ground, but included vegetation which was estimated to reach 18 m in height (see Table 2.3). 98-99
- Figure 3.4** Erosion to the valley sides exposing bedrock, 24th June 2006 satellite image 102
- Figure 3.5** (a) The pre-eruption hydrological drainage network is shown by blue lines on the three-dimensional topography (a sub-section of 2002 aerial imagery draped over the pre-eruption DEM). (b) The hydrological drainage network in February 1999 following Phase 1 volcanic activity, shown by blue lines on three dimensional topography (a sub-section of 2002 aerial imagery draped over the February 1999 DEM). The main areas of volcanic deposit are labelled. For (a) and (b), the red arrows show the direction of flow in the main channels. The Belham Catchment is delineated by the black line; the catchment 106

boundary was defined by DEM analysis using Hydro tools in ArcGIS. Note that only the upper section of the Belham Catchment near the Soufrière Hills volcano is included.

- Figure 3.6** Location of longitudinal profile (left) between the top of Gages fan (point B) and the Belham River Valley. The longitudinal profile (right) shows the change in topography due to volcanic sedimentation in Phase 1 (black to blue line) and Phases 2 to 5 (blue to red line). Changes in longitudinal profile as depressions in topography were infilled by sediment, hydrologically connected the Belham River Valley to the Gages Fan forming to the west of the Soufrière Hills volcano. Point A is the location of the base of Gages fan where vertical erosion occurred connecting Gages fan to the pre-existing drainage network near Lee’s village (see also Figure 3.7). Point C shows the location on the profile of the ridge line of the pre-eruption lower Gages valley (Photograph bottom right), which was infilled with sediment during Phase 1. Photograph (bottom right) from the British Geological Survey P536996, 01/01/1936 107
- Figure 3.7** (a) Gages Fan August 2002 (Photograph F.J. Froude), (b) Gages Fan, Satellite image 18th November 2007, (c) Looking downstream from Gages Fan to the Belham River Valley, February 2012, (d) Looking downstream from Gages fan to the Belham River Valley, February 2012 111
- Figure 3.8** (a) Location of the confluence of Lee’s village channel with the Belham River Valley. See Figure 3.5b for base map details. (b) Lahar deposition at the confluence with the Belham River Valley, September 2009. Photo courtesy Paul Cole. (c) Deposition from a small lahar on 23rd March 2011. Photo courtesy Henry Odbert. 115
- Figure 3.9** (a) Time series of monthly rainfall totals from DFID/MUL and MVO raingauges. The location of gauges is shown in Figure 2.5, and compilation of the time series data is discussed in Section 2.2.3.3. (b) The monthly rainfall totals derived from the CMAP data series are shown (black line), providing a regional scale measure of meteorological conditions. 121
- Figure 3.10** (a) The total number of category 2 and 3 lahars by month, between July 1995 and December 2013. (b) The average incidence of a lahar within a set month, based on category 2 and 3 lahars between July 1995 and December 2013. 124
- Figure 3.11** (a) Antecedent rainfall n days after Tephra fall. (b) Antecedent rainfall n days after PDC deposition in Tyres Ghaut. (c) Antecedent rainfall n days after PDC deposition on Gages fan. 130

- Figure 3.12** (a) Maximum 10-minute rainfall rate n days after Tephra fall. 131
 (b) Maximum 10-minute rainfall rate n days after PDC
 deposition in Tyres Ghaut. (c) Maximum 10-minute rainfall rate
 n days after PDC deposition on Gages fan.
- Figure 3.13** (a) Lower Belham River Valley pre-eruption, looking towards 135-
 SHV (courtesy Richard Herd). (b) Truck stuck in lahar deposits 137
 15th June 1996, situated in the Lower Belham Valley golf course
 (image still from video footage, used with permission from
 David Lea). (c) Hydraulic jump over Belham Bridge, 18th
 November 1998 (image still from video footage used with
 permission from David Lea). (d) Looking upstream from the
 Belham Bridge April 2000 (Photograph courtesy Jenni
 Barclay). (e) Looking upstream from the Belham Bridge May
 2003 (Photograph courtesy Jenni Barclay). (f) Truck stuck in
 lahar November 2005 (Photograph courtesy Jenni Barclay). (g)
 Looking cross-valley towards the north-west at the Belham
 Bridge crossing in May 2005. Boulder with red arrow is ~0.6 m
 long. Flow is from right to left (reproduced from Sušnik, 2009).
 (h) Looking upstream from B4 towards the Sappit River
 confluence on 30th May 2006. The main channel is 17 m wide
 (reproduced from Sušnik, 2009). (i) Looking upstream from 80
 m upstream of B3 at the orange house on south-side of valley
 on 23rd May 2006 shortly after large lahar (Photograph courtesy
 Jenni Barclay). (j) Looking upstream from 80 m upstream of B3
 at the orange house on south-side of valley in November 2006
 (Photograph courtesy Jenni Barclay). (k) Looking upstream
 (and across valley south- north) 100 m upstream of B5 on
 2/12/2007 bed surface (Photo courtesy MVO). (l) Buried house
 located on the south side of the valley at the Isles Bay crossing,
 November 2006 (Photo courtesy Jenni Barclay). (m) House
 shown in (l) on 7/8/2008. Pillars on the house suggest bed
 elevation has increased by ~ 1.5 m. (Photo courtesy MVO). (n)
 Looking south across channel at partially buried Orange house
 in December 2007 (see also i-j) (Photo courtesy Jenni Barclay).
 (o) Looking south across channel at partially buried Orange
 house in 30th October 2009 (Photo courtesy Emmy Aston).
- Figure 3.14** (a) Changes to the longitudinal profile of the Belham River 139
 Valley along the pre-eruption valley thalweg. The thalweg was
 defined using the River Bathymetry Toolkit in ESRI ArcGIS v.
 10.1. The pre-eruption DEM longitudinal profile contained a
 series of vertical peaks in elevation upstream of point B4.
 These are believed to represent the height of vegetation (<18 m)
 encompassed in the surface elevation, when the DEM was
 constructed from contours on the Montserrat (series E803-DOS

359, edition 6-DOS 1983) map. Topographic peaks in the June 2010 profile (bare earth) shown the occurrence of large boulders and terraces of PDC deposit. Note: the vertical scale is exaggerated by 1: 16. (b) The location of cross-channel profiles (see Figure 3.13)

- | | | |
|--------------------|-------------------------------------------------------------------------------------------------------------------------------------------------------------------------------------------------------------------------------------------------------------------------------------------------------------------------------------------------------------------------------------------------------------------------------------------------------------------------------------------------------------------------------------------------------------------------------------------------------------------------------------------------------------------------------------------------------------------------------------------------------------------------------------------------------------------------------------------------------------------------------------------------------------------------------------------------------------------------------------------------------------------------------------------------------------------------------------------------------------------------------------------------------------------------------------------------------------------------------------------------------------------------------------------------------------------------------------------------------------------------------------------------------------------------------------------------------------------------------------------------------------------------------------------------------------------------------------------------------------------------------------------------------------------------------------------------------------------------------|-------------|
| Figure 3.15 | Cross-section profiles of six transects across the Belham River Valley, locations shown in Figure 3.12b. Elevations are colour-coded to date; dates are included next to profiles. | 140-
141 |
| Figure 3.16 | Coastline change, Belham River Valley. Digitisation of coastline extent from aerial photographs and satellite imagery (see Section 2.3.2.1). Graph (bottom) shows the change in coastline with time, in relation to the pre-eruption shoreline. | 147 |
| Figure 3.17 | (a) Looking upstream at 120 m downstream of B6 (March 2011). (b) Looking upstream at 100 m downstream of B6 (March 2012). (c) Looking upstream at 250 m downstream of B6 (March 2013). (d) Vertical cracks in PDC deposit. Deposit surface is covered in pebble sized pumice (March 2013). (e) Lahar deposits on top of PDC terraces located on the south side of the Belham River Valley 300 m downstream of B6 (March 2013). (f) Looking upstream at Orange house near Belham Bridge (see also Figure 3.13o) in May 2010 (Photograph courtesy of MVO).(g) Looking upstream from ~10 m downstream of location photograph (f) was taken, in November 2010. Orange house has been buried. (Photograph courtesy of Mel Plail). (h) Looking upstream 180 m upstream of the location of (g), March 2011. (i) Looking upstream 190 m upstream of location of (g), March 2012. (j) Looking upstream 190 m upstream of the location of (g), March 2013. (k) The lower Belham River Valley, March 2011. Arrow shows common location of white house also in (l). (l) The lower Belham River Valley, May 2014. Arrow shows common location of white house also in (k; Photograph courtesy Dav Macfarlane). (m) Looking upstream 400 m upstream of B2, November 2010 (Photograph courtesy Mel Plail). (n) Looking from north-south across the same section of channel as shown in (m), position of photographer for (m) shown by arrow. Photograph shows the network of pits and boulder piles left by sand extraction in the Belham River valley, March 2013. (o) Boulders piled up having been excavated from the lahar deposits in the lower Belham (by Isles Bay crossing) in March 2011. Dan is shown for scale and is ~1.9 m tall. | 149-
151 |

Figure 3.18	Hypothetical hydrographs showing the impact of volcanic activity on catchment condition and runoff over different time scales, based on observations in the Belham Catchment and other published studies discussed throughout Chapter 3. Each hydrograph is explained in the proceeding text.	159
Figure 3.19	Model for channel response to volcanic sedimentation (adapted from Gran and Montgomery, 2005 and Manville et al., 2009)	162
Figure 4.1	Map of key monitoring locations in the Belham Catchment in the context of 13th-14th October 2012 lahar. Sites A, B1, B2 and C are shown.	167
Figure 4.2	Lahar record: 2010 to 2013. Lahar size was determined from ground observations, descriptions in MVO scientific reports and seismic records (Section 2.2.3.2)	168
Figure 4.3	Best track positions for Hurricane Rafael, 12-17 th October 2012. Track of the extratropical stage was mostly based on analyses from the NOAA Ocean Prediction Center. Track of the Tropical Storm and Hurricane stages were constructed from pressure and wind speed measurements. Reproduced from Avila (2013)	170
Figure 4.4	IR rainbow satellite image of the Western Atlantic captured by the GOES satellite on 13th October 2013 (NOAA, 2012). Montserrat is indicated by the black circle in the centre of the storm. The colour bar located at the bottom of the image indicates the intensity of outgoing long-wave radiation from low (purple) to high (red). Tropical Storm Rafael is delineated by the areas of high IR intensity, indicating a centre of thick cloud cover and associated storminess.	171
Figure 4.5	(a) Top: Rainfall rate calculated over 15 minute intervals from an adjusted rain gauge time series (Section 2.4.1) and the maximum pixel value from the Belham Catchment MFG radar image sub-section. (b) Middle: 1- minute real-time seismic amplitude (RSAM) from MBLY, MBGH and MBGB. (c) Bottom: Percentage of valley-floor width occupied by flow (red), passage of bores at Site A (grey bars) and camera (Site A) functionality.	173
Figure 4.6	(a) Image still from the camera at Site A captured before the onset of the lahar on 13/10/2012. (b) Geomorphological sketch map at Site A showing the location of the main bars within the valley –floor cross-section monitored by the camera. The red lines delimit the area of valley-floor captured by the camera in each photograph. The blue lines delimit the sub-section of the	175

image in which flow features were measured, see also Figure 4.10. The orange line shows the location of transect 1.

Figure 4.7	(a) Looking upstream 4 km from SHV. The bed surface in the image was deposited by lahars. (b) Looking cross-valley from north to south in the area of commercial sand extraction, 5.7 km from SHV. The photograph shows pits and boulder piles, as well as a network of temporary roads linking pits to the permanent road network. (c) Image still from video at Site C (Tina's House) at 20:48:00 UTC 12/10/2012. (d) Looking upstream from the same location as (b) at 16:10:00 UTC 13/10/2012 before the arrival of the first lahar front from the SHV sub-basin.	177- 178
Figure 4.8	Image stills from the camera at Site A. (a) Bore travelling downstream during the first peak in flow. (b) Bore travelling downstream during the second peak in flow.	183
Figure 4.9	(a) Waning flow of second seismic peak. (b) Flow during the second peak on 14/10/2012. (c) Bed surface after the 13 th -14 th October lahar.	185
Figure 4.10	Sketch of the main forces acting on a particle beneath a bore adapted from Khezir and Chanson (2012b).	188
Figure 4.11	Example of wave trains observed at different sites in the Belham Valley during the October 2012 lahar. (a) Wave trains 12:57:00 UTC 14/10/2012, Site B1. The three waves upstream in the train appear three-dimensional in form and two are breaking. (b) 18:42:53 UTC 14/10/2012, Site A. Wave trains were observed to form, grow and diminish in height, increase in wave number and migrate upstream during waning flow from the final flow peak.	192
Figure 4.12	Sub-section of image stills (from Site A) between 17:13:16 13/10/2012 to 17:13:24 13/10/2012 showing the migration of part of a train of water-surface-waves upstream. The wave in the centre of the photograph contains a boulder which is ejected upstream from the wave as it breaks, before rolling downstream with flow after wave breaking.	193
Figure 4.13	(a) Location of sampled waves within the camera field of view at Site A. Pixel measurements were converted to real-world coordinates based on the location of wave trains in group 1-4 and a scaling law derived from four known locations (red circles) in the image (see Section 2.5.3). The conversion was well-constrained for points between the two black dashed lines.	195

(b) Average wavelength of water-surface-waves within sampled wave trains. The different symbols differentiate the location of the sampled data within the valley-floor. The colour of each point represents the percentage of the wave train within the area well-constrained by the scaling law.

- Figure 4.14** (a) The average wavelengths of water-surface-waves present in images analysed every 15 minutes. See also Figure 4.13. (b) Mean flow velocity calculated from wave train wavelengths using Equation 4.4. 197
- Figure 4.15** Flow discharge calculated from velocity derived from water-surface wave trains, flow depth estimated from bed topography and channel width determined by the percentage width of channel occupied by flow. Measurements based on observations at Site A 199
- Figure 5.1** Diagram showing bedform formation, transition and migration direction based on increasing Froude number (Fr) and sediment size. Redrawn and adapted from Kennedy (1963) and Brakespear (2008). Stationary antidunes develop around $Fr=1$. 210
- Figure 5.2** Diagram illustrating the cyclic growth, migration and destruction of upstream migrating and breaking water-surface-waves (and antidunes). Redrawn and adapted from Duller et al. (2008). Top photograph shows an example of a water-surface-wave train before breaking, located at Site B1 during the October 2012 lahar (See Section 4.1). The spatial acceleration of flow across the bedform surface is shown by graphics at the top of each stage A-D. Areas of erosion and deposition corresponding with accelerating or decelerating flow are coloured (red= erosion and blue= deposition) in the water-bed-surface diagrams at each stage. The breaking wave may travel upstream by different amounts relative to the erosional trough of the antidune, depending on the position of the breaking wave in a wave train and the type of wave breaking (see Blair, 1999 and Cartigny et al., 2014). 212
- Figure 5.3** (a) Line drawing of flow parallel section of sedimentary structures of antidune origin deposited by supercritical flow in a laboratory flume (Alexander *et al.*, 2001; modified from Duller *et al.*, 2008). (b) Model for sedimentary structures generated by upstream migrating antidunes under aggrading conditions (Clifton, 1990; redrawn Brakespear, 2008). Type 1 laminae formed by upstream migration of the trough between antidunes. Type 2 laminae formed by sediment sorting on the upstream 213

side of the antidune.

Figure 5.4	[Left] Aerial photograph March 2012 of Pit2013 (red) showing location of Pit 2013 cross-cutting a main channel (full width of pit). [Right] Same location March 2013	218
Figure 5.5	(a) Sedimentary logs of two flow parallel sections in Pit2013 (see Figure 5.4 for location). Vertical scale, depth from the sediment surface in March 2013 and ellipsoid heights (UTM 20 N) are included in brackets. (b) Sedimentary logs of two flow parallel sections in Area 1 & 2 (see Figure 5.4 for location). Vertical scale, depth from sediment surface in March 2011 (2012_1 bed surface is February 2012) and ellipsoid heights (UTM 20N) are included in brackets. See (a) for Key	226- 228
Figure 5.6	Photograph at log site 2011_4 (see Figure 2.18). Deposit contains thick beds of Sm inter-bedded with Sl and Sh. The lower section of deposit also contains beds of Fsm. The deposit incorporates tree roots and boulders in the central upper portion.	230
Figure 5.7	Annotated photograph of deposit at 2013_2. Beneath line drawings of main sedimentary structures in the deposit.	234
Figure 5.8	Photograph of 2013_1, showing the position of FA2 within the vertical deposit. Beneath, architectural diagrams show the main structures within the deposit, discussed in Sections 5.6.2 and 5.6.3.	239
Figure 5.9	Example of FA3b within 2013_2. FA3b contained inter-beds of planar laminated sands (Sh), massive coarse sands and pebbles (Sm), sub-planar lenticular beds of massive sands and pebbles (Sm) and imbricated clast-supported pebbles in planar beds (Gh).	244
Figure 5.10	Structure in the upper unit of 2013_1 interpreted as a hydraulic jump deposit.	249
Figure 5.11	Location of Pit2013 in November 2010, looking towards 2013_2	257
Figure 5.12	Possible boundaries between lower (older deposits) and deposits from the 13 th -14 th October 2012 lahar.	259
Figure 6.1	(a) Specific sediment yield from the Belham Catchment between July 1995 and March 2013 (brown line). When this line is	270

horizontal no data is available between the start and end date of the line, and the specific sediment yield is an average value. Blue arrows highlight periods of net aggradation in the valley, red lines highlight periods of net degradation. In this case the specific sediment yield is negative representing only offshore sediment delivery. The black vertical arrows are large lahars (based on available data, grey horizontal dotted line indicates no data on large events). The horizontal grey arrows are the period during which deposition of volcanic material by PDCs was documented in the Belham Catchment (Section 3.2). (b) Specific sediment yield from the Belham Catchment between July 1995 and March 2013 based on changing sediment storage in the Belham River valley (brown line) and sediment removed from Tyres Ghaut (green line).

List of Tables

Table 1.1	Summary of some of the key events between July 1995 to March 2013, updated from Darnell (2010) after (http://www.mvo.ms/ ; Herd et al., 2005; Edmonds et al., 2006)	31
Table 1.2	Changes to the hazard level relevant to residents and users of the Belham River Valley. The hazard level was altered in response to dome extrusion and volcanic activity. This table focuses on the period from the beginning of Phase 5 to the end of the study period.	32
Table 2.1	Summary of methods used in each aspect of the study. Refer to Section 1.2 for research aims and objectives.	35- 37
Table 2.2	DEM data available that covers the entire Belham Catchment	39
Table 2.3	Imagery: archive data and data collected during this study	40
Table 2.4	Archive DEM data of the Belham River Valley	48
Table 2.5	GPS post-processing and surface generation for 2011-2013 DEMs	49
Table 2.6	Scoring system of lahar database entries	53
Table 2.7	Pole coordinates, elevations based on February 2012 bed surface	63
Table 2.8	The timing and location of ground observations (photographs and video) in the Belham River Valley, captured prior to, during and after Tropical Storm Rafael	77
Table 2.9	Facies classification for fluvial deposits, reproduced from Miall (1996). The capital letter indicates dominant grain size: G= gravel, S=sand, F= fine grained facies (includes very fine sand, silt and mud). The lower case letters serve as a mnemonic for characteristic texture or structure of the lithofacies.	79
Table 3.1	Volume estimates of primary material deposited in the Belham Catchment. It is noted that the date range used reflects the date of available data rather than the dates of intense surface activity. Volume errors were modelled using a Monte Carlo simulation for probability density function (mean= 0 m, standard deviation = 18 m, the height of vegetation included in the DEM surface model, Table 2.2) was used to generate an error surface which was added as ‘noise’ to the 1995 DEM. The same procedure was run for the 1999 DEM. The volume difference of the ‘noise’ added DEMs was calculated. This method was iterated over 100 runs. The volume difference calculated was compared to the ‘true’ surface volume	96- 97

calculation. The root mean square error (RMSE) was calculated from the volume differences of the 100 iterations. Methodology adapted from Darnell et al. (2010). Figure 3.2 shows the timing of sediment inputs to the system. Total change was calculated by direct subtraction of the 1/7/1995 DEM from the 1/6/2010 for each section of channel.

Table 3.2	Dates of significant PDCs onto Gages Fan and where available (published) volume estimates of primary material deposited.	109
Table 3.3	Tephra fall deposition, Phases 1, 2 and 5	118
Table 3.4	Lahar database summary statistics. The total number of lahars per month (between July 1995-December 2013) and by year, are shown (lahar counts). The mean column represents the average incidence of lahars by month (top) between July 1995- December 2013, providing an estimate on the typical number of lahars occurring during a set month. The standard deviation measures how much variation there is around this mean incidence value.	123
Table 3.5	Rainfall recorded on lahar days by rain gauges inside and outside of the Belham Catchment	126
Table 3.6	(a) Mean antecedent rainfall amount and rate before lahar onset. (b) Standard deviation of antecedent rainfall amount and rate before lahar onset	128
Table 3.7	Number of lahars by size that occurred within 24 hours to 60 days of deposition of primary volcanic material	132
Table 3.8	Volumes of sediment added or removed based on DEM differences. Volume errors were modelled using a Monte Carlo simulation for probability density function (mean= 0 m, standard deviation = variable) was used to generate an error surface which was added as ‘noise’ to each DEM. Standard deviations were used as follows: 1/7/1995= 5 m (unvegetated section of DEM, see Table 2.2), 1/3/2011, 1/2/2012= 0.4 m (GPS error + human error, see Table 2.5), 1/6/2010= 0.15 m (see Table 2.2.). A noise surface was added to each DEM. The volume difference of the ‘noise’ added DEMs were calculated. This method was iterated over 100 runs for each volume calculation (not all surface combinations were modelled). The volume difference calculated was compared to the ‘true’ surface volume calculation. Given that surfaces 1/2/2002-1/11/2007 and 1/3/2011-1/3/2013 were collected following the same methodology, modelling errors in the 1/2/2012 to 1/3/2011 volume calculation were considered representative of the errors expected for other volume calculations entailing GPS survey	144

surfaces. The root mean square error (RMSE) was calculated from the volume differences of the 100 iterations. Methodology adapted from Darnell et al. (2010).

Table 3.9	Net aggradation and degradation rates between survey periods	156
Table 5.1	Summary of sedimentary structures formed during flume experiments (Alexander <i>et al.</i> , 2001; Yokokawa <i>et al.</i> , 2010; Cartigny <i>et al.</i> , 2014) and interpreted as antidune origin. Observations of similar structures in field deposits are provided. All structures are described based on two-dimensional exposure parallel to palaeoflow direction unless otherwise stated. The table provides a useful reference point for interpretation of structures in architectural diagrams of lahar deposits (Section 2.5.1.4 and Section 5.5).	214- 216
Table 5.2	Descriptions of each facies (see Table 2.9) from field observations of deposits in May-June 2011, October 2012 and March 2013. Images of each facies have been included with a reference to the log location of the photograph. Sand grade facies include the grain size distribution of a sediment sample. The location of samples is shown on sediment logs in Figure 5.5. The x-axis of the grain size plot labels the upper boundary of each grain size division, where Cl denotes the boundary between clay and silt, Si denotes the boundary between silt and sand, S denotes the boundary between sand and pebbles, and Pb denotes the boundary between pebbles and cobble sized clasts.	220- 225

Acknowledgements:

Contributions, assistance and advice during the PhD

Firstly I would like to acknowledge the unwavering support of my supervisory team Professor Jenni Barclay and Professor Jan Alexander at the University of East Anglia, and Dr Paul Cole at Plymouth University (previously at the Montserrat Volcano Observatory, 2010-2012). I am lucky to have received scientific guidance from three enthusiastic academics working at the forefront of different but closely related disciplines within sedimentology and volcanology. They have advised the direction of the research and supported my desire to tackle what may be considered risky-research for a PhD; to observe and measure lahars to provide data for model validation and sedimentological interpretation. The frustrating lack of measurements of these flashy flows may result from wariness to invest time and money in developing site-specific monitoring equipment, particularly when a PhD project must be completed within 3-4 years in the UK. They have kept the faith during a period of equipment troubleshooting, provided support applying for equipment funding, and directed me to appropriate expertise to help develop successful remote-camera-based monitoring at the field site. Furthermore their constructive criticism and guidance throughout the PhD process has enabled me to complete this thesis within four years and acquire the skills necessary to continue in scientific research.

Secondly, I would like to acknowledge the funders of the research. (1) The Natural Environment Research Council (NERC) who provided the funding for the PhD, field visits and contributed to conferences. (2) The School of Environmental Sciences, UEA equipment fund who provided £2000 for the camera unit. (3) The IAVCEI2013, EGU2014 and ICFS2013 conference committees for providing fee waivers on conference attendance. (4) The British Sedimentological Research Group (BSRG) who provided field work funding to facilitate a site visit following the IAVCEI2013 conference to Mount Unzen and Sakurajima which broadened my experience of the lahar deposits and enabled me to visit some of the most extensively engineered lahar channels in the world.

Thirdly, I would like to thank the Montserrat Volcano Observatory (MVO) as an organisation for facilitating repeat field visits, providing accommodation for the first field campaign and desk space, as well as access to archival data. Many staff gave their

time to help the project succeed. Adam Stinton provided field support, carried out the 2013 aerial photograph survey and assisted in the set-up of the remote monitoring camera. Henry Odbert provided instruction on the operation of the differential GPS and advice on the camera installation. Paddy Smith provided guidance on seismic interpretation of lahars in the record and calculated the spectrograms from the seismic records, used to improve lahar identification. Karen Pascal provided GPS support from 2013. I would like to thank Pyiko Williams and Marlon Fergus for the installation of the camera unit and preparation of the field site. Drew Simpson and Richard Roberts for IT support to help enable connectivity between the field camera and the MVO.

I would like to acknowledge the contributions of David Blomfield and Alex Etchells at the University of East Anglia who installed circuitry in the camera-controller computer, and wrote the image capture code (and showed me how to edit it), respectively. I would also like to acknowledge Dav Macfarlane at the University of St Andrews and Richard Herd at the University of East Anglia for their advice on telemetry and camera set up.

Montserrat is often referred to as a science lab for volcanologists and as a consequence many studies have contributed to a vast archive of data. Specifically I would like to acknowledge the use of 2006 and 2007 digital elevation data (DEMs) produced by Amii Darnell during her PhD, 2005 DEM data collected by Janez Susnik during his PhD, and topographic surveys undertaken by Richard Herd in 2002 and 2003. Rainfall data collected by Jenni Barclay and others at the University of East Anglia during an ambitious NERC funded project considering rainfall incidence and volcanic activity.

Finally I would like to acknowledge the support of those helped me prepare equipment for field work (Richard Jacques) and accompanied me into the field (Lee Mitchell, Jonathan Stone, Sonja Melander and Pepper, the dog).

Acknowledgements: Family and friends

I believe it is important to not only acknowledge the direct contributions to the scientific study but also to recognise the support of family and friends. Undertaking doctoral research is demanding and often all-consuming. Maintaining a good support network is as crucial to a successful thesis as is good supervision.

Firstly, I would like to thank my parents who have supported me through all my ventures, encouraged me to challenge myself and ridden with me during the highs and lows of the last four years.

Secondly, I would like to thank my aunt for sharing her love of science fiction cinema and an arts perspective on post-apocalyptic drama and environmental documentary with me over the last few years. It has been refreshing to think outside the physical science box, particularly in the context of public perspective on disaster scenarios.

Thirdly, I would like to thank friends old and new for filling the last few years with adventure beyond the PhD. To Lee Mitchell, Rachel Jacques and Neill Mackay, thank you for knowing when to let me have that third glass of wine. To Johanna Scheidegger, Katie Preece, Mel Plail, Tom Read, Jennifer Weston, Anna Hicks, Jonathan Stone, Alex Poulidis and Kostas Lentas, thank you for filling the last few years with humour and cake both in and out of the office. To Sian Foch-Garrett who became a mummy during my time in Norwich and thus put perspective on any PhD challenge I encountered, I am in awe of your time management. Thanks go to all members of the Norwich Climbing and Mountaineering Club whose varied life experiences and mountain enthusiasm (unperturbed by the local Norfolk landscape) allowed me to keep one foot in the real-world.

Thank you, Francesca D’Cruz for your long term friendship, inspirational attitude and sound advice that has kept me rooted over the past few years. Thank you, Kate Goddard and Siobhan Whadcoat for your continuing friendship from one thesis to the next. Thank you, Sonja Melander for your enthusiasm and inspiring creative scientific thinking; and providing a roof (and dog) during two field seasons on Montserrat. To all friends made while on fieldwork, some remaining in paradise, some now back in the UK/ USA, thank you for filling my time on the 16 km long rock with such rich memories. Finally, to Maria Martinez De Alvaro, my comrade in arms during the thesis writing process, may we cross the finish line together.

Chapter 1:

Introduction

1.1. Introduction and research motivation

Flash floods are sudden onset subaerial phenomenon caused by excessive rainfall or sudden water release resulting in the rapid generation and propagation of a flood wave (Gourley *et al.*, 2013). Definitions vary between countries and contexts, and are based on timing, flood appearance and location (Gruntfest and Handmer, 2001; Gruntfest and Huber, 1991). Flash floods are hazardous because of extremely rapid rises in water level and velocity. The rapidly varying discharge and high peak velocities can result in high sediment transport rates. Critically, as the amount of sediment carried in the flow increases or its composition changes, the interactions between particles within the flow increase, generating internal resistance to *shear* deformation (Pierson, 2005). Historically, flows have been classified by the volumetric (or mass) ratio of sediment to water, whereby the transition from normal stream-flow to hyper-concentrated flow occurs at 0.2 (Bradley and McCutcheon, 1987; Costa, 1988) and the transition from hyper-concentrated flow to debris flow occurs at 0.6 (Costa, 1984; Pierson and Costa, 1987). The increase in sediment concentration alters flow behaviour and can exacerbate the impact of a flash flood. Other factors also control flow rheology including: sediment type, entrained air or other gas, bed roughness and velocity (Mulder and Alexander, 2001). Xu (1999) suggests that erosion rates in steep channels increase as normal stream-flow transitions into hyper-concentrated flow. Flows with higher sediment content may increase river bed aggradation at local decreases in channel gradient or increases in width (Pierson *et al.*, 1996). Excess pressures in the interstitial fluid

between coarse particles in highly concentrated flows (debris flows) increases flow mobility (Takahasi, 2014) and ability to selectively transport extremely large clasts (Vallance and Savage, 2000).

Debris flows have received significant attention in recent years because of destruction caused to inhabited mountainous regions such as the European Alps (e.g. Fuchs *et al.*, 2007; Comiti *et al.*, 2014). Over 7,000 articles have been published on the topic of debris flows since 1970, of which more than half were published in the last 10 years (based on those articles listed in the Web of Science database, 2014). Comparatively, the research output on the topic of flash floods and hyper-concentrated flows is low, 1628 and 359 publications listed, respectively, between 1970 and 2014. Issues surrounding the definition of hyper-concentrated flow have hindered research aimed at understanding processes determining flow behaviour (van Maren *et al.*, 2009a).

Beverage and Culbertson (1964) were the first to classify sediment-water flow processes into high, extreme, hyper-concentrated and mudflow categories. While coining the term hyper-concentrated flow and frequently used to define flow type, the sediment concentration boundaries appear to have been chosen arbitrarily, with the exception of the hyper-concentrated to mudflow (debris flow) boundary (Pierson and Costa, 1987). Caution should be given to uniform definitions based on sediment concentration alone for flows occurring in a variety of geographical environments, because flow rheology is governed by a number of factors including the grain size distribution of the solid phase and chemical properties of particles, as well as the sediment: water ratio. Critically, while hyper-concentrated flows are dominated by viscous fluid forces acting on channel boundaries, mud flows (debris flows) involve complex physical and electrochemical particle interactions, physical interactions between the sediment load and bed, and the sediment load and fluid (Pierson, 2005). Confusion over definition and terminology in the literature has been exacerbated by limited direct measurements of different flow types, and the use of alternative terms when classifying flows based on depositional landforms and facies; or the use of the same term for a slightly different spectrum of flow phenomenon (see Germain and Ouellet, 2013 for review). The term debris flood has been applied to sediment-water flows that maintain the characteristics of a Newtonian fluid and do not exhibit surging or pulsating behaviour (Aulitsky, 1980). Mud flood has also appeared as a synonymous term in literature (Gagoshidze, 1969; Committee on Methodologies for Predicting

Mudflow Areas, 1982). However neither terms are widely used in English-language publications (Pierson, 2005). In China, a hyper-concentrated flow is any flow possessing yield strength (Pierson and Costa, 1987); and debris flows are a special type of hyper-concentrated flow (Qian *et al.*, 1980; Wang *et al.*, 1983). The closeness of the terms debris flow and debris flood, applied to mean different flow processes, and discrepancies in the working definition of hyper-concentrated flow in different regions of the world is one element of confusion. Another is the use of a different set of terms to describe deposits from flows intermediate between water floods and debris flows; in alluvial fan literature the terms transitional flow and dilute debris flow are used for facies deposited by these types of sediment-laden flows. The two facies are differentiated by surface lobe morphology, depositional relief, deposit texture and stratification; dilute debris flow facies are matrix-rich, poorly sorted and absent of stratification, while transitional flow deposits are clast-supported with moderate sorting and some stratification (Wells and Harvey, 1987). Although some deposits are created by distinct processes, the transitory nature of flows in natural environments, and the reworking of deposited material within a single flash flood or by subsequent flows, means identification of flow type from field evidence may be ambiguous, and based on facies that do not directly correspond with flow classifications.

Turbulent sediment-laden flows are very complex not least because erosion and depositional processes are dependent on shifts in sediment concentration and composition (van Maren *et al.*, 2009a), which rapidly vary in time and space. Numerical modelling provides a tool by which to predict flow run-out, discharge and localised changes in channel capacity. Results are used by local planners when designing hazard maps or re-engineering channels to mitigate against flooding. The most recent developments in numerical modelling capture the effects of sediment density and bed deformation rate on flow, incorporating them into the physics of the model (Li, 2014). Models also account for spatial and temporal lags in sediment transport relative to flow conditions. Used in combination with a simple one-dimension empirical model to estimate flow run-out, more complex physically-based models are useful for assessing flow behaviour at critical locations (Manville *et al.*, 2009), such as channel sections in close proximity to settlement. However, three-dimensional codes remain limited in accurately modelling local behaviours such as shocks (shifts from supercritical to sub-critical), because models do not strictly abide by the laws of conservation (Li *et al.*, 2014), highlighting a need for continued research. Critically, models, whatever their complexity, are based on empirical parameters and boundary

conditions that need to be adjusted to each circumstance. Commonly, model application and development is limited by a lack of detailed, accurate and appropriate field data, primarily because of the limits of time and financial investment in site reconnaissance (Wainwright and Mulligan, 2005), but also because of the flashy nature of flows and safe access to active channels.

Sediment-laden flows are more likely to occur in catchments already prone to flash flooding (*e.g.* dryland environments), but are a particular problem in catchments that have recently been subject to an episodic mass wasting event or wide-spread change in surface runoff characteristics, for example earthquake induced landsliding, volcanic eruption, wildfire, timber harvest, dam release or mining (Rathburn *et al.*, 2013). People living within drainages from active volcanoes are particularly vulnerable, because of the prolonged, multi-hazard nature of volcanic eruptions. Sediment-laden fluvial flows are triggered directly by eruptive activity or by other processes occurring independently within the surrounding environment, and have the potential to travel hundreds of kilometres from the volcanic edifice (Pierson, 1998). They are most common on intermediate to felsic volcanoes, which develop steep flanks and an abundant supply of volcanoclastic material (Manville *et al.*, 2009).

Sediment-water flows are an important agent in the geomorphic evolution of volcanic edifices; eroding and transporting material from source to sink. Flows that entrain rock debris from a volcano are referred to in scientific literature by the Indonesian term, lahar. Given the high temperatures of recently emplaced volcanic rock, lahars may be hot or cold. While the term is well-used, the commonly cited definition provided by Smith and Fritz (1989) encompasses flow phenomenon ranging from hyper-concentrated flow to debris avalanche (Smith and Lowe, 1991), but notably excludes normal stream flow. This is a difficult working definition, considering the inter-disciplinarity of stakeholders involved in managing hazards associated with flows. As previously discussed, definitions of hyper-concentrated flow- of which there are several (Bradley and McCutcheon, 1987; Costa, 1988; Brush *et al.*, 1989; Julien, 1989; Rickenman, 1991; Xu, 1999a; Wan and Wang, 1994; Chien and Wan, 1998; van Maren *et al.*, 2009b), are based on an assessment of sediment concentration in the flow, however in reality obtaining accurate measurements of the sediment concentration of turbulent flows with high sediment calibre and flashy discharge is difficult (not least because of high equipment costs and potential equipment damage). Generally measurements are made using a non-direct method, such as seismic registration (*e.g.*

Doyle *et al.*, 2011), however sediment concentration is not the only factor controlling flow rheology and therefore a single value of this property is not a reliable means of classifying flows behaviour. Furthermore, although these set-ups are designed to be non-contact, the instrument must initially be calibrated to the site by direct sediment sampling of the flow; not only does this entail its own challenges but processing and interpretation of readings requires a high level of geophysical expertise. Recognising the challenges of measuring sediment concentration in active flows and the transitory nature of flow rheology, the definition of lahar used in this work includes all sub-aerial flows that mobilise volcanoclastic sediments and water.

Globally, lahars occurred at 58 of the 108 volcanoes that have erupted since 2000 (Figure 1.1); of these 71% are located in nations containing another lahar-prone active volcano, 45% are within 30 km of large (>100,000) population centres, 17% are within 30 km of populations of over 1 million people and 57% are located on islands (data compiled using GVP, 2014, Siebert *et al.*, 2010 and World Bank, 2014 see Appendix 1.1a). Historically, the loss of 23,080 people to a lahar triggered by crater glacier melt at Nevado del Ruiz on 13th November 1985, remains the most deadly lahar related disaster, and second deadliest volcanic disaster since 1900 (Naranjo *et al.*, 1986; Lowe *et al.*, 1986). Since 2000, only 7 deaths have been associated with lahars (4 at Manam, Papua New Guinea in 2007, 3 at Merapi, Indonesia (de Belizal *et al.*, 2013)), but it is estimated that 2.45×10^7 people were living within 30 km of active lahar-prone volcanoes (GVP, 2014, Appendix 1.1a). Developing island populations are particularly vulnerable to lahars because of inherent proximity to the volcano and complications of oversea evacuation (Auker *et al.*, 2013). Communities in the Philippines, Indonesia, Papua New Guinea, Comoros and Vanuatu fall into this category; GNI per capita ranges from US \$1210 to US \$4730 (World Bank, 2014). Indonesia and the Philippines face further challenges of protecting large populations (1.28×10^7 and 1.69×10^6 , respectively), resident around multiple active volcanoes entering new eruptive phases in short succession. As a densely populated, volcanic island nation Japan faces similar challenges, but has the economic capital (US \$46702.72 GDP; World Bank, 2014) to extensively engineer drainage routes at risk of lahars, dissipating the propagation of downstream energy and flow run out from inhabited areas (*e.g.* Sakurajima; International Sabo Centre, 2013). Where funds are limited, detailed, up-to-date hazard

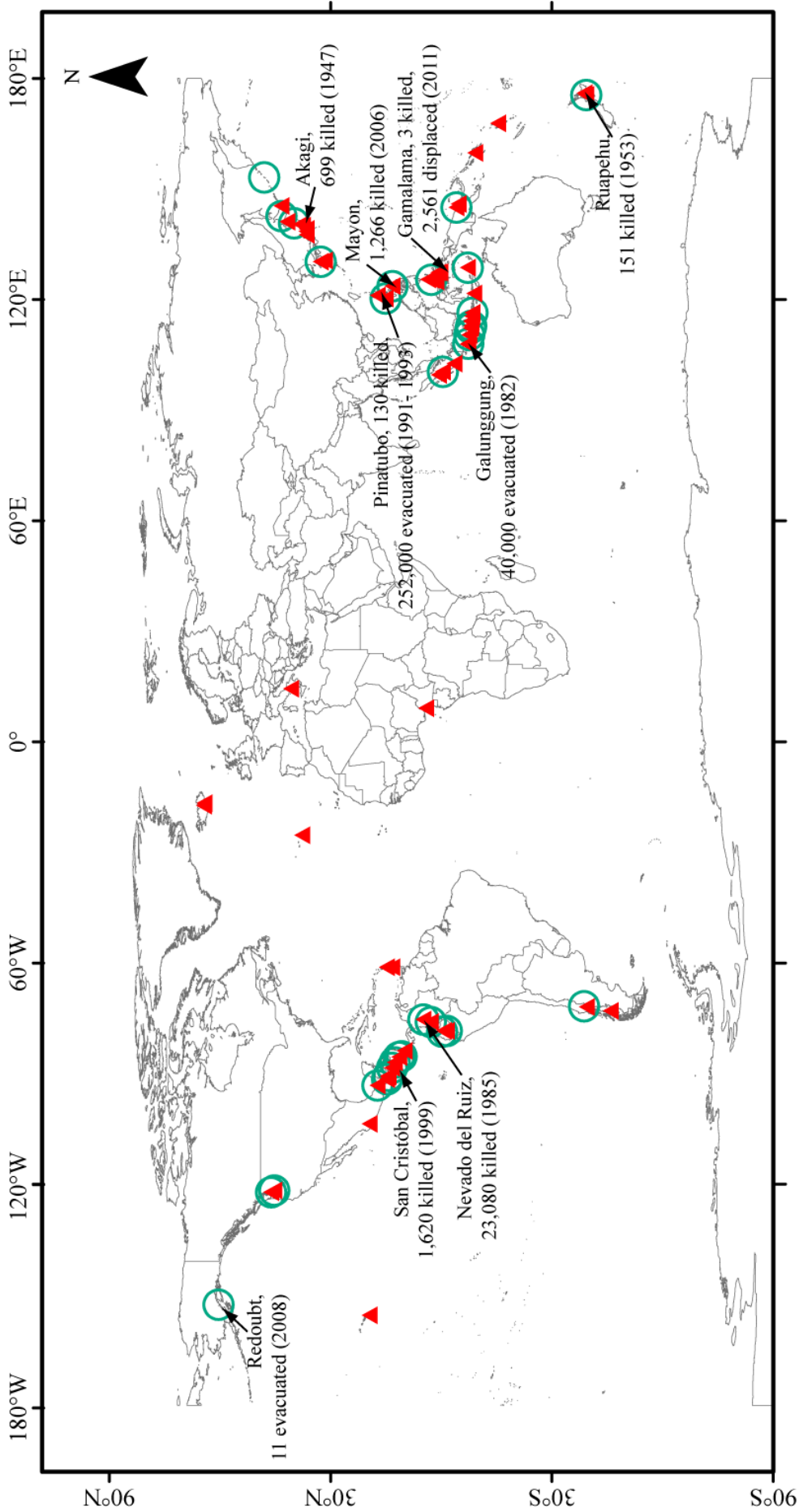


Figure 1.1 Global lahar incidence (green circles) and volcanic eruptions (red triangles) since 2000. Lahar prone volcanoes that have caused a large human impact (fatalities, permanent loss of home/livelihood and temporary evacuation) are labelled. Data compiled from GVP, 2014, Siebert *et al.*, 2010 and World Bank, 2014 see Appendix 1.1a).

maps and community driven monitoring of lahar onset have proven effective strategies in reducing fatalities (de Belizal *et al.*, 2013).

In active volcanic regions, the sedimentology of lahar deposits combined with available flow observations informs the choice of numerical models used to calculate lahar inundation risk maps (*e.g.* Cobenas *et al.*, 2012; Harpel *et al.*, 2013), and applied in the design and siting of engineering structures to retard flow (*e.g.* Nakatani *et al.*, 2008). Critically, field monitoring of lahars has focused on capturing the initiation conditions of flow (*e.g.* Merapi; Lavigne *et al.*, 2000) and downstream transitions in bulk flow dynamics (*e.g.* Semeru; Doyle *et al.*, 2011; Ruapehu; Lube *et al.*, 2012), but very few studies have directly linked inter-event observations of sediment-laden flow with depositional processes and sedimentary structures, in natural settings (Starheim *et al.*, 2013; Vazquez *et al.*, 2014). Lahar facies models have been developed from observations of deposits at Mount St Helens following the 1980 eruption (Harrison and Fritz, 1982; Scott, 1988) and provide a useful tool to describe the bulk characteristics of sedimentary units (*e.g.* Procter *et al.*, 2009), however internal architecture of sediments, particularly those deposited by turbulent normal stream-flows to hyper-concentrated flows are not well understood. Fundamentally it is difficult to recreate conditions in an experimental flume that replicate the dynamic, pulsatory nature of natural flows charged with mixtures of fine and coarse sediment. Only a small number of flume studies have provided observations relevant to lahar dynamics, such as sedimentary structures formed under supercritical flow (Alexander *et al.*, 2001; Yokokawa *et al.*, 2010; Cartigny *et al.*, 2014) and the effects of clays on bedforms in subcritical flow (Baas *et al.*, 2013). Relationships derived from experiments with the aim of reconstructing paleo-hydraulic conditions using structures in the sediment record (such as Kennedy's 1960; 1963 relationships for antidune wavelength and flow velocity and depth) should be employed with caution because they do not account for the dynamics of sediment transport in unsteady flow.

Interpretation of lahar deposits is particularly important at volcanoes showing signs of unrest with significant exposed populations and assets; for example Soufrière St Vincent (St Vincent and the Grenadines), Cuicocha (Ecuador) and Cerro Machin (Colombia) (STREVA, 2014). The preservation of tephra on steep slopes and in channels is low on lahar-prone volcanoes because of the rapid reworking of material by fluvial transport. Critically, the only evidence of an eruptive phase may reside in distal lahar deposits (*e.g.* the Kiwikiwi Formation at Mt. Ruapehu; Auer *et al.*, 2012), thereby

having significant implications on the reconstruction of eruption chronologies for volcanic risk assessment. Preservation of lahar deposits over long time scales in proximal and medial locations is considered low because of the overprinting and recycling of material by sequential flows (Manville *et al.*, 2009). In these locations historical lahar deposits may only be preserved as a series of terraces at the channel edge, with preferential preservation given to larger events with coarser deposits that are more resistant to erosion (Graettinger *et al.*, 2010). Reconstructing lahar dynamics from distal deposits is one of the key sedimentological challenges in translating deposit characteristics to hazard assessment. The second is delineating individual events within reworked deposits. Recent studies have focused on intra-event flow variability and the identification of individual rainfall triggered lahars in the sediment record (Starheim *et al.*, 2013; Vázquez *et al.*, 2014). Research has highlighted the complexities of reworking and overprinting on pre-existing sedimentary structures by sequential flows; highlighting the potential misinterpretation of deposits and parent flow. Providing a crucial link between sedimentologists, numerical modellers and hazard planners, this thesis focuses on monitoring cold lahars in medial-distal locations to improve sedimentological interpretation of deposits in the context of the long-term geomorphic evolution of a catchment perturbed by volcanic sedimentation.

1.2. Research Questions, Aims and Objectives

At the core of lahar research is the pressing need to undertake field monitoring of flows and sedimentological analysis of their associated deposits. Observations of this nature will enhance the scientific understanding of several key questions:

- (1) What is the character of the variation in flow and sediment transport within individual lahars?
- (2) What is the impact of a single lahar on the sediment record?
- (3) Are fluctuations during a flow preserved in the deposit?
- (4) Can deposits from individual lahars be delimited within an assemblage deposited by multiple events?
- (5) How does a catchment adjust to volcanic sedimentation over decadal time scales?

The Belham River Valley, Montserrat (Figure 1.2), located in the Lesser Antilles (Figure 1.4) provided a natural laboratory in which to investigate these questions. The Soufrière Hills volcano (SHV) in the south of the island remains active after five phases of activity between 1995 and May 2014 (Wadge *et al.*, 2014). Rainfall triggered lahars have occurred regularly in recent years because of high sedimentation rates around the volcano and the wet tropical climate; the island receives an average *c.*1000 mm of rainfall per year, from short duration high intensity events (Barclay *et al.*, 2007). The Belham Catchment, located to the west of SHV is relatively small (15.3 km², Figure 1.2 and 1.6), accessible and extensively covered by the established volcano monitoring network (and can be seen from the Montserrat Volcano Observatory (MVO)). The Belham River Valley has been the focus of previous lahar research (Barclay *et al.*, 2007; Sušnik, 2009; Alexander *et al.*, 2010; Darnell, 2010; Darnell *et al.*, 2012; 2013). Some of these studies focused on the lahar deposits in this location and results suggested that flows were typically normal *streamflow* to hyperconcentrated; there was very little evidence for debris flow behaviour (Barclay *et al.*, 2007; Sušnik, 2009). During the period of recent quiescence, lahars in the Belham River Valley have been the main volcanic hazard posed to occupants (residents, workers and visitors) in day-time access and permanently open hazard zones (see Section 1.7). While addressing wider scientific questions, research at this site comes at a time of heightened local interest in lahars and provides useful data for the future management of sediment in the valley.

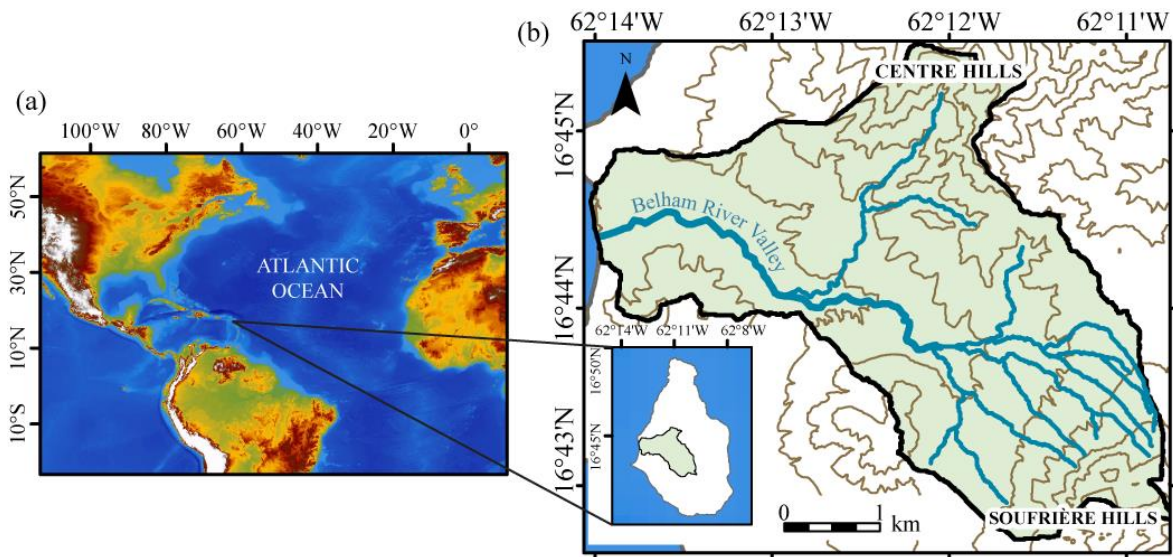


Figure 1.2 (a) Location of Montserrat. Base map: GEBCO bathymetry data (GEBCO, 2014). (b) Location of the Belham Catchment (shown in green) within Montserrat (insert). Main map shows the Belham River Valley within the Belham Catchment. The topographic base map shows contours ascending from 0 m above sea level in 100 m intervals. Contours and drainage routes were calculated from the a merged DEM from 1999 (north of island) and 2010 (south of island), WGS84 20N orthometric heights.

This study aimed to:

- (1) Investigate the possibilities of deploying automatic monitoring equipment in the Belham River Valley, that could generate data on the nature of flow and sediment transport in lahars
- (2) Improve the understanding inter-flow variability and sediment transport during a lahar in the Belham River Valley
- (3) Identify sedimentary structures formed by rapidly varying, unsteady sediment-laden flows in natural environments and consider how they can be used for interpretation
- (4) Investigate valley and catchment adjustment to volcanic sedimentation that may be used in the development of a model for other systems perturbed by multiple phases of eruption

These aims were addressed by the following objectives.

- (1) Identify and obtain the equipment that may be used to monitor a channel section in the Belham River Valley at an unmanned site.
- (2) Install a permanent remote camera to monitor a channel section of the Belham River Valley and measure and document the channel section to maximise value of camera imagery.
- (3) Record at least one lahar and combine the output with other direct observations (*e.g.* eye witness, photographs) from other sections of channel during the same event.
- (4) Compare direct observations of flow variability with other data from the volcano monitoring network (particularly rainfall, seismics)
- (5) Examine deposits and bed surface changes within the channel at the site of the camera and at other sites up and downstream of the site before and after lahars.
- (6) Compare deposits from the observed event(s) with deposits from lahars since 2010, and previous studies (Barclay *et al.*, 2007; Sušnik 2009; Alexander *et al.*, 2010)
- (7) Construct a database of lahar occurrence in the Belham River Valley since the onset of activity in 1995
- (8) Undertake an annual Kinematic GPS survey to capture topographic changes to the Belham River Valley during the study period and synthesise new data with an archive of surveys, photographs and observations to quantify valley and catchment adjustment to volcanic sedimentation
- (9) Use archive photographs, topographic data and published observations of volcanic activity at the Soufrière Hills volcano to quantify transfers of sediment between sediment storage in the Belham Catchment between 1995 and 2013.

Methodologies associated with the collection and processing of all datasets used in this study are discussed in Chapter 2. Chapter 3 brings together 19 years of archive data including volcanic sediment inputs, transfers between sediment storages in the Belham Catchment, rainfall and lahar records, and presents a model for Belham River Valley adjustment in response to volcanic sedimentation. The chapter provides useful context for subsequent analysis and discussion of specific lahars observed during the study period. Chapter 4 presents observations and measurements of a large lahar on 13th-14th October 2012 that was captured by the monitoring camera (developed during this study), providing detailed discussion on intra-flow variability. Chapter 5 discusses

the sedimentary structures preserved in the sediment record in the context of flow observations (Chapter 4). Chapter 6 discusses results from Chapters 3-5 and Chapter 7 details the conclusions of this research and recommendations for further work.

Globally the transfer of sediment from source to sink is characterised by the complex interplay of climatic and tectonic controls on: land surface denudation, fluid availability and the morphology of the cascade, operating over geological timescales. These three fundamental ingredients dictate the connectivity and nature of sediment transport within a system, placing it on a spectrum between two end member erosional regimes: *transport-limited* and *weathering-limited* (Gilbert, 1877). Volcanic activity alters the position of local sediment-cascades within this spectrum by perturbing the water and sediment flux (Major *et al.*, 2000). Post-eruption sediment yields on an annual- to decadal- scale are amongst the highest measured in mountain rivers (Korup, 2012), but the long-term ($> 10^2$ year) adjustment to drainages of voluminous eruptions is poorly constrained (Thouret, 1999). The following sections provide a useful climatic, geological and land cover context relevant to discussion of results in later chapters, as well as outlining volcanic activity and the lahar hazard.

1.3. Climatic setting

Montserrat has an equatorial, fully-humid climate (Kottek *et al.*, 2006), located at the northern edge of the Inter-tropical Convergence Zone (ITCZ). In common with ~675 active or potentially active volcanoes in the world (Simkin and Siebert, 1994; Pareschi, 1996), Montserrat's location in the Tropics means it is prone to high intensity precipitation from localised and convective storms, and less frequent large-scale synoptic tropical weather systems such as hurricanes (Gray, 1979; Matthews *et al.*, 2002). Rainfall is seasonal and the wet season is from April to November (Oppel *et al.*, 2013), with a peak in rainfall amount in May, and a second larger peak centred on September (Barclay *et al.*, 2006). The peaks in rainfall are caused by migration of the ITCZ, north during northern summer and south during northern winter (Taylor *et al.*, 2002). Most of the drainages on Montserrat are ephemeral and streamflow only occurs during, and for short periods after rainfall (Alexander *et al.*, 2010). Long duration (several days), high rainfall intensity storms (500+ mm of rainfall may fall in a single event at intensities of 50 mm hr^{-1}), can trigger flash flooding if runoff exceeds channel capacity. Hurricane Earl (category 3) triggered widespread flash flooding around drainages on Montserrat in August 2010. Flood waters carrying large metre-diameter

boulders caused damage to key bridges on the road network connecting the north and south of the island; in addition several landslips occurred (Montserrat Reporter, 2010).

Between 1995 and May 2014, twenty large-scale synoptic tropical weather systems ranging from tropical storm to category 4 hurricane strength, were documented passing within 300 km of Montserrat. Data collated from the NOAA National Hurricane Center (2014) is displayed in Figure 1.3, and shows the storm tracks of these events and their relative magnitudes. Forming from a hydrodynamic instability of the low-level easterly jet over Africa (Throncroft and Hoskins, 1994), these low-pressure systems travel eastwards with the easterly trade wind flow (Reed *et al.*, 1977), developing a coherent cyclonic circulation and a region of deep convective clouds and rainfall (Barclay *et al.*, 2006). The majority of events were registered as tropical storms with sustained wind speeds under 74 mph, resulting in typically minor localised damage to roofs and cable infrastructure. Comparatively, Hurricane Hugo, a category 4 storm caused widespread devastation on Montserrat when it passed directly over the island on 17th September 1989. Eleven people were killed, 45% of all dwelling units were totally destroyed and an additional 40% sustained serious damage; furthermore all government buildings and schools were partially or totally destroyed (Berke and Wenger, 1991). Total damage was estimated to be in excess of US\$366 million, and highlights the potential destruction from weather systems in the region, that also exacerbate efforts to manage other natural hazards, such as volcanic activity.

Storm magnitude is classified by sustained wind speed (NOAA, 2014) therefore the amount of rainfall deposited does not necessarily reflect the category of storm. Furthermore, some hurricanes are very large in diameter, containing mesoscale structures within the large-scale convection, such as cloud bands and squall lines tens of kilometres long, resulting in localised bursts of high intensity rainfall several hundred kilometres from the centre of the storm. Hurricane Floyd (category 1) tracked ~450 km to the north-east of Montserrat on 10th-11th September 1999 but rainfall was intense enough to trigger flash flooding (Montserrat Reporter, 1999). High intensity, sustained rainfall is not limited to classified tropical storms or hurricanes. Matthews *et al.* (2002) discussed two “extreme” rainfall events, the first on 20th March 2000 and the second on 29th July 2001, that corresponded with the timing of lava dome collapse and pyroclastic flow generation at the Soufrière Hills volcano. The former event was a short-lived, highly localised convective weather system (78 mm rainfall measured), while the latter was a synoptic-scale easterly wave weather system (86 mm rainfall measured).

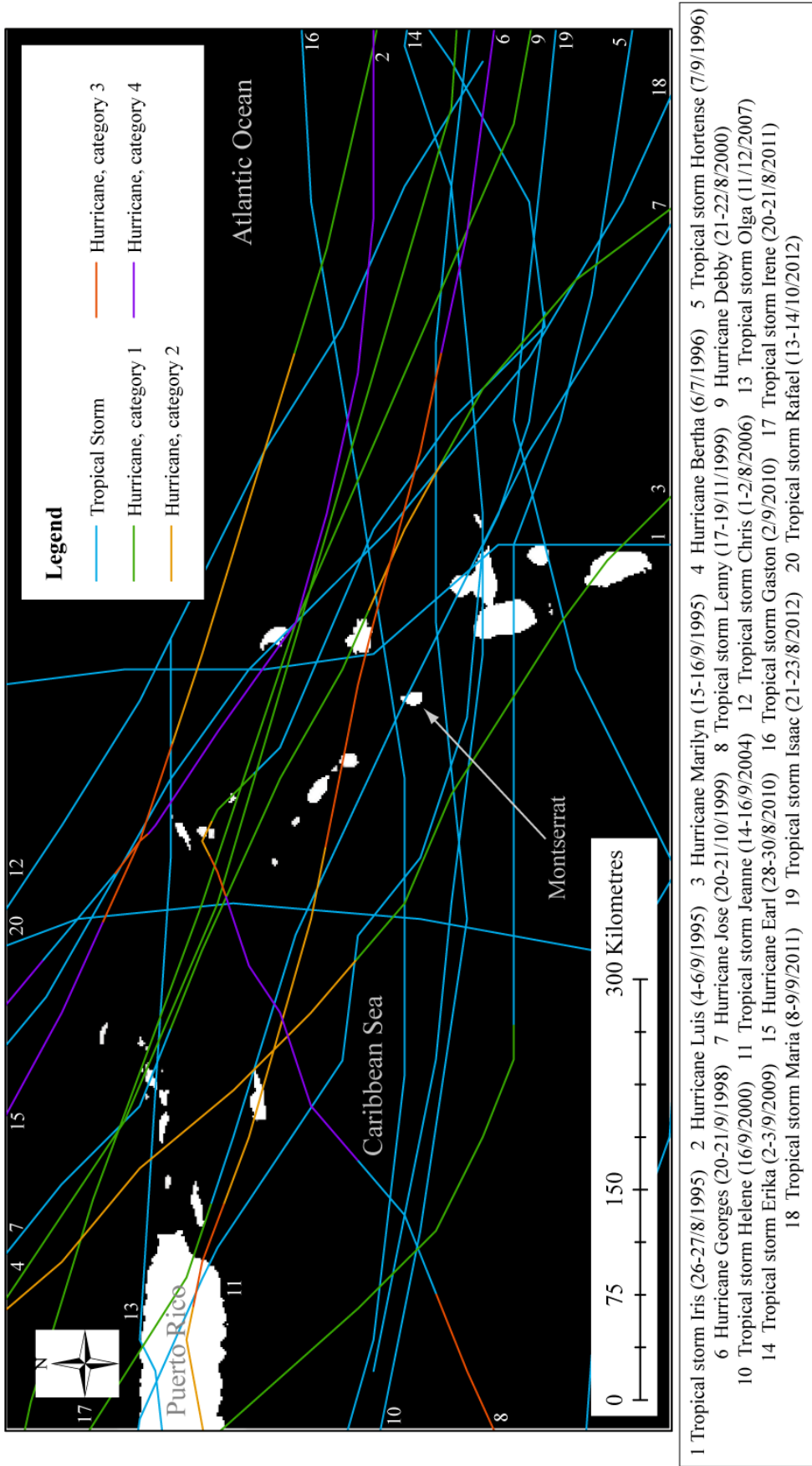


Figure 1.3 Storm track map for large-scale synoptic weather systems passing within 300 km of Montserrat between January 1995 and May 2014. Track data from NOAA (2014), redrawn in ESRI ArcGIS. Storm details (numbered) correspond to numbered tracks in the map. The storm date is the period during which a storm warning was issued for Montserrat.

Individual cumulonimbus cells and mesoscale convective complexes form rapidly, and generate very localised rainfall (<100 km across). Barclay *et al.* (2006) highlighted the influence of Montserrat's steep mountainous volcanic topography on air flow, which is forced to rise over terrain, resulting in adiabatic cooling, saturation and the formation of cloud droplets and rainfall. Analysis of rainfall measurements within their study, suggests that mountain tops on island receive 60% more rainfall than coastal regions, and the nature of terrain means there is considerable spatial variation in rainfall intensity during a single rainfall event.

Assessments by the IPCC (2013) indicate that it is unlikely that annual numbers of tropical storms, hurricanes and major hurricane counts have increased over the past 100 years in the North Atlantic, however evidence suggests a virtually certain increase in the frequency and intensity of the strongest tropical cyclones between 1970s and 2013. The precise causes of this are uncertain (Knutson *et al.*, 2010), however there is medium confidence that a reduction in aerosol forcing over the North Atlantic increased tropical cyclone incidence towards the end of the twentieth century (Dunstone *et al.*, 2013). Modelling results project a reduction in future mean precipitation but an increase in extreme precipitation from tropical cyclones in the Caribbean region; presently these projections are given a low confidence due to large errors in model simulations and the limitations of archive 100 year storm records from which future trends are projected (IPCC, 2013). Critically, projected increases in storm frequency, combined with recent trends of increasing storm intensity in the region, suggest future increases in flash flooding on Montserrat.

1.4. Geological setting

1.4.1. Tectonic setting and volcanic terrain

The Lesser Antilles arc (Figure 1.4) is formed from the subduction of the American plates beneath the Caribbean plate (Feuillet *et al.*, 2001) initiating arc volcanism ~40 Ma (Briden *et al.*, 1979; Bouysse *et al.*, 1984). The arc is split into two chains of islands, north of Martinique. Montserrat is located on the younger western chain, which developed when subduction orientation shifted during the Mid-Miocene, creating a new active volcanic arc (Bouysse *et al.*, 1984; Cassidy *et al.*, 2012). Macdonald *et al.* (2000) provide a useful review of arc magmatism in the Lesser Antilles, and a number of subsequent studies have focused on crust composition and deep structure (Christeson *et al.*, 2008; Kopp *et al.*, 2011), regional heat flow (Manga *et*

al., 2012), convergence geometry and rates (Jackson *et al.*, 2013) and the inter-regional contrasts between sedimentation processes (Picard *et al.*, 2006). The unusually wide range of magma types formed along the Lesser Antilles arc (Brown *et al.*, 1977) have also prompted a vast array of studies investigating local magma composition, using geochemical, petrological and textural analysis to better understand local drivers of volcanic eruption (Barclay *et al.*, 2010).

Recent work by the CALIPSO and SEA-CALIPSO projects (Voight *et al.*, 2010) have better constrained the tectonic context of Montserrat within the Lesser Antilles and provided more insight into the deep structure of magmatic systems on the island. Feuillet *et al.* (2010) discuss the geometries of active faults around Montserrat. Figures 1.4 and 1.5 shows that Montserrat is situated in a trans-tensional environment within a regional scale ~N-S extensional setting (Feuillet *et al.*, 2010; Kenedi *et al.*, 2010; Feuillet *et al.*, 2011). The island is composed entirely of volcanic rock produced by three volcanic centres: the Silver Hills (SH), 2.6-1.2 Ma, Centre Hills (CH), 950-550 ka and South-Soufrière Hills (SSH)- Soufrière Hills (SHV) complex (174 ka to present; Harford *et al.*, 2002). Southerly migration of volcanism with geological time is thought to reflect the westward migration of the volcanic front of the Lesser Antilles arc, at an average rate of 1 km Ma⁻¹, based on ⁴⁰Ar-³⁹Ar geochronology by Wadge (1986) relative to a single stationary mantle melting anomaly (Harford *et al.*, 2002). Over the last few million years, Montserrat has progressively grown as composite volcanoes and domes coalesce (Jackson *et al.*, 2013) (Figure 1.5); several islands in the Lesser Antilles developed from temporal volcanic migration; Basse-Terre is another example (Lahitte *et al.*, 2012). The volcanic centres define three massifs (Figure 1.6) with four topographic highs of 403 m, 741 m and 1088 m a.s.l., for SH, CH and SHV-SSH, respectively. The SH and CH massifs are predominantly andesitic, whilst the SHV and SSH massifs comprise basalts and basaltic andesites (Harford *et al.*, 2002). Inclusions of mafic lavas within the andesite are found in the SH, CH and SHV (Rea *et al.*, 1974; Zellmer *et al.*, 2003). The morphology of each massif derives from the accumulation of dome remnants and eruptive products (Block-and-ash flows (BAFs), lahars, debris-avalanches and tephra-fall; Harford *et al.*, 2002). Erosional maturity of the massifs decreases with age from north to south (Harford *et al.*, 2002; Lefriant *et al.*, 2004). Differential erosion on each massif expresses sub-surface structural discontinuities and complex local differences in lithology, surface morphology and exposure (including vegetation, aspect and elevation). Recent work by (Hautmann *et al.*, 2013), questioned previous surveys by Chiodini *et al.* (1996) and Hautmann *et al.* (2010) who attributed enhanced erosion

of the deepest valleys on Montserrat (Soldier Ghaut and Bottomless Ghaut in the Centre Hills) to a NW-SE trending fault zone located at shallow depths beneath CH. Results from the Hautmann *et al.* (2013) gravity survey do not discount the fault zone hypothesis but also entertain the possibility that enhanced erosion is driven by a structural discontinuity between high-density andesitic lava bodies and low-density flank deposits.

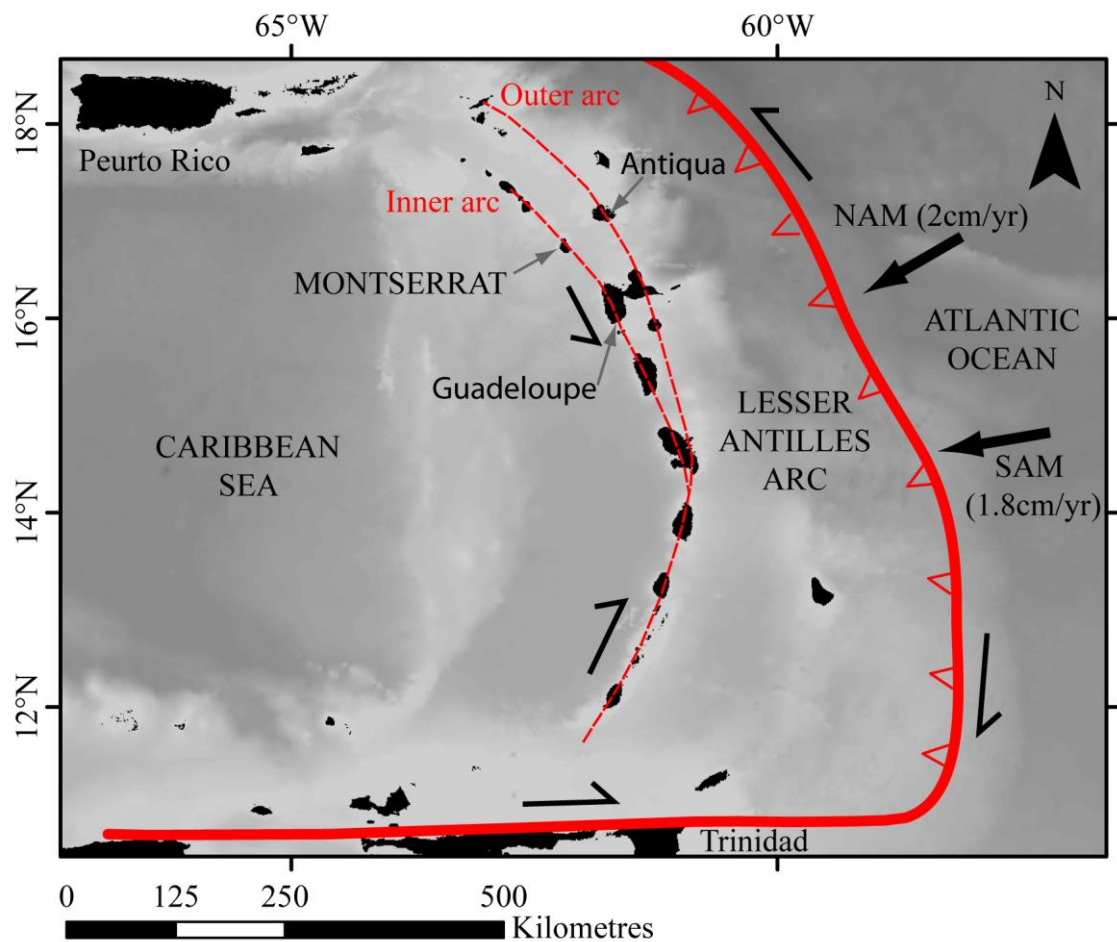


Figure 1.4 Regional tectonic context of the Lesser Antilles arc, reproduced from (Kenedi *et al.*, 2010; Cassidy *et al.*, 2012). Faults and extension directions described in (Feuillet *et al.*, 2002). Motion of the North American plate (NAM) and the South American plate (SAM) from DeMets *et al.* (2000) and Weber *et al.* (2001). Half arrows show the sinistral and dextral motion along the arc (Kenedi *et al.*, 2010). Base map: GEBCO bathymetry data (GEBCO, 2014).

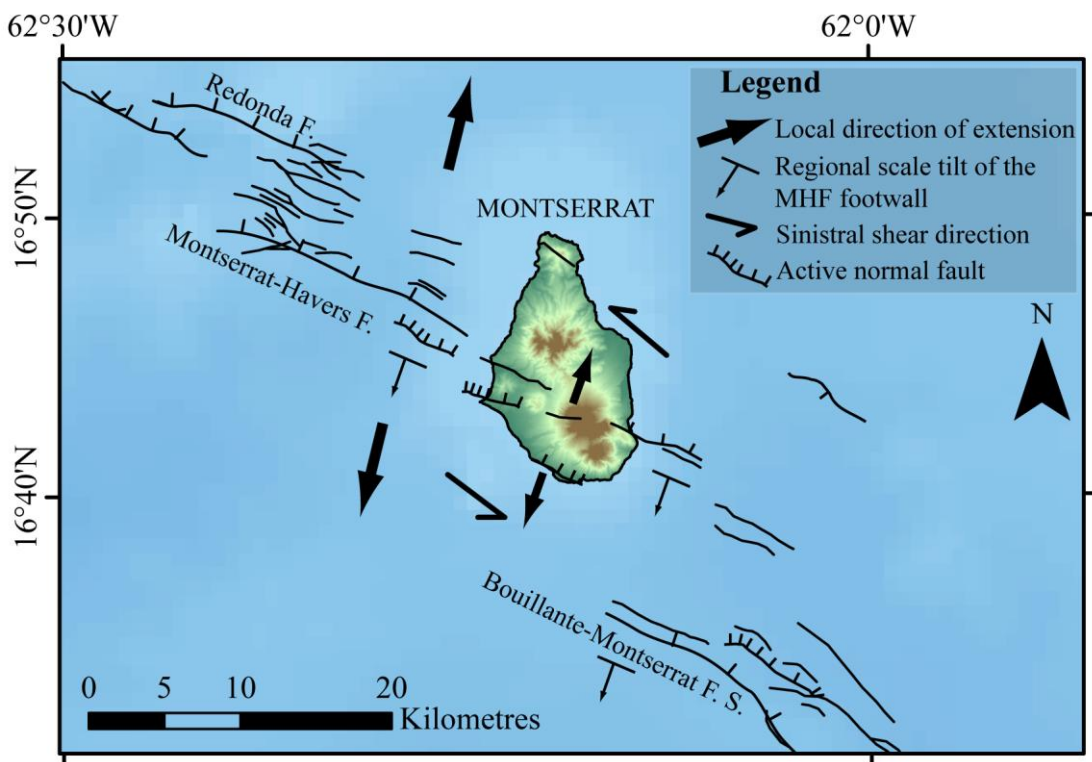


Figure 1.5 Map showing local tectonic structures offshore and onshore of Montserrat showing the Redonda Fault, Montserrat-Havers Fault, and the Bouillante-Montserrat Fault systems. Major active normal faults are indicated. Minor active normal faults are shown by a plain black line. Arrow size reflects the relative dominance of fault extension. Reproduced from Feuillet *et al.* (2010) and Cassidy *et al.* (2012). Base maps: GEBCO bathymetry data (GEBCO, 2014) and Montserrat merged Digital Elevation Model (DEM) from 1999 (north of island) and 2010 (south of the island).

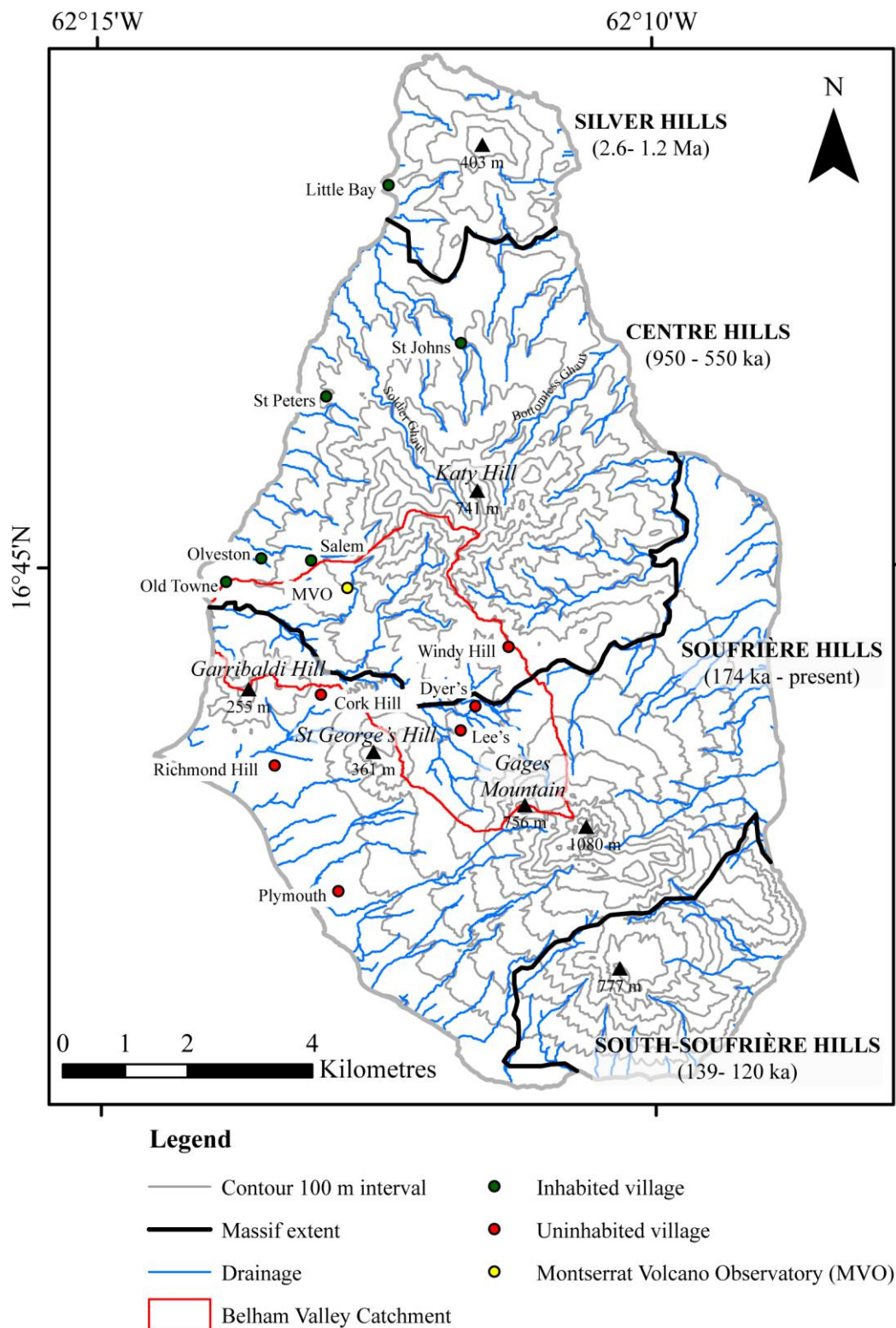


Figure 1.6 Map of Montserrat showing key locations and topographic features relevant to the study. Topographic base map: merged DEM from 1999 (north of island) and 2010 (south of the island), WGS84 20N orthometric heights. Drainage routes calculated from the topographic base map. Elevation were calculated from the topographic base map and the observed dome height of SHV, 1088 m, after the 10th February 2010 collapse (Wadge *et al.*, 2014). The volcanic complexes are delineated into three zones (based on Harford *et al.*, 2002). The Belham Valley Catchment is shown.

A drainage system of steeply-eroded channels (known locally as ghauts) and ridges, radiate from the topographic high of each massif towards the coastline (Figure 1.6; Barclay *et al.*, 2007). This study focuses on the Belham Catchment in the south of Montserrat (Figure 1.6), located predominantly on the flanks of the active SHV with additional drainage input from the Centre Hills. Tectonically, the south of the island is dominated by the Belham Valley Fault (BVF), which is a WNW-trending, NNE-dipping normal fault that extends off-shore (Kenedi *et al.*, 2010). The BVF is part of the Montserrat-Havers Fault System (MHFS), in turn part of a large scale right-stepping en-echelon structure of normal faults (MHFS, Redonda Fault System (RFS) and Bouillante-Montserrat Fault System (BMF) that accommodates left lateral shear from the regional N-S extensional environment (Figure 1.5, Feuillet *et al.*, 2002; Feuillet *et al.*, 2010; Kenedi, 2010; Kenedi *et al.*, 2010). Deformation of the BVF footwall (and other normal faults in the system) is encouraged by local stress regimes induced by the complex tectonic setting (Figure 1.4, Kenedi *et al.*, 2010). Within the Belham Catchment, this has manifested in the uplift of St Georges Hill (SGH) and Garibaldi Hill (GARRI) blocks (Kenedi *et al.*, 2010). Sub-surface surveys by Hautmann *et al.* (2013), Kenedi (2010), Kenedi *et al.* (2010) and Shalev *et al.* (2010), and field evidence discussed by EGS (2010) and Harford *et al.* (2002) indicates that GARRI and SGH are of common structural origin, composed mainly of BAFs, Pumice-and-Ash flows (PAF) and epiclastic beds, most likely sourced from SHV, that have undergone uplift and rotation to form horst structures (Kenedi *et al.*, 2010; Hautmann *et al.*, 2013).

Volcanic domes (< 170 ka) in the SHV complex are aligned with the SGH and GARRI structurally uplifted blocks, and the BVF (Figure 1.7, Feuillet *et al.*, 2010). Miller *et al.* (2010) discussed the contributions of the BVF and regional tectonics to magma ascent location, and Feuillet *et al.* (2010) and Kenedi *et al.* (2010) emphasised the complexity of evolving stress regimes around SHV and BVF. Feuillet *et al.* (2010) concludes that the young normal faulting systems on Montserrat and the volcanic alignments are the co-located consequence of the N-S crustal extension; active volcanic complexes marking ongoing, large-scale trans-tensional motion associated with subduction orientation at the Lesser Antilles arc.

1.4.2. Sub-surface geology and hydrogeology

Interest in the potential of the hydrothermal system to the west of SHV centred under SGH (Ryan *et al.*, 2013), for geothermal electricity generation, has recently led to a number of exploratory surveys providing better fault delineation relevant to the Belham catchment (Figure 1.7, EGS, 2010; Kenedi *et al.*, 2010; Ryan *et al.*, 2013). Geophysical investigation has determined the hydrothermal system lies at the intersection between the BVF and the SW orientated HPA fault (Ryan *et al.*, 2013). This corresponds with seismic swarms under SGH (see Powell, 1938; Shepherd *et al.*, 1971; Aspinall *et al.*, 1998) at ~2-4 km depth (Miller *et al.*, 2010), indicative of stress transfer within an active fracture zone (Miller *et al.*, 2010; Kenedi *et al.*, 2010b), un-associated with eruption (Roman *et al.*, 2008) and separate from the geothermal system beneath SHV (Ryan *et al.*, 2013). The HPA fault intersects the RHF, which is adjacent to BVF. Surveys indicate that the two faults are connected by a complex fracture network both at the surface and at depth, resulting in increased permeability that enables fluid circulation (Kenedi *et al.*, 2010). The stresses imposed within the transfer zones between faults and at intersections result in increased fracturing and high permeability that maintains long-lived fluid circulation (Kenedi *et al.*, 2010). The hydrogeological system is complex and specific fluid pathways constantly shift in response to local stress accommodation and mineral precipitation blocking flow (Kenedi *et al.*, 2010).

At shallow depths and above sea level, the unconsolidated sedimentary infills from recent and past SHV eruptions provide a high permeability hyporheic interface for surface flow and groundwater to interact. Exposures of ancient rocks on the coastal edge of GARRI provide insight into geological composition of the pre-1995 Belham River Valley. To the south, valley walls are composed of pyroclastic flows, pumice falls and lahar deposits derived from SHV activity between 282 ± 8 ka and 151 ± 4 ka based on ^{40}Ar - ^{39}Ar geochronology by Harford *et al.* (2002). Younger fall deposits from six later episodes of activity at SHV and SSH, between 130 ka and the present (Smith *et al.*, 2007; Cassidy *et al.*, 2013), are also likely to contribute to the stratigraphic record, although there is very little published discussion on this in the Belham River Valley context. The sequences at the GARRI coast dip up to *c.* 50° approximately NW, indicating tectonic tilting in association with block upthrusting of GARRI by the BVF (Harford *et al.*, 2002). Deposits on the south and north side of the Belham River Valley upstream of GARRI are highly weathered and vegetated, thus it is difficult to extend these observations upvalley. Borehole logs (Appendix 1.2) collected

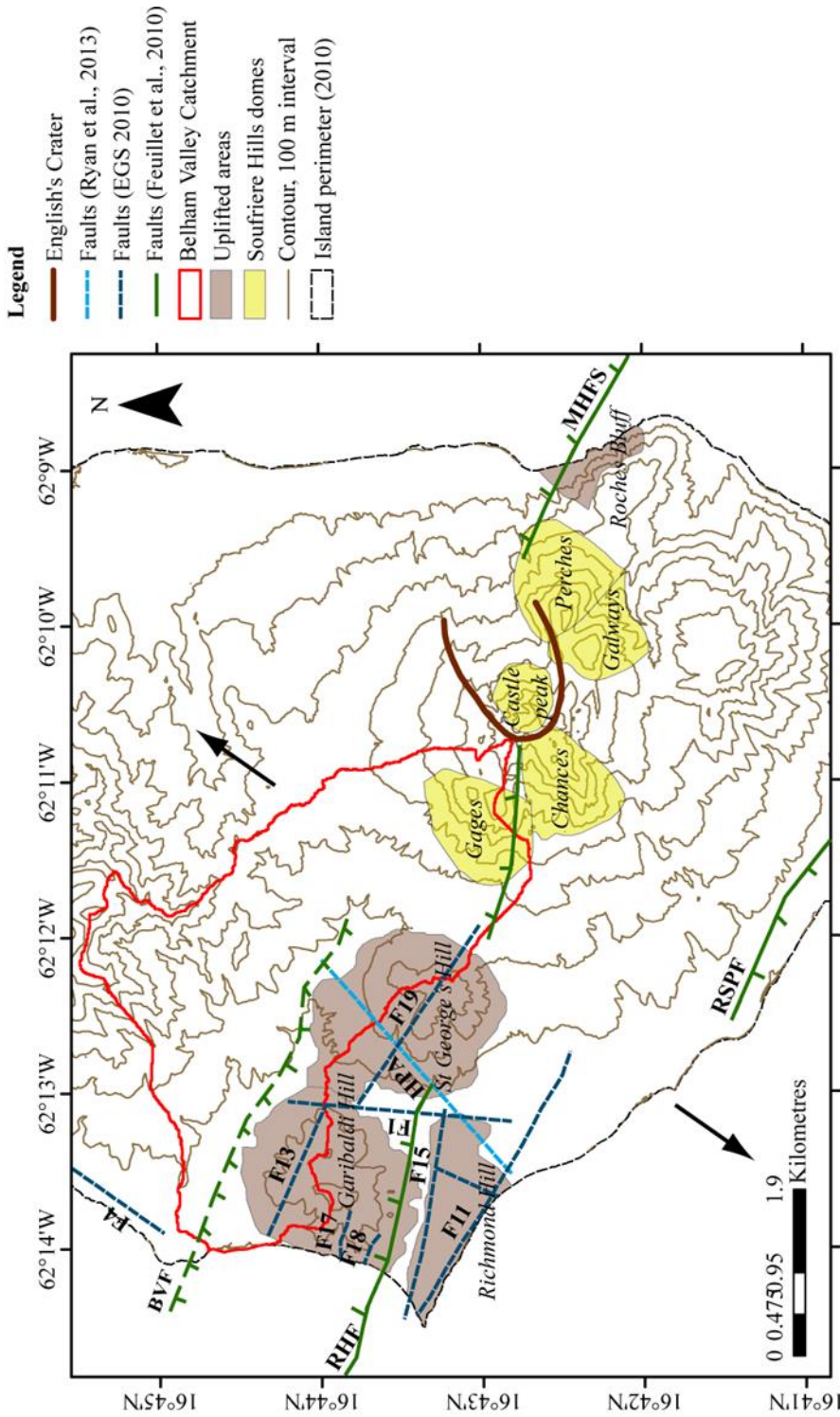


Figure 1.7 Map showing the tectonic and volcanological features in the area local to the Belham Valley catchment. Several surveys have contributed to the fault line map (EGS, 2010; Feuillet *et al.*, 2010; Ryan *et al.*, 2013) and it is noted that the surveys did not always agree. The main faults included: BVF, Richmond Hill Fault (RHF), Kinsale-St Patrick Fault (KSPF) and MHFS. Other faults are labelled arbitrarily. Local extension direction is shown (based on Feuillet *et al.*, 2010). The location of English's Crater, the Soufriere Hills domes and uplifted areas are reproduced from Harford *et al.* (2002). 100 m contour interval from 0 m at sea level.

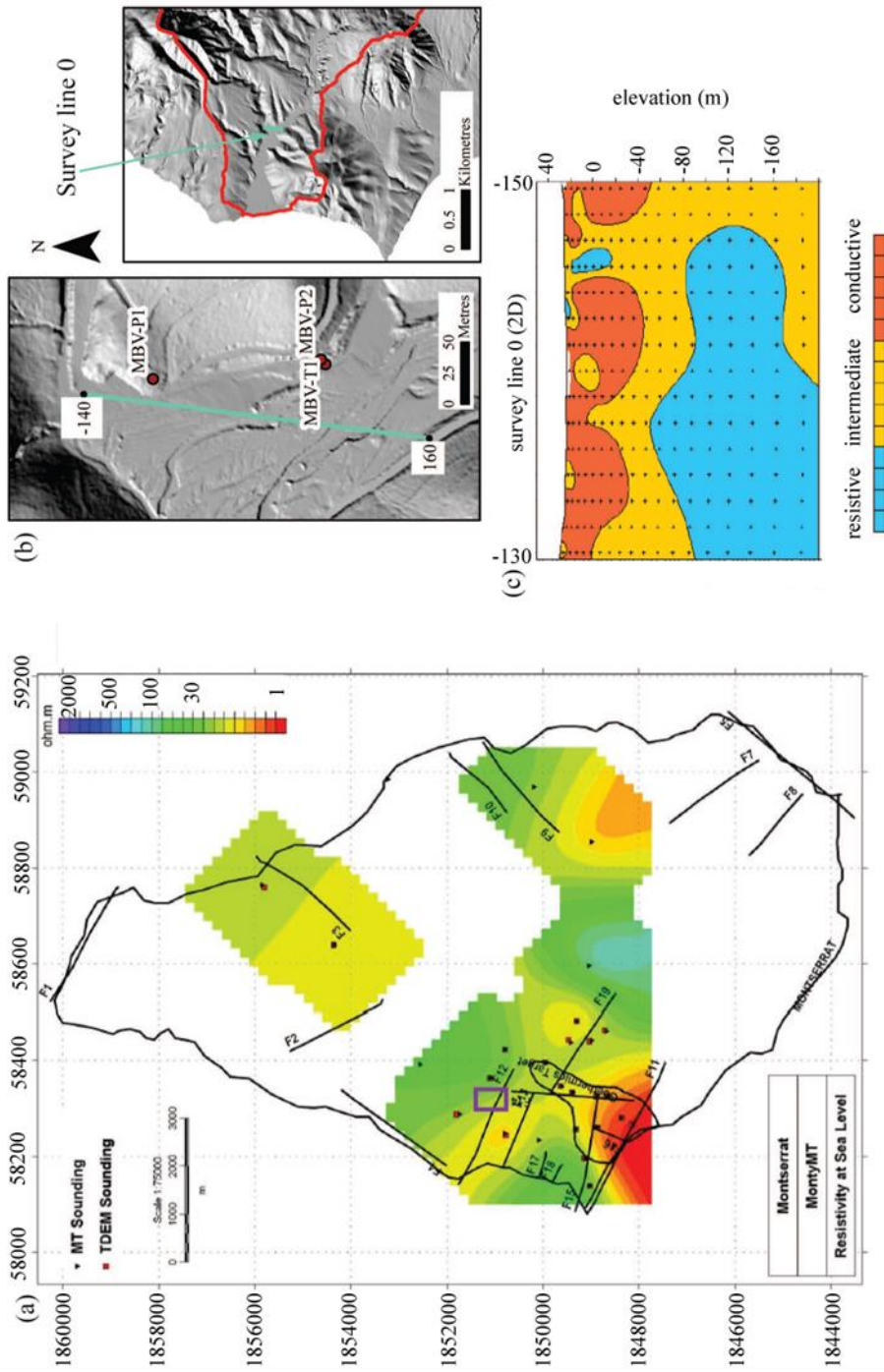


Figure 1.8 (a) Resistivity map at sea level (0 m a.s.l.). Black lines indicate fault zones. Reproduced from EGS (2010, p.36). Location of Hydrosourc, 2004 survey shown by purple rectangle. (b) Location of Belham River Valley boreholes, MBV-P1, MBV-P2, MBV-T1, MBV-T2 (red markers) and one of the ten CSAMT/ microgravity survey lines (green). Base map: 1 m resolution shaded relief model (azimuth= 315, altitude= 45) of merged DEM from 1999 (north of island) and 2010 (south of island). (c) Example of CSAMT survey, line 0. Blue indicates areas of high resistivity. Survey line ranges from -130 m to 150 m and corresponds to the survey line marked in (b)

during the installation of groundwater wells into the Belham River Valley aquifer (Figure 1.8) capture the vertical stratigraphy at a discrete location on the north side of the Belham River Valley, 5.7 km (2D Euclidean distance) from SHV .

The logs support observations of exposed deposits at GARRI, showing vertical transitions between PAFs, lahar, lapilli fall, volcanic breccias and ashfall deposits (Hydrosource, 2004). It is noted that the wells were drilled "open hole" after ~50 m (metres below sea level), as the formations were sufficiently consolidated to maintain hole integrity. Based on the location of the BVF (Figure 1.7) and topography (Figure 1.6), it is expected that north of the BVF sub-surface geology comprises flow deposits (BAFs, lahars, debris avalanche and fluvial) from the Centre Hills (950-550 ka, Harford *et al.*, 2002). Volcanic breccias and lahar deposits composed of admixtures of sands and gravels are highly permeable and form productive aquifers (Hydrosource, 2004, Bursik and Reid, 2004). Clay-rich lahar deposits and pyroclastic flow deposits rich in ash, are poor aquifers (Terzaghi *et al.*, 1996, Hydrosource, 2004). The geometric composition of deposits sub-surface controls the position of aquifers, the passage of throughflow, and influences the surface response of the Belham River Valley to rainfall.

A Magnetotellurics (MT) and time domain electromagnetic induction (TDEM) survey conducted by Ryan *et al.* (2013), results reviewed in EGS (2010) and Kenedi (2010), show a laterally extensive volume of low resistivity beneath the Belham River Valley surface, between the coast and Gage's Mountain (Figure 1.9.a-b). This has been interpreted as a clay cap (EGS, 2010), although areas of low resistivity within the Belham River Valley limits may also be attributed to open fractures containing sea water or hydrothermal fluids (Kenedi, 2010). The elevation of the top of the low resistivity zone varies spatially and is overtopped by higher resistivities (Figure 1.9b). An area of higher relative resistivity at sea level elevation (Figure 1.8a) corresponds with the location of the MBV-P1 and MBV-P2 wells that extract water from a perched aquifer located from ~-25 m a.s.l., confined in reworked gravels and alluvial deposits (Hemmings *et al.*, 2012). Results from a Controlled Source Audio frequency Magneto Telluric survey (CSAMT) conducted by HydroSource Associates in 2004 (Hydrosource, 2004), suggest the aquifer extends to depths of 200+ m (the survey limits, Figure 1.8b) and is laterally extensive within the survey limits¹ Smaller pockets

¹ A microgravity survey (Hydrosource, 2004) was also undertaken to assist aquifer identification.

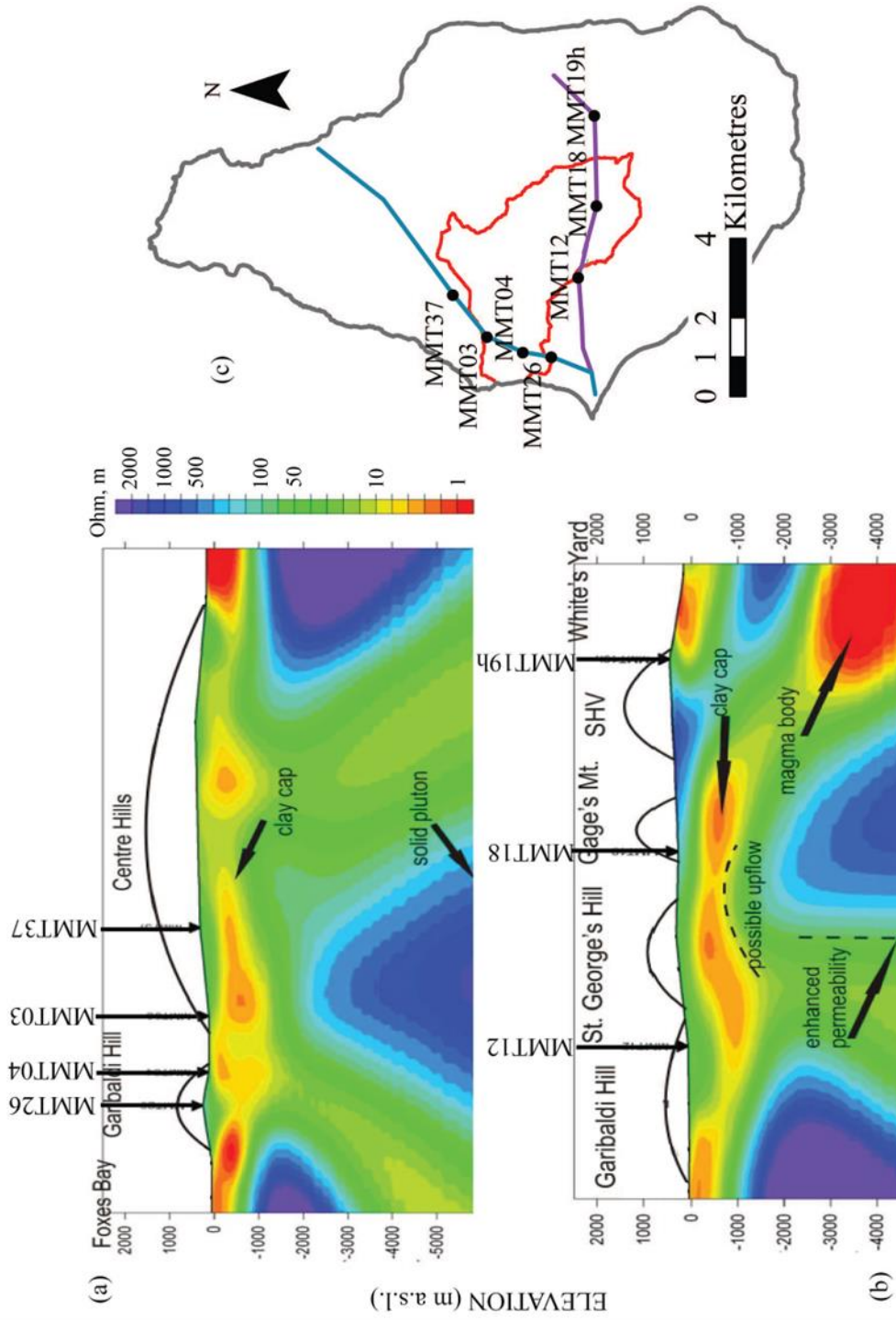


Figure 1.9 2D EQ resistivity transects from EGS (2010) survey. (a) Top transect corresponds to the blue line in (c). (b) Bottom transect corresponds to the purple line in (c). (c) The location of the Belham Catchment is shown by the red catchment outline. Key survey stations relevant to the Belham Catchment are indicated by numbered arrows in (a) and (b), corresponding to points in (c)

of higher resistivity were detected at shallow depths (>30 m a.s.l.) on all survey lines, indicating sediments with a greater water transmission capacity (*e.g.* lahar deposits and ash-and-lapilli fall with limited clay content) (Hydrosource, 2004). These areas may contain small perched aquifers, and provide pathways for through-flow of water in response to rainfall.

The interaction between geothermal activity, groundwater and volcanism on Montserrat was demonstrated by explosive phreatic eruption and phreatomagmatic eruption during the onset of major eruptive phases (*e.g.* Phase 1, Young *et al.*, 1998). Hautmann *et al.* (2010) have proposed, using a microgravity network established in 2006, that volcanic activity causes stress induced fluid migration from the north of the island to the south in response to decreased groundwater level around the SHV. Groundwater level is thought to drop because of increased evaporation through the vent as hot material ascends, and the resulting disequilibrium in aquifer head is corrected by the southward migration of an estimated $2\text{-}4 \times 10^7 \text{ m}^3$ of water (based on recorded gravity anomalies, Hautmann *et al.*, 2010). Within the Belham River Valley, water levels of MBV-P1 and MBV-P2 appear to have responded to periods of increased volcanism, showing a rise between 2005 and 2006 coincident with a switch from pause to extrusion (July 2006), and explosive activity (Hemmings *et al.*, 2012); and abruptly dropping a week after the May 2006 dome collapse (Hemmings *et al.*, 2012). Water levels have steadily increased following this collapse and in 2011 MBV-P2 became an artesian well generating surface flow into the Belham River Valley (at a rate of 3.2 L s^{-1} , November 2011, Hemmings *et al.*, 2012). The hydrogeology around SHV is very complex and changes in response to volcanism. This thesis focuses on surface transfers of water, however an awareness of sub-surface hydrology is useful when discussing infiltration response to rainfall and surface flow initiation.

1.5. Land surface cover: soil and vegetation

Soil development has been restricted by Montserrat's small size, its steep topography, and relatively young age, particularly of SHV and SSHV (Goldsmith *et al.*, 2010). Despite shallow depth the Andosol soils are fertile, supporting dense forests and agriculture. Prior to the onset of volcanic activity, 62% of the Belham Catchment was densely vegetated with: Dry Forest (29%), Mesic Forest (48%) and Wet Forest (13%) (Figure 1.10; Young, 2008). Rainfall increases with elevation (Barclay *et al.*, 2006) and the forest changes from Dry to Wet as altitude increases. A small (0.7%) of Elfin

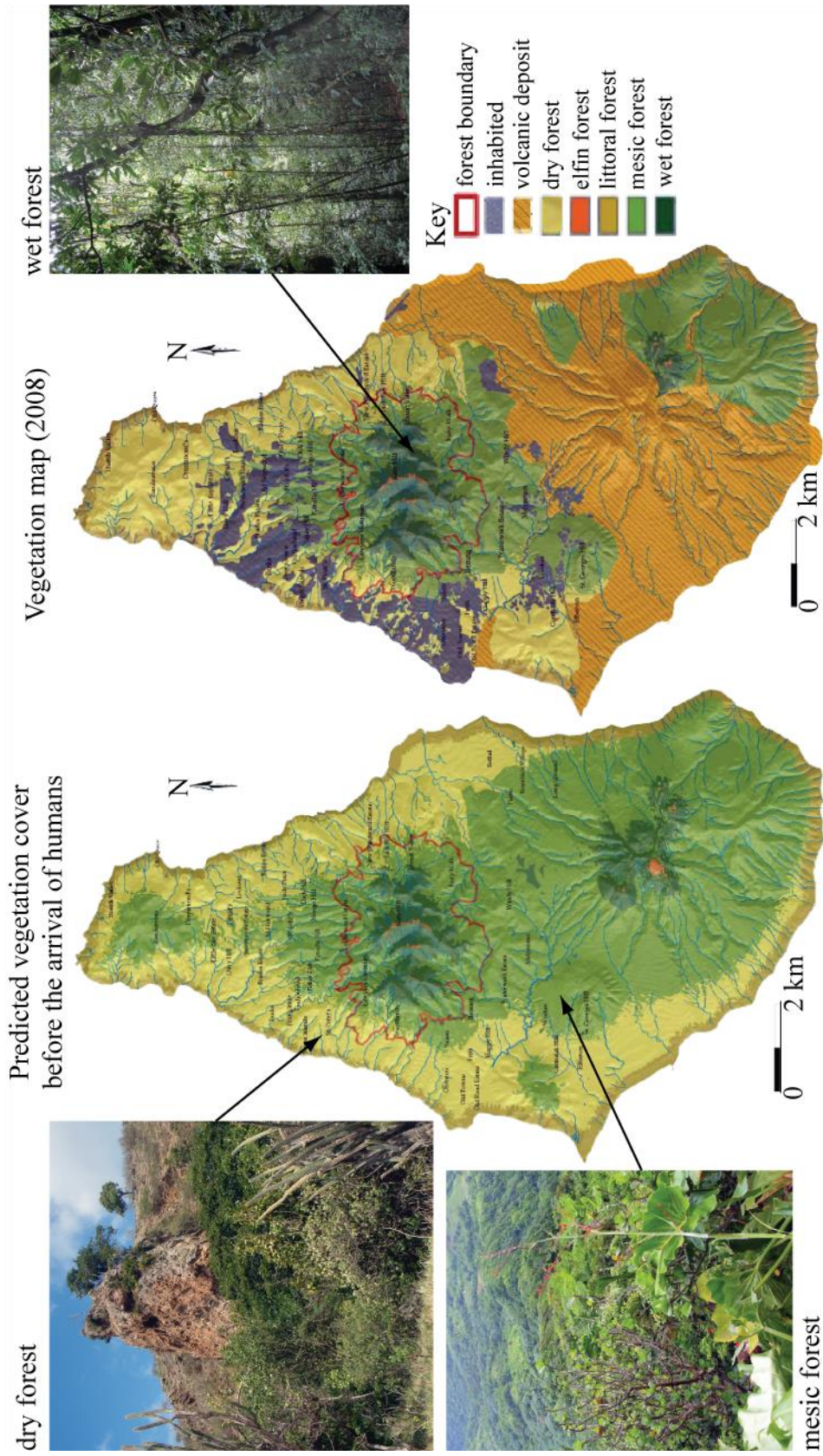


Figure 1.10 Vegetation maps of Montserrat showing the distribution of different forest types before human inhabitation (left) and after 13 years of volcanic activity (right). The left map provides some indication of vegetation lost to volcanic inundation (orange, right), although coastal areas to the south west were densely populated prior to volcanic activity. Photographs correspond to dominant vegetation types on island. Maps reproduced from Young, 2008, p. 19 and

31. Source MANSAT Arnaud, Kew, June 2007

woodland is present at the highest elevations of the north border of the Belham Catchment. Average canopy cover is highest in Mesic forest (70-75%) compared to Wet forest (60%) (Young, 2008). Inhabited areas before the eruption accounted for 9% of land area within the Belham Catchment; this includes an area in the lower reach of the Belham River, which had a gentle slope of 3° and was used as a golf course. Vegetation cover reduces soil erosion by protecting it from drop impact and stabilising it with root systems (Torri and Poesen, 2014). Soils on Montserrat are predominantly coarse (Jones, 2011) and plant roots further enhance soil infiltration capacity by increasing macroporosity (Torri and Poesen, 2014). Some smectite is present, and the mix of free-draining and clayey soil has created a series of soil aquifers as well as springs in the Centre Hills (Jones, 2011), as discussed in Section 1.4.2. Volcanic activity has profoundly altered the land surface on the flanks of volcano, destroying vegetation and altering runoff dynamics, resulting in large areas of bare earth and shifts to dry forest species on re-vegetating volcanic deposits (Figure 1.10); specific impacts are discussed in Section 3.3.

1.6. Volcanic activity

The Soufrière Hills volcano has transformed the southern end of Montserrat, rendering 64 % of the land area uninhabitable following five phases of activity over the past 18 years. Modern volcanic activity commenced in July 1995 (Young *et al.*, 1998), and the following section provides an overview of eruptive episodes and the distribution of associated volcanic products, specifically focusing on the Belham Catchment. Syn- and post- eruption rainfall has remobilised volcanic debris within the catchment, in a series of lahars (Barclay *et al.*, 2007; Alexander *et al.*, 2010), transforming the geomorphology of the Belham River Valley and coastline (discussed in Chapter 3). Figure 1.11 shows the main drainages routes from SHV (including the Belham River Valley).

Before the onset of present activity in July 1995, the SHV massif was composed of five domes: Gages Mountain, Chances Peak, Galways Mountain, Perches Mountain and Castle Peak (contained within the steep walled sector collapse scar of English's crater, Figure 1.7; Roobol and Smith, 1998). Of these, Castle Peak was most recently active $c.323 \pm 50$ years BP, involving a small andesitic dome generating $45 \pm 15 \times 10^5$ m³ of eruptive material (Young *et al.*, 1996; Young *et al.*, 1998). Pb isotopic analysis

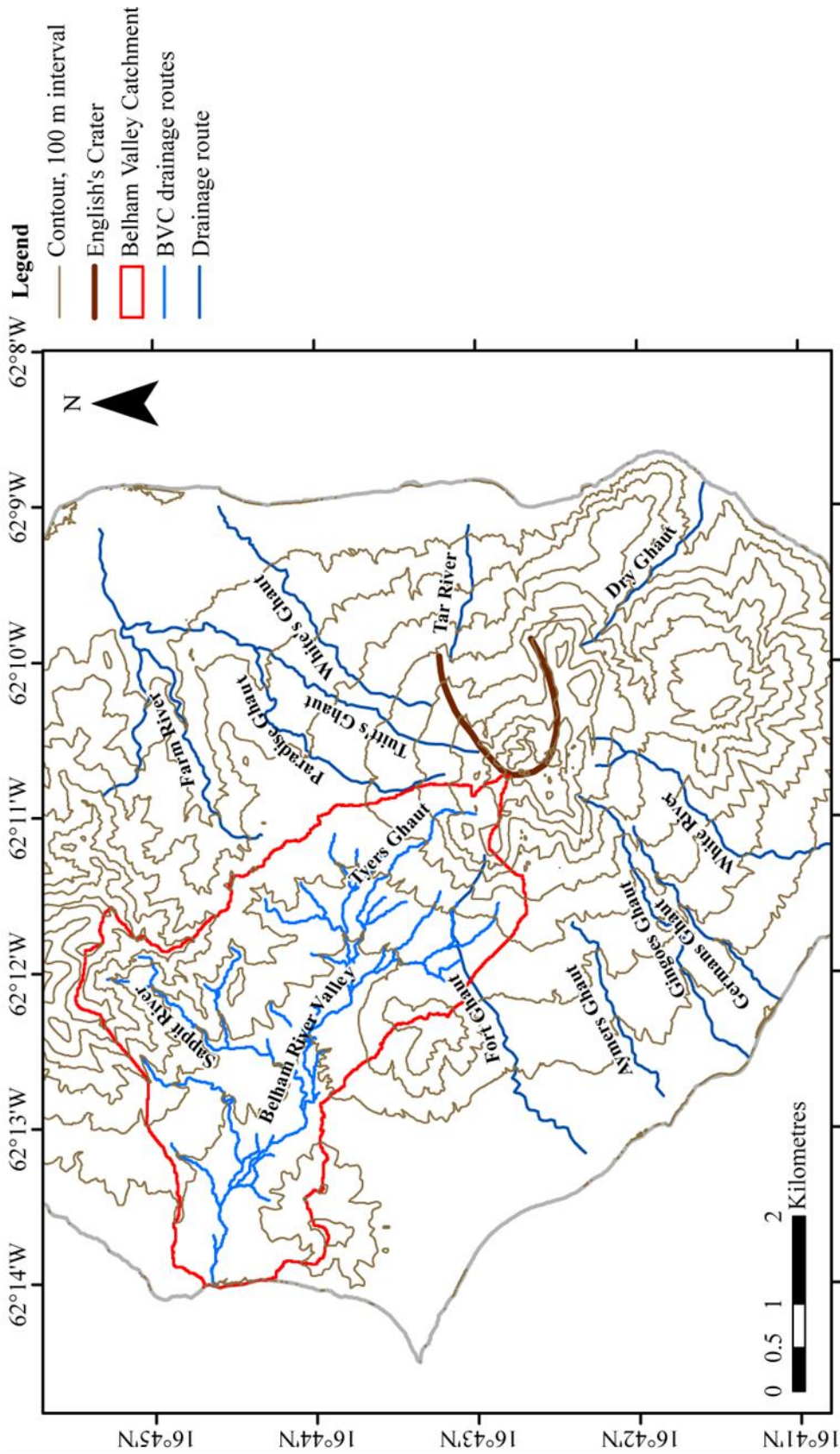


Figure 1.11 The main drainage routes from the Soufrière Hills Volcano, Montserrat. Topographic base map: 100 m contour from 0 m at sea level. Merged DEM from 1999 (north of island) and 2010 (south of the island), WGS84 20N orthometric heights. Drainage routes calculated from the topographic base map.

by (Cassidy *et al.*, 2012) have shown that SGH and GARRI are composed of material derived from the SHV complex; samples from the coastal exposure of GARRI were dated at 282 ± 8 ka by Harford *et al.* (2002), the oldest rocks associated with SHV dated. Precursors to the present volcanic episode manifested as significant increases in seismicity and hot spring activity² in 1897-98, 1933-37 (Macgregor, 1938; Perret, 1939) and 1966-67 (Shepherd *et al.*, 1971), with further marked increases in seismicity in mid-1985, 1992 and November 1994 (Young *et al.*, 1998). Seismic swarms were centred on SHV, and also reported under SGH. Eruptive activity began with a phreatic eruption on 18th July 1995 from several steam vents across the Castle Peak dome (Ambeh, and Lynch, 1996; Aspinall *et al.*, 1998); precursory seismic activity in the weeks prior to this event was unclear and not detected (Young *et al.*, 1998). Vents coalesced and phreatic explosions associated with steam and ash columns to 3 km in height continued for four months, depositing mm-thick ashfall across the south-west of Montserrat (Young *et al.*, 1998). Volcanic-tectonic (VT) seismicity dominated the phreatic phase, accompanied by shallow hybrid earthquakes during the earliest stages of dome development in late September (Young *et al.*, 1998). Dome extrusion began in November 1995 (Robertson *et al.*, 1998) and continued until March 1998, marking the end of Phase 1 (Young *et al.*, 1998). Throughout this and subsequent phases of eruption, activity has consisted of several cycles of (andesitic) magma extrusion and lava dome growth, followed by gravitational collapse and occasionally Vulcanian explosions (and ash clouds), both of which generating pyroclastic flows or surges down the flanks of SHV (Barclay *et al.*, 2007). Residual activity continued between eruptive phases (Druitt *et al.*, 2002a). Table 1.1 summarises key events from the onset of dome growth in November 1995 through five phases of volcanic activity to the present period of quiescence (2014).

The Soufrière Hills volcano (SHV) has transformed the southern end of Montserrat, rendering 64% of the island uninhabitable following five phases of activity between 1995 and 2010. Chapter 3 discusses the distribution of associated volcanic products in the Belham Catchment and remobilisation of volcanic debris in a series of lahars, transforming the morphology of the Belham River Valley.

² temperature and gas composition

Date	Volcanic activity and major evacuations
PHASE 1: July 1995- March 1998	
July 1995	First Phreatic explosions
August 1995	Partial evacuation of Plymouth
November 1995	Dome growth confirmed
December 1995	Second evacuation of Plymouth
April 1996	Evacuation of south of island
July 1996	First major dome collapses
September 1996	First major explosions
June 1997	First deaths and abandonment of Plymouth and airport
PHASE 2: November 1999- July 2003	
July 2003	Largest dome collapse (210 million m ³)
PHASE 3: August 2005- April 2007	
May 2006	Largest dome collapse (100 million m ³)
PHASE 4: August 2008- October 2008; December 2008- January 2009	
PHASE 5: October 2009- February 2010	
February 2010	Largest dome collapse since May 2006
PAUSE: February 2010- ongoing	
March 2012	Steam and ash venting, West SHV
August 2012	Ash venting

Table 1.1 Summary of some of the key events between July 1995 to March 2013, updated from Darnell (2010) after (<http://www.mvo.ms/>; Herd *et al.*, 2005; Edmonds *et al.*, 2006)

1.7. Hazard zonation and lahar assessment

Management of the volcanic crisis is discussed in detail, see Wadge *et al.* (2014) and Donovan *et al.* (2014) for review and references therein. The zonation of hazardous areas around SHV has been adjusted in response to shifts in the direction and magnitude of dome extrusion, and reductions in surface activity during pause periods. The lower Belham River Valley cross-cuts Zone B (Figure 1.12, see also Appendix 1.1b), which was evacuated during periods of Phase 5 because of pyroclastic flow risk. Residents in the south side of Zone B (Isles Bay) may be cut off for several days during a large lahar because the Belham River Valley is the only crossing point to reach other inhabited parts of the island. Zone B extends ~ 400 m upstream of the Belham Bridge (Figure 1.12), becoming Zone C which then extends up-valley becoming Zone V just upstream

of the Sappit River. At times of volcanic crisis the hazard level is elevated resulting in restricted access to certain zones around the volcano (see Appendix 1.1b for full hazard level zone restrictions). Table 1.2 shows the change in hazard level following Phase 5 during the study period.

Date	Hazard Level	Access
10 th December 2009	4	Controlled access to Zone B & C
23 rd February 2010	3	Unrestricted access to Zone B, controlled access to Zone C
4 th November 2011	2	Unrestricted access to Zone B, daytime access to Zone C
23 rd March 2012 (ash venting)	2	Unrestricted access to Zone B, no access to Zone C
27 th March 2012	2	Unrestricted access to Zone B, daytime access to Zone C
5 th August 2014	1	Unrestricted access to Zone B, unrestricted access to Zone C

Table 1.2 Changes to the hazard level relevant to residents and users of the Belham River Valley. The hazard level was altered in response to dome extrusion and volcanic activity. This table focuses on the period from the beginning of Phase 5 to the end of the study period.

Lahars are not formally monitored by the MVO however interest in them grew following a series of large flows in the Belham River Valley in 2006 and 2010. Research by Darnell *et al.* (2011; 2012; 2013) provided an inundation assessment of the Belham River Valley by lahars of different volumes using a single-direction flow routing model with an added roughness coefficient. The model was particularly useful for quick hazard assessment in response to changing valley morphology. In the Belham River Valley the key user groups were: (1) residents crossing by vehicle (permanent residents of Isles Bay, Zone B), (2) vehicles crossing to reach Zone C (non-residents), (3) recreational users (on foot, Zones B and C), (4) commercial sand extraction (in large vehicles Zones B and C). With decreasing hazard level, sand extraction has expanded upstream and more vehicles were crossing the valley to access zone C. Critically the hazard level system does not include lahars, however lahar warnings were issued by the government of Montserrat by public broadcast if large storm systems (Tropical Storms/Hurricanes) were predicted to cause heavy rainfall. Warnings are not issued for smaller storms which may trigger lahars, however signs are positioned at crossing points of the Belham River Valley warning of the potential lahar hazard, particularly during rainfall, and the MVO weekly report includes a note that lahars remain a hazard in the Belham River Valley during pauses in magma extrusion.

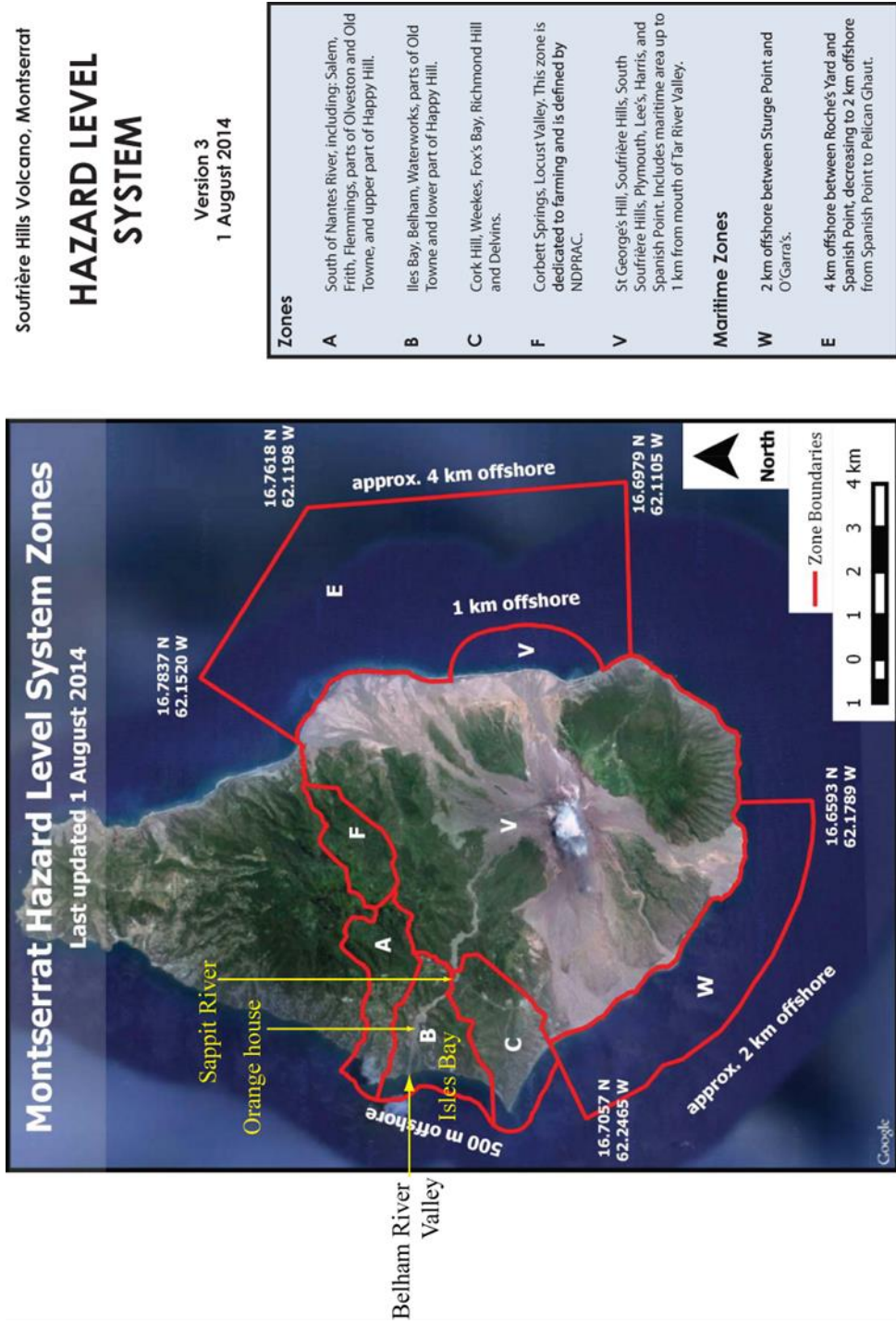


Figure 1.12 Montserrat Hazard Level System modified to include key locations in the Belham River Valley (yellow labels) and the location of the valley is labelled. (MVO, 2014)

Chapter 2

A multi-method approach to monitoring lahars: from intra-flow variability to decadal geomorphic change

2.1. Introduction

To address the aims and objectives of this research a multi-methods approach was taken. The research considered longitudinal (~20 year) changes to the Belham River Valley and catchment from repeat episodes of volcanic activity at the Soufrière Hills volcano (SHV), and aimed to develop monitoring equipment to collect new data of sediment-laden flows triggered by rainfall during the study period. The approach drew on several published methods employed to monitor long-term change in fluvial environments and traditional field geology techniques such as sedimentological logging, as well as developing a new field equipment set-up to monitor flows. Table 2.1 provides an overview of the methods used, linking methods employed and data collected with rationale derived from the research aims and objectives outlined in Section 1.2. Field work to collect primary data was undertaken in Montserrat in March 2011- May 2011, February 2012- March 2012, September 2012- October 2012 and

Attribute	Rationale/ objective	Methods	Data analysis
<p>Catchment-scale topographic change</p>	<p>Quantifying change to the Belham Catchment extent between 1995 and 2010 will indicate changes in contributing runoff area to lahar events in the Belham River Valley.</p> <p>Objective 9</p>	<ul style="list-style-type: none"> • Compared available catchment-wide DEMs generated by past studies between 1995 and 2010. • Delineated catchment boundaries using ESRI ArcGIS ArcHydro toolbox <p>Section 2.2.1</p>	<p>Chapter 3 (1995- 2010)</p>
<p>Tephra fall volume</p>	<p>To understand storage and transfer of sediment in the Belham Catchment by lahars between 1995 and 2013, volcanic sediment input volume and timing must be established.</p> <p>Objective 9</p>	<ul style="list-style-type: none"> • Assembled a database of archive surveys (DEMs, aerial/satellite vertical photographs, oblique aerial photographs) • Identified key dates of volcanic activity that directly affected the Belham Catchment using published literature and MVO observations. • Used DEM calculations and visual analysis of imagery to estimate volumes of sediment in drainage valleys in the Belham Catchment, and changes in these volumes due to fluvial reworking of sediment. <p>Section 2.2.2</p>	<p>Chapter 3 (1995-2013). Chapter 5 (2010-2013).</p>
<p>Valley-scale topographic change</p>	<p>To create or adapt (an existing) model of valley and catchment adjustment to volcanic sedimentation for use as a predictive tool when considering the impact of volcanic activity on local fluvial sediment transport and geomorphology.</p> <p>Objectives 8 and 9</p>	<ul style="list-style-type: none"> • Assembled a database of archive surveys (DEMs, aerial/satellite photographs, ground photographs). • Undertook annual kinematic DGPS surveys of the Belham River Valley, post-processed points and interpolated to form a DEM. • Compared thalweg and cross-section profiles extracted from each DEM. • Estimated volumetric change between sequential DEMs to capture fluvial transport of sediment downstream. <p>Section 2.2.3.1</p>	<p>Chapter 3 (1995-2013) Chapter 4 (2012-2013) Chapter 5 (2010-2013)</p>

Lahar occurrence	Document lahar occurrence using archive observations for events occurring in the Belham River Valley between 1995 and 2013. Estimate event magnitude (relative) and use with observations of topographic change and lahar deposits to improve understanding of sediment transfers in the Belham River Valley. Objectives 6, 7, 8 and 9	<ul style="list-style-type: none"> Analysed archive seismic helicorder and spectrogram data from seismometers in the Belham Catchment to identify long-period lahar signals. Verified seismic interpretation using MVO observations, archive rainfall data, published/ doctoral studies and personal observations. Section 2.2.3.2	Chapter 3 (1995- 2013) Chapter 4 (2010-2013) Chapter 5 (2010-2013)
Antecedent and triggering rainfall	Rainfall intensity-duration required to generate sufficient runoff to trigger a lahar depends on the impact of volcanic activity on hillslope infiltration, roughness and vegetation health, as well as prior antecedent rainfall in the weeks preceding the event. Relating rainfall measurements in the Belham Catchment with lahar timing, provides insight into changes in catchment runoff in response to volcanic activity. Peaks in rainfall during observed events may also be related with flow observations to understand intra-event flow variation. Objectives 4 and 7	<ul style="list-style-type: none"> Antecedent rainfall was calculated over periods of 60, 30, 14 and 7 days before lahar onset (day: time) using rainfall measurements from two gauges in the Belham Catchment, processed in Matlab. Peaks in triggering rainfall were calculated over 1-, 10- and 60-minutes in the 24 hours prior to lahar onset (data: time), processed in Matlab. Data from rainfall radar for one event. Sustaining rainfall (rainfall 24 hours after lahar onset) was calculated, data processed in Matlab. Section 2.2.3.3 and 2.4.1	Chapter 3 (2001-2013) Chapter 4 (13-14/10/2012)
Sedimentology of lahar deposits	The sedimentological characteristics of lahar deposits provide insight into flow conditions under which they were deposited, including intra- and inter- flow variability. Sedimentary structures from rapidly varying, unsteady sediment-laden flows are poorly understood. Combining sedimentological study with flow observations improves understanding of the formation and preservation of sedimentary structures during an event. Objectives 5 and 6	<ul style="list-style-type: none"> Geological logging of modern lahar deposits at available vertical exposures (pits excavated by commercial aggregate mining). Dip and direction of largest clasts Section 2.5	Chapter 5 (2010-2013)

<p>Particle size of lahar deposit</p>	<p>Particle size variations in the deposit preserve changes in flow competence. Particle size analysis to characterise facies within the deposit.</p> <p>Objectives 5, 6, 8 and 9</p>	<ul style="list-style-type: none"> Field-based grain size measurement for grains over <64 mm in vertical exposures. Dry sieving of sampled material 64 mm- 0.5 mm. Fines analysed in laboratory particle size analyser. Pole-aerial-photography used to measure grain size distribution of the bed surface and capture bed surface morphology at sample locations. <p>Section 2.5.1.3</p>	<p>Chapter 4 (2012-2013) Chapter 5 (2010-2013)</p>
<p>Lahar monitoring: flow velocity and depth</p>	<p>Very few strategic regular measurements of rapidly varying, unsteady sediment-laden flows exist. Developing a non-contact field instrument set-up that collects continuous data which may be interpreted to varying degrees by scientists with non-specialist expertise and members of the public, provides useful information about hazardous flows and also improves scientific understanding of flow variability.</p> <p>Objectives 1, 2, 3, 4 and 5</p>	<ul style="list-style-type: none"> Development remote camera unit and field computer, and field installation to permanently monitor lahars in a section of the Belham River Valley. Installation of permanent pole bench marks in the valley floor at the camera site, and detailed survey of the bed surface before and after a lahar. Collection of ground photographs/video at accessible locations during a flow captured by the camera. Development of processing methods to obtain flow velocities and depths from imagery. <p>Section 2.3 and 2.4.3</p>	<p>Chapter 4 (13-14/10/2012) Chapter 5 (2012-2013)</p>
<p>Lahar monitoring: flow sediment transport</p>	<p>As above.</p> <p>Objectives 1, 2, 3, 4 and 5</p>	<p>As above.</p> <ul style="list-style-type: none"> Development of processing methods to obtain velocities and travel distance of sediment travelling as bedload. Sampling of suspended sediment concentration in flow at accessible valley location (downstream of camera site). Dip samples collected. Sediment dried and analysed in the laboratory particle size analyser. <p>Section 2.3 and 2.4.2</p>	<p>Chapter 4 (13-14/10/2012)</p>

Table 2.1 Summary of methods used in each aspect of the study. Refer to Section 1.2 for research aims and objectives.

March 2013. The following chapter outlines all datasets and methods used in this study. Results are discussed throughout Chapters 3 to 5.

2.2. Monitoring decadal geomorphic change in the Belham Catchment

The geomorphology of a catchment in an active volcanic region can change very rapidly in response to volcanic processes (Gomez, 2014). Several studies in other volcanic regions have quantified long-term decadal-scale changes to topography in response to volcanic perturbation. Different methods and data sets have been used including: watershed change detection using SAR-interferometry at Mayon volcano, Philippines (Canisius *et al.*, 2008), wavelet analysis for recognition of topographic variation over different time-scales Merapi and Merababu (Gomez, 2012), and the application of recently developed techniques in SfM–MVS (Structure from Motion and Multiple-view Stereophotogrammetry) to generate 3D models from archive photographs at Sakurajima volcano, Japan for change analysis (Gomez, 2014). Other studies have focused on channel-scale change (discussed in Section 2.2.3) or monitoring summit-wide dome deformation (Major *et al.*, 2009; Walter *et al.*, 2013). There are also numerous studies documenting catchment-scale change in other active regions (*e.g.* alluvial fans, Jolivet *et al.*, 2014; earthquake induced change, Shou *et al.*, 2012; sedimentation from mining, Schneider *et al.*, 2011). In this study the catchment is defined topographically rather than hydrologically (groundwater). This is because lahar initiation is inherently controlled by rapid runoff dynamics.

2.2.1. Catchment-change

Three digital elevation models (DEMs) were available for analysis, the details of which are shown in Table 2.2. Some additional processing was required to transform the pre-eruption DEM and the 1999 DEM from Montserrat National Grid (Clarke 1880) to WGS84 UTM zone 20N. Details of the transformation are included in Appendix 2.1. In addition following coordinate transformation, elevation values were converted from orthometric heights (H), which are relative to sea-level, into ellipsoid heights (h), which are relative to the WGS84 geoid (N) using Equation 2.1.

$$h = H + N \quad \text{Equation 2.1}$$

Date	Method	Precision/ Accuracy	Pre-processing
Pre-eruption: 1987	Digitised vectors from contours of the 1:25000 topographic map of Montserrat (E803-DOS 359) Montserrat 6-DOS 1983) (Wadge and Issacs, 1988). Contour interval was ~15 m. A triangular-irregular-network (TIN) was created from which a regular 25 m elevation grid was calculated. The DEM was resampled to a 10 m grid. (Wadge, 2000) Data in Appendix 2.2a	10 m x 10 m grid spacing. Horizontal accuracy = ~25 m. Vertical accuracy = ~ 5 m. In densely forested areas vertical height includes canopy height. This is estimated to be on average 18 m (mesic forest) and 11 m (wet forest) (Young, 2008).	Transformation Montserrat National Grid to UTM. Conversion orthometric heights from feet to metres. Conversion orthometric heights to ellipsoid heights.
February 1999	Stereo-photogrammetry of SHV using airborne photographs collected in February 1999. Construction of deposit masks using photographs and published deposit descriptions. Masks were merged with 1987 DEM. Full DEM limitations are discussed in Wadge (2000). Data in Appendix 2.2b	10 m x 10 m grid spacing. Horizontal accuracy = ~25 m Vertical accuracy = ~ 5 m (based on 1987 DEM).	Transformation Montserrat National Grid to UTM. Conversion orthometric heights from feet to metres. Conversion orthometric heights to ellipsoid heights.
June 2010	Airborne light-detection and ranging (LiDAR). Data in Appendix 2.2c-d	1 m x 1 m grid spacing. Horizontal accuracy = 0.02 m. Vertical accuracy = 0.15 m	Post-processing of LiDAR point cloud was undertaken commercially (SAC, 2011).

Table 2.2 DEM data available that covers the entire Belham Catchment

The following procedures were undertaken in ESRI ArcGIS using the ArcHydro toolbox to delineate the: (1) the drainage network, (2) boundary of the Belham Catchment and (3) the boundaries of sub-basins within the catchment. All three DEMs were processed in this manner.

- Holes in the DEM were filled using a linear interpolation between neighbouring cells
- A flow direction raster was calculated based on the slope and aspect of cells
- A flow accumulation raster was calculated using the flow direction raster to find the number of cells upstream of each cell in the raster
- Streams were defined based on the flow accumulation raster; in this case streams were defined as cells in receipt of flow from 1 km² area (or 100 cells in 10 m x 10 m grid, or 1000 cells in 1 m x 1 m grid).

Date(s)	Description	Method used/ Source
25/6/1997 August 1997 22/9/1997- 21/10/1997	Map of pyroclastic flow, pumice-and-ash flow and pyroclastic surge deposit locations in Belham Catchment (Phase 1).	Digitised from Druitt <i>et al.</i> (2002b) Appendix 2.4a
February 1999	1:15000-1:10000 nominal scale colour aerial photographs covering SHV in 6 swaths orientated N-S. Scanned at 450 dpi.	Method 2 Permissions for use granted by Geoff Wadge, copyright BGS (Wadge, 2000). Appendix 2.2e, 2.3h
2002 (precise date unknown, beginning of year)	Colour aerial photograph mosaic. Covering lower half of Montserrat. 0.25 x 0.25 m resolution.	Method 2 Permissions for use granted by MVO, copyright MVO. Appendix 2.2f
1/10/2003 to 19/09/2006	Oblique colour photographs (digital) (variable resolutions)	Method 3 British Geological Survey Geoscientific archive (BGS, 2014). Appendix 2.3a-c, i, k-m, 3.1a-c
24/6/2006	Colour satellite image Coverage up to Dyers River but includes all Gages fan 0.6 x 0.6 m resolution.	Method 2 Permissions for use Darnell (2010) Appendix 2.2g
18/11/2007	Colour satellite image Coverage up to lower Tyres Ghaut, includes all Gages fan 0.6 x 0.6 m resolution.	Method 2 Permissions for use Darnell (2010) Appendix 2.2h
28/7/2008 25/08/2008 3/12/2008-3/01/2009	Map of block-and-ash flow, pumice-and-ash flow and pyroclastic surge deposit locations in Belham Catchment (Phase 4).	Digitised from Komorowski <i>et al.</i> , (2010) Appendix 2.4b
3/12/2008	Oblique colour photographs (digital) (low resolution)	Method 3 MVO Flickr (2014), permissions for use MVO. Appendix 2.3f
September 2009	Oblique colour photographs (digital) (variable resolutions)	Method 3 Permissions for use Paul Cole Appendix 2.3e, g
11/10/2009	Oblique colour photographs (digital) (low resolution)	Method 3 Appendix 2.3d
8/1/2010 5/2/2010 11/2/2010	Map of pyroclastic flow, pumice flow, pyroclastic surge and lateral blast deposits. (Phase 5)	Digitised from MVO (2010) Appendix 2.4c
December 2010/ March 2011	Quickbird Satellite image Coverage includes Farell's Plain and Gage's fan 0.6 x 0.6 m resolution.	Method 2 Image georeferenced to LiDAR DSM. Permission for use MVO. Appendix 2.2i
February 2012	Aerial photographs taken by DSLR, hand-held from helicopter. 15 megapixel images	Method 2 Undertaken during this study Appendix 2.2j
March 2013	Aerial photographs taken by GoPro fish eye lens attached to base of helicopter, corrected by Adam Stinton, MVO 4.32 megapixel images	Method 2 MVO Appendix 2.2k

Table 2.3 Imagery: archive data and data collected during this study

- The catchment was defined using stream segments (based on the stream definition and flow direction grids). Initially a series of sub-basins were defined and some manual editing was required with reference to the wider drainage

network to select sub-basins in the Belham Catchment and then merge these to form the total drainage basin.

2.2.2. Estimating tephra volume

Volcanic activity resulted in the emplacement of widespread tephra fall, valley-infilling and the development of two debris fans in the Belham Catchment. In order to understand the response of the Belham River Valley to volcanic sedimentation and how that material was (and continues to be) gradually remobilised downstream by lahars, it was important to estimate sediment volumes and rates of degradation. The following section outlines available data and volumetric calculations.

2.2.2.1. Data availability

Data was more limited in the upper Catchment of the Belham River Valley compared to more accessible downstream areas. Topographic data is summarised in Table 2.2. In addition to this vertical aerial and satellite photographs, oblique aerial photographs and published deposit maps were used. Table 2.3 details the data, source and method. Ground photographs of the Belham River Valley were not listed individually due to the large size of the archive. The catalogued archive by location and date is in Appendix 3.4a.

2.2.2.2. Valley-fills

Topographic datasets that covered the upper parts of the Belham Catchment were limited. In order to capture changes on a sub-annual basis, aerial and satellite photographs were used. One of three methods was employed depending on whether control points were available for georeferencing and if the photograph was of vertical perspective. All data processing was conducted in ESRI ArcGIS and Matlab R2010a.

Method 1: Two DEM datasets

- For each area of interest (Farrell's Plain, Tyres Ghaut and Dyers River) a polygon Shapefile was created delimiting the extent of deposition with reference to aerial photographs and published maps, from similar time periods (see Table 2.3).
- For each area of interest the polygons were merged and the maximum extent used. This area was extracted from each of the DEMs of interest for the calculation.

- The sub-sections of the DEMs were subtracted from one another (most recent minus oldest). The DEM difference was exported as a .tiff file and reshaped in Matlab into a single vector column.
- Volumetric calculations of total loss/ gain and the range of elevation changes were undertaken.
- Inclusion of channel incision in volumetric calculations of the deposits is shown in Figure 2.2 in the context of the oblique photograph method.

Method 2: Geo-referenced satellite or vertical aerial photographs

- Most images were georeferenced. One image was purchased by MVO during the study period (December 2010, March 2011, Table 2.3) which was not geolocated. The image was georeferenced in ArcGIS10.1 using the hillshade of the LiDAR digital surface model (DSM) which provided control points (buildings, roads, large identifiable trees, extremely large boulders (10 m+) in vegetated fan areas) for geo-location of the image. Forty control points were used and these were distributed across the image. The Spline transformation was used which matches source points exactly to target control points, preferentiating local accuracy over global accuracy (ESRI, 2014). This method provided the most accurate results when the transformed image was compared with other control points on the LiDAR DSM.
- Images prior to 2010 were georeferenced to Montserrat National Grid. Images were transformed into WGS84 UTM 20N (Appendix 2.2f-h).
- As a reference point the total volumetric fill that could be contained in Tyres Ghaut was calculated based on a series of cross-channel profiles. For each aerial image that covered this area the width of the valley-floor was correlated with the width change with depth of the pre-eruption valley. The percentage area of the filled part of the valley cross-section was calculated. Using multiple cross-sections the minimum and maximum % fill was calculated and used to estimate from the total valley-fill, the amount of sediment in the valley (Figure 2.1).
- Several key assumptions were made: (1) the valley did not increase in size beyond its pre-eruption boundaries, (2) the valley profile increased in width with depth, (3) when PDC deposited material in the valley the bed surface was horizontal and (4) remained horizontal as channels were incised into deposit.
- Inclusion of channel incision in volumetric calculations of the deposits is shown in Figure 2.2 in the context of the oblique photograph method.

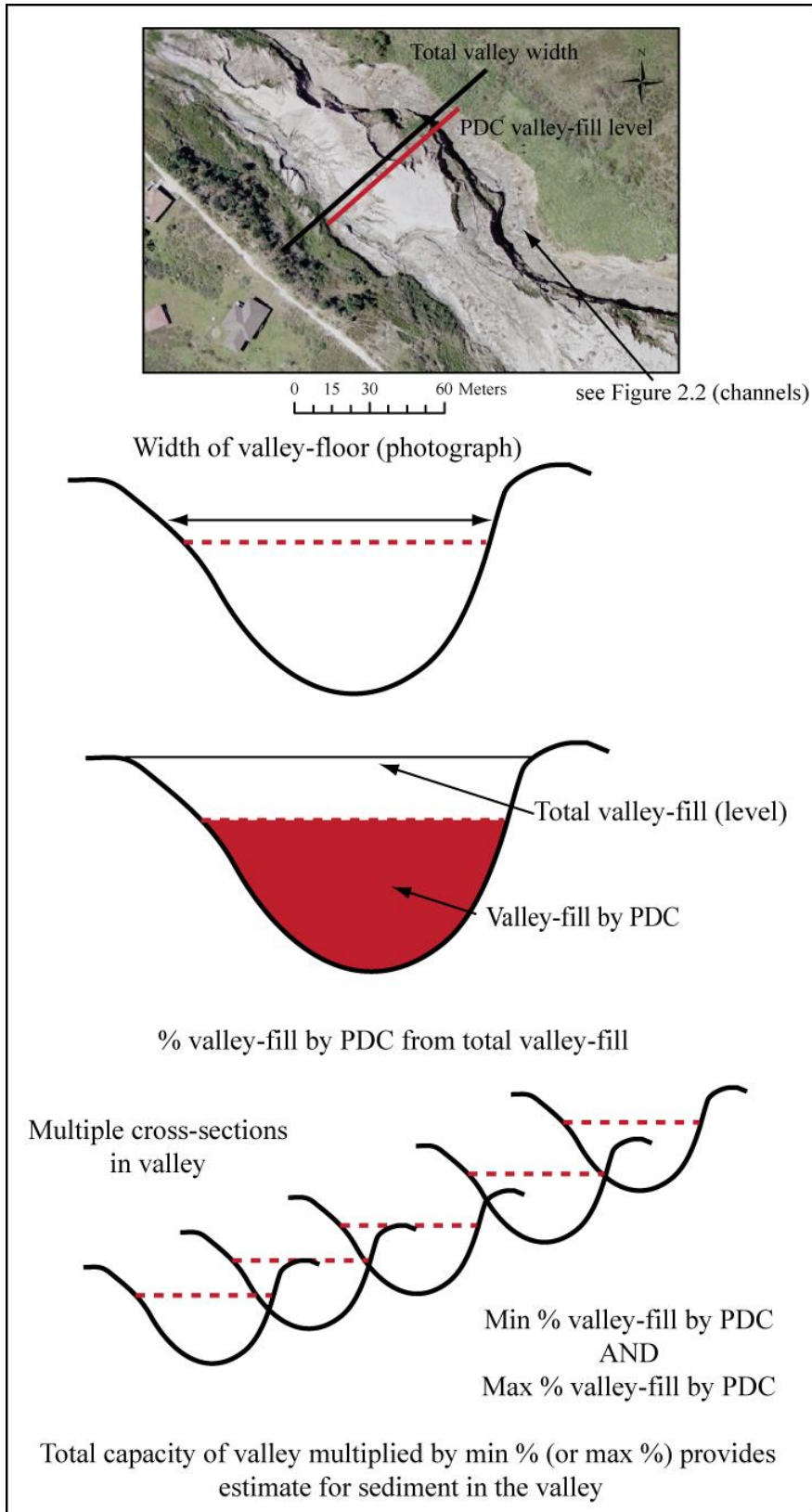


Figure 2.1 Calculation of Pyroclastic Density Current (PDC) volumes in Tyres Ghaut using vertical aerial/satellite photographs.

Method 3: Oblique aerial photographs

- Oblique aerial photographs were used with vertical aerial photographs. Oblique photographs provided more detail on the rates of channel incision into deposits because many oblique photographs were taken during observation helicopter flights and channel edges could be clearly delineated and measured relative to the total valley width and total valley fill.
- The method is shown in Figure 2.2.
- Oblique photographs were only used if: (1) common clear valley boundaries could be co-located in the oblique photographs and the vertical aerial/ satellite photographs and (2) the full valley width could be seen in the oblique photograph (looking up or down valley, not across).
- Repeat oblique and vertical photographs of the same cross-section of valley showed the infilling and evacuation of incised channels by sequential PDCs. During these periods the same PDC fill level could be used and channel-erosion rates and volume estimates of deposit removed in the channel calculated based on channel width change.
- Several key assumptions in addition to those in Method 2: (1) the channel only eroded laterally once it had reached bedrock at the base of the valley and (2) alluvial fill remaining in the base of the incised valley was not thicker than 0.5 m.

Discussion of methods

While calculations using repeat DEMs are more objective, there are only three surveys available for these drainages (Table 2.2). To supplement data, aerial/ satellite images were used (2002, 2006, 2007, 2011, 2012, 2013) and unreferenced oblique aerial photographs. The vertical aerial images provided measurements true to scale, but did not provide any depth information. The oblique photographs provided depth information depending on the orientation of the view, but the photographs contained uncorrected distortion (“pincushion distortion”) due to lens effects and relied on identifiable objects spread across the view to relate to scaled aerial photographs, in order to estimate changes. The errors involved in DEM differencing were calculated using the cell size and vertical precision of the method of topographic measurement. Aerial photographs were geo-referenced using features on the LiDAR DSM (horizontal error 1m). The method of measuring channel change in oblique photographs aimed to

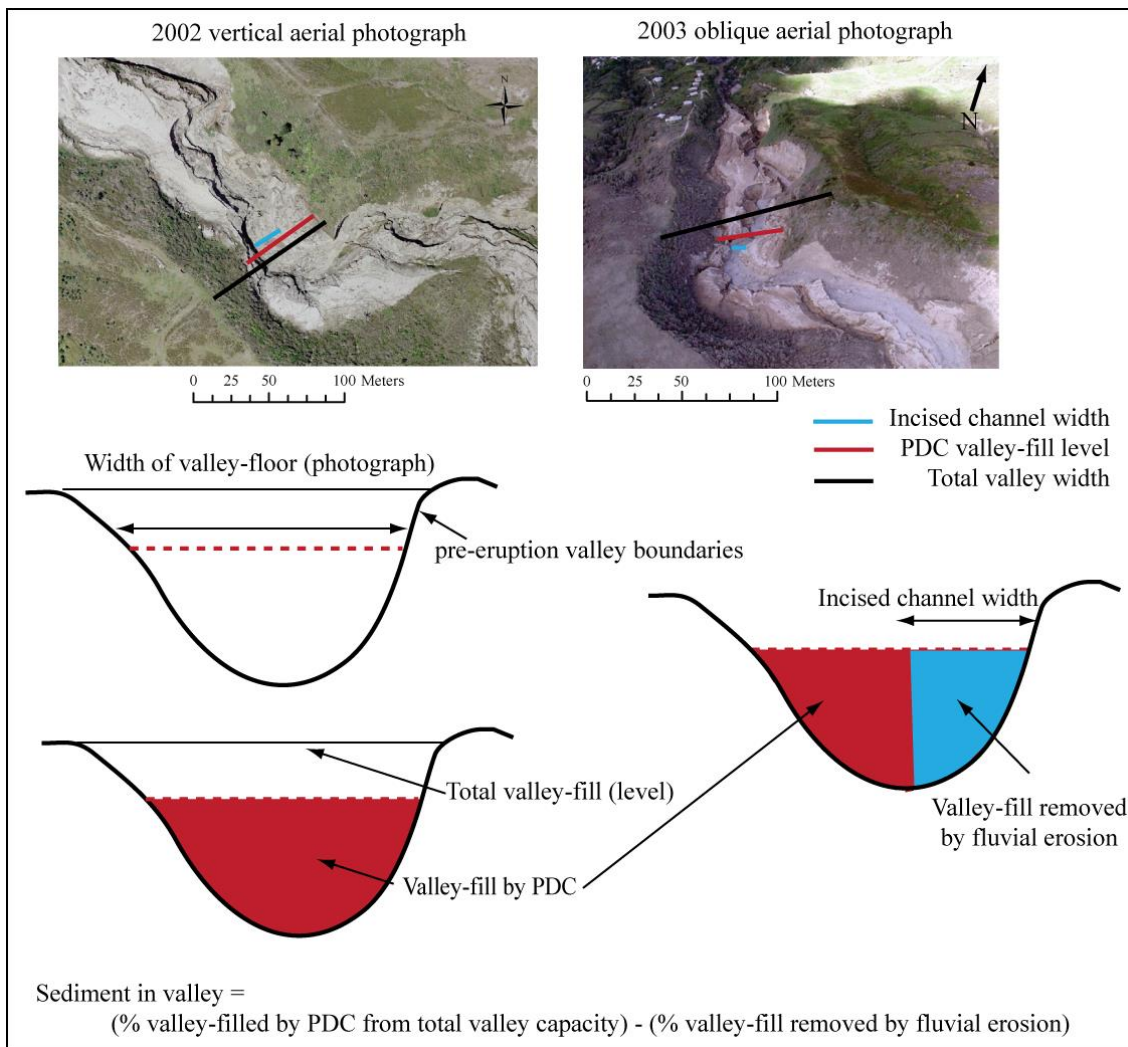


Figure 2.2 Calculation of Pyroclastic Density Current (PDC) volumes in Tyres Ghaut using oblique photographs and including measurements of channel incision.

reduce error caused by lens distortion and view angle, by considering changes to channel fill within well-constrained valley boundaries by co-locating boundaries on geo-located vertical aerial photographs (method 2); the horizontal error involved in these calculations is not thought to be significantly greater than the precision of the aerial image geo-location (horizontal error 1 m).

Estimation of valley sediment volumes using repeat aerial and oblique photographs were limited by several assumptions. The assumption was made that the depth of channel fill did not change between photographs; in the case of Tyres Ghaut, a semi-permanent (1999 to 2009) terrace of remnant PDC deposit remained in the channel and changes to the terrace (erosion) were identified relative to the fixed position of the valley wall in all photographs. Measurements capturing the rate of incised channel widening assume that flow spread laterally eroding unconsolidated fill deposits when it

hits harder bedrock at the channel base. Therefore making the assumption that (1) the base of the new channel corresponds with the pre-eruption channel boundary and (2) that no alluvial fill remained in the base of the channel before the channel started to laterally erode. This is unlikely to be the exact case, but significant bedrock erosion in Tyres Ghaut was not observed until 28/6/2005 (Appendix 2.3c) and the aerial photograph from January 2002 shows the channel bed to contain a high number of large boulders resting on areas of discolouration that correspond to the colour of bedrock. These observations suggest that volume calculations between February 1999 and June 2010 may be an underestimate because they do not account for increased channel capacity by bedrock erosion (caused by the primary flow and by secondary fluvial incision).

Vertical aerial photographs provided a greater spatial coverage than oblique photographs therefore volumes of valley-fill were calculated relative to pre-eruption topography from more cross-sections. Oblique photographs provided more regular channel coverage but only of a few valley cross-sections and not all at the same time. Calculating volume changes in valley-fill with respect to channel incision from one cross-section provides only a crude estimate of volume. However, comparison of the same cross-section through time captures the rate at which channels were widening in the PDC fill in response to fluvial activity. While Methods 2 and 3 may seem relatively simple they provide estimates of changes in valley fill and relative changes in incised channels that are appropriate for general discussion on catchment response to volcanic sedimentation in the context of more accurate measurements of catchment scale change and valley-scale change using DEM data.

2.2.2.3. Tephra fall

Tephra fall volumes and thicknesses for each volcanic phase (where data was available) were calculated by digitising published isopach maps (see references for isopach interpolation methods; Bonnadonna *et al.*, 2002; Edmonds *et al.*, 2006; MVO, 2010). The contours on the maps were used to delineate shapefiles in ESRI ArcGIS that were assigned with minimum and maximum fall thicknesses (relating to the contours). For each map the Soufrière Hills, St Georges Hill, Garibaldi Hill and Centre Hills sub-basins were extracted and the minimum and maximum thickness, and total volume were calculated. Calculations were combined to provide estimates based on volcanic phase when two or more maps were available per phase (see Appendix 3.2).

2.2.3. Belham River Valley change

Monitoring change in lahar prone valleys typically focuses on topographic scale changes to channel morphology at discrete cross-channel sections (Meyer and Dodge, 1988; Rodolfo *et al.*, 1989; 1996; Scott *et al.*, 1996; Umball and Rodolfo, 1996; Tanarro *et al.*, 2004; Muñoz-Salinas *et al.*, 2007), or using DEM differencing of the entire valley (van Western, 1997; Daag, 2003; Garcin *et al.*, 2005; Barclay *et al.*, 2007; Procter *et al.*, 2010; Darnell *et al.*, 2012). Some studies have extended volumetric analysis, categorising sub-structures within channels and levee structures (Tanarro *et al.*, 2010), in order to assess the impact of single lahars or specific periods of lahar activity on the valley morphology. This study used repeat DEM data in the context of an extensive ground-photograph archive (Appendix 3.4) and lahar database to discuss the evolution of the Belham River Valley during different Phases and pauses in the 19 year eruptive record.

2.2.3.1. Elevation

Prior to this study, previous researchers had undertaken GPS surveys of lower sections of the valley to monitor elevation change (Table 2.4). Data was in Montserrat National Grid and contained orthometric heights. Details of the GPS used, the GPS error and the accuracy of the processed DEMs are given in Table 2.4. Catchment-wide DEMs were also available (Table 2.2).

Three further GPS surveys were undertaken during the study period, one per year (in February/ March). The 2011 survey was undertaken with the Leica AT302 GPS antenna on a survey pole. The 2012 and 2013 surveys were undertaken with the Leica Viva GNSS GS15 antenna on a survey pole located in a survey rucksack (designed by Leica to support pole upright). All surveys were undertaken with the GPS set in kinematic mode and by person on foot. A quasi-systematic method was adopted, in which the perimeter of individual PDC terraces and river bars were surveyed in addition to a series of transects across the valley. Triangulated Irregular Network (TIN) surfaces retain information on steep breaks in slope if these are delineated during the data collection (Brasington *et al.*, 2000; Darnell, 2010); providing useful markers of terrace erosion between survey periods. Table 2.5 shows the post-processing procedure for data and provides an error budget depending on which GPS antenna was used. Figure 2.3 shows the post-processed GPS tracks for each survey.

Date	Coverage	GPS accuracy/ DEM precision	Source
January 2002	From 1.4 km upstream of the coast extending 610 m upstream	Leica AT302 antenna Accuracy: 10-20 mm + 1ppm Horizontal precision: 10 m x 10 m resolution	MVO/NERC Appendix 2.2i
May 2003	From 1.4 km upstream of the coast extending 930 m upstream	Leica AT302 antenna Accuracy: 10-20 mm + 1ppm Horizontal precision: 5 m x 5 m resolution	MVO Appendix 2.2m
May 2005	Coast to Sappit River	Leica AT302 antenna, CR344 controller Accuracy: 10-20 mm + 1ppm Horizontal precision: 10 m x 10 m resolution	Sušnik (2009) Appendix 2.2n
November 2006	Coast to Molyneux	Leica AT302 antenna Accuracy: 10-20 mm + 1ppm Horizontal precision: 10 m x 10 m resolution	Darnell (2010) Appendix 2.2o
November 2007	Coast to Molyneux (400 m downstream of November 2007)	Leica AT302 antenna Accuracy: 10-20 mm + 1ppm Horizontal precision: 10 m x 10 m resolution	Darnell (2010) Appendix 2.2p

Table 2.4 Archive DEM data of the Belham River Valley

Both archive DEMs and DEMs generated during this study were used to calculate elevation change and volumetric change related to lahar activity in the Belham River Valley. Due to differences in the extent of the DEMs (Table 2.3 and Figure 2.3), calculations were undertaken using common areas, and estimates were also calculated by fitting a three dimensional linear plane through data points in Matlab. Sections of this plane were used to “fill” holes in the DEM extent and provide estimates of change over larger sections of valley. Results are discussed in Section 3.5. Longitudinal profiles were calculated from each DEM using the pre-eruption valley thalweg. Cross-sectional profiles were also extracted from each DEM to show detailed morphological change.

Processing Steps	Method	Error
1 GPS survey	On-foot survey with GPS set in kinematic mode. MVO1 was used as base station. Base station was located 1.1 km from the channel. Data was saved in rinex format (.o, .n) (2011-2012) or Leica format (.m00) (2013) which was converted to rinex format in Tecq by MVO.	Leica AT302: vertical accuracy= \pm 10-20 mm, horizontal accuracy=10-20 mm. Leica GS15: vertical accuracy= \pm 15 mm, horizontal accuracy= \pm 8 mm. Human error: \pm 20 mm due to walking posture
2 Post-processing: Leica Geo-office (Appendix 2.2q)	Rinex data from the kinematic survey and the base station was imported into Leica Geo-office. Data was processed in precise mode using orbit information, precise ephemeris and antenna calibration. Full method see Appendix 2.1	
3 Data quality assessment	Resolved points were exported from Leica Geo-office into Matlab where they were assessed for quality. Points with a root-mean-square (RMS) error greater than 20 mm were removed from the data set. See Appendix 2.5 for number of points removed. See also Figure 2.3 for tracks. Spurious points which were not consistent with surrounding topography or observations were also removed, these were a particular problem at the vegetated edges of mid-reach parts of the valley.	
4 Interpolation	Points were imported into ArcGIS 10.1. Points for each survey were interpolated using a series of 'hard' breaklines (along sudden changes in slope) and a 'hard' clip which restricted the interpolation to the point cloud. Constrained Delaunay triangulation was used to connect the points in a series of triangles. Some areas of the lower Belham were not resurveyed because they were highly vegetated and showed no change. Points representing these sections in earlier surveys were included in the TIN.	
5 Elevation raster	For change analysis it is convenient for data to be in regular grids. The TIN was converted directly to an elevation raster using a linear interpolation.	10 m x 10 m horizontal precision. Vertical accuracy \pm 30-40 mm

Table 2.5 GPS post-processing and surface generation for 2011-2013 DEMs

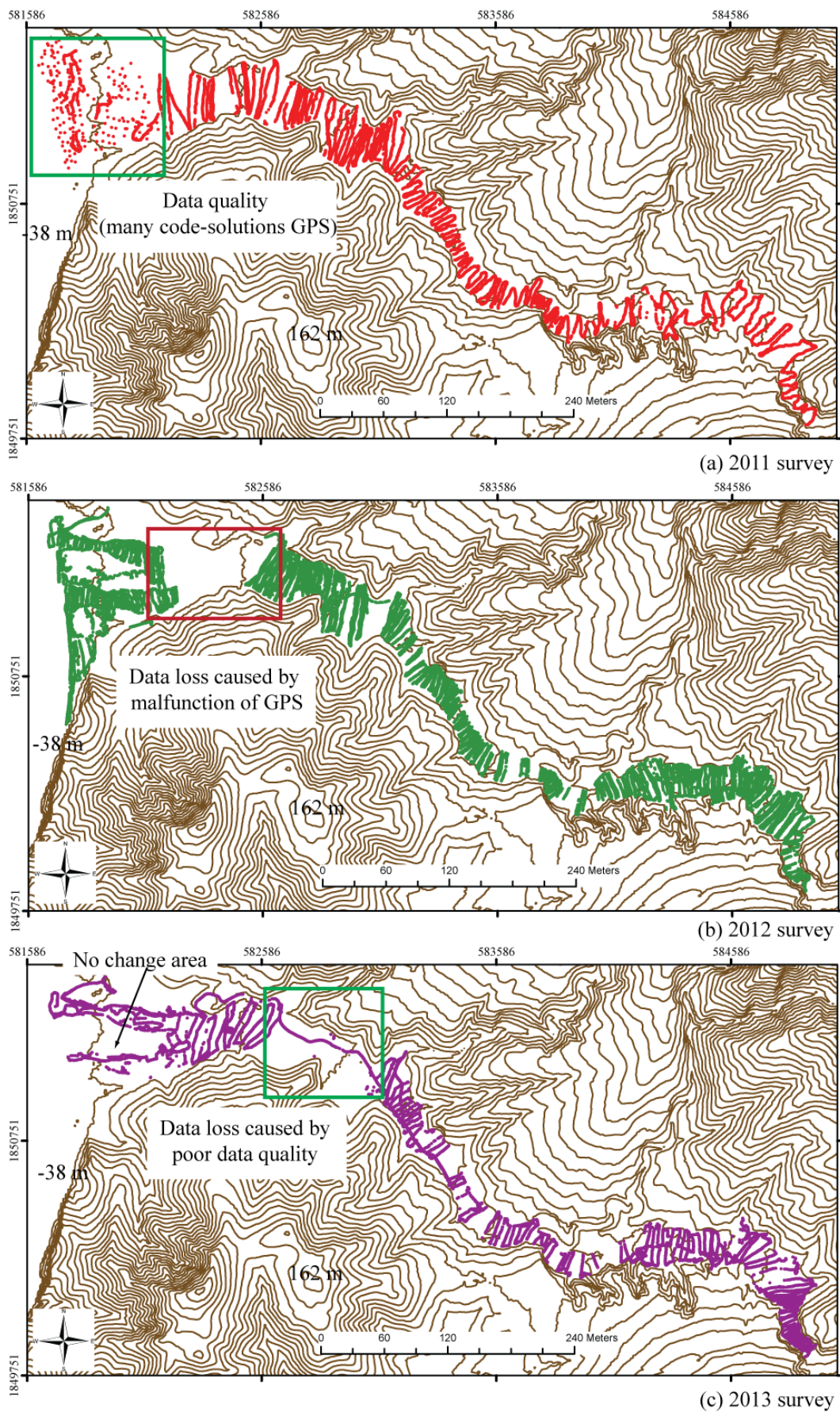


Figure 2.3 Post-processed GPS tracks from 2011-2013 surveys. The sea-level (-38 m) and top of Garibaldi Hill (162 m) are ellipsoid heights (Appendix 2.2r-t)

2.2.3.2. Lahar database

A lahar database (Appendix 2.2u) for the Belham River Valley was constructed from the record of visual observations by MVO staff (MVO, 2010), archive photographs, archive video footage and by analysis of the seismic records in cross-reference with rainfall records. Appendix 2.2v summarises seismic and rainfall data availability between July 1995 and present, relevant to the study. Lahars were identified as a very long period (~10 minutes- several hours) seismic signal (Zobin *et al.*, 2009) that had an elevated 2-5 Hz signal and peaks between 1-30 Hz, and were accompanied by seismic noise in the lower frequencies (<1 Hz). Examples are shown in Figure 2.4. During periods of intense eruptive activity it was difficult to identify lahars in the seismic record from other long-periods signals occurring repetitively, such as multiple PDCs during a partial dome collapse. Energy from wave impacts on the coast was also registered on some seismometers in the lower Belham River Valley during large storms which triggered lahars, as well as widespread wind effects, generating a complicated seismic signal. More recently migration of commercial sand extraction upstream with the day-time opening of Zone C (Section 1.7) has caused confusing periodic signals between the hours of 8 am and 4 pm that are very similar to lahars and caused by the movement of heavy machinery on the valley bed close to one of the seismometers. Furthermore, large lahars in drainages directly west of SHV generated seismic signals on local seismometers that were coincident with lahar signals registered on seismometers in the Belham Catchment. It is possible that lahars were occurring at the same time in different drainages around the volcano; however it is also possible given the same precise timing of events that a very large lahar in one drainage may have also been registered on seismometers in another, or that the signal was a composite of both events. Further investigation of this is beyond the scope of this thesis, however these observations highlight the importance of including a measure of lahar certainty in the database. It also should be noted that further analysis of seismic data beyond qualitative identification of lahars and the timings of the signal was not undertaken because the monitoring network is not preferentially located for analysis of lahar structure (see Doyle *et al.*, 2010).

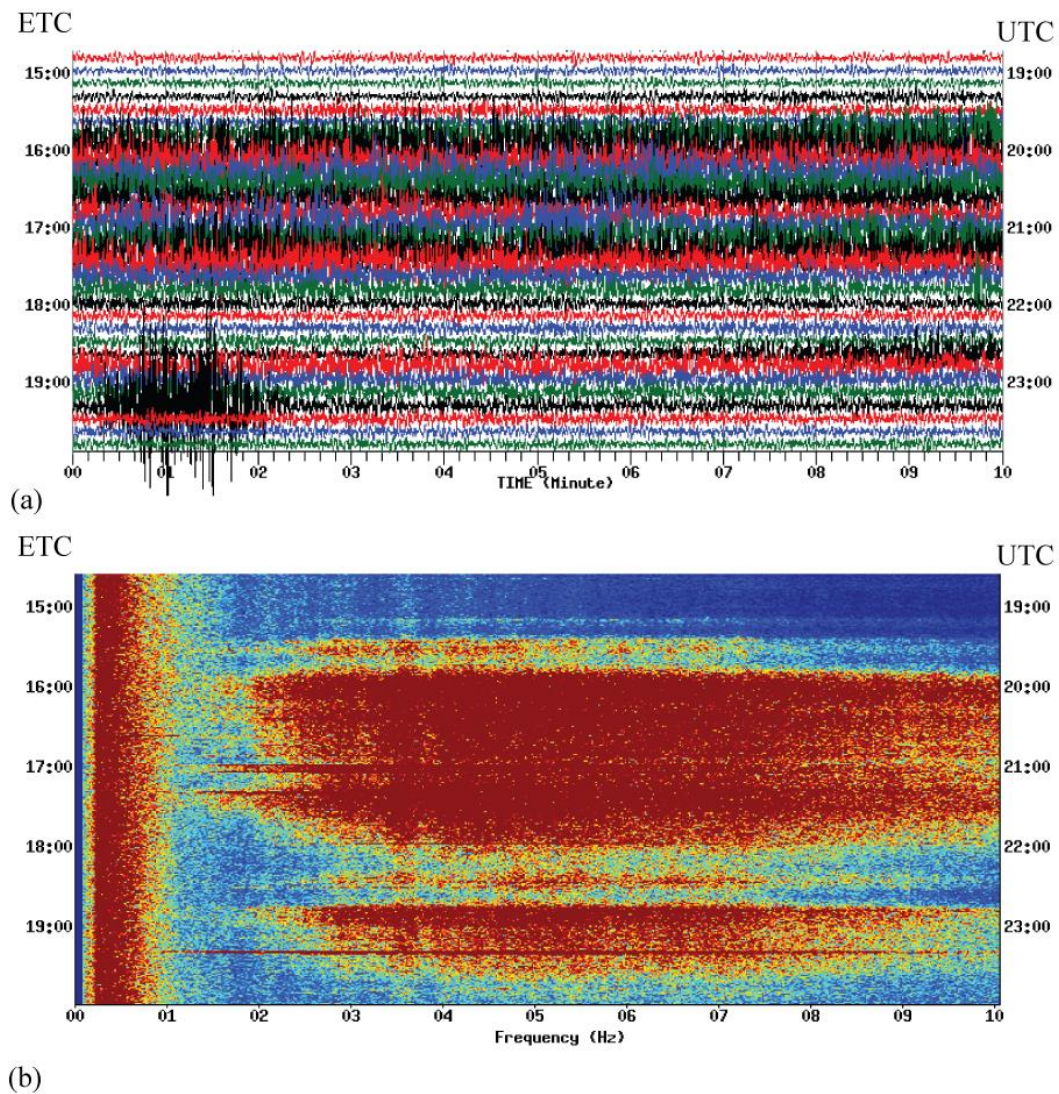


Figure 2.4 (a) Example of lahar 13/4/2010 (19:30 UTC onwards) on digital helicorder plot generated automatically by the MVO seismic network. (b) Example of lahar 13/4/2010 (19:30 UTC onwards) on spectrogram plot automatically generated by the MVO seismic network. Digital records were available from 1999.

To show the level of confidence awarded to each database entry a score system was used (Table 2.6). The scoring provided a systematic method of excluding uncertain entries from detailed analysis (Chapter 3) but also keeping uncertain entries on record for database completeness. Categories used in the scoring system were chosen to reflect: (1) conditions when lahar occurrence was more likely because of conditions in the Catchment (*e.g.* fresh volcanic deposition enhancing runoff, occurrence of rainfall), or (2) documented observations of lahars made on the specific date, and the number and precision of these observations (*e.g.* direct observation by MVO staff of lahar in the Belham River Valley scores highly, but a general lahar report with no declaration of drainage route does not score so well). Entries with a score less than 9 were classified as category 1 (uncertain), entries with a score between 10 and 24 were classified as

category 2 (lahar on west side SHV, likely Belham River Valley), and category 3 (Belham lahar, confident) entries were those with a score greater than 24.

Data	Description	Score
Volcanic extrusion	Phase	2
	Pause	1
Rainfall	Yes (data and registered rainfall)	1
	No (data, no rainfall registered)	0
Seismic signal	Clear lahar signal	7
	Unclear signal/ noise	1
	High low-frequency noise	0
Observation documented by MVO staff	Observed in the Belham, time given	24
	Observed in the Belham	23
	Lahar observed in drainage on west side of volcano	8
	Lahar observed in drainage on east side of volcano	1
Other	Hurricane/ Tropical Storm warning issued	1
	Documented by Sušnik (2009) in Belham	23
	Documented by Sušnik (2009), Belham not specified	1
	Documented by other studies (Belham specified)	8
	Documented by other studies (Belham not specified)	8
	Personal observations	24

Table 2.6 Scoring system of lahar database entries

Lahar size is typically described by total flow volume, based on measurements of discharge and duration, and observations that lahar volume controls inundation extent downstream (Iverson *et al.*, 1998). Estimates of lahar volume were not available for lahars in this study, primarily because many lahars in the database were not observed or measured. In this study large lahars were classified as those which occupied most of the valley floor at the Belham Bridge and persisted for over 24 hours with multiple peaks in discharge. Moderate lahars are defined as those which occupied at least 50% of the valley floor at the Belham Bridge, persisted for over 12 hours, possibly with multiple peaks in discharge. Small lahars were those which were confined to a single channel in the valley-floor, lasted a few hours and possibly did not reach the coast. Darnell *et al.* (2013) defined small lahars as those with total flow volumes (water and sediment combined) of 5.0×10^3 to $1.25 \times 10^5 \text{ m}^3$; the largest events they modelled in the Belham River Valley were volumes of $1.0 \times 10^6 \text{ m}^3$. When available, visual observations of “small”, “moderate” or “extensive” lahars were categorised regardless of number of peaks in discharge registered seismically; often the full duration of the lahar was not stated because observers did not include waning flow stages in duration definition, only peak discharges. When visual data was not available lahars were categorised using

seismic data into the three volume categories base on the number of seismic peaks registered in the 1-30 Hz range and the duration of those signals.

2.2.3.3. Rainfall data

Lahars in the Belham River Valley were initiated from runoff during and immediately after rainfall. Rainfall intensity-duration required to generate sufficient runoff to trigger a lahar depends on hillslope infiltration and roughness, as well as the presence, density, health and type of vegetation. It has been demonstrated on many volcanoes that rainfall intensity is the main factor for lahar generation (Lavigne *et al.*, 2000b). On Montserrat, there is considerable spatial variation in rainfall intensity during a single event (Barclay *et al.*, 2006). This presents a challenging environment in which to record rainfall peak intensity or maximum event volume, representative of rainfall received over the entire Belham Catchment (Barclay *et al.*, 2007). Direct rainfall measurements by gauges situated at elevated locations in the Belham Catchment provide the best estimates of maximum catchment rainfall due to adiabatic cooling when airflow is forced to rise over terrain (see Section 1.3). Measurements of rainfall have been collected by several parties between 1995 and 2013. Monthly rainfall summaries between 1995 and 1998 were available for Grove measuring station (deployed by UK Department for International Development and managed by Montserrat Utilities Limited), daily rainfall measurements were available between 1998 and 2002 at Hope rain gauge and sub-daily rainfall measurements were collected by multiple rain gauges and weather stations between 2001 and 2013 (excluding 2009) by UEA (Barclay *et al.* 2006) or MVO deployed systems (see Figure 2.5 and Appendix 2.2v for instrument locations). The tipping bucket rain gauges with data loggers with a 1-minute temporal resolution (Barclay *et al.*, 2002); the gauge's bucket measured rainfall with a tip every 2 mm. The weather stations (Vantage Pro 2) were deployed by MVO in 2010/2011 and contain a tipping bucket raingauge which tips every 2 mm, as well as collecting measurements of wind speed, temperature and humidity. Measurements by the rain gauges and the weather stations gauges were near-continuous, interrupted only by the tipping-motion of the bucket. Rainfall before 2001 was measured by manual rain gauges that recorded total rainfall over a set observation period. These gauges were not located within the Belham Catchment. The record after 2001 was collected by gauges within the Belham Catchment, but is not continuous because of rain gauge malfunction and shifts in the location of instruments in response to volcanic activity. Typically only one rain gauge (not necessarily the same rain gauge) was functioning within the Belham Catchment

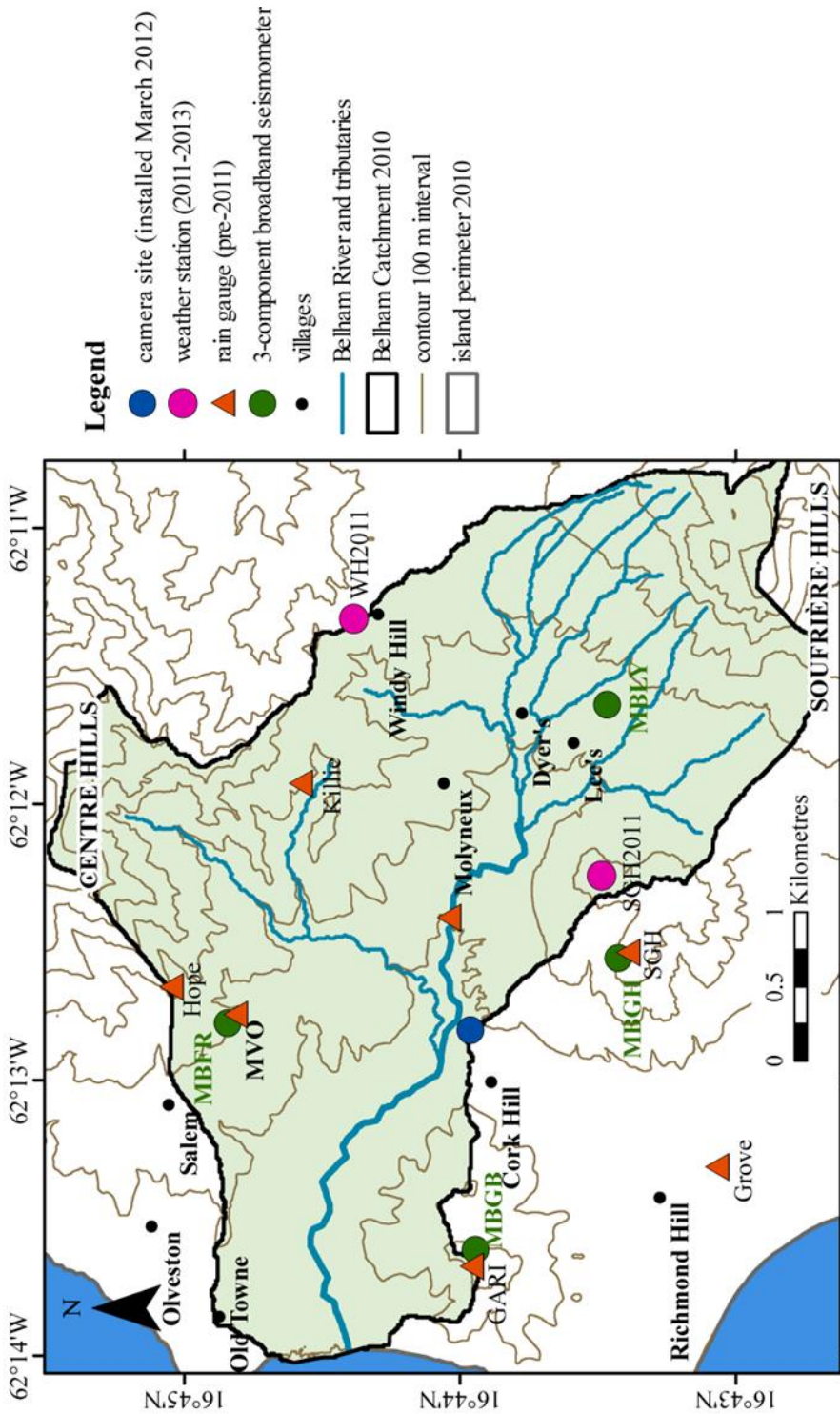


Figure 2.5 Map showing the location of the monitoring camera installed in March 2012, weather stations and seismometers operational during the period of study, and rain gauges that were operational prior to the study but provided data for analysis of rainfall on lahar days. The Belham Catchment is shaded in green. The topographic base map shows contours ascending from 0 m above sea level in 100 m intervals. Contours and drainage routes were calculated from a merged DEM from 1999 (north of island) and 2010 (south of island).

most of the time (see Appendix 2.2v for data availability), although rainfall measurements were made by other gauges located elsewhere on island.

Sub-daily rainfall data collected by SGH2011, WH2011, SGH, GARI, KILLIE, SGH and MVO2010 (Figure 2.5) were used to calculate antecedent rainfall before lahar (category 2 and 3) onset (date: time) over periods of 60, 30, 14, 7 and 1 day(s) in Matlab (see Appendix 2.2w-x). Pathiraja *et al.* (2012) advocated using up to 60 day antecedent rainfall when considering runoff dynamics in relatively flashy tropical systems. Lahar timing was determined using seismic registration where possible (see Section 2.2.3.2). Peak 1-, 10- minute and hourly rainfall was calculated for the 24 hours prior to lahar onset in Matlab (see Appendix 2.2w-x). Intervals were chosen following work by Lavigne *et al.*, (2000b) and results from Tuñgol and Regalado (1996). Rainfall sustaining flow (up to 24 hours after lahar onset) was also calculated in order to estimate total event rainfall volume, in relation to observed lahar magnitude.

2.3. In-situ instrumentation to measure intra-flow lahar dynamics

Lahar dynamics have been measured using a variety of non-contact (seismometers, geophones, cameras) and contact (dip samples, pressure cells) methods. Most non-contact methods have focused on calibrating seismic signals with lahar sediment load (Cole *et al.*, 2009; Zobin *et al.*, 2009; Doyle *et al.*, 2010; 2011), and until recently most visual based monitoring was used either as supplementary data for in-depth analysis of seismic signals or simply to indicate lahar occurrence but not intra-flow variability. This is in common with studies of flows and landslides in other locations (e.g. Debris flows, Comitti *et al.*, 2014, landslides, Yin *et al.*, 2012; river outlets, Cienfuegos *et al.*, 2014). Only a few studies have used visual data to interpret flow dynamics (Starheim *et al.*, 2013; Vázquez *et al.*, 2014) in the field.

2.3.1. Existing volcano monitoring network

The Soufrière Hills is a well-monitored volcano that has a network of ten 3-component broadband seismometers, two weather stations (installed March/ May 2011), two remote cameras monitoring the dome and a dedicated volcano observatory. Four seismometers (MBLY, MBGH, MBFL and MBGB) were located in the Belham Catchment (Figure 2.5). The two weather stations were located on boundary of the upper Belham Catchment on St George's Hill and Windy Hill.

2.3.2. Development of a bespoke remote camera unit

The camera system was designed in consultation with MVO. The system was funded by a UEA equipment grant (~£2000) and the MVO (provided power supply, expertise and installation). The following sections detail location and set-up.

2.3.2.1. Choice of site

It was important to situate the camera in a location that was both accessible and monitored a section of channel that represented the wider valley (not modified by aggregate mining), therefore best capturing event-based flow behaviour rather than site-specific dynamics. Specifically the site needed to monitor a section of the valley-floor that was: (1) unmodified by commercial sand extraction, (2) a relatively straight channel section, (3) preferably located in Hazard Zone C rather than Zone V, (4) secure (not clearly visible to road-users) and (5) within single line of sight with the MVO for telemetry between a single set of aerials. In 2011, Zone C was restricted access, and commercial sand extraction was limited in upstream extent by the Zone B- Zone C boundary just upstream of the Belham Bridge crossing (Figure 2.7). Locating the camera upstream of this point on the south-side of the valley ensured monitoring of a natural bed surface within line of sight of MVO. A site was chosen close to the old Cork Hill Primary school in Zone C (Figure 2.6), on the side of the valley 12 m above the valley-floor, looking cross-channel at a relatively straight channel-section (Figure 2.6). The site was cleared to create a field-of-view free of vegetation, and provide surfaces on which to situate solar-panels.

The choice of site had bearings on the camera set-up because the location on the south-side of the valley effectively cut off the camera for days if a large event occurred in the valley. Data collection and storage needed to be robust to periods of disconnection from the MVO and the failure of power source, in the event that the camera malfunctioned and could not be readily accessed.

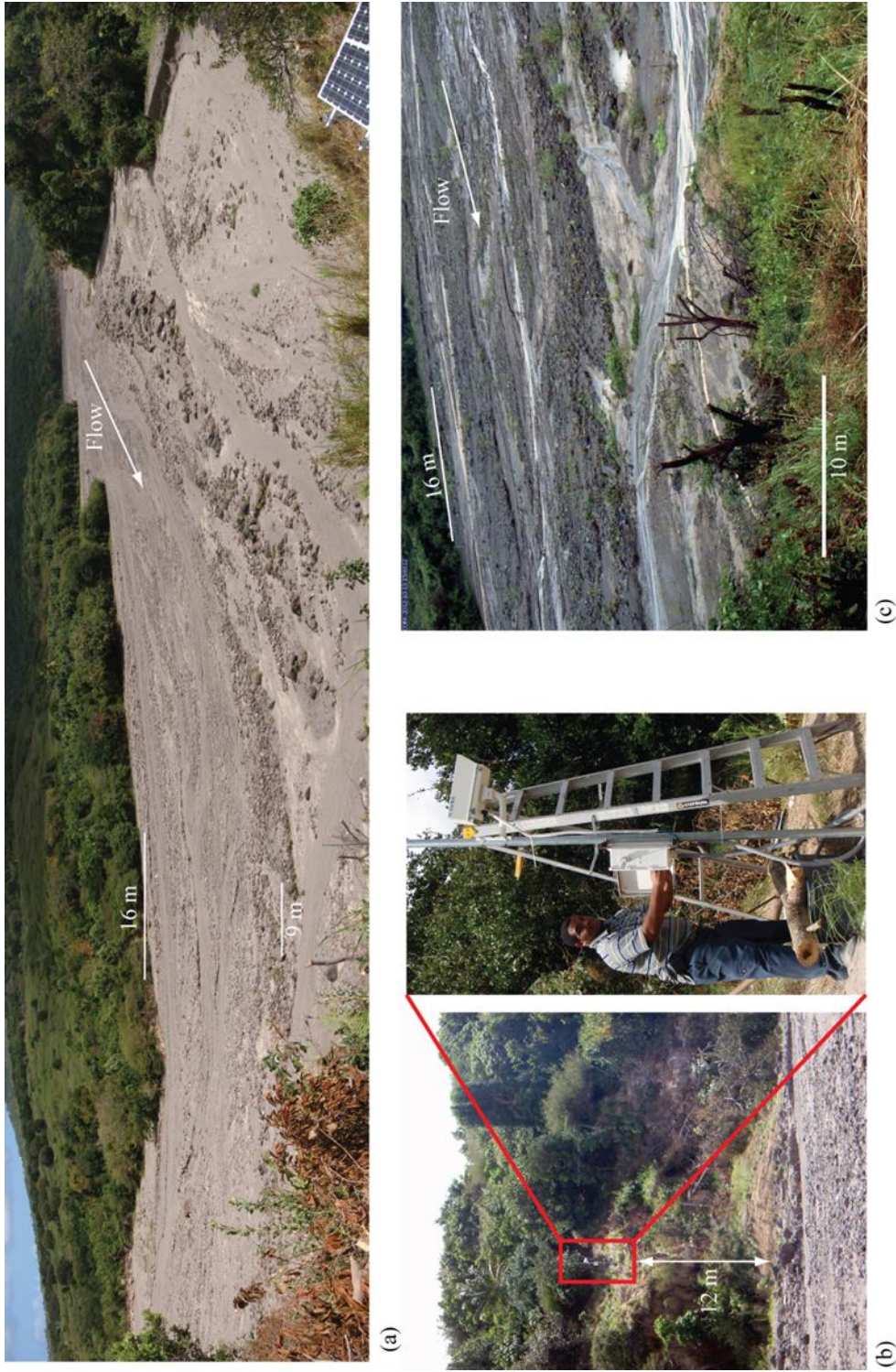


Figure 2.6 (a) Photograph looking from north to south across the valley-floor at the camera site (March 2012). (b) Camera location 12 m above valley floor and set-up on pole. (c) Example of camera image of valley floor (annotated). Multiple scale bars are included in several images showing the change in scale between the foreground and background

2.3.2.2. Instrument set-up

A Stardot SC 5mp IP camera was used in the system because cameras from the same manufacturer were already being used by MVO to monitor SHV, therefore staff at the MVO were familiar with the camera and software, and this provided added flexibility to add the camera into a network of multiple monitoring cameras at a later date. A wide-varifocal auto-iris lens was used (LEN-MV48AI) which had a 4 ~ 8mm focal length and manual focus/zoom. The camera was powered by two 100 watt solar panels which charged two 12 v car batteries. A Tycon charge controller (TP-SCPOE-1224) regulated the voltage from the batteries to the camera and telemetry. The camera was telemetered with MVO using two Ubiquiti PowerBridge M5 aeriels which created a point-to-point wireless bridge for data transfer between the remote camera site, the MVO and the UK via VPN access. This set-up had a track record of success from a concurrent project (AVTIS; NERC, 2014). The aerial was powered by power-over-ethernet (PoE) supplied by the charge controller. The camera was contained within a heavy duty outdoor enclosure (Stardot ENC-OUTD, 12") that was designed to protect the camera from the elements (Figure 2.6b). The enclosure benefitted from a wide overhang over the glass viewing window that reduced glare from bright sunlight and prevented rain-drop build up during heavy rainfall. Given the tropical climate and that lahars in the Belham River Valley were rainfall triggered the camera casing was a small but important feature for good image collection. The camera and aerial were mounted to a pole 1.7 m and 1.37 m above ground, respectively. Cabling between different elements in the system was IP67 rated.

The camera system was installed in March 2012 and functioned well in the field. Initially the camera acquisition rate remained stable at 1 frame every 4 -5 seconds (see Appendix 2.6 camera tests by Adam Stinton in June 2012), which was sufficient to capture a boulder travelling at 4 m s^{-1} across the 53 m length of channel in the image frame, with 3 images. However in July 2012 the frame acquisition rate dropped to 1 frame every 15 seconds, which was insufficient for analysis of intra-flow variability. The specific cause of this frame-rate drop is unknown; tests on telemetry, power and the camera unit were undertaken by MVO staff at the time, however it is likely that a combination of all these factors caused problems with the system. Primarily reliance on data transfer to the observatory directly from the camera meant image acquisition rate was dictated by connection speed. In addition, there were issues with the camera

rebooting after power outages at the site which were caused by long periods of overcast weather.

Given investment of time and finances in the system, the decision was made to develop a field computer to act as a bridge between the camera and telemetry, and as a controller at the site to initiate image capture. Inspiration for the computer came from the recently released low-cost (~£25) Raspberry Pi low-powered credit card sized computer that provided a basic linux operating system in which to run simple scripts. An image capture script was written by Alex Etchells at UEA (Env Software; see Appendix 2.7 for script) and was edited after field installation to adjust image capture times, frame rates and image transfer to MVO. The field computer (Figure 2.7) was built in a Peli case that was sealed to IP67 rating and contained a heat sink, the Pi computer, 120 GB low-spin rate harddrive and a power regulator. Electronics in the field computer were installed by Dave Blomfield (UEA electronics).

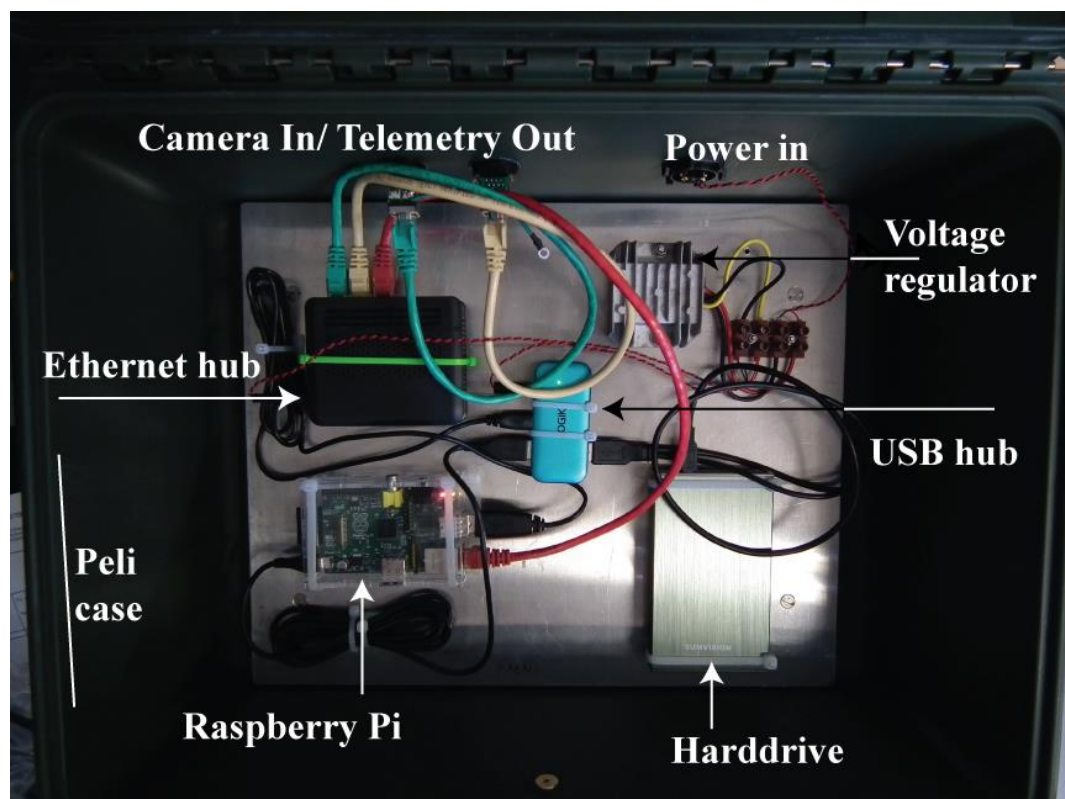


Figure 2.7 Field computer (components inside the peli-case)

Installation of the field computer in the Belham River Valley camera set-up increased the acquisition frame rate to 1 frame per second. Data was initially stored in zip files on the field computer and then transferred overnight when image capture was not ongoing. However, this was found to drain power from the batteries however

preventing the camera restarting in the morning. The storage mechanism was switched to manual transfer that was possible by two-way telemetry communication between the site and MVO. Data was automatically overwritten after ~4 days due to storage space on the hard drive, but this provided enough time to download images of interest by remote connection (or manual pick up). An example camera image is shown in Figure 2.7c.

It should be acknowledged here that as with every monitoring set-up several iterations occur before the system functions well in the field. Many different tests were run on equipment at different stages of development back in the UK; however these did not replicate conditions in a tropical volcanic environment. Specific considerations: (1) ants, (2) wasps, (3) rust and (4) wind speed have all caused problems at the site since installation. In the case of the field computer the casing cost triple the total value of the contents, however it is the computer is the only piece of equipment other than the IP camera (in an equally rugged case) that has not had to undergo significant maintenance during the study period.

2.3.3. Image processing for flow measurement

Imagery was used to measure the length of water-surface-waves in trains, the size of boulders transported in the flow, and the velocity of surge fronts and floating objects in the flow. Velocity measurements of clear objects/surges were calculated using the distance between two known points (differential GPS) in the image and the time taken for the object/surge to travel over that distance based on the image time stamp. For stationary or migrating objects in the channel more involved methods were used. There are two main methods for calculating the size of an object in an oblique photograph: (1) by photogrammetry or (2) using multiple objects of known size distributed evenly across an image to derive an image point: metre scaling law. Photogrammetry is based on the geometric relations between the camera position, focal length (of the camera lens), principle point in the photograph, inclination angle of the camera axis and horizontal and vertical angles to an object of interest in the image (Wolf and Dewitt, 2000). The coordinates of ground points in a “tilted” photograph are calculated based on camera and lens characteristics and camera position in real-world coordinates, these are used to calculate the *elements of exterior orientation* expressed as the spatial position of the camera and the angular orientation of the tilted photograph (the tilt-swing-azimuth of the system relative to the ground surface) (Wolf, 1983). Several

methods of calculating these parameters have been developed depending on available data (e.g. the Church method), and commercial software is available to automatically process images. Initially this had been the method of choice for processing camera imagery, and preliminary tests using PicWorks software developed by Richard Herd (MVO) to measure dome deformation by sets of oblique photographs showed promising results after initial troubleshooting (<1 m error, Appendix 2.8) in certain parts of the image. The method was contingent on three GPS control points that were established by three metal poles located in the foreground and background of the image (north and south of the valley-floor, Figure 2.8), and measured using differential GPS (static, Leica GS15 aerial, ± 3.5 mm vertical accuracy). However initial tests showed the software had problems resolving the internal geometry of the image using the poles because they were not located at the edges of the photograph and the tilt angle of the photograph was very acute. A fourth point towards the right side (upstream end) of the image was measured (large boulder) to improve calculation of the internal geometry and measurements (results shown in Appendix 2.8). Problems arose in May 2014 late on in the study with the GPS control point data. Conversion of the raw Leica files from the GPS controller to rinex files (obs and nav files) using Tecq had resulted in an undetected shift in vertical elevation in the output rinex data (addition was not systematic), resulting in incorrect elevation data at the camera site and the requirement to recalculate the *elements of exterior orientation*. Due to time constraints and mindful that a simple method may provide solutions with accuracies appropriate for flow analysis in this study, an alternative approach was taken.

The alternative method used the distance between two poles of known position in the background (north side of the valley, line A) in the image, and the distance between a pole and a large boulder of known position in the foreground of the image (south side of the valley, line B). Figure 2.8 shows the location of these measurements in the camera image and Table 2.7 shows the point coordinates (image scale)¹ and corresponding WGS84 UTM 20N coordinates used in the calculation.

¹ 'points' are image coordinates. Between P1 and R1 1 pt=133 pixels

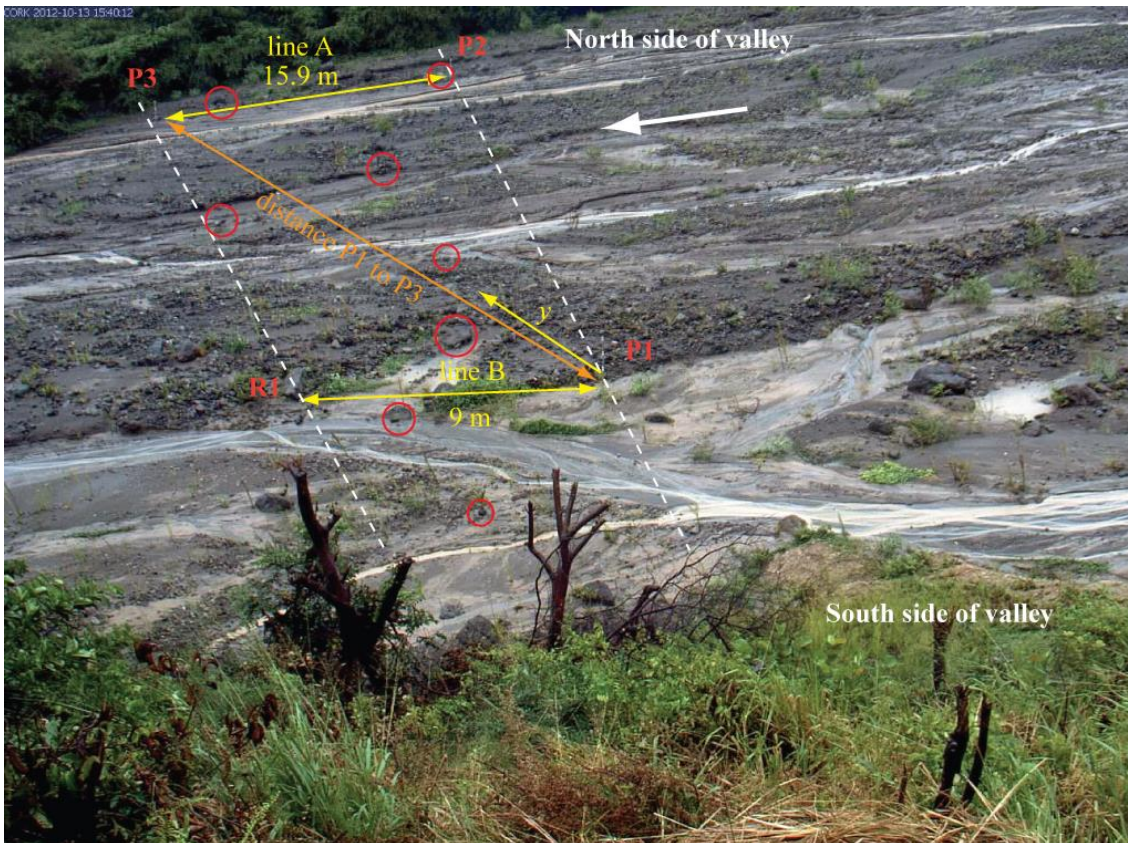


Figure 2.8 Calculation of point: metre scaling law. Red circles show the location of measured boulders used to test Equation 2.2. Multiple scale bars are included in several images showing the change in scale between the foreground and background.

Pole	Point coordinates			WGS84 UTM 20N (m)		
	photox	photoy	photoz	realx	realy	realz
P3 (bottom)	5.27	5.49	0	583887.2	1850203	28.34
P3 (top)	5.27	6.07	0	583887.2	1850203	29.324
P1 (bottom)	1.33	8.64	0	583879.9	1850267	30.23
P1 (top)	1.28	8.85	0	583879.9	1850267	31.13
P2 (bottom)	3.94	9.15	0	583895.6	1850265	29.16
P2 (top)	3.94	9.38	0	583895.6	1850265	30.14
rock (bottom)	2.55	5.29	0	583878.3	1850205	29.89
rock (top)	2.55	5.51	0	583878.3	1850205	30.24

Table 2.7 Pole coordinates, elevations based on February 2012 bed surface

The pixel: metre ratio was calculated between points in line A and line B of the image. The ratio in the foreground was 1 point: 3.35 m, the ratio in the background was 1 point: 8.59 m. These measurements in combination with the point distance between the two lines (5.05 points, from P1 to P3) were used to calculate a linear equation for change in point: metre ratio with position between line A and line B (Equation 2.2).

$$y = 1.039x + 3.35 \quad \text{Equation 2.2}$$

Where x was the distance (on the line between P1 and P3) from P1 in the foreground of the image and y was the number of metres for every point (see Figure 2.8). The point location of objects (or lengths of objects) in photographs were measured in DigitizeIt software (DigitizeIt, 2014). For water-surface-wave trains, where the lengths of all waves in the train were measured and then averaged for further calculations, the mid-point of the wave train was used to calculate x and the same y scaling coefficient was used to convert pixel distance to metres for each wave in the train measured.

The measurement of objects of known size in the photographs spread across different parts of the image within the boundaries set by R1 to P3 and P1 to P2 (shown in Figure 2.8) and application of Equation 2.2 to convert point lengths to metres showed that error was greatest on the north side of the valley furthest from the camera. Error ranged from 0.1 m in the background of the image to 0.05 m in the foreground. These errors encompass photograph measurement error (selection of the points delineating an object/ flow feature), lens distortion effects and human/ GPS error in object measurement in the field. The scaling law was not tested outside of the bounds of the image frame. In the context of water-surface-wave length measurements, which were used to derive flow velocity and depth (Chapter 4), measurements in the first instance should be compared to wave trains in the same part of the channel, to consider relative changes in flow. Absolute measurements should be discussed with caution in recognition of limitations of the method of point: metre conversion outlined in this section. See Appendix 2.2y for dataset.

2.4. Additional measurements collected during 13th-14th

October 2012 lahar

During this study a large lahar was triggered in the Belham River Valley by Tropical Storm Rafael on 13th-14th October 2012 (Section 4.3). This event was captured by the existing monitoring network (Section 2.3.1), the monitoring camera (Section 2.3.2) and in addition ground photographs/video were taken, and suspended sediment concentrations of flow estimated from dip samples. This section details the method of generating an event rainfall time series, the method of sampling suspended sediment from flow, and the location and timing of ground photographs and video.

2.4.1. Event rainfall time series

Only one rain gauge was operational during Tropical Storm Rafael (the SGH2011 station), and this developed a fault just after 04:00 UTC on 14th October 2012. This fault was diagnosed when the rainfall rate was plotted against time (Figure 2.9). Rainfall rate was calculated over time steps of 15 minutes to reduce variance in the time series by averaging out heterogeneity within the convective storm. This provided a more representative time series of catchment average rainfall intensity. Figure 2.9 shows a series of consistently high, unrealistic measurements from 274.4 mm hr⁻¹ to 288 mm hr⁻¹ over 8 hours 45 minutes (between 08:44 UTC to 17:29 UTC 14/10/2012), which would have resulted in accumulations in excess of 2,000 mm. Measurements are thought to be unrealistic because rainfall fluctuates between higher and lower intensities with time, and measurements of rainfall during the same storm on neighbouring Guadeloupe (World Meteorological Organisation, 2013), were one magnitude lower, equating to just 100 mm of accumulation in 3 hours. Measurements by the rain gauge on the 13th October are within the range anticipated (Figure 2.9).

The gauge's catch depends on environmental conditions (such as wind speed, temperature) and precipitation characteristics (Sevruk, 1982), which vary with each precipitation event (Yang *et al.*, 1995a). Tests by Yang *et al.* (1998) on the U.S. National Weather Service (NWS) 8-inch standard gauge, indicate wind speed is the only environmental factor to have a statistically significant impact on gauge catch. Yang *et al.* (1998) derived models for the daily catch ratio of the U.S. NWS 8-inch standard gauge as a function of daily wind speed at the gauge height using WMO inter-comparison data. Numerous other models have been published to correct other types of shielded and unshielded gauges, however Yang *et al.*'s (1998) is a simple textbook approach, relevant to the dimensions of the SGH2011 rain gauge (which also has a 8.75 inch rain collector diameter). The correction factor (K_{ru}) for rainfall collected in an 'unshielded' gauge is calculated for the SGH2011 rain gauge for 13th October 2012 using wind speed² measured by the SGH weather station² on which the SGH2011 gauge is situated. Windspeeds ranged between 2.2 m s⁻¹ and 19.8 m s⁻¹ (Figure 2.10a). K_{ru} is calculated for each measurement of wind speed (W_s) using Equation 2.3 (modified from Yang *et al.*, 1998 in Dingman, 2002).

$$K_{ru} = 100 \cdot \exp(-4.606 + 0.062W_s^{0.58}) \quad \text{Equation 2.3}$$

² The anemometer is located at the same height (1.5 m above ground) as the rain gauge.

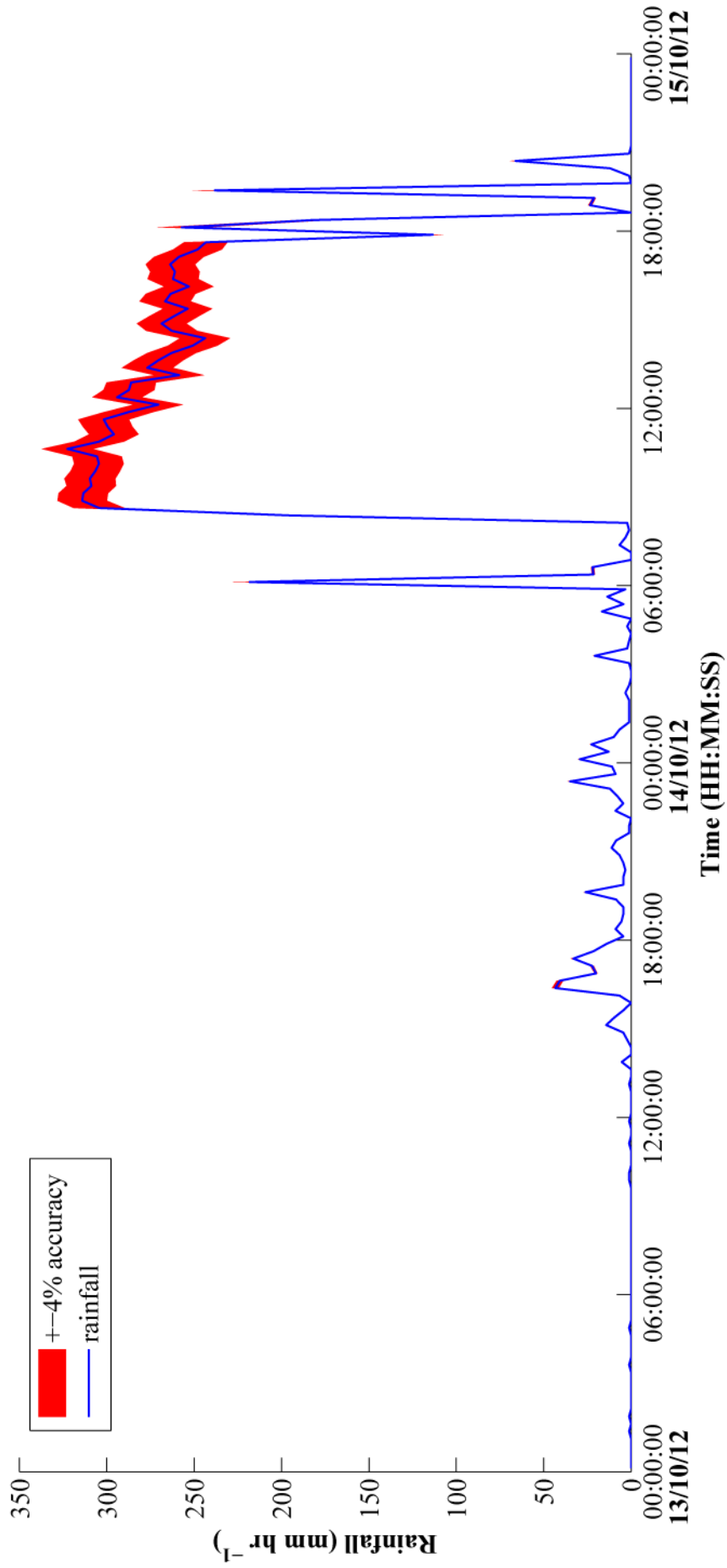


Figure 2.9 Rainfall rate calculated from 15-minute rainfall accumulation at the SGH AWS tipping-bucket rain gauge between 00:00:00 UTC on 13th October 2012 to 00:00:00 UTC on 15th October 2012. Error range shaded red is based on manufacturers guidance that instrument measurement is to within 4% accuracy (Davis Instruments, 2010).

The SGH2011 rain gauge data is multiplied with the corresponding K_{ru} value, to produce an adjusted rainfall (mm) time series for 13th October (Figure 2.10b). Wind-induced errors cause an underestimate of rainfall by between 14.5% and 42%. (Yang *et al.*, 1998) test their model on wind speeds up to 6.5 m s^{-1} ; the wind speeds measured on 13th October 2012 exceed this, and it is possible that the relationship alters with wind speeds over 6.5 m s^{-1} , resulting in a potential under- or over- estimate of K_{ru} (and adjusted rainfall). This will not be investigated as part of this study. Figure 2.11 shows the 15 minute rainfall rate (mm s^{-1}) calculated from the adjusted rainfall.

Data from the Mètèò-France Guadeloupe (MFG) rainfall radar is used to continue the time series into 14th October 2012, and provide a reference for ‘relative’ peaks in rainfall over the entire storm event. The MFG radar is a GEMATRONIK 28 GHz S-band Doppler, non planimetric system with a maximum range of 400 km (Tabary, 2006). Montserrat is 30 km from Guadeloupe and is located within the MFG 100 km maximum range rainfall intensity product (Figure 2.12). The raw reflectivity values (Z , dBZ) were not available and the exact method of calibration and adjustment between Z and rainfall (R) is not specified (data is processed by Mètèò-France’s CASTOR 2 computer, Tabary, 2006). The radar has been calibrated using local rain gauge measurements on Guadeloupe. Adjustment of the calibrated radar data to correct for range, orographic occlusion³ and orographic enhancement⁴ have not been undertaken for Montserrat and are beyond the scope of this project. Therefore, rather than an estimate of absolute rainfall intensity, the MFG radar data is useful in showing relative peaks in rainfall intensity.

The MFG radar data set (13/10/2012- 14/10/2012) is composed of 530 time-stamped images, with a pixel: spatial resolution of 1 pixel: 500 m^2 and a sampling resolution of 5 minutes. Images were manipulated in MATLAB (see Appendix 2.2z-aa). Pixels contained within the Belham Catchment were extracted from each radar image, converted from the RGB colour scale in the image (Figure 2.12) to rainfall intensity values (mm s^{-1}) and the average and maximum value in the catchment for each time step was calculated. The time series was converted from 5-minute to 15-minute intervals to provide continuity with the rain gauge time series for 13th October 2012.

³ Large topographic obstacles may partially block the radar beam (Andersson, 1991). The SHV interrupts the lowest 914 m of the radar beam, partially shadowing radar registration of rainfall in the Belham Catchment between 0 and 914 m elevation.

⁴ Specifically the seeder-feeder mechanism: the uplift of strong moist low level flow over hills, leading to the formation of capping clouds which scavenge precipitation from synoptic scale systems above (Purdy *et al.*, 2005).

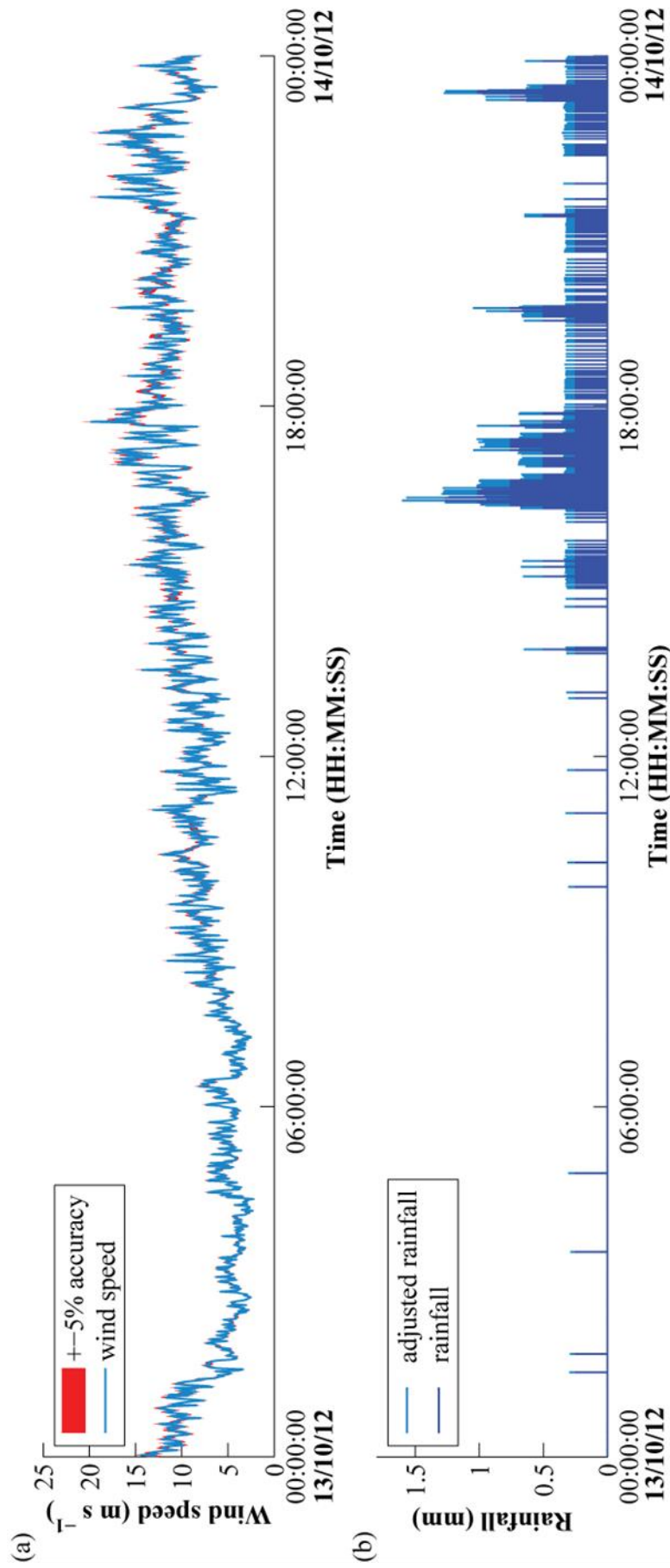


Figure 2.10 (a) Wind speed at the SGH AWS tip bucket rain gauge between 00:00:00 UTC on 13th October 2012 to 00:00:00 UTC on 14th October 2012. Error range shaded red is based on manufacturers guidance that instrument measurement is to within 5% accuracy (Davis Instruments, 2010). (b) Rainfall (mm) measured by the SGH AWS tip bucket rain gauge every minute between 00:00:00 UTC on 13th October 2012 to 00:00:00 UTC on 14th October 2012 (blue). Adjusted rainfall (mm) using the (Kru) correction factor is shown in light-blue. Errors (not displayed) were 4% for rainfall (described in Figure 4.3). Adjusted rainfall error 11% equates from the manufacture's guidance for rain gauge and anemometer measurement accuracy (Davis Instruments, 2010), and the performance accuracy of (Yang et al., 1998)'s model, reported at 2% (Yang et al., 1995b).

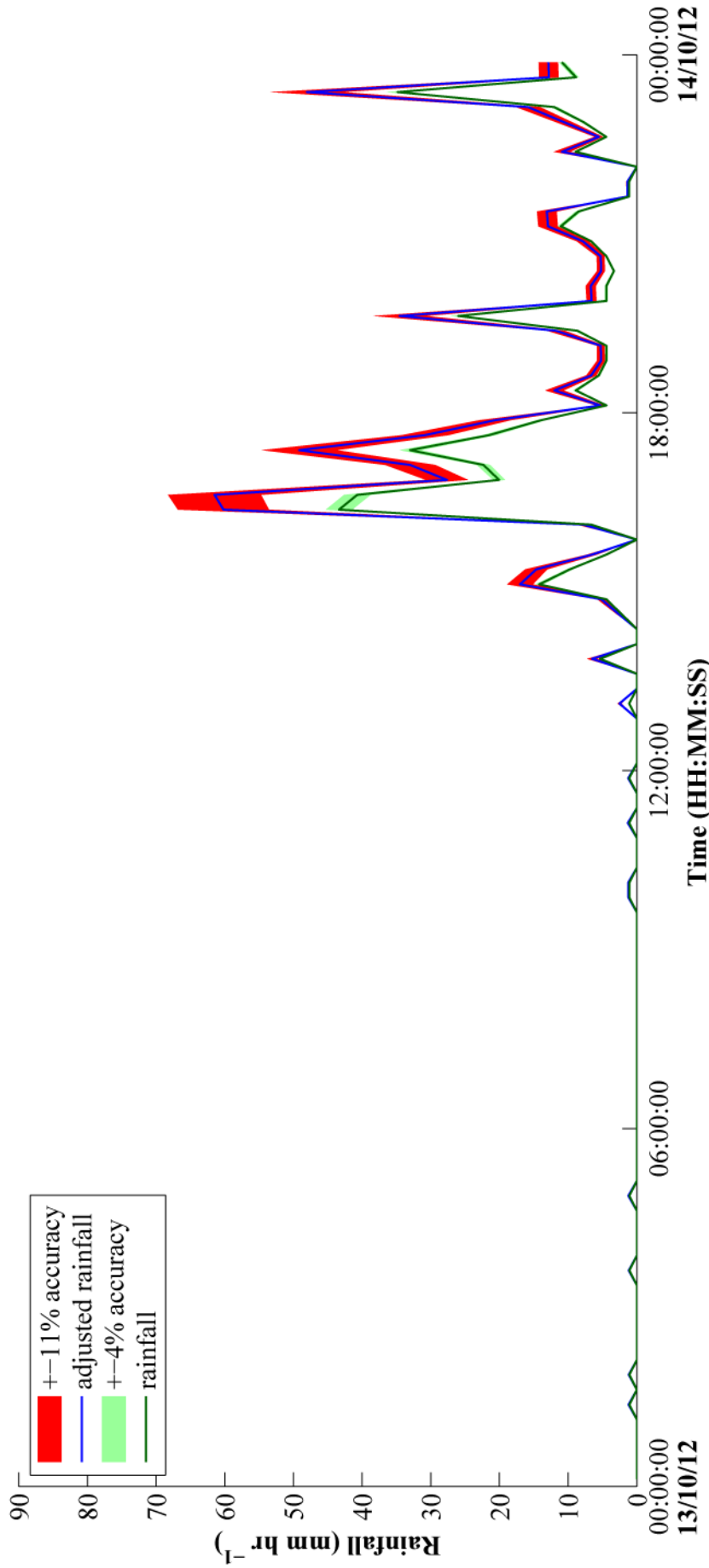
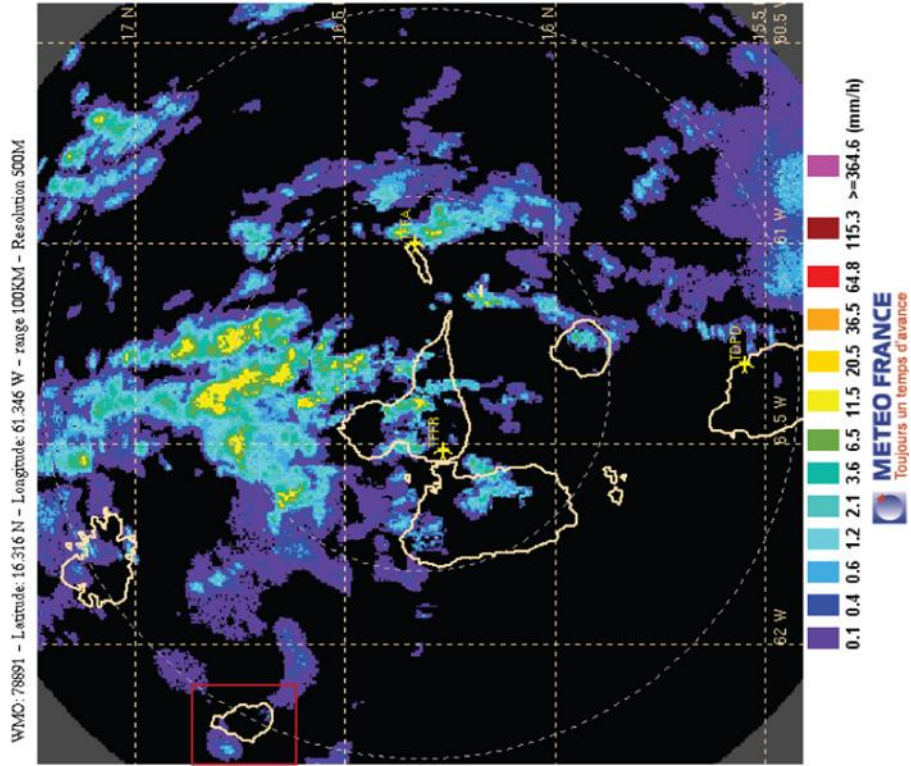


Figure 2.11 Rainfall rate calculated from adjusted rainfall over 15-minute intervals between 00:00:00 UTC on 13th October 2012 to 00:00:00 UTC on 14th October 2012 (blue). See Figure 4.5 for adjusted rainfall error (red) description. Also shown, original rainfall rate (green) calculated from 15-minute rainfall accumulation at the SGH AWS tip bucket rain gauge between 00:00:00 UTC on 13th October 2012 to 00:00:00 UTC on 14th October 2012. See Figure 2.9 for rainfall error (green) description

(a) **Radar GUADELOUPE (FWI) 12/10/2012 23H00 UTC (Loc+4H)**



(b)

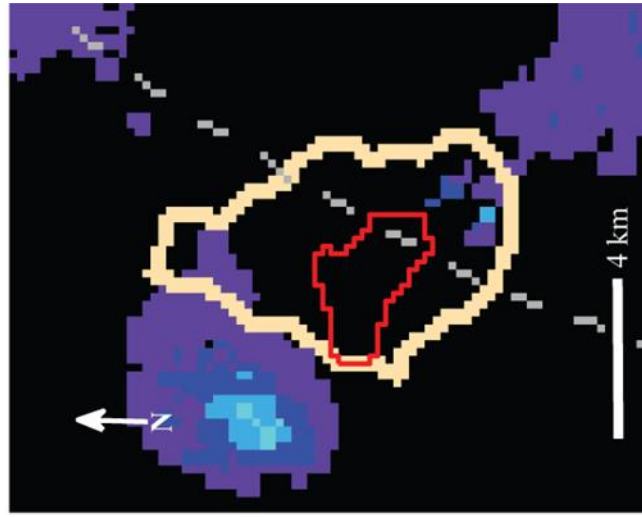


Figure 2.12 (a) Example of MFG radar image. Montserrat is located in the red box to the north-west. (b) Location of the Belham Catchment in Montserrat, on the radar image. Pixels were extracted from the radar image within (and inclusive) of the red catchment boundary.

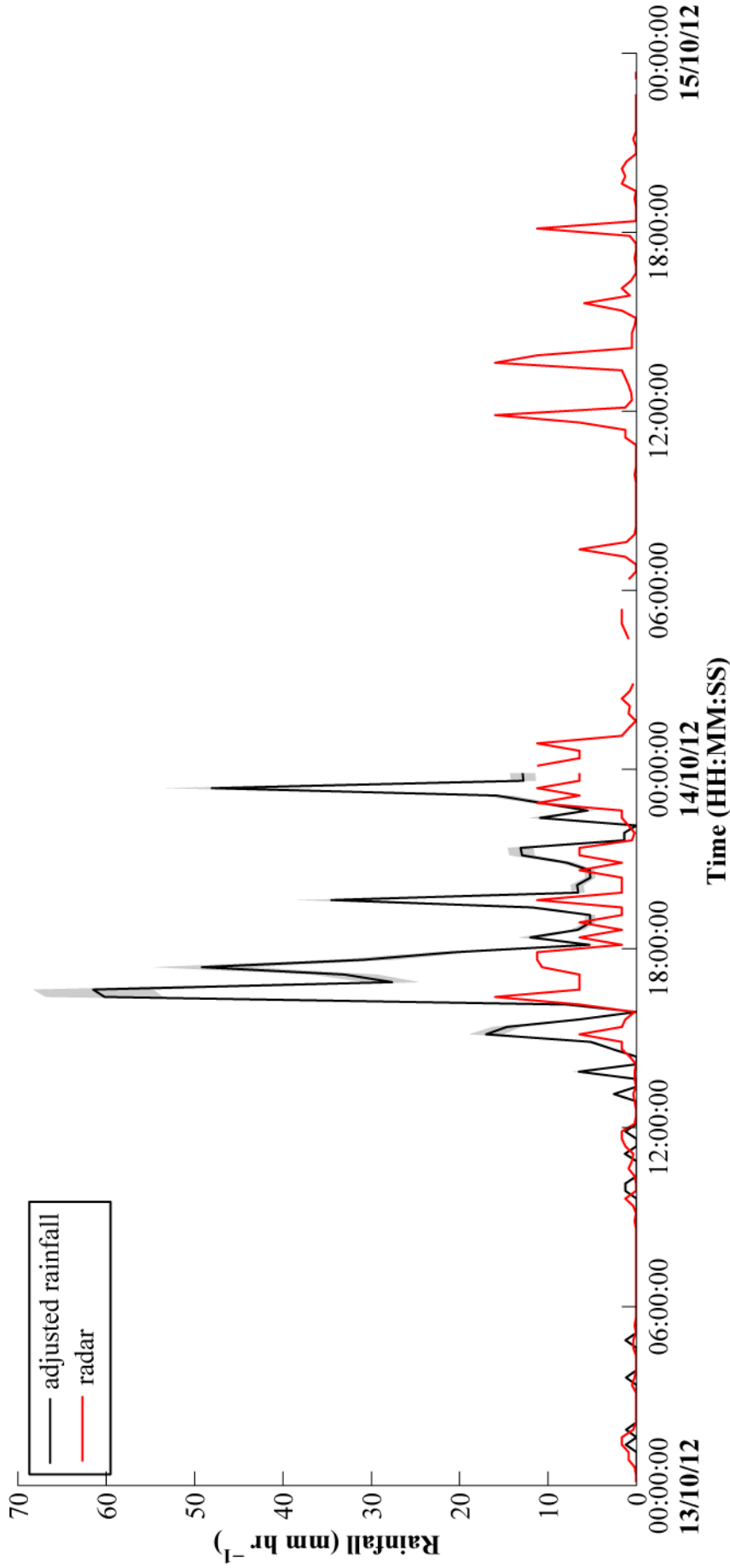


Figure 2.13 Rainfall rate calculated over 15 minute intervals from adjusted rainfall (black), the maximum value of the Catchment radar sub-section (red). Error range shaded in grey, 11%.

The averaged and maximum radar time series were compared to the rain gauge time series for 13th October 2012. The averaged radar time series underestimated rainfall intensity compared to the rain gauge by approximately 1.5 orders of magnitude, while the maximum radar time series produced estimates within the same order of magnitude as the rain gauge. The number of ‘no rain’ intervals was reduced in the maximum radar time series by 28% (compared to the rain gauge series), indicating that the point based rain gauge measurement may miss instances of rainfall within the wider catchment. Critically, the timing of peaks in radar rainfall intensity corresponded reasonably well to the rain gauge time series (Figure 2.13), indicating that both datasets captured peaks in catchment rainfall, that may then be related to observations of peaks in discharge to understand runoff lag dynamics (Chapter 4). Figure 2.13 shows the full two day rainfall time series.

2.4.2. Suspended sediment

There are two main strategies for measuring suspended sediment concentration in flow: (1) manual sampling by dipping a container into flow to collect a set volume of water (and sediment) or (2) an automated sampling device permanently situated at a fixed location to sample flow at set-intervals (possibly near-continuously) (Wren *et al.*, 2000). Gauged stations employed at other lahar prone volcanoes (*e.g.* Mount St Helens, Major *et al.*, 2000) were installed on bridges or other substantial engineered channel structures. The only available structures in the Belham River Valley of this nature were the edges of partially buried houses or telephone poles; however both were situated within an area of commercial aggregate extraction (Figure 2.5) placing expensive instrumentation in close proximity to heavy machinery working on the valley-bed surface. The alternative was to install instrumentation upstream; this was not an option because of the mobile alluvial bed surface and magnitude of sediment transport, resulting in rapid shifts in river morphology that would potentially destroy any instrumentation on the valley-floor within a single lahar event. Additionally lahars in the Belham River Valley do not always occupy the entire valley-floor in a single event, and channel boundaries shift within and between flows, so a point based measurement from fixed instrumentation, whether installed on a building or valley-floor may not measure flow if channel boundaries shifted away from the instrument location.

A manual sampling approach was adopted in this study. Several lahar studies have used “dip” samples to collect water and sediment samples from flow to obtain

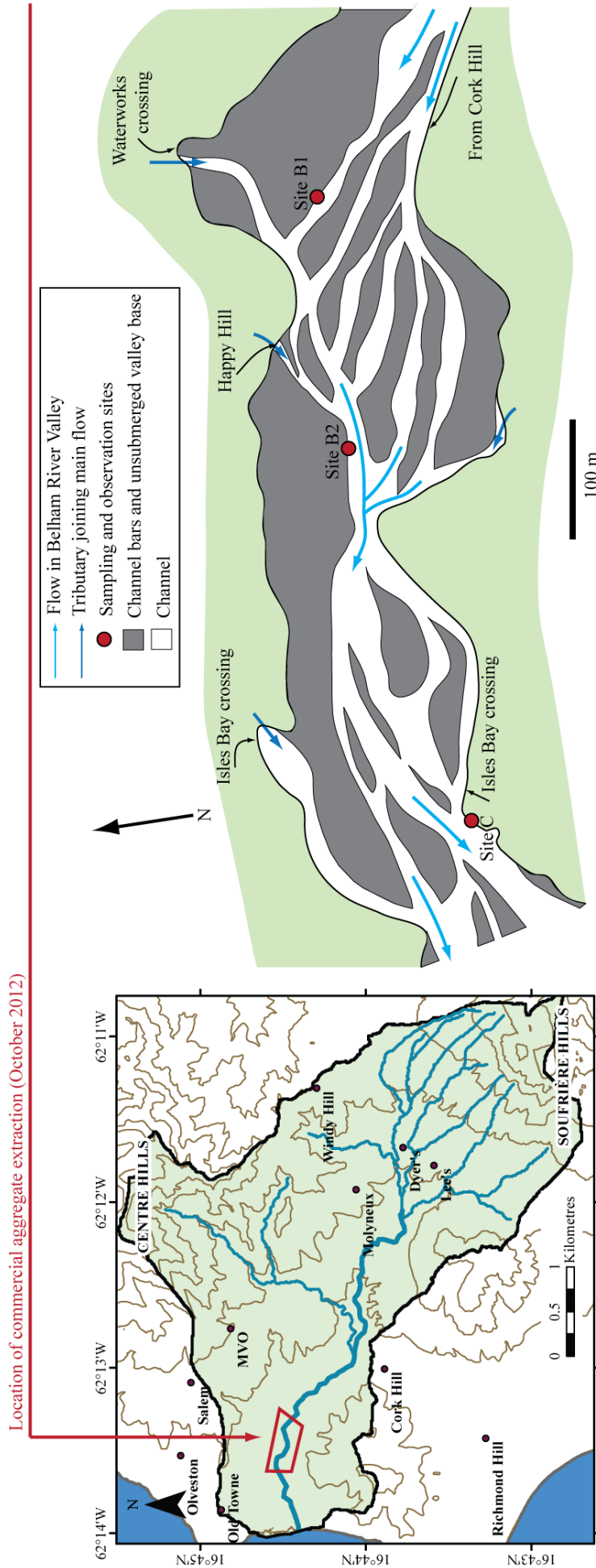


Figure 2.14 [left] Location of commercial aggregate extraction during 2012 (shown in red). The Belham Catchment is shaded in green. The topographic base map shows contours ascending from 0 m above sea level in 100 m intervals. Contours and drainage routes were calculated from a merged DEM from 1999 (north of island) and 2010 (south of island). [right] Sketch map of the channel structure within the area of commercial aggregate extraction (October 2012).

estimates of suspended sediment concentration, however very few published studies provide detailed accounts on methodology (Martinez *et al.*, 1996; Rodolfo *et al.*, 1996; Tüngol *et al.*, 1996; Lavigne *et al.*, 2000; 2000b). Cronin *et al.* (1997) sampled flow using a 5 litre plastic container with 100 x 30 mm holes cut into its top. Sampling was undertaken from a bridge into the centre of flow (top 1 m). This strategy was not appropriate for the Belham River Valley, and both the position of sampling in flow and the size of container were modified. Access was limited to lower reaches of the Belham River Valley during the 13th-14th October 2012 large lahar, because the event occupied most of the valley floor just upstream of the Belham Bridge where the valley narrows (Figure 2.5, 2.14). Commercial aggregate extraction directed the path taken by flow in the lower reach, which followed the temporary roads and network of pits generated by excavation. The location of the main temporary roadway was in the centre of the valley-floor and flow preferentially followed the roadway depression; once formed this main channel was surrounded on either side by narrower channels that formed when flow avulsed from the main channel or entered the valley from a tributary. Figure 2.14 shows a sketch map of the network of channels formed within this modified section of the Belham River Valley. Sampling of flow in the centre of the main channel was not possible and the entire main channel was not accessible during peak flow stages due to flow in surrounding narrower channels. Three opportunistic measurements were collected during the lahar at the edge of the main channel (site B2); two samples during the rising limb of flow (16:16:00 UTC, 13/10/2012, 16:21:00 UTC, 13/10/2012) and a third during waning flow (21:00:00 UTC, 14/10/2012). Figure 2.15 illustrates the sampling method, which used a 500 ml drinking water bottle (the volume advocated by Thomas *et al.*, 1985) to take a dip sample at 30 cm above the bed surface (shin height) in flow 50 cm deep (knee height). The cap of the bottle was opened at 0.3 m from the bed surface, the bottle was steadily lifted (Figure 2.15) through the vertical water column and then closed at the water surface (bottle was full). This method was adapted from Vanoni (2006), which aims to provide a more representative sample of flow suspended sediment than a point-measurement; a depth-integrated sampling unit was substituted with a drinking container. The distance from the edge of the channel varied depending on flow depth but the method was consistent with each measurement and samples were collected from the same cross-section and channel edge each time.

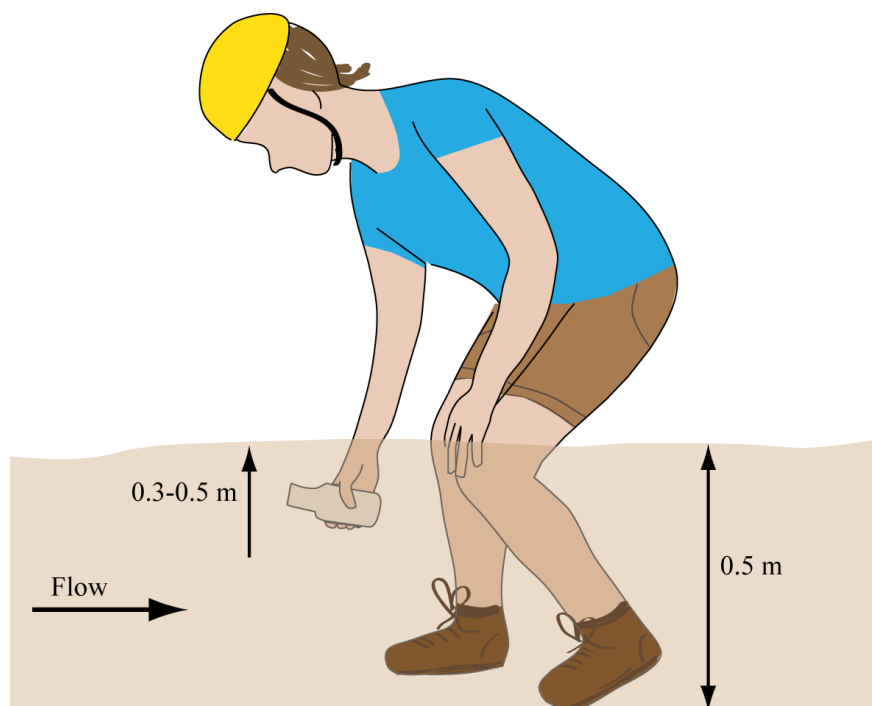


Figure 2.15 Illustration for method of collecting a suspended sediment sample with a 500 ml bottle at Site B2 during the 13th-14th October 2012 lahar. The bottle was inserted (with lid on) to 0.3 m above the bed surface. The lid was removed and water (and sediment) filled the container until full as it was lifted at a uniform rate upwards for 0.2 m. Data in Appendix 4.1g

Deposits from the event showed that boulder sized clasts were mobilised downstream, and observations from the camera and in-person at Site B2, identified cobble and boulder transport as bedload. However, the opaque nature of flow and challenges sampling, meant it was difficult to ascertain the maximum grain size in the transport by suspension. The container chosen to sample flow had a 2.5 cm opening. Potentially this restricts the grain size of sediment that may be sampled, however based on sampling by Sušnik (2009) of a lahar in the Belham River Valley of a similar flow velocity ($<3 \text{ m s}^{-1}$ surface velocity from floating objects), samples did not contain grains larger than 6 mm diameter. Therefore this container was considered appropriate for the flow being sampled. Critically, measurements of suspended sediment concentration and grain size distribution were analysed to consider relative changes (Chapter 4) and were not compared to other published studies because the measuring device and strategy can affect results.

The total weight of the sample (minus bottle weight) was calculated and the sample was filtered using three sheets layered coffee filter paper (filters above 10-20 microns). Coffee filter paper was used as this was what was available in the field. The solid fraction of the sample above 10-20 microns was retained in the filter paper, dried

at 90°C for 24 hours (Shreve and Downs, 2005) in the laboratory in the UK. The dried sample was weighed to the nearest 1 milligram. The dry mass was used to calculate the mass of the suspension and then the sediment volume assuming a water temperature of 15°C and a sediment density of 2650 kg m⁻³ (density of quartz). From this the suspended sediment concentration (g l⁻¹) was calculated.

The dried sample was weighed and a sub-sample of 5 mm³ (1 level teaspoon) was extracted from the main sample. The sample was placed into suspension with distilled water containing three drops of Calgon and distilled water. The suspension (and beaker) was weighed and a magnetic stirrer was then used to extract a heavy mineral magnetite from the sample. Grains of magnetite did not stay in suspension during stirring and were removed to prevent damage to analytical equipment. The magnetite equated to up to 5% of the sample weight, and grain size of this sub-set was not analysed. Laser-diffraction analysis was used to ascertain the grain size distribution of particles in the remaining suspension. The Malvern Mastersizer 2000 was used and automatically generated a particle size distribution ranging from 0.1 microns to 2 mm.

2.4.3. Ground photographs and video

Photographs and video were collected during the lahar on 13th-14th October 2012 using several hand-held cameras. These observations were opportunistic based on accessibility to the valley-floor during the storm event. One set of photographs/video were collected by a resident situated at the Isles Bay crossing (Site C, Figure 2.14, equipped with a camera as part of a community monitoring project managed by Jonathan Stone, UEA. Ground photographs and video were taken in person at this site also and two other sites (Site B1 and B2). The timing, location and data collected are listed in table 2.8.

Observations provided useful information on the timing of peak flow stages at downstream locations, changes in discharge (occupied valley width by flow), the presence of flow features such as stationary water-surface-waves and their geometries, the size of boulders in bedload transport, apparent flow turbulence (indicated by white water on the surface of flow), and the timing of rainfall. These visual observations were correlated with visual observations at the camera site upstream and instrumental measurements around the catchment during the tropical storm.

Date/ Time (UTC)	Site
12/10/2012 18:58- 19:00	C
12/10/2012 20:10-20:11	C
13/10/2012 16:00- 17:00	B1
13/10/2012 16:24- 16:53	C
13/10/2012 16:55- 17:24	C
13/10/2012 17:27	C
13/10/2012 17:28- 17:41	C
13/10/2012 17:30- 18:15	B2
13/10/2012 18:17-18:23	C
13/10/2012 18:46- 19:04	C
13/10/2012 19:44- 20:05	C
13/10/2012 20:45-21:15	B1
14/10/2012 12:00- 14:00	B1
14/10/2012 13:40	C
14/10/2012 14:21- 14:51	C
14/10/2012 14:51- 15:21	C
14/10/2012 15;24- 15:53	C
14/10/2012 21:00- 21:30	B2
15/10/2012 12:30	C

Table 2.8 The timing and location of ground observations (photographs and video) in the Belham River Valley, captured prior to, during and after Tropical Storm Rafael (Appendix 4.1d-f)

2.5. Sedimentology

The character of deposits is influenced by lahar size, origin and depositional environment. Sedimentologists use facies to delineate bodies of sediment/rock that formed under a unique set of physical, chemical and biological conditions representing a specific depositional environment. An assemblage of contemporaneous genetically related facies provides information on the nature of a depositional system. Lahars (by definition in this thesis, Section 1.1), transcend flow phenomenon from normal streamflows to debris flows. Transitions in flow as it propagates downstream and inter-event variations in flow rheology may lead to complex sequences of facies and stark variations in deposit character between proximal and distal areas. This thesis draws on

the widely used lithofacies scheme (Table 2.9) for fluvial systems by Miall (1985; 1996) to describe the character of sediments in the Belham River Valley. Identifying facies within vertical exposures of deposit provides the building blocks to understanding the mode of deposition. Scott's (1988) facies scheme for lahars differentiated between lahar flow facies based on observations at Mount St Helens. While the scheme presented individual facies for channel, floodplain *etc.* (Figure 2.16), the composition of each of Scott's (1988) facies was equivalent to an assemblage of Miall's (1985; 1996) lithofacies. Although Scott's (1988) scheme provided some insight into flow rheology and the location of channel boundaries, it did not include the level of detail required to discriminate variability within and between flows of the type seen in the Belham River Valley; typically streamflow to hyperconcentrated flows, rather than debris flows. The rapidly varying, unsteady dynamics of some lahars lead to dramatic variation between vertical sequences of deposit located in close lateral proximity (metres apart).

To move beyond simply classifying the bulk character of the lahar in different locations and to begin relating measurements of flow velocity and depth (from monitoring) with features in the preserved deposit to test empirical relationships derived in laboratory flume experiments, this study employed architectural element analysis. The approach focuses on sedimentary structures within laterally extensive vertical exposures of deposit, associating internal geometry, facies assemblage and external form with a "component" of the depositional system such as channels, scours and bars (Miall, 1985). Several recent studies on jökulhlaup deposits (Duller *et al.*, 2008; Lang and Winsemann, 2013) constructed detailed architectural panels from laterally extensive exposures of sediment. Duller *et al.* (2008) used architectural analysis to distinguish and analyse sedimentary structures within a single facies, leading to the reconstruction of flow parameters from preserved bedset geometries (Figure 2.17). While Lang and Winsemann (2013) described a series of sedimentary structures with varying characteristics (presented as individual facies), associating each to a sedimentary bedform. Interpretations of deposits in these schemes were based on published observations from laboratory flume experiments (*e.g.* Alexander *et al.*, 2001; Yokokawa *et al.*, 2010) and previous field observations, however some facies in the latter scheme were associated with more than one bedform, because understanding was limited in distinguishing certain upper flow regime bedforms based on sediment structure alone.

Facies Code	Facies	Sedimentary Structures	Interpretation
Gmm	Matrix supported massive gravel	Weak grading	Plastic debris flow (high-strength, viscous)
Gmg	Matrix-supported gravel	Inverse to normal grading	Pseudoplastic debris flow (low strength viscous)
Gci	Clast supported gravel	Inverse grading	Clast-rich debris flow (high strength), or pseudoplastic debris flow (low strength)
Gcm	Clast-supported massive gravel	-	Pseudoplastic debris flow (inertial bedload, turbulent flow)
Gh	Clast-supported, crudely bedded gravel	Horizontal bedding, imbrication	Longitudinal bedforms, lag deposits, sieve deposits
Gt	Gravel stratified	Trough cross-beds	Minor channel fills
Gp	Gravel stratified	Planar cross-beds	Transverse bedforms, deltaic growths from older bar remnants
St	Sand, fine to very coarse may be pebbly	Solitary or grouped trough cross-beds	Sinuuous –crested and linguoid (3D) dunes
Sp	Sand, fine to very coarse may be pebbly	Solitary or grouped planar cross-beds	Transverse and linguoid (3D) dunes
Sr	Sand, very fine to coarse	Ripple cross-lamination	Ripples (low flow regime)
Sh	Sand, very fine to coarse, may be pebbly	Horizontal lamination parting or streaming lineation	Plane-bed flow (critical flow)
Sl	Sand, very fine to coarse may be pebbly	Low angle (<15 deg) cross-beds	Scour fills, humpback or washed out dunes, antidunes
Ss	Sand, fine ot very coarse, may be pebbly	Broad, shallow scours	Scour fill
Sm	Sand, fine to coarse	Massive or faint lamination	Sediment-gravity flow deposits
Fl	Sand, silt, mud	Fine laminations, very small ripples	Overbank, abandoned channel or waning flood deposits
Fsm	Silt, mud	Massive	Backswamp or abandoned channel deposits
Fm	Mud, silt	Massive, desiccation cracks	Overbank, abandoned channel or drape deposits
Fr	Mud, silt	Massive, roots, bioturbation	Root bed, incipient soil
C	Coal, carbonaceous mud	Plant, mud films	Vegetated swamp deposits
P	Paleosol carbonate (calcite, siderite)	Pedogenic features: nodules, filaments	Soil with chemical precipitation

Table 2.9 Facies classification for fluvial deposits, reproduced from Miall (1996). The capital letter indicates dominant grain size: G= gravel, S=sand, F= fine grained facies (includes very fine sand, silt and mud). The lower case letters serve as a mnemonic for characteristic texture or structure of the lithofacies.

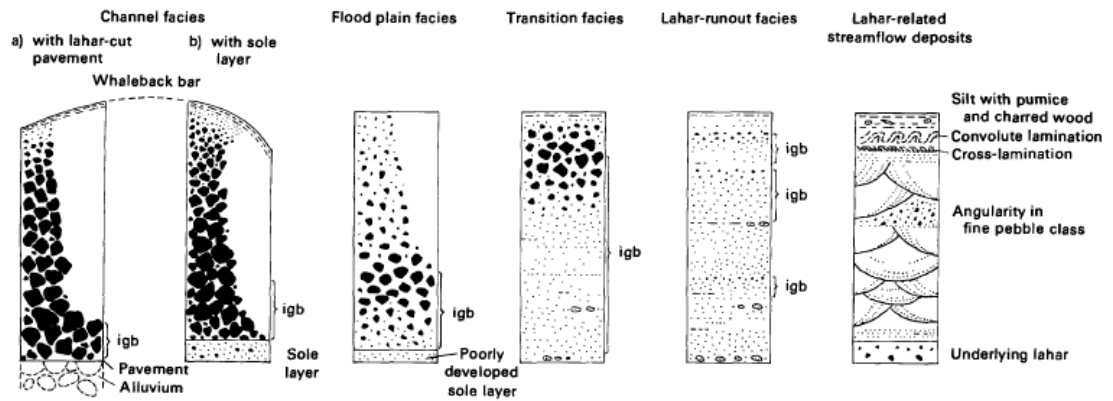


Figure 2.16 Lahar facies types, reproduced from Scott (1988, p.A19). igb = Inversely graded bedding

2.5.1. Sediment logging

2.5.1.1. Log sites

Field work was undertaken between 2011 and 2013. During this period of time channel incision into modern deposits in accessible sections of the valley (Zones B and C, see Figure 1.12) was minimal (mostly 0-0.2 m, but generally under 0.5 m) and did not provide extensive vertical exposures of sediment. Commercial sand and aggregate excavation by the backhoe pit method in lower- middle reaches of the Belham River Valley (Figure 2.18), created a series of temporary vertical exposures of sediment (typically <1.5 m tall) that extended between 2 m and 150 m long. Excavation was focused in area 1 (Figure 2.18) in 2011 and expanded upstream into area 2 when the hazard level was reduced from 3 to 2 on 4th November 2011; this permitted day time access to Hazard Zone C (Section 1.7). Deposits were surveyed in May-June 2011 (area 1), October 2012 (area 1) and March 2013 (Pit2013, area 2; Figure 2.18).

Exposures were logged when they fulfilled the following criteria:

1. They could be accessed safely by the field worker.
2. They were over 0.5 m in vertical extent and greater than 2 m in lateral extent. These dimensions provided sufficient exposure of deposit to not only view micro-scale structures but also identify vertical transitions in deposit pertaining to changes in flow character.
3. Sediment within exposures was deposited by natural processes. Care was taken when working in areas where sand and aggregate mining had excavated and piled large volumes of sediment.

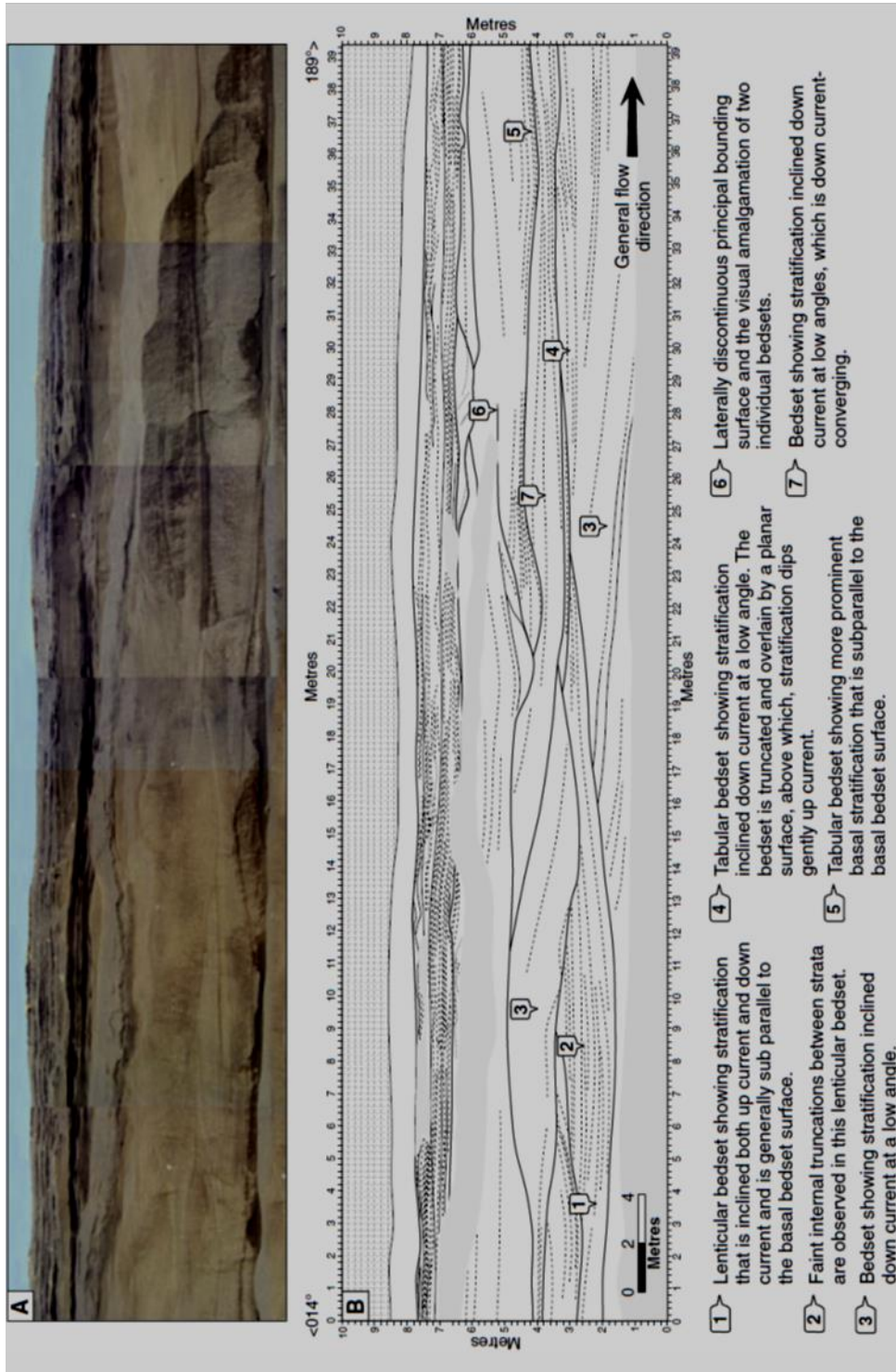
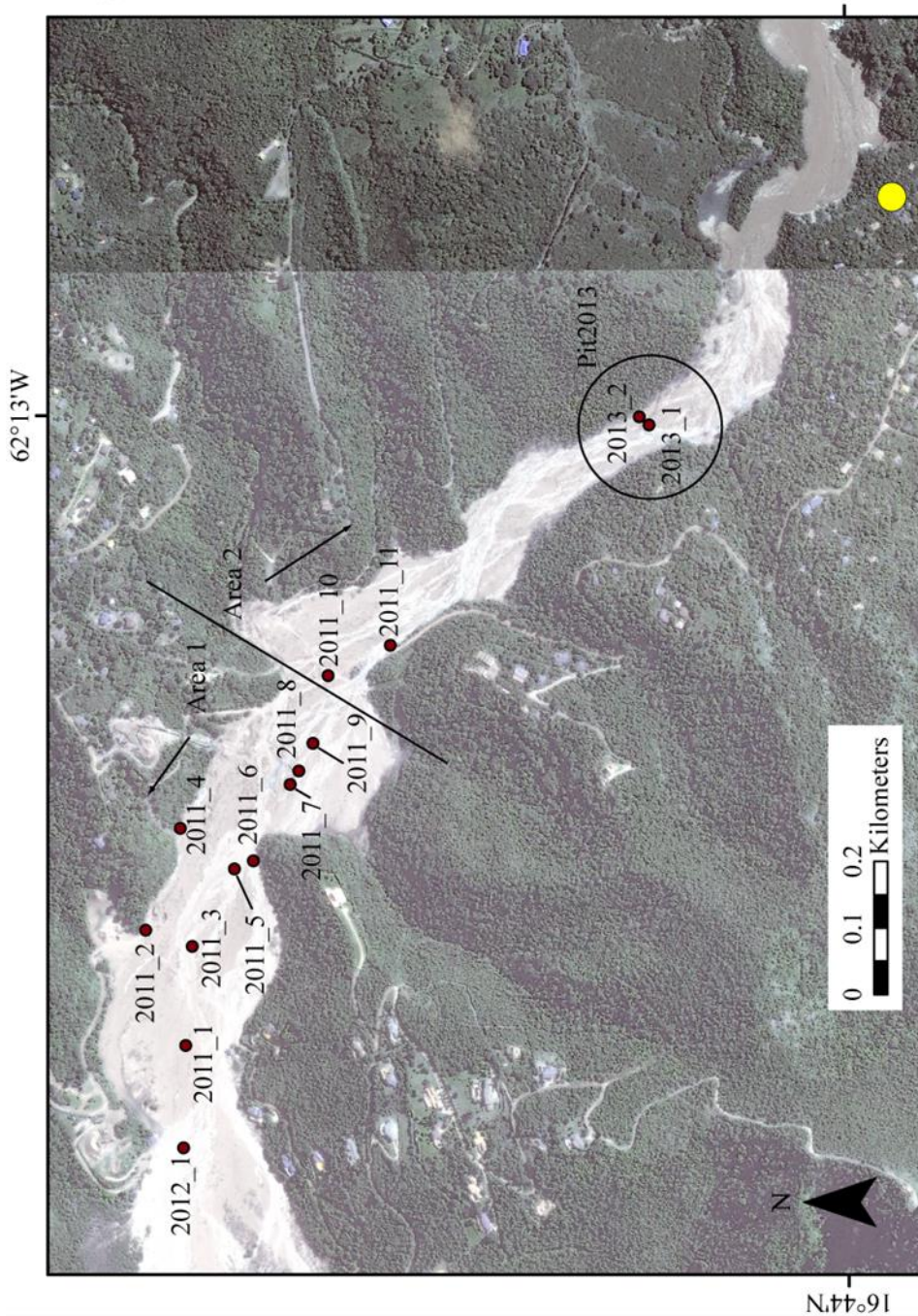


Figure 2.17 (A) Photomontage of 1918 jökulhlaup deposits in the area of Mýrdalssandur, to the south of the Mýrdalsjökull ice cap and Katla Volcanic System. (B) Line drawing highlighting the main architectural features of interest within the middle vertical section (unit 2) of the deposit. Figure reproduced from Duller *et al.* (2009), p.949



It is important to note here, this study was not able to govern the location of pits in the valley, nor could prior notification be obtained as to where new pits were planned. Undertaking excavation on the scale required to log a sufficient exposure of sediment, was not logistically possible within this study, therefore sediment logs were limited to sites governed by commercial activity. Commercial sand extraction did not operate as far upstream as the remote camera was situated within the study period (Figure 2.14). However, a large 150 m long pit (Pit2013, Figure 2.18) was established ~400 m downstream of the camera, situated cross-cutting one of the main channels within a previously unmodified (by commercial activity) section of valley. The valley at this location was relatively proximal to the camera site, was similar in width (68m and 79 m, respectively) and had comparable bed surface morphology and channel structure. Therefore flow was thought to be approximately the same average velocity, depth and composition at both locations. Given this, imagery from the camera was used to interpret deposits in Pit2013. A fuller description of the sites is provided in Section 5.3-5.4.

2.5.1.2. Logging method

Sediment was logged with reference to Miall's facies scheme (Table 2.9), which was adapted in the field to capture all features of the deposit (see Section 5.4). Logging in the field was systematic and worked from bottom to top of each vertical exposure of interest using a simple scheme of symbols to document features in the deposit (Section 5.4). The vertical location of boundaries between packets of sediment visually sharing the same textural characteristics, and the nature of these boundaries (sharp, gradational, erosional *etc.*, and dipping angle and direction) were noted on the log. The characteristics of laminae and bedding within each packet of sediment were described. Dip and dip direction measurements were obtained using a compass/ clinometer.

The grain size composition of sediment was estimated in the field using a grain size card (63 μm to 10 mm), clast measurements (measurement of b-axis of a minimum of 30 clasts within each packet of sediment measured for grain sizes above 16 mm) and the collection and analysis of samples (see Section 2.5.1.3 for method). Vertical changes in the bulk grain size broadly correspond to changes in flow competence (the maximum grain size a given flow at a given time can transport); sediment of a given grain size is deposited when flow rates drop below the fall velocity for a particle of that size (refer to the classic work of Hjulström, 1935). In natural systems the relationship between flow velocity and particle grain size is complicated by individual grain

characteristics (shape, structure, density), as well as the flow characteristics of the fluid medium (Perry and Taylor, 2007). However, observations of relative shifts in grain size, within and between packets of sediment from the same source within a vertical exposure of deposit, may indicate changes in flow stream power during a single event or differences in stream power between multiple events.

The degree of sediment sorting was estimated for each packet of sediment identified in each vertical exposure, by visual comparison to a standard grain size sorting chart. Observations were undertaken by the same field worker to ensure consistency, although an element of subjectivity was expected. The results were treated in relative terms, but provided a useful indication on the rate and/or duration of deposition, pertaining to the mechanism of sediment transport. Paleoflow direction was determined from repeat aerial and ground photographs between 2010 and 2013 (Table 2.3).

Sediment logs were constructed for each exposure documented using the boundaries identified between vertical packets of sediment, and the description of sediment texture together with measurements of grain size (from analysis of samples, Section 2.5.1.3), which enabled field observations to be associated with Miall's facies scheme (Table 2.9), and the facies code to be integrated into the sediment log. Some sediment packets contained several facies, and these associations were discussed in relation to sediment transport mechanisms and flow observations in Section 5.5.

2.5.1.3. Sediment sampling

Samples were collected from packets of sediment visually sharing the same textural characteristics (as delineated during the process of sediment logging) containing grains <16 mm. Samples were excavated using a trowel, and it is acknowledged that there is inherent bias in this method towards finer sediment. Most samples were processed during field work in non-laboratory conditions. All samples were weighed (to ± 0.1 g), dried at $\sim 90^{\circ}\text{C}$ in a kitchen oven for 12 hours, re-weighed after drying (to ± 0.1 g) and sieved with mesh sizes from 64 mm to 0.5 mm (1 mm, 2 mm, 4 mm, 8 mm, 16 mm, 32 mm). A mechanical shaker was not available; sieves were shaken vigorously by hand for 10 minutes. These methods were deemed acceptable for this study which focused on large scale sedimentary structures and bulk shifts in deposit character.

The grain size distribution of samples under 0.5 mm was analysed using laser sizing to access the distribution of fine sands and silts more accurately. The sample was placed into suspension with distilled water containing three drops of Calgon and distilled water. The suspension (and beaker) was weighed and a magnetic stirrer was then used to extract a heavy mineral magnetite from the sample. Grains of magnetite did not stay in suspension during stirring and were removed to prevent damage to analytical equipment. After removal the suspension was re-weighed and run through the Malvern Mastersizer 2000. Results were combined with sieve measurements to generate complete grain size distributions (Appendix 2.2ab).

2.5.1.4. Architectural diagrams

Photographs of each exposure were taken from a fixed vantage point at ground level. If multiple photographs were taken to ensure sufficient horizontal coverage, photographs were merged into a single panoramic image using Adobe Photoshop automated *photomerge* function (*reposition* mode). The photographs were used in conjunction with field observations to create a series of architectural panels showing the bounding surfaces and internal structures within the surveyed exposures of deposit. The characteristics of structures (sharp, diffuse) and the presence of clasts larger than 64 mm (cobbles) were recorded in the panels. Final versions of the panels were drawn in Adobe Illustrator.

2.5.2. Bed surface grain size and geomorphological mapping of the valley-floor at the camera site

Pole-aerial-photography (PAP, Figure 2.19a, Appendix 4.1a) was employed as a rapid method of capturing high resolution imagery of the valley-floor at the camera site (Figure 2.5). The camera was held in the self-levelling cradle that ensured the camera lens was parallel with the bed surface to ensure photographs were vertical rather than at an oblique angle. The camera cradle was attached to a 3 m long pole that was secured to the surveyor by a waist pole mount (typically used for fishing poles) and a neck strap (Figure 2.19a); this set-up allowed the pole to maintain a consistent angle from the ground, and therefore the camera to be held at a consistent height. Photographs were captured every metre along an 85 m long transect across the valley-floor at the camera site (marked by a tape measure in the field), corresponding to the camera image sampling transect shown in Figure 2.8. A survey of this transect was undertaken on 12th October 2012 before the lahar, and then on 15th October 2012 after the lahar. Camera

lens distortion was minimal and corrected in Adobe Photoshop. One pixel length in each photograph equated to 0.7 mm on the valley floor. The grain size was measured and presence/absence of vegetation was sampled in the imagery every 10 cm along the tape measure, which was included in each photograph (Figure 2.19b). Silt and sand sized sediment (< 2 mm) were a single category due to the challenges differentiating individual grains < 2 mm within imagery; medium-, coarse- and very- coarse pebbles, cobbles and boulders were measured at each sample point.

Geomorphological sketch maps showing the location of channel bars were drawn for the camera site in conjunction with the two PAP surveys. Measurements of bar geometry were undertaken and the PAP survey was extended to capture the full extent of the valley-floor covered by the remote monitoring camera. Images were joined using using Adobe Photoshop automated *photomerge* function (*collage* mode). The imagery provided a base-map on which a geomorphological map was drawn in Adobe Illustrator, with reference to the field sketches. The maps showed changes in the valley-floor channel structure resulting from the 13th-14th October 2012 lahar.

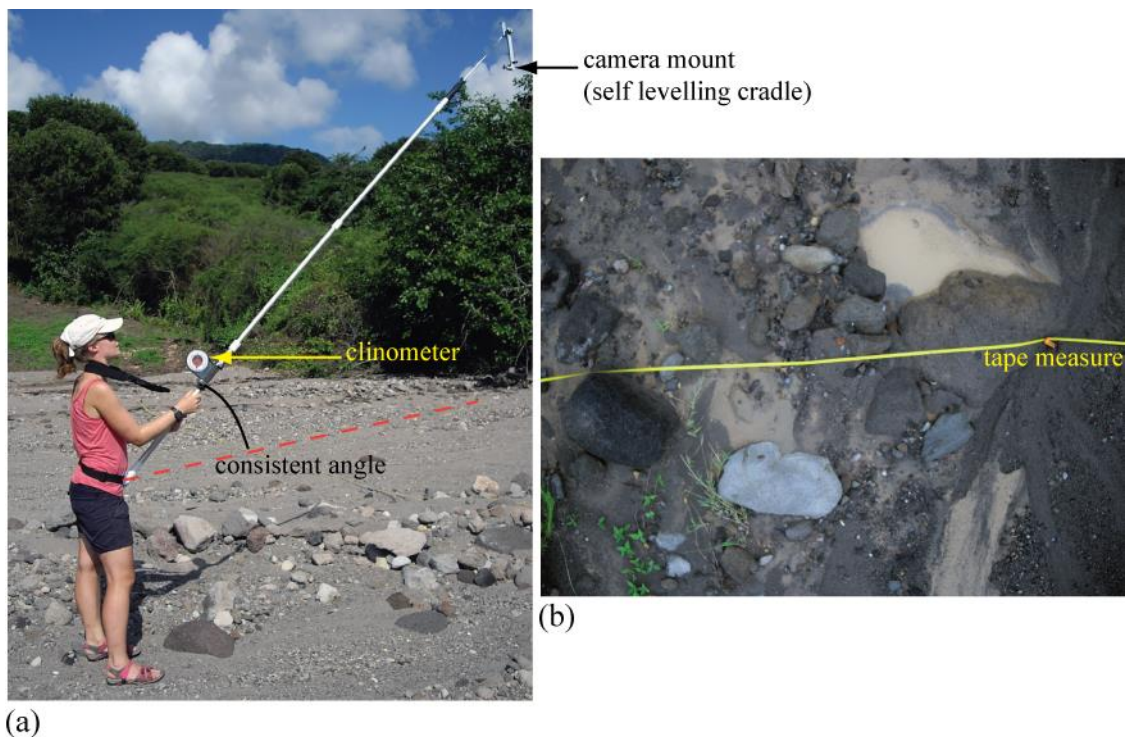


Figure 2.19 (a) Pole-aerial-photography (PAP) set-up. The pole was kept at a consistent angle using a waist pole mount, neck strap and clinometer. The camera (not shown in photograph) was secured to a self-levelling camera mount. (b) Example photograph from PAP. Tape measure is shown within the image.

Chapter 3:

Response of the Belham Catchment and channel to 18 years of volcanic perturbation

3.1. Introduction

The long-term adjustment of local drainages to rapid volcanic sedimentation has only been studied following a couple of types of modern event; (1) after a single period of intense volcanic activity (e.g. Mount St Helens, Major *et al.*, 2000; Mount Pinatubo, Hayes *et al.*, 2002), or (2) after a single large lahar triggered by a single sudden release of water (e.g. crater lake outburst at Mount Ruapehu, Procter *et al.*, 2010). To date, there are no longitudinal studies of drainage adjustment during a long-term eruptive episode.

The adjustment of a system to volcanic sedimentation is strongly related to the nature of volcanoclastic input (volume, composition), the pre-volcanic geomorphology, the duration of volcanic activity and the local climate regime. These factors are site specific and complex. Sedimentological interpretation of ancient deposits to derive rates of sediment transfer can be misleading; partial preservation of tephra units, sediment diagenesis and tectonic modification (Vessell and Davies, 1981) restrict interpretation of sediment transfer mechanisms and rates. In order to manage progressive sediment delivery downstream into inhabited areas in volcanic regions undergoing repeat sub-decadal periods of eruptive activity, it is useful to quantify the rate of sediment remobilisation from tephra deposits, by lahars, and the contexts in which these sediment transfers are taking place. Only a few studies have systematically

monitored lahars, and quantified the rates of sediment transfer and changes in local morphology in response to multiple phases of volcanic activity; Volcán de Colima, Mexico (Vázquez *et al.*, 2014), Mount Semeru, Indonesia (Doyle *et al.*, 2010; Thouret *et al.*, 2007), Mount Mayon (Rodolfo *et al.*, 1991) and Mount Merapi, Indonesia (Lavigne, 2004); these have typically focussed on short concentrated observations of longer lived systems. This chapter provides new data and synthesises earlier observations to evaluate the response of the Belham Catchment, Montserrat (Chapter 1) to 18 years of volcanic perturbation. The systematic examination across 18 years of rainfall data, lahar activity and observations of system response provides the first study of prolonged volcanic perturbations (multiple phases of volcanic activity with pause periods) and response in an active lahar drainage.

Since the start of eruptive activity in 1995, drainage routes around the SHV have undergone change in response to inputs of volcanic material; valleys have been choked with pyroclastic debris (Cole *et al.*, 2002; Komorowski *et al.*, 2010; Stinton *et al.*, 2014), hillslopes have been draped in tephra fall (Bonadonna *et al.*, 2002a; Edmonds *et al.* 2006; MVO, 2010), channel incision has altered the location, connections and densities of channels, and the coastline has been extended by the development of debris fans (Kenedi *et al.*, 2010). Located at a significant hazard boundary, topographic modification of the Belham River Valley has been monitored by repeat topographic and photographic surveys (aerial and ground) over the last two decades. The dates of primary sediment influx into the valley from pyroclastic flows and tephra fall were well documented by MVO daily-weekly observation and are discussed in reports to the Scientific Advisory Committee (SAC). The remobilisation of these deposits as lahars has been captured by the local seismic network, MVO observations, and past research projects (including this study); in addition rainfall measurements are available from several discontinuous networks.

During this study three annual Kinematic GPS surveys were undertaken to capture topography between 2011 and 2013. Ground and aerial photographic surveys were carried out within a few days; the aerial surveys also covered areas upstream of the GPS track- too hazardous to reach on foot. Previous DGPS surveys conducted in 2002, 2003, 2005, 2006 and 2007 (Barclay *et al.*, 2007; Sušnik, 2009; Darnell *et al.*, 2010), and island-wide topographic surveys conducted pre-eruption and updated in 1999 (Wadge, 2000) were transformed from Montserrat National Grid into UTM and heights were converted from orthometric to ellipsoid heights using the WGS84 geoid (Section

2.2.1, 2.2.3.1). Satellite imagery was acquired for March 2011 and was geo-referenced to a 2010 LiDAR DSM; sections of aerial surveys conducted in 2012 and 2013 were also geo-located for analysis (Section 2.2.2.2). Archive photographs and video from a number of different sources (including local residents) were collated. Some of these photographs were suitable for valley-change analysis, particularly in the upper catchment where data is more limited. These photographs were used to reconstruct channel infilling upstream (Section 2.2.2.2) and to increase the temporal resolution of the record of valley-floor surface change in the Belham. Visual and seismic observations were collated to construct an 18 year record of lahar incidence (Section 2.2.3.2). Rainfall measurements from several networks were used to compare the timing of registered lahar occurrence with antecedent rainfall intensity and duration, as well as the amount of sustaining rainfall protracting the flow duration.

Work by Stinton *et al.* (2014) and Ogburn (2014) have considered the impact of changing catchment and channel morphology on pyroclastic flow hazards. Research by Sušnik (2009) discussed the response of the Belham Catchment to volcanic activity between 1995 and 2007, and extrapolated valley evolution under two volcanic scenarios. Detailed analysis of lahar initiation during a dome collapse on 20th May 2006, provided insight into the critical control of runoff on extreme flood generation (Alexander *et al.*, 2010). Building on past work, this chapter evaluates connections between sediment inputs, catchment conditions, rainfall and the characteristics of lahars over time. The chapter discusses the complexity of factors in multi-phase eruptive environments that condition catchment response to rainfall.

3.2. Morphological changes to the Belham Catchment

The Belham Catchment is the largest topographically defined drainage on the island. The size of the basin is primarily governed by the distance between and morphology of the Centre Hills and Soufrière Hills volcanic centres; a result of the local tectonic setting, characteristics of ancient and modern volcanic activity and local erosion (see Chapter 1). Ground water migration into and out of the catchment, and the location of perched aquifers are important in ephemeral settings, however the complexities of modelling the sub-terrain system response to rainfall and volcanic activity are beyond the scope of this work (see Hemmings *et al.*, 2012). This section highlights significant modifications to the surface morphology of the Belham Catchment over the last 18 years, and the effects this had on the system.

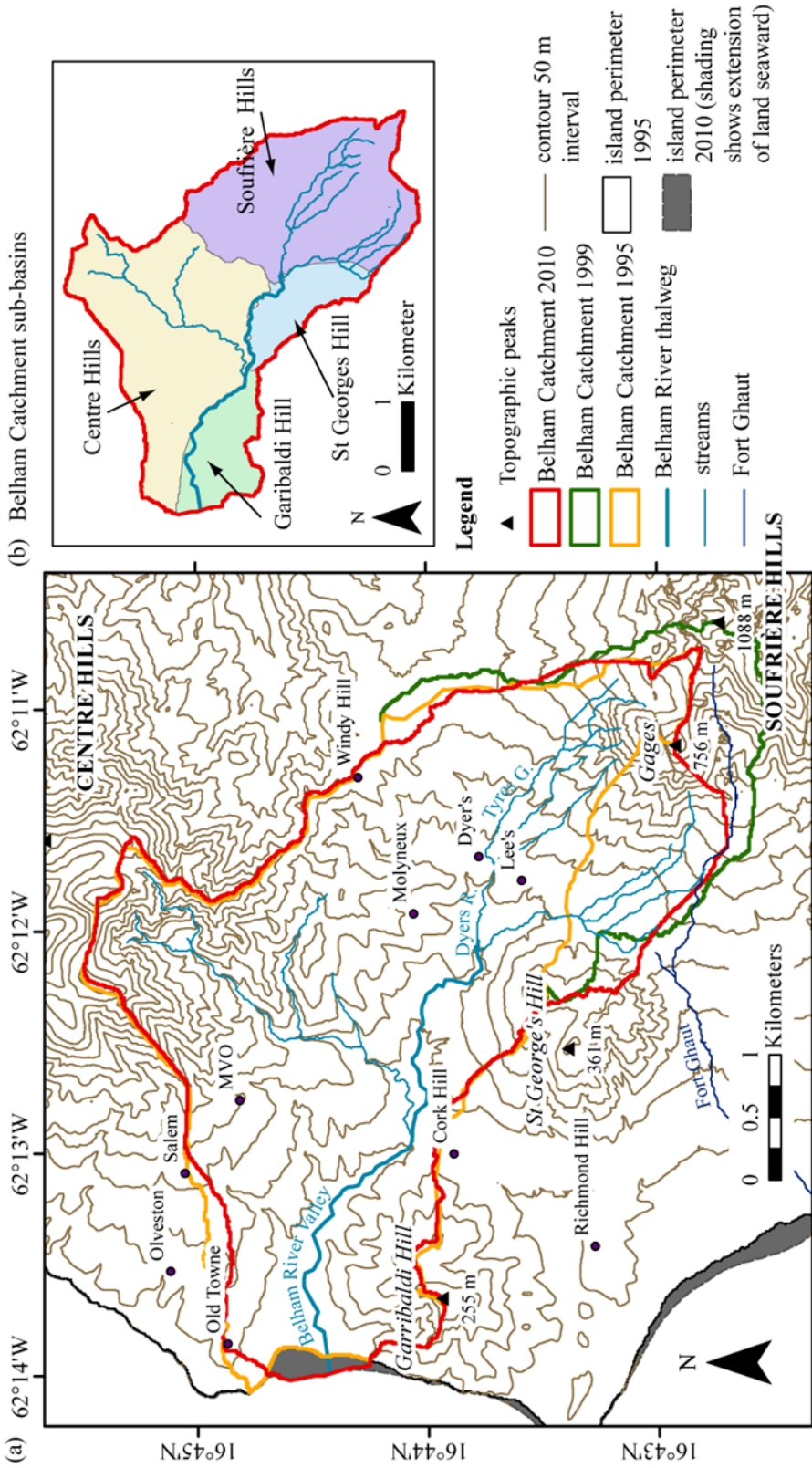


Figure 3.1 (a) Change to surface extent of the Belham Catchment between 1995 and June 2010, in response to sediment deposition from multi-phases of volcanic activity. Catchment extent based on DEM analysis using Arc Hydro tools in Arc GIS software. Change in coastline between 1995 and 2010, from sediment mobilisation downstream by lahars is shown by grey shading. Contour intervals of 50 m displayed from 0 m at the coast; orthometric heights used. (b) Sub-basins within the catchment were defined using the June 2010 LiDAR DEM. These surface divisions represented drainage area contributing runoff to the Belham River Valley at different locations along the channel

Prior to the onset of volcanic activity, the Belham Catchment had a surface area of 13.7 km², which was sub-divided into four topographically defined areas (Figure 3.1). Following five phases of lava extrusion resulting in modification to Tyre's Ghaut and Gage's Valley, the Belham Catchment had increased in size to 16.3 km². Tyre's Ghaut drains from the topographic low between Gage's Mountain and Castle Peak (Figure 1.7; in 2014 this was the location of a new dome), joins with Dyer's River after 2.5 km, which then becomes the Belham River at the tributary with an unnamed Ghaut (draining through Lee's Village), just upstream from Molyneux (Figure 3.1). The source of Gage's Valley is located between Gage's Mountain and Chance's Peak (to the west). While the route taken by Tyre's Ghaut has not significantly deviated in the last 19 years, the course of Gage's Valley has undergone significant change. The route taken prior to volcanic activity saw the channel initially drain from SHV in a north-west direction with a bearing of 295°N, and then be deflected in a south-west direction (bearing 265°N) when it reached the base of St George's Hill, joining Fort Ghaut which hugs the southwest base of St George's Hill (Figure 3.1). Critically, Tyres Ghaut has always been a significant drainage route from the Soufrière Hills into the Belham River Valley. Gage's Valley was not part of the Belham Catchment before Phase 1 and modification to this channel, resulting in it becoming connected with the Lee's Village channel, accounts for the largest gain in area to the Belham Catchment (Section 3.2.2). The following sections detail the cumulative deposition of sediment by (1) dome collapse block-and-ash flows, (2) pyroclastic surges associated with and generated above pyroclastic flows, (3) secondary pyroclastic flows derived from late-stage pyroclastic surges, and (4) pumice-rich flows associated with fountain collapses (Calder *et al.*, 1999). The timing of these inputs is summarised in Figure 3.2.

3.2.1. Contributions of sediment by Farrell's Plain and Tyre's Ghaut-Dyer's River

Debris fan development on the northern slopes of SHV commenced in early June 1997. Shortly after this a dome collapse on 25th June 1997, triggered a block-and-ash flow (BAF) in to Mosquito Ghaut (to east of Tyres Ghaut, see Figure 3.1), BAFs into Tyres Ghaut and pyroclastic surges into the Belham River Valley. Further minor collapses during July 1997 shed material to the north and west, infilling Mosquito Ghaut. Volumes of material deposited during the events were sufficient to alter the position of

Volcanic deposition

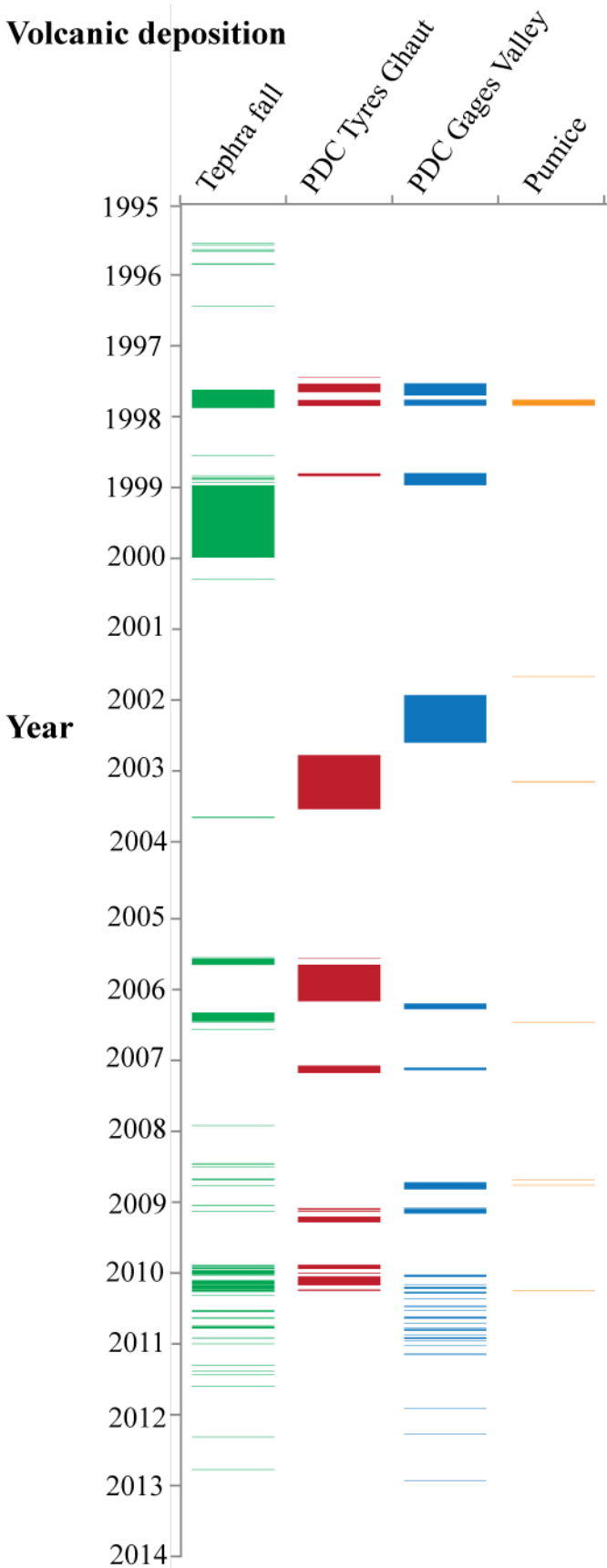


Figure 3.2 The timing of volcanic inputs to the Belham Catchment. Tephra fall represents periods of repeat dome collapses and explosions resulting in multiple fall deposits (see Section 3.3) and single significant events. The record of events was compiled from Cole *et al.*, 1998, Young *et al.*, 1998, Cole *et al.*, 2002, Loughlin *et al.*, 2002, Druitt *et al.*, 2002a, Druitt *et al.*, 2002b, Norton *et al.*, 2002, Carn *et al.*, 2004, Herd *et al.*, 2005, Edmonds *et al.*, 2006, Barclay *et al.*, 2007, Wadge *et al.*, 2009, Alexander *et al.*, 2010, Komorowski *et al.*, 2010, MVO, 2010, Wadge *et al.*, 2014, Stinton *et al.*, 2014. While it does not represent a complete record of activity, it is complete based on available published observations.

the eastern Belham Catchment boundary by modifying the position of the ridge between Tyres Ghaut and Mosquito Ghaut, extending the catchment area by 0.2 km². This new boundary did not significantly change with future inputs of sediment, suggesting that sequential events onto Farrell's plain were topography mantling rather than topography modifying (Manville *et al.* 2009).

Material was added to Tyres Ghaut in response to north-west dome extrusion, during unconfined dome growth, significant explosions and by unstable remnant dome rock in periods of volcanic repose. Figure 3.2 shows the timing of pyroclastic density currents onto Farrell's Plain and into Tyres Ghaut. Table 3.1 provides estimates of sediment volumes resulting from periods of intense surface activity. The method of volumetric calculation is also referenced; readers are directed to Section 2.2.2.2 for full description.

Figure 3.3 shows the change in cross-sectional profile at two locations down Tyres Ghaut. A third profile is included for Dyers River, however only the pre-eruption and 2010 DEM were included because quantitative observations of change were limited in this stretch of channel. Estimates of change were also compounded by the significant downstream variation in pre-eruption valley width and depth that resulted in different patterns of deposition and erosion. Qualitative observations were made and included in the following discussion. During Phase 1 and in the months immediately following, BAFs and rockfall filled 40% of the total depth of Tyres Ghaut valley with sediment. Photographs (Appendix 2.3h-i) show that primary flows did not erode the interlocking spurs of the upper sections of Tyres Ghaut but significant channel straightening occurred downstream at the transition from Tyres Ghaut to Dyers River. Where the valley narrows and shallows at the top of Dyers River, aerial photographs from 1999 show the removal of vegetation and avulsion of flow, as buoyant PDCs were forced up the valley sides. This pattern of deposition was persistent until Dyers Bridge; at this location the channel reduced in width from 17 m to 5 m. Only a couple of BAFs and one surge travelled past this point during- and immediately after- Phase 1. This shows that initially most material from this period of volcanic activity was stored upstream of Dyers Bridge.

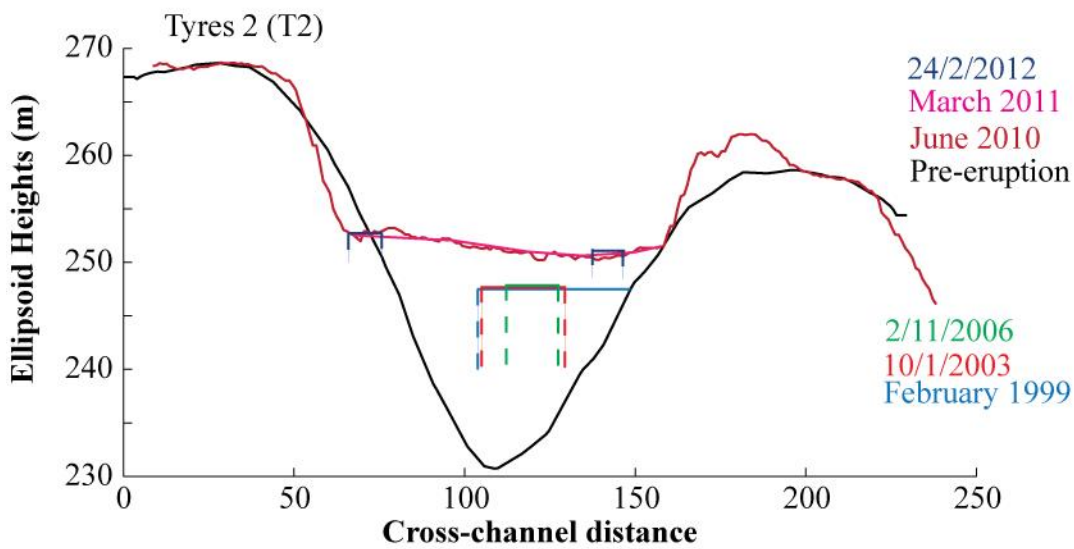
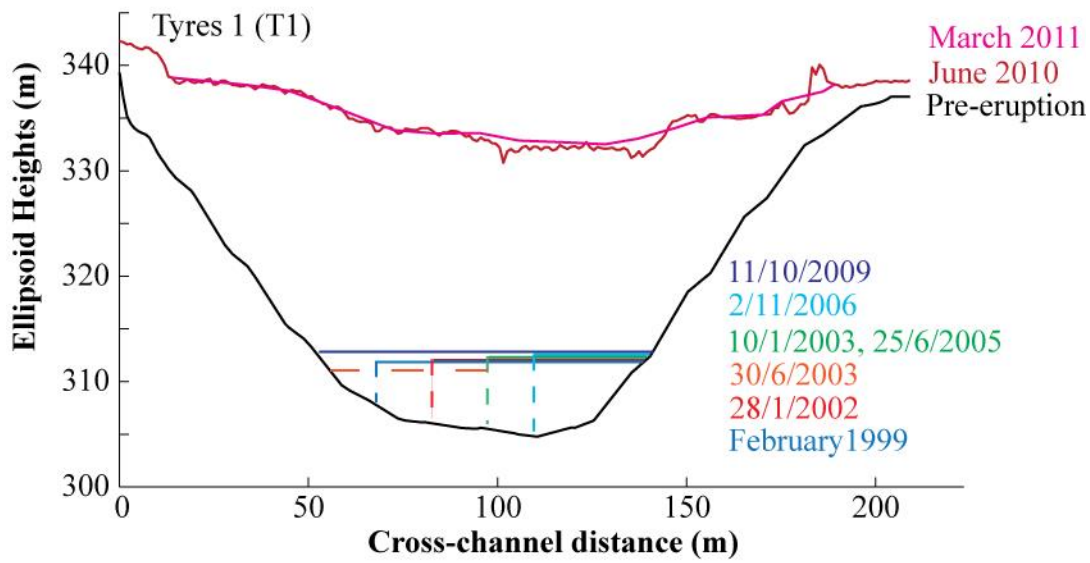
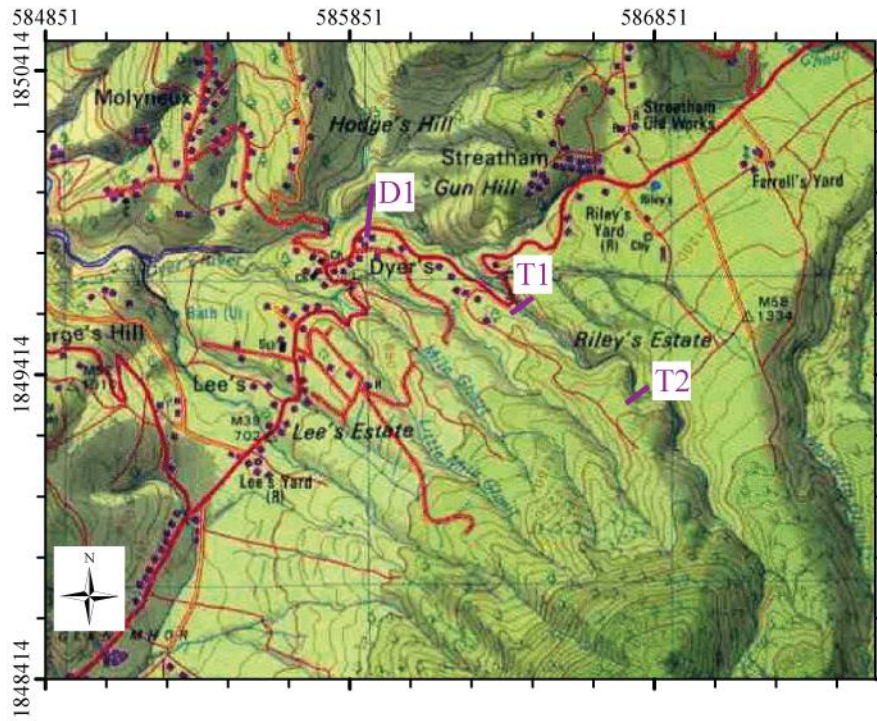
Date range	Flow Type	Maximum downstream distance	Source	Volume added	Method
1/6/1997- 1/2/1999 25/6/1997 surge	Surge-derived from BAF	4.5 km (Cork Hill)	Druitt <i>et al.</i> , 2002a	0.087 x 10 ⁶ m ³	Published
22/9/1997-21/10/1997	BAFs triggered by Vulcanian explosions	3.6 km (Dyer's Village)	Cole <i>et al.</i> , 2002; Druitt <i>et al.</i> , 2002b	Tyres Ghaut 4.39 x 10 ⁶ ± 2.8 x 10 ⁴ m ³ Farrell's Plain 7.71 x 10 ⁶ ± 2.8 x 10 ⁴ m ³ Max depth 180 m	Comparison of 1999 DEM (Wadge, 2000) and pre-eruption DEM (Wadge, 2000)
1/3/1998-1/2/1999	BAFs/ rockfall- dome degradation	13/10/1998- flow into top of Belham Valley (to Molyneux Village)			
1/9/2002- 30/6/2003	BAFs Significant run-outs: 7/11/2002, 9/11/2002, 28/12/2002, 3/01/2003, 10/1/2003, 26-27/01/2003	2.9 km (Dyer's bridge)	MVOobs, 2014	Tyres Ghaut 2.28 x 10 ⁶ ± 2.8 x 10 ⁴ m ³	Single oblique photograph (Appendix 2.3a-2.3b) and aerial photograph (2002)
2/11/2006- 22/1/2007 26/12/2006- 22/01/2007	BAFs		MVOobs, 2014	Tyres Ghaut 3.16 x 10 ⁶ ± 2.8 x 10 ⁴ m ³	Observations (De Angelis <i>et al.</i> , 2007; Wadge <i>et al.</i> , 2014) and aerial photograph (2002)
8/1/2007 Partial dome collapse	BAF	5 km (Cork Hill)	Hards <i>et al.</i> , 2008	4.5 x 10 ⁶ m ³	Published
3/12/2008- 31/1/2009	BAFs triggered by Vulcanian explosions, pumice flows Significant flows: 20-, 21-, 23-, 25/12/08, 2/1/09		MVOobs, 2014; Komorowski <i>et al.</i> , 2010	Tyres Ghaut 3.16 x 10 ⁶ ± 2.8 x 10 ⁴ m ³ 0.5-0.8 x 10 ⁶ m ³	Single oblique photograph (Appendix 2.3d- 2.3e) and aerial photograph (2002)
2/1/2009 Partial dome collapse	BAF	3.5 km (top of BV)	Ogburn, 2013		Published

Table continued to next page

1/10/2009-1/6/2010	BAFs, surges derived from BAFs, pumice flows (11/2/10) and lateral blast		Stinton <i>et al.</i> , 2014	Tyres Ghaut 5.8 x 10 ⁶ m ³ Max depth 30 m	Published
8/2/2010 Partial dome collapse	BAF and surge	6 km (terminated ~300 m upstream of Belham Bridge)	Cole <i>et al.</i> , 2014	3.4 x 10 ⁶ m ³	Published
1/7/1995- 1/6/2010 Total change				Tyres Ghaut 9.79 x 10 ⁶ ± 2.8 x 10 ⁴ m ³ Max depth 70.8 m Dyers River 1.23 x 10 ⁴ ± 2.8 x 10 ⁴ m ³ Max depth 33.1 m Farrell's Plain 9.52 x 10 ⁵ ± 2.8 x 10 ⁴ m ³ Max depth 180.3 m	Comparison of pre-eruption DEM (Wadge, 2000) and June 2010 LiDAR survey (MVO, 2010)

Table 3.1 Volume estimates of primary material deposited in the Belham Catchment. It is noted that the date range used reflects the date of available data rather than the dates of intense surface activity. Volume errors were modelled using a Monte Carlo simulation for probability density function (mean = 0 m, standard deviation = 18 m, the height of vegetation included in the DEM surface model, Table 2.2) was used to generate an error surface which was added as 'noise' to the 1995 DEM. The same procedure was run for the 1999 DEM. The volume difference of the 'noise' added DEMs was calculated. This method was iterated over 100 runs. The volume difference calculated was compared to the 'true' surface volume calculation.

The root mean square error (RMSE) was calculated from the volume differences of the 100 iterations. Methodology adapted from Darnell et al. (2010). Figure 3.2 shows the timing of sediment inputs to the system. Total change was calculated by direct subtraction of the 1/7/1995 DEM from the 1/6/2010 for each section of channel.



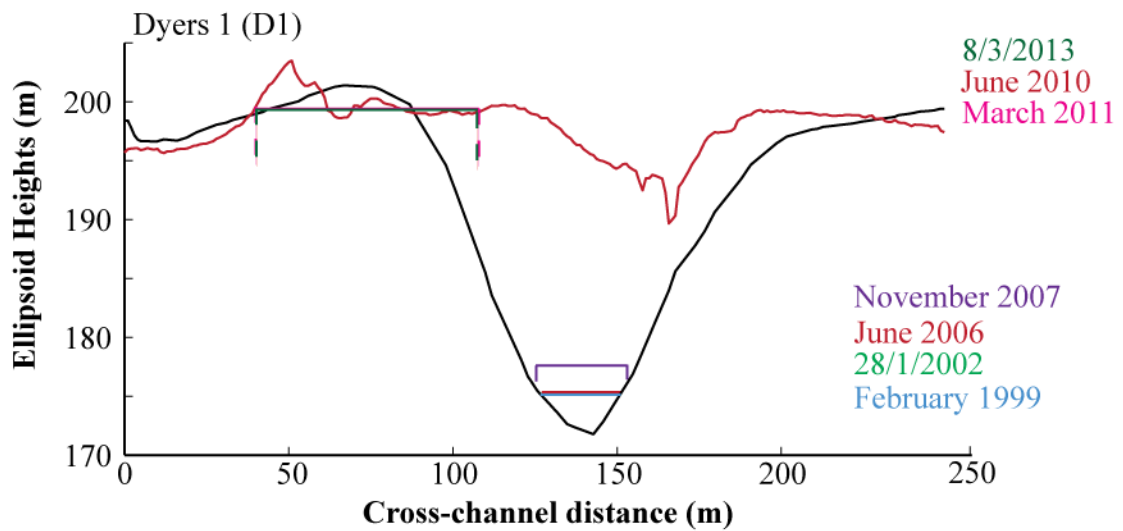


Figure 3.3 Channel cross-sections of Tyres Ghaut and Dyers River. Apparent erosion to the pre-eruption bed surface may be in part representing the loss of vegetation; the pre-eruption DEM was not strictly bare ground, but included vegetation which was estimated to reach 18 m in height (see Table 2.3).

Erosion into valley fills was evident in the 1999 aerial photographs as a single channel located along the east bank of Tyres Ghaut, however the base of the valley in Dyers River appeared to contain braiding and there were no clear terraces of relict deposit. This suggests that most of the material from Dyers was remobilised. The elevation of the bed surface was expected to be higher than the pre-eruption elevation however there was no depth information available for this time (1999 DEM did not cover this stretch of channel). Erosion of Farrell's Plain created a parallel network of near-straight drainage channels <10 m wide with a high density of sometimes discontinuous, high order channels, draining into Tyres Ghaut via 11 new tributaries. Farrell's Plain remained un-vegetated and littered with loose rockfall, while surge deposits from 25th June 1997 that blanketed areas of Riley's Yard and Stretham at the northern limits of the fan, had been largely removed by overland flow (road networks are still visible suggesting deposits were removed rather than re-vegetated) (Appendix 2.3j). Between October 1998 and September 2002, activity onto Farrell's Plain was limited to rockfall and ashfall (Figure 3.2). The reduced disturbance to lower sections of Farrell's Plain between October 1998 and September 2002 allowed significant vegetation recovery (Appendix 2.3k). Formation of new channels at the top of Farrell's Plain fan and the connectivity of these channels with the (incised) 11 tributaries into Tyres Ghaut would have increased peak discharge and channel capacity, resulting in larger lahars downstream in the Belham River Valley.

The rate of channel incision to Tyres Ghaut at cross-section *Tyres 1* (Figure 3.3) shows that erosion rates decreased with increasing time from valley fill deposition. Between October 1998 (last significant PDC down Tyres) and February 1999, fluvial incision in Tyres Ghaut was widening the channel by $9.25 \text{ m month}^{-1}$. This decreased between February 1999 and January 2002 to 0.1 m month^{-1} . This equates to estimated losses of $8.36 \times 10^5 \pm 2.8 \times 10^4 \text{ m}^3$ in the first 4 months following deposition of material, and $2.91 \times 10^5 \pm 2.8 \times 10^4 \text{ m}^3$ in the following 35 months. By January 2003 channel width had increased by 14 m (an increase in erosion rate to $1.17 \text{ m month}^{-1}$), however the incised channel was being filled by BAFs from renewed north-west dome growth. Notably on the 30/6/2003, fresh loose debris was contained within the hydraulically incised channel within relict PDC deposits within the valley (Appendix 2.3b). This showed that significant amounts of material- at least $2.11 \times 10^6 \text{ m}^3 \pm 2.8 \times 10^4 \text{ m}^3$ - remained in storage in Tyres Ghaut between Phase 1 and 2. The aerial photographs from January 2002 showed that the upper sections of Dyers River near Dyers village contained a relatively flat, braided channel bed, similar to that shown in February 1999 aerial photographs. Channel incision appeared to have occurred, potentially into bedrock in the narrow section of channel immediately downstream of Dyers Bridge. Where the channel width increased again, upstream from the tributary with the drainage through Lee's Village, clear multi-level erosional terraces formed between February 1999 and January 2002, within the 33m valley base. This degradational response was likely triggered by reductions in sediment supply from deposits in Tyres Ghaut and on Farrell's Plain.

Increased primary surface activity during September 2002 and May 2003 effectively reset erosion to the valley fill deposit in Tyres Ghaut. Drainages on Farrell's Plain remained active and PDCs did not travel past Dyers Bridge, so the lower section of Dyers River did not receive material from primary flow activity during this time. Channel width in the valley fill deposit increased at an estimated rate of 2.3 m month^{-1} between June 2003 and June 2005. At least $2.28 \times 10^6 \text{ m}^3 \pm 2.8 \times 10^4 \text{ m}^3$ of material was removed from Tyres Ghaut during this period. An oblique photograph taken on 28/6/2005 (Appendix 2.3c) showed significant vertical fluvial erosion into bedrock. Volumetric estimates were calculated using pre-eruption channel boundaries. Evidence of significant bedrock erosion suggested that more material than estimated was removed from the valley fill in Tyres Ghaut and that material transported in flows (lahars) also contained ancient lithic fragments. Critically, vertical channel incision occurred rather

than lateral erosion into unconsolidated valley fill. Runoff from the slopes of Farrell's Plain as well as via channels in the fan, would enhance erosion to the east valley slope of Tyres. However, the presence of alluvial fill within the base of the incised channel suggested bedrock erosion may have taken place during primary activity, caused by BAFs rather than fluvial incision.

A small BAF entered Tyres Ghaut at the end of June 2005 and it is likely deposits were confined to the channel within the valley fill. By November 2006 a further 14 m of erosion had occurred to the terrace of primary deposit in Tyres Ghaut (at *Tyres 1*, Figure 3.3). Downstream oblique photographs (Appendix 2.3l) showed three discontinuous terrace levels, resulting from inter-flow and intra-flow shifts in lahar magnitude. Bedrock underlay terraces in Dyers River where the channel incised in response to confinement by steep valley walls (Appendix 2.3k). Erosion rates downstream in the lower sections of Tyres Ghaut and Dyers River were expected to be higher than upstream because of the addition of water to flow by runoff from Farrell's Plain. Observations also showed that material from upper sections of Tyres Ghaut (and likely Farrell's Plain) was being transported downstream into the Belham River Valley, rather than being deposited as channel storage in parts of Dyers River. The 2006 satellite image showed patchy colouration differences on the channel bed of Dyers River downstream from Dyers Village (Figure 3.4). Based on colour relative to alluvial deposits, imagery suggested parts of the channel bed were stripped of material to bedrock. Bedrock was not visible in this area in the 2002 aerial photograph, suggesting that erosion between June 2003 and November 2006 was greater than between February 1999 and January 2002.

The rate of sedimentation into Tyres Ghaut and Dyers River changed after December 2006 from (1) multiple small-moderate PDCs cumulatively adding to valley fill to include (2) volumetrically significant PDCs generated by partial dome collapses to the north and north-west. Three significant flows occurred- 8/1/2007, 2/1/2009 and 8/01/2010- and all events terminated within the Belham River Valley (Table 3.1). The BAF on 8/1/2007 deposited more material than the entire fill volume of Tyres Ghaut during Phase 1. Volumetrically it was also the largest single BAF to the north-west, although the BAF on 8/10/2010 had a longer run-out. Photographs of Tyres Ghaut following 8/1/2007 were limited, however MVO observations described the valley as "full" (MVOobs, 2014) and an oblique photograph (Figure 3(d) in De Angelis *et al.*, 2007) showed channel fill to occupy a similar depth to deposits in 1999. Since the

valley was not full in the photograph, but the incised channel (e.g. Appendix 2.3i) had been filled and deposits appeared to correspond with approximate fill depths of relict PDC terraces from before January 2007 activity, it was believed that deposition in the upper section of Tyres Ghaut was contained within the incised channel. Satellite imagery was available for 18/11/2007 of Dyers River and the Belham River Valley.

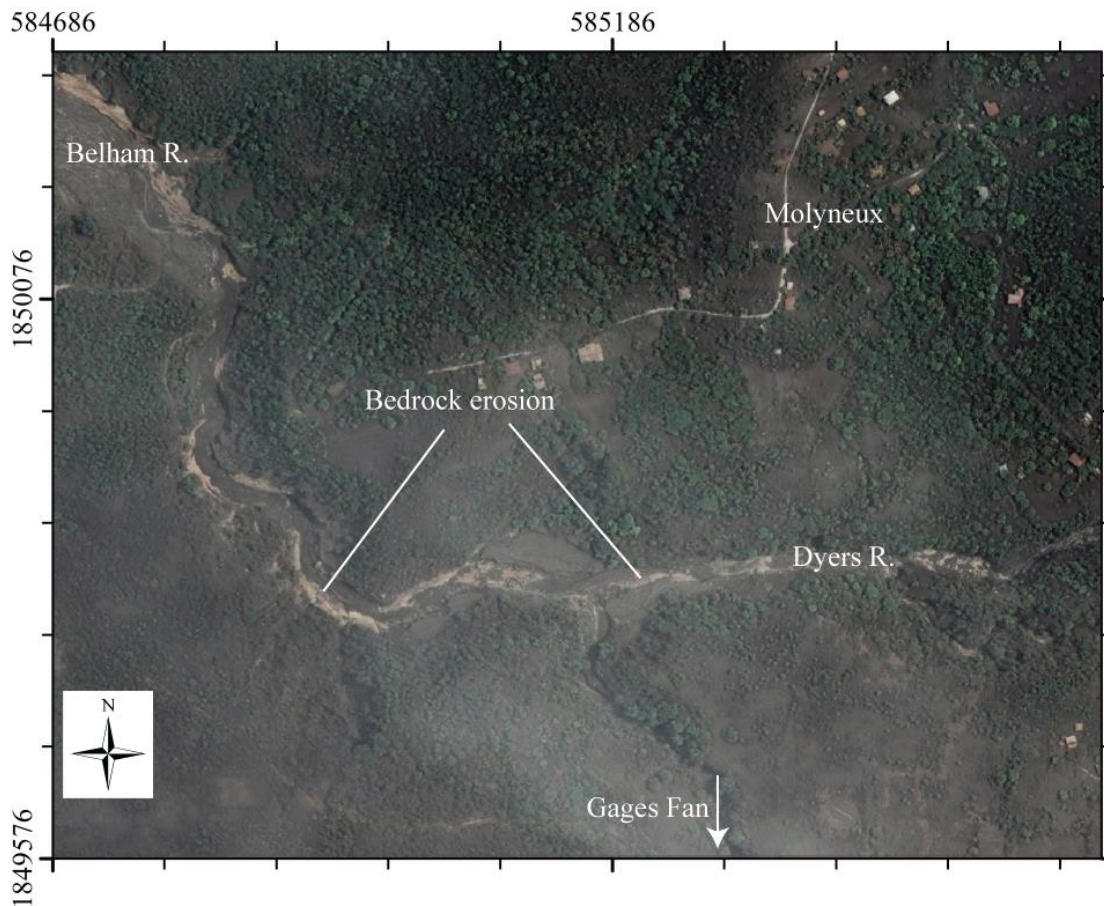


Figure 3.4 Erosion to the valley sides exposing bedrock, 24th June 2006 satellite image

Imagery showed significant widening and infilling of Dyers River by BAFs compared to imagery from 24/6/2006. It is likely that these changes were associated with the voluminous 8/1/2007 event. Just upstream of Dyer’s Bridge, channel width increased from 46 m to 60 m. Dyers Bridge, which was visible in the 2006 image has been buried. Significant deposition occurred immediately upstream of Dyers Bridge because the valley narrowed at the bridge location, reducing channel capacity resulting in channel avulsion by the PDC and deposition of suspended material. Just downstream (0.37 km) from Dyer’s bridge, the channel widened from 21 m to 68 m; at the confluence of the drainage from Lee’s Village (marking the start of the Belham River Valley, 0.63 km from Dyer’s bridge), channel width increased from 67 m to 140 m.

Critically, imagery suggested that most deposition from the 8/1/2007 event occurred downstream of Tyres Ghaut in Dyers River. It was hypothesised that this happened because the flow had enough energy to carry material down the relatively straight steep section of Tyres Ghaut but responded to the reduction in channel gradient, change in channel direction and reduction in valley width by depositing significant volumes of material near Dyers Village. Reworking of deposits by rainfall was evident in the 18/11/2007 satellite image. Upstream of Dyers Bridge channel incision occurred (between January and November 2007) and terraces of PDC material with multiple steps were identified in the centre and on the edges of Dyers River Valley. Channels occupied ~ 30% of the valley width; the remaining width was filled with primary deposit. Downstream of Dyers Bridge the valley base was covered in a complex network of multiple narrow (<10 m) channels, fed from deposits upstream. Notably, the shift from channelized terraces to braiding occurred after Dyers bridge when the channel widened and fluvial flows lost energy.

There were only two oblique photographs available for Tyres Ghaut before and after the 2/1/2009 event. The first image (Appendix 2.3d) showed that by 3/12/2008 deep incision had occurred to deposits in the top section of Tyres Ghaut that was likely to correspond downstream to the formation of channels similar to those in November 2006. The second image (taken September 2009; Appendix 2.3e) showed Tyres Ghaut was filled with sediment to similar depths as during Phase 1. Estimates of volumetric gain for this period (Table 3.1) were very crude but suggest comparable amounts of fill to that in 2007 (in this section of channel). Only a few very narrow superficial channels were apparent on the September 2009 image, although a shallow terrace of PDC deposit was present in the valley meander and drainages on Farrell's Plain have been re-established. The endurance of Phase 4 PDC deposits in Tyres Ghaut meant that flows at the onset of Phase 5 quickly avulsed from the valley ridges. Following the voluminous BAF on 8/10/2010 (Table 3.1), Tyres Ghaut became intrinsically linked to Farrell's Plain, becoming part of the continuous debris fan, rather than a distinct major drainage channel. Of the estimated $1.4 \times 10^6 \pm 2.8 \times 10^4 \text{ m}^3$ of material that was deposited in Tyres Ghaut and Dyers River between November 2009 and June 2010, an estimated $3.6 \times 10^6 \pm 2.8 \times 10^4 \text{ m}^3$ of material (including sediment deposited prior to November 2009) was removed by fluvial erosion between the end of Phase 5 (February 2010) and June 2010, with unquantifiable amounts of material mobilised from drainages on Farrell's Plain. The PDC deposits were easily erodible, because of their high (at least 30%, Cole,

2014) sand content. By June 2010 a dense network of parallel channels had developed on the Farrell's plain- Tyres Ghaut debris fan. Drainage density of this area had increased from 7.11 km^{-1} to 9.52 km^{-1} during the five phases of eruptive activity but predominantly due to deposition in Phase 5. Once established the channel network in the debris fan continued to erode laterally, at variable rates depending on location. Just downstream from Dyers Village the channel widened by 4 m month^{-1} between June 2010 and March 2011, $0.18 \text{ m month}^{-1}$ between March 2011 and February 2012, and $0.08 \text{ m month}^{-1}$ between February 2012 and March 2013 (calculations based on repeat aerial imagery, 2011-2013). Erosion was driven by flow undercutting deposit terraces that delimited channel width, resulting in mass collapse of sediment into the channel that was then reworked and entrained by flow.

3.2.2. Development of Gage's Valley Fan

The most significant change to catchment size during the 18 years of volcanic activity occurred in Phase 1 during periods of dome collapse in July 1997 and explosive activity between the 4th-12th August 1997 and 22nd September- 21st October 1997. Rapid dome growth and large collapse events to the north and west during July 1997, initiated the building of a debris fan between Gage's Mountain and St George's Hill, centred over Gage's Valley. Pyroclastic flows generated down Gage's Valley lost energy when deflected by St George's Hill (Figure 3.5a). This resulted in some deposition in and proximal to the Gage's Valley channel, accompanied by erosion to the south-west slopes of St George's Hill. This occurred as buoyant pyroclastic flows were forced upwards by topographic barriers in the flow pathway. The material added to the Gage's fan during 31st July- 4th August 1997, was predominantly in the form of BAFs; a large flow (Table 3.2) that descended the length of Fort Ghaut on 3rd August 1997. Eight explosions generated pumice-and-ash flows during 5th-12th August 1997 (Druitt *et al.*, 2002a), and deposited pumice rich material on Gages Fan. Further PDCs and rockfalls in response to westward dome growth continued to add material to Gage's fan until 19th August 1997. Material was added to the Gages Valley fan during a second period of explosive activity (22nd September- 21st October 1997) involving a total of seventy-five Vulcanian explosions (Cole *et al.*, 2002); forty-one explosions resulted in pumiceous pyroclastic flows down Gage's Valley (Druitt *et al.*, 2002b).

Although there was a pause in magma extrusion between March 1998 and November 1999, rockfalls and pyroclastic flows from the west side of the unstable

dome continued to deposit material Gage's Valley fan. Activity increased in October 1998 during which time a series of small volume dome collapses triggered pyroclastic flows in several drainages. A small volume dome collapse on 31st October 1998 deposited material to the west, 3 km from the dome. Pyroclastic flows also occurred down Gage's Valley during a larger collapse event on 12th November 1998. By the end of November 1998, degradation of the dome had excavated a deep (150 m x 30 m wide) gully into Gage's Valley, which extended through the dome to the north-east, effectively splitting the dome into two peaks (Norton *et al.*, 2002).

The accumulation of material onto the Gage's Valley fan during Phase 1 and the pause between Phases 1 and 2 modified the boundary between the Belham Catchment and the Gages Catchment. Figure 3.5 shows the change to the local drainage network calculated from repeat topographic surveys and photographs (see Section 2.2.1). Between July 1995 and February 1999 the Belham Catchment had increased in size by $1.24 \times 10^6 \text{ km}^2$. Prior to the onset of activity Gage's Valley was disconnected from drainages in the Lee's Village area, and therefore from the Belham River Valley, by an elevated piece of land (Lee's Yard, Figure 3.6). By February 1999 pyroclastic flow deposition had infilled upper Fort Ghaut (point A, Figure 3.5a), creating a continuous slope from the head of the Gage's Valley (point B, Figure 3.5a) through Lee's Yard to join the ghaut draining from Lee's Village into the Belham River Valley. Although the photographic record of this area is limited between 1997 and 1998, based on records of volcanic activity and available photographs (Appendix 3.1a-b), it is suggested here that Gage's fan was *hydrologically* connected to Lee's Village drainage from 3rd August 1997 following the voluminous BAF down Gages valley into Fort Ghaut.

Between August 1997 and October 1997 runoff and erosion resulted in the formation of a drainage divide on the fan, separating it into two sub-basins: one draining to the north and one to the west (Figure 3.5). The north basin remained connected to the outlet of Gages Valley (point B, Figure 3.6), while the west basin drained from the fan to join the lower reaches of Fort Ghaut (Figure 3.5b), which flowed through Plymouth. Initially the main channel draining the north fan skirted the base of Gages Mountain joining pre-existing drainage routes in a northwards direction. By 1st October 1998 the deposit at the outlet of Gages Valley had been dissected by a new channel heading directly westward towards Plymouth, from which the north basin of Gages fan was

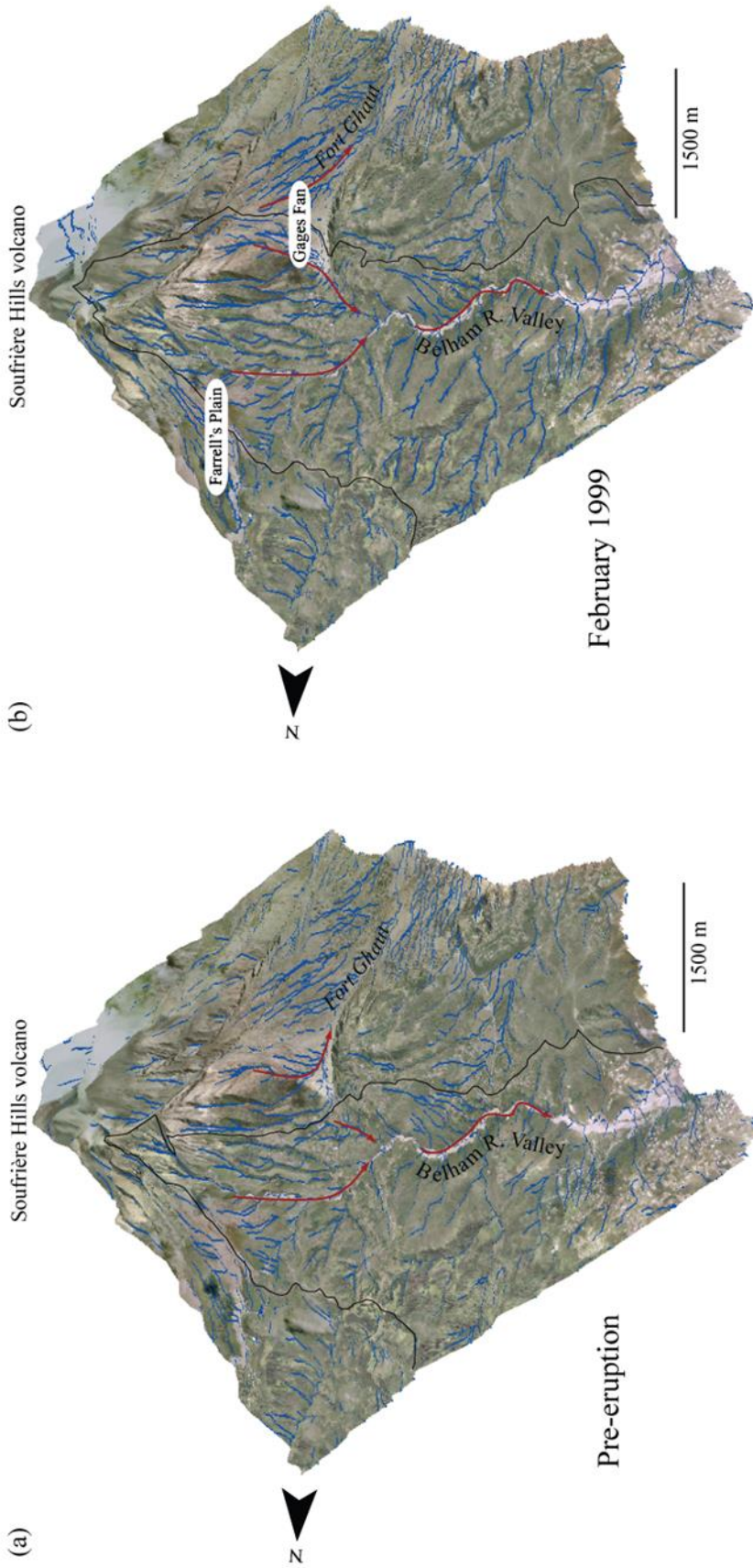


Figure 3.5 (a) The pre-eruption hydrological drainage network is shown by blue lines on the three-dimensional topography (a sub-section of 2002 aerial imagery draped over the pre-eruption DEM). (b) The hydrological drainage network in February 1999 following Phase 1 volcanic activity, shown by blue lines on three dimensional topography (a sub-section of 2002 aerial imagery draped over the February 1999 DEM). The main areas of volcanic deposit are labelled. For (a) and (b), the red arrows show the direction of flow in the main channels. The Belham Catchment is delineated by the black line; the catchment boundary was defined by DEM analysis using Hydro tools in ArcGIS. Note that only the upper section of the Belham Catchment near the Soufrière Hills volcano is included.

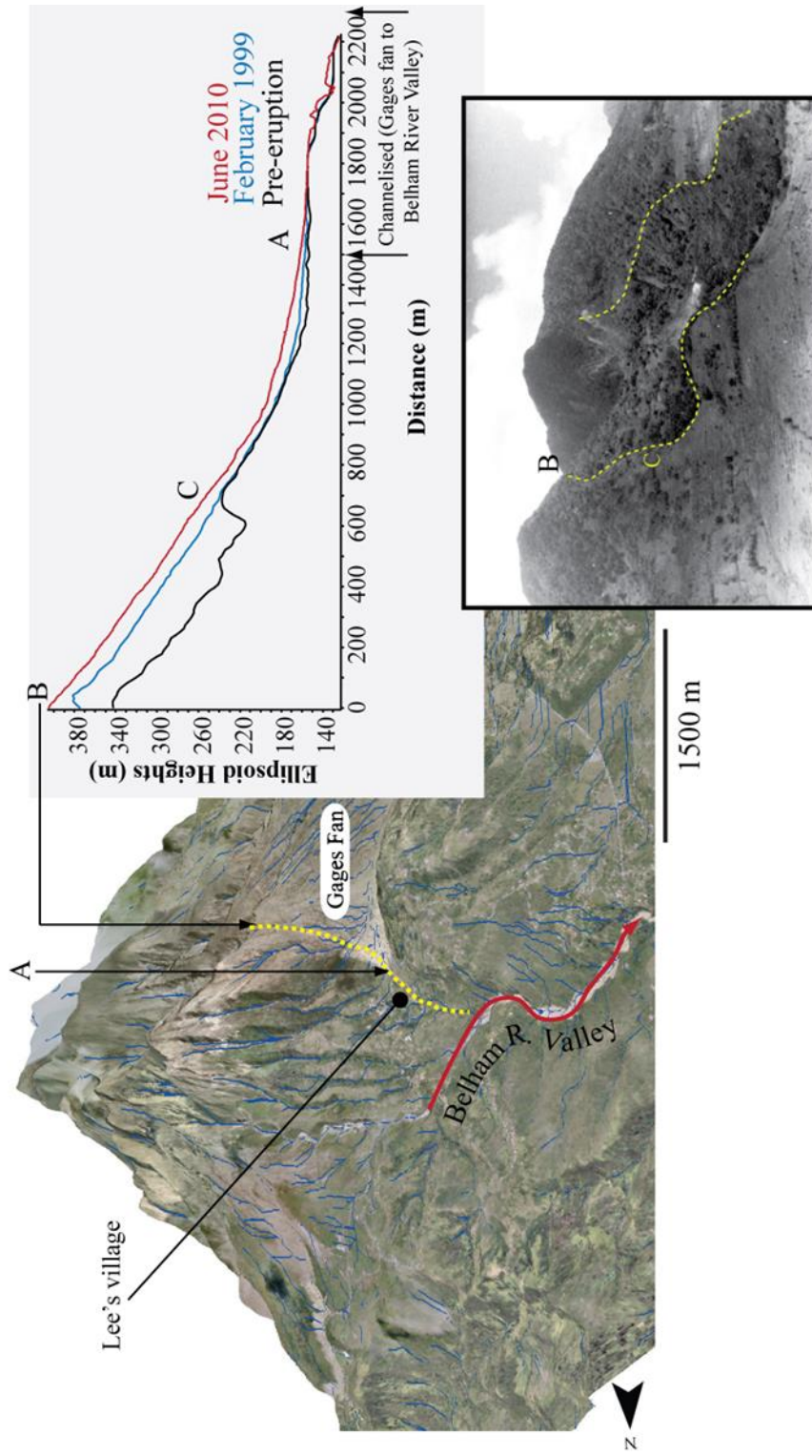


Figure 3.6 Location of longitudinal profile (left) between the top of Gages fan (point B) and the Belham River Valley. The longitudinal profile (right) shows the change in topography due to volcanic sedimentation in Phase 1 (black to blue line) and Phases 2 to 5 (blue to red line). Changes in longitudinal profile as depressions in topography were infilled by sediment, hydrologically connected the Belham River Valley to the Gages Fan forming to the west of the Soufrière Hills volcano. Point A is the location of the base of Gages fan where vertical erosion occurred connecting Gages fan to the pre-existing drainage network near Lee's village (see also Figure 3.7). Point C shows the location on the profile of the ridge line of the pre-eruption lower Gages valley (Photograph bottom right), which was infilled with sediment during Phase 1. Photograph (bottom right) from the British Geological Survey P536996, 01/01/1936.

connected by the small channel at the base of Gages Mountain. Given the deposition of material westwards by dome collapses during October and November 1998, it is anticipated that the north basin on Gages fan remained connected to the Gages Valley outlet in December 1998. Critically, from December 1998 the north basin of Gages fan was connected to the gully which had formed through the dome (Norton *et al.*, 2002), facilitating the movement of large volumes of material onto this part of the fan and potentially beyond into the Belham Valley.

On 26th February 1999, the volume of material on the north basin of the Gages fan available for re-entrainment was estimated at $1.2 \times 10^7 \text{ m}^3 \pm 2.8 \times 10^4 \text{ m}^3$ over an area of $6.95 \times 10^5 \text{ m}^2 \pm 625 \text{ m}^2$, of the total fan volume of $1.44 \times 10^7 \text{ m}^3 \pm 2.8 \times 10^4 \text{ m}^3$ (area $2.93 \times 10^6 \text{ m}^2 \pm 625 \text{ m}^2$) (see Chapter 1 for catchment delineation). The maximum deposit thickness was 219 m. The fan was connected to the Belham River Valley via a single new channel across Lee's Yard joining the pre-existing channel draining from Lee's Village into the Belham River Valley just below Dyers (Figure 3.5a). DEM analysis did not capture any changes to the existing 400 m length of channel, which at its narrowest point was ~7 m wide.

Water and sediment were transported from the Gages fan into the Belham River Valley, while the two were hydrologically connected. Gages fan and the Belham River Valley became disconnected when there was a 'temporary' blockage in the channel connecting the fan and Belham River Valley, or when the Gages fan morphology altered, directing flow westwards. While connected to the dome via the Gages outlet (point B, Figure 3.5a), the north Gages fan continued to receive fresh material via rockfall and PDCs. However, this connectivity between the dome and north Gages fan depended on the balance between deposition of material from the west-side of the dome, and erosion into these deposits by rainfall. Since February 1999 the Gages fan remained connected to the Belham River Valley via the Lee's Village drainage, however direct connection with the dome was intermittent. Table 3.2 summarises periods of increased sedimentation on the north Gages fan. When incision of the westward channel draining from Gages outlet to Plymouth outpaced the rate of incision of channels exiting the Gages outlet onto the north part of the fan, material was not fed from the dome onto the fan unless it avulsed the deep westward channel or was deposited from air transport. Rockfall from St George's Hill and the north-west slopes of Gages Mountain contributed material to the fan, but volumes were insignificant compared with PDCs. Channel incision between March 1999 and 26th February 2001

North Gages fan connected with Gages outlet	Significant flows	Deposit type	Volume estimate ^[1]	Source
July 1997- (March 1999- 26 th February 2001)	3/8/1997	BAF	9.1 x 10 ⁶ m ³ DRE	Cole <i>et al.</i> , 2002
15 th September 2006- March 2007	4/1/2007 8/1/2007			MVOobs, 2014
28 th July 2008- early 2009	28/7/2008 3/12/2008 3/1/2009	Pumice-fallout BAF and surge Pumice-fallout	1.36 x 10 ⁶ m ³	Komorowski <i>et al.</i> , 2010
6 th November 2009- present	28/10/2009 18/1/2010	BAF BAFs	1.5 x 10 ⁶ m ³ ^[2]	Stinton <i>et al.</i> , 2014

^[1] Volume estimates do not discriminate by fan location- flow volume was distributed across the entire Gages fan

^[2]Total volume for Phase 5 deposited

Table 3.2 Dates of significant PDCs onto Gages Fan and where available (published) volume estimates of primary material deposited.

(Appendix 3.1c-) deepened and widened the Gages outlet to similar geometries as the pre-1995 Gages Lower Soufrière and Gages Valley (see Photograph in Figure 3.6). Small rockfalls and pyroclastic flows during 2002 and 2003 were contained within the Gages outlet (MVOobs, 2014), which fed into a deep, 18 m wide channel leading to Plymouth. The source fan for the Gages outlet was not heavily incised illustrating the regularity of input material into this zone. Erosion to deposits was not readily observed following other periods of sedimentation; the record of observations after Phase 1 cannot specifically date the disconnection of the north Gages fan with the dome- a range from March 1999 to 26th February 2001 was used based on available photographs (Appendix 3.1c-d). Therefore the date of disconnection of the north Gages fan from the Gages outlet in Table 3.2 must be treated as an estimate from available photographs.

Between February 1999 and June 2010 an estimated $5.21 \times 10^6 \text{ m}^3 \pm 2.8 \times 10^4 \text{ m}^3$ (area $5.48 \times 10^5 \text{ m}^2 \pm 625 \text{ m}^2$) of material was deposited on the north section of Gages Fan; the total fan volume gained between 1999 and 2010 was $1.04 \times 10^7 \text{ m}^3 \pm 2.8 \times 10^4 \text{ m}^3$ (area $3.09 \times 10^6 \text{ m}^2 \pm 625 \text{ m}^2$). Of the total volume ($1.08 \times 10^7 \text{ m}^3 \pm 2.8 \times 10^4 \text{ m}^3$, area $5.47 \times 10^5 \text{ m}^2 \pm 625 \text{ m}^2$) deposited on the north Gages fan between July 1995 and June 2010, at least 48% of material was deposited by 1999 (greater if erosion included in calculation), while deposition from Phase 1 equated to 52% of the total fan volume. Volumetric inputs by individual flows or a concurrent phase of activity, were considerable and equated to 115% of the entire Gages fan volume. Of course some material from these events was deposited offshore or just outside the boundaries defined for the Gages fan in this analysis, however it is likely that much of the material from the three events (periods) in Table 3.2 remained stored in Gages fan.

Photographs (Appendix 3.1a-c) showed that it initially took over 2 years to establish clear channels on the north section of Gages fan and a further 2 years for these to extend from the fan apex to toe (Figure 3.7a). Once established, these channels were excavated and then re-occupied by deposit following further sedimentation, between 15th September 2006 and March 2007. Satellite and aerial imagery from January 2002, June 2006 and November 2007 showed the preservation of terraces within the channels before and after primary flows, suggesting that deposition during these events only mantled topography and did not alter channel morphology. Channel migration from mid-way down the fan (point C, Figure 3.6) was likely to have been slow due to the underlying bedrock morphology; in this section the deposit was only ~ 1 m thick and erosion was likely focused. There was a distinct absence of coarser (boulder) material

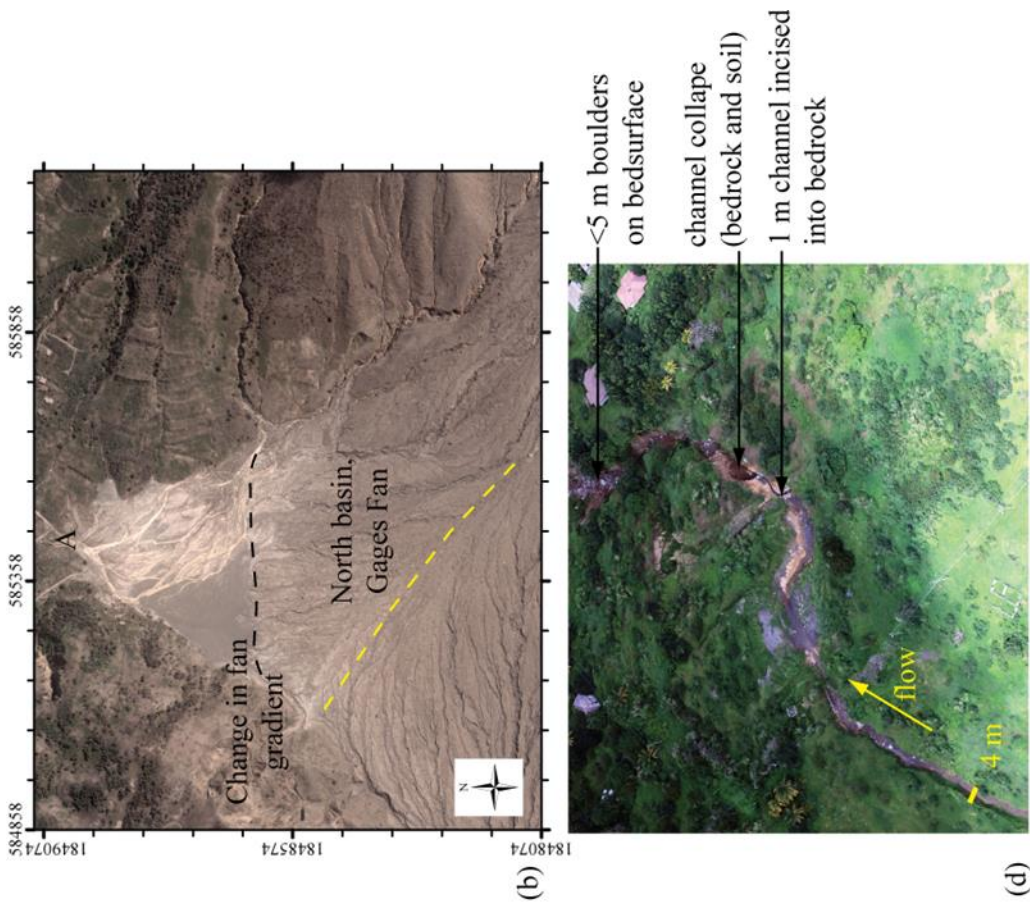


Figure 3.7 (a) Gages Fan August 2002 (Photograph F.J. Froude), (b) Gages Fan, Satellite image 18th November 2007, (c) Looking downstream from Gages Fan to the Belham River Valley, February 2012, (d) Looking downstream from Gages fan to the Belham River Valley, February 2012

in the lower section of the fan because of the decrease in slope gradient (determined by pre-eruption topography) 1.3 km from Gages outlet; coarser material was preferentially deposited immediately downstream of this point. The channel structure abruptly changed in response to the decrease in slope angle (9° - 3.8°), and the lower fan section contained a high density of braided channels (Figure 3.7b). Critically, the change-point in slope gradient advanced up the fan suggesting that the thickness of material in the lower section of the fan was increasing (between 2002 and 2007, Figure 3.6 and 3.7b). This was not captured by the limited DEM record, but was important because it shows the ready supply of sediment close to the outlet into the drainage channel between Gages fan and Lee's Village was increasing. The change in slope angle promoted significant deposition between 2008 and 2010 near the toe of the fan (Figure 3.5b) and reset channelization upstream. Small PDCs were observed to the west in the years following the end of Phase 5 (MVOobs, 2014); particularly in the first year after the February 2010 dome collapse. If activity were to resume with voluminous PDCs to the west into the north section of Gages fan, it is likely that the debris fan toe would advance further northwards and possible that primary flows would continue from the fan into the channel between Gages and the Belham River Valley. In 2014 hydrological connectivity was limited to an entrenched steep channel with a low width: depth ratio of 1.3. Prior major dome collapses were focused to the east, south and north (Wadge *et al.*, 2014), and PDCs all terminated on the Gages debris fan. If activity were to resume and large primary flows were to continue north from Gages fan towards the Belham River Valley it is likely the connecting channel would quickly be infilled, dramatically altering runoff between Gages fan (and the west side of the dome) and the Belham River Valley. This would significantly increase the magnitude (water and sediment) and frequency of lahars entering the Belham River Valley.

The channel between the Gages Fan and the Belham River Valley was narrow, 4 m wide by 4 m deep draining from the base of the north Gages fan over the top of a relict road structure. The channel was straight for the first 0.25 km and then increased in width at its first bend. Figure 3.7d is an aerial photograph taken in March 2012 and shows the 4m deep, 1 m wide incision into the channel bed that was made just downstream of the second meander. Channel incision here was likely to have been prompted by a discontinuity in geology- note the landslide scarp at the channel collapse labelled in Figure 3.7d. Erosion into the bedrock exposed a layer of conglomerate with a high content of boulder sized clasts- relative to adjacent rock. Immediately downstream from this incision was a fresh bank collapse containing large (estimated ~5

m) boulders; this was one of many bank failures in the channel. Photographs showed that from this point the bed surface of the channel was littered with boulders, some of them occupying >50% of the channel width. The boulders do not show any organised bed structure and many were arranged within heaps of mixed material (grain size, soil and rock). This suggested that they originated from bank collapse rather than from the Gages debris fan. Just upstream of the confluence with the Belham River Valley, where the channel was wider (27 m), there was evidence of fluvial organisation in the form of terraces and a mid-channel bar (Figure 3.7d), however this was a very short (0.16 km) stretch of channel.

The increase of the Belham Catchment to include an active debris fan draining (at times) directly from the dome and to the west of SHV, provided a sub-basin containing: (1) a large volume of loose debris, (2) a sediment supply that was sustained beyond the period of eruption when the fan was connected with the Gages outlet and the dome, and (3) an extension to the Belham Catchment to the west coinciding with east-to-west preferential wind direction and therefore an increased incidence of tephra fall (Section 3.3). The small-scale nature of short-duration, high intensity weather systems, characteristic of Montserrat's location in a tropical climate system, result in rainfall that may only affect part of the Belham Catchment. Furthermore, recent work by Poulidis *et al.* (2014), investigated the role of heated terrain as a forcing mechanism for convection and storm generation. Numerical modelling results showed that localised rainfall to the west and south-west generated by this mechanism is possible under 'favourable atmospheric conditions'. Enlargement of the Belham Catchment to include Gages fan provided coverage of this westerly area, facilitating the triggering of lahars into the Belham River Valley by locally generated rainfall over SHV.

The increase in catchment size increased the surface area intercepting rainfall and therefore the probability of intercepting small-scale weather systems. The volume of water contributing to surface runoff depends on the surface characteristics of the fan. In 2012 the fan remained largely un-vegetated, promoting high run-off rates; limited revegetation occurred on the upper sections of the fan in 2007 (shown November 2007 satellite image) but this was short lived. Tephra fall from both explosions and PDCs onto the fan was observed in other parts of the catchment to temporarily reduce infiltration into the bed surface (Section 3.3); therefore increasing runoff. Channelization of the fan increased the efficiency of runoff and the intensity of peak discharge. There were a number of factors that controlled the amount of water entering

the channel between Gages and the Belham River Valley. Channel incision rates into the bedrock were extremely high, 333 mm year^{-1} corresponding to a channel depth change of 5 m (in the new section of channel near Gages fan), between 1995 and 2010. Although the vertical error on the 1995 DEM was $\pm 23 \text{ m}$ (Wadge, 2000), oblique aerial photographs (Figure 3.7c-d) support DEM calculations. The steep, deep and narrow geometry of the channel linking the Gages fan and the Belham River Valley was likely to result in high flow velocities and rapid delivery of runoff between the two sections of catchment. The presence of piles of bedrock and soil debris in the base of the channel from mass wasting as flow incised into the channel base and destabilised the vertical channel sides (Figure 3.7c-d), suggested that flow may bulk and transform into a hyperconcentrated or debris flow depending on flow hydraulics and available sediment in the channel. A photograph from September 2009 (Figure 3.8a), shows the en-masse deposition of coarse material within the channel at the tributary with the Belham River Valley. It is likely that this deposit resulted from the sudden loss of flow capacity as it exited the narrow channel in the wider main channel.

Critically observations suggested that expansion of the Belham Catchment and development of the Gages fan and connecting channel, enhanced lahar magnitude in the Belham River Valley by increasing runoff area, the potential of rainfall inception and sediment supply. It is also possible that the arrival time of flow in the Belham River Valley after rainfall decreased, because of the increasing efficiency of the channel linking Gages fan with the Belham River Valley. Observations after a small lahar on 23rd March 2011 (Figure 3.8) showed that drapes of fine sediment deposited during the flow seemed to originate from the Gage's fan-Belham link channel, and that the deposit had not been cross cut by flow from upstream (Tyers-Dyers River) suggesting that the lahar may have been solely come from Gage's fan or that Gage's fan provided a second lahar peak.

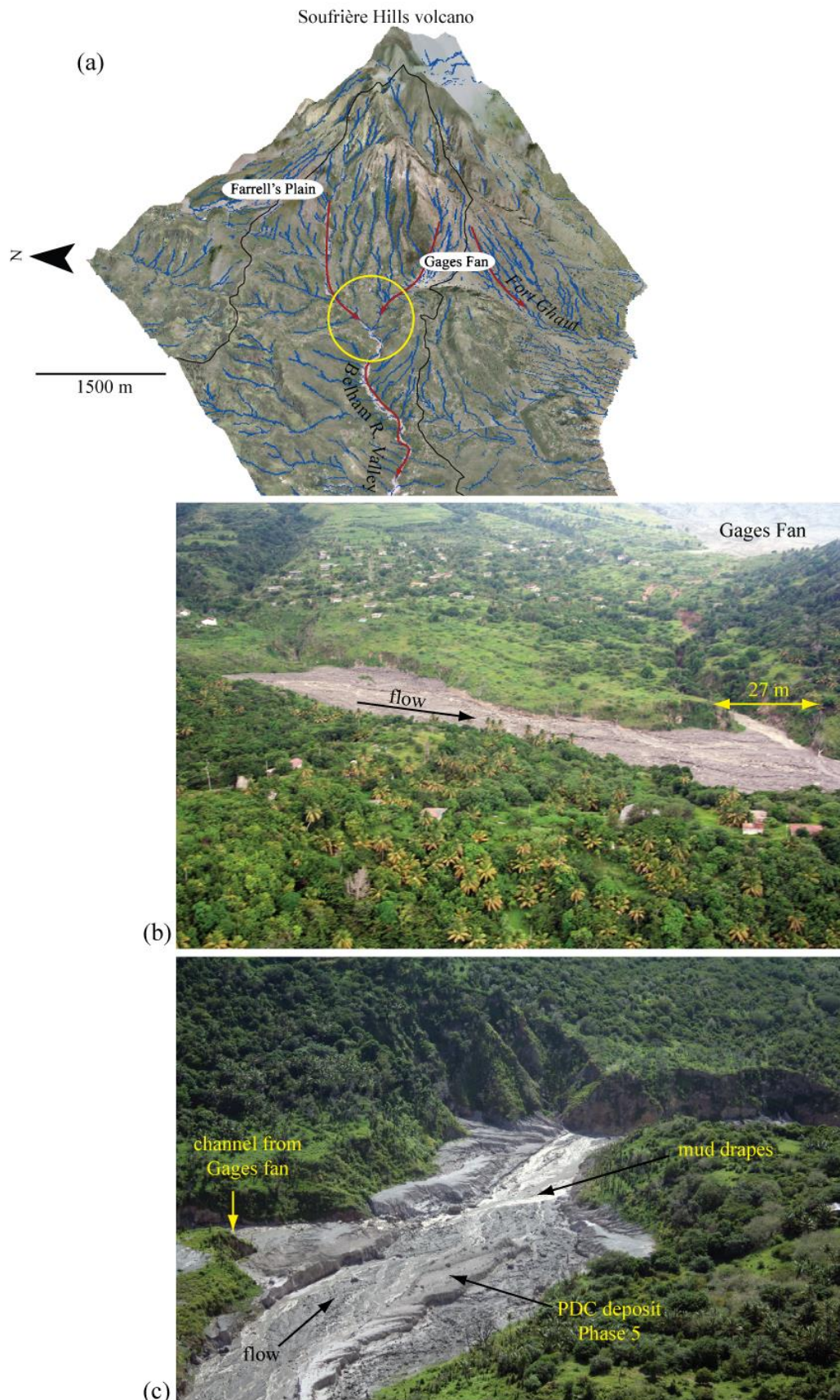


Figure 3.8 (a) Location of the confluence of Lee's village channel with the Belham River Valley. See Figure 3.5b for base map details. (b) Lahar deposition at the confluence with the Belham River Valley, September 2009. Photo courtesy Paul Cole. (c) Deposition from a small lahar on 23rd March 2011. Photo courtesy Henry Odbert.

Results from this section showed that:

1. The size of the Belham Catchment increased to include some of Gage's fan early in the 19 years of volcanic activity; by August 1997.
2. Inclusion of Gage's fan increased catchment runoff area, the probability of rainfall inception during mesoscale weather systems and sediment supply (and storage).
3. 80% of the total PDC deposition in Tyres Ghaut, Dyers River and Farrell's Plain originated from three large partial dome collapse events during Phases 3 to 5 (Table 3.1): .8/01/2007, 2/01/2009 and 8/02/2010.
4. Inputs of sediment to Farrell's Plain and Gage's Fan were strongly linked to north-west or west dome extrusion, respectively, as well as patterns of gully erosion on the debris fan and at the edifice.
5. The lateral erosion of channels in PDC deposits decreased with increased time from eruption. Based on measurements from 1998 to 2002, and 2010 to 2013, lateral erosion decreased by an order of magnitude the year after volcanic emplacement.
6. Bedrock erosion was observed on valley sides and in the base of channels on debris fans and in areas previously unoccupied by flow.

3.3. Tephra fall and runoff dynamics

Tephra fallout occurred during all five phases of eruption and had the potential to alter (1) infiltration rate and runoff efficiency, (2) add sediment to a lahar and (3) alter lahar rheology (Alexander *et al.*, 2010). Fallout material was generated by (1) magmatic explosive eruptions, (2) elutriation of fines from dome-collapse block-and-ash flows and rockfalls, (3) ash-venting, and (4) phreatic explosions (Bonadonna *et al.*, 2002). The term tephra fall is used to describe all particles ejected from the volcano irrespective of size, shape and composition. Unless specified, reported tephra fall thickness and thereby calculated volumes may include a mixture of ashfall, pumice fragments and dome fragments (detailed descriptions were not always given by observers). The prevailing direction of low-level wind is from east to west, thereby where coverage of fall deposits are not given by observers, it is likely that the Gage's Fan area of the catchment to the west of SHV received some fallout, and possible that fallout was catchment wide, including slopes draining into the Belham River Valley to the northwest of SHV.

Phreatic eruptions from 18th July 1995, including explosions on 28th July, 20th, 22nd and 28th August generated mm thick ash fall around SHV. Explosions on 21st August, 31st October, 4th and 5th November generated cold base pyroclastic surges to the west, which deposited thin (mm) ash layers (Young *et al.*, 1998). Prior to the onset of dome extrusion in mid-November 1995 (Robertson *et al.*, 1998), the ash derived from fine fragments of older domes (Young *et al.*, 1998). Following the onset of Phase 1, tephra fall included juvenile material. Table 3.3 summarises tephra fall depth and volume calculated from published isopach maps that were digitised and combined in ArcGIS (Appendix 3.2). It is noted that the isopach divisions (min and max) for each delimited map section were maintained when the maps were combined and the total tephra depth was calculated. Tephra fall volumes were calculated using the minimum and maximum tephra fall depths for the area of each sub-catchment.

Vegetation increases the surface storage of rain water because it can more than double the total surface area to be wetted before drops wet the soil and accumulate on the soil surface. Vegetation protects the soil surface from drop impact and retards soil surface sealing. Soil aggregates are more stable if organic matter is present in the soil, which is usually more abundant under (permanent) vegetation cover. Plant roots increase macroporosity and hence infiltration capacity. Furthermore, vegetation increases friction to overland flow, decreasing runoff velocity and absorbing part of the flow energy. Roots increase the resistance of topsoil to flow detachment (De Baets *et al.*, 2007), which is equivalent to increasing soil cohesion (De Baets *et al.*, 2008; Torri *et al.*, 2013). The increase of soil resistance with root density (0-15 kg m⁻³) is initially very close to a power law and corresponds to an increase in soil cohesion at saturation of 4 to 8 kPa (Brunori *et al.*, 1989; De Baets *et al.*, 2008). This brings the soil to an almost non-erodible condition.

Volcanic activity damages or completely destroys vegetation by several mechanisms, dramatically altering surface runoff response to rainfall. (1) Sulphur chloride emissions from SHV in the plume mix with water in the atmosphere and generate acid rain, which damages leaves and limits chlorophyll production. Significant damage was observed to cloud forest at Masaya volcano, Nicaragua (Johnson and Parnell, 1986), although certain weedy composites flourished in the hostile conditions (2) Thin layers of tephra fall may adhere to wet leaves from prior rainfall, and generate hydrochloric and sulphuric acid, resulting in similar leaf damage as acid rain. Outdoor crops suffered from tephra adherence, resulting in reduced harvest yields, following the

Date	Catchment	Tephra Fall Depth (range) (mm)	Tephra Fall Volume (m ³)	Source
Phase 1 2/6/96-25/6/97 4/8/1997-21/10/97	Soufrière Hills	30- 458	7.86 x 10 ⁵ to 1.66 x 10 ⁶	Bonadonna <i>et al.</i> , 2002
	St Georges Hill	100- 330	6.13 x 10 ⁵ to 1.25 x 10 ⁶	
	Garibaldi Hill	32- 210	1.71 x 10 ⁵ to 4.03 x 10 ⁵	
	Centre Hills	1- 214	5.87 x 10 ⁵ to 1.42 x 10 ⁶	
	Entire	1- 458	2.16 x 10 ⁶ to 3.46 x 10 ⁶	
Phase 2 12-15/7/03	Soufrière Hills	0- 100	1.27 x 10 ⁵ to 2.38 x 10 ⁵	Edmonds <i>et al.</i> , 2006
	St Georges Hill	60- 120	1.10 x 10 ⁵ to 1.36 x 10 ⁵	
	Garibaldi Hill	80- 140	1.56 x 10 ⁵ to 1.83 x 10 ⁵	
	Centre Hills	0- 140	3.88 x 10 ⁵ to 5.05 x 10 ⁵	
	Entire	0-140	6.71 x 10 ⁵ to 1.06 x 10 ⁶	
Phase 5 19/11/09-7/2/10	Soufrière Hills	1.2- 15.7	1.60 x 10 ⁴ to 6.41 x 10 ⁴	MVO, 2010
	St Georges Hill	1.7- 14.6	3.88 x 10 ³ to 1.72 x 10 ⁴	
	Garibaldi Hill	0.7- 13.8	1.95 x 10 ³ to 1.55 x 10 ⁴	
	Centre Hills	0.7- 14.6	1.34 x 10 ⁴ to 3.82 x 10 ⁴	
	Entire	0.7- 15.7	3.52 x 10 ⁴ to 1.35 x 10 ⁵	

Table 3.3: Tephra fall deposition, Phases 1, 2 and 5

2011 Shinmoedake eruption (Magill *et al.*, 2013). (3) Heavy tephra fall (over 50 mm) may break tree branches and bury low-lying vegetation; depending on residence time of the deposit, burial may result in complete vegetation loss in areas of thick tephra fall. Zobel and Antos (1997) investigated the dynamics of understorey vegetation recovery in the context of the characteristics of volcanic disturbance, following the Mount St Helens eruption in 1980. (4) Burial or burning by PDC may completely destroy vegetation over large areas. De Rose *et al.*, (2011) documented land cover change on Mount Pinatubo using satellite imagery to identify areas of burnt vegetation, amounting from 3-45% of land within a watershed.

A combination of these processes in April- May 2006 resulted in an estimated 68% of vegetation loss or damage across the Belham Catchment; estimated using aerial imagery by Alexander *et al.* (2010). This was responsible in part for a large lahar on 20th May 2006 that was triggered and sustained by non-extreme rainfall (Alexander *et al.*, 2010). Widespread vegetation damage in April and early May, combined with the second largest dome collapse since 1995 ($\sim 115 \times 10^6 \text{ m}^3$ removed from the dome, most within 40 minutes, Loughlin *et al.*, 2006), and synchronous rainfall and tephra fall resulted in an acute catchment response to rainfall. Coarser material from the dome collapse (fall deposit) was distributed to the east, however finer fallout tephra (silt and sand) was deposited across the catchment reducing infiltration rate by up to two orders of magnitude (assuming observations by Major and Mark, 2006 at Mount St Helens), increasing runoff, directly bulking active flows with sediment and increasing damage vegetation damage that persisted beyond the lahar (Alexander *et al.*, 2010).

Vegetation damage decreases surface roughness, increasing overland flow velocity and bed shear stress, enhancing erosion rates and sediment entrainment (Bryan, 2000). It is anticipated that initially water will rapidly boil and evaporate from the surface of newly emplaced, hot ($>100^\circ \text{ C}$) PDC deposits. Research by Hicks *et al.* (2010) investigating rainfall infiltration on lava domes provides some insight into the effects of hot volcanic deposits on infiltration, depending on rainfall rate, highlighting that the higher the rainfall rate, the faster the cooling of the deposit to below 100° C at which infiltration of water may occur. At the time of writing no systematic study (to this author's knowledge) was available on the cooling of hot volcanic deposits in response to rainfall; this was likely due to the challenging logistics of undertaking field studies and cost of laboratory work. Depending on rainfall rate, it is anticipated that the

surface of the deposit quickly (under 1 hour) cools to below 100° C facilitating runoff and infiltration (rather than the boiling) of rainfall. On fresh PDC deposits, under 100° C in temperature, runoff was initially very high because of the layer of fine ashfall at the top of the deposit (Collins and Dunne, 1986). Rills may develop within minutes as runoff rapidly erodes into the top of fresh tephra deposits (Mosley, 1974). In areas where deposits are thick, rill networks develop into wider and deeper gullies (Meyer *et al.*, 1989). Where deposits are thinner, erosion by overland flow may strip burned soils and expose large areas of bedrock (Figure 3.4). This impedes revegetation and promotes bedrock erosion. On thicker deposits, over time, channels widen stabilising despite deep entrenchment, because mobilisation of large sediment volumes becomes dependent on sufficient discharge to occupy the full channel width and incise the base of PDC terraces (Gray and Montgomery, 2005).

3.4. Rainfall and Lahar record

The relationship between rainfall and lahar occurrence is not simple because surface runoff is the dominant agent in the transfer of sediment from the upper Belham Catchment into the Belham River Valley, and this varies in space and time with the infiltration capacity of the soil/rock. Understanding the type of rainfall (amount, intensity, duration) that triggers lahars and how this changes with time in relation to volcanic perturbation, provides insight into the effects of volcanic activity on surface runoff and lahar initiation. Chapter 2 summarises data coverage and processing.

Monthly rainfall between 1995 and 2013 is shown in Figure 3.9. The CPC Merged Analysis of Precipitation (CMAP) data set is a satellite derived measure of precipitation (see Xie and Arkin, 1997), and is included here to provide an overview of regional scale meteorological conditions, particularly at times when no local rainfall data is available. Montserrat's location on the northern edge of the Inter-tropical Convergence Zone (ITCZ) means that it experiences a rainfall season between April and November. Data shows that the season annually contains 1-3 pronounced peaks in rainfall and that one of these peaks may occur outside of the regional rainfall season; annual peak monthly rainfall ranges from 149 mm (December 1997) to 519 mm (September 1995). Inter-annual rainfall variability, primarily associated with sea-surface temperature (SST) anomalies (Barclay *et al.*, 2006), was evident in the CMAP dataset. Although some inter-annual variability was seen in local rainfall measurements, the variation in monthly rainfall at different locations was far more

significant, emphasising the strong orographic rainfall effect resulting in up to 60% more rainfall at high elevations compared to coastal areas (Barclay *et al.*, 2006).

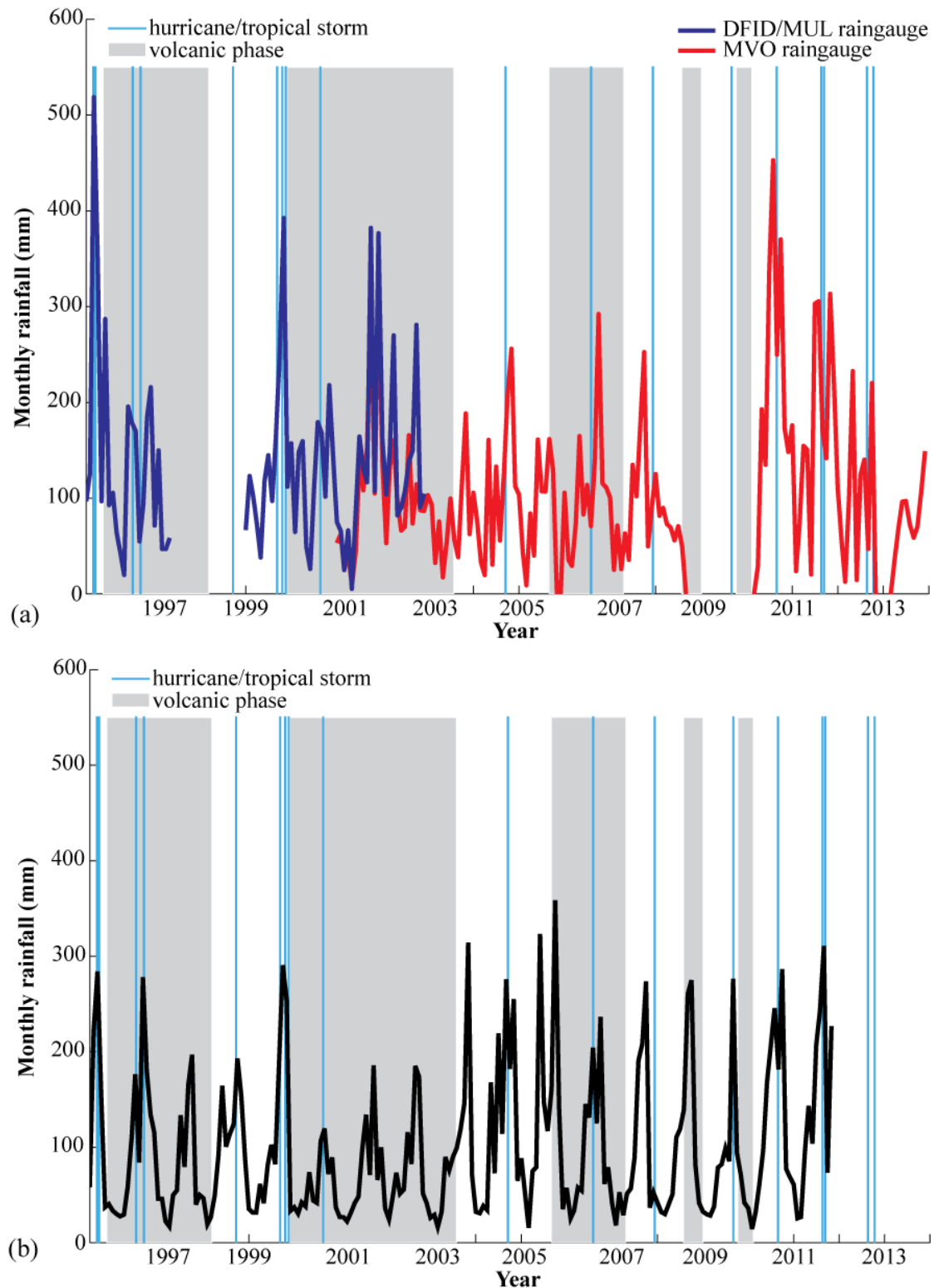


Figure 3.9 (a) Time series of monthly rainfall totals from DFID/MUL and MVO raingauges. The location of gauges is shown in Figure 2.5, and compilation of the time series data is discussed in Section 2.2.3.3. (b) The monthly rainfall totals derived from the CMAP data series are shown (black line), providing a regional scale measure of meteorological conditions.

Collated from observations and seismic records (see Chapter 2 for methodology), Table 3.4 presents the number of lahar days per month, between 1995 and 2013. The lahar record was categorised using a confidence score, assigned to each lahar occurrence (date and time) based on the number of different sources of information available and the confidence of seismic interpretation (Section 2.2.3.2). Data from all three categories: (1) uncertain signal, (2) lahar to north-west/west and (3) lahar in the Belham are included in Table 3.4 as *all* (categories 1-3) and *Belham* (categories 2-3). Although category 2 lahars have not been validated by visual observation as occurring in the Belham River Valley, personal observations during field work 2011-2013 were made that every very long-period signal registered when rainfall was also recorded, correlated with the occurrence of a lahar in the Belham River Valley. Given the location of the seismometer there was the possibility that the lahar signal was composed of tremors registered by active flows in multiple drainages around SGH (Section 2.2.3.2), however investigating this was beyond the scope of this thesis. Critically, rainfall to the west of SHV was likely to initiate surface flow in Spring Ghaut (draining into Plymouth) and the Belham River Valley when it was hydrologically connected to the north section of Gage's Fan (*c.* August 1997; Section 3.2.2). Therefore, lahars were likely to be occurring synchronously in drainages around the SGH seismometer during island wide and westerly focused weather-systems. Category 2 records were therefore events that 'likely' occurred in the Belham River Valley but were not validated by visual observation. It was also noted that on days of multiple lahar occurrence the highest confidence score was used to represent and categorise the daily lahar record.

Figure 3.10a-b shows significant variation in the number of lahars occurring per month. The highest numbers were observed in October 2006 (9 lahar days, category 2 and 3, Table 3.4). The month October had the highest average incidence of lahars (3.4 days per month), while February had the lowest incidence 0.3 days per month. The standard deviation of lahars per month ranged from 0.7 days (February) to 3 days (October) highlighting higher inter-annual variability in monthly lahar occurrence during the rainfall season. This variability in part was related to the different tracks taken by Tropical Storms and Hurricanes during the North Atlantic Hurricane Season; passage of large storms over the island resulted in multiple days of high-intensity rainfall and multiple lahars, triggered during the period of rainfall (see Figure 3.8, blue vertical lines show significant storms between 1995- 2013). In 166 of the total lahar

events were confirmed in the Belham (category 3), a further 186 were likely to have occurred in the Belham (category 2) and 584 further uncertain events were identified.

Month	Category 2 and 3				All			
	Total	Mean	Standard Deviation	Maximum	Total	Mean	Standard Deviation	Maximum
1	13	0.7	1.1	4	68	3.6	4.2	15
2	7	0.4	0.8	3	65	3.4	4.9	15
3	18	0.9	1.2	4	68	3.6	4.5	14
4	30	1.6	1.6	5	77	4.1	3.2	9
5	27	1.4	2.1	7	52	2.7	3.1	9
6	26	1.4	2.0	7	82	4.3	3.3	10
7	37	1.9	2.2	8	101	5.3	4.6	14
8	34	1.8	2.0	6	73	3.8	3.9	11
9	37	1.9	1.7	5	89	4.7	3.7	14
10	66	3.5	3.0	9	114	6.0	4.6	16
11	35	1.8	2.0	6	71	3.7	3.8	14
12	21	1.2	2.0	7	76	4.5	4.3	13
Year	Category 2 and 3				All			
	Total	Monthly			Total	Monthly		
		Mean	Standard Deviation	Maximum		Mean	Standard Deviation	Maximum
1995	9	0.75	2.05	7	9	0.75	2.05	7
1996	29	2.42	2.23	5	35	2.92	2.94	8
1997	13	1.08	1.44	4	13	1.08	1.44	4
1998	13	1.08	2.07	7	17	1.42	2.50	7
1999	14	1.17	1.59	4	14	1.17	1.59	4
2000	10	0.83	1.40	4	20	1.67	3.03	10
2001	15	1.25	1.82	6	60	5.00	3.88	14
2002	22	1.83	1.40	4	36	3.00	2.34	8
2003	21	1.75	2.67	8	60	5.00	3.36	12
2004	21	1.75	1.76	5	68	5.67	3.20	12
2005	10	0.83	1.53	5	53	4.42	4.52	14
2006	23	1.92	2.71	9	86	7.17	2.79	11
2007	21	1.75	1.66	5	71	5.92	3.40	13
2008	34	2.83	2.04	7	106	8.83	5.24	16
2009	17	1.42	2.87	8	26	2.17	3.88	12
2010	28	2.33	1.78	5	68	5.67	3.68	12
2011	25	2.27	1.74	6	102	9.27	3.41	15
2012	22	2.00	2.53	7	67	6.09	3.33	9
2013	4	0.33	0.65	2	25	2.08	2.61	8

Table 3.4 Lahar database summary statistics. The total number of lahars per month (between July 1995- December 2013) and by year, are shown (lahar counts). The mean column represents the average incidence of lahars by month (top) between July 1995- December 2013, providing an estimate on the typical number of lahars occurring during a set month. The standard deviation measures how much variation there is around this mean incidence value.

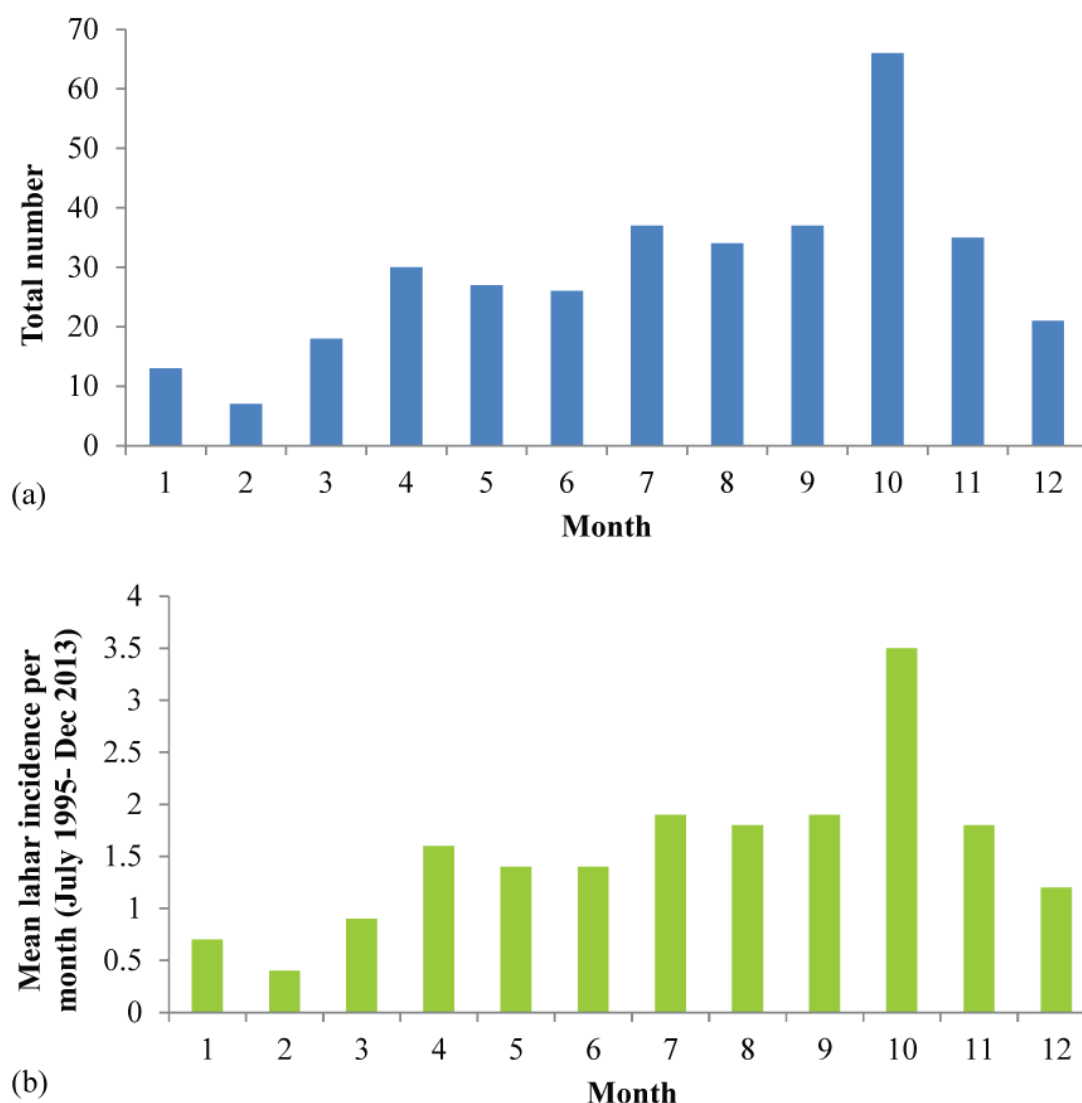


Figure 3.10 (a) The total number of category 2 and 3 lahars by month, between July 1995 and December 2013. (b) The average incidence of a lahar within a set month, based on category 2 and 3 lahars between July 1995 and December 2013.

3.4.1. Daily rainfall and lahar occurrence

The relationship between rainfall and volcanic (primary and secondary) activity was investigated during 1998-2003 by Barclay *et al.* (2006). This section extends the lahar aspect of their study to include data between 1999 and 2013. Rainfall was registered by at least one rain gauge on 83% of lahar days between 1999 and 2013. Category 2 and 3 lahars are discussed here, however statistics for the entire lahar database (including less certain dates) only varied from those presented by <2 %. Less than 1 mm of rainfall was recorded on 16 % of lahar days; only 34% of these measurements were made by a rain gauge within the Belham Catchment, while other measurements were recorded by instruments situated in elsewhere on island. Given the nature of rainfall on Montserrat, delivered by both synoptic scale and localised (<100

km) weather-systems, it is anticipated that rainfall recorded outside of the catchment may not be representative of rainfall intercepted within the catchment. Records show daily measurements of rainfall (on lahar days) varied by 0- 89 mm between rain gauges inside and outside of the Belham Catchment. Table 3.5 summarises the rainfall recorded by rain gauges inside the catchment during lahar days, and the equivalent measurements (where available) outside the catchment. It is noted that while the two weather stations (data after 2011) record zero rainfall, making it easy to identify when a gauge has stopped recording, earlier rain gauges do not make a record of zero rain. This means that it is difficult to differentiate between 'no rainfall' and days of gauge malfunction. While every effort was made to remove data during periods of known gauge malfunction, spurious days of drop out may have occurred.

On lahar days when rainfall was recorded in the Belham Catchment, $0 < x \leq 1$ mm was registered on 25.8% of days, $1 < x < 10$ mm was registered on 47.3% of days, $10 \leq x < 20$ mm was registered on 11.3% of days, $20 \leq x < 40$ mm was registered on 9% of days and $x > 40$ mm was registered on 6.5% of days. On days when rainfall was coincidentally measured outside of the Belham Catchment (excludes no data), of the days measured with less than 1 mm of rainfall, 37% of days were also registered with less than 1 mm of rainfall, 54% of days were registered with rainfall $1 \leq x < 10$ mm and 8% of days were registered with rainfall greater than 10 mm. Conversely, on lahar days with more than 10 mm of rainfall in the Belham Catchment, 88% of coincident measurements of rainfall outside the catchment (excluding zero rain/ no data) were greater than 10 mm; on lahar days with more than 20 mm of rainfall in the Belham Catchment, 75% of coincident measurements were greater than 20 mm; and on lahar days with more than 40 mm of rainfall in the Belham Catchment, 71% of coincident measurements were greater than 40 mm. These results show that when available, rainfall measurements outside of the catchment provide a good estimation of catchment rainfall for synoptic scale weather-systems, such as during a Tropical Storm or Hurricane. Concurrent with observations by Barclay *et al.* (2006), lahars occurred on most days when rainfall over 40 mm was registered inside the Belham Catchment; category 2 and 3 lahars were identified on 72% of days (74% including all possible lahars). Examining the (11) days when lahars did not occur when over 40 mm of rainfall was registered show: (1) several high readings the day after the passage of a significant (Tropical Storm/ Hurricane), (2) possible under-reporting of lahar activity

Rainfall recorded by rain gauges in Belham Catchment		Outside of catchment recording (% of total lahar days)						
Rainfall (mm) per day	Number of days	% of total recorded lahar days	No data	0>x<1	1<=x<10	10<=x<20	20<=x<40	x>=40
No data	166	23.1	123	15	24	6	1	0
x=0	3	0.004	3	0	0	0	0	0
0>x<1	142	19.7	83	22	32	3	1	1
1<=x<10	260	36.2	175	9	54	16	4	2
10<=x<20	62	8.6	41	0	3	10	5	3
20<=x<40	50	7.0	37	1	0	3	8	1
x>=40	36	5.0	29	1	0	0	1	5
Total	716							

Table 3.5 Rainfall recorded on lahar days by rain gauges inside and outside of the Belham Catchment

because of an absence of seismic data and insufficient detail in MVO observations (MVOobs, 2014; ‘multiple lahars over one week’ or large lahars listed but others not included), and (3) high rainfall readings coincident with dome collapse and ash fall. These observations and intermittent operating life of instruments (Appendix 2.2v) points to the difficulties in maintaining a rain gauge network around an active volcanic subject to intense storms. The limitations of the lahar database were also highlighted. Lahars that were not seismically registered or observed, or lahars that occurred during a time of intense volcanic activity which concealed the seismic lahar signal, were not included in the database. Indicating that the number of lahars in the database underestimated the true number; with potential bias towards the under-reporting of small events that did not reach lower sections of the Belham River Valley. In addition, the conditions leading to a lahar do not necessarily operate over 24 hour periods defined by 00:00 to 23:59 hours. Irrespective of data completeness and inconsistent rain gauge location, available data covers a significant proportion (~65 %) of the 18 year period and shows that the relationships between rainfall and lahar activity were complex, determined by multiple interconnected processes operating over several timescales.

3.4.2. Lahar magnitude and antecedent, triggering and sustaining rainfall

Methods of assigning relative lahar size for flows in the lahar database were discussed in Section 2.2.3.2. Antecedent rainfall was calculated over periods of 60, 30, 14 and 7 days, and 24 hours based on time of initiation of all category 2 and 3 lahars using available rainfall data (Section 2.2.3.3). There was a clear correlation between sustaining rainfall and lahar size; on average small lahars were sustained by 12 mm of rainfall, moderate by 18 mm and large by 85 mm. Relatively high standard deviations (17 mm, 22 mm, 83 mm) suggested that rainfall recorded during a lahar of similar size was highly variable. It was likely some of this variability may be explained by rain gauge dropout due to malfunction or that the gauge may not have captured rainfall representative of the whole catchment. Comparison of data from two weather stations installed on St George’s Hill and Windy Hill (edge of Belham Catchment) in 2011, showed that of the 73 lahar days of combined recording, daily rainfall varied by an average 7 mm between sites and a maximum of 60 mm. However, variations in lahar size were mostly thought to be due to differences in catchment condition affecting runoff and delivery of water to the Belham River Valley.

Phase/Pause	Antecedent rainfall (mm within n days)					Rainfall rate 24 hours before lahar (mm/n minutes)	
	n=1	n=7	n=14	n=30	n=60	n=10	n=60
Phase 2	2.37	12.23	21.99	64.60	123.57	0.84	1.30
Phase 3	1.99	32.73	53.96	91.94	171.79	0.80	1.00
Phase 4	0.90	6.13	9.88	41.23	87.50	2.07	2.27
Pause 2-3	11.76	44.17	71.09	129.24	223.87	4.04	5.70
Pause 3-4	1.78	7.78	17.30	29.20	58.05	0.63	0.65
Pause after 5	7.83	34.49	55.09	103.20	206.37	2.03	3.29

Table 3.6a Mean antecedent rainfall amount and rate before lahar onset

Phase/Pause	Antecedent rainfall (mm within n days)					Rainfall rate 24 hours before lahar (mm/n minutes)	
	n=1	n=7	n=14	n=30	n=60	n=10	n=60
Phase 2	3.54	12.14	16.80	38.73	57.26	1.01	2.29
Phase 3	3.06	31.30	49.87	69.78	116.83	1.08	1.76
Phase 4	1.92	7.89	12.73	21.51	23.40	2.47	2.80
Pause 2-3	11.75	30.65	39.86	61.98	88.60	2.88	5.24
Pause 3-4	2.61	6.04	13.86	17.66	29.08	0.96	1.02
Pause after 5	10.77	37.82	47.14	87.35	172.52	2.11	4.24

Table 3.6b Standard deviation of antecedent rainfall amount and rate before lahar onset

Table 3.6a shows the mean antecedent rainfall over different periods that triggered a lahar. Data was only available for three volcanic phases and three pause periods. Generally, less rainfall triggered lahars during volcanic phases, and more during pause periods for all antecedent periods of time considered. This relationship breaks down for the pause between Phases 3 and 4, when lahars occurred after less antecedent rainfall; similar values to active volcanic periods. This pause period was short compared to the other pauses considered, just 466 days compared to 735 days (Pause 2-3) and over 1682 days (as of 20/9/2014 the pause after Phase 5 is ongoing). The low rainfall required to trigger lahars during this period was likely a reflection on the persistence of conditions pertaining to high runoff rates, caused predominantly by the large partial dome collapse on 8/1/2007, which deposited substantial BAF volumes in the Belham Catchment (Table 3.1). Large primary flows during Phase 2 were directed eastwards and deposits in the Belham Catchment were not as thick or as spatially extensive as those during Phases 3, 4 and 5.

During the pause following Phase 5 the difference between the amount of antecedent rainfall triggering sequential lahars decreased with time from eruptive activity. Although on average antecedent rainfall (Table 3.6a) was higher than during

volcanic phases, the standard deviation was higher during the pause period between Phase 2-3 and after Phase 5. This was due to the continued degradation of the volcanic dome and tephra fall, rockfall and small PDCs during pause periods. During Phase 5 24-hour antecedent rainfall before a lahar decreased from 11 mm to 4 mm, if tephra fall was recorded in the Belham Catchment within 7 days of the lahar. Two lahars were triggered on the same day as tephra fall during Phase 5, by only 2 mm of rainfall (recorded). The effect of tephra fall on lahar 24-hour antecedent rainfall did not persist when tephra was deposited over 14 days before a lahar, suggesting that tephra fall during pause periods modified catchment runoff conditions over time scales of weeks rather than months. This makes sense because tephra fall during pauses were less extensive and thin compared with volcanic phases, leading to more rapid vegetation recovery and shorter periods of infiltration reduction.

Using data from Figure 3.2 containing the dates of tephra fall and PDCs into Tyres Ghaut and onto Gages fan, trends in 24-hour antecedent rainfall and lahar size were considered in the context of time from deposition of primary material. The number of lahars included in the analysis are shown in Table 3.7. There was no clear trend between lahar incidence (or size) and time from deposition of primary material; the table does highlight (as expected) there were more small lahars than moderate events, and more moderate events than larger flows. Figure 3.11(a) shows that antecedent rainfall generally increased with time from tephra fall. Moderate and large lahars were triggered by more antecedent rainfall when tephra fall occurred on the same day as the lahar, however this may be a function of lahar timing. For small and large lahars the positive trend persists up to 60 days after deposition, while the moderate sized lahar data showed varying amounts of antecedent rainfall with no clear trend. It was possible that small lahars were more sensitive to changing catchment runoff because they were sustained by shorter periods of rainfall that deposited less water directly to the channel. The sharp increase in antecedent rainfall between 30 and 60 days for large lahars may relate to the reworking of tephra fall by small- moderate lahars between tephra fall emplacement and the larger event. Small-moderate events were more frequent and the analysis here does not explicitly consider the first event after tephra fall.

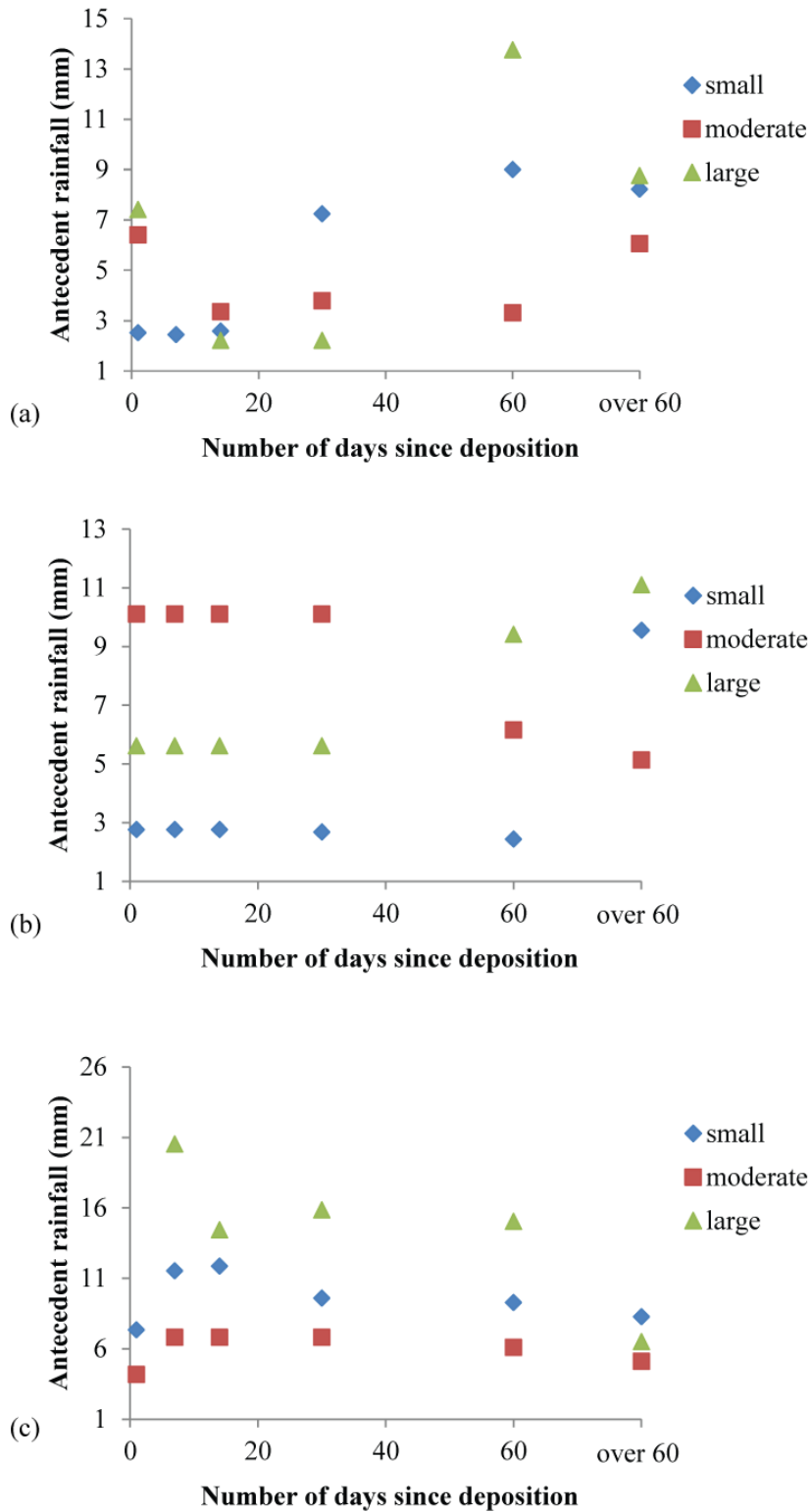


Figure 3.11 (a) Antecedent rainfall n days after Tephra fall. (b) Antecedent rainfall n days after PDC deposition in Tyres Ghaut. (c) Antecedent rainfall n days after PDC deposition on Gages fan.

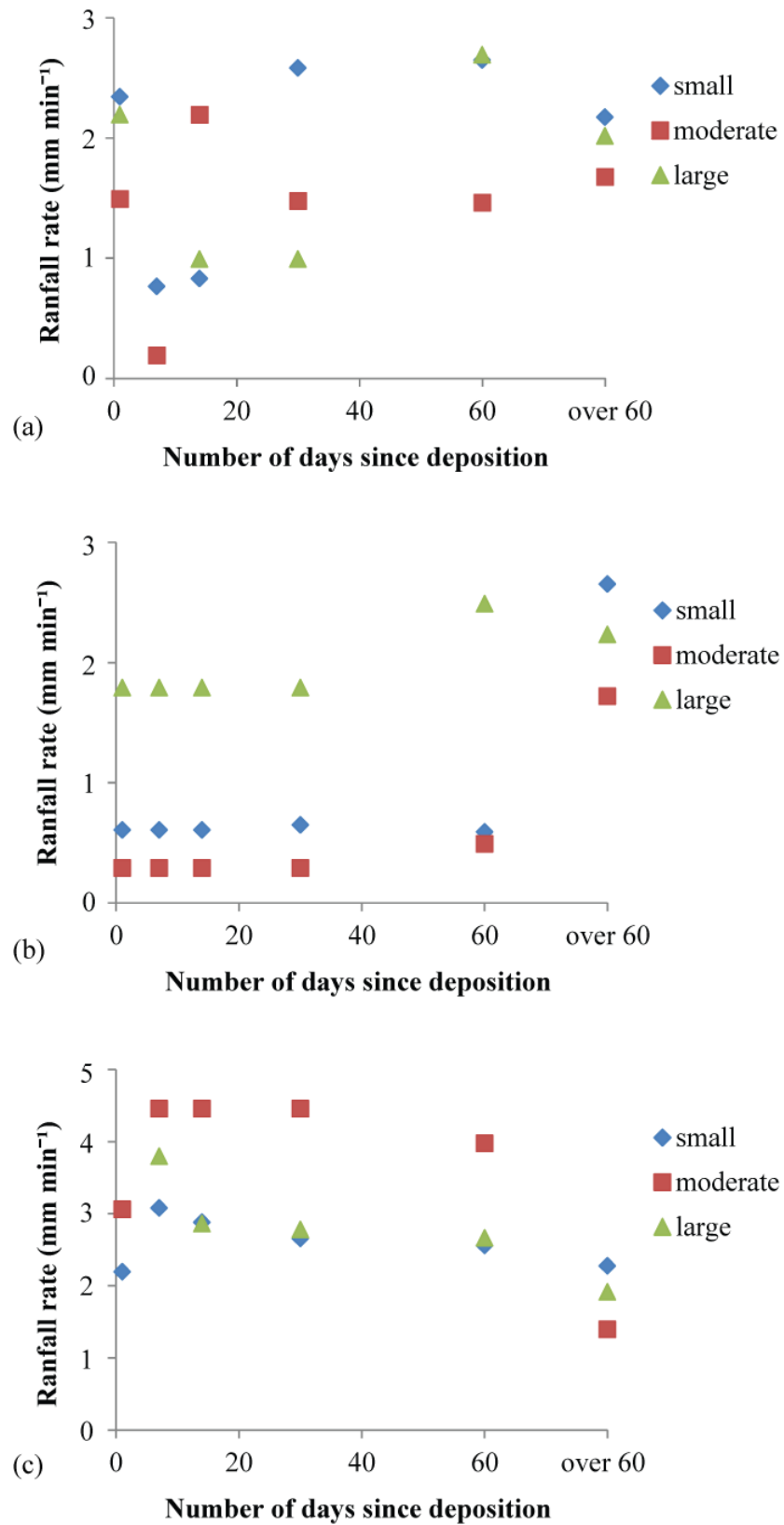


Figure 3.12 (a) Maximum 10-minute rainfall rate n days after Tephra fall. (b) Maximum 10-minute rainfall rate n days after PDC deposition in Tyres Ghaut. (c) Maximum 10-minute rainfall rate n days after PDC deposition on Gages fan.

		Lahar size					
		small	moderate	large	small	moderate	large
Total number		110	49	10	Percentage (%)		
Tephra fall	same day	4	2	2	4	4	20
	within 7 days	8	3	0	7	6	0
	within 14 days	12	4	1	11	8	10
	within 30 days	30	10	1	27	20	10
	within 60 days	42	15	4	38	31	40
No tephra fall within 60 days		14	15	2	13	31	20
PDC in Tyres	same day	13	2	1	12	4	10
	within 7 days	13	2	1	12	4	10
	within 14 days	13	2	1	12	4	10
	within 30 days	14	2	1	13	4	10
	within 60 days	16	4	2	15	8	20
No PDC in Tyres within 60 days		41	37	4	37	76	40
PDC in Gages	same day	8	5	1	7	10	10
	within 7 days	13	5	1	12	10	10
	within 14 days	20	5	1	18	10	10
	within 30 days	29	5	1	26	10	10
	within 60 days	30	6	1	27	12	10
No PDC in Gages within 60 days		10	23	5	9	47	50

Table 3.7 Number of lahars by size that occurred within 24 hours to 60 days of deposition of primary volcanic material

The 10-minute peak rainfall intensity during 24-hour antecedent rainfall (Figure 3.12a) did not correlate well with time from tephra fall. There was a general increase in rainfall rate with time for small and large lahars between 7 and 60 days from tephra fall, but the trend was weak. This may be due to complex interactions between spatial variation in runoff rate and spatial variation in rainfall rate across the catchment. Conversely, the maximum 10-minute peak rate of antecedent rainfall remained consistent with increasing time from PDC emplacement in Tyres Ghaut from 24 hours to 30 days, and then increased with time. This may be due to the incidence of rainfall events that even during low runoff conditions, deposit a large enough amount of rainfall or rainfall at a high-enough rate to initiate a lahar. This threshold may be as low as 0.9 mm, based on results in Table 3.6a. More rainfall events during the wet season (June to December) resulted in a lahar; 33% of rainfall events generated lahars compared to 24% during the dry season (January to May). Primarily, this was because weather systems during the wet season were dominated by regional tropical storms and hurricanes, which may persist for several days. Irrespective of season, data between 2001 and 2013

showed two lahars were triggered on average per month, however only one lahar was triggered in 40% of the months in the dataset. The increase in lahar triggering rainfall rate after 30 days of PDC emplacement in Tyres Ghaut was strongly related to lahar incidence, simply that after 30 days it was likely a single lahar had already occurred and eroded finer fall deposits on the top of the PDC deposit, exposing coarser material increasing infiltration and thereby increasing the amount of rainfall required to trigger a lahar. This suggested that irrespective of size, the occurrence of one or two lahars altered runoff dynamics in the catchment.

The shift from increasing to decreasing antecedent rainfall amount and delivery rate with time from the deposition of PDCs on Gages fan (Figure 3.11c, 3.12c) may relate to observations of bedrock incision in central sections of the fan, where PDC deposits were only ~1 m thick (Section 3.2.2). Initially runoff rates from fresh deposits may be inhibited by boiling of rainwater if the deposit is over 100°C, however once below this temperature runoff rates were expected to be high, particularly given the steep gradient of Gages fan and if a surface layer of fine ash was resident, inhibiting infiltration. Channels established in the bedrock by erosion after Phase 1 were repeatedly infilled by PDCs and then excavated by runoff during rainfall events. The process of excavation and exposure of bedrock may explain the decrease in antecedent rainfall after 7 days (large lahars) and 14 days (small-moderate lahars) following PDC emplacement. Surface runoff from bedrock was expected to be higher than from channel fills of volcanic deposits, resulting in lahar initiation from less antecedent rainfall (Figure 3.11c, 3.12c).

Results discussed in this section show that:

1. Measuring rainfall alone provides limited information on lahar incidence. Lahar rainfall thresholds need to take into account catchment condition in relation to the deposition of primary volcanic material.
2. Lahar size was dependent on the amount of sustaining rainfall in the 24 hours after lahar onset, irrespective of volcanic activity.
3. Lahars were more readily triggered during or immediately after volcanic activity, particularly after phases involving voluminous PDC deposition.
4. Tephra fall during pauses in volcanic activity reduced the 24 hour antecedent rainfall required to trigger a lahar to similar values as those during volcanic phases.

5. The infiltration and runoff of PDC deposits altered after one or two lahar events (or within ~ 30 days of PDC emplacement).
6. Bedrock erosion and exposure in channels may increase lahar incidence by increasing runoff.
7. Recording of rainfall by one rain gauge, or by a rain gauge outside or on the peripheries of the catchment may not be representative of catchment rainfall for meso-scale weather systems.

3.5. Impacts of lahar activity on the Belham River Valley

The following sections describe changes to the Belham River Valley between July 1995 and March 2013. The time period was separated into sub-divisions based on archive data and data collected during this study period. Change in the Belham River Valley was captured by archive photographs and video footage, repeat GPS surveys, and satellite and aerial photographs. Processing methods were described in Section 2.2.3.1.

3.5.1. 1995- 2010

Prior to the onset of volcanic activity the Belham River was contained in a narrow (2-3 m) ephemeral channel within a steep-sided valley bounded by the Centre Hills to the north, Soufrière Hills to the south-east, and St George's Hill and Garibaldi Hill to the south. The valley floor widened progressively downstream and close to the coast the river channel dissected the island's golf course. Here the valley gradient was 0.014 (0.8°); on average the valley slope was 0.02 (1.15°) measured from the pre-eruption topographic map (Crown Copyright, 1983). The lower Belham River Valley was an area used primarily for recreation (including the golf course and tennis courts), and contained a number of large residential properties (Figure 3.13a). At the coast there was a broad sandy beach lined with palm trees; a small harbour was located at the north end of the beach with a depth of ~ 10 m (B.A.N.C., 1986) and the Belham River mouth (4-5 m wide) was located at the south end of the beach. Upstream of the golf course was the Belham Bridge, a key part of Montserrat's infrastructure this was the main road bridge connecting the north-west mainly residential part of the island with the capital, Plymouth, in the south-west. The bridge was elevated 6 m above the channel, and the width of the valley-floor was 18 m. The valley-floor between the Belham Bridge and the Sappit River confluence was narrow (~2 m) and vegetated with Dry and Mesic forest.



(a)



(b)



(c)



(d)



(e)



(f)



(g)



(h)



(i)



(j)



(k)



(l)



(m)



(n)



(o)

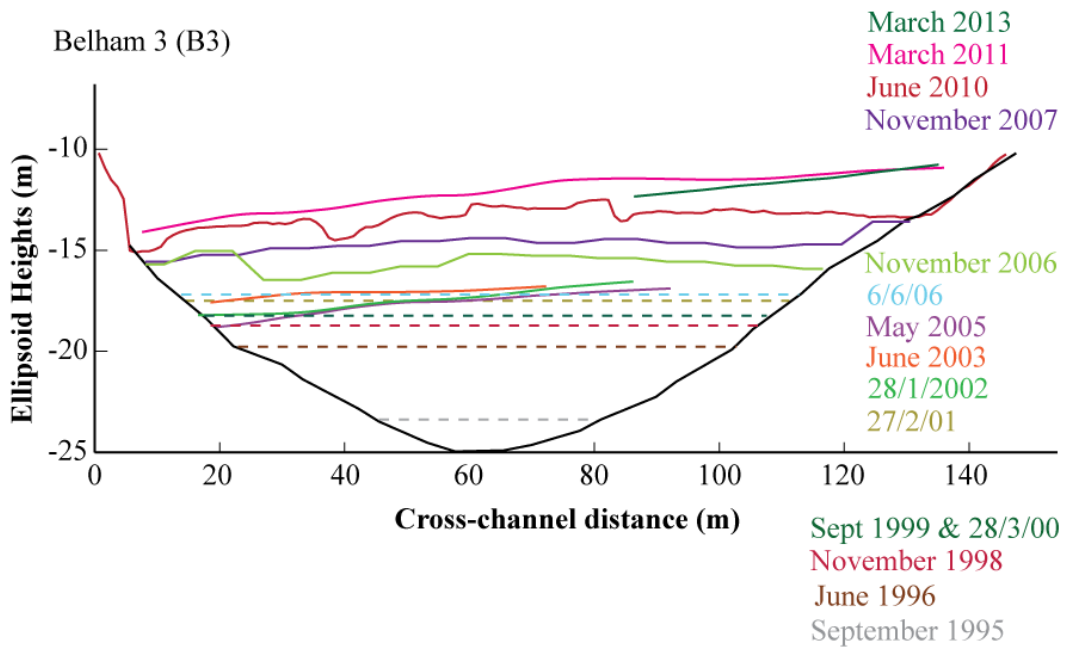
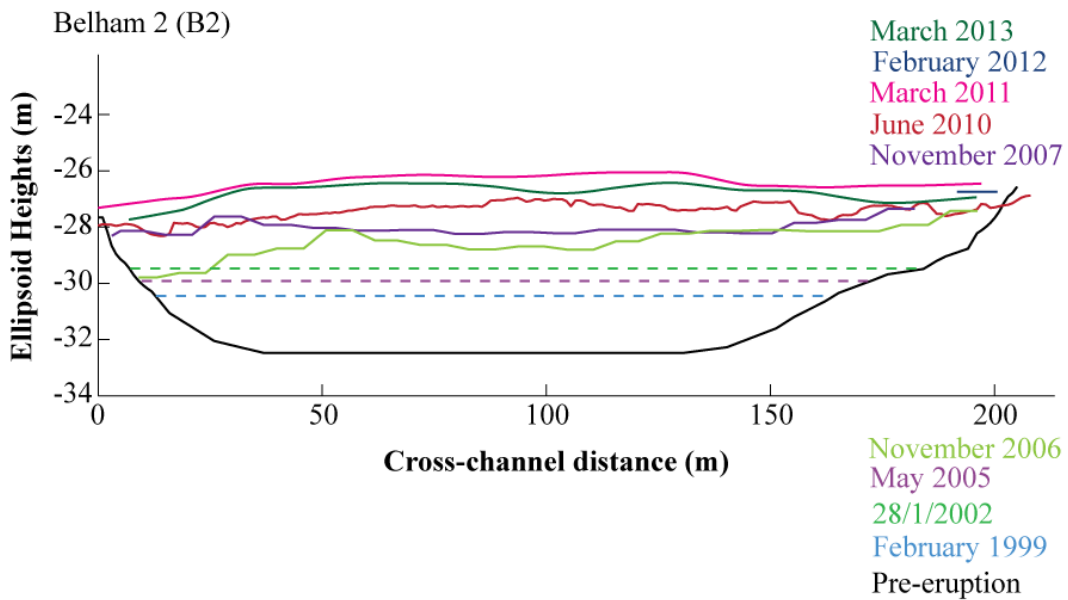
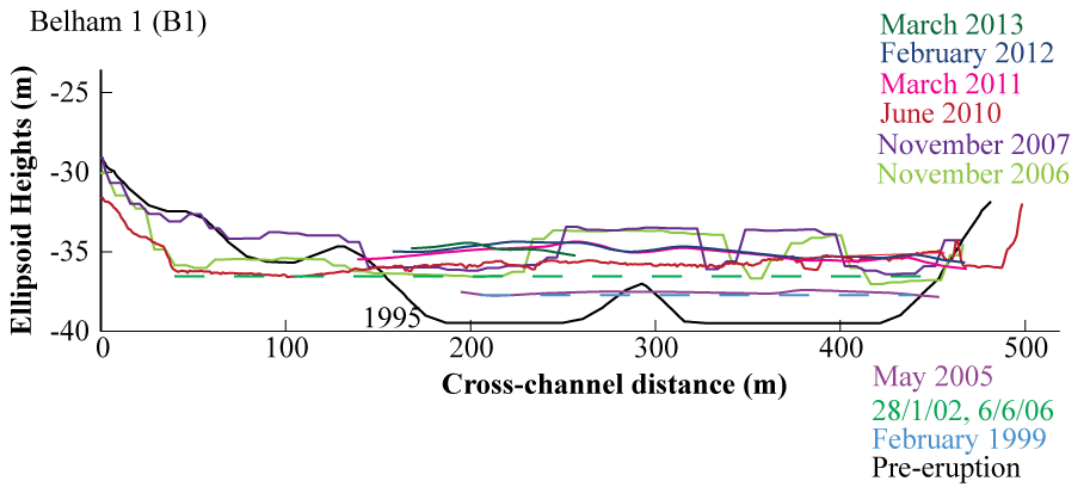
Figure 3.13 (a) Lower Belham River Valley pre-eruption, looking towards SHV (courtesy Richard Herd). (b) Truck stuck in lahar deposits 15th June 1996, situated in the Lower Belham Valley golf course (image still from video footage, used with permission from David Lea). (c) Hydraulic jump over Belham Bridge, 18th November 1998 (image still from video footage used with permission from David Lea). (d) Looking upstream from the Belham Bridge April 2000 (Photograph courtesy Jenni Barclay). (e) Looking upstream from the Belham Bridge May 2003 (Photograph courtesy Jenni Barclay). (f) Truck stuck in lahar November 2005 (Photograph courtesy Jenni Barclay). (g) Looking cross-valley towards the north-west at the Belham Bridge crossing in May 2005. Boulder with red arrow is ~0.6 m long. Flow is from right to left (reproduced from Sušnik, 2009). (h) Looking upstream from B4 towards the Sappit River confluence on 30th May 2006. The main channel is 17 m wide (reproduced from Sušnik, 2009). (i) Looking upstream from 80 m upstream of B3 at the orange house on south-side of valley on 23rd May 2006 shortly after large lahar (Photograph courtesy Jenni Barclay). (j) Looking upstream from 80 m upstream of B3 at the orange house on south-side of valley in November 2006 (Photograph courtesy Jenni Barclay). (k) Looking upstream (and across valley south- north) 100 m upstream of B5 on 2/12/2007 bed surface (Photo courtesy MVO). (l) Buried house located on the south side of the valley at the Isles Bay crossing, November 2006 (Photo courtesy Jenni Barclay). (m) House shown in (l) on 7/8/2008. Pillars on the house suggest bed elevation has increased by ~ 1.5 m. (Photo courtesy MVO). (n) Looking south across channel at partially buried Orange house in December 2007 (see also i-j) (Photo courtesy Jenni Barclay). (o) Looking south across channel at partially buried Orange house in 30th October 2009 (Photo courtesy Emmy Aston).

The location of the Belham River channel was modified during the construction of the golf course to go through the centre and south side of the valley; prior to this the channel was located on the north side of the valley (Lea, 2011). This is the location of the Belham Valley Fault (Section 1.4.2). The old river course was occupied by a road parallel to the edge of the valley connecting the Belham Bridge with Old Towne (Figure 3.1). Anecdotal evidence suggested that the channel had been overtopped by floods on an approximately annual basis, resulting in overbank deposits of small lateral extent and volume (Barclay *et al.*, 2006; Harriet Joan Peakes, 2010). The devastating Hurricane Hugo in 1989 was expected to have generated significant flooding in the valley; however this was not specifically documented because damage was widespread across the island and recovery was focused on commercial and residential areas.

The onset of volcanic activity in July 1995 (Section 1.6) coincided with the passage of Tropical storm Iris (26-27/8/1995), Hurricane Luis (4-6/9/1995) and Hurricane Marilyn (15-16/9/1995), depositing significant rainfall on the island; 284 mm of rainfall was recorded in September, primarily from the hurricanes. Video footage from the September storm (Appendix 3.4b) showed that the Belham River flooded parts

of the golf course; flow was opaque and appeared to contain a high suspended sediment load. An estimated 1.7 m of aggradation occurred under the Belham Bridge based on analysis of archive video (Appendix 3.4c, Figure 3.15-B3). The channel under the bridge widened to occupy the full ~18 m valley-floor and on the bed surface small bars of pebble-sized pumice clasts were deposited separated by ~6 m wide sand bedded sub-channels. Low-lying vegetation in and around the channel was damaged and partially buried. Lahars between September 1995 and 15th June 1996 resulted in further deposition under the Belham Bridge (Figure 3.15-B3, estimated from photographs, Appendix 3.4a) and avulsion of the golf course section of the channel by up to 114 m near the coast. Although flow appeared shallow it posed a hazard to those both on foot and in vehicles within the valley (Figure 3.13b). There was very little information on the condition of the Belham River Valley in 1997 because of escalations in the volcanic crisis and evacuations of Plymouth (Section 1.7).

By November 1998, lahars had overtopped the Belham Bridge by ~ 0.4 m and the channel at this location was 62 m wide (estimated from video footage of a lahar at the end of November 1998, Appendix 3.4a). Boulder sized clasts up to 0.7 m in diameter were located on the bridge; smaller boulders were seen rolling and sliding in footage of the November flow. Cobble and boulder bars with sand sub-channels had been deposited across the bridge, and were continuous with bar structures upstream. A hydraulic jump naturally formed around the downstream side of the Belham Bridge (Figure 3.13c) resulting in a difference of ~1.2 m between the bridge and valley floor. Downstream of the bridge substantial bank erosion occurred and flow preferentially occupied the roadway on the north-side of the valley. The lahar at the end of November 1998 occupied 125 m of the valley-floor but remained shallow; downstream of the Isles Bay crossing flow split into two wide channels (~62 m), which persisted during waning flow, reducing in size to ~2.5 m. The northern channel was described as being located on the site of the old channel (Lea, 2011). Trees and taller vegetation formed islands in the centre of wide channels, and the truck abandoned at the golf course (Figure 3.13b) was buried by a further 0.5 m of material (June 1996- November 1998). Two sediment fans formed at the coast and water colour suggested substantial volumes of sediment had remained in suspension as flow exited into the sea.



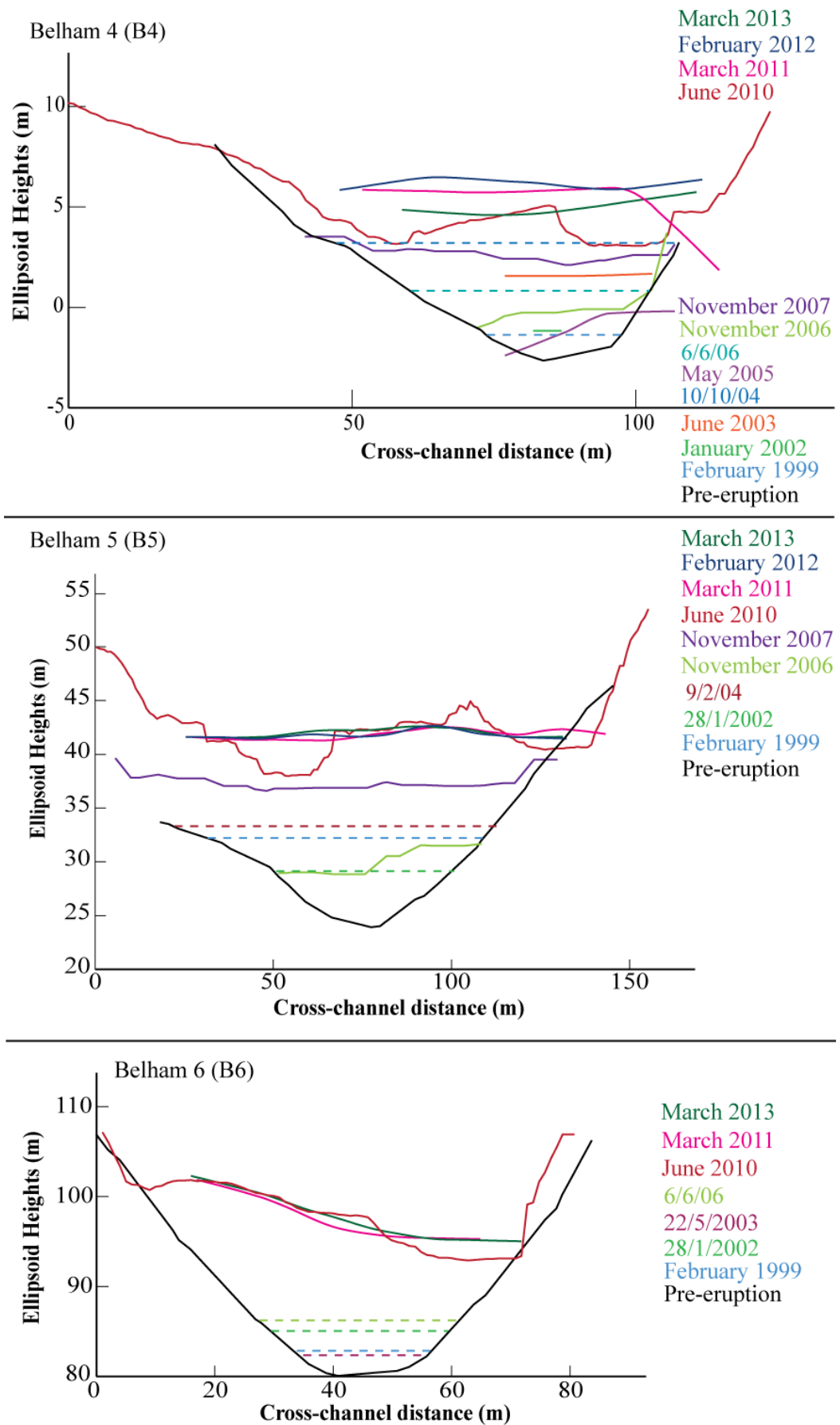


Figure 3.15 Cross-section profiles of six transects across the Belham River Valley, locations shown in Figure 3.12b. Elevations are colour-coded to date; dates are included next to profiles.

An aerial survey conducted in February 1999 to update the DEM of the Soufrière Hills volcano was used to estimate elevation change in six sections (Figure 3.14) of the Belham River Valley based on the width of the valley-floor (in the photograph) relative to the pre-eruption valley cross-sectional profile (Pre-eruption DEM, Appendix 2.2a). Bed surface elevation at the cross-sections was estimated to have increased between July 1995 and February 1999 by an average 2.85 m, ranging from 1 m (at B4 Figure 3.15) to 8 m (at B5, Figure 3.15). Cross-channel profiles (Figure 3.15) showed deposition resulted in valley-widening at all locations; the valley-floor was sinuous at the base of a series of interlocking spurs descending from the slopes of the Centre Hills and St George's Hill. Downstream of the Belham Bridge the channel divided into two as the valley widened: one following the location of the north-side of valley road exiting into the harbour, and the other down the centre of the valley exiting at the south end of the beach. By this date, the entire lower valley was covered in differing thicknesses of deposit and only isolated patches of trees remained. A debris fan from the north channel extended the coastline by 64 m.

Lahars triggered by Hurricane Floyd on 10th-11th September 1999 were observed "steaming" as they travelled down valley (Montserrat Reporter, 1999). BAFs deposited during Phase 1, remained hot for years after emplacement. Temperature measurements 1 m beneath the surface at Trants in 2011 showed the deposit remained above boiling point over a year after it had been deposited, during the Phase 5 dome collapse in February 2010. Large hot lahars were also observed in the Belham River Valley on 13th April 2010 (Appendix 3.4d). Hot flows posed an additional hazard not only personal injury by direct contact with the hot flow, but also steam obscuring visibility across the valley to communities located on the south side of the valley.

Very little elevation change occurred around the Belham Bridge between September 1999 and April 2000, however the bed surface of the valley at this site had become very coarse. Immediately upstream of the bridge the bed surface was covered with 0.5- 1 m boulders that were resting (not buried) on a sand base (Figure 3.13d). Wood debris was also scattered across the valley floor, and by March 2001 there was evidence of revegetation, suggesting that very few or only small lahars occurred between 2000 and 2001 (Appendix 3.4a). By September 2001, 10 m wide sub-channels had formed between the boulders at the Belham Bridge site and by October 2001, a braided channel structure had developed from the reworking of the bed surface by lahars. Wood debris had also been washed downstream to the coast. Photographs

(Appendix 3.4a) also showed the first evidence of sand extraction between the Isles Bay crossing and the Belham Bridge on the south side of the valley. The coarsening of the bed surface, revegetation and signs of on-foot workers in the valley coincided with periods during Phase 2, when dome extrusion was focused to the east.

The longitudinal profile from a 70 m long sub-section of valley near the Belham Bridge surveyed in 2002 showed that the gradient of the valley underwent very little change between July 1995 and January 2002, 0.035 (2°) to 0.03 (1.72°) (Figure 3.14a). A similar gradient was measured from the DEM derived by GPS survey during June 2003 (0.03, 1.72°). The ~2 km long section of survey conducted in May 2005 provided a more complete picture of longitudinal valley change since eruptive activity began. The gradient of the valley was 0.02 (1.15°), and the survey showed that the gradient of sections of valley upstream of the Sappit River tributary had reduced since 1995 (0.025 to 0.02, 1.43° to 1.15°) but increased since 1995 in sections of the valley downstream of this point (0.014 to 0.02, 0.8° to 1.15°), as sediment was mobilised and deposited downstream by lahars.

Block-and-ash flows deposited material in Tyres Ghaut and Dyers River during the end of 2002 and beginning of 2003, however following this, most primary material deposited in the Belham Catchment was derived from rockfall and tephra fall (see Section 3.2.1) until the end of 2006. There was already evidence that the valley was shifting from a net aggrading to net degrading regime around 1999: (1) bed surface coarsening, (2) very little elevation change (gain) (Table 3.8), (3) the formation of terracing in lahar deposits upstream of the Sappit River, and (4) coastline retreat (20 m retreat at the south side of the valley between 25/10/2001 and 28/1/2002, Appendix 3.4a). Although fresh PDC deposits were emplaced in the upper catchment during Phase 2, flows did not travel past Dyers Bridge and lahar incidence was limited to small flows between January and July 2003 (see Appendix 2.2u). Aerial imagery from 2002 showed the bed surface was braided between B5 and B2, and ground imagery on 22/5/2003 at the Belham Bridge (Figure 3.13e) showed that bed surface grain size was finer, as sequential flows had deposited sand-sized sediment infiltrating between gravels on the bed surface in April 2000 (Figure 3.13d). Between 28/01/2002 and 30/6/2003 only 0.3 m of elevation gain was measured at the Belham Bridge (B3, Figure 3.15), equating to an estimated net gain of $1.77 \times 10^5 \text{ m}^3$ based on extrapolations of survey data (Table 3.8) from the $2.57 \times 10^4 \text{ m}^2$ surveyed area upstream. Remobilisation of substantial volumes of the estimated $2.28 \times 10^6 \text{ m}^3$ of primary

Date range	Volume(m ³)			Elevation difference (m)				Area included in calculation (m ²)		Method
	Gained	Loss	Error (± m ³)	Mean	Standard Deviation	Range	Error (± m)	Area (m ²)	Error (± m ²)	
1/7/1995 to 1/1/2002	1.90 x 10 ⁵	-9.57 x 10 ³	9.2 x 10 ³	5.30	3.57	-11.6- 10.87	5	3.41 x 10 ⁴	625	DEM - DEM
	6.51 x 10 ⁵	-5.47 x 10 ⁵	9.2 x 10 ³	0.46	6.87	-32.02- 10.65	5	2.26 x 10 ⁵	625	extrapolated DEM - DEM
	1.69 x 10 ⁴	-2.43 x 10 ³	4.08 x 10 ³	0.56	0.79	-2.55- 9.71	0.4	2.57 x 10 ⁴	100	DEM- DEM
1/1/2002 to 31/5/2003	1.77 x 10 ⁵	0.00 x 10 ⁰	4.08 x 10 ³	0.78	0.16	-0.303- 1.05	0.4	2.26 x 10 ⁵	100	extrapolated DEM - extrapolated DEM
	6.46 x 10 ²	-5.10 x 10 ⁴	4.08 x 10 ³	-1.45	1.38	-13.12- 2.30	0.4	3.47 x 10 ⁴	100	DEM- DEM
31/5/2003 to 1/5/2005	5.33 x 10 ⁴	-5.19 x 10 ⁴	4.08 x 10 ³	0.01	0.62	-1.52- 2.70	0.4	2.15 x 10 ⁵	100	extrapolated DEM - extrapolated DEM
	6.35 x 10 ⁵	-1.65 x 10 ⁴	4.08 x 10 ³	2.11	1.80	-5.66- 11.43	0.4	2.90 x 10 ⁵	100	DEM- DEM
1/5/2005 to 1/11/2006	1.26 x 10 ⁶	-9.28 x 10 ⁴	4.08 x 10 ³	2.83	4.74	-3.62- 37.88	0.4	1.20 x 10 ⁵	100	DEM - extrapolated DEM
1/11/2006 to 1/11/2007	1.72 x 10 ⁶	-2.15 x 10 ⁵	4.08 x 10 ³	2.02	4.10	-25.87- 23.17	0.4	7.47 x 10 ⁵	100	DEM- DEM
1/11/2007 to 1/6/2010	1.59 x 10 ⁶	-4.94 x 10 ⁵	7.38 x 10 ⁴	1.45	4.64	-27.67- 36.48	0.4	7.59 x 10 ⁵	100	DEM- DEM
	5.83 x 10 ⁵	-1.47 x 10 ⁵	7.38 x 10 ⁴	0.68	1.24	-4.86- 4.71	0.4	6.43 x 10 ⁵	100	DEM- DEM
1/6/2010 to 1/3/2011	5.91 x 10 ⁵	-1.49 x 10 ⁵	7.38 x 10 ⁴	0.57	1.16	-4.89- 4.65	0.4	7.71 x 10 ⁵	100	modified DEM- DEM
	9.92 x 10 ⁴	-1.01 x 10 ⁵	4.08 x 10 ³	-0.02	0.98	-3.06- 5.4512	0.4	4.77 x 10 ⁵	100	DEM- DEM
1/3/2011 to 1/2/2012	1.26 x 10 ⁵	-1.55 x 10 ⁵	4.08 x 10 ³	-0.04	0.56	-2.90- 3.77	0.4	7.68 x 10 ⁵	100	modified DEM- DEM
	4.68 x 10 ⁴	-5.49 x 10 ⁴	4.08 x 10 ³	-0.03	0.53	-4.87- 2.04	0.4	5.12 x 10 ⁵	100	DEM- DEM
1/2/2012 to 1/3/2013	1.44 x 10 ⁵	-9.27 x 10 ⁴	4.08 x 10 ³	0.07	0.51	-3.77- 3.73	0.4	7.63 x 10 ⁵	100	modified DEM- DEM

Table 3.8 Volumes of sediment added or removed based on DEM differences. Volume errors were modelled using a Monte Carlo simulation for probability density function (mean= 0 m, standard deviation = variable) was used to generate an error surface which was added as 'noise' to each DEM. Standard deviations were used as follows: 1/7/1995= 5 m (unvegetated section of DEM, see Table 2.2), 1/3/2011, 1/2/2012= 0.4 m (GPS error + human error, see Table 2.5), 1/6/2010= 0.15 m (see Table 2.2.). A noise surface was added to each DEM. The volume difference of the 'noise' added DEMs were calculated. This method was iterated over 100 runs for each volume calculation (not all surface combinations were modelled). The volume difference calculated was compared to the 'true' surface volume calculation. Given that surfaces 1/2/2002-1/11/2007 and 1/3/2011-1/3/2013 were collected following the same methodology, modelling errors in the 1/2/2012 to 1/3/2011 volume calculation were considered representative of the errors expected for other volume calculations entailing GPS survey surfaces. The root mean square error (RMSE) was calculated from the volume differences of the 100 iterations. Methodology adapted from Darnell *et al.* (2010)

material deposited upstream in December 2002- January 2003 (Table 3.1) was delayed until larger lahars on 12th-13th July 2003 coincided with a dome collapse (Barclay *et al.*, 2006).

Observations immediately after this event were limited for the Belham River Valley (the dome collapse was to the east), but descriptions of vegetation burial on the golf course and the stripping of tree branches suggests damage and deposition from at least one large lahar. Aerial photographs from March 2004 (Appendix 3.4a) showed new earth levees in the lower Belham in front of houses on the south side of the valley, highlighting that residents were mitigating against lahars directly using engineered structures for the first time. The coastline was also extended by 57 m on the north side of the valley (Appendix 3.4a) between 14/3/2003 and 30/3/2004, suggesting voluminous lahars and net deposition.

Commercial sand extraction was more active during this time (Photograph February 2004, Appendix 3.4a), creating a network of low-lying areas within the deposit between the Belham Bridge and the Isles Bay crossings. Channelisation resulted in deeper flows in this section of valley and may have contributed to a vehicle getting stuck in a larger lahar on 9/11/2004 (Figure 3.13f); the opaque flow texture and the shallow depth of the flow in wider (unquarried) sections of the valley may have given the driver of the vehicle a false perception of flow depth, which was observed to be fast flowing and at least waist deep. Water-surface-waves were documented during the event, which occupied most of the valley width at B3, except for gravel bars in the centre of the channel, some of which were vegetated. Bed surface coarsening in combination with elevation loss ranging from 4.5 m between October 2004 and May 2005 at B4 to 0.6 m between June 2003 and May 2005 at B3 (Figure 3.15), showed that the valley was shifting to net-degradation (Table 3.8). Prior to October 2004, B4 was experiencing net elevation gain, suggesting that the large lahar observed on 19/11/2004 quarried material from the valley-floor. Following the event the valley-floor was dominated by gravel bar forms, some containing large (0.5 m) boulders and vegetation debris.

Observations of the valley bed surface in May/June 2005 (Sušnik, 2009) described a shift in character from medium to very coarse sand and sandy-gravel (vegetated in places) upstream of B4, to cobbles and boulders (<1.5 m diameter) with sand-rich ribbon (<0.2 m) channels at B3 (Figure 3.13g), and then to planar sand beds downstream of B2. Naturally incised channels were not observed, however by end of

May 2006, deep 2 m channels had formed upstream of B4 (Figure 3.13h), boulders were more abundant and larger around B3, and shallow channels (<0.7 m) had formed between B2 and B1 (Sušnik, 2009). Bedrock incision was also observed at B6 (Appendix 3.4a). This study attributed changes in valley-floor morphology to a large lahar on 20th-21st May 2006 that occurred during a large dome collapse (Alexander *et al.*, 2010), however a large lahar was also filmed at the Belham Bridge (Lea, 2011; Appendix 3.4c) on 30th July 2005 and descriptions of the valley bed surface after the event (Lea, 2011) suggest that this lahar may have contributed to channel formation upstream. The 20th May 2006 event was described as an extreme hydrological response because of enhanced runoff caused by extensive vegetation damage in the catchment in combination with parallel dome collapse (Alexander *et al.*, 2010). Given the degree of channel incision relative to previous events, it may be suggested that this marked the peak in valley degradation, because measurements in November 2006 (Figure 3.15) showed an average elevation increase of ~ 1 m (B2, B3, B4, Figure 3.15), and the coastline had extended by 65 m at the south end and 69 m at the north end (between June- November 2006, Figure 3.14). Photographs of the Orange house (Figure 3.13i-j) just upstream of the Belham Bridge showed the infilling of channels by at least 12 lahars (Appendix 2.2u), between June and November 2006. Based on satellite imagery from 6th June 2006 and estimates of depth change, $1.1 \times 10^5 \text{ m}^3$ to $2.4 \times 10^5 \text{ m}^3$ of sediment was deposited between the Belham Bridge and B6. The shift from net degradation to net aggradation may have resulted from changes in catchment runoff; deposition of primary material by PDCs was not documented until December 2006 (Table 3.1, Figure 3.2), therefore sediment that infilled the channel was mobilised from storage in the upper catchment (Phase 1 and 2 PDC deposits).

The partial dome collapse on 8th January 2007 deposited $4.5 \times 10^6 \text{ m}^3$ of primary material into Tyres Ghaut and Dyers River (Hards *et al.*, 2008). Between January and November (when the valley was resurveyed; Darnell, 2010) at least 21 lahars mobilised an estimated $1.72 \times 10^6 \text{ m}^3$ of material downstream, resulting in 76 m of coastline extension at the south end and an increase in valley gradient between B5 and B6 from 0.02 (1.15°, November 2006) to 0.05 (2.86°, November 2007); the valley-floor gradient did not alter downstream of B5 between 2006 and 2007 (based on DEM measurements). Elevation gain ranged from 0.7 m (B2) to 7.2 m (B5, Figure 3.15). Observations from satellite imagery from November 2007 and an oblique photograph (Figure 3.13k)

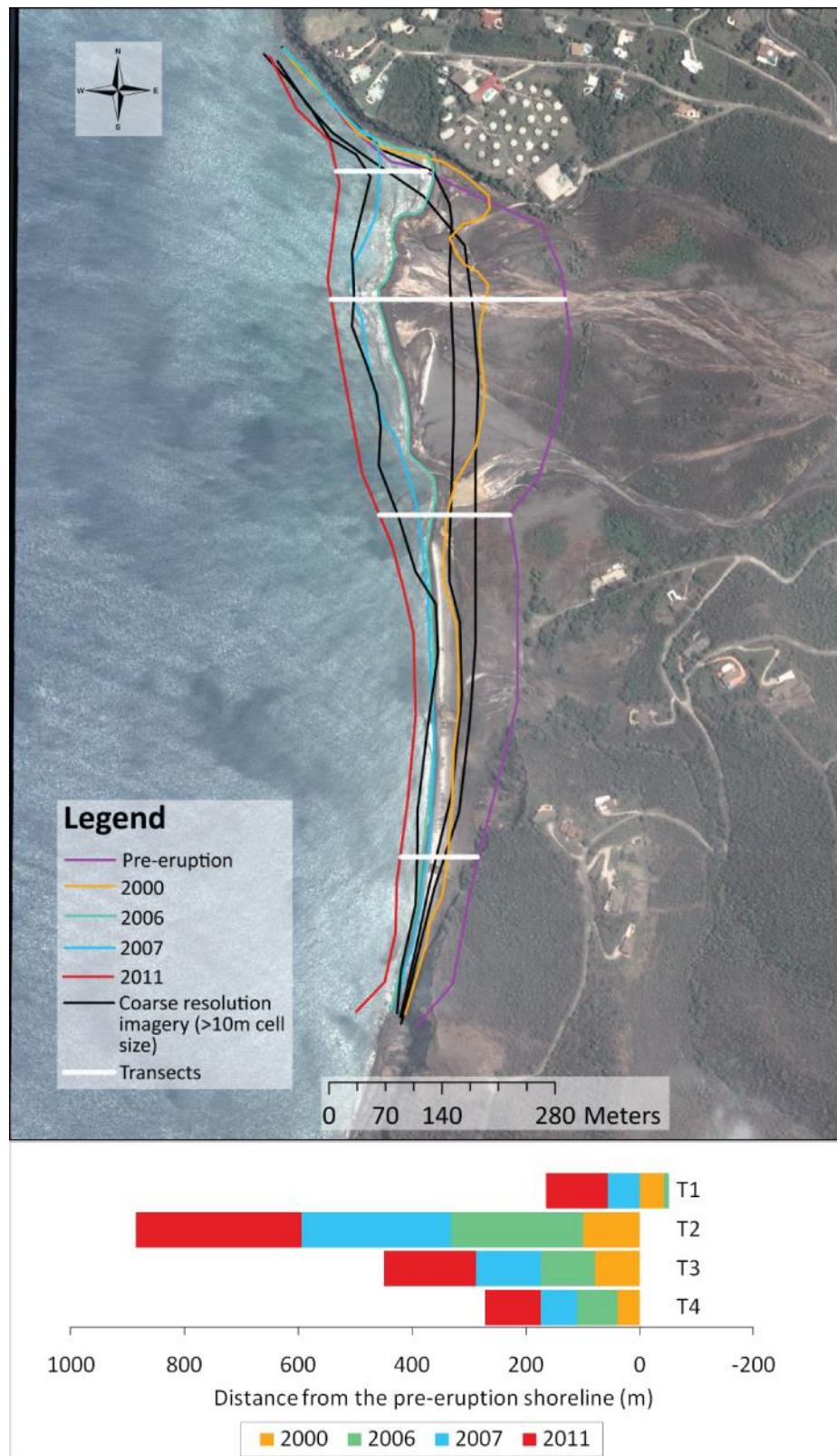
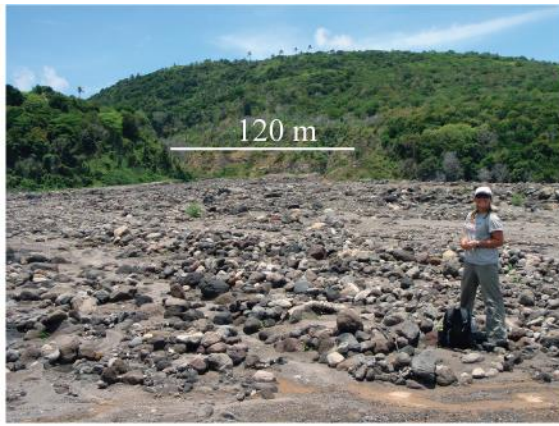


Figure 3.16 Coastline change, Belham River Valley. Digitisation of coastline extent from aerial photographs and satellite imagery (see Table 2.3). Graph (bottom) shows the change in coastline with time, in relation to the pre-eruption shoreline.

showed that the base of the valley contained wide boulder bar forms separated by sand-based channels in the section of valley upstream of the Sappit River, and a predominantly sand bed downstream of the Belham Bridge. Imagery and data between November 2007 and June 2010 was limited because attention was focused on two further phases of eruptive activity in short succession. Photographs of a house at the Isles Bay crossing (Figure 3.13l-m) showed 1.8 m of elevation gain, and 0.8 m of elevation gain was observed at the Orange house (Figure 3.13n-o). The continuation of net aggradation in the Belham River Valley during this time was expected because of the large volume of material emplaced in the upper Catchment during Phase 3, the deposition of more material in Tyres Ghaut (Table 3.1) and on Gages Fan (Table 3.2) during Phase 4 (29/7/2008 and 3/1/2009), and the short pause in dome extrusion between Phases 4 and 5, leading to near-continuous volcanic perturbation of the Belham Catchment between December 2008 and February 2010.

3.5.2. 2010- 2013

Between November 2007 and June 2010, the gradient of the Belham River Valley upstream of the Sappit River confluence increased from 0.045 (2.56°) to 0.05 (2.86°) in response to deposition of material by PDCs, the largest terminating at B4 (Figure 3.12a) on 8th February 2010 (partial dome collapse, Table 3.1). PDC deposits in the Belham River Valley from Phase 5 thickened with distance upstream, and immediately following Phase 5, the bed surface upstream of the Sappit River confluence was fully covered in BAF deposit. A large lahar on 13th-14th April 2010 and five smaller flows remobilised an estimated $1.10 \times 10^5 \text{ m}^3$ of material from the PDC deposits within the Belham River Valley, between February and June 2010, forming an 18 m – 56 m channel in deposits. By March 2013 a further $1.3 \times 10^4 \text{ m}^3$ was remobilised and a 65 m wide channel had formed at B5 (Figure 3.14b). In March 2011, at B6 the bed surface was covered in cobble-boulder sized clasts resting on sand beds and organised in ~10 m wide bar structures (Figure 3.17a). Narrow channels were present between the gravel bars and some contained small amounts of vegetation (Figure 3.17a). Cobble-boulder bars were partially buried by sand and channels had widened relative to bars and were covered in sand to medium sized pebbles, in March 2012 (Figure 3.17b). Twenty-five small to moderate lahars were recorded during this period, resulting in the gradual fining of the bed surface. By March 2013 flow had incised into the base of wider channels (by ~0.2m) and gravel bars delineated channel boundaries (Figure 3.17c). Small blocks of PDC deposit remained on the edges of the valley, and on the



(a)



(b)



(c)



(d)



(e)



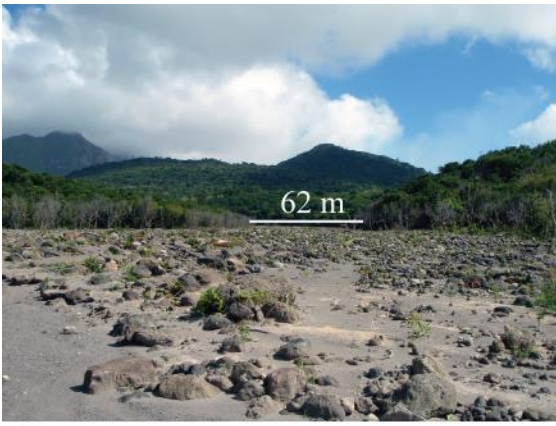
(f)



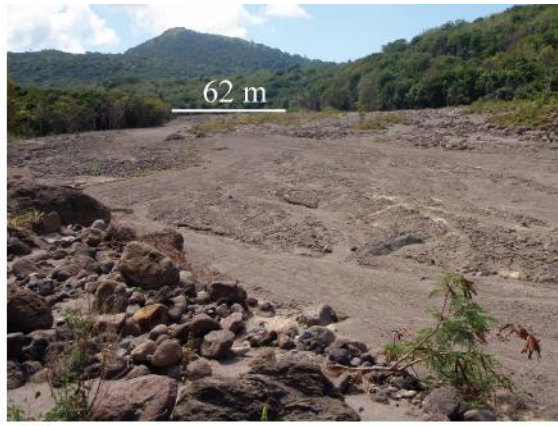
(g)



(h)



(i)



(j)



(k)



(l)



(m)



(n)



(o)

Figure 3.17 (a) Looking upstream at 120 m downstream of B6 (March 2011). (b) Looking upstream at 100 m downstream of B6 (March 2012). (c) Looking upstream at 250 m downstream of B6 (March 2013). (d) Vertical cracks in PDC deposit. Deposit surface is covered in pebble sized pumice (March 2013). (e) Lahar deposits on top of PDC terraces located on the south side of the Belham River Valley 300 m downstream of B6 (March 2013). (f) Looking upstream at Orange house near Belham Bridge (see also Figure 3.13o) in May 2010 (Photograph courtesy of MVO). (g) Looking upstream from ~10 m downstream of location photograph (f) was taken, in November 2010.

Orange house has been buried. (Photograph courtesy of Mel Plail). (h) Looking upstream 180 m upstream of the location of (g), March 2011. (i) Looking upstream 190 m upstream of location of (g), March 2012. (j) Looking upstream 190 m upstream of the location of (g), March 2013. (k) The lower Belham River Valley, March 2011. Arrow shows common location of white house also in (l). (l) The lower Belham River Valley, May 2014. Arrow shows common location of white house also in (k; Photograph courtesy Dav Macfarlane). (m) Looking upstream 400 m upstream of B2, November 2010 (Photograph courtesy Mel Plail). (n) Looking from north-south across the same section of channel as shown in (m), position of photographer for (m) shown by arrow. Photograph shows the network of pits and boulder piles left by sand extraction in the Belham River valley, March 2013. (o) Boulders piled up having been excavated from the lahar deposits in the lower Belham (by Isles Bay crossing) in March 2011. Person in photograph is shown for scale and is 1.85 m tall.

outside of meander bends as isolated blocks of material (Figure 3.17c). PDC material was integrated into flow by the undercutting of terraces by shallow flow, destabilising a vertical block of material that may topple or slump into the channel. Tension cracks present in the tops of PDC deposits (Figure 3.17d) highlighted terraces that had been eroded by recent flows. As the channel widened, erosion to PDC terraces decreased because higher magnitude (less frequent) flows were required to mobilise material. Lahar deposits on top of the PDC terraces (Figure 3.17e) in March 2013, showed that fluvial flow had occurred over the top surface of the PDC deposit, and that subsequent lahars had incised vertically (by <0.8 m) and excavated a channel, between June 2010 and March 2013.;

Elevation change between 30th October 2009 and June 2010 during Phase 5 was not captured by DEM data, however photographs of the Orange house at the Belham Bridge crossing (Figure 3.13o and Figure 3.17f) showed ~0.7 m of elevation gain. Most of this material was deposited during a single lahar on 13th-14th April 2010. The elevation gain at this location between November 2007 and June 2010 DEMs (Table 3.8) was the same as the elevation gain measured using the Orange house as a scale (~1.8 m). This suggests that the six small-moderate lahars proceeding the April event (13th April- June 2010) had no measurable impact on bed surface elevation. A large

lahar triggered by Hurricane Earl (29th- 31st August 2010) resulted in an increase in bed surface elevation at B3 (Figure 3.15) by 0.8 m, however between March 2011 and March 2013 the bed surface was eroded and 0.2 m of vertical material removed. Figure 3.15(f-j) showed the change in bed surface at B3 from May 2010 to March 2013. Photographs and field surveys (2011-2013) showed the bed surface coarsened between May 2010 and November 2010 (Figure 3.17f-g) from predominantly sand sized sediment with a low percentage (~5 %) pebble-cobble fraction of predominantly pumice clasts, to ~40% gravel: 60% sand bed surface with cobble-boulder bars in the centre of the valley and sand-pebble bars in the centre of sand channels (~15 m wide). The bed surface did not alter significantly between November 2010 and March 2012 (Figure 3.17g-i). Gravel bars were unmodified in their central parts and vegetation was growing suggesting minimal disturbance. Lahars during this period were categorised as small-moderate events that were contained within channels formed between coarser gravel bar forms. The width of these channels increased with time (~8 m to ~27 m March 2011-March 2013) highlighting that smaller lahars gradually reworked coarser material delineating channel boundaries. The fine (orange-brown) sediment in Figure 3.17h was deposited during the lahar flow front (observed in March 2013, Appendix 3.4e and Section 4.4.1). During 2011, a series of seven small lahars between March 2011 and June 2011, terminated progressively further down valley from B3 (Figure 3.14b) to the coast on 30th April 2011 (fourth lahar in sequence). The lahars were between 2 months and 4 days apart. Critically, they all followed the same flow path and between events fines deposits persisted creating a smooth bed surface for preferential flow. From available data lahars two to four in the sequence of seven flows, were triggered by less than 10 mm of rainfall, however the lahar on the 30th April 2011 was sustained by 60 mm of rainfall compared to ~10 mm for the other events. Once one lahar had reached the coast other proceeding lahars also travelled the full valley length, despite being sustained by lower amounts of rainfall, ~15 mm (see Appendix 2.2w). This observation showed a relationship between lahar frequency, magnitude and travel distance for flows of small volume.

The large lahars in 2010 reset the bed surface both topographically and texturally, however the large lahar (by classification) on 13th-14th October 2012 reworked the bed surface and altered channel boundaries but did not induce significant elevation loss or gain (~0.2 m at B3). Figure 3.17j taken at approximately the same location as Figure 3.15h showed that channels widened and some incision occurred. Channel widths increased by ~12 m in this location. Areas that were not heavily modified (gravel bars)

showed increased percentage vegetation cover; vegetation species abundance and height provide a useful indicator of lahar occurrence (Jones, 2011). Significant revegetation occurred between March 2011 when the Jones (2011) study was undertaken and May 2014 (Figure 3.17k-l); it would be useful to update this work and consider impacts of vegetation roughness on lahars.

Downstream between B3 and B2 (Figure 3.14b) lahars were constrained by topographic lows created by commercial sand extraction. The change in bed surface in this location was shown in Figure 3.17m-n documenting the construction of a series of pits between November 2010 and March 2013. The network of roads and pits altered channel dimensions compared to areas up and downstream, by decreasing channel width:depth ratio, and therefore the hydraulics of lahars in this location. Extraction, which has also increased in scale since March 2011, has removed an estimated $9.0 \times 10^4 \text{ m}^3$ of sand-pebble sized material from the area between March 2011 and February 2012, leaving larger cobbles and boulder sized clasts in-situ (Figure 3.17o). Excavated boulders present on the valley floor during the study period were up to 2.37 m in diameter (b-axis), and were excavated from material deposited by lahars between November 2007 and March 2011. Boulders up to 0.5 m were observed rolling downstream in a medium sized lahar on 30th October 2009 (Appendix 3.4b). Given the size of the boulders (Figure 3.17o) it is suggested that they were transported as bedload (rolled) during a large lahar; four large events were listed in the database for this period (13/4/2010, 29/8/2010, 4/10/2010 and 6/10/2010). Extremely large boulders were observed protruding from the bed surface of finer material in November 2010 (Figure 3.17m), these were not evident in video and photographs taken at the same valley location on 30th October 2009, supporting boulder emplacement by a large lahar in 2010. Stream power represents the rate of energy expenditure at a particular point in a river system. Employing empirical published equations from Costa (1983, Equations 3.1-3.2) provides an estimate of critical stream power (ω) required to initiation clast motion; maximum stream power may be far greater than clast initiation conditions.

$$\omega = 0.009Di^{1.686} \quad \text{Equation 3.1}$$

$$\omega = 0.030Di^{1.686} \quad \text{Equation 3.2}$$

Where Di is mobilised clast size (in this case 2370 mm is used), the parameters in each equation were determined based on reconstructions from analysis of paleoflood deposits

at specific locations, appropriate for clast sizes over 0.05 m. The equations suggest a critical stream power in the range of 4400 Wm^{-2} to 14700 Wm^{-2} , the range representing differences in possible flow depth, bed surface roughness and channel slope (Costa, 1983). Sušnik (2009) found that theoretically based equations such as those by Petit *et al.* (2005) provided lower estimates of critical stream power, than empirical based methods, because they accounted for protrusion and clustering of particles on the bed surface, and the bed surface grain size distribution. The estimates of critical stream power here provide a useful flood magnitude for large lahars in 2010 the Belham River valley. The stream power is comparable to that predicted for large lahars in the Belham River Valley on 20th May 2006 by Sušnik (2009), who estimated maximum (local) stream power of *c.* 8000 Wm^{-2} .

Results in this section showed that:

1. Lahars in the Belham River Valley have occurred since the onset of eruptive activity in July 1995. The effects of volcanic sedimentation were enhanced by a series of synoptic scale weather systems early on in the eruption, resulting in sediment deposition infilling pre-eruption channels by November 1998 (based on observations at the Belham Bridge site).
2. The Belham River Valley has undergone three periods of net aggradation (1995-1999; 2002-2003; 2006-2011), two periods (one still ongoing) with very little net loss or gain (2000-2002; 2012-2013), and one period of net degradation (2004-2006), during which time a large lahar (20th May 2006, see Section 3.5) incised 2 m deep channels into the bed surface, dramatically altering valley morphology.
3. Large lahars undertook the most geomorphic work, resulting in significant (> 0.2 m) changes in bed surface elevation (e.g. 13th April 2010). The amount of change to the valley depended on the combined sediment-water volume of the lahar; this was evidenced by surface measurements and observations of the valley floor in relation to lahar activity between March 2011 and March 2013.
4. Smaller lahars with the same volume had longer runouts if they occurred after other small events, because fines deposition by the flow front reduced bed surface roughness.
5. In total $\sim 9 \times 10^6 \text{ m}^3$ of sediment ($6.75 \times 10^6 \text{ m}^3$ solid volume) was in storage in the Belham River Valley in March 2013. Of this $3.85 \times 10^6 \text{ m}^3$ was deposited within 1 km off-shore, resulting in 880 m of sea-ward coastline extension.

3.6. Discussion

Since the onset of volcanic activity in July 1995, an estimated $5.06 \times 10^7 \text{ m}^3$ of material has been deposited in the Belham Catchment by five phases of volcanic activity. At least 351 rainfall-triggered lahars (< 585 including category 1) in conjunction with tephra fall and other minor fluvial and aeolian processes, have progressively remobilised over $9.97 \times 10^6 \text{ m}^3$ of primary material downstream into channel storage within the Belham River Valley ($4.89 \times 10^6 \pm 2.8 \times 10^4 \text{ m}^3$, 51 %) and out to sea to form a sub-aerial debris fan (49%). Approximately $4.44 \times 10^6 \text{ m}^3 \pm 2.8 \times 10^4 \text{ m}^3$ of sediment remains in storage in the Belham River Valley. Several authors (Barclay *et al.*, 2006; Barclay *et al.*, 2007, Sušnik 2009) have compiled sections of the data archive to explore relationships between rainfall, lahar activity and changing valley morphology, focusing on activity between 1999 and 2007. Since then a further two phases of volcanic activity have contributed over $1.20 \times 10^7 \text{ m}^3$ of material to Farrell's Plain, Tyre's Ghaut and Gages Fan (Section 3.2), some of which was remobilised by 130 (<394 including category 1) lahars, resulting in $2.45 \times 10^6 \text{ m}^3$ of deposition in the Belham River Valley. The following discussion uses the complete longitudinal dataset (updated to include events between 2007 and 2013, Sections 3.2- 3.5) to assess conditions under which significant changes to valley morphology occurred.

Morphological changes to the Belham River Valley between 1995 and 2013 were strongly controlled by sediment inputs to Farrell's Plain and Tyres Ghaut associated with volcanic activity in phases of extrusion, and degradation of the dome in periods of repose (Section 3.2). In common with other systems perturbed by large sedimentation events, there were clear periods of valley net aggradation and subsequent shifts to degradation as sediments in the upper system were evacuated or stabilised (e.g. Mount Pinatubo, Gran and Montgomery, 2005). In the Belham River Valley, these transitions occurred relatively rapidly, conditional on patterns of rainfall and changing runoff characteristics. Based on the record of volcanic activity alone, five periods of sedimentation occurred between 1995 and 2013: (1) July 1995 to October 1998, (2) September 2002 to June 2003, (3) December 2006 to January 2007, (4) December 2008 to January 2009 and (5) November 2009 to February 2010. These periods of sedimentation broadly corresponded with north-west to west dome extrusion. Net degradation was recorded by topographic surveys between June 2003 and May 2005, and between March 2011 and March 2013 (present). Observations between 1995 and 2002, and November 2007 and June 2010 were limited to a few photographs, but

showed evidence of bed surface incision- channelization in 2001, 2002 (Barclay *et al.*, 2007), terracing upstream of the Sappit River in September 2009 (Appendix 2.3e) - and selective erosion (Dietrich *et al.*, 1989) resulting in bed surface armouring, observed upstream of the Belham Bridge crossing in March 2001 (Appendix 3.4a). These features were characteristic of degradation to the valley bed but without further evidence it is difficult to comment if net degradation was occurring valley-wide.

Date range	Number of category 2 & 3 lahars	Rate (m lahar ⁻¹)	Rate (m year ⁻¹)
1/7/1995 to 1/1/2002	105	0.05	0.86
1/1/2002 to 31/5/2003	24	0.02	0.47
31/5/2003 to 1/5/2005	43	-0.03	-0.77
1/5/2005 to 1/11/2006	25	0.09	1.46
1/11/2006 to 1/11/2007	24	0.10	2.31
1/11/2007 to 1/6/2010	60	0.035	0.8
1/6/2010 to 1/3/2011	22	0.04	1.2
1/3/2011 to 1/2/2012	23	-0.009	-0.22
1/2/2012 to 1/3/2013	23	-0.005	-0.1

Table 3.9 Net aggradation and degradation rates between survey periods

Table 3.9 contains calculations of the rate of aggradation/degradation per lahar and per year in the valley, using available DEM data. Rates were averaged over the combined spatial coverage of the two surfaces in the calculation. The highest yearly rate of aggradation was recorded between 1/11/2006 to 1/11/2007 and was related to the voluminous PDCs that entered the Belham River Valley on 8th January 2007. The PDCs deposited $4.5 \times 10^6 \text{ m}^3$ of material (Table 3.1) between the top of Tyres Ghaut and Cork Hill (Figure 3.1). This was captured in the valley’s longitudinal profile (Figure 3.12a, Section 3.5), where there was a distinct shift at 1700 m (distance upstream) from ~1m to ~3 m, of elevation gain, upstream of the Sappit River confluence (and Cork Hill). Lahars between January and early October 2007 were initiated with very low rates of rainfall; the peak 10-minute rainfall in the 24 hours before lahar initiation was just 0.2 mm (for all events) and the average total 24 hour rainfall was 0.88 mm, compared with the average 12.6 mm for the GARI rain gauge data set (Section 3.4). Antecedent 7-day rainfall increased in June- August 2007 but values were still below the dataset average 24 hour rainfall amount. Two main possibilities explain these observations: (1) the surface characteristics of the catchment changed in response to volcanic activity, enhancing the runoff of rainfall or (2) the location of the GARI rain gauge was not representative of rainfall over the upland areas of the catchment, where

lahars were being initiated (this is the only rainfall record at this time). While (2) may explain the low 10-minute intensity values recorded, it does not fully account for the fact that recordings were low relative to the full ~7 year rain gauge dataset.

Volcanic activity in early 2007 affected the entire catchment and primary flows deposited material to the north-west down Tyres Ghaut and to the west onto Gages Fan. When tephra is rich in fine ash (<0.125 mm) and under 100° C, infiltration rates on tephra-blanketed surfaces may be reduced by orders of magnitude (Murata and Okabayashi, 1983; Leavesley *et al.*, 1989) increasing runoff production. All PDCs developed buoyant ash plumes that were typically deposited down-wind of the flow (Cole *et al.*, 2002); given the predominant east-west wind direction, fallout from flows to the north-west will have affected large areas of the Belham Catchment. Tephra fall deposits from the 12-15 July 2003 dome collapse, analysed by Edmonds *et al.* (2006) contained 50-70 wt. % <0.063 mm sediment and exhibited a similar grain size distribution to co-PF tephra fall observed by Bonnadonna *et al.* (2002). It is suggested that fall deposits in 2007 were of similar composition. Major and Mark (2006) demonstrated that the influence of tephra fall on surface infiltration rate decreased rapidly after deposition. On PDC deposits, the infiltration rate significantly increases after fine fall deposits are removed by overland flow (Yamakoshi *et al.*, 2005), followed by the initiation of rill incision. The prevalence of lahars triggered by comparatively low rainfall between January and early October 2007 suggested that conditions of enhanced runoff persisted for months after initial PDC and fall deposition. The spatial extent of deposition, thickness and composition of fall deposits, replenishment by fresh ashfall (*e.g.* 15th March 2007 ashfall) and debris from shedding of the west side of the dome (north Gages fan was connected until ~ March 2007), as well as the nature of rainfall, low sustaining 24 hour rainfall (Section 3.4) deposited by meso-scale weather systems (<100 km in size) where rainfall may not have been catchment wide, were all factors that would increase the duration of fine fall deposit coverage.

Lahar magnitude was characterised by flow volume, rheological character, run-out and duration. In 2007, lahars between January and early October were triggered by similar amounts of rainfall, delivered at similar rates. Sustaining rainfall (in the following 24 hours after flow is triggered) varied from 0 mm to 8.4 mm. By comparison lahars on 23/10/2007 and 26/10/2007 were triggered by 21 mm and 22 mm of rainfall, with peak 10 minute intensities of 9 mm and 4 mm, and 24 hour sustaining rainfall of 4 mm and 55 mm, respectively. Once infiltration capacity is reached and

overland flow initiated, excess rainfall becomes runoff and contributes to flow discharge; manifested either by increased flow duration or peak discharge primarily dependent on channelization in the system. The duration of seismic registration for the lahar on 26/10/2007 was longer than that on 23/10/2007 due to sustaining rainfall. Rainfall relationships in the Belham Catchment were complex (Section 3.4) and dependent on time since primary volcanic material has been emplaced, the spatial extent of volcanic perturbations and the spatial distribution of rainfall in the catchment. While 'valley-wide' large lahars were observed during the passage of large synoptic weather systems (e.g. Hurricane Earl 2010, Section 3.5), highly erosive flows causing significant modification to the valley bed have also been observed following average rainfall with synchronous tephra fall and at a time of prolonged vegetation damage (Alexander *et al.*, 2010). Critically large valley-wide lahars that persisted for days rather than hours, undertook the majority of geomorphic work; small lahars did not mobilise large volumes of material or significantly alter bed surface morphology.

The impact of multi-phase volcanic eruptions on catchment runoff response operates over sub-daily to decadal timescales. Figure 3.18 shows the effect of volcanically induced catchment modification on runoff response. Modification of the topographic catchment boundary in Phase 1 remained permanent, resulting in a bimodal hydrograph response (Figure 3.18A), if rainfall was uniform across the catchment. The Belham River Valley longitudinal profile steepened (Section 3.5) in response to voluminous PDCs on 8/01/07 and 8/01/10, increasing runoff velocity and peak discharge relative to a lesser channel gradient (Figure 3.18B), assuming uniform bed surface roughness. In the SHV sub-catchment, drainage density increased and the pattern of channels changed from dendritic to parallel between 1995 and June 2010. Development of channels following the emplacement of large volumes of primary deposit, was rapid after Phase 5 because of a number of large rainfall events and the erodibility of the deposit. Increased drainage density increases the efficiency of delivery of water from hillslopes upstream into the Belham River Valley, thereby increasing peak discharge and decreasing the time between rainfall and the arrival of

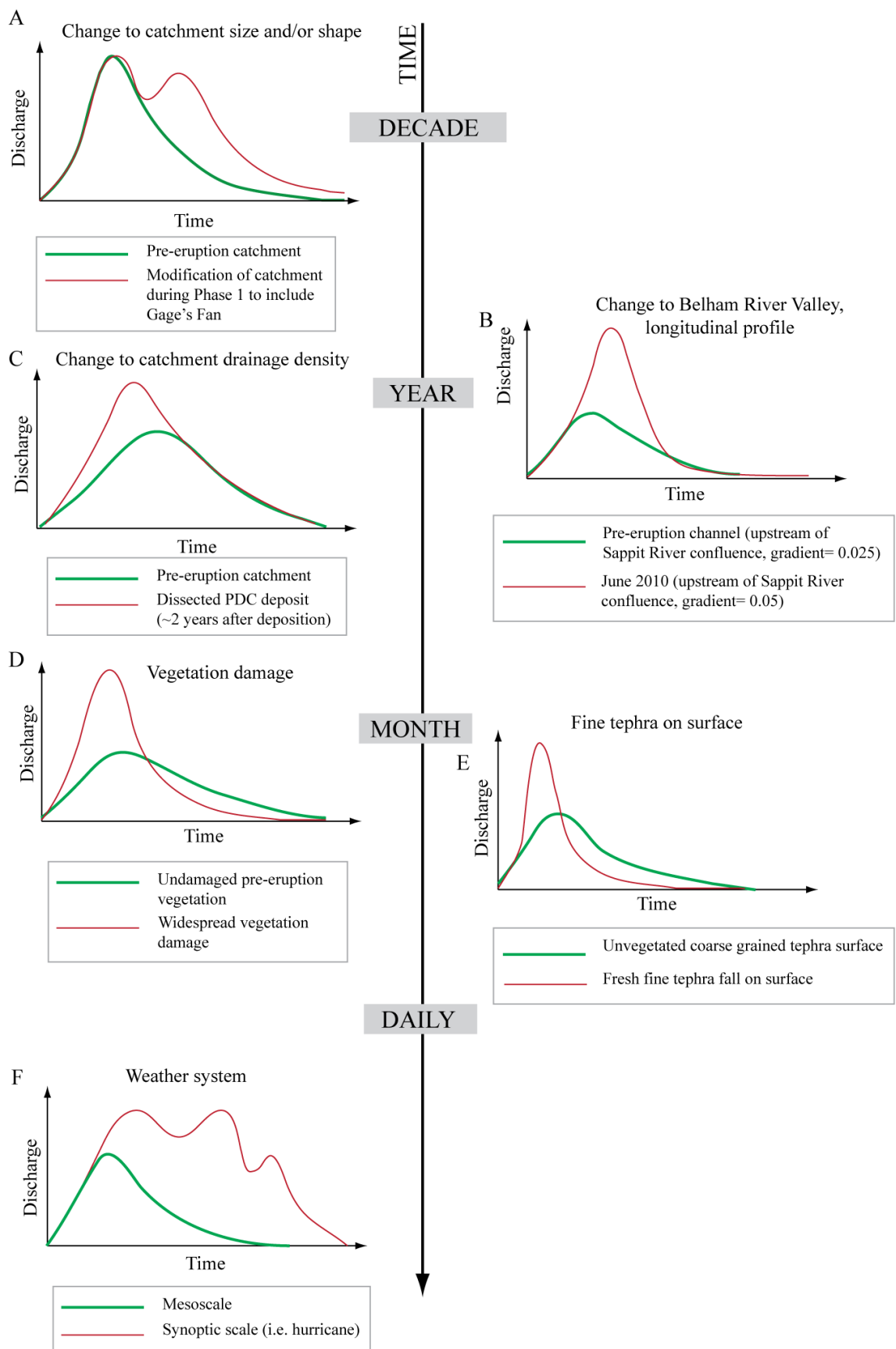


Figure 3.18 Hypothetical hydrographs showing the impact of volcanic activity on catchment condition and runoff over different time scales, based on observations in the Belham Catchment and other published studies discussed throughout Chapter 3. Each hydrograph is explained in the preceding text.

peak flow (Figure 3.18C). Areas of vegetation damage and fresh tephra deposition increase runoff by decreasing bed surface roughness, and the interception and storage of water (Section 3.3). Rapid rates of revegetation on Montserrat resulted in shifts in local infiltration rates and rainfall inception in areas affected by volcanic activity (Figure 3.18D). Depending on rainfall (frequency and magnitude) and the thickness of tephra, runoff rates decreased with time as fine ashfall was entrained leaving a coarser more permeable deposit (Figure 3.18E). Runoff rates may initially be low if tephra deposits are over 100°C in temperature, however the rate of cooling of deposits during rainfall is difficult to quantify because of variable cooling rates dependent on rainfall intensity (Hicks *et al.*, 2010). More rainfall was required to trigger lahars with time from tephra fall emplacement. These two processes operated over scales of days to months. Finally, the size and duration of the weather system dictated where rainfall was deposited within the catchment, how much was deposited and how long rainfall sustained a lahar (Figure 3.18F).

In natural volcanic systems these processes do not operate independently, but in combination over different time scales shows conditions that may lead to the formation of large lahars, the unexpected generation of lahars by relatively low amounts and/or intensities of rainfall, and inter-and intra-flow variability. Theoretically the largest lahars occur during the passage of synoptic scale weather systems synchronously or immediately after a large partial dome collapse following a prolonged phase of eruptive activity and widespread vegetation damage. This set of circumstances is not dissimilar to catchment conditions during Hurricane Earl in late August 2010, which generated large lahars contributing to $5.83 \times 10^5 \text{ m}^3 \pm 4.08 \times 10^3 \text{ m}^3$ of volumetric gain in sediment storage in the Belham River Valley between June 2010 and March 2011. Several large lahars were also associated with rainfall synchronous dome collapses on 3rd July 1998, 20th March 2000, 29th July 2001 and 12th– 13th July 2003 (Barclay *et al.*, 2006); lahars were driven by high runoff conditions and bulking by tephra fall directly into the flow, similarly to the large lahar on 20th May 2006 (Alexander *et al.*, 2010). Although large lahars naturally attract more scientific interest because they pose the greatest hazard to local people and infrastructure, it is equally important to document smaller lahars in event databases. In the absence of a tropical storm or hurricane sized weather system, the prevalence of small lahars increased relative to moderate-large events, with increased time from volcanic activity. This was due in part, to the amount and distribution of rainfall sustaining a lahar, but also to decreased runoff and decreased finer sediment availability, which are signs of fluvial recovery.

Models for catchment adjustment to sedimentation have been discussed by various authors in volcanic environments (Pinatubo, Philippines, Gran and Montgomery, 2005; Mt St Helens, USA, Major and Mark, 2006; Mt Ruapehu, New Zealand, Manville *et al.*, 2009). Gran and Montgomery's (2005) model was adopted and modified (Figure 3.19) based on observations presented in this chapter and review of catchment adjustment to volcanic sedimentation by Manville *et al.* (2009). The model shows the progressive adjustment of the fluvial system to volcanic sedimentation by morphological changes to the valley and by changes in channel bed form and texture; in the context of changing runoff dynamics and weather systems. Inputs of primary volcanic material during Phases 2 to 5 effectively reset the position of the Belham River Valley within the model; during Phase 2 PDCs were deposited gradually over time and observations were made that deposition was contained within channels in Tyres Ghaut that had been established in Phase 1 PDC deposits by fluvial activity. Observations suggested that transitions up the model (Figure 3.19) were slow during this period, but rapid progression down the model ensued after Phase 2. Bedrock erosion was observed in Tyre's Ghaut, Dyers River and the channel between Gages fan and the Belham River Valley, as the system tried to adjust to increased runoff from steep volcanic fans, that remained active between Phases, and depleting sediment supplies, as valley-fill was transported downstream.

Large volume inputs of sediment during Phases 3 to 5 (Table 3.8) rapidly changed the state of the Belham River Valley, resetting channel stabilisation and resulting in slower progression from aggrading to degrading conditions. Since geomorphic work was undertaken by the lahars, the size of the lahar and therefore the amount of rainfall and catchment condition governed the progression through the model. This was evidenced in 2010 when a series of large lahars mobilised an estimated $7.7 \times 10^5 \text{ m}^3$ of material shortly after emplacement of $3.4 \times 10^6 \text{ m}^3$ of sediment during 8th February 2010 partial dome collapse in Phase 5. Deviations from the model may also occur if runoff is enhanced when the channel has shifted to net degradation (20th May 2006 lahar, Section 3.5.1). The specific sediment yield of the system is discussed in Section 6.2.

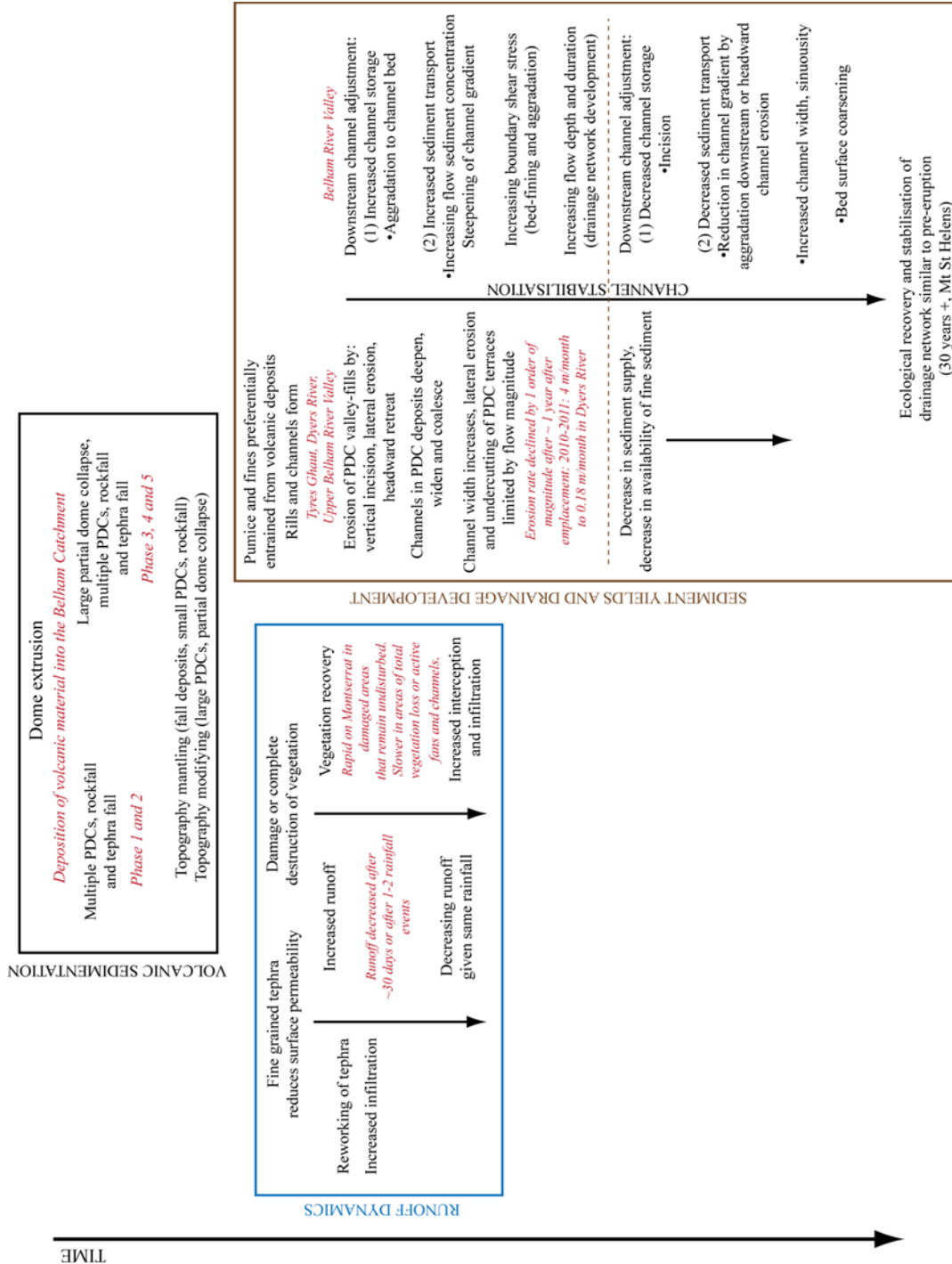


Figure 3.19 Model for channel response to volcanic sedimentation (adapted from Gran and Montgomery, 2005 and Manville *et al.*, 2009)

3.7. Conclusions

1. The size of the Belham Catchment increased from 13.7 km² to 14.8 km² to include Gage's fan early in the 19 years of eruptive activity. This altered the catchment response to rainfall and increased sediment storage (and availability). The increase in size also increased the probability of rainfall inception during mesoscale weather systems that may only affect sub-sections of the catchment.
2. 80% of the total PDC deposition in Tyres Ghaut, Dyers River and Farrell's Plain originated from three large partial dome collapse events during Phases 3 to 5 (Table 3.2).
3. The Belham River Valley responded to volcanic sedimentation by increasing channel storage, slope gradient and decreasing bed surface roughness by decreasing grain size.
4. In the Belham River Valley, three periods of net aggradation are identified (1995-1999; 2002-2003; 2006-2011), two periods with very little net loss or gain (2000-2002; 2012-2013) and one period of net degradation (2004-2006).
5. The shift from net aggradation to net degradation was described using a model adapted from Gran and Montgomery (2005) and Manville *et al.* (2005).
6. The rate at which the system passed through the different stages of this model was dependent on the number of large lahars and the amount of sediment deposited by volcanic activity in the Belham Catchment. The rate of erosion to primary deposits decreased with increased time from eruption, typically the erosion rate decreased by one order of magnitude the year after volcanic emplacement. Although large volumes of sediment were stored in the upper catchment, the system was limited by the lahar magnitude required to occupy the full channel width and initiate undercutting of PDC terraces.
7. Lahar size was dependent on the amount of sustaining rainfall in the 24 hours after lahar onset, irrespective of volcanic activity. However, lahars were more readily triggered during or immediately after volcanic activity.

8. In total $\sim 4.4 \times 10^6 \text{ m}^3$ of sediment ($3.3 \times 10^6 \text{ m}^3$ solid volume) was in storage in the Belham River Valley in March 2013. Of this $3.85 \times 10^6 \text{ m}^3$ was deposited within 1 km off-shore, resulting in 880 m of sea-ward extension. An estimated $10.7 \times 10^6 \text{ m}^3$ ($8.06 \times 10^6 \text{ m}^3$ solid volume) was in storage in the upper Belham Catchment (Tyres Ghaut, Farrells Plain, Dyers River) in June 2010.

Chapter 4:

Characteristics of multi-order discharge fluctuations observed in lahars triggered by Tropical Storm Rafael, 13-14th October 2012, and impacts on sediment transport

4.1. Introduction

Sediment-laden flash floods are extremely destructive, but remain poorly documented and understood, particularly in terms of their fingerprint within the sediment record. Coupled observations of rapidly varying unsteady flows and the sedimentology of resultant deposits in natural channels are few (Starheim *et al.*, 2013; Vazquez *et al.* 2014). This is because of the unpredictability of sudden onset ‘flashy’ events, the challenges of measuring flow parameters in alluvial channels with highly mobile beds, and difficulty in observing and re-visiting vertical exposures of deposits. There are some published studies on experimental flow and sedimentary structures relevant to flashy systems (Kennedy, 1960; Middleton, 1965; Jopling and Richardson, 1966; Yagishita and Taira, 1989; Cheel, 1990a; Alexander *et al.*, 2001; Yokokawa *et al.*, 2010; Cartigny *et al.*, 2014), and a few interpretations of ‘flashy’ event deposits in the rock record (Power, 1961; McKee *et al.*, 1967; Hand *et al.*, 1969; Picard and High, 1973; Tunbridge, 1981; Rust and Gibling, 1990; Fralick, 1999; Duller *et al.*, 2008; Lang

and Winesmann, 2013), but these observations combined are not sufficient to confidently recognise sedimentary structures formed by sediment-laden flash floods.

Lahars in the Belham River Valley (Chapter 3) vary considerably because of changes in catchment response to rainfall, driven by volcanic activity. Observations of sub-channel structure over time (Section 3.5) using photographs and video (<5 minute clips) of lahars (1995-2010), record rapid discharge changes recurring during individual flood events. This has significant implications for sediment transport dynamics, the sediment record and also for the management of lahar related hazards.

Monitoring lahars in the Belham River Valley was challenging because of restricted 'safe' access. In-person visual observation of valley-wide lahars was limited to sites >5 km from the volcanic edifice in an area modified by commercial sand extraction. In order to monitor a section of the natural channel a remote indirect approach was used. In March 2012, a remote camera was installed 3.8 km from the volcano edifice (Figure 4.1; Site A) (see Section 2.3.2 for details on installation and technical specifications). The camera was continuously operational, capturing an image (Figure 4.2) at a rate of 1 frame per second. On 13-14th October 2012, over 170 mm of rain, from Tropical Storm Rafael, fell on the Belham Catchment, triggering multi-peaked lahars.

This chapter presents direct observations, analyses camera data and discusses the inter- and intra-flow variability of lahars in the Belham River Valley between 2011 and 2013. The observations in this chapter were directly related to sedimentary structures in the resultant deposits (Chapter 5).

4.2. Lahars 2010 to 2013

Seventy-seven lahars (category 2-3, Section 3.4.2) occurred between the end of Phase 5 in February 2010 and the beginning of 2014. Lahar size was defined in Section 2.2.3.2. Total rainfall during 2010 was 2091 mm, higher than 2012 (1574 mm) and 2013 (760 mm)¹, but lower than in 2011 when 2722 mm was recorded. There were many small and a couple of moderate lahars during 2011, however based on available data (Appendix 2.2w) the average 24-hour rainfall prior to lahar onset in 2010 and 2011 was similar; 14.2 mm and 12.2 mm respectively. Rainfall data and onset times were only available for 63% of events in 2010, but 100% for 2011 (recordings were spread across

¹ Rainfall was not recorded for the entire year due to instrument malfunction, see Appendix 2.2v

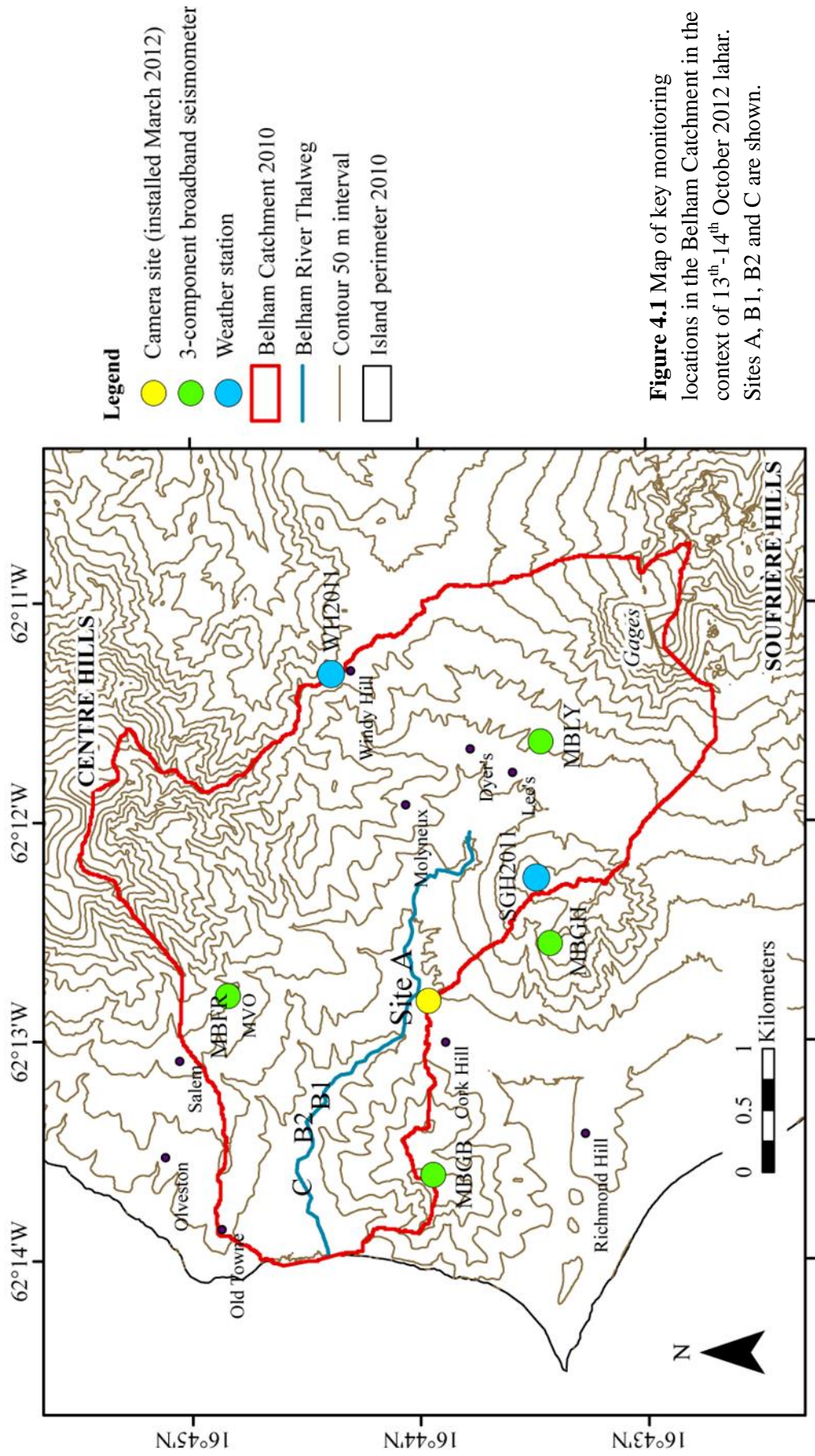


Figure 4.1 Map of key monitoring locations in the Belham Catchment in the context of 13th-14th October 2012 lahar. Sites A, B1, B2 and C are shown.

two automated weather stations). Available data shows that 24-hour rainfall prior to lahar onset was more variable in 2010 compared to 2011. Sections 3.3 and 3.4.2 discussed the impact of tephra fall on surface runoff and lahar magnitude. In 2010 minor tephra fall persisted in the upper Belham Catchment after the end of Phase 5 due to dome degradation and in common with extensive vegetation damage, surface runoff was enhanced, increasing lahar volume. As discussed in Section 3.6 a combination of catchment conditions were capable of generating very large lahars from rainfall that may otherwise only trigger a moderate sized flow.

Figure 4.2 shows the incidence of lahars (category 2 & 3) between 2010 and 2013 and an estimate of size (based on descriptions, photographs and in-person observations). Of those lahars that were visually observed in 2010 there were an equal number of small lahars to moderate-large events. Comparatively between 2011 and 2012, most lahars were small. These events did not significantly modify the valley-floor and left little trace in the sediment record (Section 3.5.2). Only one large lahar occurred during this time, triggered during the passage of Tropical Storm Rafael on 13th-14th October 2012. The remote camera (Section 2.3.2) was operational between March 2012 and early 2013, however the rate of image acquisition was significantly increased from 1 frame every 15 seconds to 1 frame every second in October 2012. This event was the largest lahar captured by the camera and reworked sediments on the valley-floor, indicating that the flow contributed to the sediment record.

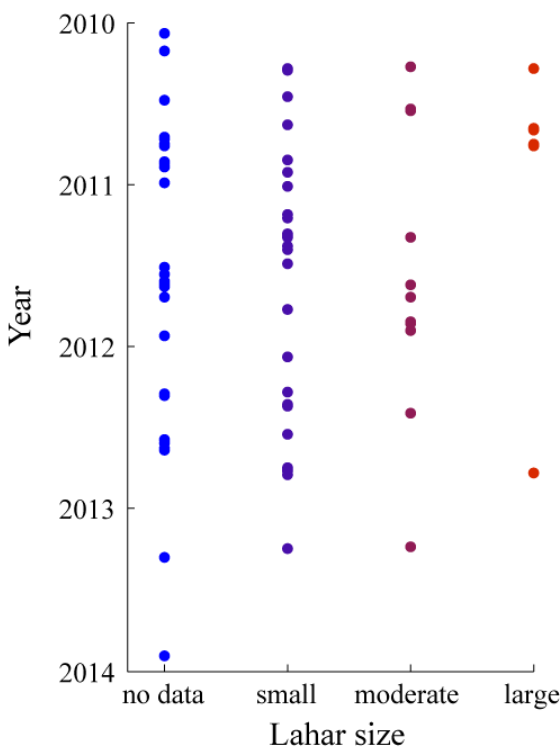


Figure 4.2 Lahar record: 2010 to 2013. Lahar size was determined from ground observations, descriptions in MVO scientific reports and seismic records (Section 2.2.3.2)

4.3. Tropical Storm Rafael

Tropical Storm Rafael formed from a tropical wave that originated off of the west coast of Africa on 5th October 2012 and tracked westward across the Atlantic (Avila, 2013). This track was typical of other tropical cyclones (Chapter 1). The tropical wave developed closed circulation on 12th October at 18:00 UTC about 200 nautical miles south-southeast of St Croix in the US Virgin Islands. The Tropical Storm then proceeded northwards, shown by the *best* track chart (Figure 4.3). Montserrat issued a tropical storm warning for Rafael between 00:00 UTC on 13th October and 09:00 UTC on 14th October. Rainfall was widespread across the whole island but was not continuous over the entire ~48 hour storm passage. Peaks in rainfall intensity were observed to last no more than 30 minutes, although rainfall continued for several hours. Near-gale to gale force wind speeds were inferred from visual observations of whole trees in motion, high and toppling waves with dense foam streaks at the coast, and large twigs in windblown debris. Air temperature ranged between 22°C and 28°C (measured on the SGH2011 weather station). There was minor direct damage to property (fence collapses, fallen roof tiles) and the road network (small-scale shallow landslips and rockfall from hillside road cuts, some minor cracking on tarmac edges). Lahars occurred in the Belham River Valley (Section 4.4) and other uninhabited drainages around SHV. Ephemeral *ghauts* draining from the Centre Hills and Silver Hills were occupied by turbulent streamflow during the storm and in the following 3 days but the *ghauts* did not flood onto road bridges crossing over them. The sand was washed off beaches in small bays along the west coast of the island, and the beach profiles steepened and shortened. Temporary ~2 m wide channels were generated by *ghauts* draining across beaches.

Regionally, the only fatality directly resulting from the storm, drowned while driving through a flooded river on Guadeloupe. This incident was associated with localised flooding in the southern Basse-Terre, resulting from more than 100 mm of rain in 3 hours and almost 300 mm of rain in 24 hours, on 13th October (WMO, 2013). Montserrat is ~ 30 km northwest of Guadeloupe. Satellite imagery from GOEs (e.g. Figure 4.4) and data from Meteo France Guadeloupe radar (Appendix 2.2x) indicated that the highest rainfall intensities on Guadeloupe were sustained for significantly longer than on Montserrat. Initially on the 13th October rain bands circulated from the south-east to the north-west directly across Guadeloupe, with peak intensities tracking just north of Montserrat. Shifts in circulation altered this direction from south-west to

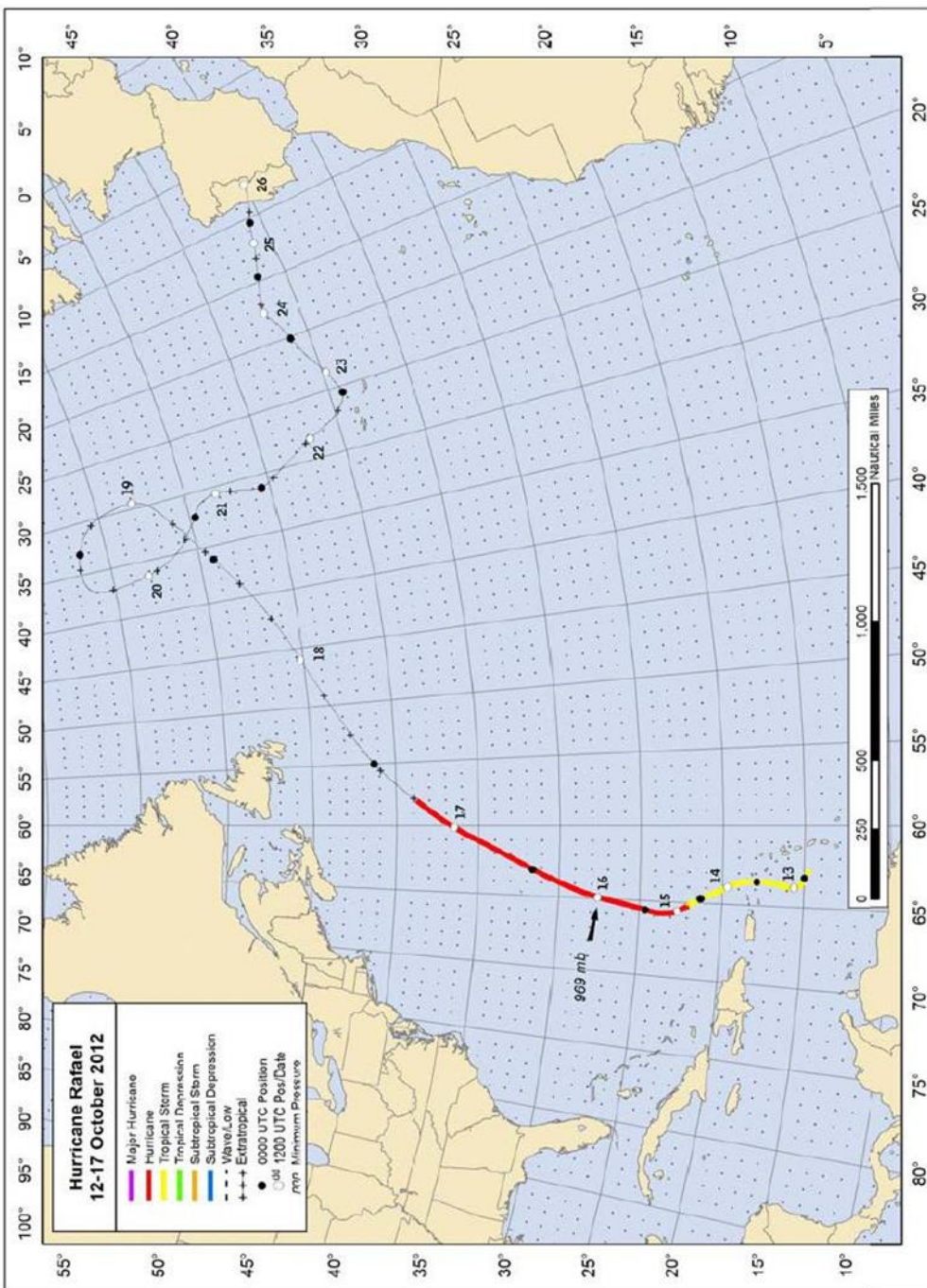


Figure 4.3 Best track positions for Hurricane Rafael, 12-17th October 2012. Track of the extratropical stage was mostly based on analyses from the NOAA Ocean Prediction Center. Track of the Tropical Storm and Hurricane stages were constructed from pressure and wind speed measurements. Reproduced from Avila (2013)

north-east at around 18:00 UTC on 13th October. This resulted in more sustained periods of higher intensity rainfall on Montserrat until around 2:20 UTC on 14th October when the rain bands narrowed and convective clusters converged, passing directly over Guadeloupe in a south-south-west to north-north-east direction. By 11:00 UTC the rain band had begun to disperse into a laterally more extensive system containing a series of convective cloud clusters that generated lower intensity, short duration bursts of rainfall as they tracked across Montserrat. Rainfall continued with this pattern gradually becoming more dispersed until it ceased at 21:40 UTC on 14th October. Radar data from the event not only provided a useful regional picture of the passage of rain, but was also used to supplement local direct rainfall measurements.



Figure 4.4 IR rainbow satellite image of the Western Atlantic captured by the GOES satellite on 13th October 2013 (NOAA, 2012). Montserrat is indicated by the black circle in the centre of the storm. The colour bar located at the bottom of the image indicates the intensity of outgoing long-wave radiation from low (purple) to high (red). Tropical Storm Rafael is delineated by the areas of high IR intensity, indicating a centre of thick cloud cover and associated storminess.

4.3.1. Rainfall

Direct rainfall measurements were made by the tipping-bucket rain gauge located at the St George's Hill (SGH) weather station (SGH2011, Figure 4.1). This was the only rain gauge operational during Tropical Storm Rafael and it developed a fault

just after 04:00 UTC on 14th October. To supplement these data, rainfall intensity estimates were extracted from images from the Mètèo-France Guadeloupe rainfall radar (Section 2.4.1). Image pixels associated with the Belham Catchment area were extracted and the maximum value from each sub-section was used to create a 15-minute rainfall time series. While the SGH2011 weather station provided a direct point measurement of rainfall in the Belham Catchment, the radar estimates rainfall intensity from the reflection of a radar pulse by precipitation. The radar was calibrated with rain gauges on Guadeloupe to calculate rainfall from the intensity of the radar reflections. The radar was not calibrated for Montserrat which was located on the outer reaches of the 100 km radar range. The radar time series underestimates peak rainfall intensity but correlates well with the timing of rainfall peaks registered on the SGH2011 weather station on 13th October when it was functioning. Data are shown later in this chapter, in Figure 4.5.

On 13th October 2012 the radar underestimated rainfall by 46%; 119 mm was registered at the SGH2011 weather station. The rainfall radar estimated 35 mm of rainfall fell on 14th October, however applying the same percentage underestimate as the previous day suggests that rainfall was closer to 50 mm. Based on these measurements the total volume of rainfall received in the Belham Catchment on the 13th October was estimated at $1.94 \times 10^6 \text{ m}^3$ and on the 14th October, $8.27 \times 10^5 \text{ m}^3$; in total $2.77 \times 10^6 \text{ m}^3$ across the two days. Most rainfall was received during three intense periods lasting between 60 to 130 minutes on 13th October and two 60 minute periods on 14th October.

4.4. Observations 11th -15th October 2012

Visual observations of the lahar in the Belham River Valley on 13-14th October 2012 were recorded by the remote camera (upstream, Site A Figure 4.1a), by the author (at two locations, sites B1 and B2, Figure 4.1a) and by a resident situated at the Isles Bay crossing (site C Figure 4.1a) equipped with a camera as part of a community monitoring project (managed by Jonathan Stone, UEA, see Section 2.4.3). Ground vibration associated with the lahar was captured by all four seismometers located in the Belham Catchment (MBLY, MBGH, MBGB and MBFL; Figure 4.1). In addition, the flow was sampled for suspended sediment using a simple bottle dipping method (Section 2.4.2); results are included in the following section. The following sections collate data to discuss arrival of the flow front, flow variability and waning flow.

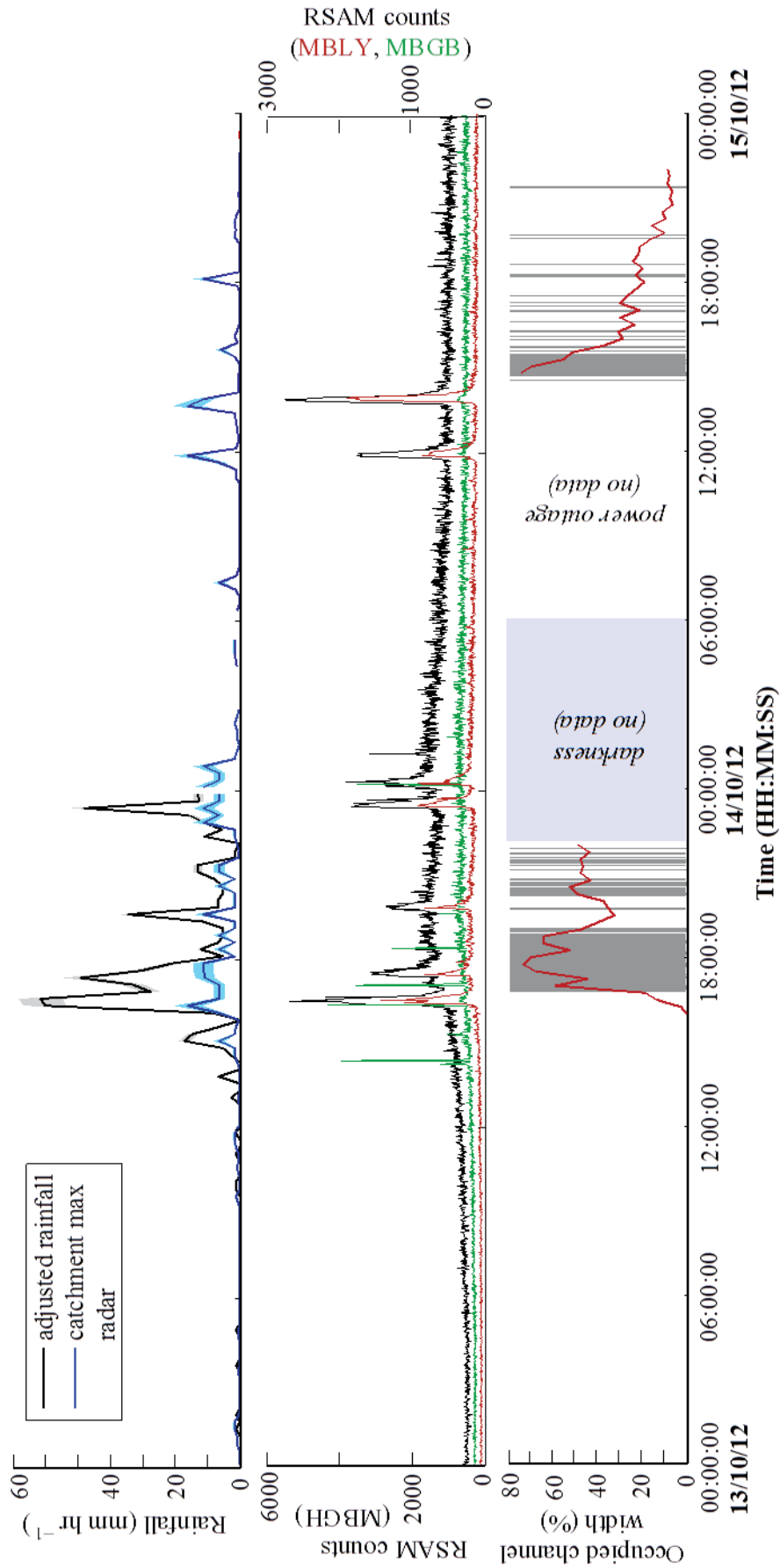


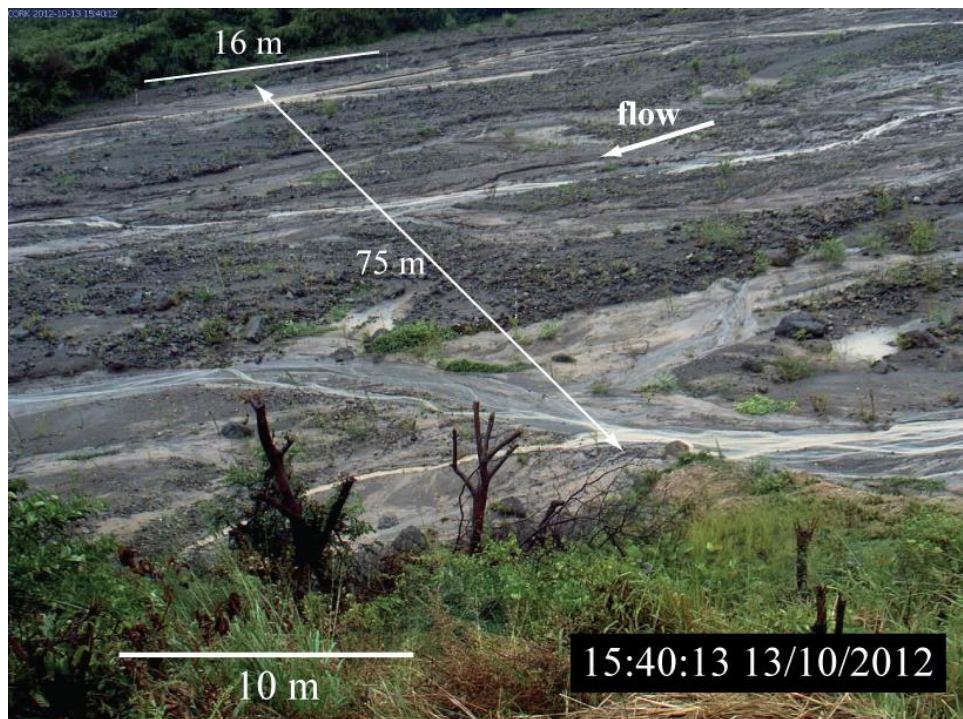
Figure 4.5 (a) Top: Rainfall rate calculated over 15 minute intervals from an adjusted rain gauge time series (Section 2.4.1) and the maximum pixel value from the Belham Catchment MFG radar image sub-section. (b) Middle: 1- minute real-time seismic amplitude (RSAM) from MBLY, MBGH and MBGB. (c) Bottom: Percentage of valley-floor width occupied by flow (red), passage of bores at Site A (grey bars) and camera (Site A) functionality.

4.4.1. Bed surface and flow prior to the onset of the lahar on 13th

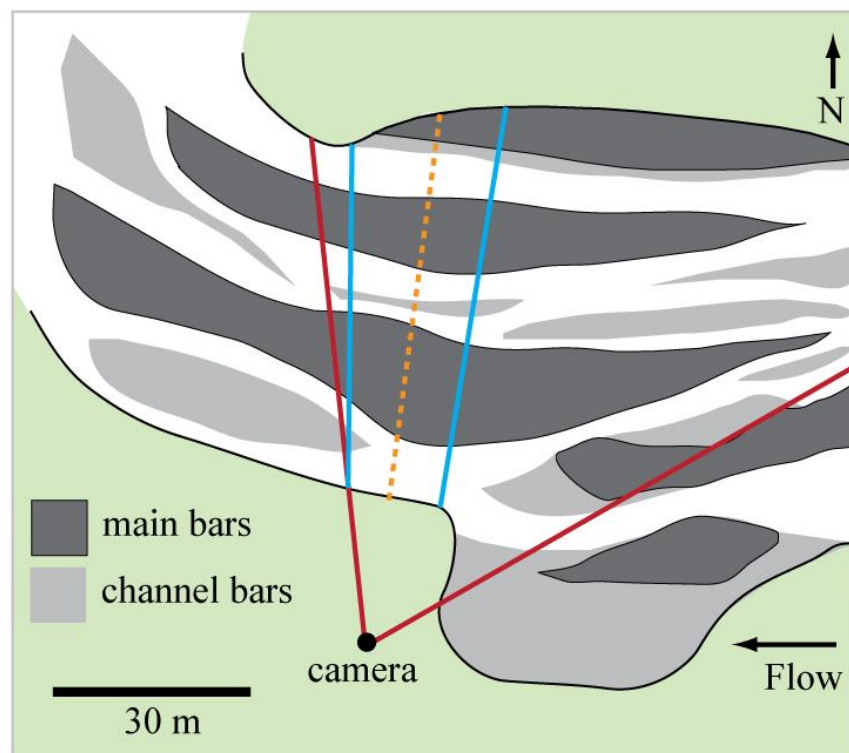
October 2012

The valley-floor surface character determines the preferential path of the lahar, particularly in the early stages of waxing flow. The pre-lahar bed surface at the camera site was very heterogeneous and in places vegetated (Figure 4.6a). The valley base was divided into three shallow (<0.2 m deep) channels by two bars (Figure 4.6b). Analysis of vertical photographs transect 1 photographs (Section 2.5.2, Appendix 4.1a) suggests that 65% of the bed consisted of pebbles and finer clasts (silt, sand), 12% medium pebbles (8 to 16 mm), 11% coarse- very coarse pebbles (16 to 64 mm), 10% cobbles (64 to 256mm) and 2% boulders (<256 mm). Fifteen percent of the bed was draped with light-brown fine sediment, which was deposited by lahars on 9th-10th October 2012 that occupied all three channels, but did not spread over the valley floor. The bed composition at the camera site was similar to the valley floor between Molyneux (2 km upstream, Figure 4.1 and 4.7a) and at the site of Pit2013 (0.7 km downstream, Figure 2.18).

Vegetation (mainly grasses and sedges) occupied 12 % of the valley floor at this site occurring in discrete patches, mainly on bar tops. The vegetation height and coverage indicated the level of disturbance and therefore the occupation of valley by recent flows (Jones, 2011). There had not been any large valley-wide flows since the end of 2010, but 50 lahars were seismically registered. The presence of established plants (> 20 cm in height) and multiple species was similar to photographs in March 2011 of this section, suggesting that channel pattern remained unchanged between early 2011 and October 2012.



(a)



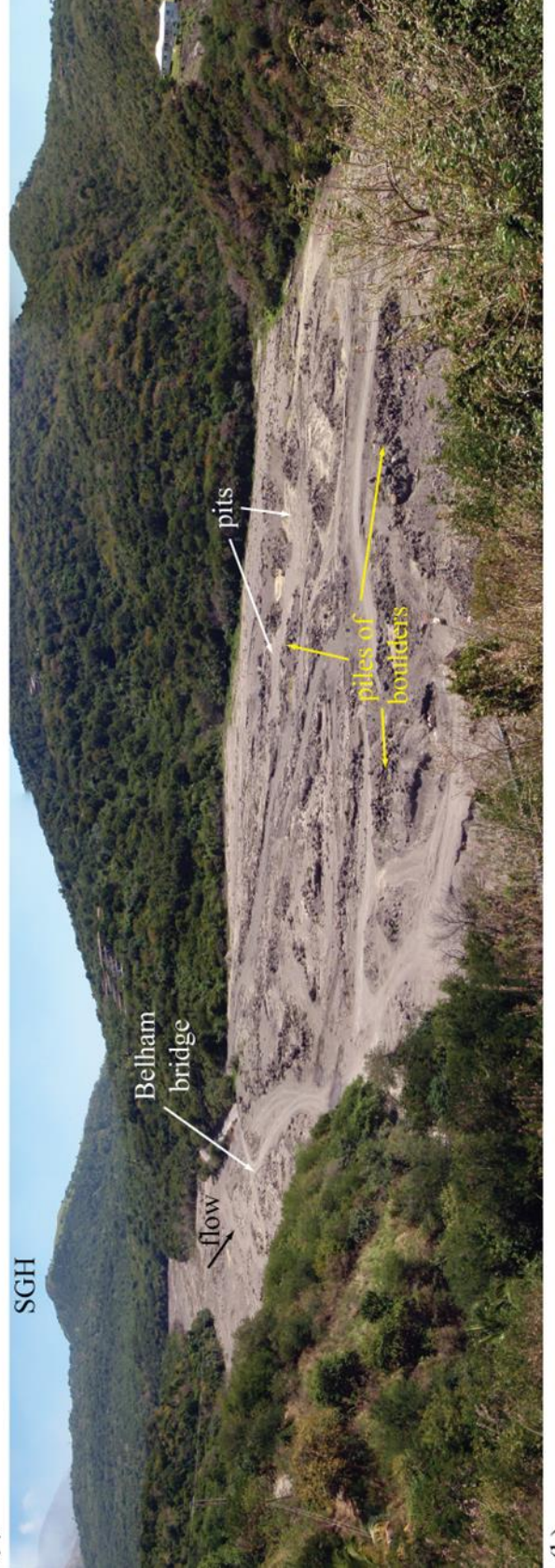
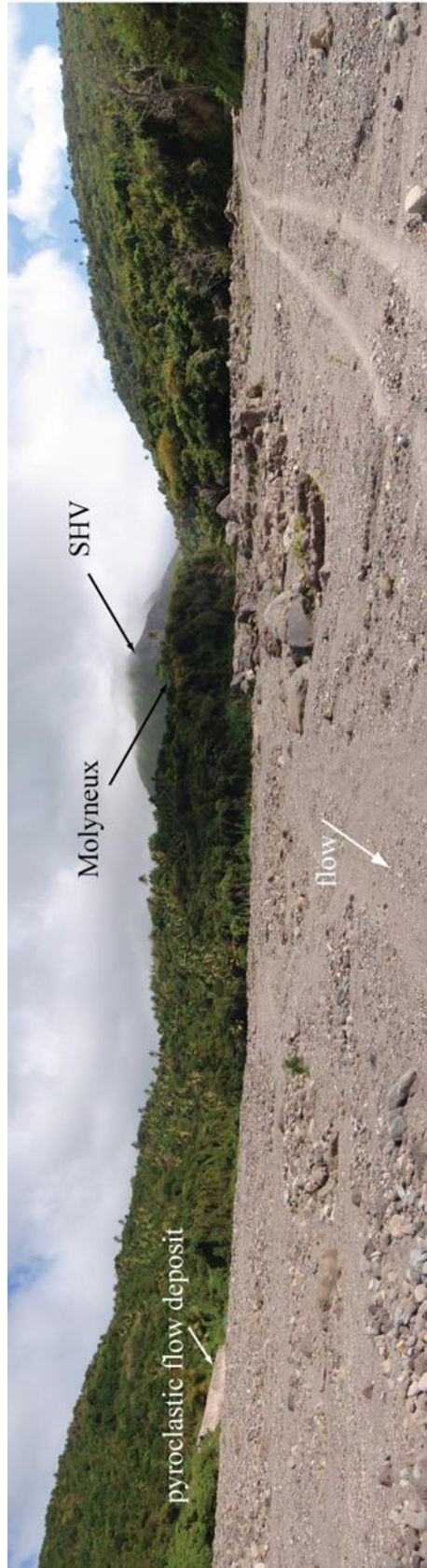
(b)

Figure 4.6 (a) Image still from the camera at Site A captured before the onset of the lahar on 13/10/2012. (b) Geomorphological sketch map at Site A showing the location of the main bars within the valley –floor cross-section monitored by the camera. The red lines delimit the area of valley-floor captured by the camera in each photograph.

The blue lines delimit the sub-section of the image in which flow features were measured, see also Figure 4.10. The orange line shows the location of transect 1.

Intermittent rainfall began at 07:01:00 on 11th October 2012 as rain bands on the periphery of the storm reached the island. Five millimetres of rainfall was recorded by the SGH weather station on 11th October, and 14 mm on 12th October. The maximum 10-minute rainfall of 2.8 mm occurred at 9:21:00 on 11th October and did not trigger a lahar that was seismically registered or observed. Images from the remote camera on 11th October show that valley bed surface was wet but surface flow had not occurred (Appendix 4.1b). By midday on 12th October some of the fine-grained drapage deposited on 9-10th October 2012 had been washed off the surface of the channel in the nearest the camera and water had started to pool in a low-lying section of the mid-channel bar (Appendix 4.1b). This suggested either the local water table had risen in response to rainfall or ponding was occurring above an area of low permeability. Before the onset of surface flow, there was a gradual increase in the coverage of the channel bed by surface water in response to ongoing rainfall. Rainfall between 18:01:00 and 20:05:00 UTC (5.6 mm, SGH weather station) initiated surface flow at 20:02:52 UTC lasting until 20:12:16 UTC; rainfall was observed at Site A to pond, spread and flow downstream. Images showed flow was clear with a relatively low sediment load, contained within narrow (<0.1 m), shallow (few cm) sub-channels within the south and middle channels (Appendix 4.1b). The SGH weather station did not register rainfall intensity $> 0.25 \text{ mm min}^{-1}$ during this time, however the station was 3.6 km from the monitored channel section and periods of intense rainfall were recorded in camera images. Surface runoff in the channel was probably generated by a combination of highly localised intense rainfall (over a short period of time, minutes) at the camera site and runoff from the upper catchment.

Video captured at 20:48:00 UTC downstream at Site C (Figure 4.7c; Appendix 4.1f) showed that surface flow had occurred in a ~0.3 m wide channel in the foreground (south side of the valley). Pondered water occupied 0.5 m of a 1.8 m deep trench in the background of the image; associated with rising water table because of both rainfall and storm surge (pressure driven sea level rise). Both the surface flow and water in the trench were light brown, suggesting it contained a lot of fine sediment. The flow was different from upstream because of the greater sediment load. Surface flow at Site A was short-lived (<15 minutes) compared with downstream observations that showed





(c)



(d)

Figure 4.7 (a) Looking upstream 4 km from SHV. The bed surface in the image was deposited by lahars. (b) Looking cross-valley from north to south in the area of commercial sand extraction, 5.7 km from SHV. The photograph shows pits and boulder piles, as well as a network of temporary roads linking pits to the permanent road network. (c) Image still from video at Site C (Tina’s House) at 20:48:00 UTC 12/10/2012. (d) Looking upstream from the same location as (b) at 16:10:00 UTC 13/10/2012 before the arrival of the first lahar front from the SHV sub-basin.

prolonged sub-channel occupation (observations at 22:10 show flow was still present in the channel). Water and sediment in flow observed at Site C may have been from the main channel, valley side runoff or from the Sappit River. Fine sediment in suspension was probably derived by erosion of lahar deposits from September and October 2012 (see photographs Appendix 3.4a), particularly from ‘traps’ of surficial fines deposited in the area of valley mined for aggregate (Figure 2.14 and 2.18). Prior to rainfall on 11th October the base of the trench (Figure 4.7c) was coated in a thick layer of fines; elutriation by ground water rise and erosion by through-flow entering the trench from the upstream cut-face are thought to have entrained fines in trench water.

Sporadic rainfall was registered by the SGH weather station between 01:27:00 UTC and 13:52:00 UTC on 13th October, equating to 3.8 mm, and rainfall became near-continuous from 14:34:00 UTC (Figure 4.5a). The first flow front arrived at Site A at 16:13:53 UTC in the north-side channel (Appendix 4.1c) travelling at 1.8 m s^{-1} . Before this, the valley was occupied by very narrow (<10 cm) flows that entrained fine sediment (change in water colour from clear to light brown) when the flow passed over older fine-grained surface drapes. Downstream at Site B1 at 16:10:00 UTC flow was already established in a 1-2 m wide single channel on the north side of the valley (Figure 4.7d). The channel meandered through the section of valley modified by aggregate mining, constrained by spoil heaps. Upstream of Site B1 flow remained in a single channel on the north side of the valley. The suspended sediment concentration measured at 16:16:00 UTC at Site B1 was 5.25 g l^{-1} , composed of 28.3% very fine-fine sand, 57.4% silts and 14.3% clay-sized particles (Appendix 4.1g).

The arrival of the flow front observed at Site A, at the Sappit River confluence and the merging of the two flows increased the volume of the lahar. Assuming that the velocity of the flow did not alter by more than $2\text{-}3 \text{ m s}^{-1}$, water and/or sediment from the flow front had not arrived at Site B1 by 16:16:00 UTC, therefore the first suspended sediment sample did not contain sediments from the SHV sub-basin. The velocity of flow at Site C at 16:21 UTC 13/10/2012 was 2.9 m s^{-1} (Appendix 4.1f). A second sample at Site B1 at 16:56 UTC showed suspended sediment had increased to 106.5 g l^{-1} , composed of 9% very fine sand, 78.3% silts and 12.2% clay-sized particles. If average flow velocity between Site A and Site C was 3 m s^{-1} , it was estimated the flow front (after merging with flow from the Sappit River) would take ~11 minutes to reach Site C, arriving at ~16:30 UTC. The second flow sample showed that changes to the flow by the arrival of the lahar from the SHV sub-basin increased suspended load with contributions from the upper Belham Catchment and sediment mobilised from the valley-floor. Of the seven samples collected during the October lahar, the second contained the highest concentrations of sediment. The lahar persisted for over 29 hours following the passage of the first flow front at 16:13:53 UTC on 13/10/12.

4.4.1.1 Discussion

As the front of the flow travels downstream, it will lose water by infiltration, but gain it by flow into the front from the trailing flow. The trailing flow is generally faster than the flow front as was observed during the October 2012 lahar (Section 4.4.1 and Section 4.4.2) and as was observed during other smaller events in the Belham River

Valley. The flow front, whether or not it is a wetting front, tends to entrain material (both denser and less dense than water) and may become sediment charged. The changing sediment load (both type and quantity) will lead to changes in bulk viscosity and thus flow behaviour.

Propagation of the flow front on 2/10/2012 was filmed by handheld camera at Site B1 (Appendix 3.4d). The flow front behaved as a debris-flow surge (Iverson, 2005). The head of the flow was steep, non-turbulent and recirculation was observed; individual coarse-sand sized grains were identified in circulation at the surface of the flow, indicative of particle size segregation (Pierson, 1986). The flow front rapidly spread laterally to fill local depressions on the bed surface; flow was confined within relict sub-channels from previous event(s) or on temporary roadways in the aggregate mining section of valley, but behaved as an unconfined flow because of the relatively large channel widths. Flow behind the head, where the flow front was <1 cm stream length had a very different character. Turbulent eddies were visible on the flow surface, and water was travelling at over twice the speed of the flow front (0.06 m s^{-1}), driving the front like a moving dam and causing localised surges. Granular-sized material was seen in bedload but grains of this size were not suspended.

As the flow expanded downstream and laterally, the flow front took the form of fingers; lateral instabilities generated by particle segregation. This form was temporary and rapidly changing. However, observations of fines draped on the bed surface derived from the flow front, suggested that flow was creating a stable bed surface. Recently, Kokelaar *et al.* (2014) proposed a mechanism for the generation of fines-lined leveed channels during granular flow run-out. Using physical experiments they showed that slow moving flows with segregated fronts, composed of a fine-grained fraction less resistant to flow than coarser-grained fractions, could self-organise to ensure a fines-rich basal flow, which shears over the substrate; lining the conduit with fines. In fines-rich flows water may become dynamically over-pressured because the small size of particles reduces flow permeability (Iverson, 1997). Heightened fluid pressure reduces the shear strength of the flow, permitting it to flow freely on low slopes. This mechanism may be appropriate to sediment-charged fines rich flow fronts in the Belham River Valley.

Recognition that the flow front of the 2/10/2012 lahar lined the bed surface with fines is important for two reasons. (1) It showed that the flow front not only stabilised the bed surface but also reduced frictional energy loss to the bed by reducing surface roughness. Furthermore, the persistence of fines due to fluid over-pressure during

180

steady shearing flow lowered the permeability of the bed surface, reducing infiltration and increasing lahar volume and run out. (2) Drapes of fine sediment were typically interpreted as waning flow origin, both as exposed alluvial bed surface deposit and in the sedimentary record. Under the mechanism proposed by Kokelaar *et al.* (2014) and observed during the 2/10/2012 lahar, drapes of fines derive from depositional processes at the flow front. Drapes of fines, including terminal lobes, were preserved on the bed surface after multiple small flows between 2011 and 2013. Fines drapes were not preserved following the 13th- 14th October 2012 lahar.

4.4.2. Rapidly varying unsteady flow during 13th-14th October 2012 interpreted from monitoring data

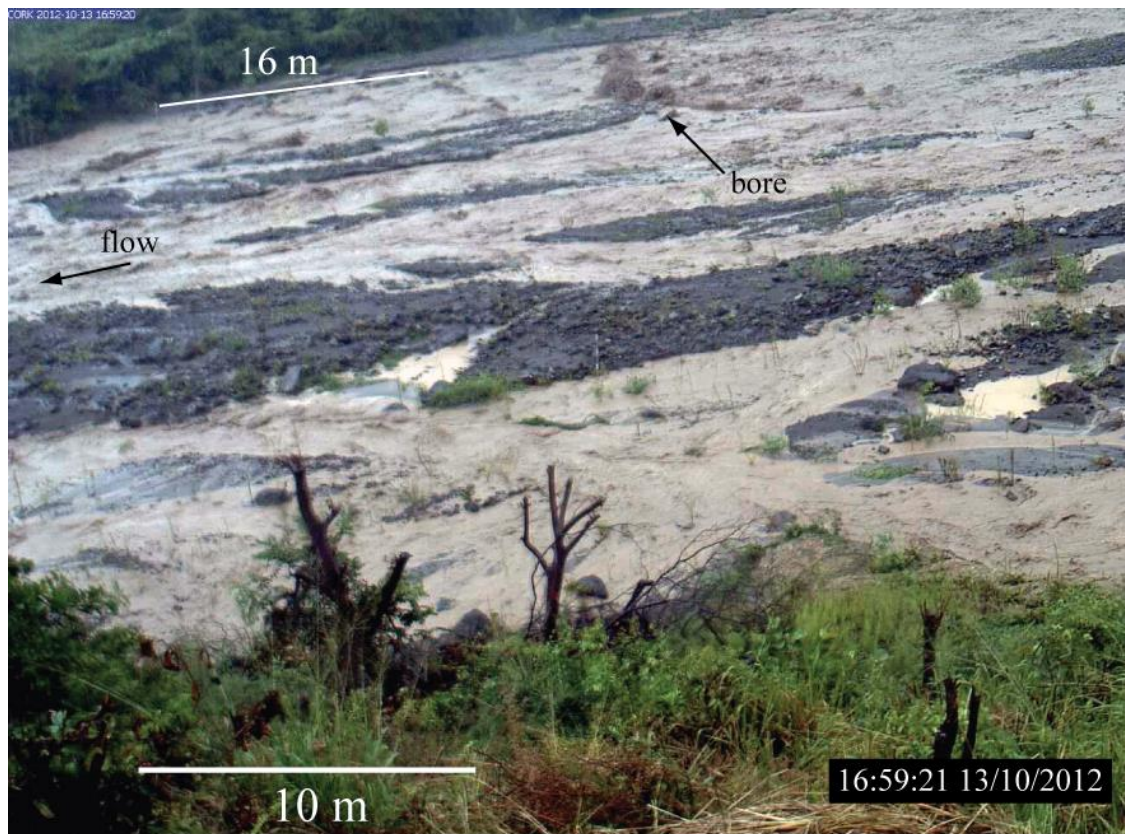
The lahar was very unsteady, turbulent and sediment-laden, changing character downstream. The number of sub-channels, their depth and boundary characteristics altered throughout the event, causing changes to flow behaviour and sediment transport. Between 3 and 75% of the total valley-floor width was occupied by flow during the lahar. Based on pre- and post-event bed surface topography it was estimated that flow depth was no greater than 0.5 m at Site A, however traversing active sub-channels by foot downstream of Site C on 13/10/2012, suggested that at this point in the valley, preserved bed surface topography underestimated the true depth of flow by ~60%; an observation that may be relevant elsewhere in the valley. Three hundred and forty-nine turbulent surges (bores) were recorded during the lahar, and stationary and upstream migrating trains of water-surface-waves were a pervasive feature of the flow at Site A, B1, B2 and C. Figure 4.5 summarised data collected during the two-day lahar event.

Peaks in seismicity (Figure 4.5b) lagged peaks in rainfall intensity (Figure 4.5a); the lag ranged from 1 to 28 minutes (± 7.5 minutes, due to the temporal sampling resolution of the rainfall dataset). Elevated seismicity corresponds to increased turbulence, flow volume or sediment load (Doyle *et al.*, 2011). Peaks in rainfall were not always followed by a peak in seismicity, and peaks in seismicity did not always correlate between stations. Seven seismic peaks were registered at MBLY and MBGH (Figure 4.1), where MBGH lagged behind MBLY by 1 to 7 minutes. Decomposed, these peaks in seismicity corresponded to a strong signal between 1 and 30 Hz (see spectrograms Appendix 4.2). Background noise was registered between 0.2- 0.5 Hz and this was elevated during the lahar. Elevated signals between 2 and 5 Hz were also observed on the spectrograms during this time. Only five seismic peaks were registered

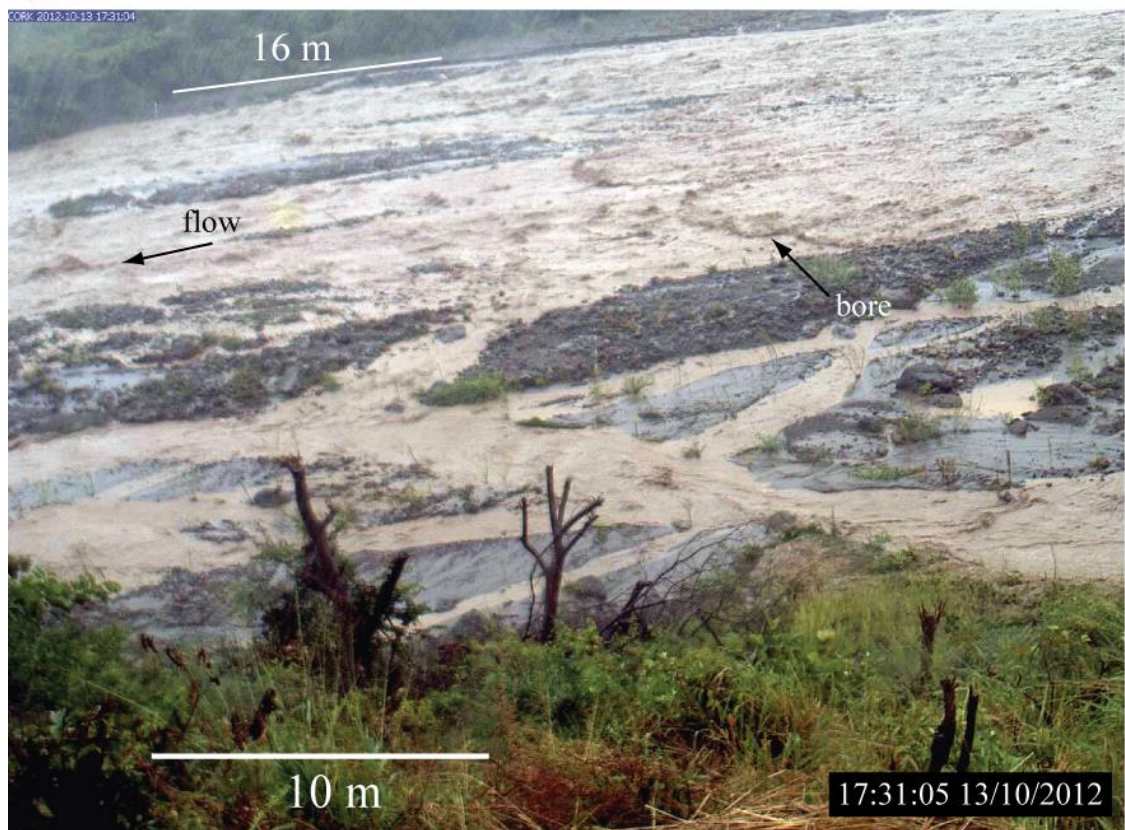
on the MBGB station and of these only three were associated with peaks registered upstream at MBGH and MBLY. The lag between peaks at MBGH and MBGB, ranged from 33 to 56 minutes, equating to travel speeds of 0.8 m s^{-1} to 1.4 m s^{-1} (over a distance of $\sim 2.8 \text{ km}$). One seismic peak was registered at MBGB at 14:25:59 UTC 13/10/12 before flow was observed at Site A, suggesting that discharge from the Sappit River and valley-side runoff was able to transport sediment load to be registered seismically. The second seismic peak registered at MBGB was after peaks registered at MBGH and MBLY, however it was unlikely to relate to flow propagation from the SHV sub-catchment. While the second seismic peak registered at MBGB ahead of peaks in seismicity registered by MBGH and MBLY, represented the propagation of flow from the SHV sub-catchment, reaching Site A at 16:13:00 UTC travelling at $\sim 2 \text{ m s}^{-1}$, and therefore MBGB at $\sim 16:30:00 \text{ UTC}$. The spectrogram of the MBGB signal (Appendix 4.2) was much noisier in the lower frequencies ($<1 \text{ Hz}$) than the MBGH and MBLY because of the proximity to the coast and the heightened sea conditions. Lahar occurrence was captured by an elevated 2-5 Hz signal and peaks between 1-30 Hz, however these were less discernible at MBGB compared with MBGH and MBLY. Comparison of the time lags between MBLY to MBGH and MBGH to MBGB suggested that the seismically registered packets of the lahar were decelerating as they travelled downstream; the first peak registered by MBLY decelerated from 9.4 m s^{-1} to 1.4 m s^{-1} , while the second peak registered by MBLY decelerated from 2.7 m s^{-1} to 0.8 m s^{-1} . Critically, the timing of peaks in seismicity at MBGB correlated with increased apparent turbulence and bore frequency at Site A (allowing for downstream propagation time); there was less correlation between peaks in seismicity at MBLY and MBGH and the timing of observations at Site A, however this may be because of the increased distance of 2.8 km compared with 1.5 km between the seismometer and camera site.

4.4.2.1. Bores

Channel-wide bores propagating downstream with a distinct breaking front were observed at irregular intervals, 6 to 6002 seconds, from 16:46:23 UTC 13/10/2012 to 21:25:12 UTC 14/10/2012 (Figure 4.5c). White water in the vicinity of the wave front suggested that turbulent eddies were present, and change to this appearance between bores and across the channel suggested that turbulence varied (Figure 4.8). The bores travelled at an average velocity of $\sim 6 \text{ m s}^{-1}$ and induced temporary increases in depth of



(a)



(b)

Figure 4.8 Image stills from the camera at Site A. (a) Bore travelling downstream during the first peak in flow. (b) Bore travelling downstream during the second peak in flow.

flow of up to half a metre; during waxing flow bores gradually increased flow stage, however during waning conditions depth change was associated with the front and did not increase flow stage. Bores initiated boulder motion, propelling boulders (up to 0.4 m long axis) along the bed by rolling and bouncing for tens of metres depending on the magnitude of the bore (see Appendix 4.1c: 16:51:44 to 16:53:15). Boulders did not necessarily travel in the flow front, in many cases the impact of the bore arrival was observed on the boulder, initiating slow downstream boulder rotation that accelerated as the bore passed (see Appendix 4.1c: 17:03:00 to 17:03:37 13/10/12). Larger boulders were progressively rolled downstream by this process (coming to rest between bores), and were partially exposed in the flow indicating local flow depth was less than the boulder diameter; up to 0.4 m. Bore arrival increased flow depth and modified channel boundaries by mobilising boulders that were on the edges of unit bars (Figure 4.6b). Between 16:45:00 to 17:00:00 UTC 13/10/2012 occupied valley floor width at Site A increased from 18 to 60 % (Figure 4.5c) in response to twenty-eight bores and increases in discharge. Flow occupied over 48% of the valley floor width between 17:00:00 to 19:00:00 UTC 13/10/2012 during which time bores occurred on average every 40 seconds. A reduction in occupied valley width, to 32% by 19:30:00 UTC correlated with an absence of bores between 19:01:05 to 19:40:46 UTC.

Figure 4.9a and 4.9c show that vegetation was stripped from areas of the bed inundated by flow. Approximately 0.1 m of vertical erosion occurred in area *A* on Figure 4.9a to form a narrow sub-channel, exposing a 0.56 m boulder that remained in position for the duration of the lahar. Immediately upstream of this boulder in the sub-channel, erosion preferentially removed finer material from a pre-event unit bar, leaving a gravelly bed surface. The boundaries of the channel in the foreground (*B*) in Figure 4.9a changed with the deposition of a central gravel bar cross-cutting the pre-event channel; vegetation at the edge of the bar was partially buried suggesting deposition rather than erosion in this instance

Re-occupation of the valley by flow occurred gradually between 19:30:00 to 20:11:00 UTC in the absence of significant bore activity (i.e. the stage went up). Flow was confined within a straight channel on the north side of the valley (58 m wide, *C* Figure 4.9a) and initially there was vertical (until 20:05:00 UTC) then lateral erosion of the bed. Lateral erosion accelerated with the onset of a period of more vigorous (both in frequency and size) bore activity from 20:11:00 UTC 13/10/2012; bores occurred on average every 2.5 minutes. Onset of this period was registered upstream by MBGH and

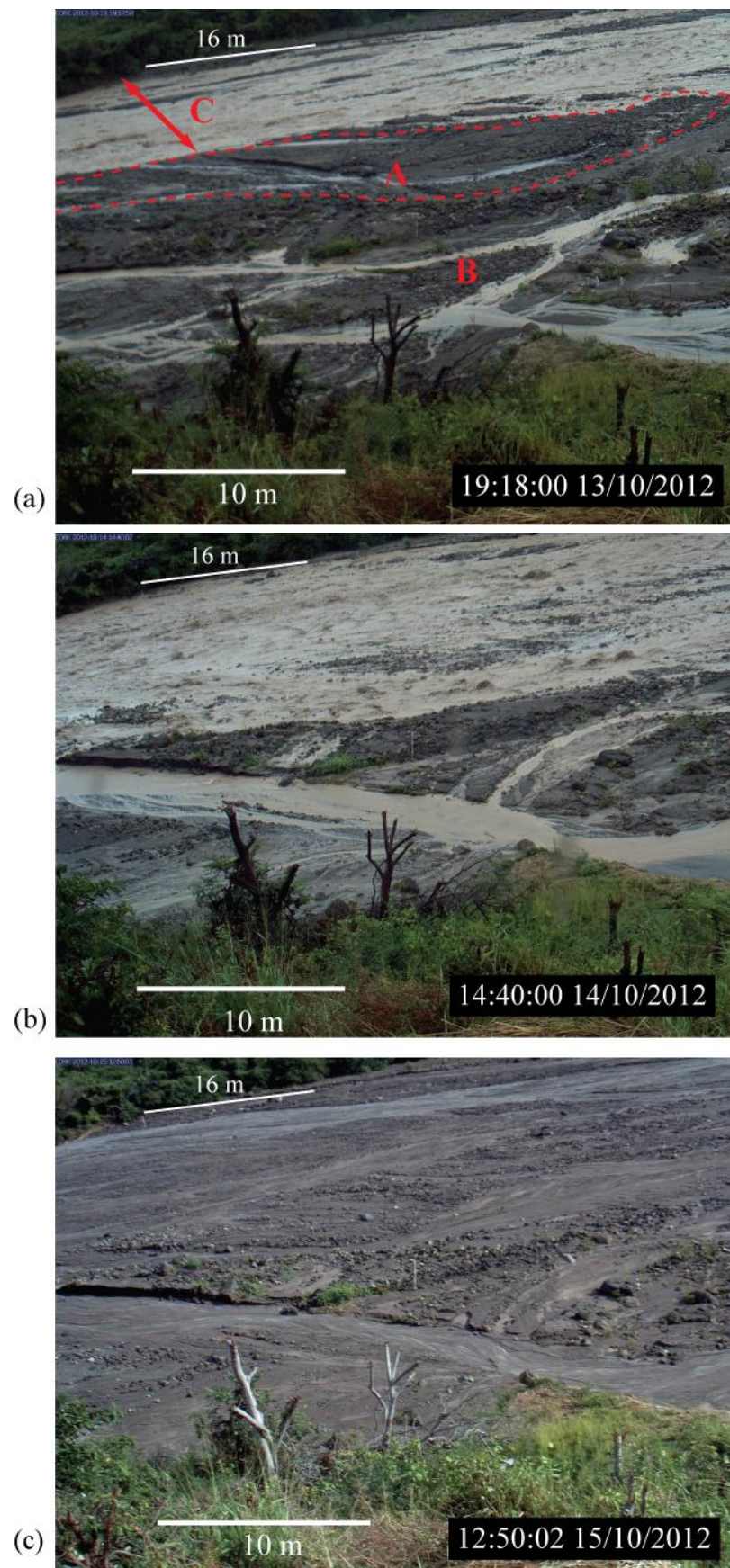


Figure 4.9 (a) Waning flow of second seismic peak. (b) Flow during the second peak on 14/10/2012. (c) Bed surface after the 13th-14th October lahar.

MBLY, but not downstream at MBGB. The travel speed between MBLY and MBGH was estimated at 2 m s^{-1} , however the velocity of the bore fronts at Site A was up to 7.5 m s^{-1} (at 20:16:52 UTC), suggesting that the bores may have accelerated as they propagated downstream, but dissipated before reaching the lower Belham.

Resumption of recording at Site A (Figure 4.9b) showed that the lahar occupied 75% of the total valley width (the largest coverage during the event) and that flow had incised and widened the channel in the foreground of the image (south side of valley), having overtopped the gravel bar at 19:40:00 UTC the previous day. Seventy centimetres of channel incision was observed downstream at Site B1. Two seismic peaks were registered overnight at MBLY and MBGH; MBGB registered the first peak, 50 minutes after registration at MBGH. The intensity of signal registered in the 2 to 5 Hz range gradually decreased from 01:00:00 UTC to 11:45:00 UTC on 14/10/2012 (Appendix 4.2), and it is likely that the flow stage decreased during this period. Radar images show that Montserrat received relatively little rainfall overnight, with rain bands focused over Guadeloupe. Rainfall resumed and peaked at 11:59:00 and 13:44:00 UTC on 14/10/2012 (± 7.5 minutes), correlating with peaks in seismicity at MBLY and MBGH at 11:51:17 and 13:49:40 UTC, and 11:55:31 and 13:53:14 UTC, respectively. Image coverage at Site A did not capture the arrival of either of these flow peaks (predicted to have reached Site A ~ 15 minutes after registration at MBGH), however imagery from 14:31:00 to 15:44:00 UTC showed a series of bores occurring on average every 59 seconds. The visual appearance of the bores implies that their turbulence decreased as their velocity decreased (3.75 m s^{-1} at 14:42:00 to 3 m s^{-1} at 15:20:00 UTC) and the flow occupied less of the valley. The size and number of boulders set in motion by the bores also decreased. The last bore was registered at 21:25:12 UTC 14/10/2012.

Discussion

The bores were striking features of the lahar, and were thought to play a key role in sediment transport and reshaping bed morphology. Bores are hydraulic jumps in translation, representing a hydrodynamic shock wave (Lighthill, 1978) involving a sudden increase in pressure, depth and flow velocity. The shape of the *positive surge* is closely linked with its Froude number F_s , for downstream propagating surges this is defined by

$$F_s = \left(\frac{(V_w - U_1)}{(gh_1)} \right)^{\frac{1}{2}} \quad \text{Equation 4.1}$$

where V_w is the surge celerity, U_1 is the initial flow velocity, g is the gravity acceleration and h_1 is the initial flow depth (Henderson 1966; Lieggett, 1994; Chanson 2013). Selecting two bores of differing frontal character (both breaking but one more vigorously than the other; Figure 4.8), the bore F_s was estimated using calculations of flow velocity derived from water-surface-wave measurements (see Sections 2.3.3 and 4.4.2.2). The more vigorous bore travelled at 6.4 m s^{-1} , initial flow velocity was $3.5 \text{ m s}^{-1} \pm 0.19 \text{ m s}^{-1}$; $F_s = 1.47$. Experiments have shown that for $F_s > 1.4$ the bore front was breaking, turbulent and with a marked roller (Khezri and Chanson, 2012a). Accounting for the propagation of error in the calculation, $1.23 \leq F_s \leq 1.81$. F_s estimates were most sensitive to depth variation. Calculation of mean water depth (h_m) using the water-surface-wave length (λ) and Equation 4.2 (Kennedy, 1960) suggested that flow depths estimated from bed surface topography miscalculated flow depth by -1.1 m to 0.26 m (Section 4.4.2.2).

$$\lambda = 2\pi h_m \quad \text{Equation 4.2}$$

Critically, the application of the equation here was not without its own problems, but considering the lower bounds of the depth error in the equation, increases the value of F_s to 1.69. Chanson *et al.*, (2012) showed that the size and strength of the bore increased with increasing Froude number. Comparatively, the less vigorous bore front travelled at 4 m s^{-1} , initial flow velocity was $2.45 \text{ m s}^{-1} \pm 0.15 \text{ m s}^{-1}$; $F_s = 1.11$. Flume experiments on mobile beds suggested that bores were undular when $F_s < 1.3$ (Khezri and Chanson 2012c). While this bore front did not appear as turbulent as the first discussed, it still showed some turbulence. Consideration of depth calculated from water-surface-wave lengths (Equation 4.2) suggested flow depth ranged between 0.14 - 0.17 m rather than 0.2 m (used in the F_s calculation); note that three wave trains were measured in this section of the valley at this time. Recalculating F_s with this value increased it up to 1.32. The difference in initial depth across the channel, suggested that the bore front (which occupied the entire channel width) may vary in form across the channel, so that some sections of the front were more turbulent than others. This has not been described in experiments on *positive surges*. Typically experimental set-up maintains a uniform bed surface, and bores propagate with a consistent form across the front (with some boundary effects from the flume tank edge); bed topography was not varied across the flume width, as is the situation in natural channels.

The propagation of bores play a major role in the initiation of sediment motion in other environments (Jiyu *et al.*, 1990; Chanson, 2011), and experiments by Khezri and Chanson (2012c) showed that turbulent breaking bores set a large number of particles into motion, compared with undular bores for which sediment motion was negligible. The bores during the 13-14th October 2012 lahar appeared most turbulent during rising and peak flow stages. Critically, Khezri and Chanson's (2012a-c) study considers tidal bores, where the bore is propagating upstream. The decrease of the longitudinal pressure gradient force (acting downstream) in response to the depth increase downstream induced by the bore, resulted in an adverse pressure force opposing fluid motion (and sediment transport) downstream. In combination with increased drag (shear) force the change in pressure conditions drove the onset of sediment motion upstream (Khezri and Chanson 2012a). Reversal of the initial flow direction, as was the case for the Belham bores, attributes the initiation of sediment motion during the propagation of the surge front to drag and higher pressure gradient force, facilitating sudden increases in sediment load (Figure 4.10).

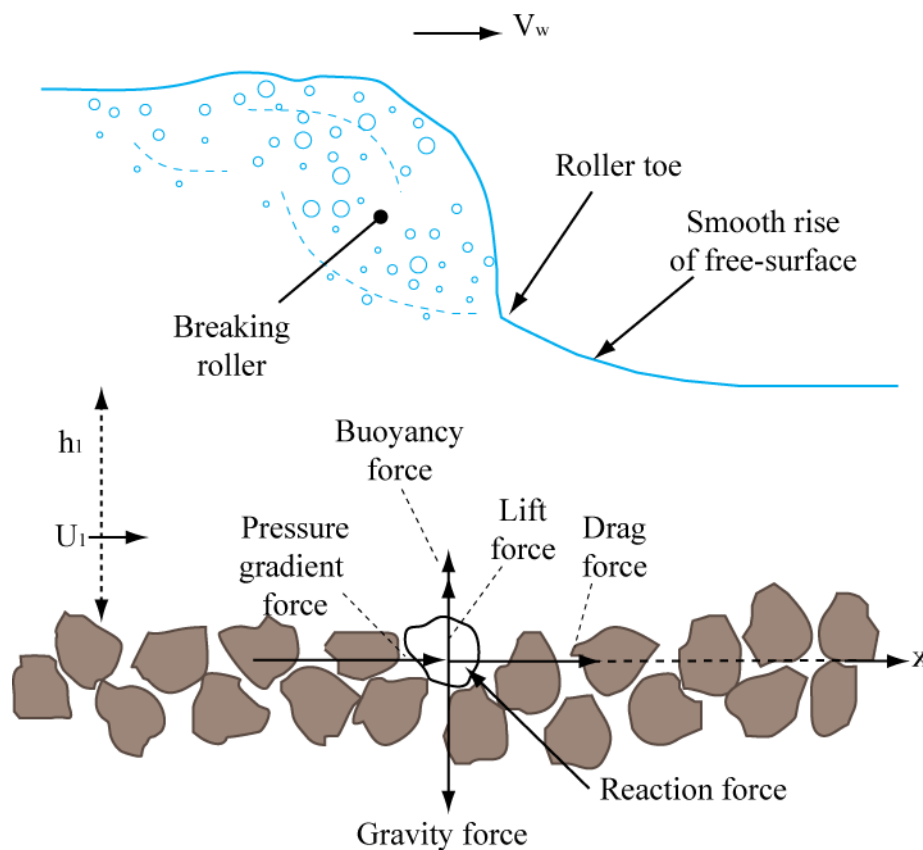


Figure 4.10 Sketch of the main forces acting on a particle beneath a bore adapted from Khezir and Chanson (2012b).

Positive surges (aka bores) during lahars have been observed before at Semeru (Doyle *et al.*, 2010; Doyle *et al.*, 2011) and Pinatubo (Hayes *et al.*, 2002; Gran and Montgomery 2005). Doyle *et al.* (2010; 2011) attributed these ‘packets’ to differential arrival times of flow from spatially and temporally distributed lahar sources. Observations by Hayes *et al.* (2002) attributed the bores to the release of water stored in water-surface-wave trains when they break upstream, then undergo flow reversal to propagate as a hydraulic bore downstream (Grant, 1997). However, Gran and Montgomery (2005) specifically identified the bores as roll waves, but do not discuss their formation. Doyle *et al.* (2010; 2011) discounted the possibility that surges observed at Semeru were roll waves, because the ‘packets’ were not observed as frequently as is expected with this phenomenon (≤ 100 s), and low channel slope ($\sim 3^\circ$) with subcritical flow did not favour roll wave formation. The frequency and return-period (ranging between 6 and 6000 seconds) of bores observed between 13th-14th October 2012 in the Belham River Valley does not discount the roll wave phenomenon. Bore generation by the arrival of peak flow from tributaries and valley-slope runoff is possible but seems unlikely to explain alone, periods of flow during which bores re-occurred every few seconds. Furthermore, the depth change and cross-channel coverage of the bores relative to the occurrence of water-surface-wave trains and their size (Section 4.4.2.2) does not correlate with the notion that the bores were being generated solely by the destabilisation of wave trains. There was a clear interaction between the bores and wave trains (Section 4.4.2.2), and wave breaking immediately prior to the bore passage was expected to enhance it by bulking water-sediment volume (discussed in Section 4.4.2.2.1). Theoretically, en-masse breaking of wave trains progressively downstream cannot be disproved as a mechanism for generating and propagating a series of bores, but it was also possible that flow was inherently unstable during certain periods of the lahar, resulting in the formation of roll waves.

Roll waves form from small perturbations, generated by flow variability, evolving by expanding to form large shock-like waves (Huang, 2013). The formation of roll-waves depends on the interaction between flow and the rough boundary wall; analytically if channel resistance is zero, the size of water-surface-waves will approach zero (Dressler, 1949). Conversely Rouse (1938) highlighted that roll waves do not form if the channel bed is too irregular, because resistance to flow prevents the formation of perturbations. Roll waves occur when the relative kinematic wave celerity is greater than the relative dynamic wave celerity; such that transport of mass in the kinematic wave (waves in which a balance is struck between friction and gravitational forces)

travels faster than transport of energy in the dynamic wave (governed by inertial and pressure forces). Models describing the behaviour of these waves were derived by Saint-Venant to describe gradually varied unsteady flows (Saint Venant, 1971). The ratio of the celerity of the dynamic wave to the mean velocity U and relative celerity of the kinematic wave is described by the Vedernikov number, Ve (Vedernikov 1945; 1946). This criterion is used to identify unstable flow and states that roll waves will form when $Ve \geq 1$. Defined by Equation 4.3,

$$Ve = m \left(1 - R \frac{dP}{dA} \right) Fr \quad \text{Equation 4.3}$$

where R is the hydraulic radius, P the wetted perimeter, Fr the Froude number, A the cross-sectional area and m is defined from the Manning's or Chezy's equations of mean flow velocity (Chow, 1959); whereby $m = 2/3$ when Manning's is used and $m = 1/2$ when Chezy's is used for turbulent flow. Substitution of measurements from Site A suggest that there are periods when $Ve \geq 1$ using the Manning's equation, indicating unstable flow conditions conducive to roll wave formation (Appendix 2.2y). These calculations were crude because they did not account for measurement error, relied on the value of m coefficient predetermined for turbulent water flow (turbulence was only apparent during the lahar not specifically measured and sediment concentration was not measured at the site) and did not consider formative conditions of the roll waves upstream, rather whether flow conditions at Site A were unstable.

Further research is required to observe lahar events upstream of Site A in order to better understand bore initiation. Fundamentally, bore occurrence was governed by principles of continuity and momentum, defined by the Saint Venant equations for unsteady flow. Momentum includes terms for friction and channel/flow geometry that vary in a downstream direction. The bores were not observed at Sites B1, B2 and C, located in an area of modified channel topography (from sand extraction). Here flow remained in man-made valley depressions that were narrower and deeper than channels at Site A; in addition depressions did not always join to form straight channels, instead increasing the channel sinuosity in the area of modified channel relative to upstream at Site A. The change to channel structure altered the width to depth ratio, altering the stability of flow.

4.4.2.2. Water-surface-waves and flow unsteadiness

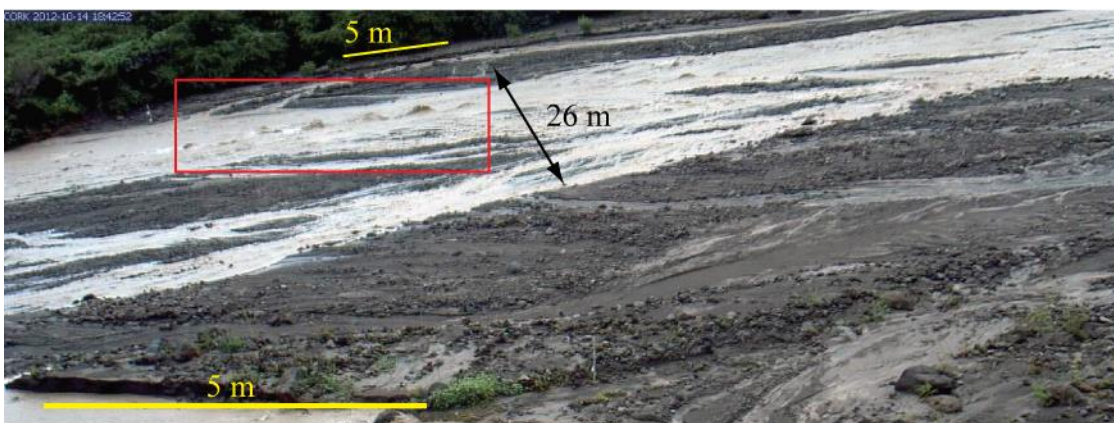
Trains of water-surface-waves were prevalent in flow at all observation sites (Figure 4.11). The wave trains remained stationary for periods of up to 6 minutes or migrated upstream, formed at multiple locations within flow, sometimes occupied the full sub-channel width or occurred discretely within a sub-channel. When a bore approached (within ~10 m) a wave train from upstream, often the waves appeared to destabilise and break altogether (en-masse) generating a localised short-lived upstream positive surge, that was engulfed by the bore travelling downstream. Waves reformed immediately after the surge in the same location. Boulders were observed to move short distances upstream in these surges, then back downstream as the bore passed (Figure 4.12). Waves within some trains that did not break during the passage of a bore temporarily reduced in height. In the absence of a bore, waves persisted for longer, growing and diminishing in height; waves within a train broke individually, sometimes triggering the breaking of adjacent waves. The characteristic ‘rooster tail’ wave form was observed in the foreground channel (*B*) in Figure 4.9a at Site A, and also at Site B1 and Site C (Figure 4.11a and Appendix 4.1d-f). This represents the inference pattern between two wave trains with differing crest orientations (Kennedy, 1960), indicating that the wave train has taken on a three-dimensional form (as opposed to two-dimensional). It was possible that wave trains in other channels at Site A also took this form but camera perspective made it difficult to identify this confidently.

Clusters of cobbles and small boulders were seen moving in periodic bursts within the shallowest parts of the channel; the material moved at variable rates depending on precise location in the channel and size. In imagery at Site A the boulders appeared to slide downstream, but observations at Site B1 (close-up, not limited by image resolution) showed large pebbles rolling downstream in <0.1 m deep flow (Appendix 4.1d). At Site A larger boulders rolled directly through trains of stationary and upstream migrating waves; in some cases the boulder rolled continuously through the waveforms and downstream, however in other cases boulder motion was halted within one of the waves and was then carried a short distance back upstream. The boulder (of smaller diameter than the wave amplitude) caught in the wave, wobbled within it, was sometimes tossed about, before being ejected either out the side of the wave or when the wave breaks. The boulder was then either flicked into a wave downstream in the train or was propelled downstream out of the train. Waves were

sometimes added to the train, formed in the immediate wake of the boulder's route downstream after ejection.



(a)



(b)

Figure 4.11 Example of wave trains observed at different sites in the Belham Valley during the October 2012 lahar. (a) Wave trains 12:57:00 UTC 14/10/2012, Site B1. The three waves upstream in the train appear three-dimensional in form and two are breaking. (b) 18:42:53 UTC 14/10/2012, Site A. Wave trains were observed to form, grow and diminish in height, increase in wave number and migrate upstream during waning flow from the final flow peak.

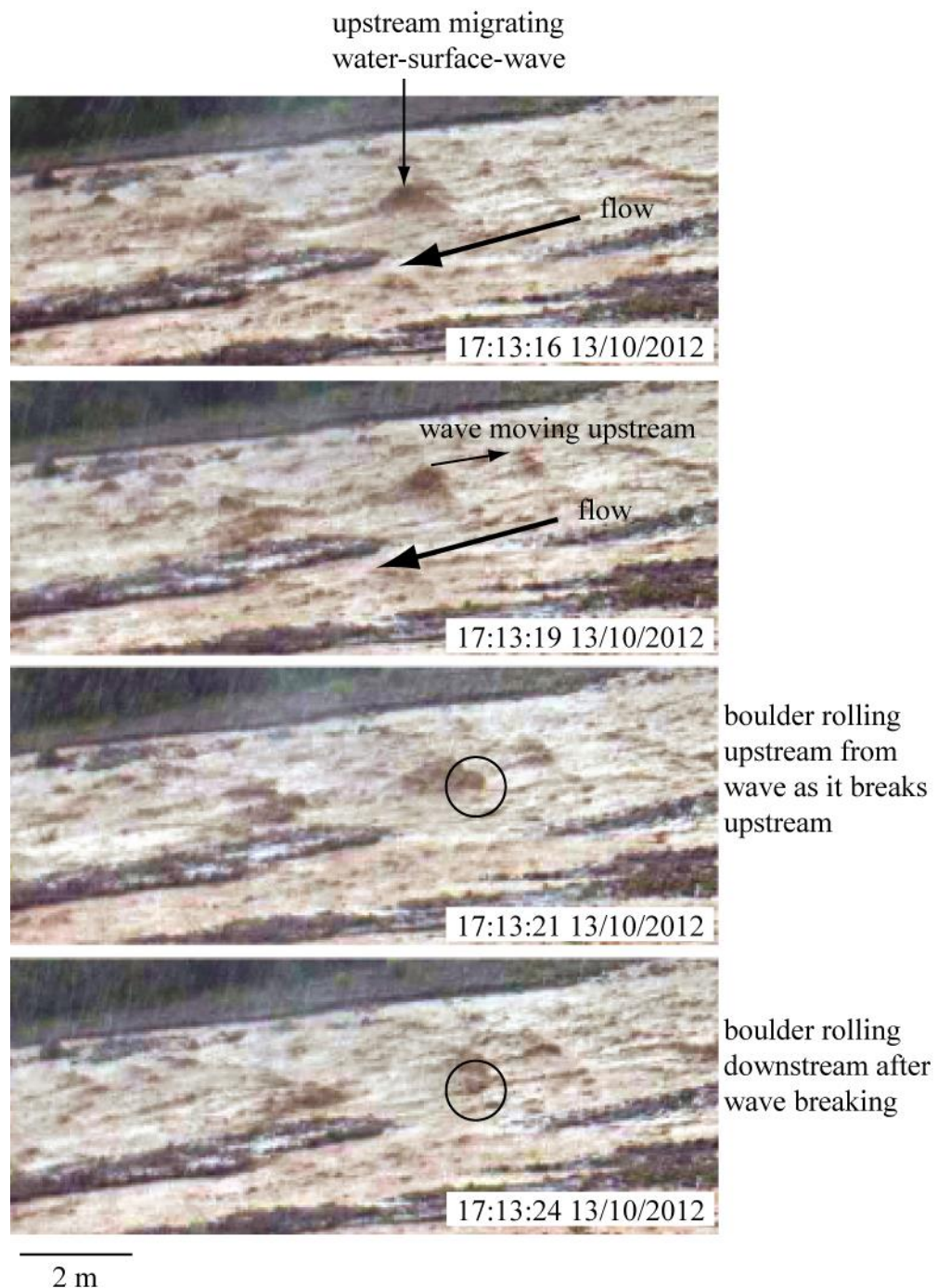


Figure 4.12 Sub-section of image stills (from Site A) between 17:13:16 13/10/2012 to 17:13:24 13/10/2012 showing the migration of part of a train of water-surface-waves upstream. The wave in the centre of the photograph contains a boulder which is ejected upstream from the wave as it breaks, before rolling downstream with flow after wave breaking.

Discussion: calculations of flow velocity from wavelength

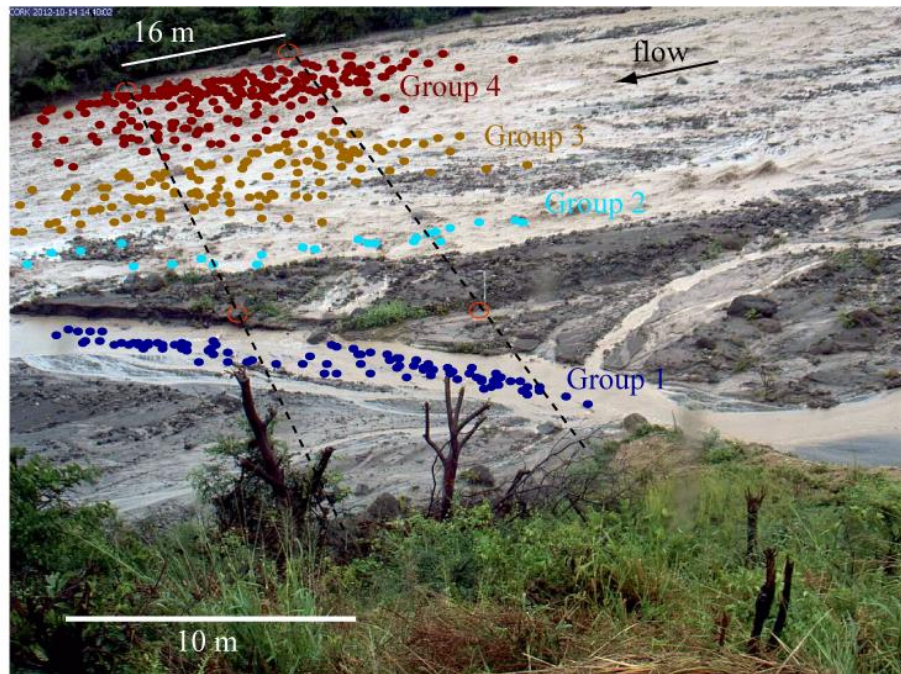
The coverage of channels by multiple wave trains that migrated upstream, changed form and broke, created a pulsating highly unsteady flow operating at a sub-scale to the passage of turbulent bore fronts. Wave trains form when inertial forces are

equal to or dominate over gravitational forces in flow; such that, the celerity of the wave is greater or equal to the mean velocity of flow. This relationship is defined by the Froude number (Fr), whereby water-surface-waves can move upstream when $Fr > 1$, and remain stationary when $Fr = 1$ (although stationary waves may form when $0.84 > Fr < 1$ if surface flow velocity is greater than mean flow velocity; Kennedy, 1963). Antidunes are bedforms that develop under water-surface-waves and are predominantly in-phase with them. Kennedy (1963) found that the wavelength λ of water-surface-waves (and antidunes) is related to the mean flow velocity v , Equation 4.4.

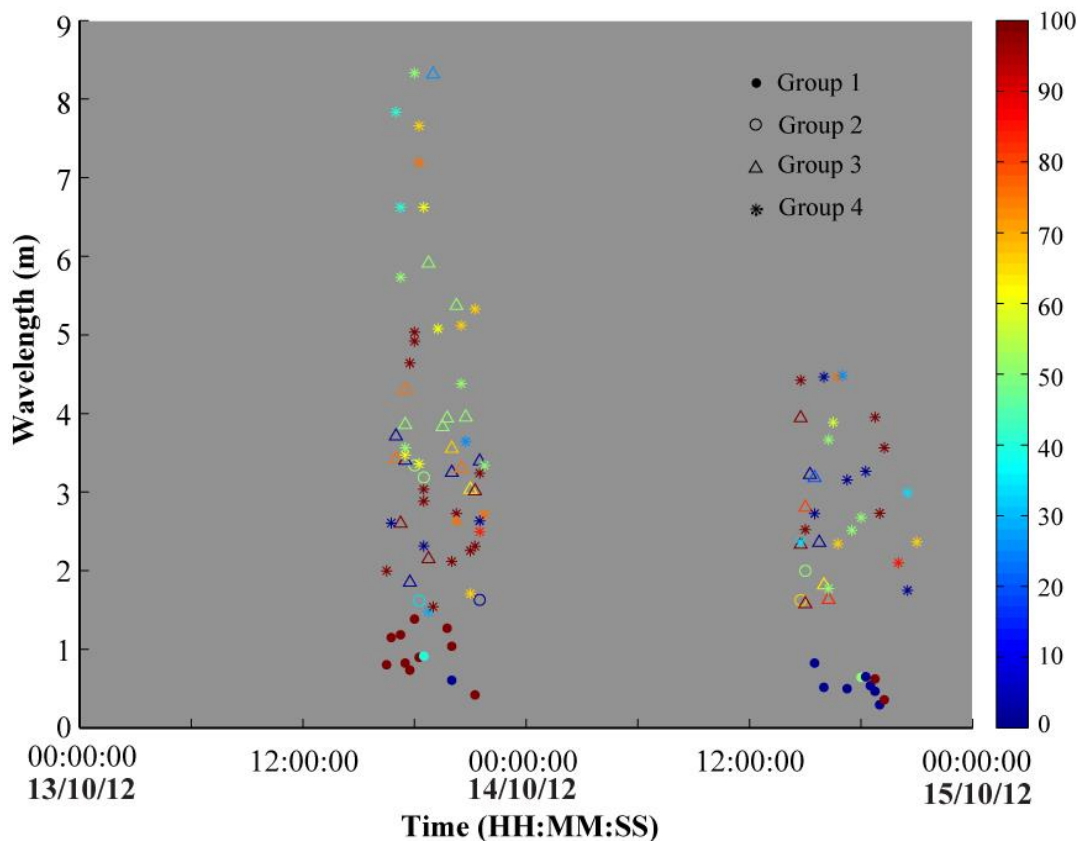
$$v = \sqrt{\frac{g\lambda}{2\pi}} \quad \text{Equation 4.4}$$

This equation was derived for two-dimensional antidunes; those which have continuous crest lines transverse to flow. The formative conditions for three-dimensional antidunes, which present with discontinuous crests or mound shapes (e.g. Carling and Breakspeare, 2006), are more specific because their occurrence depends on conditions lateral to the wave train (Robillard and Kennedy, 1967). The average wavelength within trains was measured from imagery recorded at Site A (see Section 2.3.3) and was used in Equation 4.4 to estimate v . Imagery was sampled every 15 minutes between 16:15:00 UTC 13/10/2012 and 22:00:00 UTC 14/10/2012, and where possible multiple wave trains were measured to capture flow conditions in different occupied sub-channels across the valley width. Figure 4.13a shows the sampling location of wave trains. Wave trains were measured at similar channel locations but specific wave trains could not be tracked through the entire sequence of images, because most individual wave trains did not persist for longer than 10 seconds.

Figure 4.13b shows measured wavelength by location, and the percentage of the wave train that was located within the area of well-constrained measurement error (Section 2.3.3). Wavelengths in the foreground channel (group 1, Figure 4.13 a) were smaller than those measured in the main channel (groups 2 to 4), ranging between 0.3 to $1.4 \text{ m} \pm 0.05 \text{ m}$ compared to 1.48 to $8.33 \text{ m} \pm 0.44 \text{ m}$. Sub-channel width in the foreground remained $< 2.2 \text{ m} \pm 0.2 \text{ m}$ and single wave trains occupied between 11 and 100% of the channel width. The main channel was occupied by 2 to 3 sub-channels that merged to form a large 58 m wide channel during peak discharge. When sub-channels were greater than 8 m wide, waves did not cover more than 30% of the channel width; although multiple wave trains occurred in different parts of the channel. Wave trains consisted of three to eleven waves and in 30% of cases the entire wave train was located



(a)



(b)

Figure 4.13 (a) Location of sampled waves within the camera field of view at Site A. Pixel measurements were converted to real-world coordinates based on the location of wave trains in group 1-4 and a scaling law derived from four known locations (red circles) in the image (see Section 2.3.3). The conversion was well-constrained for points between the two black dashed lines. (b) Average wavelength of water-surface-waves within sampled wave trains. The different symbols differentiate the location of the sampled data within the valley-floor. The colour of each point represents the percentage of the wave train within the area well-constrained by the scaling law.

within the area of well-constrained error (Figure 4.13 a). For the rest of the data set, one or more waves in the train were located outside this area, but peripheral to it. As discussed in Section 2.3.3, the location of measured objects in the camera field of view restricted the extension of error assessment across wider sections of the image. Measurement accuracy decreased with distance from the camera; wavelength error ranged from 0.05 m in group 1 waves to 0.8 m in group 4. Errors are shown on Figure 4.14a and are propagated into calculations of velocity (Equation 4.4; Figure 4.11 b).

The velocity in the foreground channel did not exceed $1.5 \text{ m s}^{-1} \pm 0.02 \text{ m s}^{-1}$, while in the main channel it peaked at $3.6 \text{ m s}^{-1} \pm 0.1 \text{ m s}^{-1}$ at 19:00:00 UTC 13/10/2012. Broadly the data showed that flow in the main channel accelerated from $1.77 \text{ m s}^{-1} \pm 0.4 \text{ m s}^{-1}$ at 16:30:00 UTC to $3.50 \text{ m s}^{-1} \pm 0.2 \text{ m s}^{-1}$ at 17:00:00 UTC on 13/10/2012 and trended towards gradual deceleration from 18:30:00 UTC on 13/10/2012 (although flow may have accelerated during the *no data* period). The velocity of floating objects (e.g. coconuts) carried by flow in the centre of the channel at Site B1 at ~12:00:00 UTC 14/10/2012 was between 2.7 and 3.9 m s^{-1} ; one of the objects was also recorded in flow at Site C, travelling at 2.37 m s^{-1} .

The velocity fluctuation was cyclic in the far (north) side of the valley (group 4) Figure 4.13, varying by ~0.5 to 1.5 m s^{-1} over periods of < 1 hour; some cyclicity was seen in other parts of the valley also. The variation in velocity correlated with shifting channel boundaries (recording discharge fluctuations) and with propagation of bores. The valley-wide peak velocity of $3.6 \text{ m s}^{-1} \pm 0.1 \text{ m s}^{-1}$ at 19:00:00 UTC 13/10/2012 corresponded to the temporary shift in the main streamline from the north side to the centre of the valley. Velocity increased in response to peak rainfall at 18:23:30 UTC 13/10/2012 (± 7.5 minutes) and decreases in channel roughness- reduced by the mobilisation of boulders during the passage of bore fronts. Velocities measured in the front channel (group 1) were steadier because the channel boundaries were constrained by a mid-channel bar that was not overtopped during the lahar. When multiple wave trains were sampled in the same time-stamped image, velocity was seen to vary by up to $2.05 \text{ m s}^{-1} \pm 0.5 \text{ m s}^{-1}$ across the valley; the mean cross-valley variation was $1.06 \text{ m s}^{-1} \pm 0.34 \text{ m s}^{-1}$ and the standard deviation was $0.43 \text{ m s}^{-1} \pm 0.35 \text{ m s}^{-1}$. In-channel variation of velocity, the instance when more than one wave train formed at the same time within the same channel, was up to $1.20 \text{ m s}^{-1} \pm 0.2 \text{ m s}^{-1}$ at 18:45:00 UTC 13/10/2012 in the centre section of valley (group 3).

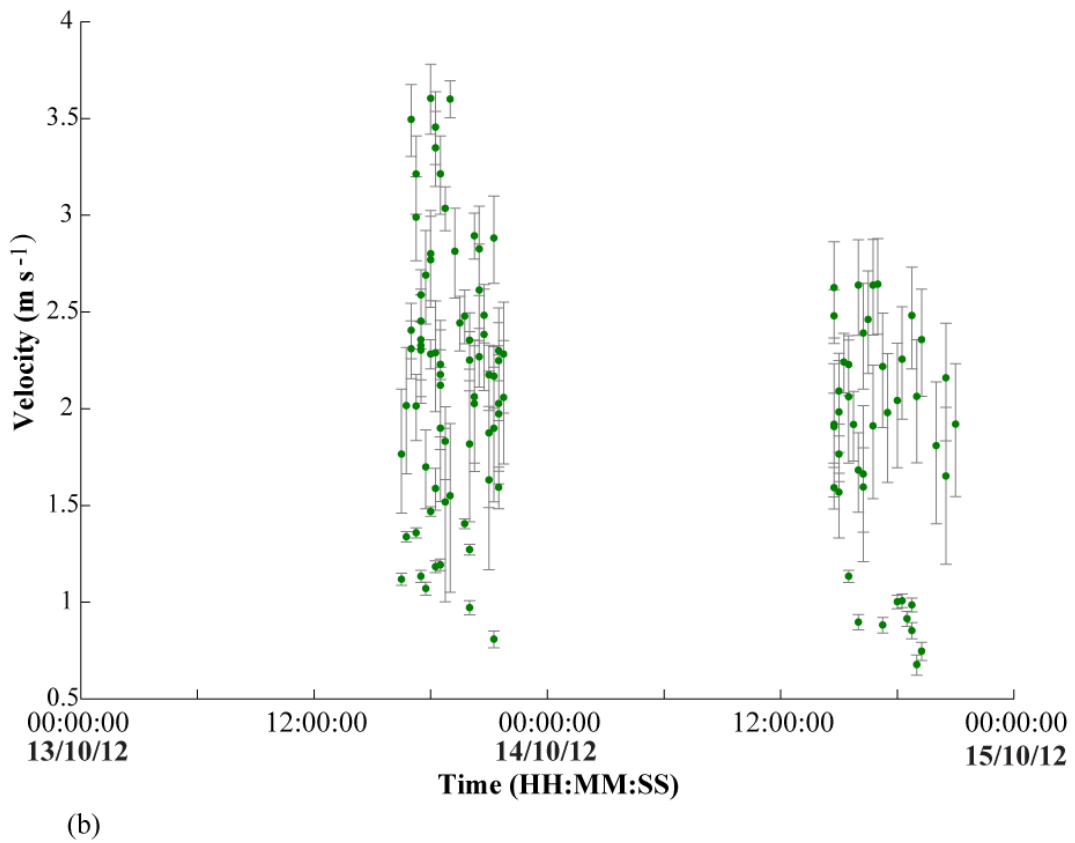
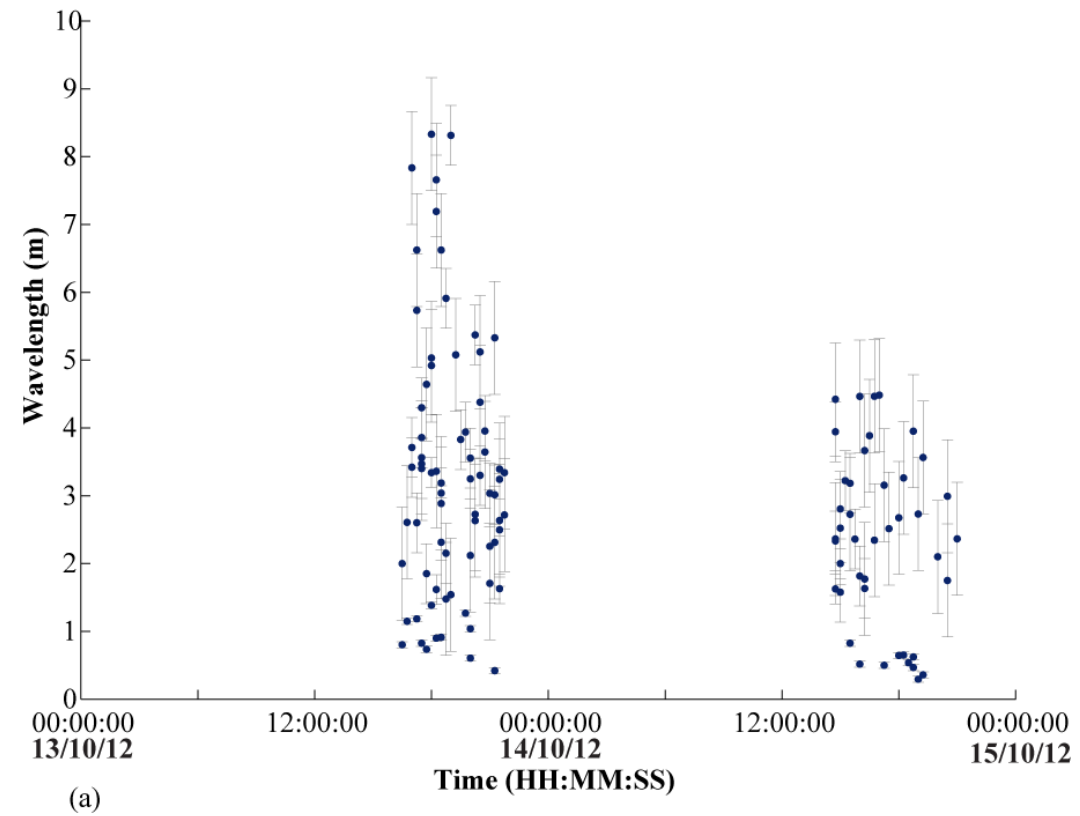


Figure 4.14 (a) The average wavelengths of water-surface-waves present in images analysed every 15 minutes. See also Figure 4.13. (b) Mean flow velocity calculated from wave train wavelengths using Equation 4.4.

Three-dimensional wave trains were observed in the flow at multiple sites. Application of Equation 4.5 (Kennedy, 1960) allows one to compare the velocity derivation dependant on wave-train form.

$$v = \sqrt{\frac{g\lambda}{2\pi}} \cdot \left[1 + \left(\frac{\lambda}{\lambda_t}\right)^2\right]^{\frac{1}{4}} \quad \text{Equation 4.5}$$

All wavelength measurements were included in the calculations because of uncertainty in identifying three-dimensional wave forms in the imagery; λ is the wavelength of the streamwise wave train and λ_t is the transverse wavelength of the waveform. Velocities calculated using Equation 4.5 ranged between $0.75 \text{ m s}^{-1} \pm 0.48 \text{ m s}^{-1}$ and $8.78 \text{ m s}^{-1} \pm 0.79 \text{ m s}^{-1}$ compared to $0.68 \pm 0.05 \text{ m s}^{-1}$ to $3.6 \pm 0.1 \text{ m s}^{-1}$. The difference in velocity calculated using Equations 4.4 and 4.5 ranged from 0.02 m s^{-1} to 5.29 m s^{-1} ; the relationship between the two-dimensional (x) and the three-dimensional estimate (y) may be modelled using a power-law $y = 1.2769x^{1.3163}$, $R^2 = 0.8227$, suggesting that velocity was underestimated if the two-dimensional equation was used on three-dimensional wave trains, and that the underestimation increased in magnitude with increasing wavelength. Yokokawa *et al.* (2010) showed in the flume that two-dimensional wave-trains formed three-dimensional wave trains, when waves resonated with those in a second wave train of a different orientation. Three-dimensional wave trains diminished when the difference in wavelength between waves interacting from each train, became too large; else the wave train persisted becoming steeper and breaking. Two dimensional wave trains formed after breaking; Yokokawa *et al.* (2010) found that two-dimensional and three-dimensional wave trains (and antidunes) formed alternately. Three-dimensional wave trains identified at Site B1 were breaking (Appendix 4.1d), but the waves did not catastrophically break, rather they shifted between an undular and breaking form over a period of minutes. This change in form was modulated by antidune growth underneath each wave in the train, whereby deposition occurred at the crest and erosion in the trough of the bedform (see Section 5.2). As the bedform grew the flow depth remained greater than the bedform height, such that the flow depth over the antidune crest was greater than that above the trough (Alexander *et al.*, 2001). The waves become over-steepened asymmetrically leading to breaking upstream. Breaking observed at Site B1 was not catastrophic suggesting that turbulence induced at the crest by wave over-steepening eroded material from the crest and deposited in the trough, readjusting the ratio of flow depth at the crest and trough of

the bedform. The critical height for breaking water-surface-waves is approximately 1.5λ (Bridge, 2003)

Discussion: calculations of discharge

Discharge was estimated from the average velocity calculated from two-dimensional wave trains in group 2 to 4 at each time step (Equation 4.4, Section 4.4.2.2), depths estimated from bed topography and channel width derived from percentage valley-floor coverage. Figure 4.15 shows that discharge ranged between $0.1 \text{ m}^3 \text{ s}^{-1} \pm 0.2 \text{ m}^3 \text{ s}^{-1}$ at 18:30 UTC on 14/10/2012 and $13.7 \text{ m}^3 \text{ s}^{-1} \pm 0.4 \text{ m}^3 \text{ s}^{-1}$ at 19:15 UTC 13/10/2012, the largest variance in discharge over the 15 minute sampling interval was $8.9 \text{ m}^3 \text{ s}^{-1}$ indicating a sudden drop in flow.

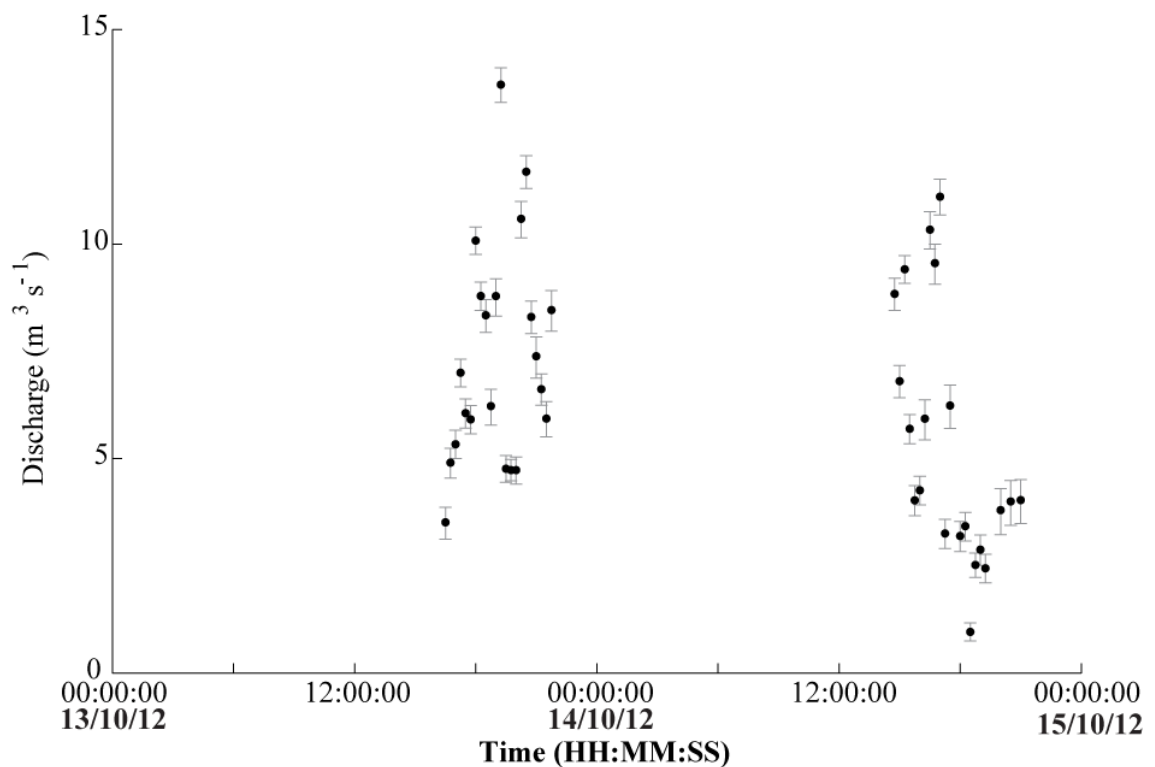


Figure 4.15 Flow discharge calculated from velocity derived from water-surface wave trains, flow depth estimated from bed topography and channel width determined by the percentage width of channel occupied by flow. Measurements based on observations at Site A

Discharge estimates varied if velocity derived from three-dimensional wave trains (Equation 4.5, Section 4.4.2.2) was applied, or if flow depth was calculated from wave train wavelength (Equation 4.3) rather than bed topography. Tests showed that discharge increased by up to 210 % (equating to $12.8 \text{ m}^3 \text{ s}^{-1}$ increase) if wave train three-dimensionality was included, discharge increased by up to 397% (equating to 15.9

$\text{m}^3 \text{s}^{-1}$ increase) if water depth was calculated using Equation 4.3; in combination these two elements increased discharge estimates by up to 812% (equating to $38 \text{ m}^3 \text{ s}^{-1}$ increase). The average difference in discharge calculation from three-dimensional wave train velocities was $4.6 \text{ m}^3 \text{ s}^{-1}$, the average difference using water depth calculated by Equation 4.3 was $3.6 \text{ m}^3 \text{ s}^{-1}$, and the average difference based on the combination of both elements was $10.9 \text{ m}^3 \text{ s}^{-1}$. As discussed in Section 4.4.2.2, velocity calculated assuming wave trains were three-dimensional was greater than velocity calculated assuming wave trains were two dimensional; the relationship is described by a power law. This relationship propagated through the calculation of discharge to show that misinterpretation of wave train dimensionality will lead to significant over or under estimates of discharge, particularly during peak conditions.

Estimates of water depth using bed topography were lower than depths derived from Equation 4.3; up to 0.59 m less. Accounting for the different methods of calculating velocity and depth, and their impact on discharge we see that calculation of mean discharge ranged from $6.4 \text{ m}^3 \text{ s}^{-1}$ to $17.2 \text{ m}^3 \text{ s}^{-1}$, and peak discharge $13.7 \text{ m}^3 \text{ s}^{-1}$ to $43.3 \text{ m}^3 \text{ s}^{-1}$. If these figures were extrapolated over 48 hours, the duration of the October 2012 lahar, the total flow volume (water and solid load) was estimated between $1.1 \times 10^6 \text{ m}^3$ to $2.9 \times 10^6 \text{ m}^3$. The estimated total rainfall volume was $2.77 \times 10^6 \text{ m}^3$ (based on a catchment extrapolation of raingauge and radar rainfall measurements) and it was clear from calculations that depending on the equations used to derive flow velocity and the method chosen to calculate flow depth, estimates of flow volume and interpretation of the catchment runoff response could vary. The limitations of the calculations are acknowledged: (1) Equations 4.3, 4.4 and 4.5 have only been tested for clear water flows in flume environments and may need adjustment for flows containing a higher suspended load, (2) spatial variations in flow were not specifically considered in calculations only intrinsically included using mean values at each 15 minute time step, and (3) calculations assumed consistent wave train dimensionality for the whole event, whereas observations were made that the form of a single wave train changed in time and wave trains occurring at the same time in different parts of the flow were different. However discharge estimates using wave train equations provided a useful estimate of flow volume and lahar magnitude.

4.4.3. Waning flow

Following the last peak in flow at 13:44 UTC on 14/10/2012, flow gradually occupied less of the valley-floor, from 74.8% at 14:45 UTC to 6.5% at 20:45 UTC. Bores persisted every 10 to 180 seconds until 15:58 UTC, becoming less frequent and distinguishable in the flow (becoming undular in form from ~15:00 UTC). Wave trains were present in the channel closest to the camera (area B, Figure 4.9a) until 19:15 UTC and the channel furthest from the camera (area C, Figure 4.9a) until 21:00:00 UTC (light conditions made it difficult to discern flow features after this time). Wave trains repeatedly formed in the same part of the channel; in the centre of area C (Figure 4.9a & Figure 4.9a) a wave train repeatedly formed in the same location after breaking from 14:45 UTC to 21:00 UTC. The average wavelength of waves in the train ranged from 2.52 m at 15:15 UTC to 3.88 m at 16:30 UTC. The residence time of the wave train was ~ 2 minutes at 15:15 UTC but over 6 minutes at 16:30 UTC, in fact some of the waves in the train at this second time persisted through waves breaking upstream, decreasing in height but quickly re-growing, and trains included up to 15 waves. The wave train at 21:00 UTC did not persist for more than 1 minute although another train containing waves of similar wavelength quickly formed. Flow in areas surrounding the wave train had a smooth surface texture.

Downstream at Site B1 at 21:00 UTC flow was shallow (< 0.2 m deep). Wave trains were observed in multiple locations in this lower section of valley at this time; one train (Appendix 4.1d) persisted for nearly 10 minutes, retaining a wavelength of ~0.5 m. Suspended sediment concentration (see Section 2.4.2 for methodology) measured at this location at 21:00 UTC, was 20 g l⁻¹ composed of 5% very fine sands, 81.2% silts and 12.9% clay- sized sediment (Appendix 4.1g). Suspended sediment concentration measured at the same location at 13:00 UTC was 17.5 g l⁻¹ composed of 8.3% very fine sands, 79.7% silts and 12% clay-sized sediment (Appendix 4.1g). Samples showed that suspended sediment concentration did not significantly vary in this location during the final waning period of flow. Comparatively, suspended sediment concentration was highest (106 g l⁻¹) during the waxing stage of the first lahar peak at 16:30 UTC on 13/10/2012 (registered on MBGB), but contained a similar sediment grain size distribution as waning flow samples from 14/10/2012. This suggested that flow competence and available sediment did not change.

Seismicity in the 2-5 Hz range remained elevated into 15/10/2012 (Appendix 4.2), declining to background levels overnight between 15/10/2012 and 16/10/2012.

Flow at Site A persisted until at least 13:00 UTC on 15/10/2012 in a shallow channel at the north-side of the valley. Flow from the Sappit River continued for several days confined to a narrow (<2 m) wide channel that did not reach the coast. Surface flow was not observed on 20/10/2012.

4.4.3.1. Bed surface change

At Site A elevation changed between 0 m and 0.1 m (based on February 2012 and March 2013 surveys, Section 2.2.3.1), over ~80% of the valley-floor within the cameras field of view. The bed surface composition estimated from PAP images at transect 1 (Figure 4.6b, Appendix 4.1a) showed that 3.5% was boulders, 17% was cobbles, 21% pebbles (>16 mm), 22% pebbles (<16 mm), 37% silts-sands and 0.2% fines brown coloured sediment drapes. The bed surface composition was coarser than prior to the event in the same location. Drapes of fine sediment from the passage of the flow front were not preserved on the bed surface, as was the case during smaller lahars. Vegetation had also been stripped and buried during the passage of the October 2012 lahar, only 1.4% of the bed surface was occupied by vegetation. This was located on the edge of a channel bar that separated the small channel closest to the camera from the rest of the valley floor. Lateral and vertical incision by the small channel removed ~0.5 m width of the channel bar at its downstream end. Elsewhere at Site A, bar structures in the channel base were reorganised during the event (Figure 4.6b and Figure 4.9c), but were not incised by sub-channels to create steep sided channel boundaries. The absence of distinct stepped channel terraces on the valley-floor corresponded with the long period of waning flow and high channel width to depth ratio. Channels were not entrenched and flow gradually spread out and then in as discharge increased and decreased.

Downstream at Site B1 and B2 flow was confined within narrower channels defined by piles of boulders and pits created by commercial sand extraction. The narrowest channels were incised by up to 0.5 m on the outside of meanders (Figure 4.911a), and the wider channels down the centre of the valley contained a series of shallow (<0.05 m) stepped terraces from the gradual decrease in discharge. Vegetation was stripped from areas of the valley-floor occupied by flow and brown fines drapes were not present on the bed surface between the Sappit and coast. DEM calculations from available data estimated a net loss of $8100 \text{ m}^3 \pm 4 \text{ m}^3$ which equates to 2 cm of loss over the surveyed area of $5.12 \times 10^5 \text{ m}^2$. The lahar on 13th-14th October 2012 was the largest event to have occurred since 2010 and was estimated to have a total volume

of over 1 million m³; however its impact on modifying valley morphology was barely registered. This suggested that erosional and depositional processes over the course of the whole lahar were balanced, resulting in the reworking of sediment but not large-scale geomorphic change. The impact that this has on the sediment record is discussed in Chapter 5.

4.5. The implications of observations between 11th and 15th October 2012 on other lahars in the Belham River Valley

Observations from the October 2012 lahar showed that large lahars in the Belham River Valley triggered by multi-day storm systems rapidly varied over several different temporal and spatial scales. These were (1) multiple peaks in catchment discharge in response to rainfall (hours), (2) channel-wide bores (minutes-seconds) and (3) local formation of water-surface-wave trains within part of a channel (seconds). RSAM data (Figure 4.5b) contained seven seismic peaks during the event that corresponded to a strong signal between 1 and 30 Hz. The peaks in seismicity were associated visually at Site A with increases in discharge, apparent turbulence, bore incidence and cobble-boulder transport. Average bore velocity ($\sim 6 \text{ m s}^{-1}$) was nearly double that of peak flow velocity ($3.6 \text{ m s}^{-1} \pm 0.1 \text{ m s}^{-1}$ at 19:00:00 UTC 13/10/2012), and bores were responsible for reworking channel boundaries and increasing flow depth. Peaks in seismicity appeared to decelerate by up to 1.4 m s^{-1} between registration on MBLY and MBGH seismometers, and this may infer bore deceleration if the bores were directly related to peaks in seismicity; this requires further research. Critically, seismic peaks of these frequencies were characteristic of seismic registration during other lahars in the Belham Valley, other valleys around the Soufrière Hills Volcano, and in other lahar prone seismically monitored systems (Cole *et al.*, 2009; Zobin *et al.*, 2009; Doyle *et al.*, 2010). It was possible that in the case of sediment-charged stream flows, seismic peaks may relate to packets of turbulence in the flow induced by inherent flow instability that manifested as a series of bores (or irregularly occurring roll-waves). It is suggested thus, that bores may be a common feature of lahars in the Belham Valley in upstream areas and in other lahar prone valleys, but are not readily observed, perhaps because of safe upstream channel vantage points or an undular front.

Froude numbers calculated for the bore (Section 4.4.2.1) suggested that the front of the surge was turbulent. Observations of cobble-boulder transport at Site A indicated

that propagation of a bore increased shear stress resulting in erosion to the bed surface. It is proposed that turbulent eddies in the bores reworked the bed sediments, gradually stripping finer material and transporting it in suspension, and propelling larger clasts short distances downstream in traction. As turbulence in the bore decreased or they occurred less frequently due to changing flow stability, the flow was thought to debulk as it travelled downstream. This pattern of erosion and deposition, corresponding to the passage of packets of turbulence was similarly described by Doyle *et al.* (2011). It supports measurements of low bed surface elevation change despite observations of long periods of traction at Site A during the October 2012 lahar; inferring that approximately equal volumes of sediment were locally removed and then replaced during the passage of this single lahar.

Trains of water-surface-waves during the flow broke and rapidly formed in different parts of the valley-floor, representing periods during which the flow free-surface was in-phase with the bed (Kennedy, 1960). These were pervasive flow features, present during all stages of flow. Wave trains were stationary and migrated upstream, depositing antidunes. Bedform preservation in October 2012 was only likely to have occurred during waning flow and in overbank-locations because of the bores; the rapid shifts in occupied valley-floor observed during waning flow following peaks in discharge reduced reworking of deposits (Alexander and Fielding, 1997). Water-surface-waves form when $Fr > 0.84$ (Kennedy, 1960) and wave trains have been observed in other lahars of different magnitudes in the Belham Valley between 2010 and 2013, and in 2001 (Barclay *et al.*, 2007); and deposits from 2005 and 2006 contained structures attributed to antidunes (Sušnik, 2009). It was likely that wave trains frequently developed in stream-flows in the Belham Valley, particularly during moderate-large events. Observations of wave trains during the October 2012 lahar provide some of the first direct measurements of water-surface-wave train behaviour in naturally rapidly varying flows. Coupling these observations with the interpretation of deposits from the event (Chapter 5) contributed significant new knowledge towards improving the interpretation of similar lahars in other systems.

Relationships between wavelength, flow velocity and flow depth developed by Kennedy (1960;1963) experimentally in the flume estimated peak flow velocity $3.6 \text{ m s}^{-1} \pm 0.1 \text{ m s}^{-1}$ by Equation 4.4 (or $8.78 \text{ m s}^{-1} \pm 0.79 \text{ m s}^{-1}$, Equation 4.5) across channel at Site A during the October 2012 lahar. Further research is required to test these equations in natural environments, consider flows containing different concentrations of

sediment and to improve identification criteria for two- and three- dimensional wave forms in rapidly varying flows that do not easily permit parallel measurement of flow parameters (such as those used to define three-dimensional antidunes in the flume, Yokokawa *et al.*, 2010). However, despite limitations, measurements of wave trains and other visual flow features facilitate the estimation of key flow parameters that are useful in managing the hazards associated with lahars. Calculations of lahar volume, flow velocity, flow depth, travel time and inundation area were advocated by Darnell *et al.* (2012) as the most important characteristics of lahars for hazard assessment. Estimations of the volume of the 13th-14th October 2012 lahar suggest it was an order of magnitude higher than the volume of “large” flows in the Belham River Valley between January 2001 and April 2004, estimated by Darnell (2010) using discharge estimates of 15-45 m³ s⁻¹ for a braided channel from Barclay *et al.* (2007). In this instance the flow duration was only 2 hours, based on eye-witness accounts, pertaining to a smaller flow volume compared to the lower discharge, longer duration event observed on 13th-14th October 2012. The event was an order of magnitude lower than estimates of the syn-eruption South Fork lahar at Mount St Helens on May 18th 1980, whose volume was estimated at 1.3 x 10⁷ m³ (Scott, 1988). Although lahars of an order of magnitude lower (3.8 x 10⁵ m³) than the Belham Valley October event were also reported at Blue Lake and Butt Canon, around Mount St Helens at this time (Major, 1984; Major and Voight, 1986; Iverson *et al.*, 1998).

The October 2012 lahar in the Belham Valley was a large event relative to those observed between 2011 and 2013 but much more “extensive” flows were documented by MVO staff in 2010. These are discussed in the context of lahar deposits in Chapter 5.

4.6. Conclusions

- On the 13th-14th October 2012 a large lahar (estimated volume 2 x 10⁶ m³) occurred in the Belham River Valley, triggered by rainfall during the passage of Tropical Storm Rafael. The lahar was recorded by a permanent remote camera installed at Site A, 3.8 km from SHV which captures an image every 1 second.
- In combination with rainfall measurements, seismic data and visual observations from other sites downstream, images from Site A provided new insight into

lahar dynamics, relevant to other flows in this valley and other lahar prone systems.

- The lahar was characterised by seven peaks in seismicity which were attributed to “packets” of flow turbulence. Increases in seismicity corresponded with visual observations at Site A of increased in discharge, apparent turbulence, bore incidence and cobble-boulder transport.
- Three hundred and forty-nine bores were identified at Site A, travelling downstream at irregular intervals of 6 to 2002 seconds. The bores played a significant role in the initiation of sediment motion and their formation is attributed to roll-wave dynamics.
- Trains of water-surface-waves were prevalent in flow at all observations sites. Application of equations derived by Kennedy (1960;1963) to measurements of wavelength provided estimates of flow velocity, depth and in turn discharge. Flow velocity fluctuation in the main channel (area C) was cyclic, varying by ~ 0.5 to 1.5 m s^{-1} over periods of < 1 hour. Variation in velocity correlated with shifting channel boundaries (recording discharge fluctuations) and with propagation of bores.
- Flow parameters derived from water-surface-wave geometry provide useful measurements of flow variability for model validation in sites that are difficult to monitor with contact instrumentation. However, further research is required to test equations in scenarios relevant to sediment-laden natural flows.
- Observations of small lahars during 2011 to 2013 (Chapter 3) indicated that bed surface modification was minimal. While the change in elevation at Site A was small (0 to 0.1 m) during the October 2012 lahar, it was proposed that flow eroded into the bed surface and bulked during peaks in discharge (and bores). Sediments deposited during waning flow may include antidune bedforms and other sedimentary structures associated with the upper flow regime.

Chapter 5

Sedimentary structures formed by lahars in the Belham River Valley

5.1. Introduction

Observations of a large lahar on 13th-14th October 2012 (Chapter 4) provided new insight into the dynamics of flows in the Belham River Valley that was relevant to sediment-laden stream flows in valleys in other locations that have similar channel width: depth ratios and discharge. Trains of water-surface-waves were prevalent in the flow at all observation sites: during waxing and waning stages, and in multiple valley-floor locations at the same site at the same time. These wave trains indicated that the bed surface was in-phase with the flow free surface during much of this time, pertaining to the formation of antidune bedforms. Preservation of antidune sedimentary structures (and sometimes morphology) was commonly attributed to rapidly decelerating flows under aggradational bed conditions (Alexander and Fielding, 1997; Russell and Arnott, 2003; Fielding, 2006; Duller *et al.*, 2008; Winsemann *et al.*, 2009; Lang and Winsemann, 2013). During the October 2012 lahar, three hundred and forty-nine bores (Section 4.4.2.1) were associated with increased discharge, turbulence and cobble-boulder transport. Periods of increased bore frequency coincided with “packets” of seismically registered sediment transport that were associated with net bed surface erosion; net deposition occurred during waning flow. Sedimentary structures attributed to antidunes preserved in the sediment record, were therefore likely to have been formed

during the final waning flow stage or in-between peaks in discharge in valley-floor locations that were not re-occupied by subsequent waxing flow.

This chapter discusses sediments deposited by lahars between Phase 5 (9/10/2009- 11/2/2010) and October 2012 in the Belham River Valley. Published studies of lahar deposits have typically focused on identifying traces of large crater-lake outburst events in the rock record as indicators of eruption (*e.g.* Mount Ruapheu, Auer *et al.*, 2012) or have discussed the bulk shifts in character of the deposit to delineate debris-, hyperconcentrated- and stream- flow phases in downstream or vertical successions (*e.g.* Merapi, Lavigne *et al.*, 2003). Those studies in volcanic environments that have considered sedimentary structures in detail were limited to jökulhaup deposits, emplaced by voluminous glacial outburst floods (Branney and Gilbert, 1995; Duller *et al.*, 2008). To the author's knowledge the study of deposits in the Belham River Valley is the first to discuss in detail sedimentary structures formed by multiple rainfall triggered lahars in the context of direct flow observations with measurements of wave train wavelength. There is a significant foundation to the theoretical understanding of antidune bedform geometries and flow dynamics (see review in Allen, 1982; Carling and Shvidchenko, 2002), and as a result, the transverse spacing of antidunes is a powerful tool in the estimation of paleoflow water depth and velocity (Allen, 1982; Equations 4.2 and 4.4 Sections 4.4.2.1 and 4.4.2.2). However the perceived low preservation potential of antidunes leads to under-recognition of them in the rock record (Fielding, 2006); and few published studies have reconstructed flow dynamics from the geometry of preserved structures (Alexander and Fielding, 1997; Fralick, 1999; Fielding, 2006; Duller *et al.*, 2008). Furthermore, there is a limited understanding of the sedimentary structures associated with antidunes that have formed during rapidly varying unsteady flows with heterogeneous sediment loads; in comparison to the sedimentary architecture derived experimentally in steady-flow flume runs (Kennedy, 1961; 1963; Middleton, 1965; Simons *et al.*, 1965; Jopling and Richardson, 1966; McBride *et al.*, 1975; Shaw and Kellerhals, 1977; Clifton, 1990; Yokokawa *et al.*, 2000; Alexander *et al.*, 2001; Kubo and Yokokawa, 2001; Wren *et al.*, 2005; Yokokawa *et al.*, 2010; Carling *et al.*, 2014). Very few studies have documented the detailed sedimentary structures resulting from observed water-surface- waves in natural alluvial channels in non-glacial outburst settings (Harms and Fahnestock, 1965; Barwis and Hayes, 1985; Langford and Bracken, 1987; Alexander and Fielding, 1997; Blair and McPherson, 1999; Blair, 2000). This chapter provides a description of sediments using the facies scheme outlined in Section 2.5, presenting a series of logs from vertical

sections exposed by sand mining in the Belham River Valley between March 2011 and March 2013. The chapter describes sedimentary structures using architectural diagrams (Section 2.5.1.4) of sub-sections of the exposed deposit, and discusses the inter- and intra-flow variations inferred from sediment structures and changes in deposit character, with reference to relevant flume and field studies.

5.2. Antidunes

Antidunes are one of several upper flow regime bedforms which form when the bed surface is in-phase with the flow free-surface and Froude number is greater than $Fr > 0.84$ (Kennedy, 1963). Upper flow regime bedforms include transitional dunes, planar beds, antidunes, chute-and-pools and cyclic steps (Simonset *et al.*, 1961; Cartigny *et al.*, 2014) and low amplitude bed waves (Best and Bridge, 1992). Some of these bedforms form in sub-critical or critical flow conditions, but most form during supercritical flow where inertia dominates over gravity. Section 4.4.2.1 discussed the formation of bores during ‘unstable’ flow when relative kinematic wave celerity is greater than the relative dynamic wave celerity, defined when the Vedernikov number is greater than 1. Water-surface-waves (and antidunes) form at the onset of unstable flow, while periodic fluctuating flows at higher Froude numbers form chutes-and-pools and cyclic steps (Guy *et al.*, 1966; Alexander *et al.*, 2001; Spinewine *et al.*, 2009; Cartigny *et al.*, 2014).

5.2.1. Formation and flow dynamics

Antidunes may form from upper stage plane beds, dune covered beds or even lower stage plane beds depending on grain size (Southard and Boguchwal, 1990; Allen, 1982). Formation from a planar alluvial bed occurs when internal periodic non-uniformity develops in uniform turbulent shear flow resulting in the deformation of streamlines and their interaction with the bed surface (Carling and Shvidchenko, 2002; Yalin and da Silva, 2001). Three theories have been used to explain instantaneous bedform initiation from a flat bed: (1) perturbation theory, (2) generation of bed defects by turbulence, and (3) instability interface theory (see Venditti *et al.*, 2013 for review). Bedforms may also be initiated by flow separation around debris defects on the bed surface (see Raudkivi 1963; 1966). Although this method of initiation is less common in antidune flume studies, which typically commence runs from a planar bed of near-uniform grain size; it is relevant to natural channels. Increasing grain size of the planar bed, results in increases in the lag time between flow regime change and bedform

adjustment (Engelund and Fredsøe, 1974). This is thought to be driven by inertia in the sediment phase (Wieprecht, 2000) and results in dunes persisting as antidunes develop in response to flow regime changes (*e.g.* Carling and Shvidchenko, 2002).

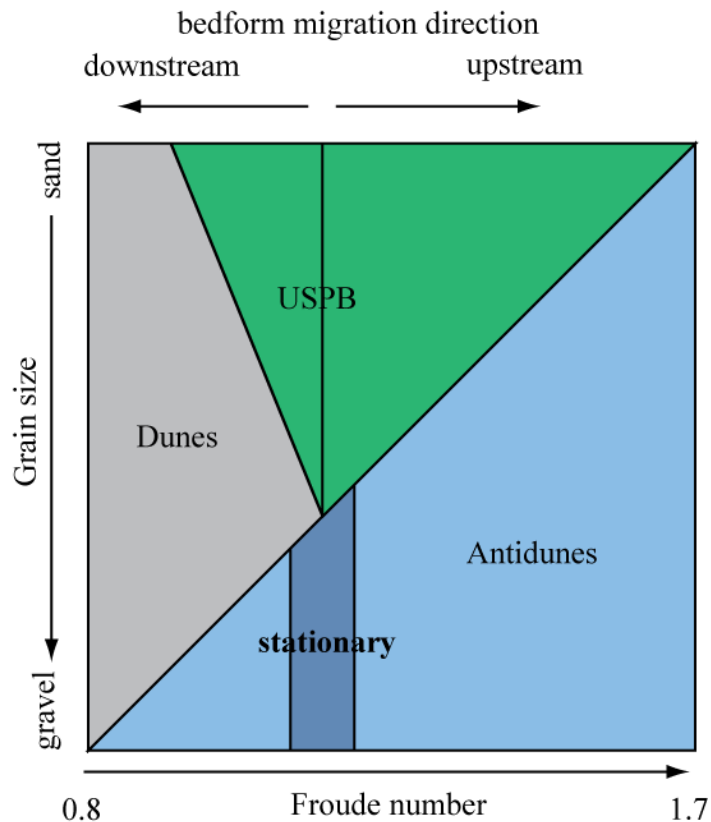


Figure 5.1 Diagram showing bedform formation, transition and migration direction based on increasing Froude number (Fr) and sediment size. Redrawn and adapted from Kennedy (1963) and Brakespear (2008). Stationary antidunes develop around $Fr=1$.

Antidunes formed in different hydrodynamic situations result in characteristic sets of deposits. Figure 5.1 presents a framework for bedform formation and transition with respect to increasing Froude number (Fr) and grain size. Antidunes do not form when sediment is very coarse and poorly sorted (Wilcock, 1993), because the magnitude shear stress required to mobilise coarse material is infrequent and finer sediment suitable for bedform formation is preferentially stripped from the bed surface (Brakespear, 2008). In coarser sediment downstream-migrating antidunes form in low Froude numbers. Antidunes remain stationary when $Fr \approx 1$ and migrate upstream for all sediment sizes with higher Fr ($Fr < 1.7$) (Kennedy, 1963). The direction of migration is thought to relate to the intermittent and erratic streamline detachment from the downstream slope (leading to downstream migration) or the upstream slope (leading to upstream migration); this mechanism favours downstream migrating antidunes forming during a period of transition from dune to antidune, where the irregularity and

asymmetry of these bedforms in transition promotes flow separation (Núñez-gonzález and Martín- Vide, 2011). Fundamentally antidunes in natural flows develop under unstable flow regimes in which the free-surface and bed surface are changing continuously; for upstream-migrating antidunes under water-surface-waves that amplify and break, this process is a cyclic, composed of bedform growth, migration and destruction (Alexander *et al.*, 2001; Figure 5.2). Blair (1999) discussed three types of water-surface-wave breaking: (1) wave dissipation that eroded the antidune crest and flattened the bed surface but preserved laminae, (2) moderate breaking which preserved laminae in erosional trough deposits, and (3) violent breaking which eroded all fine material and left coarse beds of sediment, followed by a fines bed as turbulence dissipated. The complex nature of these bedforms pertains to an array of different sedimentary structures and bedform morphologies dependent on flow regime and sediment characteristics. These are reviewed in the following section and used in combination with the facies scheme discussed in Section 2.5 to interpret lahar deposits from Phase 5 to 2013.

5.2.2. Deposit characteristics

Studies on antidunes have considered structures of different scales, from individual laminae indicative of bedform migration to assemblages of different sediments representing a sequence of free-surface wave behaviour over time. Most research has focused on fine-medium sand in flumes (Middleton, 1965; Yagishita and Taira, 1989; Yokokawa *et al.*, 2000; Alexander *et al.*, 2001; Yokokawa *et al.*, 2010; Cartigny *et al.*, 2014) and these experiments have provided useful insight into the internal structures of stationary and upstream migrating antidunes, including those that break. Very few flume studies (McBride *et al.*, 1975; Núñez-gonzález and Martín-vide, 2011) have generated downstream migrating antidunes. Figure 5.3 summarises flume observations using an example of structures generated by a train of breaking water-surface-waves during a flume run with medium sand (Alexander *et al.*, 2001). Experiments from various authors have linked specific structures in deposits with water-surface-wave behaviour (combined observations summarised in Table 5.1). The precise origin of antidune laminae is debated (Bridge, 2003), and two main theories have been proposed: (1) shear sorting (Barwis and Hayes, 1985) and (2) low-amplitude bedwaves (Alexander *et al.*, 2001 following Best and Bridge 1992). Grain scale processes are not

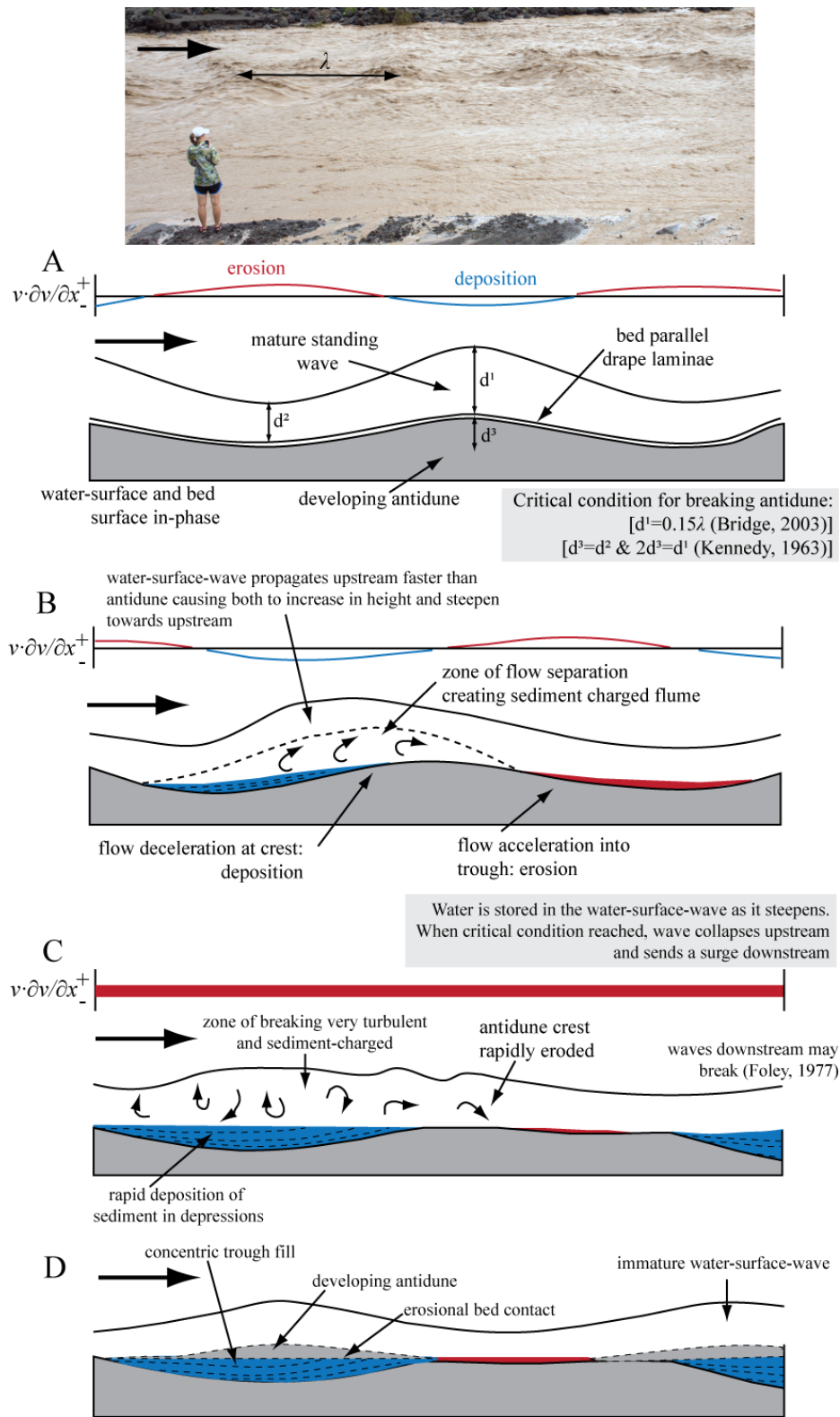


Figure 5.2 Diagram illustrating the cyclic growth, migration and destruction of upstream migrating and breaking water-surface-waves (and antidunes). Redrawn and adapted from Duller *et al.* (2008). Top photograph shows an example of a water-surface-wave train before breaking, located at Site B1 during the October 2012 lahar (see Section 4.1). The spatial acceleration of flow across the bedform surface is shown by graphics at the top of each stage A-D. Areas of erosion and deposition corresponding with accelerating or decelerating flow are coloured (red= erosion and blue= deposition) in the water-bedsurface diagrams at each stage. The breaking wave may travel upstream by different amounts relative to the erosional trough of the antidune, depending on the position of the breaking wave in a wave train and the type of wave breaking (see Blair, 1999 and Cartigny *et al.*, 2014).

discussed in detail in this study, but it is important to be aware of possible processes and recognise antidunes form from a combination of traction, saltation and suspension sedimentation.

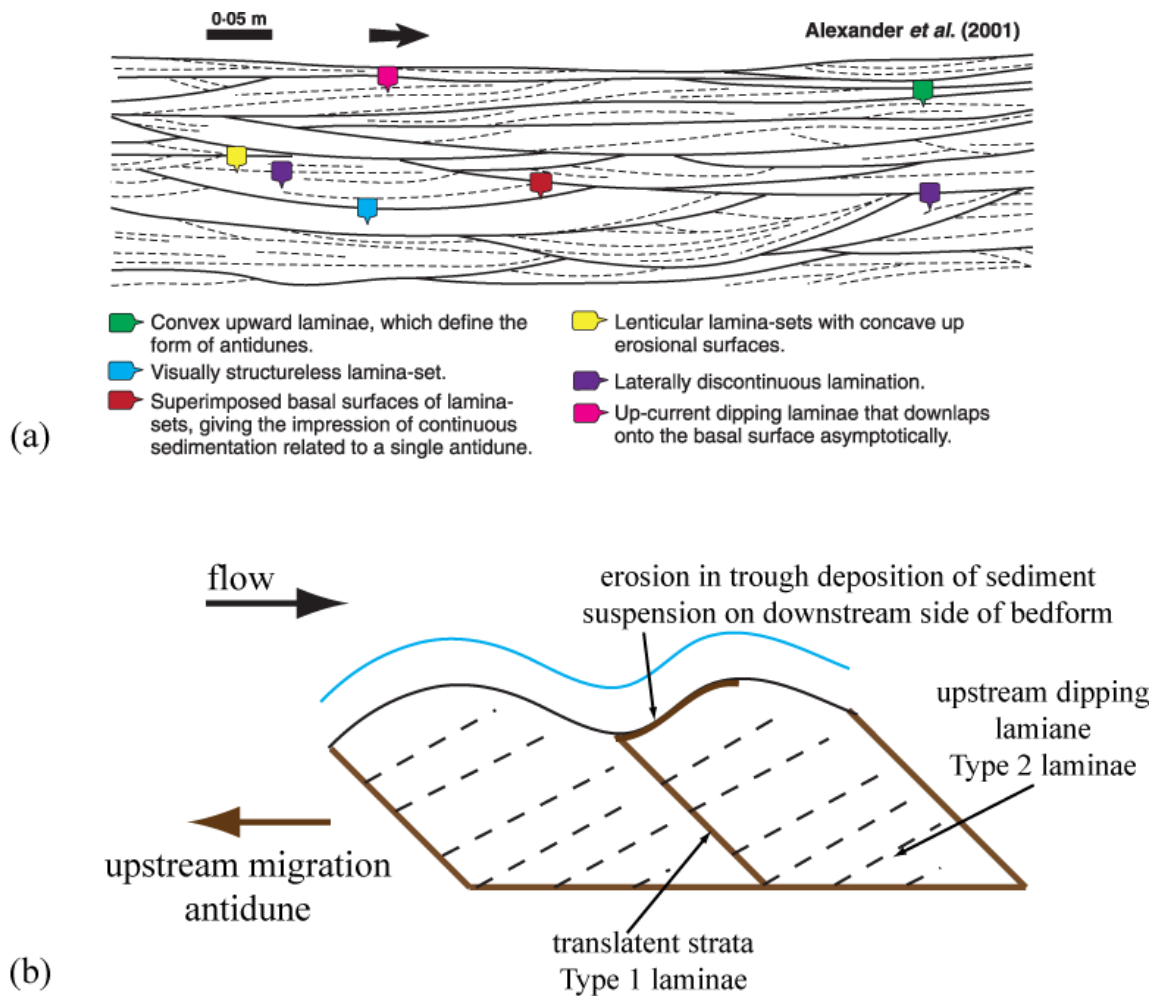


Figure 5.3 (a) Line drawing of flow parallel section of sedimentary structures of antidune origin deposited by supercritical flow in a laboratory flume (Alexander *et al.*, 2001; modified from Duller *et al.*, 2008). (b) Model for sedimentary structures generated by upstream migrating antidunes under aggrading conditions (Clifton, 1990; redrawn Brakespear, 2008).

Type 1 laminae formed by upstream migration of the trough between antidunes. Type 2 laminae formed by sediment sorting on the upstream side of the antidune.

Deposit	Interpretation	Field example
<p>Variations of convex-upward laminae sets (symmetrical) and convex-up laminae that transition to concave-up laminae upstream; concave-up sets have erosional bases (Alexander <i>et al.</i>, 2001). Parallel unidular beds that are symmetrical (Brakespear, 2008)</p>	<p>In-phase non breaking stationary water-surface-waves. Progressive deposition on antidune crest that thins out on the flanks (Allen, 1985). Boundary shear stress is highest beneath the wave crest and lowest in the trough resulting in difference in deposit thickness (Chanson, 2000). Preserved when flow is quasi-steady (Cheel, 1990; Lang and Winsemann, 2013) and aggradation persists for prolonged periods (Middleton, 1965). Erosional contacts of concave-up laminae indicate aggradation is non-continuous (Duller <i>et al.</i>, 2008). Normal to flow laminae sets are parallel to set boundaries or inclined less than 10°, rarely up to 20° (Bridge, 2002)</p>	<p>Saalian ice-marginal sand-rich deposits: northern Germany (Lang and Winsemann, 2013). Waveforms in deposit have lengths of metres to decametres and amplitudes lower than 0.25 m. Normal to flow deposits with similar form (convex-up) were interpreted as three-dimensional antidunes or two-dimensional antidunes formed in narrow channels. Across flow structures had a smaller length compared with thickness.</p>
<p>Upstream dipping (low angle) laminae sets organised in planar to –sub-planar bedsets</p>	<p>Upstream migrating in-phase water-surface-waves that do not break or significantly change in amplitude. Deposition on the upstream side of the antidune. Complete laminae length is ~0.5 times the wavelength of the antidune (Leclair <i>et al.</i>, 1997). Laminae thickness is related to bedform amplitude which depends on aggradation rate. Stacked sets of laminae correspond to the progressive sedimentation from an antidune train, and have subhorizontal to gently inclined boundaries (Cartigny <i>et al.</i>, 2014). Sets of laminae in Cartigny <i>et al.</i>'s (2014) experiments were typically upward thinning, corresponding to decreasing water-surface-wave amplitude within a train.</p>	<p>Low-angle cross-beds beneath wave or dome forms that appear to dip upstream within Late Devonian formation in Southern Ireland, interpreted to be antidunes formed on low-angle fluvial fan at coast (Cotter and Graham, 1991).</p>
<p>Downstream dipping laminae (high angle) with trough shaped basal bed boundary</p>	<p>Laminae dipping more than 20° downstream generated by the rapid migration of asymmetrical bedwaves with a steep downstream face, that propagate downstream after surface wave breaking and during bed smoothing (Alexander <i>et al.</i>, 2001). Downstream dipping laminae are usually contained in a bed with a trough-shaped (concave up) base.</p>	<p>Lang and Winesmann (2013) discuss “sigmoidal downflow parallel cross-sets” which are attributed to trough fills when the brink (separating topsets and foresets) trajectory is sub-horizontal. If the brink trajectory is climbing (upwards) and the sets are downflow divergent, deposits are attributed to humpback dunes.</p>

Deposit	Interpretation	Field example
<p>Upstream dipping laminae (low angle) with trough shaped basal boundary</p>	<p>Dips up to 20° (but generally less than this) at the top of the bed, decrease in dip towards the base of the set resulting in concave-upward laminae with bases sub-parallel to parallel with the trough shaped base of the set. (Bridge, 2003). Laminae flatten out upward to fill the trough. Form during the gradual reduction in height of water-surface-waves or during wave breaking. Cartigny <i>et al.</i> (2014) suggested that upstream dipping low-angle laminae were formed during wave breaking and the propagation of a surge upstream. Formation was dependent on the maximum upstream position reached by the surge relative to the deepest point of the trough; upstream dipping laminae were formed when the surge did not propagate further upstream than the deepest centre part of the trough, depositing material on the upstream side of the antidune.</p>	<p>Troughs infilled with concave-up upstream dipping laminae. Base of the trough has erosional contact. Common in the proximal or lower parts of the vertical succession of the glacial outburst floods at Porta fan Northern Germany (Lang and Winsemann, 2013).</p>
<p>Downstream dipping laminae (low angle) with trough shaped basal boundary</p>	<p>Cartigny <i>et al.</i> (2014) suggested that downstream dipping low-angle laminae were formed during wave breaking and the propagation of a surge upstream. Formation was dependent on the maximum upstream position reached by the surge relative to the deepest point of the trough; downstream dipping laminae were formed when the surge reached the downstream face of the upstream antidune. Most likely formed by breaking of the first waves in an antidune train which were observed as generating surges which travelled the furthest upstream.</p>	<p>In the Burkedin River, Australia, Alexander and Fielding (1997) discussed gravel antidune formation during short high discharge flows. Internally the bedforms (which were up to 19 m in length) contained low-angle cross-bedded structures interpreted as downstream migrating antidunes. The cross-beds were located downstream and above a set of steeper downstream dipping cross-beds that were interpreted as dune origin. These structures were thought to represent dunes truncated and deflated by supercritical flows.</p>
<p>Visually structureless with trough-shaped basal bed boundary</p>	<p>From rapid deposition from direct suspension fall-out during wave breaking. Propagation of a surge of water downstream, induced a reduction in traction upstream of the surge, resulting in sedimentation by suspension. (Cartigny <i>et al.</i>, 2014). Sometimes process forms structureless fines beds at the base of troughs which are overlain by dipping laminae (Alexander <i>et al.</i>, 2001).</p>	<p>In a Carboniferous South Bar Formation in Nova Scotia, apparently structureless, poorly-sorted sandstones in tabular beds extending 10-30 m were interpreted as possibly forming from breaking of water-surface-waves and en-masse deposition (Rust and Gibling, 1990; Fielding, 2006)</p>

Deposit	Interpretation	Field example
Truncation of trough sets	Overlapping beds with trough shaped bases, formed by water-surface-waves that break or significantly vary in amplitude over a period of time. Erosional troughs do not develop in the same location during sequential antidune formation resulting in truncation of the top of the previously deposited trough form by erosion by the most recent trough.	Truncated structureless beds were observed by Rust and Gibling (1990) at a Carboniferous Sand Bar Formation in Nova Scotia. The beds were truncated by the overlying bed and the bedsets are interpreted as breaking antidune origin.
Superimposed trough sets	Rare case: erosional troughs are formed in the same location, resulting in a deposit with the appearance of a concave-up laminae trough fill, rather than superimposed bedsets (Alexander <i>et al.</i> , 2001).	Superimposed trough sets were observed in 1918 jökulhlaup deposits by Duller <i>et al.</i> (2008). The bedsets were not described but were interpreted as deposited by two cycles of antidune growth in aggrading conditions.
Downstream dipping laminae (low angle) with planar to sub-planar bed boundary	Deposition on the downstream face of an antidune and indicative of downstream bedform migration (McBride <i>et al.</i> , 1975). Water-surface-waves do not break . Limited observations.	Duller <i>et al.</i> (2008) Mýrdalssandur, Katla volcano, Iceland. Sand-rich jökulhlaup deposits. Tabular or lenticular bedsets showing stratification inclined down current at a low angle (5-10 °) interpreted as down-current migrating antidunes.

Table 5.1 Summary of sedimentary structures formed during flume experiments (Alexander *et al.*, 2001; Yokokawa *et al.*, 2010; Cartigny *et al.*, 2014) and interpreted as antidune origin. Observations of similar structures in field deposits are provided. All structures are described based on two-dimensional exposure parallel to palaeoflow direction unless otherwise stated. The table provides a useful reference point for interpretation of structures in architectural diagrams of lahar deposits (Section 2.5.1.4 and Section 5.5).

5.3. Location of logged vertical exposures in the depositional record

Field work between 2011 and 2013 documented deposits exposed by commercial aggregate extraction (Photographs in Appendix 5.1a-d). The location of pits constructed by the backhoe method was dependent on plans of the commercial companies operating in the valley, and typically workings were focused on the lower reaches of the Belham River Valley between 2011-2012 (Figure 2.18). There were very few natural vertical faces in the deposit between 2011 and 2013. The method of logging was detailed in Section 2.5.1.2 and the location of each exposure is shown in Figure 2.18. The valley bed-surface elevation was surveyed annually (in February/March 2011-2013) and in combination with an airborne LiDAR survey conducted in 2010, captures the impact of lahars (and sediment extraction) on topography between the coast and Molyneux for the duration of the study period (Section 2.2.3, analysis Section 3.5). Lahar incidence during this time (Section 4.2) occurred as a series of large valley-wide, multi-day lahars in 2010; flows were smaller in 2011 until October 2012 when Tropical Storm Rafael triggered a two-day lahar documented in Chapter 4.

Several large flows occurred between June 2010 and November 2010 (Section 3.5 and 4.2). Deposition between November 2007 and June 2010, caused surface elevation to rise between $0.08 \text{ m} \pm 0.04 \text{ m}$ and $3.6 \text{ m} \pm 0.04 \text{ m}$ in Area 1, and between $0.33 \text{ m} \pm 0.04 \text{ m}$ and $2.66 \text{ m} \pm 0.04 \text{ m}$ in Area 2. Two of the pits were present in the June 2010 DEM in area 1 and the lower section of area 2 (Figure 2.18), representing up to $1.86 \text{ m} \pm 0.04 \text{ m}$ of elevation loss by sand extraction. Topographic changes between March 2011 and February 2012 were predominantly less than $0.5 \text{ m} \pm 0.04 \text{ m}$ in areas unaffected by sand extraction. There was more deposition at the upstream end of Area 2, but generally on the natural bed surface there were areas of erosion corresponding with shallow ($<0.2 \text{ m}$) channels and deposition overbank and on channel bars. Sand extraction during 2011, contributed up to 2.78 m of elevation reduction in Area 1; flows during 2011 to 2013 were constrained to depressions in the bed within Area 1, created by temporary roads connecting extraction pits. Twenty-three lahars (category 2 & 3, Section 3.4) were registered between March 2011 and February 2012, and also between February 2012 and March 2013. Only one event occupied most of the valley-floor and lasted more than a few hours, all other lahars were confined in $<0.2 \text{ m}$ wide channels.

The large lahar on 13-14th October 2012 did not result in significant elevation change in the valley despite observations of intense periods of erosion during peak flow and vertical and lateral changes to channel boundaries (Section 4.4.3.1). At Site A (upstream of the Sappit River confluence, Figure 4.1), deposition was prevalent but gains in elevation were no greater than $0.15 \text{ m} \pm 0.035 \text{ m}$. More deposition occurred upstream in the vicinity of Phase 5 pyroclastic flow terraces (upstream of Site A, Figure 4.1), than downstream towards the coast, however erosion and deposition was locally patchy, varying between $-0.52 \text{ m} \pm 0.035 \text{ m}$ and $0.5 \text{ m} \pm 0.035 \text{ m}$ in Area 2 (Figure 2.18).

A pit (Pit2013) was excavated in early 2013 downstream of the Sappit River confluence, in an area previously un-modified by sand extraction (Figure 2.18). It crossed the widest channel of three in this valley reach (Figure 5.4), providing a 150 m stream-parallel by 1.5- 4 m high exposure, a 20 m wide by 4 m high cross-channel section and a 94 m long section that varied between stream-parallel and cross-channel orientation (1.5- 4 m high). Upstream and beside the pit, the sediment surface elevation change between $-0.14 \text{ m} \pm 0.035 \text{ m}$ and $0.45 \text{ m} \pm 0.035 \text{ m}$ between February 2012 and March 2013, is attributed to the October 2012 lahar.

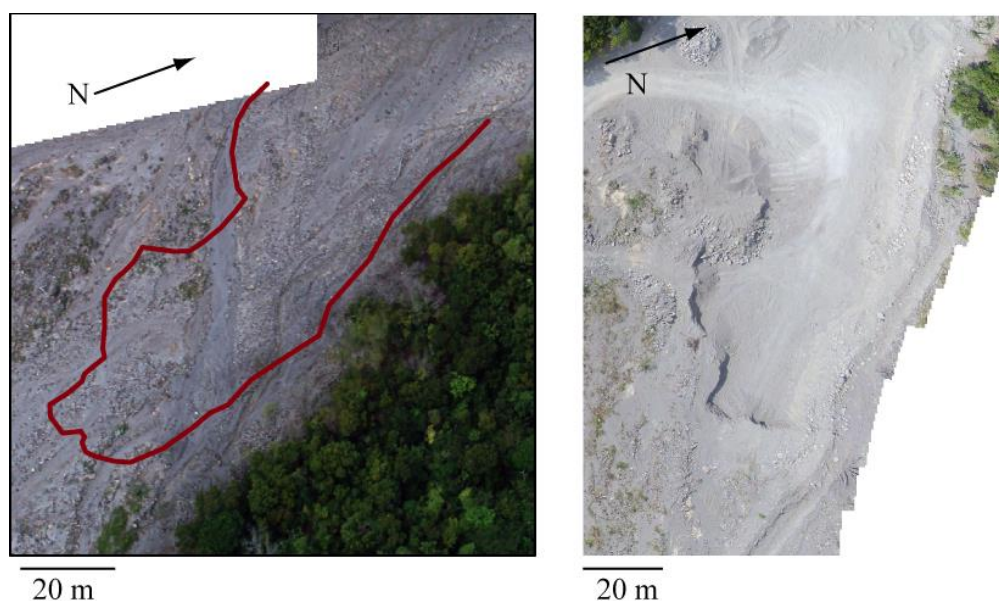




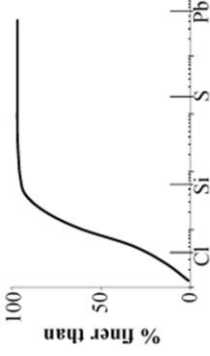
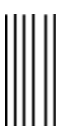

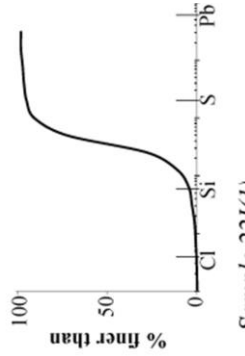
Figure 5.4 [Left] Aerial photograph March 2012 of Pit2013 (red) showing location of Pit 2013 cross-cutting a main channel (full width of pit). [Right] Same location March 2013

5.4. Deposit description



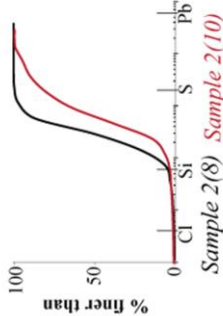



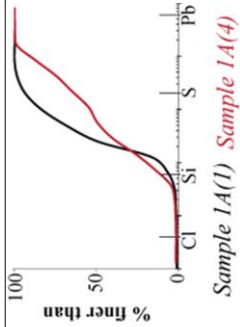
Sediment logging methodologies and the facies scheme (Table 2.9) used were discussed in Section 2.5. Table 5.2 contains descriptions of each facies (including the addition of a facies to the scheme, Sw), visual examples and relevant grain size

distributions from sediment samples of sand grade facies (see Section 2.5.1.3 for method). Two parts of Pit2013 were logged in detail. Log 1 (Figure 5.5a) was parallel to palaeoflow direction in the centre of one of the main channels occupied during the October 2012 lahar. The log was 1.83 m thick and contained massive gravels at its base (Gmm), laminated sands (Sh), matrix-supported gravel lenses (Gmg), thick beds of massive sands (Sm) and beds of clast-supported gravels (Gcm) organised in a lenticular pattern at the top. Log 2 (Figure 5.5a) was located parallel to paleoflow direction at the edge of the valley. The log was 2.84 m thick and contained laminated sands (Sh) and dipping sand and pebble beds (Sl) in its lower half, with some obstacle scours and matrix-supported gravel lenses (Gmg). Above this were laminated sands (Sh) and gravels (Gh) with a bed of open framework gravels and clast-supported gravels (Gcm) inter-bedded with sands (Sm) in its central-upper section and laminated beds of sands (Sh) and pebbles (Gh) at the top.



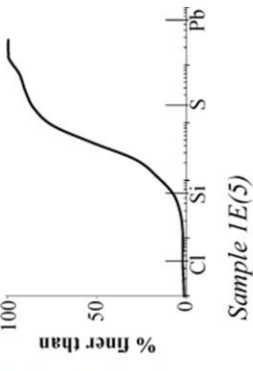


Twelve logs document deposits in the lower Belham Valley (downstream of the orange house) between Phase 5 and 2011 (Figure 5.5b). Three of these logs were transverse to palaeoflow direction, generally at 90° to channels identified on the bed surface from the LiDAR full-feature DSM. The other logs were parallel to palaeoflow. Logs 2012_1, 2011_2 and 2011_4 were between 0.98 m and 3.11 m thick and were composed of predominately sand sized sediment in horizontal (Sh) and dipping planar laminated beds, low-angle cross-beds (Sl) or massive (Sm) tabular beds. 2011_4 contained a 0.3 m thick bed of silts and sands that was brown (compared with other beds that were grey); 2011_6 contained a similar bed of approximately the same thickness. 2011_1, 2011_3, 2011_5, 2011_6, 2011_7, 2011_11 contained beds of ranging from 0.2 m to 1.05 m thick of clast-supported gravels (Gci, Gcm) with different sorting and clast a-b plane orientation; in some beds clasts dipped upstream however in other beds clasts did not share a clear dip and the beds appeared massive and/or were matrix supported (Gmg, Gmm). 2011_5, 2011_6, 2011_9 and 2011_10 contained massive sands (with pebbles) in lenses. Some logs contained sharp boundaries of silts and fine sands (Fsm) that were mm to 10 cm thick (2011_2, 2011_4, 2011_11); many logs contained beds with gradational boundaries. There was no predominant shift in grain size between logs up and down-stream, nor from the base to the top of logs.

Facies	Description	Example and grain size distribution
Massive mud (Fsm) 	<p>Found in millimetre thick to 0.08 m thick beds. Thicker beds were not as laterally extensive as thinner beds, max 1.8 m at 2013_2. Thinner beds were observed to extend nearly continuously for over 100 m. many of the thicker beds contained live plant material. Sharp basal boundary. Light brown to dark orange.</p> <p>Some evidence of desiccation cracks (Fm) in thicker beds.</p>	  <p style="text-align: center;">Sample laharmarch2011</p>
Horizontal laminated sands (and silts) (Sh) 	<p><0.05 m thick horizontal beds. Short lateral extent, 0.4 m at 2013_2. At 2013_20.07 m thick, laterally continuous for 8 m. At 2012_1 0.06 m to 0.12 m thick, laterally continuous for 12 m. Lamination of varying grain size, a few millimetres thick. Individual laminae appeared massive. Included sands and silts of all grades. Sharp upper and lower boundary</p>	  <p style="text-align: center;">Sample 22I(1)</p>



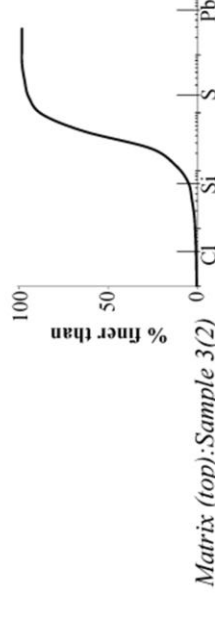

(Table 5.2 continued to next page)

Facies	Description	Example and grain size distribution
<p>Low angle (<15 deg) cross-beds of sands (S1)</p> 	<p>Solitary or grouped (predominantly) planar low-angle cross-beds in tabular to sub-tabular beds. Inclination may be downstream or upstream, although most dip upstream. In longer exposures the bed dip was seen to change from upstream to downstream. The transition point in dip direction was not preserved at 2013_2. Some beds were wavy, but this was not a widespread feature. At 2013_2 solitary laminae (under 10 mm thick) were laterally extensive for tens of metres. At 2011_2 laminae of 1-3 mm dipped 8° upstream, bed thickness was 0.02 m, cross-beds laterally extended for 0.3 m becoming Sh.</p> <p>Sharp basal and top boundaries. Found in exposures parallel to paleoflow direction. Predominantly sands of all grades but also silts, granules and small pebbles.</p> <p>Laminae texture- internally massive composed of admixtures of sands and pebbles which varied between beds. Depending on thickness some beds were visibly inward coarsening.</p>	<p>2013_2</p>   
<p>Massive sand-pebbles (S_m)</p> 	<p>Sand of all grades to small pebbles, with no visible internal structure. At 2013_1 beds were planar, 0.12 m thick and laterally extensive for <10 m. At 2011_2 beds were 0.03-0.05 m thick and extended for ~5 m. Thicker beds had diffuse boundaries, thinner beds boundaries tended to be sharp. At 2013_2 some beds of coarse sands and pebbles, were a few millimetres to 0.02 m thick, laterally extending for <10 m. The beds were horizontal or had a low-angle dip (10°) upstream or downstream. Also within 2013_2 were 0.02 m – 0.18 m thick low-angle massive sand (and pebble) beds that were laterally extensive for <5 m. These beds were upstream divergent in thickness when inclined upstream and downstream divergent in thickness when inclined downstream. Beds at 2013_1 and 2013_2 that were lenticular in geometry (parallel to paleoflow direction), between 0.26 m and 2.21 m in bed length, 0.01 m to 0.05 m thick. Lens thickness:length ratio = 1:6 to 1:10 varied with on location. Most beds had sharp upper and lower boundaries. A few lenses had wavy tops that were symmetrical. The beds were predominantly sand but did contain some pebble sized clasts (max clast size = 48 mm). In some locations lateral exposure limited measurement of lens geometry but the basal boundary was convex-up and the top boundary may be concave-up.</p>	 


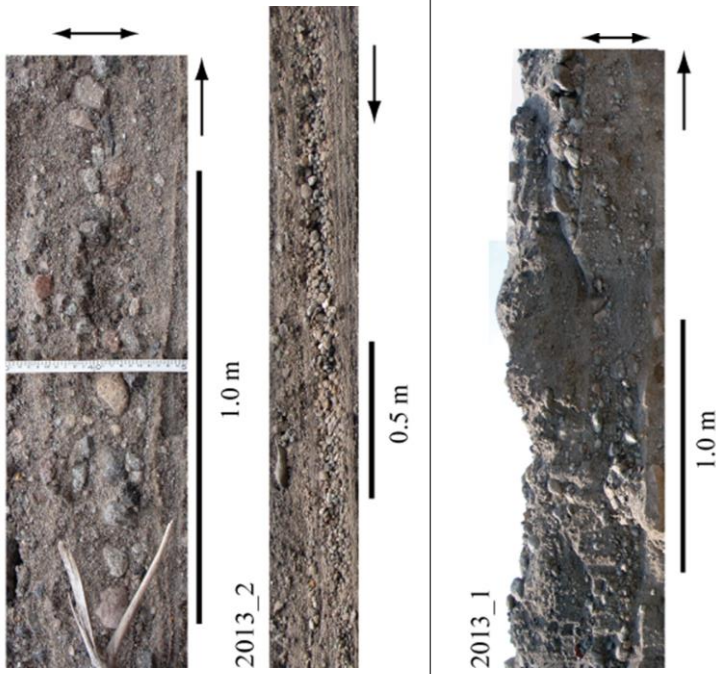

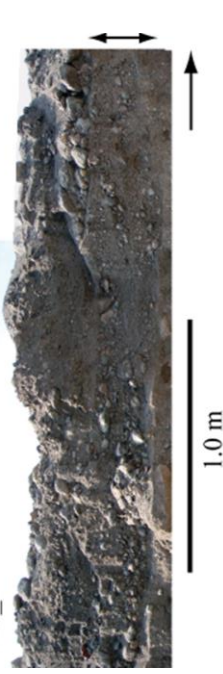
(Table 5.2 continued to next page)

Facies	Description	Example and grain size distribution
<p>Wavy laminated sand (Sw)</p> 	<p>Located above cobbles-boulders (Gmg) also occurs above Sh and Sm. Not laterally extensive, 0.3 m, 0.1 thick at 2013_2. Laminae formed of different grain size: v-fine to fine sand and coarse-v-coarse sand. Finer laminae were thinner (few millimetres), coarser laminae are thicker (~10 mm). Laminae were not concordant, thickness of the coarser laminae decreased in troughs. The waves were symmetrical. Parallel to paleoflow direction. Sharp basal and top boundary.</p>	 
<p>Massive matrix-supported massive gravels (Gmm)</p> 	<p>Gravels (fine pebbles- boulders; variable) in a coarse-sand-pebble matrix. At 2011_10 the bed extended laterally for at least 4 m and was 0.2 m thick. Here the exposure was orientated at 90° to paleoflow. The base of the bed was curved with a sharp boundary that was delimited by a sudden change in grain size to Sm. The inward dip of the sides of the basal boundary towards the centre was 10°. The top of the bed was also curved but with a lesser dip of 4° outwards from the bed centre. Clasts were largest in the middle-top part of the bed consisting of boulders. Clast a-b plane dip varied from 0° to 40°. The largest clasts were arranged in a wavy pattern within the bed, but if cobble-boulder sized clasts were absent the bed is massive. Locally around the largest clasts there were weak concordant structures. At the edges of the bed (lateral) clast a-b plane dipped at a low-angle (<10°) towards the centre of the bed. Max clast size= 270 mm</p> <p>At 2013_1, poorly sorted cobbles-boulders were supported by a pebble matrix. Max clast size was 300 mm. The facies was well-exposed in discontinuous (2 m wide) thick beds (0.68 m - 0.73 m) that were transverse (45-90°) to palaeoflow direction, or less-well exposed (at the base of exposures 2013_1) in longer beds (~10m) in exposures parallel to palaeoflow direction. The thicker beds had erosional bases that were steeply curved to the top of the bed (channel-shaped). The bed shape was asymmetrical with a steeper boundary (dipping inward <85°) on one side than the other (dipping inward <20°). On the shallower side of the curved bed the boundary was delineated by large boulders with a-b planes that dipped 30-35° towards the centre of the bed. Some weak concave-up structures were observed in the deposit shown by the dip of clast visible long-axis concordant with the base of the bed.</p>	

(Table 5.2 continued to next page)

Facies	Description	Example and grain size distribution
<p data-bbox="411 1892 470 2098">Matrix-supported gravel (Gmg)</p> 	<p data-bbox="411 862 534 1836">Gravels (medium pebbles- boulders) supported by a matrix of medium sands-fine pebbles. The precise grain size varied between beds; beds containing a finer gravel fraction contain higher matrix content, while coarser beds have lower matrix content. The internal texture of the deposit was variable.</p> <p data-bbox="566 862 726 1836">The bed boundaries were mainly gradational and curved, although at 2013_2 the beds had sharp curved basal boundaries. Beds ranged from 0.3 m to 1.7 m long and 0.05 m to 0.2 m thick. The thickness: length ratio was 1:85. Here the bed fabric changed from imbrication a-b pebble plane of 10° upstream to horizontal with weakly reversed grading downstream (concordant with the base boundary). Max clast size = 26 mm (outsized).</p> <p data-bbox="758 840 997 1836">At 2013_1 beds had gradational curved boundaries that gave the appearance of reverse grading from the base to the centre to the centre vertical part of the bed, then normal grading in the upper half of the bed. The bottom of the bed was convex-up and the top of the bed was concave up. This gives the bed a lenticular shape (when viewed parallel to paleoflow direction). Bed lengths ranged from 0.84 m to 3.16 m and bed thickness ranged from 0.11 m to 0.45 m. The average thickness: length ratio was 1:7. The boundaries of the bed were determined by an increase in gravel fraction, however in many places the matrix of the bed was the same as surrounding material (Sm). Max clast size: 258 mm.</p> <p data-bbox="1029 862 1308 1836">At 2011_2 the bed was exposed for ~30 m parallel to palaeoflow. Bed thickness exposed was ~1 m. Cobble and boulder sized clasts were in a sand matrix (predominantly m-vc sands and fine pebbles). Clast size ranged from 50 mm -900 mm. Clasts were in trains in planar or wavy pattern within the matrix when parallel to palaeoflow direction (2011_2). This pattern was the same when at 90° to palaeoflow direction. Clasts a-b plane dipped upstream up to 30°, downstream up to 30° or were horizontal. The largest clasts were typically horizontal. The matrix fabric varied vertically and laterally. At the top of the bed the matrix contained wavy laminae (Sw) and planar laminated sands (Sh). The majority of the matrix was massive sands (Sm). The amount of matrix varied vertically and laterally.</p>	  

(Table 5.2 continued to next page)

Facies	Description	Example and grain size distribution
<p>Clast-supported, crudely bedded gravel (Gh)</p> 	<p>Clast-supported pebbles- cobble sized clasts arranged in wavy beds (parallel to palaeoflow) or showing imbrication in tabular beds that thin and fine laterally.</p> <p>At 2013_2 imbrication of pebbles was in an upstream direction up to 30°. Grain size increased towards the centre of the lateral exposure of 3.22 m (parallel to flow direction). Here the bed was 0.41 m thick. At the edges of the lateral extent the bed thinned and fined to 0.08 m thick. The bed was well sorted with a maximum clast size of 31 mm.</p> <p>At 2011_2 the beds were composed of pebbles-cobble sized clasts arranged in a wavy pattern (parallel to paleoflow) with a sand-granule matrix between clasts which is thicker at the top than then bottom of the bed giving the appearance of gradational boundaries. The beds were discontinuous and the clasts on the ends of the bed (upstream and downstream) were matrix-supported. Typically the beds were < 1 m long and 0.08 m thick. Clasts a-b plane dipped upstream (<20°) and downstream (25°), and some were horizontal. The dip varied along the length of the beds, giving the bed a wavy appearance.</p>	
<p>Clast-supported massive gravel (Gcm)</p> 	<p>Gravel beds organised in lenticular patterns with erosional bases which varied in size, dip angle and internal fabric. At 2013_1 the bed was 0.46 m thick, laterally continuous for 31 m parallel to palaeoflow direction. At 2013_2 the bed was 0.2- 0.49 m thick, laterally continuous for >50 m parallel to palaeoflow direction. Within these two exposures lenses were delineated by clast a-b plane orientation and grain size. A layer of massive coarse sands- vf pebbles (0.01 m to 0.12 m thick) was located at the base of each lens. The length of lenses ranged from 0.36 m – 1.08 m and the thickness between 0.05 m and 0.1 m. The thickness: length ratio was variable between 1:6 to 1:10. Some of the lenses were truncated by the erosional base of a lens deposited above. The tops of the lenses were also sharp.</p> <p>Internally, the lenses were composed of poorly sorted pebbles and cobbles. Fabric was massive, inverse-graded or clasts were arranged in concave-up or an upstream-dipping pattern. Structures were shown by a change in grain size and clast a-b plane dip, up to 45° parallel to paleoflow direction. Max clast size = 96 mm</p>	

(Table 5.2 continued to next page)


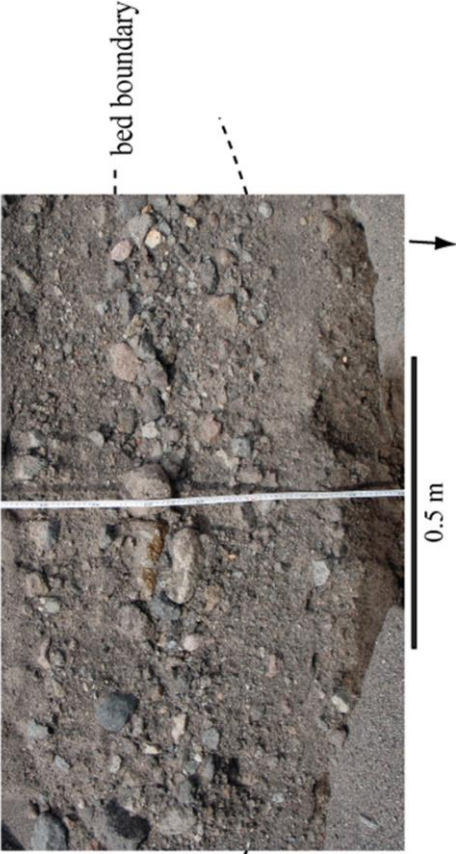
Facies	Description	Example and grain size distribution 2011_1
<p>Inverse-graded clast supported gravel (Gci)</p> 	<p>Description</p> <p>At 2011_1 the inverse-graded well-sorted gravel bed that was matrix-supported at its base and clast-supported at its top. Clast size increased with increased vertical height from the bed base. Max clast size at the base was 30 mm at the top it was 150 mm. The bottom of the bed had a gradational boundary and there was a high matrix content (coarse sand-fine pebbles) that gave the deposit the appearance of being massive. The abundance of matrix decreased towards the top of the deposit.</p> <p>Observed in an exposure orientated 90° to paleoflow at 2011_1. Only 2.5 m of bed length was exposed, but the bed was believed to have extended beyond this, the bed was 0.36 m thick in the centre of the exposure.</p> <p>The curved base dipped inwards to the centre of base of the bed by ~ 10°. The base of the deposit was gradational with an 5m layer. The base of the bed was delineated by the reduction in fine pebbles content; the base of the deposit was ~50% fine pebbles, 50% sands (estimated by eye in field).</p> <p>The top of the bed appeared sub-tabular with the largest cobble-sized clasts orientated parallel with the top of the bed.</p>	

Table 5.2 Descriptions of each facies (see Table 2.9) from field observations of deposits in May-June 2011, October 2012 and March 2013. Images of each facies have been included with a reference to the log location of the photograph. Sand grade facies include the grain size distribution of a sediment sample. The location of samples is shown on sediment logs in Figure 5.5. The x-axis of the grain size plot labels the upper boundary of each grain size division, where *Cl* denotes the boundary between clay and silt, *S_i* denotes the boundary between silt and sand, *S* denotes the boundary between sand and pebbles, and *Pb* denotes the boundary between pebbles and cobble sized clasts. Grain size distribution data (Appendix 2.2ab)

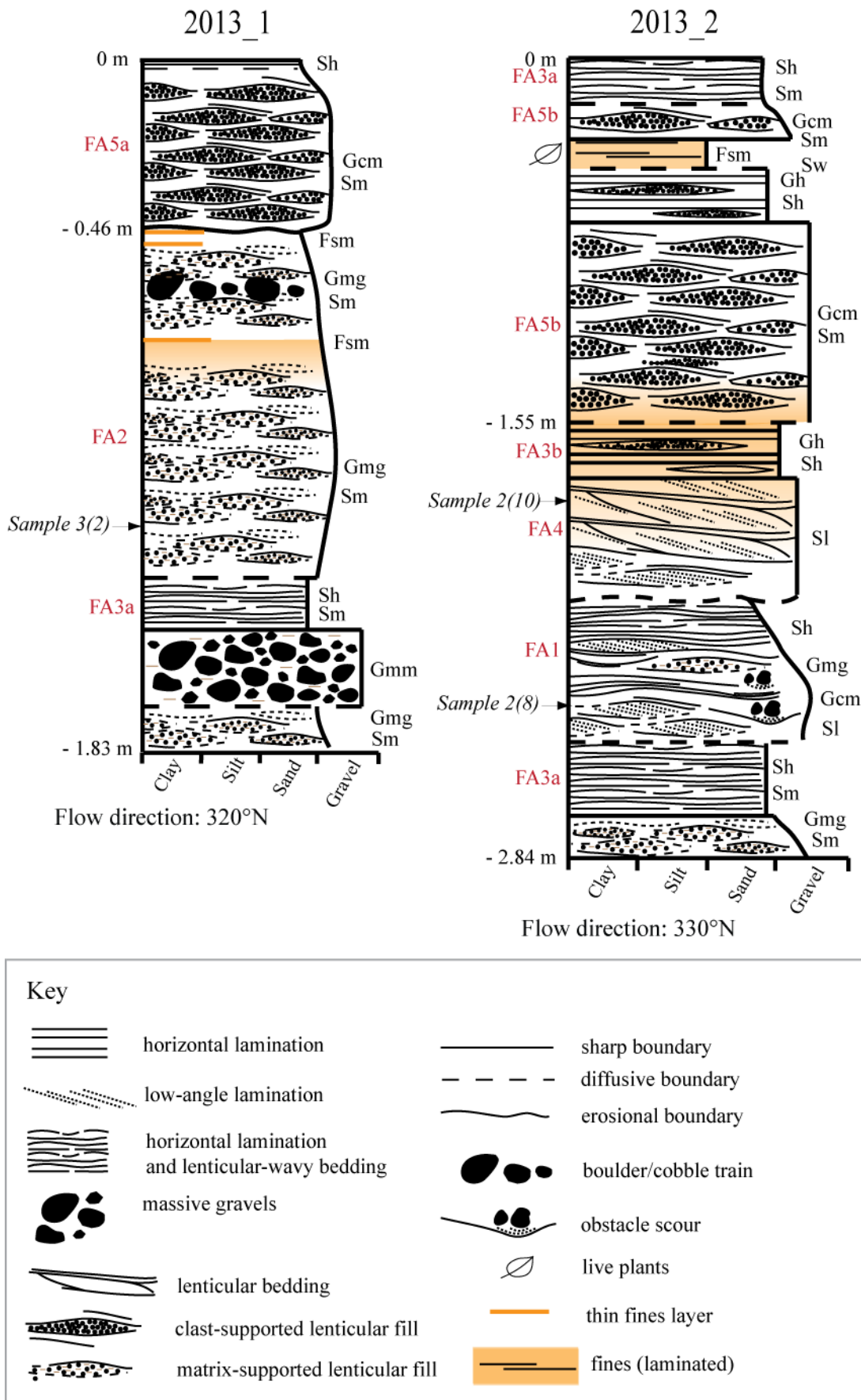
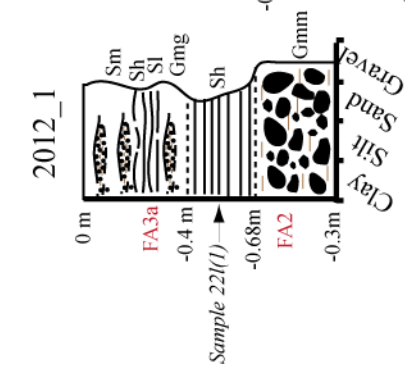
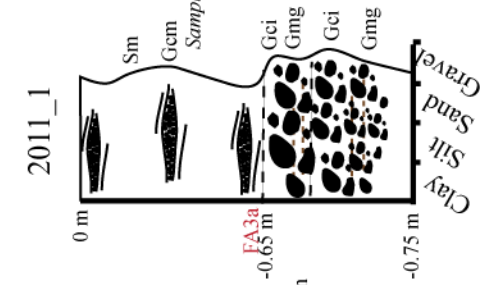
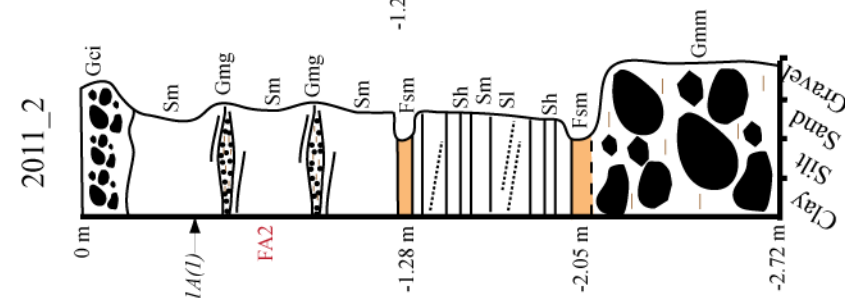
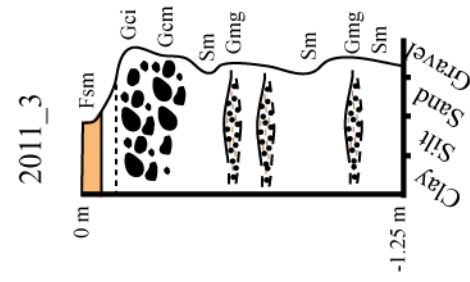
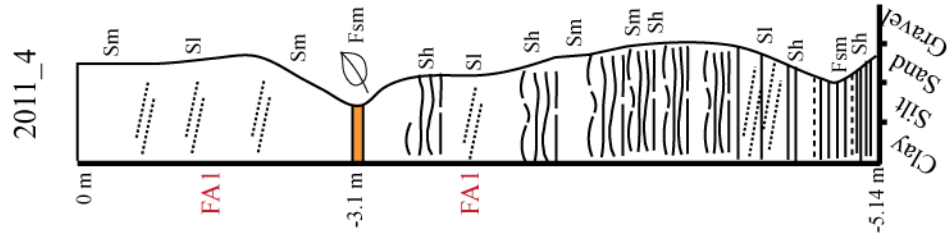
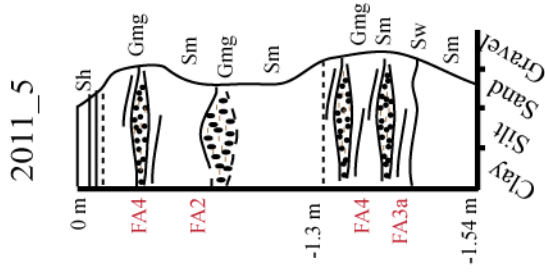


Figure 5.5 (a) Sedimentary logs of two flow parallel sections in Pit2013 (see Figure 5.4 for location). Vertical scale, depth from the sediment surface in March 2013 and ellipsoid heights (UTM 20 N) are included in brackets.



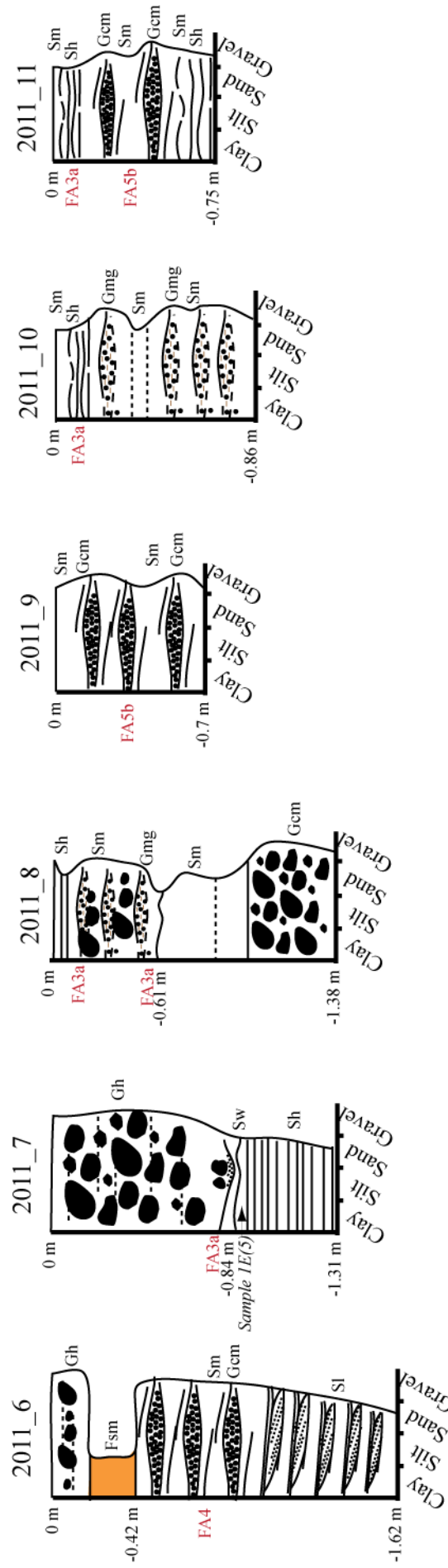


Figure 5.5 (b) Sedimentary logs of two flow parallel sections in Area 1 & 2 (see Figure 5.4 for location). Vertical scale, depth from sediment surface in March 2011 (2012_1 bed surface is February 2012) and ellipsoid heights (UTM 20N) are included in brackets. See (a) for Key

5.5. Facies associations (FA)

The following sections discuss assemblages of facies that were deposited by slightly different processes operating in broadly the same flow conditions. The facies associations do not include all documented facies because some were considered standalone, for example facies Gmm. These are discussed more generally in Section 5.8.

5.5.1. FA1: Dipping sand and pebble beds with pumice clasts

Description

Composed predominantly of low-angle inclined beds of laminated sand and silt (Sl) inter-bedded with low-angle inclined beds of massive pebbly sand (Sm). This facies association was not common in the 2011- 2013 sediment record, and varied in character at different exposures, however FA1 was laterally extensive for over 10 m at every exposure logged. At site 2011_4 (Figure 5.5b; Figure 5.6) and at 2011_2 (Figure 5.5b), thick beds of massive sand (Sm) and planar laminated sand and silt (Sh) were also incorporated in FA1. The combined FA1 at these sites was over 1.5 m thicker than at site 2013_2 (located upstream; Figure 5.5a). The beds have varying low-angle dips, parallel to paleoflow direction and at $\sim 90^\circ$ to palaeoflow. FA1 at 2011_2 was not as vertically extensive (0.5 m thick) and extended laterally for ~ 8 m. FA1 at 2011_4 incorporated root systems of trees at the edge of the valley. The log was measured on the north-side of the valley and dense dry forest vegetation was immediately upslope of the exposure. Boulders were in the deposit between patches of tree roots.

Upstream at site 2013_2, Sl beds (predominantly sands but ranging from silts to pebbles) were in a convex-up structure that was ~ 5 m long and on average 0.8 m thick (Figure 5.7) dipping 14° downstream and 10° upstream. Although the full structure was not exposed, deposition on the upstream end of the structure (beds dipping upstream) was more vertically extensive (both in thickness and number) than on the downstream end. The shift from downstream to upstream dipping beds was obscured by a scour feature (Gmg) that was not part of FA1 (Figure 5.7). Beneath downstream dipping beds of Sl, were beds of Gh containing a relatively high matrix content that was finer than other beds in logged deposits. The beds had curved bases that varied in contact (sharp- gradational) and were ~ 0.8 m long and up to 0.16 m thick. The downstream bed truncated the upstream bed (Figure 5.7). Above these beds a shift from

downstream to upstream dipping Sl was observed creating concave-up forms that were thicker towards the centre than at the edges.

Upstream of the scour feature (Gmg) in the centre of FA1 at site 2013_2, beds of Sl were present with dipping planar beds of outsized clasts (similar to Gh) that were also dipping at a low angle upstream, parallel with finer beds. Over half the clasts were pumice and ranged in size from fine pebbles to 300 mm boulders. Concave-up laminations of sands (Sw), and massive sands and pebbles (Sm) were located at the base and sides of larger clasts. The beds of Sl that dipped upstream appeared to diverge (increase in thickness) with distance upstream. Large scale structures such as that at site 2013_2 were not observed at site 2011_4; here the exposure was not so continuous laterally and the beds were shorter in length and cross-cut one another. Outsized clasts were also absent unless in close proximity to vegetation.



Figure 5.6 Photograph at log site 2011_4 (see Figure 2.18). Deposit contains thick beds of Sm inter-bedded with Sl and Sh. The lower section of deposit also contains beds of Fsm. The deposit incorporates tree roots and boulders in the central upper portion.

Interpretation

FA1 was deposited by flow carrying a load abundant in sand sized sediment. This was evidenced by the thick continuous sand beds at sites 2011_4 and 2013_2, which contained structures indicative of critical to supercritical normal stream flow (see

Table 5.1). Beds and bedsets varied both vertically and between the upstream and downstream exposures. At site 2011_4 structures were less visible because Sm beds were thicker and contained a higher proportion of sand relative to pebbles. This led to less visual differentiation of individual beds. Sl beds were interpreted as antidune origin. The low-angle dip upstream suggested deposition on the upstream side of an antidune during migration (Kennedy, 1960). The difference in character of Sl beds at site 2011_4 and site 2013_2 (see also Figure 5.6 and Table 5.2, respectively) was thought to correspond with the dominance of different depositional mechanisms. The planar laminations of Sl beds at 2013_2 suggest water-surface-waves did not break violently, preserving the layers of the deposit. However the predominance of massive sands and poor clarity of layers at 2011_4 suggests rapid deposition inhibiting preferential settling, i.e. from more violent wave breaking.

The lower sections of FA1 at 2013_2 contained several distinct features including local scour features around single larger (non-pumiceous) clast, and beds of Gh. The largest clasts at the bed base were contained within trough-shaped scours that had eroded into upstream dipping beds of sands (Sl). The Gh beds immediately downstream of this were interpreted to have been formed by water-surface-waves. The clasts were deposited when flow lost energy, and were likely in transport by traction. There was a stronger clast orientation on the upstream side of the pebble-cobble wave. Alexander and Fielding (1997) found that the strong flow over the upstream face of antidunes produced well orientated clasts on the upstream side of the bedform relative to the downstream side. They also found that larger clasts accumulated at the crest of the bedform and lacked strong orientation. While the largest clasts were not necessarily those that were located in parts of the bed which had largest clast dip variation, the sections of bed containing clasts most varied in dip were those immediately downstream of clasts with a common upstream dip. This pattern is suggestive of antidune origin. The matrix content of Gh beds and trough-shaped bases, were indicative of fill deposits from breaking water-surface-waves in the upstream antidune trough. Here material was deposited very rapidly as flow lost capacity and/or competence due to flow unsteadiness under water-surface-waves, resulting in a poorly sorted, relatively structureless deposit. These beds were similar to those observed in flume studies (Alexander *et al.*, 2001; Yokokawa *et al.*, 2000; Cartigny *et al.*, 2014); containing weak concave-up structures. There were also layers of finer sand at the base of the trough fills that were observed by Alexander *et al.* (2001) and interpreted as sediment that had settled from suspension in rapidly decelerating sediment-charged flow as it travelled upstream through the

antidune trough. The length of the downstream trough that was not truncated was 0.9 m, equating to flow velocities of 1.2 m s^{-1} (using Equation 4.4). This velocity was low relative to observations at Site A during the October 2012. The scour structure upstream of these troughs may have been incorporated in the wave train, and it was possible that the larger clast (30 mm) in the scour provided a bed defect on which an undular hydraulic jump formed.

The upper section of FA1 at site 2013_2 was more difficult to confidently interpret. Beds of S1 dipped upstream, which was suggestive of antidune origin (Table 5.1). However, if the upstream dipping beds were from deposition on the upstream face of a migrating antidune (in common with structures at Buschhaus fan; Lang and Winsemann, 2013) this would infer very long antidunes and therefore very high velocities, which does not correspond with the sediment grain size. If the beds represented deposits from a wave train migrating upstream, based on Clifton's (1990) model, the beds should dip downstream and contain upstream dipping laminae. One hypothesis is the upstream dipping beds may be part of a low-amplitude chute-and-pool or cyclic step. This theory is based on similarities to the documented internal architecture of chute-and-pools and cyclic steps by Cartigny *et al.* (2014) in sand-sized sediment in the flume. Several key features of the deposit support this hypothesis: (1) gently dipping upstream beds that extend for long distances, (2) a sharp and steep erosional boundary immediately downstream of the upstream dipping beds that cross-cut them (see Figure 5.7), (3) massive lenses with trough-shaped erosional boundaries downstream of the sharp steep erosional boundary and (4) the presence of larger clasts (some pumice) in upstream dipping beds at the base of the upper section of FA1 (although vertically midway up dipping sand beds) that were deposited from traction, in common with 'dropout armour' (Foley, 1977). Based on extrapolation of experimental data (Guy *et al.*, 1966; Mastbergen and Winterwerp, 1987; Alexander *et al.*, 2001; in Cartigny *et al.*, 2014) for median particle diameters of 0.5 mm (median grain size sample 2(10)) in shallow flow (0.06-0.1 m), chute-and-pools form in velocities between 2 and 2.5 m s^{-1} , and cyclic steps at higher velocities. These values were not unrealistic for flow in the Belham River Valley. Furthermore estimates of flow velocity from trough lengths deposited in the lower part of FA1 fall within the range estimated from experimental data for antidune formation.

In the absence of flow measurements and more laterally extensive exposure it was difficult to differentiate chute-and-pool from cyclic step deposits. Upstream

dipping beds of Sm may represent rapid fall-out directly from suspended sediment downstream of a hydraulic jump. Observations in the flume identified massive grading to laminated beds (formed by traction carpets) downstream of a cyclic step hydraulic jump (Cartigny *et al.*, 2014). This description is similar to the inter-bedding of Sl and Sm observed. Upstream divergence was observed in some Sl beds and this corresponds with observations from the flume of deposits upstream of a hydraulic jump; interpreted as minor aggradation from continuous traction. The thickness of Sl beds was controlled by sediment from the hydraulic jump; hydraulic jump migration was step-wise in chute-and-pool structures because of local breaking antidunes downstream of the hydraulic jump compared with cyclic steps. This infers that beds of more regular thickness may be associated with cyclic step formation, however other factors such as fluctuations in flow suspended sediment upstream of the jump must also be considered, highlighting the complexity of bed thickness: aggradation rate relationships.

Comparison of the deposit at 2011_4 with that at 2013_2 suggests that FA1 at site 2013_2 may have been a much thicker deposit than what is preserved beneath the deposits of subsequent flows. Preservation at site 2011_4 was extensive and it is likely that this was because of its peripheral position on the north-side of a wide section of the lower valley (see Figure 2.18). It was not possible to determine if this deposit was formed by one or multiple similar lahars, although the grain size and facies were similar through the succession, there were erosional structures and clear boundaries within FA1 that suggested changes to or breaks in flow. At Site 2011_4 these were bedsets of Sh approximately halfway up the deposit. However at Site 2013_2, these features were erosional trough fills and scours around large clasts that have eroded into upstream dipping bedsets (Figure 5.7). The erosional upstream dipping base of FA1 at site 2013_2 was suggestive of chute-and-pool or cyclic steps, indicating that with changing flow velocities (and Froude numbers) bedforms transitioned between planar beds and antidunes (lower deposit, see Figure 5.7 and FA3a), to chute-and-pools and/or cyclic steps, and back again. This created a vertical succession of upper flow regime bedforms that were relatively well preserved in the sediment record because deposits extended to the valley-floor edge and were formed by highly aggrading flow. Given the pumice clasts, sediment composition and availability, it is likely that FA1 was deposited during or shortly after deposition of primary material in the Belham Catchment during Phase 5 volcanic activity. The presence of pumice with other clasts thought to be deposited by traction suggests that pumice clasts became waterlogged and sank in flow. The density of pumice clasts of ~60 mm more than doubles (to above the density of water), when

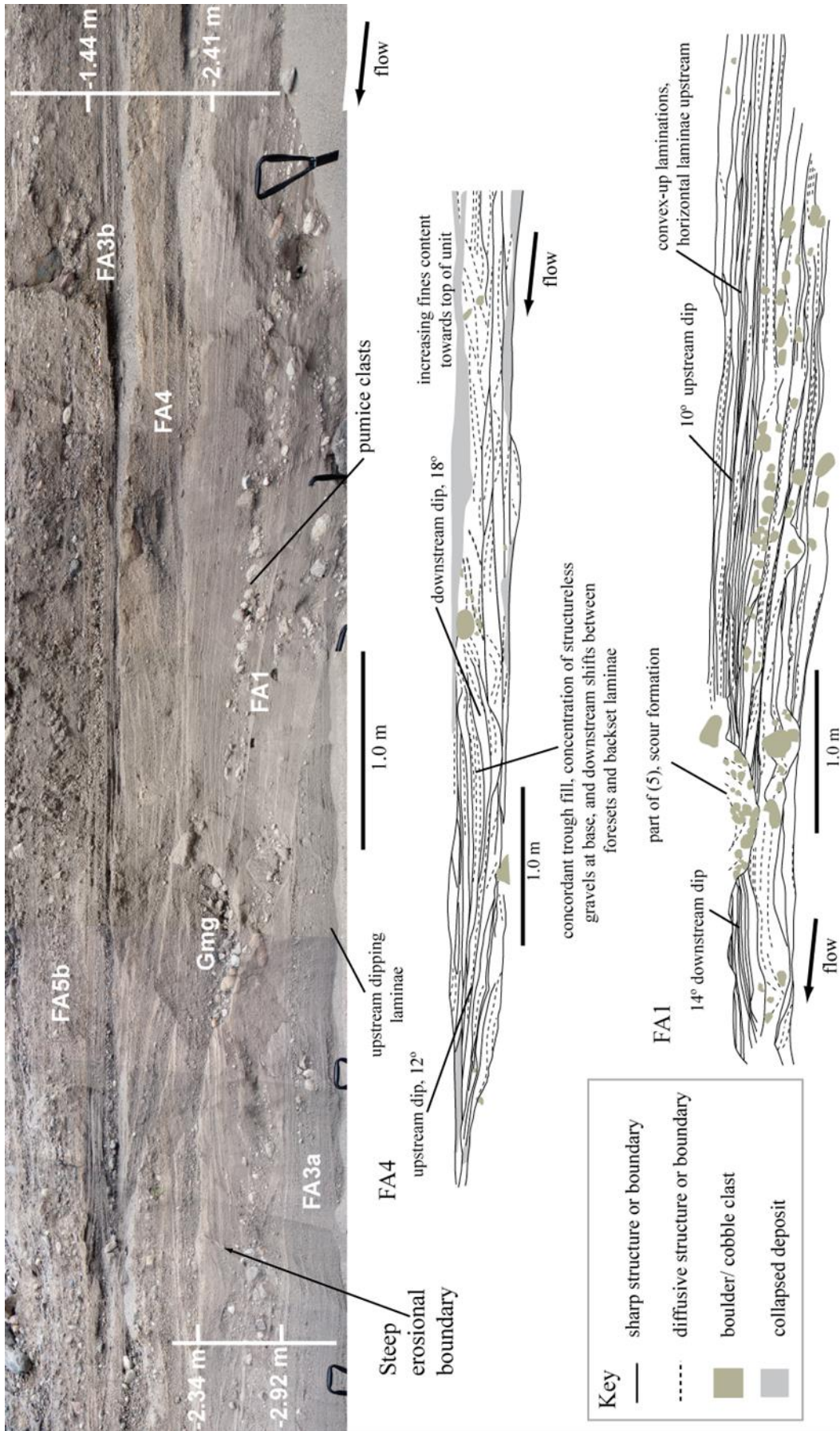


Figure 5.7 Annotated photograph of deposit at 2013_2. Beneath line drawings of main sedimentary structures in the deposit.

clast vesicles fill with water (Manville *et al.*, 2002). The rate at which the clast becomes saturated depends on its volume, vesicularity and temperature. Cold pumice clasts of ~100 mm diameter (as observed in FA1, site 2013_2, Figure 5.7) may take in the region of 10000 hours to sink (saturate) in flow (based on settling experiments undertaken on Taupo pumice, Manville *et al.* 2002). However, hot coarse pumice clasts may sink immediately when immersed in water because rapid cooling and the contraction of interior gases draw water inwards (Whitham and Sparks, 1986). This suggests pumice clasts in the deposit at site 2013_2 were mobilised by flow when they were hot, shortly after emplacement by primary volcanic processes. The elevation of the base of the pit at 2013_2 is within 0.1 m of the elevation of the valley floor in June 2010; this suggests that FA1 was deposited by a flow after the June 2010 survey, but before March 2011. This is discussed further in Chapter 6.

5.5.2. FA2: Massive sand beds containing matrix-supported gravel lenses

Description

FA2 was composed of thick beds of massive to planar laminated sand (Sm, Sh) that contained lenses of matrix-supported gravel (Gmg). The gravel lenses had gradational boundaries with a matrix sand that was similar to that in the surrounding Sm and Sh beds. At site 2013_1 an exposed unit of FA2 was 1.37 m thick (Figure 5.5a) and was laterally extensive for 62 m of exposure which also changed orientation. Gravel lenses at this site varied from 0.84 m to 3.16 m long and were 0.11 m to 0.45 m thick with high thickness:length ratios (see Table 5.2). The coarsest material was in the centre (vertical) part of the bed, therefore the bottom of the bed was reverse-graded and the top of the bed was normal graded. The largest clast in the Gmg beds were 258 mm; boulders were also present in Sm beds. The lenses were separated by 0.01 to 0.04 m thick beds of Sh or thicker (~0.1 m) beds of Sm. The Gmg bed at the base of 2013_1 was distinct from other beds because it contained much larger clasts (cobbles to boulders) and most clasts a-b plane dipped upstream (Figure 5.18). Other beds of Gmg contained clasts with more variable dips. This type of deposit was not seen within FA2 at other downstream locations.

FA2 was not well exposed at site 2012_1 (Figure 5.5b) and was identified by the gradational upper boundary between beds of Gmg and Sh, and the high matrix content between clasts. At site 2011_2 FA2 had a higher Sm component in a 1.08 m thick

deposit (Figure 5.5b). The Gmg beds were smaller both in thickness, length and clast size; ranging from 0.35 m to 1.4 m in length, 0.02 m to 0.15 m in thickness and with a maximum clast size of 45 mm. Outsized cobble sized clasts were present in the Sm beds. The sites 2013_2, 2012_1 and 2011_2 were all located parallel to paleoflow direction based on interpretation from aerial and satellite photographs of bed surface morphology (Section 2.5.1.2). Site 2011_5 was transverse to palaeoflow by between 45° and 90°. It was difficult to estimate paleoflow direction because the site was located in a central section of valley floor where channel boundaries altered between lahars. Furthermore beds in the exposure were either massive in texture or had similar three-dimensional internal architecture. FA2 at site 2011_5 (Figure 5.5b) was composed of longer, thicker and coarser lenses (Gmg) at the base of the deposit separated by thinner beds of Sm (0.02 m to 0.05 m) and smaller finer beds of Gmg at the top of the deposit separated by thicker beds of Sm (~0.1 m). The largest clast in the coarser Gmg beds was 90 mm.

At site 2013_1 there was a sharp boundary between FA2 and FA3a at the base of the deposit, a bed of Sh within the deposit at 8.98 m (see Figure 5.5a) and a gradual shift from FA2 to FA5b. At site 2012_1 the boundary between FA2 and FA3a was gradational. There was a clear boundary at the base of FA2 at site 2011_2, marked by a thick (0.12 m) bed of Fsm. The top of the deposit in this location had been partially reworked by commercial sand extraction. At site 2011_4 the bottom of FA2 had a gradational boundary with FA5a and FA3a depending on bed location.

Interpretation

Similarly to FA1, FA2 was deposited by a flow carrying a load high in sand sized sediment. The inter-bedded gradational relationship of facies Gmg with facies Sm confirm their common flow origin. It was not clear at any location, if the bedset was deposited by one lahar or multiple small-moderate events, because gradational boundaries may represent a reactivated bed surface with mixing, and tabular beds of sands within the bedset may have been deposited during waning flow (Vazquez *et al.*, 2014). Examples of FA2 contain large parts with little variation in the grain size of Sm or the thickness in Gmg beds, suggesting a single event was responsible. If the deposit formed from multiple lahars those flows must have been similar and undergoing rapid fluctuations in velocity or sediment grade flux to generate the vertical alternations in grain size.

There are three plausible interpretations by comparison with studies of sheetflood deposits and observations of the October 2012: (1) deposition by traction carpet, (2) deposition by breaking antidunes, or (3) deposition by roll waves; or by more than one of these mechanisms operating synchronously. From the high sand content observed in the flow, massive fabric of the deposit and gradational boundaries between Gmg and Sm, it is inferred that the three hypothesised mechanisms were occurring during flow with a high suspended sediment concentration, in either: a vertically stratified flow (1, 3), streamflow (2, 3) or hyperconcentrated flow (all). Traction carpets are highly concentrated bedload layers that developed beneath and are driven by shear stress from a more dilute turbulent overlying flow, gravity and inertia (Sohn, 1997). They form in flows with a high sediment load and aggradation rate, or in those undergoing rapid lateral expansion (Todd, 1989; Sohn, 1997). Vertical flow stratification is driven by the segregation of particle size, shape and density within flow (Fagents *et al.*, 2013). Deposits from traction carpets are variable in texture but include matrix-supported, massive beds and inversely graded beds (Benvenuti and Martini, 2002), in common with Gmg. Sequences of Gmg and Sm/Sh may be interpreted as deposited by a series of flood waves with a non-cohesive debris flow front, hyperconcentrated body and streamflow tail (Sohn *et al.*, 1999). Under this hypothesis Gmg beds were deposited as the front of a shallow flood wave slowed due to energy loss by friction at the bed, the interface between Gmg and Sm/Sh formed as the flow behind the coarser front overrode this deposit, and Sm beds represented suspended sedimentation from the flood wave tail (Lirer *et al.*, 2001). While most Gmg beds were massive, a bed at the base of 2013_1 contained upstream dipping clast fabric (Figure 5.8). The dipping clasts have been associated with piecemeal deposition by either a hyperconcentrated or debris flow over a period of time (Vallance and Scott, 1997; Jakob and Hungr, 2005). Evidence based on careful measurement of debris flow clasts have shown that some deposits exhibit alignment and imbrication of elongate clasts, suggesting incremental accretion (Vallance, 2000).

The lenticular geometry of Gmg beds and their discontinuous nature brings into question the traction bed hypothesis, deposits which were typically described as laterally extensive, and parallel-planar to slightly wavy or low angle (Cornwell, 1998; Carling *et al.*, 2009a;b; Carling, 2013). An alternative hypothesis is deposition by water-surface-wave trains. Blair (2000) presented a model for planar gravel couplets inter-bedded with low-angle upstream dipping sands and fine gravels. The model was based on antidune cyclicity (see Figure 5.2); finer beds were deposited by upstream

migrating antidunes, while the coarser couplets represented violent breaking of water-surface-waves that destroyed antidunes (that formed under the wave) and redeposited material parallel to the bed, with some preferential deposition by grain size as turbulence abated. A sharp bed contact existed between coarser and finer material associated with the breaking wave mechanism, and this was linked with differences in deposition rate; rapid during washout and sustained during suspension fall out of finer material (Blair, 2000). FA2 had distinct differences to deposits discussed by Blair (2000) however a similar interpretation of deposit origin is adopted here. The key differences between deposits including sharp (gradational) boundaries, grading and imbrication (massive), were attributed to differences in flow sediment load. Poorly-defined depositional surfaces, poor sorting, structureless and diffusely stratified deposits (Postma *et al.*, 1988; Arnott and Hand, 1989) have been associated with high suspended sediment concentrations and limited clast segregation by traction (Duller *et al.*, 2008). Breaking waves have been observed in hyperconcentrated flows (Pierson and Scott, 1985; Dinehart, 1999; Cronin *et al.*, 1999, 2000), with shifts from stationary or upstream migrating to breaking water-surface-waves corresponding with increased suspended sediment concentration and decreased flow discharge (Simons and Richardson, 1963; Dinehart, 1999). Based on adaption of Blair's (2000) model to flows containing higher concentration of suspended sediment, it is suggested that beds of Gmg were formed by the reworking of antidunes during wave breaking, and thick beds of Sm deposited by gradual suspended sedimentation. The presence of Sh beds with Sm beds suggests that planar beds form between antidune cycles.

The third hypothesis for FA2 formation draws on observations from the October 2012 lahar of frequent bores, attributed to roll waves formed during unstable flow (defined by the Vedernikov number, Section 4.4.2.1). During the passage of bores with apparently turbulent fronts, large cobbles and boulders were seen rolling and bouncing within the front and directly behind it. These large clasts came to rest both at the edges and in the centre of channels. Channel bed surface grain size was not observed during the flow however surveys after the lahar showed that larger clasts (>0.1 m) were buried by differing amounts of sand-medium pebble sized material arranged in elongate trains around the larger clast. In vertical section these deposits presented as oversized clasts with differing local erosional structures around the clasts, formed by scour (Mather and Hartley, 2005). In FA2 at 2013_1 oversized clasts were located within Gmg beds. The visible long axis of clasts showed differing dips orientated parallel, at 90° to and at 30° to horizontal; some were surrounded by clear erosional scours, and others were within a

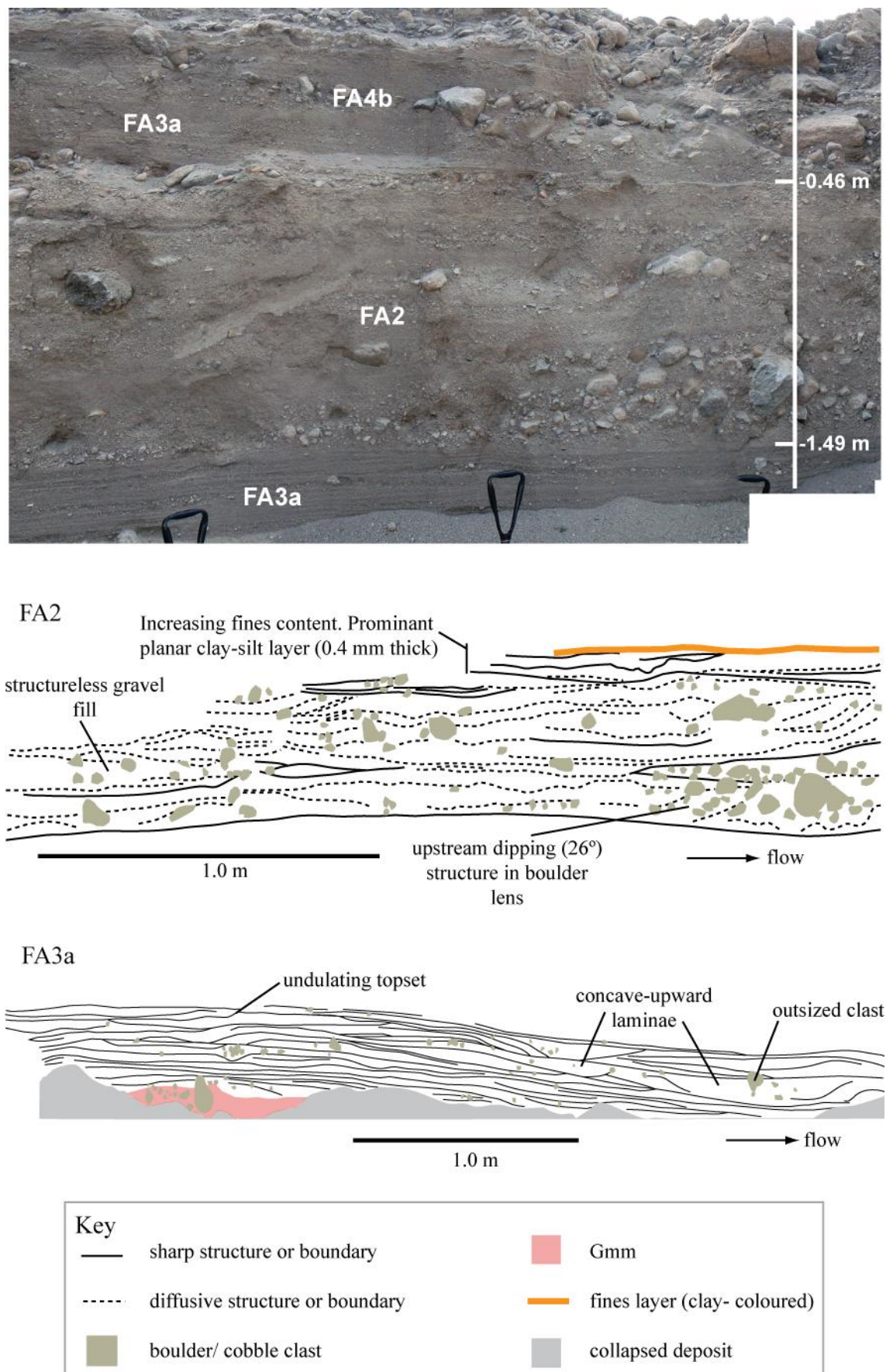


Figure 5.8 Photograph of 2013_1, showing the position of FA2 within the vertical deposit. Beneath, architectural diagrams show the main structures within the deposit, discussed in Sections 5.5.2 and 5.5.3.

massive sand-gravel deposit characteristic of Gmg. In this interpretation, inception of large clasts by bores mobilised clasts as bedload short-distances downstream (as observed in Section 4.4). Beds of Gmg formed by combination bedload and saltation sedimentation during the passage of the bore, while beds of Sm during the suspended sedimentation in wake of bore during rapid flow deceleration. The gradational boundaries between beds, and the high proportion of sand matrix between clasts represented overlap of sedimentation processes at the turbulent bore, and a rapid shift to predominantly suspended sedimentation. Roll wave formation was dependent on channel geometry, roughness and flow Froude number. The thickness of Gmg beds and lenticular orientation suggest shallow flow in a wider channel, conducive to the development of flow instability and roll waves.

5.5.3. FA3: Inter-bedded planar sands and pebbles

This facies association was divided into two FA3a and FA3b. Both types of deposit were thought to be formed by the same process but in flow containing different compositions (grain size and amount) of suspended sediment.

Description

FA3a was composed of inter-beds of planar laminated sands (Sh) and sub-planar lenticular beds of massive coarse sands and pebbles (Sm). The deposit was relatively common in exposures between 2011 and 2013 but typically did not occur in thick sections. At site 2013_1, the deposit was 0.2 m thick (Figure 5.5a) and extended for 8 m laterally parallel to palaeoflow. Figure 5.18 shows part of the deposit at this site and the variation in thickness of Sm beds, between 0.01 m and 0.053 m. Bed length ranged between 0.26 and 2.21 m. Internally most coarse Sm beds were massive and composed of sands, although in the thickest beds larger pebbles dipped inward towards the centre base of the bed creating concave-up structures. Beds of Sh were under 0.02 m thick. Most beds were planar but some dipped at a low-angle as coarse Sm beds beneath thinned out. Beds near the top of the deposit at 2013_2 contained several discrete waveforms that were 0.08 m long and symmetrical (Figure 5.7).

FA3a was identified at seven other log sites in the valley 2012_1, 2011_1, 2011_5, 2011_7, 2011_8, 2011_10, 2011_11 and 2013_2. The vertical thickness ranged from 0.05 m to 0.45 m and the lateral extent from 2.3 m to 8.2 m. The thickness of Sh and coarser Sm beds were similar to site 2013_1 but coarse Sm appeared to

contain more sand-sized sediment to the proportion of pebble-sized clasts at sites downstream of pit2013. The length of coarse Sm beds could not always be ascertained because of the limits of the exposures; however based on fully visible beds of coarse Sm, the high thickness: length ratio of lenses at site 2013_1 was also observed in other locations including at exposures transverse to palaeoflow direction. The boundary of this deposit with other facies associations and its location in the vertical succession varied between locations.

FA3b was composed of inter-beds of planar laminated sands (Sh), massive coarse sands and pebbles (Sm), sub-planar lenticular beds of massive sands and pebbles (Sm) and imbricated clast-supported pebbles in planar beds (Gh). The deposit was only observed at site 2013_2 (Figure 5.5a) but was laterally extensive at this site for over 100 m, with a maximum thickness of 0.2 m. The base of the deposit contained a one to two beds of coarse Sm which were up to 35 mm thick in the middle of the bed, thinning upstream and downstream of this point to 5 mm. The bed contained pebble sized clasts that were matrix-supported in the thickest part of the bed but clast-supported in the thinner sections (Figure 5.9). The beds were 0.4 m to 1.5 m in length; thinner beds were shorter. Coarse beds of Sm were inter-bedded with fine beds of Sm that were ~3 mm thick. The fine Sm beds could be traced tens of metres laterally in the deposit. Above this bedset were inter-beds of coarser beds of Sm. The thickness of finer Sm beds did not vary; beds of coarser Sm beds were between 6 to 8 m thick and were laterally extensive for tens of metres. There was a distinct colour change from grey at the base to light-brown at the top of the bedset. At the top of the deposit was a bed of Gh, that was 2.21 m in length and up to 0.05 m. Composed of clast-supported coarse pebbles that dipped up to 30° upstream, the centre of the bed contained very little matrix; this part of the deposit may be described as open-framework. The upstream and downstream edges of the bed were thinner and contained fine-medium sized pebbles and a small amount of sand matrix. The bed was located between two 0.3 m thick beds of Sm; there was a sharp contact between Gh and the Sm bed beneath, but the upper contact of Gh with the second Sm layer was gradational. The Gi bed was only present at the log site shown in Figure 5.9, and did not occur elsewhere within the laterally extensive FA3b deposit in this location.

Interpretation

FA3a and FA3b are interpreted as upper stage planar beds deposited during flows of different magnitudes with different sediment load compositions. Upper stage

plane beds are stable under upper-flow regime conditions (Simons and Richardson, 1960). Their formation has been observed between Froude numbers of 0.8 and 1.3 (Bridge and Best, 1997). Parallel lamination forms by grain segregation over low-amplitude long wavelength bed waves (Cheel, 1990a; Bridge and Best, 1992). Laminae thickness is related to the height of its formative bed wave, and in turn the rate of bed aggradation (Yokokawa *et al.*, 2007); lateral stream-wise variation in thickness reflects variations in trough elevation in response to changing flow conditions (Bridge and Best, 1997). Lamina sequences are thought to result from turbulent bursts and sweeps, which sort and deposit grains, and drive bed wave migration (Cheel and Middleton, 1986). Observations from the October 2012 lahar suggested that upper stage plane beds were deposited in multiple channel sections in all flow stages, because flow rapidly shifted in criticality locally in space and time (Section 4.4). However the deposits formed in these conditions have low preservation potential because of reworking by breaking water-surface-wave trains and the bores. Deposits were only likely preserved during aggrading flow, in the waning stages of a lahar or by flow deceleration in flow with a high sediment load (Russell and Arnott, 2003).

Variations in the definition of laminae have been related to deposition rates (Yokokawa *et al.*, 2008); whereby sharply defined laminae represent low rates of bed-aggradation, while gradational structures were deposited at higher rates of bed aggradation (Arnott and Hand, 1989; Yokokawa *et al.*, 2005). FA3a (Figure 5.18) was interpreted as originating from flow with a higher aggradation rate than FA3b (Figure 5.9). The two inter-bedded facies comprising FA3a, Sm and Sh, suggest that flow competence and/or capacity varied cyclically. In coarser sediments UPSB stability decreases (Fielding, 2006), because as grain size increases, near-bed turbulence generation is enhanced, and bed waves develop in height in response to increased erosion in troughs (Bridge, 2003). The lenticular form of coarse Sm beds and their internal massive texture suggest formation by small water-surface-waves that wash out due to fluctuations in flow, resetting the planar bed. The variability of lenticular length suggests that bed waves persisted for different periods of time or that the magnitude of flow fluctuation varied. If the length of coarse Sm beds corresponded to trough-fill geometry of the bed waves (and therefore bed wave length), mean flow velocity is estimated to range between 0.6 m s^{-1} and 1.86 m s^{-1} using Equation 4.4. These velocity estimates correspond with flow observations from the small channel at Site A and during waning flow between flow peaks in larger channel at Site A during the October 2012 lahar (Section 4.4.2.2). Bed length of coarse Sm in FA3a varied between 0.26 m

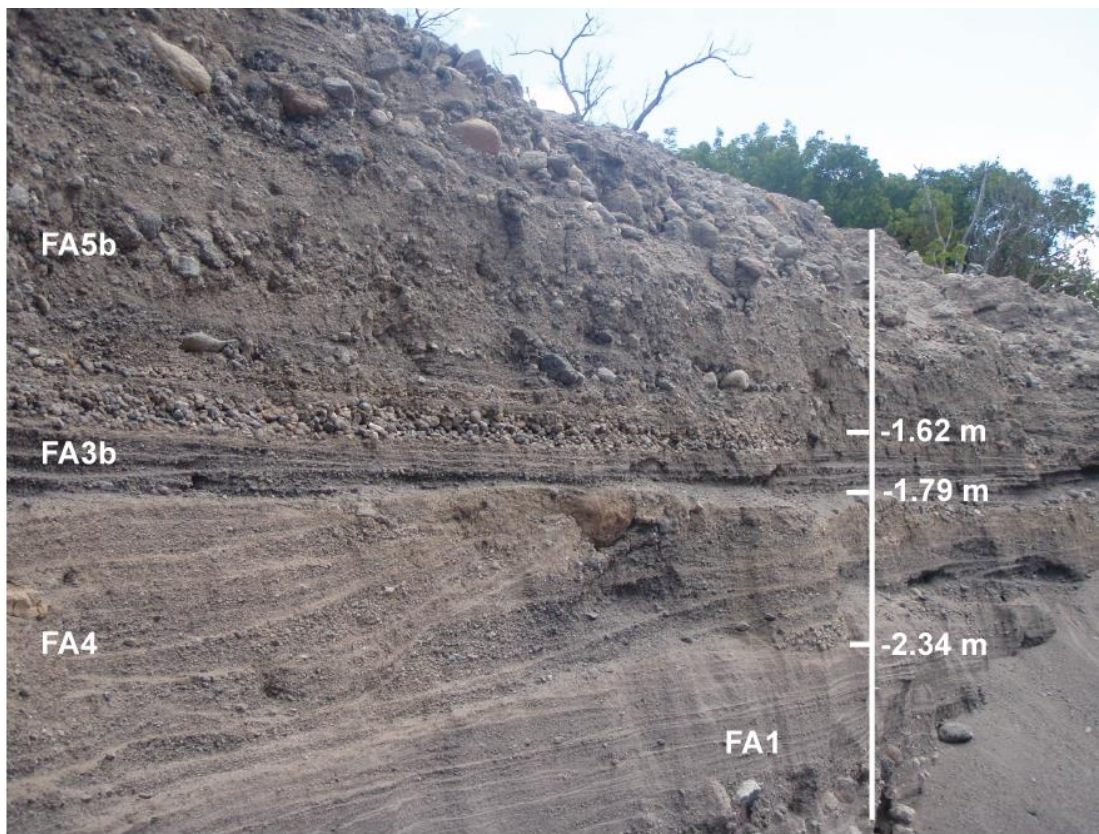
and 2.21 m (Table 5.2) across nine sites suggesting the preservation of waning or low flow deposits at different sites across the valley. The consistency of the bedset vertically at all locations suggests it was deposited by a single flow, but it may have been deposited by sequential small flows of similar character.

FA3b (Figure 5.9) is interpreted to have been deposited by the same mechanisms as FA3a but in flow that was either carrying a lower suspended sediment concentration than that depositing FA3a, or in an environment with less silt-sand sized sediment available for transport. The sequence of inter-bedded coarse Sm and fine Sm, shifting vertically to Sh and Gh, overtopped by Sm, suggests that FA3b was deposited by flow(s) fluctuating between conditions pertaining to antidune formation and then upper-stage-planar-beds. The Gh bed may have been formed by the gradual transport and deposition of pebbles in low flow conditions. The bed was likely to have formed around a downstream bed defect that reduced flow velocity causing competence loss and particle freezing. The open framework texture of the bed and Sm bed above suggests that flow rapidly shifted from this channel location or ceased completely, depositing a thin bed of finer material above Gh.

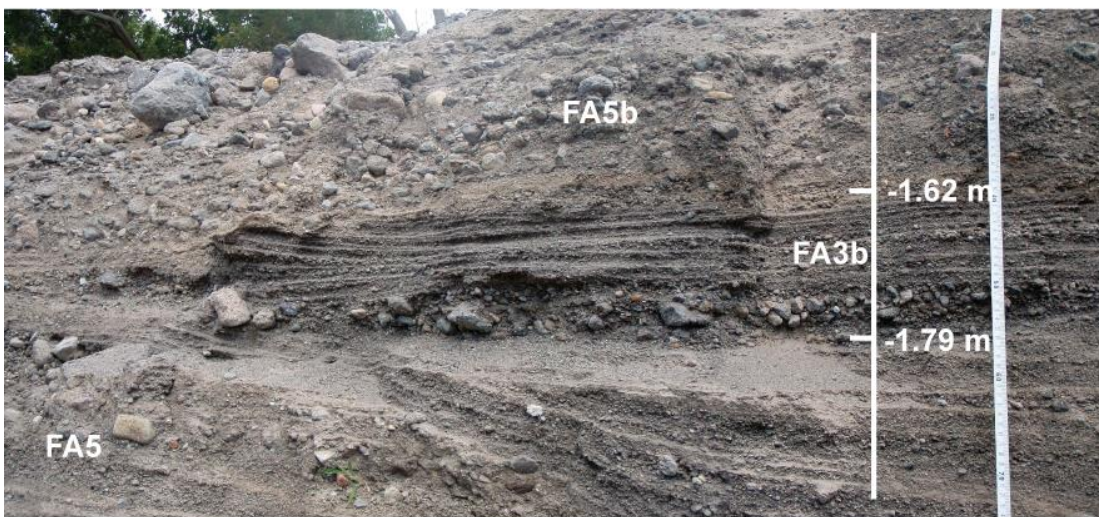
5.5.4. FA4: Dipping sand and pebble beds in planar and trough bedsets

Description

FA4 was composed of sands and pebbles that dipped at a low angle upstream internally within a bed that was planar to sub-planar dipping at a low angle downstream (Sl); inter-bedded massive sands and pebbles (Sm, Gmg) that were parallel to the base and top of Sl beds. These inter-beds (Sm and Gmg) were also arranged in ~3 m long trough shaped structures at site 2013_2 (Figure 5.7). Facies combinations characteristic of FA4 were identified at other log sites (2011_5 and 2011_6, Figure 5.5b) which included sections transverse to flow, however the deposits were not well exposed at these locations and larger scale structures were not visible. At site 2013_2 (Figure 5.5a), planar inter-beds of Sm and Sl were 0.4 m thick and were laterally extensive for 3.5 m; it was probable that the beds extended further than this however they were covered by piles of debris (shown in Figure 5.9). The beds of Sl varied between 0.11m and 0.18 m thick and had a median grain size of 1mm. The bed contained weak laminations that dipped 8°-10° upstream. The colour of the bed varied from grey to light brown both vertically and laterally. The Sm beds were ~ 1.2 mm thick and orientated with the same



(a)



(b)

Figure 5.9 Example of FA3b within 2013_2. FA3b contained inter-beds of planar laminated sands (Sh), massive coarse sands and pebbles (Sm), sub-planar lenticular beds of massive sands and pebbles (Sm) and imbricated clast-supported pebbles in planar beds (Gh).

downstream dip as the S1 beds (see Figure 5.7). The base of the bedset was erosional and trough-shaped scour fills (Gmg) of different sizes were present. The largest had a steep 40° upstream side and a slightly shallower 30° downstream side, was 0.88 m wide and 0.2 m deep. Internally the trough was filled with normal graded gravels; clast a-b plane in the upstream part of the fill dipped steeply downstream at angles of 40°. Upstream of the scour the bed was horizontal and a large cobble (160 mm) was located on the brink of the scour (Figure 5.7). Downstream of the scour a bed of S1 dipped upstream at a low angle. The scour and this bed were continuous in grain size and texture. Above this bed were downstream dipping inter-beds of S1 and Sm.

Inter-beds of Sm and Gmg were organised in a larger scale trough-shaped structure in the deposit at site 2013_2, downstream of planar beds described above. The upstream side of the trough shaped bedset dipped 18° downstream and the downstream side of the bedset dipped 12° upstream. Individual beds of Gmg were lenticular and organised within the trough-shape bedset in a series of concave-up layers; lenses were truncated in the bottom of the trough. Sm beds were parallel with the boundaries of Gmg, and did not alter in thickness. Laminae deposited concordant with the base of the bed were present in the Gmg beds at the upstream end and top of the trough bedset. Sediments dipped upstream within the Gmg beds at the downstream end of the trough, and contained the largest clasts of the bedset. Two lenticular beds of similar thickness (0.11 m) and length (1.18 m) that dip upstream are stacked on top of one another at the downstream end of the trough; these were the longest dipping beds in the sequence.

Interpretation

FA4 at site 2013_2 was interpreted to have formed under upstream migrating water-surface-waves and upstream migrating hydraulic jumps. The inter-beds of Gmg and Sm that together dip at a low-angle downstream and contain low-angle upstream dipping laminae (GSli) were characteristic of the translent strata model produced by Clifton (1990) to illustrate upstream migration of antidunes under aggrading conditions (Figure 5.3). Upstream dipping laminae (Type 2 structures) were thought to be less readily preserved because they were formed during the growth stage of the antidune (see Figure 5.2B). Based on Clifton's (1990) model the downstream dip of the bed and more specifically beds of Sm (Type 1 structures) were formed at the erosional antidune trough as it progressively migrated upstream overriding beds of S1. Based on this model the length of laminae in S1 may be related to antidune wavelength; the mean length of laminae in the cross-set is related to wavelength by the ratio 0.4 to 0.6: 1 (based on data

from Barwis and Hayes, 1985; Langford and Bracken, 1987; Alexander *et al.*, 2001; Bridge, 2003). This relationship has not been well tested in the field, however provides an estimate on antidune wavelength here that is useful in palaeoflow reconstruction. The mean laminae length in the cross-sets was 0.24 m suggesting antidune wavelength was 0.4 m to 0.6 m. From these measurements, mean flow velocity may be estimated using Equation 4.4; 0.79 m s^{-1} to 0.97 m s^{-1} and flow depth between 0.13 m to 0.15 m. Based on these estimations and the character of this part of FA4 it is suggested that the bedset formed under a train consisting of at least five water-surface-waves that migrated at least four metres upstream (from exposed deposit at site 2013_2).

The water-surface-waves (described above) formed upstream of a scour feature that was interpreted as a chute-and-pool (see Figure 5.7). The steep upstream side of the scour and downstream dipping clasts at this end of the trough fill were formed by erosion as the hydraulic jump migrated upstream (Cartigny *et al.*, 2014). The downstream dipping bed of S1 and clasts within the downstream end of the trough fill were deposited rapidly both by traction (large pebbles-cobbles) and suspended sedimentation (S1 bed). The deposit beneath the scour (FA1) contained cobble sized clasts in trains and in clusters (Section 5.5.1). Based on the geometry of water-surface-wave trains upstream and the texture of these beds it was likely that the coarse clasts in the scour fill downstream were from the lower deposit as the hydraulic jump excavated and reworked the material. The chute-and-pool formed just downstream of the large cobble sized clast at the brink of the jump (Figure 5.7), and it was likely that acceleration of flow on the downstream side of this clast may have enabled the transition to chute-and-pool formation. The chute-and-pool stopped migrating upstream when it reached the large clast, suggesting that the position of the clast limited migration of the jump. Flow deceleration would lead to a reduction in Froude number and weakening of the hydraulic jump (Bradley and Peterka, 1955; Chow, 1959; Lennon and Hill, 2006). This may occur if water with a high suspended sediment concentration recirculated upstream by the jump interacted with flow on the downstream side of the boulder, causing local deceleration, and fall in capacity, causing the remainder of the chute-and-pool trough to fill.

The third structure in FA4 was the inter-beds of Sm and S1 organised in a large scale trough structure (Figure 5.7). This was a complicated bedset and it bore similarities to structures interpreted as breaking antidune or chute-and-pool origin (Alexander *et al.*, 2001; Duller *et al.*, 2008; Yokokawa *et al.*, 2010; Lang and

Winsemann, 2013; Cartigny *et al.*, 2014, see also Table 5.1). The structure differed in morphology, geometry and fill to the chute-and-pool discussed earlier in this section. This may have been because of the composition of sediment the jump eroded into, the hydraulics of the flow, channel morphology or bed surface roughness. Although a boulder sized clast was located at the upstream end of the trough, a hydraulic jump generating a chute-and-pool structure of this scale would have formed at least 2 m downstream of this point; this does not discount hydraulic jump and chute-and-pool formation over a different topographic knick-point. The longer length of lenses at the downstream end of the trough dipping upstream, relative to the lenses at the upstream end of the trough, were similar to observations of regular bedsets interpreted as chute-and-pools by Duller *et al.* (2008). Concordant concave-up laminae in lenses at the upstream end of the trough, and truncation of these lenses may suggest breaking wave antidune origin; in chute-and-pool deposits the prevalence of structureless lenses was higher (Alexander *et al.*, 2001). Based on these observations and the interpretation of similar bedforms in the rock record (Lang and Winsemann, 2013), it was possible that the structure was formed by a hydraulic jump, possibly associated with a chute-and-pool that transformed into breaking water-surface-waves due to a drop in Froude number. Bedforms can be superimposed on one another in response to changes in flow (Rubin and Hunter, 1982). Occurrence of the structure suggests deposition by supercritical flow with high aggradational rates because the bedsets are well-preserved.

5.5.5. FA5: Clast-supported gravel beds with lens patterns

Clast-supported gravel beds that were lenticular with sharp or gradational boundaries are the key feature of this facies association. Two different sub-types are described below: FA5a has sharp boundaries, FA5b has gradational boundaries.

Description

FA5a is composed of clast-supported gravel beds organised in lens patterns (Gci) with sharp erosional boundaries delineated by beds of massive sands (Sm). Figure 5.10 shows a unit of FA5a at site 2013_1 0.46 m thick that was laterally extensive for 31 m parallel to flow. FA5a was not observed elsewhere. The lenses varied in size and internal fabric (Table 5.2). The lens width ranged from 0.32 m to 2.92 m and thickness from 0.06 m to 0.15 m. Some of the lenses were truncated by the erosional base of a younger lens. The largest lenses contained concave-up structures that were shown by the dip of clasts inward towards the centre of the bed. The smallest

lenses contained finer gravels (relative to the whole deposit) and were massive. At the base of most lenses was a thin layer (<0.02 m) of medium-v.coarse sand (Sm). When lenses overlapped, the space between lenses was filled with sands (Sm), some of which filled gaps between larger clasts at the top of the lens. Most lenses were matrix poor.

FA5b was composed of clast-supported pebbles and cobbles in wavy beds (Gh) that have gradational boundaries with massive sands and pebbles (Sm). The deposit was documented at 2013_2 (Figure 5.5a), 2011_9 (Figure 5.5b) and 2011_11 (Figure 5.5b). Site 2013_2 had the longest exposed length of deposit (over 4 m length), that contained a series of stacked Gh beds that ranged from 0.6 m to 1.7 m in length, and from 0.05 m to 0.2 m in thickness. Bed thickness was often dictated by the largest clast in the bed. Beds were separated by massive sands and pebbles that varied in thickness from a few centimetres to 0.08 m. The basal boundary of FA5b with FA3b was gradational. As a whole FA5b was a complex deposit and beds were not well defined compared with other facies associations. Beds of Gh were sometimes discontinuous and sections of the boundary between gravels and sands were mixed, creating discrete sections of massive deposit. At sites 2011_9 and 2011_11, gravel beds were smaller in length and thickness (0.3 m to 0.95 m and 0.03 to 0.17 m, respectively).

Interpretation

FA5 was interpreted to have been deposited by upstream migrating and breaking water-surface-waves; the differences between FA5a and FA5b are attributed to differences in flow magnitude and sediment load. The lenticular structures in FA5a (Figure 5.10) were similar to those formed under water-surface-waves in the flume (see Figure 5.3, Alexander *et al.*, 2001; Yokokawa *et al.*, 2010; Cartigny *et al.*, 2014). Based

on this interpretation, the erosional base of each lens correspond to the trough of an antidune (see Figure 5.2) and sediment inside each lens, predominantly deposited during upstream water-surface-wave breaking. The internal fabric of the lenses varied and lamina were not well-defined within the lenses because of the coarse grain size relative to the scale of the lenticular structure; however the lenticular shape, sometimes truncated troughs and convex-up internal structures were characteristic of upstream migrating antidunes with a stationary element (Cheel, 1990; Duller *et al.*, 2008). The internal fabric of lenses has been discussed in relation to the distance upstream the breaking wave travelled relative to the trough and the violence with which the wave

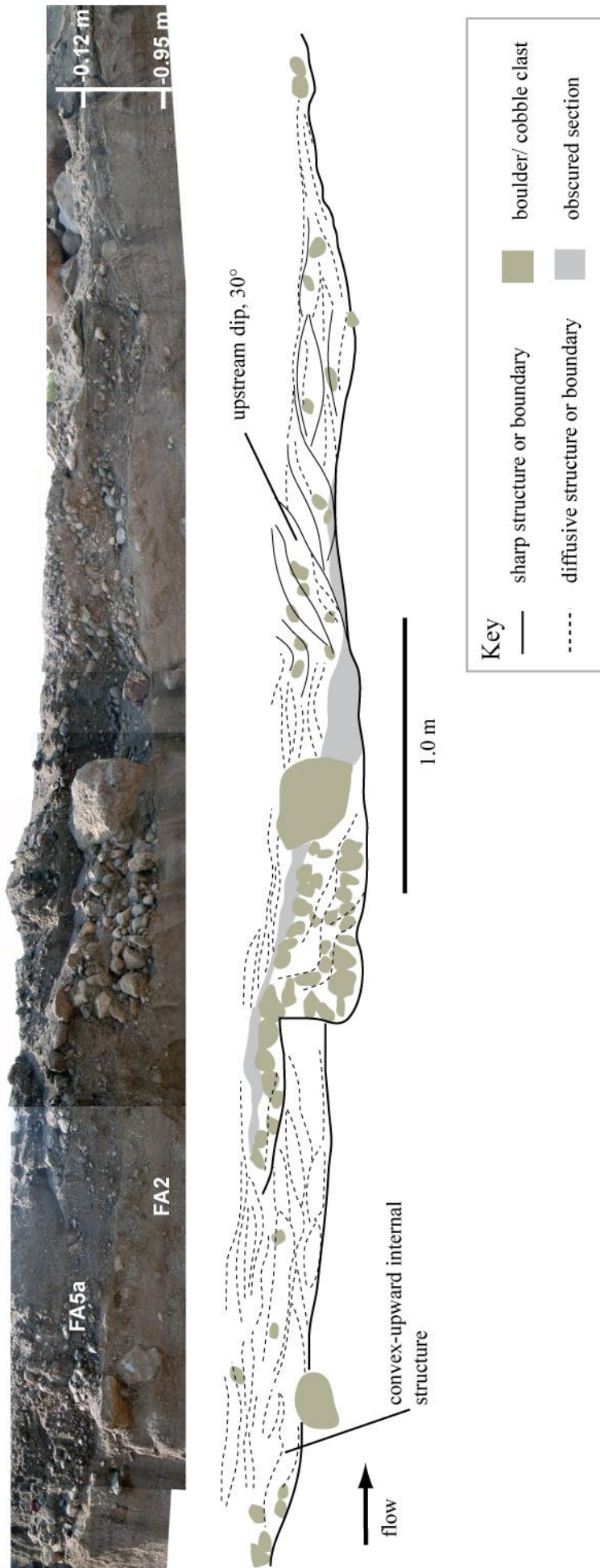


Figure 5.10 Structure in the upper unit of 2013_1 interpreted as a hydraulic jump deposit.

broke. Upstream dipping structures were thought to form when the surge from wave breaking did not propagate further than the centre (deepest) part of the trough (Cartigny *et al.*, 2014), while structureless fills may have been deposited during particularly violent wave breaking (Blair, 2000). Most lenses were delineated by a layer of sands formed after wave breaking by the direct fall-out of material from suspension as flow rapidly decelerated (Alexander *et al.*, 2001; Figure 5.3). Yokokawa *et al.* (2010) extended this association to the transition from three-dimensional antidunes to planar beds and two-dimensional antidunes because of the presence of weak planar to wavy structures in the sand layers and discordance with the erosional trough base; this was also apparent in parts of the upper unit of 2013_1.

The clast-supported gravel texture of FA5a suggests deposits originated from flow that was not carrying a high suspended sediment load, or did not lose capacity during antidune formation. Preservation of structures suggests deposition during aggrading conditions either due to gradual flow deceleration in the waning stages of a lahar or due to high sediment load. If the lens length is taken as the preserved length of the antidune trough, Kennedy's (1960;1963) equations (Equations 4.2 and 4.4) may be used to reconstruct palaeoflow velocity and depth. Lens length ranged from 0.36 m to 1.08 m at 2013_1. The flow velocity is estimated to range between 0.7 m s^{-1} to 1.30 m s^{-1} , while flow depth is estimated between 0.06 m to 0.17 m. These estimates were similar to those calculated using video observations at Site A, during waning flow conditions of the October 2012 lahar (Section 4.4.2.2). However, it is likely that the lens length underestimates the antidune wave length as the crests of the structures were not preserved and particularly where younger lenses cut into older ones the lens length could only give minimum estimates of flow velocity and depth.

FA5b was interpreted to be deposited by the same mechanism as FA5a but with more violent wave breaking (Blair, 2000). This interpretation was supported by the discontinuous lateral extent of Gh beds, the gradational boundary between Gh and Sm beds, and the poor delineation of Sh beds. These features suggested antidune origin, bed reworking and rapid deposition of finer material by suspended sedimentation, respectively. One of the hypotheses proposed for FA2 referred to Blair's (2000) interpretations of gravel couplets inter-bedded with low-angle upstream dipping sands and fine gravels (Section 5.5.2). The model was based on antidune cyclicity and may be applied also to interpret FA5b. The variation in texture of this deposit with FA2 was interpreted to have resulted from differences in the grain size composition of available

sediment and flow hydraulics; sediment grain size distribution was thought to be more heterogeneous with a higher median grain size than that available to flow responsible for FA2.

5.6 Other structures

Description

At 2013_1 a more complex structure was observed (Figure 5.10), which shows a clear irregular-based disconformity within the top unit focused on a 0.30 m (diameter) boulder, located at the downstream end of the longitudinal extensive deposit. Upstream of the boulder was a fill of clast-supported cobbles that were orientated concordant with the $\sim 90^\circ$ 'L-shaped' erosional boundary. A series of stacked concave-up clast-supported gravel lenses (Gci) were located upstream of the disconformity. Clear delineation of the lenticular structures in the deposit was by a subtle reduction in grain size. The erosional boundary persisted downstream of the boulder, tapering towards the bed surface. Furthest from the boulder, structures were inward coarsening, stacked lenses containing a centre of clast-supported cobbles and pebbles. In common with those in the rest of the upper 2013_1, the lenses were delineated by a layer of sands (Sm) but the lenticular fills were both convex- and concave-up. A second set of coarser gravel lenses closer to the boulder dipped upstream by 30° , stacked progressively upstream of one-another. Between these lenses and the boulder was a coarse sand-gravel deposit that contained weak wavy structures, and this deposit is pervasive both immediately upstream and downstream of the boulder.

Interpretation

The structure shown in Figure 5.10 was deposited by a hydraulic jump, possibly a chute-and-pool. The large boulder situated within the pool was rolled into location by highly competent flow, perhaps during the passage of a bore; boulders of similar size were observed in bores during the October 2012 lahar at Site A (Section 4.4). Upstream migration of the jump was preserved by the l-shaped erosional boundary. Downstream of the boulder the deposit contained steeply upstream dipping (30°) lenticular structures of clast-supported gravels (including cobbles), and these were comparable to the structures observed in the flume by Macdonald *et al.* (2013) and in the field (Duller *et al.*, 2008), formed by the growth of a series of unit bars each upstream of the previous. There were differences between the flume observations and the structures shown in Figure 5.3. The massive basal bed that formed from suspension fallout was not a

prominent feature of the deposit compared to the flume example; while a poorly structured deposit was present at the downstream end of the unit bar assemblage, it was not thick, nor extensive. Instead the shape of the basal erosional boundary seemed to control upstream angle (and change in inclination angle) of each unit bar structure. Internally the lenses did not contain downstream dipping lamina; the internal structure is weak and described as wavy. This was likely a function of grain size. The deposit immediately downstream of the boulder was not so well preserved during the process of excavation, and the weak wavy structures that were pervasive both downstream and upstream of the boulder were likely deposited by a train of water-surface-waves centred on the boulder as a series of undular jumps.

5.7. Discussion

Analysis and interpretation of deposits from lahars between Phase 5 and 2013 in different parts of the valley, suggested that the sediment record was dominated by upper flow regime bedforms. In-phase water-surface-waves were discussed as a mechanism for the deposition of most facies associations, chute-and-pool structures and even cyclic steps were suggested in FA1 and FA4, and Upper Stage Planar Beds were prevalent in the sediment record. This interpretation was supported by observations of migrating and breaking water-surface-waves, bores and rapid flow variations during the October 2012 lahar (Chapter 4). Variations in the texture of bedsets interpreted to have formed by the same mechanism were caused by differences in the particle size distribution, density and amount of sediment stored in the upper Belham Catchment and in the channel, as well as differences in catchment runoff and discharge of the parent flow. At site 2013_2 there was a clear vertical trend in median grain size from sands (FA1) to admixtures of sands and gravels (FA2, FA3, FA4), to predominantly gravel beds (FA5). Most bedsets had erosional bases and where estimations were possible palaeoflow reconstructions indicated that velocities remained low (relative to calculations during October 2012); range between 0.7 m s^{-1} to 1.30 m s^{-1} . The location of the 2013_2 exposure at the side of the valley in combination with net aggrading conditions, preserved both intra-flow variations in deposition as well as inter-flow differences. Other sites documented were exposed to lesser extents or were located in central sections of the valley which, based on GPS survey data, were thought to be heavily reworked by successive flows. The following sections discuss the preservation of intra-flow and inter-flow variations in the sediment record.

5.7.1. Variations in structures interpreted as antidune origin

Flume-studies in fine-medium sand provide examples of antidune deposits from which to interpret sediment structures and textures in modern and ancient deposits. However, flume studies were limited in their consideration of the impact of coarser sediment (Foley, 1977; 1978; Shaw and Kellerhals, 1977) or sediment of mixed size (Foley, 1977; Baas *et al.*, 2013) on bedform morphology and internal architecture. Shaw and Kellerhals (1977) used coarser sediment ($D_{50} = 8$ mm) and concluded equations governing antidune geometry (Equations 4.2 and 4.4) were applicable to gravel forms; internal sedimentary structures were not discussed.

In this study, several facies associations were interpreted as deposited by water-surface-waves in flows containing different amounts and compositions of sediment load. Structures directly comparable with those formed in the flume were observed in FA1 at 2013_2, and this is thought to reflect the high sand content of the component facies. Deposited by flow with a high load of sand-sized sediment, structures were well preserved in the deposit because of rapid fluctuations in flow discharge or thalweg migration (Yagishita and Taira, 1989); location of the deposit at the far north side of the valley in a wider valley section suggests that deposits were formed during waning flow stages and were preserved as flow vacated the channel in response to decreased discharge. FA4 contained structures compared to Clifton's (1990) model for upstream antidunes containing type 1 and type 2 laminae and formed under aggrading conditions. These structures were identified in several settings including lahar deposits at Mount St Helens (Clifton, 1990). Low-angle cross-laminae (Type 2) were thought to be less readily preserved (Clifton, 1990) however several authors have identified these within the sediment record for different mixes of sediment size (Barwis and Tankard, 1983; Barwis and Hayes, 1985; Mack *et al.*, 1996; Blair and McPherson, 1999; Giannetti and De Casa, 2000). Based on the vertical succession of structures in FA4 (discussed in 5.8.2) it is suggested the structures interpreted as upstream migrating antidunes were preserved despite shifts in flow regime to breaking water-surface-waves or singular hydraulic jumps (chute-and-pool). The persistence of the upstream migrating wave train (without breaking) was due in part to the steadiness of the flow and also to the bulk uniformity of grain size at the bed surface (FA4 structures are composed of similar sized sediment). Given the same flow conditions, bedforms composed of similar sized sediments are more stable than those of mixed sized, (Lang and Winsemann, 2013). This is because critical shear stress for initiation of sediment motion varies and is

particularly affected by the sediment grain size distribution and sorting. The upstream migrating antidune deposit may therefore have been preserved because of its lateral extent and vertical thickness.

The gradational boundaries between inter-beds of coarser and finer sediment, the discontinuous lateral extent of coarser beds and poor delineation of the coarser beds were features identified in both FA2 and FA5b, commonly interpreted (or one possible interpretation- FA2) as deposited by violently breaking water-surface-waves. The differences between FA2 and FA5b: matrix-supported (clast-supported), sand sized matrix (sand-pebble matrix) and massive texture (wavy structure), indicate formation under different flow conditions. FA2 was deposited by a flow with a high sand load (likely in suspension) that rapidly lost capacity and/or competence in response to flow unsteadiness, whereas FA5b was deposited by a flow that was transporting a coarser load. The vertical location of FA5b in the deposit (Figure 5.8) relative to FA2 and the location of the elevation of the June 2010 bed surface, suggests that FA2 was deposited closer in time to the deposition of primary material in the Belham Catchment during Phase 5, than FA5b. This interpretation was based on observations of selective transport of finer sediments (Komar, 1987) that result in the evacuation of the finer bed fraction and the coarsening of the bed surface with increased time from volcanic sedimentation (Section 3.5). The reduction in sand-sized sediment with time from volcanic deposition due to preferential entrainment of small grain sizes by flow resulted in coarsening of the bed surface and gravel bedforms.

5.7.2. Preservation of structures interpreted as transitions between different upper flow regime bedforms during the same flow

Transitions between different bedforms depends on flow velocity, flow depth, sediment load, grain size, bed roughness and slope and changes in any or all of those (Van den Berg and van Gelder, 1993; 1998; Van den Berg and Nio, 2010; Cartigny *et al.*, 2014). Field and flume studies have shown lateral continuity in the structures characteristic of upper-stage-planar-beds and low-angle cross-stratification and convex-up bedding indicative of antidune formation (Fielding, 2006); particularly in high aggrading conditions (Cartigny *et al.*, 2014). In mixed sediments from sheetfloods at the Hell's Gate alluvial fan, California (Blair and McPherson, 1999; Blair, 2000), planar gravel couplets were inter-bedded with upstream dipping (5-24°) sandy-gravelly beds, interpreted as antidune migration and washout, followed by upper-stage-planar-beds.

Curved based bedsets at Mýrdalssandur, Katla volcano, Iceland contained concave-up laminae that become well-defined planar laminae interpreted as a shift from antidune to upper-stage-planar-beds in sand-sized sediments (Duller *et al.*, 2008). Undulations within the upper-stage-planar-beds indicated a transition back to antidune conditions. These examples illustrate the different types of deposits formed by similar flow transitions in different sediment mixes.

Similar transitions were identified in FA3 and FA4; between upper-stage-planar-beds and antidunes, and antidunes and chute-and-pools, respectively. FA3a contained inter-beds of Sh and Sl which were interpreted as cyclic shifts in bed wave initiation from upper-stage-planar-beds, growth under an in-phase wave and then dissipation in response to flow fluctuation. The deposit was prevalent in logged exposures in the valley; located at the top of 2012_1, the most downstream exposure, at the bottom of exposures 2011_5, 2011_7 and 2011_8 located centrally in area a (Figure 2.18), and at the bottom of 2013_2 and 2011_11 located at the edge of the valley at Pit2013 and at the orange house, respectively. The deposit was well preserved suggesting deposition by flow with a high aggradation or by flow that rapidly decreased in velocity. The location of beds beneath coarser deposits with erosive boundaries suggests that beds of FA3a may have been thicker than what was preserved, suggesting sustained periods of fluctuating waning flow.

Work by Cartigny *et al.* (2014) suggested that the transition from upper-stage planar beds to antidune is governed by flow velocity and depth, however chute-and-pool and cyclic step formation is more dependent on flow-sediment interactions, which are a function of flow velocity, fluid density, grain density and size, and bed surface roughness. However more work is required to consider the formation of bedforms in mixed and coarser grain sizes. At the current state of knowledge it is not possible to reliably distinguish between structures formed by breaking waves and chute-and-pool (complicated by the fact that they can occur together in the same flow). Cartigny *et al.* (2014) considered antidunes formed under breaking waves and chute-and-pools as intermediate stages of bedform transitions between stationary antidunes and cyclic steps. The superposition of bedforms is more readily studied in the lower flow regime (e.g. Rubin and McCulloch, 1980; Vendetti *et al.*, 2005).

5.7.3. Preservation of deposits from the 2012 flow

At Site A during the 13th-14th October 2012 lahar, observations were made that flow variability operated with different magnitudes over different spatial extents (valley-floor wide or channel specific) and over different time scales (over the order of seconds to hours). This resulted in pulses of sediment delivery and removal. Observations were made that the flow was locally erosive and this is supported by comparison of GPS surveys conducted in 2012 and 2013 (Section 3.5 and 5.3). The upper section of 2013_1 (Figure 5.3) composed of FA5a and the hydraulic jump structure (Section 5.6) has a clear erosional boundary with the lower deposit, the log is located in the centre of the larger channel occupied during the 13-14th October 2012 lahar shown (Figure 5.4), orientated parallel to flow and is the upper-most main unit at the 2013 bed-surface. It is proposed that this unit was deposited by the October 2012 lahar. The change in bed surface (0.3 m) at this location does not correspond to the thickness of the unit (0.46 m) suggesting (as per the erosional boundary) that material was removed from the bed surface by the flow before deposition of this unit occurred. Given the texture of FA5a in 2013_1, the lenticular structures in this deposit were interpreted as antidunes, supported by the following evidence: water-surface-waves were readily observed during the October 2012 lahar, the deposit location corresponded to the main channel occupied during the October 2012 lahar, and, material above the erosional base boundary of this deposit was emplaced during the October 2012 event. Lahars after this date but before the date of the sediment survey were small and did not significantly alter the bed surface.

The minimum flow velocity (0.7 m s^{-1} to 1.30 m s^{-1}) and flow depth (0.06 m to 0.17 m) estimated from length of gravel lenses in FA5a corresponded with flow within waning flow conditions (Figure 4.11, Section 4.4.2.2). It is possible this figure underestimates flow because of truncation to the gravel lens length by stacked and overlapping bedsets, however the estimate was unlikely to increase much above 2 m s^{-1} , still placing the deposit within the waning flow velocity range based on water-surface-wave train measurements in Section 4.4.2.2. The rapid changes in discharge and consequential shifts in channel occupation (Section 4.4) during waning flow, would have resulted in antidune preservation (Alexander and Fielding, 1997). It is likely given the erosion of the hydraulic jump into FA5a that FA5a at 2013_1 was emplaced before the hydraulic jump formed, suggesting that rather than deposition during waning flow of the final peak in the October 2012 event, FA5a may have been deposited during the

waning phase of one of the other lahar peaks, therefore being preserved during a sequential increase in flow discharge.

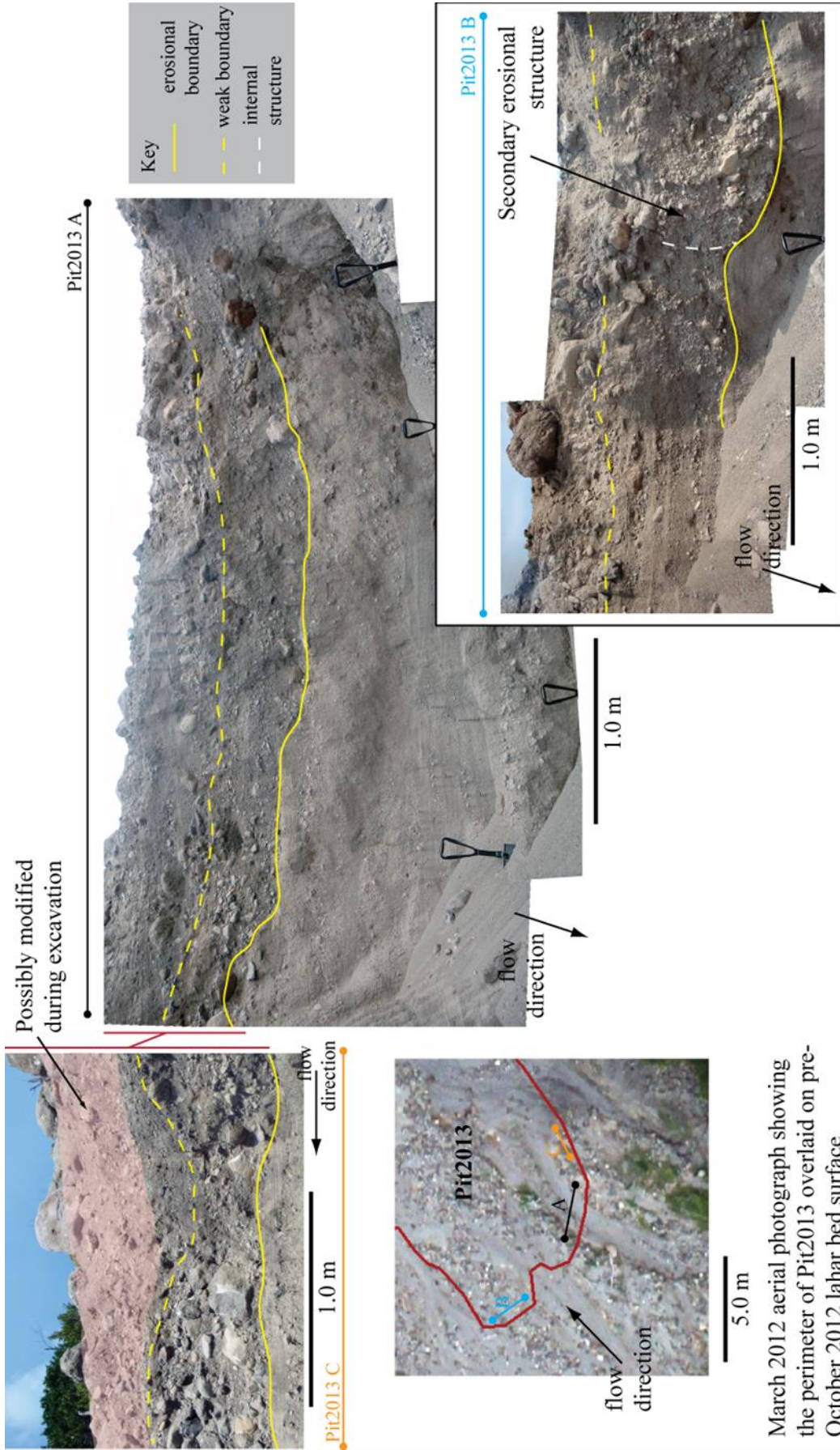


Figure 5.11 Location of Pit2013 in November 2010, looking towards 2013_2

Observations at Pit2013 in November 2010 identify the source of the Fsm bed in 2013_2 at 0.36 m beneath the March 2013 surface, as a fines rich deposit (Figure 5.11) deposited during low flow conditions. This suggests the upper 0.36 m of deposit containing FA5b and FA3a (2013_2, Figure 5.5a) was deposited by flows after November 2010, and possibly by the October 2012 lahar. This bed surface was not preserved in 2013_1. In some parts of the deposit exposed in Pit2013, where the natural 2012 bed surface could be identified, the upper unit of deposit was only a few 10s of centimetres thick before there was a distinct change in vertical character (e.g. Figure 5.7). The base of this upper unit could be traced laterally (albeit discontinuously) to tie in with erosional features and deposit associated with the October 2012 lahar at 2013_1. Sediment deposited beneath the thin upper-section (Figure 5.7) was topped with fine laminations and was very different in character to facies associated with the October 2012 lahar. This observation highlights the spatial variability and discontinuity of packets of deposit associated with a single flow that included periods of bed surface incision.

A boundary representing the base of deposition associated with the October 2012 lahar was not identified in some parts of the Pit2013 deposit because the upper sections of the deposit were vertically gradational and similar in character to

observations of the bed surface prior to the event (Figure 5.4). An example is shown in Figure 5.12; here the upper section of deposit was very variable showing FA5b, but also some cross-cutting lenticular sand structures, some interlamination of sands and fine pebbles, and some weakly structured scour features. Although an erosional boundary may be traced for over 100 m laterally, the vertical location of this boundary relative to the surface varied between 0.45 m and 1.4 m, and the lower unit of sands was not characteristic of all parts of the pre-October 2012 bed surface in this section of the valley-floor. Instead it is hypothesised that the upper complex deposit built up over several events. A weak boundary halfway up the section (shown in Figure 5.12) was delineated laterally by a change in deposit character, either a change to the inclination of lenticular structures, the presence of a fines layer (Fsm) or a colouration change to sediment. This does not necessarily mark an event boundary but it does suggest a change in channel boundary conditions, flow competence or transported sediment character. Figure 5.12 also highlights the difficulties of interpreting deposits that have been excavated rather than naturally incised. The top sections of some exposures in Pit2013 had completely collapsed and were unintelligible, while in other areas deposit had been piled on top of the bed surface leading to uncertainty in the identification of the natural bed surface prior to pit excavation.



March 2012 aerial photograph showing the perimeter of Pit2013 overlaid on pre-October 2012 lahar bed surface

Figure 5.12 Possible boundaries between lower (older deposits) and deposits from the 13th -14th October 2012 lahar.

5.8. Conclusions

- Ten facies were described in the deposits and five facies associations were discussed; a large number of facies were used to discriminate an appropriate level of detail from the highly variable deposit. Of these FA5a in 2013_2, clast-supported gravel beds with lens patterns, was interpreted to have been deposited by the 13th-14th October 2012 lahar discussed in Chapter 4. The deposit had an erosional boundary and flow had eroded ~ 0.2 m below the February 2012 bed surface elevation. Thinner deposits of FA3a (inter-bedded planar sands and pebbles) and FA5b (similar to FA5a but with gradational boundaries) were located in deposit identified as post November 2010 (2013_2), however these deposits could not be attributed to a specific lahar.
- Material interpreted as deposited by the 13th- 14th October 2012 lahar also contained a hydraulic jump structure composed of clast-supported gravel beds with lens patterns that were planar and dipped 30° upstream, contained within a 3 m long, 0.3 m deep ‘L-shaped’ erosional boundary. This structure was one of very few well documented examples of hydraulic jump deposits in sediment record.
- A suite of facies have been attributed to water-surface-waves and antidune bedforms deposited by flows containing different amounts and compositions of sediment load, and by water-surface-waves that migrated upstream and also breaking waves. Structures in FA4 were interpreted in relation to Clifton’s (1990) laminae model for upstream migrating antidunes; the preservation of both types of laminae (which are considered ‘rare’ in the sediment record) suggests deposition by flow that was rapidly decelerating. Structures in FA5a (deposited by the October 2012 lahar) were very similar to those from flume experiments of breaking water-surface-waves by Alexander *et al.* (2001), despite large differences in grain size. This supports the relevance of flume experimentation for understanding bedform deposition in natural channels with mixed sediment load.
- Transitions in flow character were preserved in the sediment record by shifts between upper-planar-beds and antidunes, and antidunes and chute-and-pools.

Chapter 6:

Discussion

6.1. In-situ monitoring for lahar detection and scientific analysis

Cameras with different sensors and set-ups have been employed on active volcanoes around the world to monitor different volcanic processes; Hawaii (Harris and Thornber, 1999; Patrick *et al.*, 2014), Mount St Helens, USA (Krimmel and Post, 1981, 1981; Major *et al.*, 2009; U.S.G.S., 2014), Soufrière volcano, St Vincent (Sparks and Wilson, 1982), Soufrière Hills, Montserrat (Herd *et al.*, 2005; MVO, 2011), Merapi Indonesia (Lavigne *et al.*, 2000), Etna, Italy (Spampinato *et al.*, 2011). Monitoring environmental change using visual data is not a new technique in volcanic environments, and is avidly used because it provides a remote method of measuring large scale phenomenon occurring in inaccessible and dangerous locations. Critical to the study of lahars is the ability to capture rapidly changing behaviours that will affect flow travel distance and therefore inundation extent (Darnell *et al.*, 2012). This goes beyond simply providing an event warning using telemetered cameras. Still-image and video camera systems have been deployed to monitor sediment-laden flows in volcanic and non-volcanic locations. Most permanent stations with cameras capturing an image frame more than once per minute, were connected into the local power grid (e.g. debris flows in the European Alps, Comiti *et al.*, 2014; lahars at Sakurajima, Japan, International Sabo Centre, 2014), or were powered locally but captured high rate image sequences over short periods of time (e.g. 5-minutes of 1 fps images of lahars at Mount

Merapi, Suwa and Sumaryono, 1995). In some cases siting instrumentation required substantial development of a structure engineered to withstand lahar impact (lahars at Mount Ruapehu, Campbell Scientific, 2014); a costly endeavour both in terms of materials and outsourcing of expertise. Other studies have used standard video cameras on tripods at non-permanent sites, monitoring lahars over short field seasons (Doyle *pers. comm.*, 2012), but collecting high frame rate, high quality data.

One of the key challenges of this study was to balance equipment cost, image collection rate and image quality, while permanently monitoring the Belham River Valley over long-periods of time. In total the camera unit cost ~ £2000, which included two aerials for telemetry to and from the site, a high-spec IP camera, power control, power source (batteries and solar panels), site installation and the field computer (see Section 2.3). Electrical and software expertise were donated in kind by staff at the University of East Anglia and the Montserrat Volcano Observatory, so the true cost if this project were repeated elsewhere is likely to be higher. Lahars in the Belham Valley were contained in pre-existing river valleys, negating the development of reinforced siting for monitoring equipment, which may be installed out of reach of flow on valley-sides; thus reducing cost. Recent educational thinking in combination with technological advance has driven the development and availability of low-cost, low-powered, small (credit-card) sized computers. The development of the camera system in 2011-2012 coincided with the release of the Raspberry Pi computer (early 2012), which was used as a control device to mediate between image capture from the camera, and the storage and transmission of data to the observatory. This allowed images at the monitoring site to be captured at less than 1 frame per second at 5 megapixels, providing sufficient temporal and spatial resolution to identify 0.46 m objects in the background of the image, moving at rates of 19 m s^{-1} (with 2 frames).

The remote camera at Site A (see Figure 4.1, Section 2.3.2) captured oblique images of a section of the Belham River Valley that contained four control points (objects) of known position sited at the foreground and background of the image. A scaling law (see Section 2.3.3) was used to convert pixel based measurements of flow features into metres. The control points were also used as markers between which objects carried in the flow were tracked through sequential images to calculate surface flow velocity. Using this set-up, image analysis was extended beyond qualitative time-stamped observations of flow onset and bulk dynamics, to include estimates of flow velocity, depth and lahar volume (Section 4.4). These measurements were facilitated by

empirical equations derived in experimental flume studies that relate the wavelength of water-surface-waves with mean flow velocity (Kennedy, 1961; Kennedy, 1963). Very few floating objects (such as vegetation debris) were observed during the passage of the lahar in October 2012, most discernible objects were transported by traction; however wave trains were abundant because the high width:depth ratio of channels in the Belham Valley and catchment runoff characteristics which resulted in shallow, fast flow. Water-surface-waves formed from internal flow instabilities (Jeffreys, 1925; Vedernikov, 1945; 1946), generated by localised changes in flow velocity and/or viscosity (Fryirs and Brierley, 2012) caused by variations in depth and/or roughness (Lawless *et al.*, 2004). Distortion of the free-surface into a waveform by internal instability represented a transition from supercritical flow upstream to subcritical flow downstream; forming an undular hydraulic jump. Wave trains were observed in other stream-flows in the Belham River Valley (Section 4.5), but were not discernible at Site A during small lahars, perhaps because of size rather than absence.

Application of empirical relationships to estimate flow velocity provided a non-contact method of quantifying flow variability over a range of different scales, because wave trains were abundant in multiple channel locations during the majority of the large October 2012 lahar. Measurements of this frequency and coverage would be very difficult to obtain with contact methods, because of the challenges involved in installing instrumentation on an alluvial bed to withstand scour and damage by clast impact; fundamentally instrumentation that requires direct contact with flow to make a measurement is unlikely to be robust enough to have a long enough life span to justify equipment cost. However, the measurement method applied in this study is not without significant limitations because it is contingent on the presence of wave trains, and therefore the hydraulics of the flow. Furthermore, errors attached to measurements were derived from the positional accuracy of the control points and accuracy of the image coordinate (point): metre scaling law (Section 2.3.3), and do not include estimates of the precision of empirical relationships between water-surface-wave length and velocity. These relationships were derived in flume experiments with low viscosity flow, sand-sized sediment and steady conditions (Kennedy, 1960, 1963); tests of the equations have not been undertaken for water-surface-waves forming in unsteady flows, viscous water-sediment mixtures or on different compositions of erodible bed, which are more relevant conditions to sediment-charged flashy flows such as lahars.

Water-surface-waves were documented during lahars in other volcanic systems; at Mount Pinatubo, Philippines (Hayes *et al.*, 2002) and Mount St Helens, USA (Pierson and Scott, 1985), indicating the transferability of measurement techniques for flow velocity employed in the Belham Valley to other locations, including other flash flood prone systems not discussed here. Imagery enhances the value of datasets from other monitoring instruments because visual evidence is more easily interpreted, and may be used to calibrate signals in numeric data with observed physical flow dynamics; this was demonstrated in this study by the association of bores with increased seismicity (see Section 4.4.2.1). In a set-up designed to monitor intra-flow dynamics to improve scientific understanding or for numerical model development and validation, camera-based monitoring benefits from the parallel installation of seismic monitoring and if possible load cells (e.g. Manville *et al.*, 2007), which in combination may be used to quantify the sediment load and therefore the rheological dynamics of the lahar. It is only possible to estimate relative changes in suspended sediment load in imagery based on flow colour and texture, and bed load when clasts breach the free water surface; severely limiting complete analysis of sediment transport dynamics. In applications for lahar early warning, camera-based monitoring of at-risk channels has been criticised as expensive and man-power intensive (manually analysing imagery) compared with automated seismic detection (USGS, 2014). As a primary lahar detection system, these arguments hold true, however the power of visualising hazardous natural phenomenon to improve public understanding of risk was advocated by IFRC (2014), because no matter what level of scientific understanding a person may possess, everyone can gain useful information from visual data.

6.2. Preservation of flow variability in the sediment record

Examination of deposits from 2011-2013 in Chapter 5 showed that shifts in flow velocity, flow depth, sediment load, grain size, bed roughness and slope were preserved in sedimentary structures interpreted as upper flow regime bedforms (Section 5.7.2). The characteristics of flow attributed to these deposits was difficult to reconstruct in detail because, of the factors listed above, some could only be commented on qualitatively (sediment load, bed surface roughness), and while it was possible to estimate palaeoflow velocity and palaeoflow depth for a few bedforms, using relationships derived from experimental flume studies (Kennedy, 1960; 1963), the empirical equations have not been well tested for rapidly varying flows with mixed-sediment loads. The massive fabric and gradational boundaries between beds in some

facies associations (FA2) in combination with a high sand component were interpreted to have been deposited by flow carrying a high concentration of suspended sediment, resulting in high rates of aggradation in response to rapid decelerations of flow. These observations suggest that some flows may have contained hyper-concentrations of sediment (Mulder and Alexander, 2001), however it should be clear that evidence of cohesive flow is limited to observations of the behaviour of lahar flow fronts, which were not specifically sampled (Section 4.4.1.2). A suspended sediment sample from immediately behind the flow front contained 17% clay-sized particles (March 2011 lahar, Appendix 4.1g) and it is possible that smectite and kaolinite were present in the sample (based on observations on water chemistry by Jones *et al.*, 2011 and the presence of a clay cap beneath parts of the Belham River Valley; EGS, 2010), however detailed mineralogical analysis was not undertaken on samples as part of this study. Flows in the Belham River Valley were non-cohesive and predominantly Newtonian, with the exception of thicker beds of Fsm containing pumice (observed in 2011_6 and March 2000, Barclay *et al.*, 2007), which were interpreted to as non-Newtonian origin. Extensive analysis by Sušnik (2009) also discounted non-Newtonian behaviour for emplacement of deposits between 2005 and 2006 in the Belham River Valley.

Observations from the remote camera during the 13th-14th October 2012 large lahar showed that increases in cobble-boulder bedload transport corresponded with visual observations of increased discharge, apparent turbulence and bore incidence (Chapter 4). These peak periods during the flow were similar to the “packets” of flow described by Doyle *et al.* (2011). Trains of water-surface-waves were also prevalent in flow at all observation sites however preservation of antidunes was limited to waning flow phases, although not strictly to waning flow of the final peak in discharge (Section 5.7.3). The presence of a hydraulic jump overprinted on sedimentary structures interpreted as antidunes, both from the October 2012 lahar, suggests that structures formed during a waning flow phase could persist through subsequent increases in discharge. It is likely these structures were preserved by a shift in sub-channel boundaries within the wider main channel; the transitory occupation of different parts of the shallow-wide channels by flow was observed at Site A by the camera (Section 4.4.2). Transitions between deposits interpreted as upper-stage-planar-beds and antidunes were preserved at the edges of channels in upstream areas and at the top of deposits at downstream locations in central parts of the channel. The length of lenticular Sm beds in FA3a was used to reconstruct flow velocity and depth, and suggested minimum velocities of 0.6 m s^{-1} and 1.86 m s^{-1} at Pit2013 upstream and velocities at the lower end of the range at

downstream valley locations (Section 5.5.3). Flow velocities corresponded with those observed during waning flow stages of larger flows and with the flow velocity during small lahars.

Based on these observations it might be suggested in common with previous studies of upper flow regime bedforms in modern alluvial channels, that preservation of sedimentary structures was limited to shallow flows that readily approached $Fr=1$ (Langford and Bracken, 1987; Fielding, 2006) or flow that rapidly decelerated either during waning flow or from a sudden shift in channel boundaries (Alexander and Fielding, 1997). While this fits with observations of FA3 and FA5 deposits, it does not correspond with sedimentary structures in FA4 at 2013_2, which were interpreted to have been deposited by upstream migrating water-surface-waves overprinted by breaking water-surface-waves/ chute-and-pool during the same flow. If deposits were formed by breaking water-surface-waves, the transition represents a variation in flow velocity, depth or sediment load, promoting non-steady bedform growth that outpaces upstream migration causing the antidune under the water-surface-wave to grow, enhancing trough erosion, resulting in the over-steepening and breaking of the water wave upstream. Formation of a chute-and-pool structure from upstream migrating waves would have required a much greater shift in velocity or a decrease in sediment load median grain size (Cartigny *et al.*, 2014). The texture of S1 and Gmg beds in FA4 was relatively uniform across the deposit, suggesting that formation was controlled predominantly by flow velocity, likely in response to an increase in discharge. Structures in the deposit were preserved because of a high aggradation rate (Duller *et al.*, 2008; Lang and Winsemann, 2013) and the location at the edge of the valley-floor.

Material deposited between June 2010 and March 2013 at Pit2013 showed an upward coarsening trend. The June 2010 bed surface from the LiDAR DEM was located 0.7 m below the bottom of 2013_1 and 1 m below the bottom of 2013_2, indicating that the full deposit from June 2010 was not exposed; the deposit may have been thicker than this if flows eroded into the June 2010 bed surface. The lahar record for 2010 to 2013 (Section 4.2) showed that two large lahars occurred, one in August and one in October 2010, followed by a series of small and moderate events and then the large lahar on 13th-14th October 2012. Observations of large lahars during 2010 suggested they were much larger events (by volume) than the lahar in October 2012, particularly the lahar triggered by Hurricane Earl on 29th-31st August 2010. This lahar was triggered within 9 months of the deposition of $3.4 \times 10^6 \text{ m}^3$ (Table 3.1, Section 3.2,

3.4.2) of primary material in the upper Belham River Valley, Dyers River and Tyres Ghaut (and Farrell's Plain) by a large synoptic system that deposited ~290 mm of rainfall over the Belham Catchment (Appendix 2.2w). The availability of large volumes of sediment containing a high sand fraction (Cole, 2014) in storage in the Belham River Valley from the location of Pit2013¹ upstream to SHV, in combination with large volumes of water from rainfall and relatively high runoff rates² resulted in a lahar that eroded substantial volumes³ of sediment from PDC deposits upstream and was highly aggradational downstream, contributing to up to 4.71 m of elevation gain. Given that large lahars undertake the majority of geomorphic work (Section 3.6) and three large lahars⁴ occurred between the June 2010 and March 2011 surveys, it is suggested that FA2 in 2013_1 was deposited by the October 2010 lahars, FA3a beneath this deposit was emplaced during smaller flows in August to October 2010 and deposits from the lahar triggered by Hurricane Earl were beneath this bedset. This interpretation is based on: (1) the gradational boundaries of FA2 which suggest rapid deposition by flow carrying a high sediment load by one or more flows, (2) the sharp boundary between FA3a and FA2 at 7.95 m (see Figure 5.5a, Section 5.4) suggesting a sudden change in flow behaviour (or a separate event), (3) the interpretation of FA3a as low flow or waning flow origin, (4) the presence of Gmm beds beneath FA3a in the log suggesting that flow with greater transport capacity and competence occurred prior to a series of smaller events (or waning flow stage), and (5) the deposit above FA2 in the sequence and the boundary between this upper deposit and FA2 corresponds with the elevation of the March 2011 bed surface, suggesting this upper deposit was emplaced by a series of small-moderate lahars between March 2011 and October 2012.

While much of this evidence was conjectural because no direct observations were made of these lahars at this location, the interpretation is logical based on interpretations of individual facies associations (Section 5.5), their thicknesses and the sequence in which they appeared at 2013_1, relative to topographic change and the lahar record. It suggests that large lahars may be identified within deposits emplaced within a few years of the event. This is dependent on reworking of material (discussed later). At this location large lahars occupy ~80% of the valley-floor and aggradational events are likely to appear in the sediment record at most locations. Downstream of the Belham

¹ termination of 8th February 2010 PDC

² widespread vegetation damage from Phase 5

³ estimated $1.47 \times 10^5 \text{ m}^3$ loss of material in Belham River Valley from PDC deposits between June 2010 and March 2011

⁴ two in short succession, 4th, 6th October 2010

Bridge where the valley widens (< 214 m), deposits were not easily interpreted in the context of the lahar record because exposures were not as deep and were less laterally extensive. Deposits at 2011_2 and 2011_4 contained thick beds of sands (including FA2 and FA1) and it was likely these were deposited by large lahars in late 2010. These deposits were well preserved because of their location at the far side of a wide section of the valley. Commercial sand extraction created a ~30 m wide channel down the centre of the valley (between the Belham Bridge and Isles Bay) to provide access to a series of pits that were gradually excavated between 2010 and 2013. Flow was channelised (preventing the reworking of deposits at the edge of the valley) within the network of temporary roads resulting in changes in flow behaviour (Section 4.4.2). The bed surface of this road network was altered almost instantaneously after a lahar by excavation equipment, which often resumed within hours of an event. This made it difficult to monitor the effect sand mining had on deposit thickness or bed surface composition. More importantly, sand extraction modified both the hydraulics of lahars and the sediment record, preferentially preserving deposits at the edge of the valley (at the edge of pits), but excavating and depositing material in the central areas of the valley. As sand extraction is a common economy in lahar prone valleys (e.g. Merapi, de Belizal et al., 2013), the impact of anthropogenic activity on deposit preservation, is an important consideration when interpreting structures in the modern sediment record.

Preservation of deposits over longer time scales (years to decades) is dependent on the shift from net aggrading to net degrading conditions in the valley (Gran and Montgomery, 2005). In Section 3.6 a model was presented for the progressive channel adjustment to volcanic sedimentation. Catchment conditions and weather system rainfall delivery, controlled lahar size, which governed the amount of geomorphic work each lahar undertook relative to channel-bed shear stress, and also governed the speed of transition from a net aggrading (transport-limited) to a net degrading (supply-limited) system, and ultimately to fluvial and ecological recovery of the catchment (Gran and Montgomery, 2005). The shift from high availability of fine sediment to the development of gravel clusters and bed armour, and channel incision with decreasing sediment supply was captured by the sediment record between June 2010 and March 2013 at Pit2013 following Phase 5 deposition, and by a previous study of deposits in the Belham River Valley conducted during 2006 by Sušnik (2009), which included sediments deposited between May 2003 and November 2006, after Phase 2 (Appendix 6.1).

The specific sediment yields between July 1995 and March 2013 were calculated using the solid sediment volume (75% of total volume, Table 3.8, Section 3.5) based on DEM differences (net gain) in the Belham River Valley and the 2010 catchment size of 16.3 km². The estimate represents the minimum amount of sediment to pass through the Belham River Valley. Over 3.77×10^6 m³ (submarine volume required to extend Belham coastline to March 2013 position) has been deposited offshore and 4.4×10^6 m³ remained in storage in the Belham River Valley, however significant amounts of material were transported offshore by flows in addition to smaller amounts of material by wind, as well as volumes (4.4×10^4 m³ between March 2011 and March 2013) removed by sand and aggregate mining. The precise volume of material transported offshore was difficult to qualify because survey work by others *e.g.* Le Friant *et al.* (2004). Figure 6.1a shows the change in specific sediment yield per year averaged over periods between available Belham Valley DEM data. The estimates were two orders of magnitude higher than the average for world rivers (Milliman and Syvitski, 1992; Sušnik, 2009), they were comparable to measurements at drainages around Sakurajima with similar sized catchments to the Belham River Valley (Lavigne, 2004) but were two orders of magnitude lower than estimates of drainages around Pinatubo (Lavigne, 2004). Figure 6.1b uses limited observations of erosion at Tyres Ghaut (Section 3.2.1, solid sediment volume calculated from total volume) to calculate specific sediment yield for the catchment and shows that specific sediment yield may be underestimated by at least one order of magnitude using change in the volume of sediment storage in the Belham Valley alone. This shows that the majority of material eroded from Tyres Ghaut was transported directly offshore, rather than being stored in the Belham River Valley, which is not surprising given the size of the catchment, volume of material in storage, channel gradient and the length of the Belham River Valley.

The detail of the Belham River Valley record is useful when considering the relative changes in sediment yield over time in response to volcanic sedimentation. Analysis of elevation data in combination with archive photographs in Section 3.5 showed that three periods of net aggradation (1995-1999, 2002-2003, 2006-2011), two periods with very little loss or gain (2000-2002, 2012-2013) and one period of net degradation (2004-2006) have occurred in the Belham River Valley. Some of these time periods were visible in changes to the specific sediment yield (Figure 6.1a), which showed the dramatic decrease in sediment yield in the years immediately after volcanic sedimentation during Phase 3 and Phase 5. The shifts in sediment yield highlighted the rapid transitions through

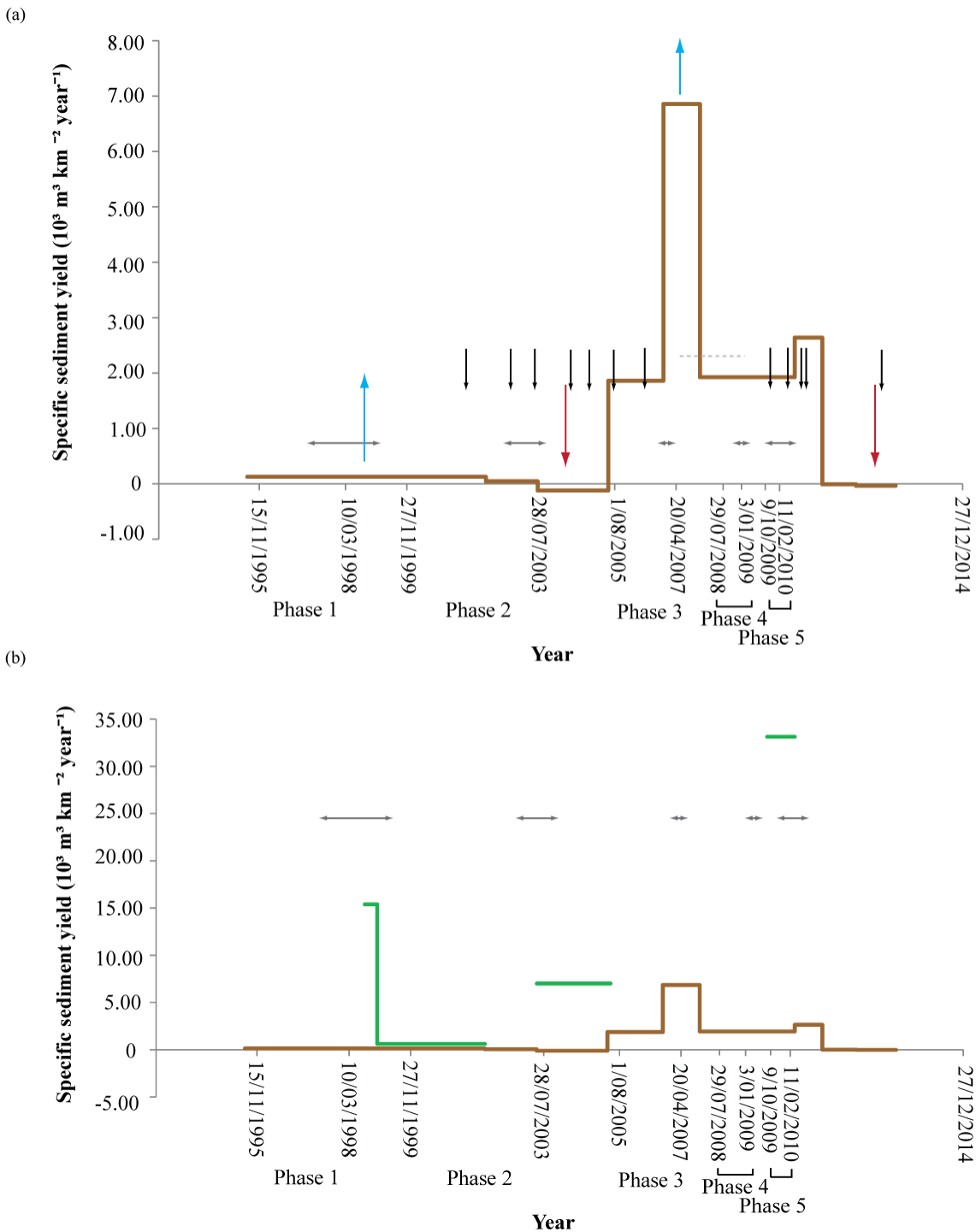


Figure 6.1 (a) Specific sediment yield from the Belham Catchment between July 1995 and March 2013 (brown line). When this line is horizontal no data is available between the start and end date of the line, and the specific sediment yield is an average value. Blue arrows highlight periods of net aggradation in the valley, red lines highlight periods of net degradation. In this case the specific sediment yield is negative representing only offshore sediment delivery. The black vertical arrows are large lahars (based on available data, grey horizontal dotted line indicates no data on large events). The horizontal grey arrows are the period during which deposition of volcanic material by PDCs was documented in the Belham Catchment (Section 3.2). (b) Specific sediment yield from the Belham Catchment between July 1995 and March 2013 based on changing sediment storage in the Belham River valley (brown line) and sediment removed from Tyres Ghaut (green line).

different stages of the channel-response model (Figure 3.19, Section 3.6) in the months after volcanic sedimentation. After Phase 5, transitions in channel stability were driven by several large lahars in 2010, which remobilised $7.7 \times 10^5 \text{ m}^3$ of material deposited in the Belham River Valley within the first 8 months. Observations after the 13th-14th October 2012 lahar suggested that in narrower parts of the valley channel incision ($\sim 0.2 \text{ m}$) was occurring; at the camera site (Site A, Figure 4.1) observations were made of erosion to the bed surface during peak discharge and deposition during waning stages of flow. This was also inferred from deposits at Pit2013 (Section 5.4) which contained an erosional boundary $\sim 0.46 \text{ m}$ beneath the March 2013 bed surface, in a location of 0.3 m of elevation change, indicating a shift from erosion to deposition during the lahar.

Although a large volume of sediment remained in storage in the upper catchment (Farrell's Plain, Gage's fan) in March 2013, erosion to terraces in channels was limited by lahar magnitude because of channel width. In the absence of a large lahar able to undercut PDC terraces, sediment is quarried from the channel bed; fines are removed preferentially to coarser material, resulting in the development of gravel patches and eventually armoured beds form (Gran and Montgomery, 2005; see Figure 3.19, Section 3.6). In the absence of further volcanic sedimentation large lahars incise into the bed surface (e.g. 20th May 2006), releasing finer sediment trapped beneath gravel armour (depending on transport capacity and competence of the flow); PDC terraces are also undercut. Large lahars (of sufficient volume) reduce channel stability by reworking bed armouring and removing vegetation.

By nature, dome-building volcanic environments are characterised by relatively short-term eruptive phenomenon and erosional processes operating over longer time scales, degrading volcanic edifices (Davidson and De Silva, 2000). With time (decades) repeated cycles of channel incision and reworking of sediments deepen and widen channels in the valley, transporting sediment out of the system; drainage networks stabilise close to pre-eruption configuration (Manville *et al.*, 2009). The dynamics of channel stabilisation has profound impacts on the sediment record because channel incision over time removes evidence of periods of lahar activity (Graettinger *et al.*, 2010). Although some indication of lahar stream power may be gained by looking at the largest remaining clasts in a channel (Section 3.5.2) and their location in relation to source areas, the transport mechanism (and number of flows in the case of multiple boulders) is difficult to interpret in the absence of other finer deposits. Sedimentary structures in lahar deposits may only be preserved on the edges of wider valley sections

and in distal debris fans (*i.e.* lower Belham River Valley). Critically these deposits typically represent the waning flow of large lahars or bear no relation to the dynamics of flow upstream (*i.e.* changes in flow stability with changing channel width:depth ratio). However if sedimentary structures, are preserved in deposits paleoflow may be reconstructed using empirical relationships such as those used to calculate flow velocity from antidune wavelength (Kennedy, 1960; 1963). Further research is required to better understand deposition during different types (size, sediment load, intra-flow variation) of individual lahars (building on work by Vázquez *et al.*, 2014), and deposit preservation after multiple lahars (of differing character). One of the most effective means of gathering this information is to use visual monitoring of the flow and bed surface in combination with other instrumentation to determine sediment load, and repeat site surveys to capture changes in bed surface and elevation. Extending this study over different periods of time to monitor an upstream section of channel, in parallel with a sedimentological study of material deposited by observed events in distal areas, would help develop facies and facies associations for palaeoflow reconstruction. This would help link sedimentary structures deposited during waning flow in distal locations that are more readily preserved in the rock record, with lahar dynamics upstream. This type of analysis requires detailed strategic documentation of deposits at multiple exposures on a distal debris fan, in combination with lahar observations at locations proximal-medial to the volcano. Although this approach was not possible in the Belham River Valley study due to active commercial sand extraction which dictated exposure location and altered natural channel dynamics, the method would be a viable option at other lahar prone volcanoes, such as Semeru, Indonesia, Tungurahua, Ecuador or Redoubt, USA (refer to global lahar database, Appendix 1.1a).

Chapter 7

Conclusions

Within this thesis lahar variability during a single event using a remote monitoring camera and over longer time scales using archive topographic surveys and visual data, has been investigated. Observations from a large lahar on the 13th-14th October 2012 in the Belham River Valley, Montserrat showed that flow was rapidly varying, unsteady and sediment-laden, changing character downstream; trains of upstream migrating and breaking water-surface-wave trains and bores were observed during the event in flow. Deposits were interpreted using these observations and upper-flow-regime bedforms have been described by a series of facies and facies associations. The preservation of these deposits was discussed over different time scales in the context of catchment adjustment to volcanic sedimentation.

The aims and objectives of this thesis were set-out in Section 1.2 based on recognition of the pressing need to monitor the intra-flow dynamics of lahars and examine event deposits to improve sedimentological interpretation of structures deposited (and preserved) by sediment-laden unsteady flows. Improved understanding of the sediment record in active volcanic regions is important because it provides the basis for hazard assessment and planning. The following section outlines the aims of the thesis, key contributions to knowledge and recommendations for future research.

(1) Development and deployment of automatic monitoring equipment to generate data on the nature of flow and sediment transport in lahars

During this study a remote monitoring camera was installed in the Belham River Valley, Montserrat to continuously monitor a section of channel providing an image at least once every second. Images were analysed in the context of measurements made by other instruments in the MVO monitoring network and provided information on flow variability over different temporal scales.

Key findings and contributions to knowledge

- Deployment of a remote camera was an effective method of identifying flow variability over different temporal scales and estimating variations in flow velocity, depth and discharge using measurements of flow features and floating objects in the flow.
- Estimations of flow velocity, depth and discharge were made using the length of water-surface-waves in trains which formed when the flow Froude number was greater than 0.84. The high width:depth ratio of channels in the Belham River Valley resulted in fast shallow flows that fluctuated between sub- and supercritical flow, resulting in the formation of hydraulic jumps. These flow features have been observed in other lahar prone valleys (*e.g.* Pinatubo, Philippines; Hayes *et al.*, 2002) and in other flashy systems in non-volcanic locations (*e.g.* desert environments; Reid and Frostick, 1987)
- The prevalence of water-surface-waves in flow in these types of systems has not been previously documented in a systematic manner. Observations from this study showed that water-surface-waves formed frequently and could be used to make regular estimates of flow velocity, depth and discharge from repeat camera images. This data is difficult to collect by instrumentation that requires direct contact with the flow because the flow is rapidly varying, turbulent and carries a coarse bedload that may damage instrumentation. In addition instrumentation is expected to have a short lifespan when installed on alluvial bedded channels that may undergo metres of change during a single flow. Image analysis provides greater spatial coverage of the flow (rather than a point based measurement) and is non-contact, therefore justifying equipment cost by increased lifespan.

- The prevalence of water-surface-waves in shallow non-cohesive water-sediment flows in this system (wave trains observed during multiple lahars in the 19 year record) suggests camera-based flow measurement may be applied to monitor similar flows in other locations. This shows visual data can play a key role in flow monitoring.
- Functionality of the camera was dependent on the development of a bespoke field computer to control image capture by the camera, and this was strongly facilitated by the availability of the low-cost low-powered Raspberry Pi computer that was released in 2012. Similar systems from other manufacturers were also available. Development of the computer required specialist support but is a feasible option for other field monitoring applications, and is a crucial element when attempting to capture higher frame rate, higher resolution images from camera systems, particularly those that may not be in a telemetered network.

Recommendations for future research

- Development of the camera system to include multiple cameras pointing at the same channel section from different positions to create stereo-pairs of channel sections to increase the accuracy of measurements in the channel and provide data on which to build repeat DEMs of the bed surface.
- Illuminating channel sections with infra-red (IR) lights and using a camera which does not filter IR wavelengths is the cheapest method of extending the monitoring time of the camera beyond daylight. Many lahars occurred in darkness hours in the Belham River Valley, on Montserrat, and the camera used in this study only monitored the channel in daylight, missing substantial sections of the lahar record.
- Testing of Kennedy's (1960, 1963) equations relating water-surface-wave length to flow velocity and depth is required for flows with different sediment loads and in rapidly varying, unsteady conditions to constrain the accuracy of flow estimates in natural systems, and refine the use of image analysis as a tool for flow measurement. This is particularly important for testing the sensitivity of

numerical models if data is used to validate model runs. Improving the understanding of measurement error from these empirical relationships is likely to increase the uptake of camera-based monitoring for flow measurement.

(2) Improve the understanding of inter-flow variability and sediment transport during a lahar in the Belham River Valley

Observations from a large lahar on 13th -14th October 2012 showed that the lahar was characterised by multiple peaks in seismicity that were attributed to “packets” of flow with increased discharge, apparent turbulence, bore incidence and cobble-boulder transport. Three-hundred and forty-nine bores were identified travelling downstream at irregular intervals of 6 to 2000 seconds during the 12 hours of imagery captured by the remote monitoring camera (in total the lahar lasted 29 hours). The bores played a significant role in the initiation of sediment motion.

Key findings and contributions to knowledge

- Flow was rapidly varying, unsteady and sediment-laden; flow variability was recorded over different temporal (hours to seconds) and spatial (in-channel to reach) scales. Measurements of flow at the resolution (seconds) obtained in this study have not previously been made for shallow water-sediment flows in natural channels.
- Multiple peaks in seismic signal between 1-30 Hz were registered during “moderate” to “large” lahars in the Belham River Valley. These peaks were interpreted as peaks in discharge (including increased bore incidence, turbulence and bedload transport) based on coincident observations of flow from camera images.
- Multiple peaks in discharge represented the catchment response to fluctuations in rainfall intensity, particularly during synoptic scale weather systems and also to the spatial variability of rainfall over different parts of the catchment. Modification of topographic catchment boundaries by volcanic sedimentation in Phase 1 increased catchment size to include a second debris fan to the west of SHV. Volcanic sedimentation can instantaneously alter catchment boundaries and this may have significant impacts on event volume, duration and run-out. Reactive recalculation of catchment boundaries in response to volcanic activity

is important for numerical-model based assessment of lahar run-out; particularly given that runoff rates increase due to tephra fall and vegetation damage during eruptive activity. In combination, these effects may result in an unexpectedly large and dangerous lahar, particularly in systems in which lahars of similar size occur regularly.

- Bores were interpreted as roll waves, and have been observed at other lahar prone systems (Hayes *et al.*, 2002). Formation is dependent on channel geometry, and flow velocity and depth. Studies of roll waves in the laboratory have emphasised their regularity resulting in problems of interpretation in natural channels (Doyle *et al.*, 2011). This study has shown that bores occurred irregularly but frequently in flow and based on preliminary calculations of the Vedernikov number, flow conditions were unstable, conducive to roll-wave formation. The irregularity of the bores is attributed to fluctuations in discharge (and channel boundaries) due to catchment runoff response, altering the stability of flow.
- The bores suddenly increased the flow depth and sediment transport capacity. Camera image sequences showed the initiation of cobble-boulder sized clasts as bedload by the bore. Multiple clasts of this size were rolled several metres downstream with the passage of each bore. In addition to entrainment of sediment in suspension which was inferred from the apparently turbulent bore fronts (and based on flume measurements of bores, Khezri and Chanson, 2012a), observations of bedload transport showed that the bores transported large volumes of sediment downstream. The specific contribution of bores to sediment yield is unknown, however observations of bores during lahars on Pinatubo, Philippines in combination with the high sediment yields measured at this system (Gran and Montgomery, 2005), and based on the high rate of recurrence (based on observations in the Belham River Valley, Montserrat), suggests the bores transport a large percent of the annual sediment yield from the system.
- The bores were only observed at the camera site and were not observed downstream in areas accessible in-person during a lahar. The bores have not been observed in previous flows, however it was thought this was due to limited access to upstream areas of the valley. Absence of the bores in flow

downstream was thought to be related to changes in channel width and depth. Primarily caused by modifications to the channel bed surface by commercial sand and aggregate extraction, which created a network of narrow depressions in the valley-floor.

- Upstream migrating trains of water-surface-waves were observed in multiple locations across the valley-floor in upstream and downstream parts of the valley throughout the lahar. The upstream migration and breaking of water-surface-waves was cyclic, in common with behaviour observed in the flume. When a bore front came into close proximity (within ~10 m) upstream of a train of water surface waves, they appeared to destabilise and break altogether (*en-masse*) generating a localised short-lived surge of water upstream, that was covered by the bore travelling downstream. Those wave trains that did not break during the passage of a bore temporarily reduced in height. In both cases, water surface waves formed immediately after the surge in the same location. In the absence of a bore, waves persisted for longer, growing and diminishing in height; waves within a train broke individually, sometimes triggering the breaking of adjoining waves. Observations of water-surface-wave trains lasting through bore fronts, and of stationary and upstream migrating waves persisting for up to 6 minutes suggests antidune bedforms may have been preserved in deposits. These observations are important steps in linking measurements of water-surface-waves and antidune bedforms in the flume with the natural environment.
- Observations of flow front propagation during a smaller lahar showed that the front was fines rich and deposited a drape of fines on the bed surface as it travelled downstream. These drapes of finer material have previously been interpreted (in the sediment record) as deposited during waning flows. The drapes of fine material may provide an important mechanism for flow propagation downstream on a coarse highly permeable bed surface. In addition, the persistence of the drapes on the bed surface between small lahars was thought to increase the run-out of subsequent events, by reducing the permeability and roughness of the bed surface.

Recommendations for future research

- Flume experimentation should be extended from bores travelling upstream (*i.e.* to tidal bores, Khezri and Chanson, 2012a) to downstream propagating bores to improve understanding of sediment transport dynamics.
- Research is required to better understand the seismic signal generated by bores and if possible what contribution this has on the whole lahar signal.
- Commercial sand extraction is a common economy in lahar-prone volcanic drainages (de Belizal *et al.*, 2013), and although criticised for placing employees in harms way of lahars (not to mention other volcanic flows), sand extraction could simultaneously modify the valley-floor to mitigate lahar impact downstream in inhabited areas, particularly in countries that cannot afford to invest in channel re-engineering. Further research is required both from an engineering stand-point and in the context of risk and livelihood literature, to better understand whether sediments could be extracted in a manner that could also mitigate lahar risk downstream, whilst not exposing sand workers to unacceptable risk.

(3) Identify sedimentary structures formed by rapidly varying, unsteady sediment-laden flows in natural environments and consider how they can be used for interpretation

Examination of deposits from lahars between June 2010 and March 2013, in combination with detailed flow observations from a large lahar in October 2012, and other observations in the Belham River Valley archive, has facilitated the interpretation of a number of different structures based on the identification of 10 facies in the sediment record.

Key findings and contributions to knowledge

- Deposits from upstream migrating water-surface-waves, breaking waves and hydraulic jumps were preserved in the sediment record of a sediment-laden rapidly varying, unsteady flow. There are very few published examples of upper-flow-regime bedforms in the modern sediment or rock record (Fielding, 2006); at many sites in this study over 90% of the deposit is interpreted as

upper-flow-regime origin. Only a couple of studies on antidune deposits have observed the flow (or similar flow) by which the deposit was emplaced (*e.g.* Alexander and Fielding, 1997). This study observed 12 hours of a large lahar and was able to identify deposits from the event in the sediment record.

- Some bedsets resembled those formed in the flume by supercritical water flows over aggrading sand beds. These included sands and pebbles in low angle downstream dipping bedsets with low-angle upstream dipping laminae (FA4), comparable to the laminae model defined experimentally in the flume by Clifton (1990) for upstream migrating water-surface-waves. Clast-supported gravel beds with lens patterns that were inter-bedded with structureless sands (FA5a) were interpreted as deposited by breaking water-surface-waves observed during the 13th-14th October 2012 lahar; these structures have also been observed by Alexander *et al.* (2001) and others (Yokokawa, *et al.*, 2010; Cartigny *et al.*, 2014) in the flume.
- Other bedsets of matrix supported gravels in lenticular beds with gradational boundaries surrounded by massive sands (FA2), were also interpreted as possible antidune origin. Inter-flow transitions in sediment availability were interpreted from textural difference in deposits in the vertical succession, particularly at Pit2013. Older deposits in the sequence contained a higher sand fraction despite being deposited by larger lahars (2010 flows). Occurring within months of volcanic activity, flows preferentially remobilised sand sized sediment from fresh PDC deposits in the upper catchment resulting in lahars with a high load of finer grained sediment. These flow conditions favoured high rates of aggradation and thick deposits. As the sediment supply coarsened upstream, the texture of deposits changed and gravel bedforms in thinner beds were preserved. This inter-flow transition was best observed in narrower mid-reach locations in deposits at the edge of channels. Downstream the sediment record became harder to interpret because of multiple flow pathways that were not occupied by every event (and in the case of the Belham River Valley, disruption to deposits by commercial sand extraction). Recognition of this is important because lahars have a low preservation potential and only deposits from the highest magnitude events may be preserved, only in distal areas in the rock record.

- Intra-flow transitions between upper-stage-planar beds and antidunes, and antidunes and chute-and-pool structures were also preserved in deposits at the edges of the valley-floor, in both sands and gravels. Empirical equations were used to calculate flow velocity and depth from lenticular trough fills (with awareness of truncation of the troughs). Palaeoflow reconstructions were comparable to waning flow velocities observed in the 13th-14th October 2012 lahar and peak flow during smaller lahars. This suggests that sedimentary structures preserved at the edges of the valley-floor were deposited in the waning stages of large lahars, and indicates that the sediment record of lahar prone catchments may be dominated by sediments deposited during waning flow.
- Furthermore, erosion into the bed surface during the 13th-14th October 2012 lahar preserved in the sediment record, in combination with observations following a large lahar on 20th May 2006 of ~ 2 m of vertical incision, show that as sediment supply upstream reduces, downstream the bed coarsens and net degradation occurs to the valley-floor. Over-time this results in the reworking and transport of sediment downstream and the formation of channels which gradually widen and deepen, effectively “deleting” past lahars from the sediment record. This shows the difficulties in using the sedimentological record to interpret the characteristics of past lahars, and highlights the need for improved sedimentological models for distal deposits (that are more readily preserved) based on detailed observations of lahars in upstream areas. The link between upstream and downstream is important because vertical sequences of deposits on distal fans may not represent sequential lahars (and the variation in flow character with time), because each flow may not occupy all of the wide debris fan, so the vertical sediment record at a single point may not capture significant changes in lahar character in response to volcanic sedimentation upstream. In this instance multiple vertical sequences at strategic points across a distal debris fan must be studied to obtain a more complete picture of activity. Reconstructing lahar activity from complex distal fan deposits is important for lahar hazard assessment because it helps to determine the magnitude and frequency of future lahars, and additionally helps to identify phases of volcanic eruption.

Recommendations for future research

- Experiments considering the stability of upper flow regime bedforms in mixed sediments would assist palaeoflow reconstruction in the field for further studies of this nature that consider sedimentary structures deposited by rapidly varying sediment laden flows.
- Building on this, further experimental work is required with mixed sediments to better improve the identification and differentiation of sedimentary structures deposited by breaking antidunes and by chute-and-pools. These bedforms are difficult to differentiate from one another in the rock record based on current knowledge.
- Fundamentally it is hoped that this study paves the way for further research that uses camera-based monitoring to measure flow and link observations with preserved deposits at the same site. While sediments may be difficult to interpret because of reworking and the components of flow variability in the natural environment hard to quantify, more observations of natural phenomenon assist in the design of laboratory experiments that more closely replicate natural flow and increase understanding of the relative importance of the nature and magnitude of flow variability on bedform development.

(4) Investigate catchment adjustment to volcanic sedimentation that may be used in the development of a model for other systems perturbed by multiple phases of eruption

Sixteen years of archive data on the Belham River Valley, Montserrat was analysed in addition to three elevation surveys, ground photographs and video collected during this study. Catchment response to volcanic perturbation was discussed in the context of antecedent rainfall analysis, and a model for channel stabilisation after volcanic sedimentation based on adapted models proposed by Gran and Montgomery, (2005) and Manville *et al.*, (2009) was discussed.

Key findings and contributions to knowledge

- Lahar size was dependent on the amount of sustaining rainfall in the 24 hours after lahar onset, irrespective of volcanic activity. However lahars were more readily triggered during or immediately after volcanic activity. Discussion of rainfall data highlighted the difficulties of defining rainfall thresholds for lahars even in small catchments because of the often sub-daily changes in catchment condition and the spatial variability of rainfall indicating that point-based rainfall measurement does not represent widespread runoff initiation. This is an important consideration, while lahar rainfall thresholds may be a useful tool given sufficient data, they are difficult to apply confidently during periods of volcanic activity.
- The Belham River Valley responded to volcanic sedimentation by increasing channel storage, slope gradient and decreasing bed surface roughness by decreasing grain size. This has been observed in other lahar prone systems (*e.g.* Pinatubo, Philippines; Gran and Montgomery, 2005; Gran *et al.*, 2011). In the Belham River Valley, three periods of net aggradation were identified (1995-1990; 2002-2003; 2006-2011), two periods with very little net loss or gain (2000-2002; 2012-2013) and one period of net degradation (2004-2006). The rate at which the system passed through different stages of the channel stabilisation model (Figure 3.19, Section 3.6) was dependent on the number of large lahars and the amount of sediment deposited by volcanic activity in the Belham Catchment. The rate of erosion of primary deposits decreased with time from eruption, typically the erosion rate decreased by one order of magnitude the year after volcanic emplacement. Although large volumes of sediment were stored in the upper catchment, the system was limited by the lahar magnitude required to occupy the full channel width and initiate undercutting of PDC terraces.

Recommendations for future research

- Monitoring of PDC terraces to better estimate erosion rates in response to lahar activity and to better constrain stabilisation of drainages with time from volcanic emplacement. This may be done using a terrestrial laser scanner and repeat

surveys to create repeat DEMs of vertical terraces, analysed in the context of the lahar record.

- Increasing data collection of DEMs in lahar prone systems at a sub-yearly interval to better constrain patterns of channel stabilisation. This may be achieved using SfM-MVS approaches that stitch large collections of aerial photographs together to create a three-dimensional surface.

Appendix

Appendix 1

1.1 Digital appendix

- **Appendix 1.1a:** world lahar occurrence database = *worldlahars.xlsx*
- **Appendix 1.1b:** MVO hazard zones, www.mvo.ms
= *MVOhazardlevelzone2014s.pdf*

1.2. Borehole logs, Belham River Valley, locations in Figure 1.8, p. 23

HYDROSOURCE ASSOCIATES WELL LOG

CLIENT: Montserrat Water Authority

Well ID: MBV-T1

Geologist: Erik Anderson, Roland Hoag

Description of Location: Belham Valley

Dates Drilled: 3/17/04 to 3/22/04



Depth	Well Diagram	Lithological Description	Air Lift Yield (gpm)	TDS
0	6" Casing to 188 ft.			
		Coarse Ash Flow, Pumice, Blocks		
31		Channel		
40		La pilli Fall		
43				
		Lahar		
68				
75		Lapilli Fall	3	382
		Volcanic Breccia	50	486
115				
		Lahar	106	400
145				
150		Volcanic Breccia	120	330
		Lahar	118	290
188				
190		Clay -Ash	120	
		Probable Channel	200	300
218				
		Channel Coarse Gravel and Weathered Pebbles	243	306
240				
243		Pumice-Lapilli and Claystone	243	
247		Volcanic Breccia	243	
		Lahar	264	293
260				
269		Probable Channel Weathered Pebbles	265	
		Lahar with Possible Small Channels	293	301
296				
298		Clay	293	298
		Fine Grained Ash Fall	280	
319				
		Fine-medium Grained Ash/ Lapilli Fall	290	300
360				

Appendix 1.2a Well log for MBV-T1, reproduced from Hydrosorce, 2004 (Appendix)

HYDROSOURCE ASSOCIATES WELL LOG

CLIENT: Montserrat Water Authority

Well ID: MBV-P1

Geologist: Erik Anderson

Description of Location: Belham Valley



Dates Drilled: 3/24/04 to 4/6/04

Depth	Well Diagram	Lithological Description	Air Lift Yield (gpm)	TDS
0	12" Casing to 195 ft.			
		Coarse Ash Flow, Pumice, Blocks		
31				
40		Channel		
43		Lapilli Fall	20	
		Lahar	20	
68				
75		Lapilli Fall		
		Volcanic Breccia	350	348
115				
		Lahar	420	350
145				
150		Volcanic Breccia	400	
		Lahar	500	330
180				
188	8-inch riser			
190		Clay-Ash		
195				
200	8-inch 20 slot ss screen	Probable Channel	460	303
218		Channel Coarse Gravel and Weathered Pebbles	875	
240				
243		Pumice-Lipilli and Claystone	1500	281
247		Volcanic Breccia		
260		Lahar		
265	5-foot sump Gravel pack			

Appendix 1.2b Well log for MBV-P1, reproduced from Hydrosorce, 2004 (Appendix)

HYDROSOURCE ASSOCIATES WELL LOG

CLIENT: Montserrat Water Authority

Well ID: MBV-P2

Geologist: Erik Anderson

Description of Location: Belham Valley



Dates Drilled: 4/8/04 to 4/15/04

Depth	Well Diagram	Lithological Description	Air Lift Yield (gpm)	TDS
0	12" Casing to 163 ft.			
18		Weathered Volcanic Breccia	0	
30		Weathered Channel	0	
75		Weathered Ashflow	0	
80		Weathered Lahar	0	
86		Channel	0	
98		Volcanic Breccia	0	
133		Lahar	0	
150	6-inch riser	Channel	90	365
158			190	324
163	6-inch 20 slot ss screen	Volcanic Breccia	630	327
179		Lapilli flow	843	309
190	3-foot sump			
193	Gravel pack			

Appendix 1.3c Well log for MVB-P2, reproduced from Hydrosorce, 2004 (Appendix)

Appendix 2

2.1. Montserrat National Grid (Clarke 1880) to WGS84 UTM 20N transformation (GPS processing notes by R.Herd, 2006 for Darnell, 2010)

Transformation into Montserrat Grid coordinates

Transformation from WGS84 to the local Montserrat Grid system can be made using the “Datum and Map” option in Leica GeoOffice. There are third party and freeware solutions, as well as spreadsheets from the Ordnance Survey website with which you can perform these transformations. It is convenient however when working with Leica GeoOffice to be able to perform all the transformation in the software and this is described briefly.

The Montserrat Grid is a Transverse Mercator projection made onto the Clarke 1880 ellipsoid.

The 1:25,000 tourist map of Montserrat gives the full projection information. This is entered into GeoOffice as a new Projection in the TM directory:

Name	MONCAD.SET
False Easting	400000.0000
False Northing	0.0000
Latitude of Origin	0° 00' 00.00000" N
Central Meridian	62° 00' 00.00000" W
Zone Width	6° 00' 00.0"
Scale Factor at Origin	0.99950000000

The actual transformation is entered in GeoOffice as a new 3D transformation. This transformation maps the WGS84 coordinates generated from the GPS processing into the local grid coordinates on the Clarke 1880 ellipsoid. The details of the two ellipsoids are:

	Semi-major axis (a)	Reciprocal flattening (1/f)
WGS 1984	6378137.0000	298.2572235630
Clarke 1880	6378249.145	293.4650

Transformation parameters were calculated in 1996 when GPS was introduced to the Montserrat Volcano Observatory. The Montserrat DOS (Department of Surveying) benchmarks were occupied with dual-frequency GPS receivers for several days. The data were processed in a single point mode to derive independent accurate and precise coordinates for each benchmark in WGS84. The DOS provided their station coordinates in easting, northing and height and a routine from Leica calculate the displacement, rotation and shear factors detailed below:

Name	gps2grd
Ellipsoid A	WGS 1984
Ellipsoid B	Clarke 1880

Height Mode	Ellipsoidal
Model	Bursa Wolf
dx	132.9380
dy	-128.2850
dz	-383.1110
Rx	0.00000
Ry	0.00000
Rz	12.79960
SF	9.9976
X0	-
Y0	-
Z0	-

2.2. Digital Appendix data files:

- **Appendix 2.2a:** Pre-eruption DEM= *pre_dem.tif*
- **Appendix 2.2b:** 1999 DEM= *1999dem.tif*
- **Appendix 2.2c:** June 2010 DEM= *2010dem.tif*
- **Appendix 2.2d:** June 2010 DSM= *2010dsm.tif*
- **Appendix 2.2e:** 1999 aerial photographs= *Wadge1999 folder*
- **Appendix 2.2f:** 2002 (precise date unknown)= *2002aerial.tif*
- **Appendix 2.2g:** 2006 satellite image= *2006satellite.tif*
- **Appendix 2.2h:** 2007 satellite image= *2007satellite.tif*
- **Appendix 2.2i:** 2010/2011 Quickbird image= *March2011survey*
- **Appendix 2.2j:** Aerial survey corrected March 2013= *March2013survey folder*
- **Appendix 2.2k:** Aerial survey corrected February 2012= *February2012survey folder*
- **Appendix 2.2l:** 2002 DEM= *2002dem.tif*
- **Appendix 2.2m:** 2003 DEM= *2003dem.tif*
- **Appendix 2.2n:** 2005 DEM= *2005dem.tif*
- **Appendix 2.2o:** 2006 DEM= *2006dem.tif*
- **Appendix 2.2p:** 2007 DEM= *2007dem.tif*
- **Appendix 2.2q:** Leica processing method= *leicaprocessingnotes.pptx*
- **Appendix 2.2r:** 2011 DEM= *2011dem.tif*
- **Appendix 2.2s:** 2012 DEM= *2012dem.tif*
- **Appendix 2.2t:** 2013 DEM= *2013dem.tif*
- **Appendix 2.2u:** Lahar database: *lahardatabase.xlsx*
- **Appendix 2.2v:** Monitoring data availability = *monitoring.xlsx*
- **Appendix 2.2w:** Antecedent rainfall data= *rainfall.xlsx*
- **Appendix 2.2x:** Matlab script antecedent rainfall = *antecedentproc.m*
- **Appendix 2.2y:** Wavelength data= *wavelength.xlsx*
- **Appendix 2.2z:** MFG radar images= *MFGimages folder*
- **Appendix 2.2aa:** MFG matlab script= *MFG.m*
- **Appendix 2.2ab:** Deposit samples: *grainsize.xlsx*

2.3. Oblique aerial photographs



Appendix 2.3a: Photograph looking upstream of Tyres Ghaut, 1/10/2003. BGS (2014), P563210



Appendix 2.3b: Photograph looking upstream of Tyres Ghaut, 30/6/2003. BGS (2014), P565273



Appendix 2.3c: Photograph looking upstream of Tyres Ghaut, 28/6/2005. BGS (2014) P650542



Appendix 2.3d: Photograph of Tyres Ghaut 3/12/2008.
(<http://www.montserratvolcano.org/frogs2.htm>, downloaded 14/3/2013)



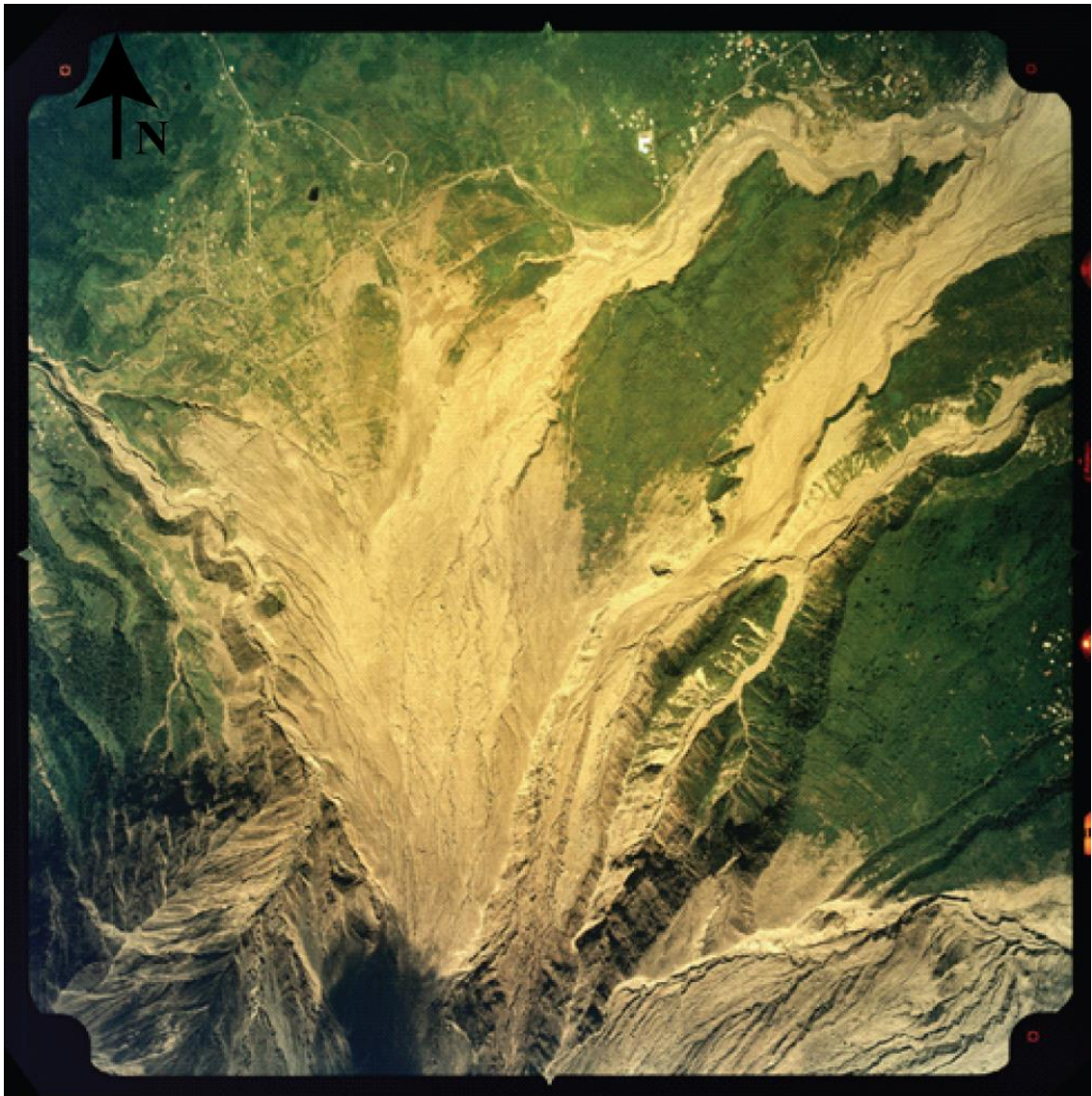
Appendix 2.3e: Photograph looking upstream of Tyres Ghaut, September 2009. Reproduced with permission from of Paul Cole, University of Plymouth



Appendix 2.3f: Photograph looking upstream of Tyres Ghaut, 11/10/2009. MVO flickr, <https://www.flickr.com/photos/mvo/>. Downloaded: 14/6/2014. Valley fill pre-PDC estimated.



Appendix 2.3g: Photograph looking upstream of Tyres Ghaut, September 2009.
Reproduced with permission from Paul Cole, University of Plymouth



1.5 km

Appendix 2.3h: Photograph of Farrell's Plain looking north from the vertical aerial survey conducted in February 1999. Reproduced with permission from Geoff Wadge, University of Reading



Appendix 2.3i: Photograph looking downstream from Tyres Ghaut into Dyers River, 10/1/2003. BGS (2014), P563204



Plate 9. (A) Aftermath of 25 June 1997. Upper reaches of Mosquito Ghaut (centre) are substantially filled with block-and-ash flow deposits. Pyroclastic surge deposits blanket Farrell's plain west of Mosquito Ghaut, northwards as far as lower parts of Windy Hill and Streatham village (middle and right). Houses of Dyer's village are visible on the extreme right, across Tyre's Ghaut. Note the broad singe zones (vegetation turned brown) and tendency for the deposit extremities to extend into topographic depressions (photo by G. E. Norton, 28 June 1997; © NERC).

Appendix 2.3j: Photograph of Farrell's Plain, looking towards SHV after 25/6/1997 BAF and surge. Re-produced from Kokelaar *et al.*, 2002 (Plate 9A). Original photograph copyright to NERC



Appendix 2.3k: Photograph of Farrell's Plain, looking towards SHV, 2/9/2002. BGS (2014), P560595



Appendix 2.3l: Photograph looking downstream of Dyers River, 17/8/2006. BGS (2014), P657685

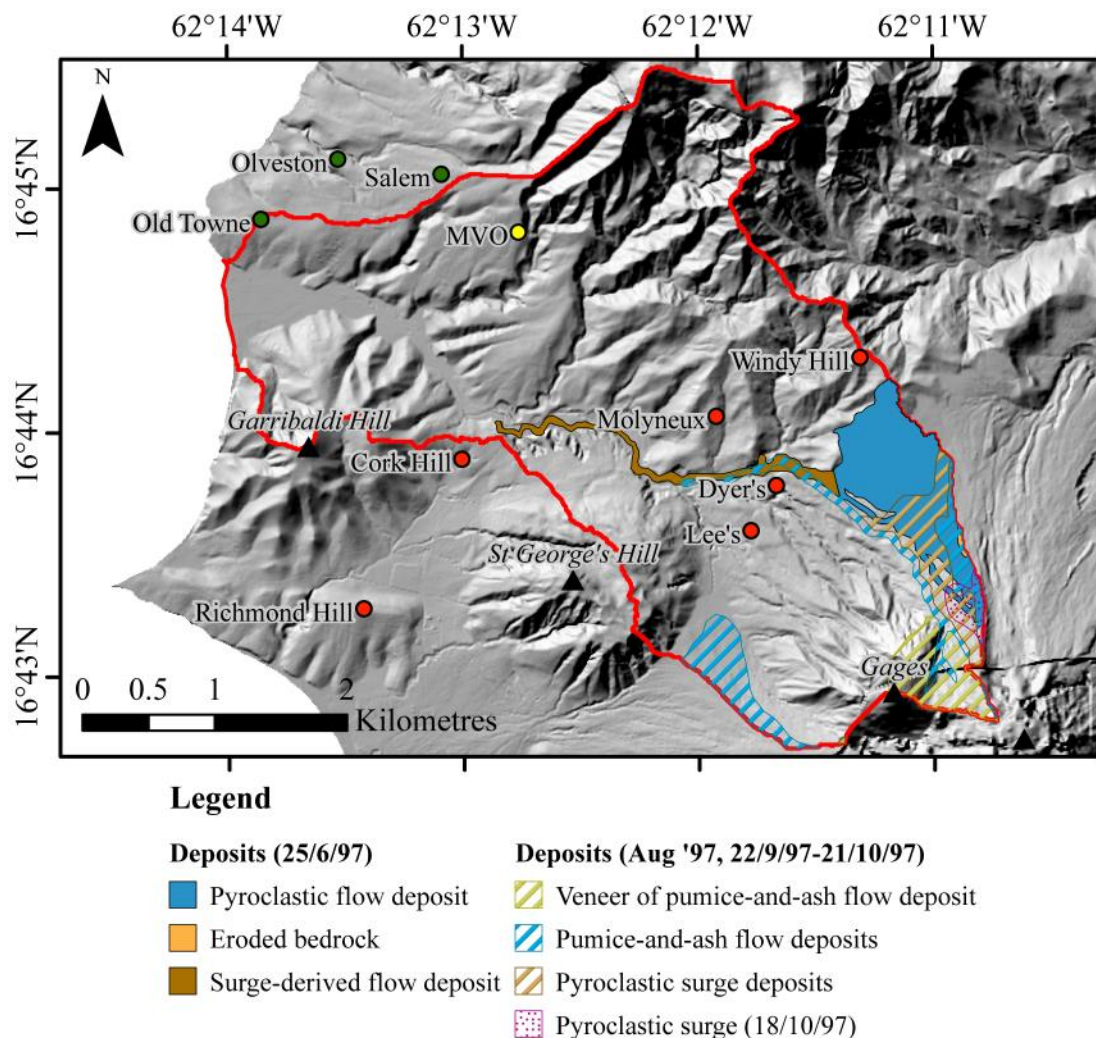


Appendix 2.3m: Photograph looking downstream into Tyres Ghaut and Dyers River, 19/9/2006. BGS (2014), P65449

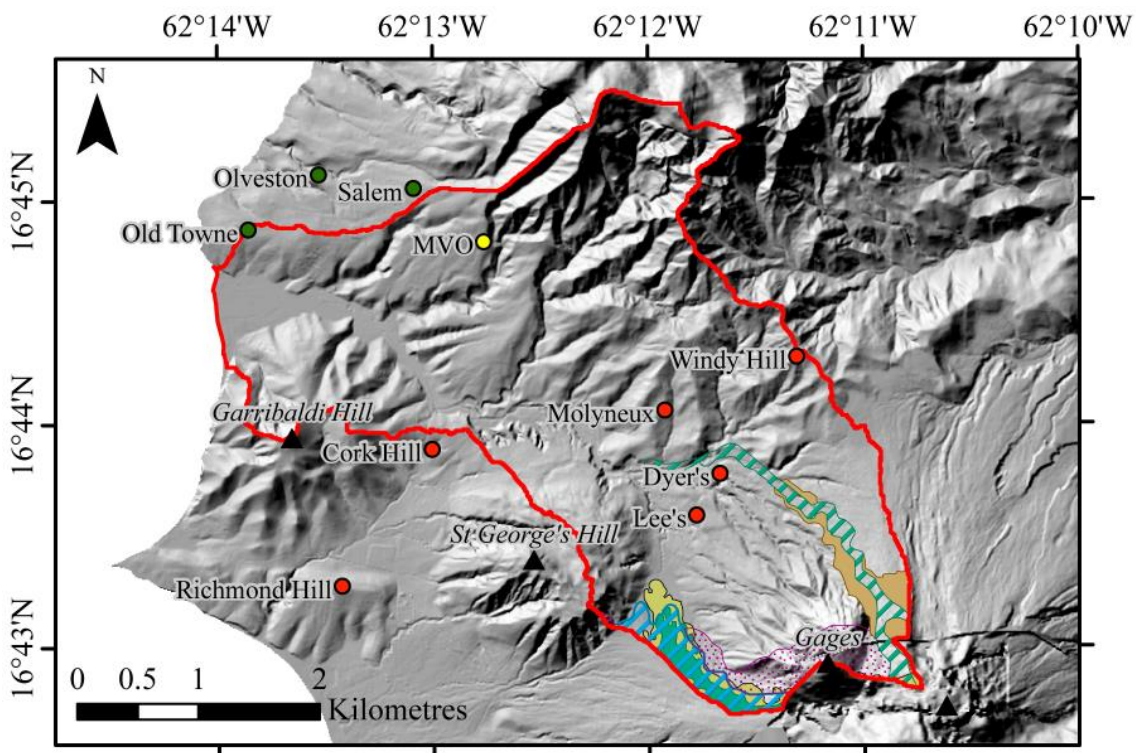


Appendix 2.3n: Photograph looking upstream into Tyres Ghaut, 8/1/2007. Re-produced from De Angelis *et al.* (2007), Figure 3(d). Original photograph copyright MVO/BGS/NERC.

Appendix 2.4 Digitised flow deposit maps from publications



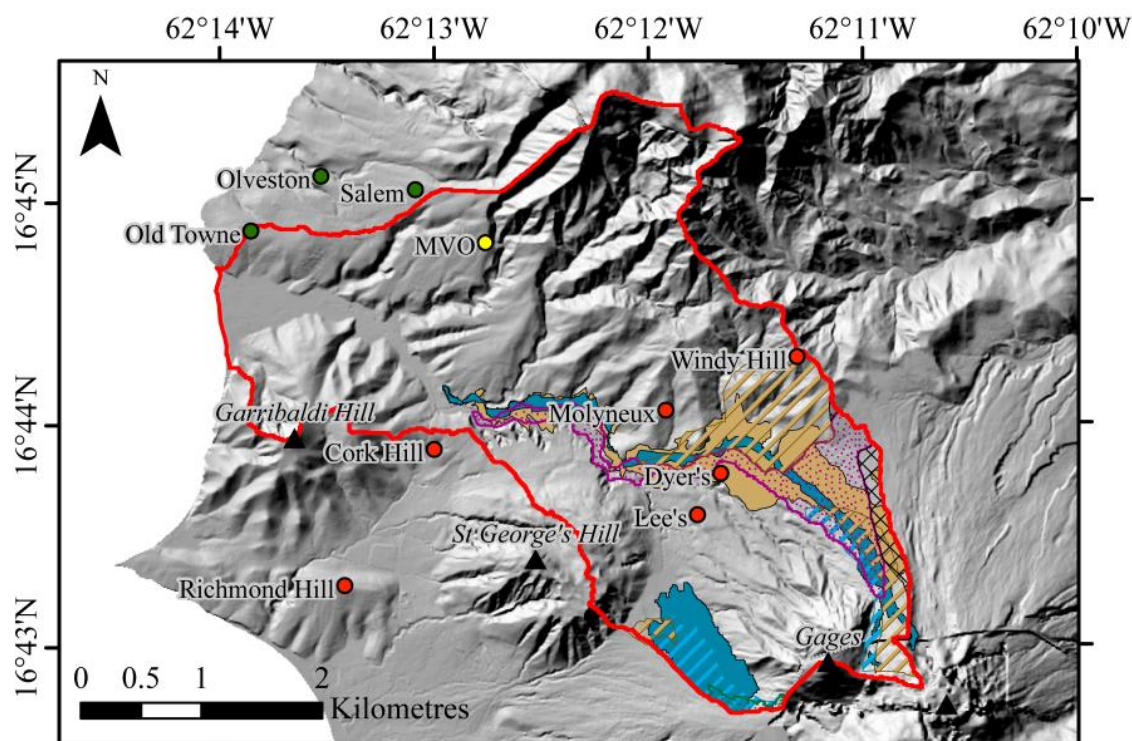
Appendix 2.4a Map showing the extent of pyroclastic flow and pyroclastic surge deposits recorded during Phase 1 within the BV catchment (red perimeter). Inhabited (green) and abandoned (red) villages, and the MVO (yellow) are shown. Local topographic highs are shown by labelled black triangles. Base map: shaded relief model (azimuth= 315, altitude= 45) of merged DEM from 1999 (north of island) and 2010 (south of island) *Druitt et al.* (2002b).



Legend

- Pumice flow deposits (28/7/08)
- Pyroclastic surges (5/12/08-3/01/09)
- BAF deposits (25/08/08)
- BAF deposits (2/01/09)
- Explosion surge deposit (3/12/08)
- BAF and pumice flows (3/12/08-2/01/09)

Appendix 2.4b Map showing the extent of pumice flow, BAF and pyroclastic surge deposits recorded during Phase 4 within the BV catchment (red perimeter) (Komorowski *et al.*, 2010). Inhabited (green) and abandoned (red) villages, and the MVO (yellow) are shown. Local topographic highs are shown by labelled black triangles. Base map: shaded relief model (azimuth= 315, altitude= 45) of merged DEM from 1999 (north of island) and 2010 (south of island).



Legend

Deposits (8/1/10)	Deposits (5/2/10)	Deposits (11/2/10)
■ Pyroclastic flows	▨ Pyroclastic flows	▨ Pumice flows
■ Pyroclastic surges	▨ Pyroclastic surges	▨ Lateral blast
	▨ Pyroclastic surges	▨ Pyroclastic surges
		▨ 'Dome collapse' flows

Appendix 2.4c Map showing the extent of pyroclastic flow, pumice flow, pyroclastic surge and lateral blast deposits recorded during Phase 5 within the Belham catchment (red perimeter) Cole et al. (2010b). Inhabited (green) and abandoned (red) villages, and the MVO (yellow) are shown. Local topographic highs are shown by labelled black triangles. Base map: shaded relief model (azimuth= 315, altitude= 45) of merged DEM from 1999 (north of island) and 2010 (south of island)

Appendix 2.5 GPS Data quality assessment

Date	Number of points	Number of phase points	Number of points kept RMS ≤ 20 mm
6/3/13	10246	8527	5289
7/3/13	16237	13623	10313
9/3/13	26401	17037	10410
13/2/12	12280	10784	8261
14/2/12	7666	5760	4724
15/2/12	16984	10883	8549
16/2/12	20774	17719	13868
21/2/12	15898	13440	11365
22/2/12	4864	4690	3968
26/1/11	3293	2660	966
28/1/11	5254	4027	3202
1/2/11	3611	2906	2417
4/2/11	3988	3839	3311
29/3/11	199	193	174
31/3/11	7959	7865	6700

Appendix 2.6 Frame Rate Testing - Updated 27 June 2012 Adam Stinton - MVO

Transfer of images by FTP from the Cork Hill camera to MVO tested at 4 and 5 second intervals with three different image sizes. Results are shown below. No tests on 24 June due to power outage at MVO affecting Wifi receiver on mast.

5 second interval:

Image Dimensions	Ave Filesize (kb)	Date	Time (UTC)	Transfer rate (min:secs)		
				Average	Maximum	Minimum
1296 x 960	146	21 June	13:15 to 23:00	00:14	04:03	00:05
	159	22 June	09:00 to 13:16	00:09	00:16	00:05
1280 x 960	117	22 June	13:16 to 23:00	00:05	00:11	00:05
	119	23 June	09:00 to 21:02	00:06	00:16	00:04
1024 x 768	110	23 June	21:02 to 23:00	00:13	00:16	00:10
	95	25 June	13:00 to 15:56	00:11	01:10	00:05

Gap frequency stats:

1296 x 960 on 21 June			1296 x 960 on 22 June			1280 x 960 on 22 June		
Gap	Count	%	Gap	Count	%	Gap	Count	%
4	0	0.0	5	526	29.7	5	5731	88.6
5	218	8.7	6	24	1.4	6	273	4.2
6	12	0.5	10	1050	59.2	10	412	6.4
7	0	0.0	11	122	6.9	11	53	0.8
10	473	18.9	12	1	0.1			
11	51	2.0	15	45	2.5			
12	2	0.1	16	6	0.3			
15	1297	51.8						
16	260	10.4						
20	54	2.2						
21	14	0.6						

25	64	2.6						
26	24	1.0						
> 30	35	1.4						

1280 x 960 on 23 June			1024 x 768 on 23 June			1024 x 768 on 25 June		
Gap	Count	%	Gap	Count	%	Gap	Count	%
4	1	0.0	10	207	38.1	5	9	1.0
5	5505	79.0	11	27	5.0	10	613	66.5
6	275	3.9	15	256	47.1	11	76	8.2
7	1	0.0	16	53	9.8	15	171	18.5
10	669	9.6				16	35	3.8
11	86	1.2				> 20	18	2.0
15	341	4.9						
16	88	1.3						

4 second interval:

Image Dimensions	Ave Filesize (kb)	Date	Time (UTC)	Transfer rate (min:secs)		
				Average	Maximum	Minimum
1280 x 960	123.7	26 June	09:00 to 23:00	00:07	00:07	00:04

1280 x 960 on 26 June		
Gap	Count	%
4	3338	43.9
5	182	2.4
8	3072	40.4
9	424	5.6
12	337	4.4
13	88	1.2
16	117	1.5
17	40	0.5

Appendix 2.7: MudPi.py code (Author Alex Etechells, UEA; edited by M. Froude)

```
#!/usr/bin/python
#above line because the script is an executable
'''
        mud Pi
    automated ip camera image capture and ftp upload
        13 Aug 2012
    @author: Alex Etechells    envsoft@uea.ac.uk
'''
#libraries
import os
import urllib2
import datetime
import zipfile
import ftplib
import traceback
import time
import glob
import socket

#*****
#*****
#                KEEP A COPY RUNNING!!!!
#crontab calls this script every 10 mins
#so we need to see if it is already running and, if so, quit

#make sure we always run in the same directory
os.chdir("/home/pi/alex/python")

#if we get past looking for other copies running we store our
pid
#in mudpi.pid, so let's look for that
if os.path.isfile("mudpi.pid"):
    f = open("mudpi.pid")
    pid = f.readline()
    f.close()
    #if the prog is running /proc/pid/cmdline will contain
mudPi.py
    prcl = "/proc/" + str(pid) + "/cmdline"
    if os.path.isfile(prcl):
        f = open(prcl)
        cl = f.readline()
        f.close()
        #if it does contain mudPi.py, we are already running and
        #this instance and can quit
        if "mudPi.py" in cl:
            quit()

#if we get to here, this is the currently running instance and
needs
#to save its pid
f = open("mudpi.pid", "w")
f.write(str(os.getpid()))
f.close()
#*****
#*****
```

```

#settings
#cameraSource = "http://envserver3.env.uea.ac.uk/temp/mud.jpg"
#1280 x 960 test image
cameraSource = "http://139.222.96.16/image.jpg" #env ip cam -
smaller image
#cameraSource = "http://172.20.0.121/image.jpg" #Mel's Montserrat
IP Cam
filePrfx = "image"
#ftpHost = "172.20.0.16" #Montserrat FTP
ftpHost = "139.222.96.130" #UEA test FTP
ftpPort = 21
#ftpPassword = "I have no idea what your password is" #Montserrat
FTP
ftpPassword = "v0lcan0"      #UEA test FTP
#ftpUsername = "mvo"         #Montserrat FTP
ftpUsername = "mudpi"       #UEA test FTP
#ftpRemotePath = "data/MVO_IMAGERY/RemoteCameras" #Montserrat FTP
#if above does not work try
#ftpRemotePath = "/home/mvo/data/MVO_IMAGERY/RemoteCameras"
#Montserrat FTP
ftpRemotePath = "data"      #UEA test FTP
#localFileLocation = "/home/pi/alex/python/"
localFileLocation = "/media/BIPRA 120GB/"
daylightStart = datetime.time(5,0,0,0) #GMT! e.g 6:30 =
datetime.time(6,30,0,0)
daylightEnd = datetime.time(19,0,0,0)
captureDelay = 200 #minimum time between image captures in
microseconds 200
#
#           should mean no more than 5 per sec
minSpace = 1 #the minimum number of gb still free when the
system decides to
#
#           ftp - this should be bigger than the size of the
zip files

#globals
currentZipTime = -1

socket.setdefaulttimeout(10)

#need to set up a reference to z
z = zipfile.ZipFile(localFileLocation + "temp.zip","w")
z.close()
os.remove(localFileLocation + "temp.zip")

#delay between captures
nextImageTime = datetime.datetime.now()

def grab_a_snap():
    global nextImageTime #function needs to know its using a
global because it modifies it
    # wait until specified time has past since last snap
    while datetime.datetime.now() < nextImageTime:
        #waiting for next image
        #we need some operation in the while block apparently
        one = 1
    try:
        nextImageTime = datetime.datetime.now() +
datetime.timedelta(microseconds = captureDelay * 1000)

```

```

    # open the web page picture and read it into a variable
    opener1 = urllib2.build_opener()
    page1 = opener1.open(cameraSource)
    my_picture = page1.read()
    return my_picture
except:
    print "problems accessing camera"
    #give it a sec before it trys again
    time.sleep(1)
    return "NO IMAGE FILE"

def freeGbSpace(p):
    """
    Returns the number of free gb on the drive that ``p`` is on
    """
    s = os.statvfs(p)
    return s.f_bsize * s.f_bavail / 1000000000.0

def ftpUpload():
    zipFiles = glob.glob(localFileLocation + "image*.zip")
    for eachZip in zipFiles:
        if os.path.isfile(eachZip):
            try:
                print "FTP of " + eachZip
                ftp = ftplib.FTP()
                ftp.connect(ftpHost,ftpPort)
                print ftp.getwelcome()
                try:
                    ftp.login(ftpUsername, ftpPassword)
                    ftp.cwd(ftpRemotePath)
                    f= open(eachZip,"rb")
                    ftp.storbinary("STOR " +
os.path.basename(eachZip), f)
                    print "upload success"
                    f.close()
                    #delete zipfile if upload successful
                    os.remove(eachZip)
                finally:
                    ftp.quit()
            except:
                traceback.print_exc()
        except:
            print "buggrit ftp problems!"

#program loop
while True:
    print "day or night?"
    #is it daylight or not?
    if datetime.datetime.now().time() >= daylightStart and
datetime.datetime.now().time() <= daylightEnd:
        print "day"
        #DAYLIGHT
        #if it's time for a new zip check available disk space
        print "10min interval no " + str(currentZipTime) + " of
the day. Remaing disk space(gb) =" +
str(freeGbSpace(localFileLocation))

```

```

        if currentZipTime != (datetime.datetime.now().hour * 6 +
datetime.datetime.now().minute / 10) and
freeGbSpace(localFileLocation) < minSpace:
    #do an ftp upload
    #close currently open zipfile
    try:
        z.close()
    finally:
        #ftp the day's zip files
        print "No space: ftp"
        ftpUpload()
        #give things 5 secs to settle down
        time.sleep(5)
else:
    #acquire an image
    now = datetime.datetime.now()
    fnm = str(now.year) + "_"
    if now.month < 10:fnm += "0"
    fnm += str(now.month) + "_"
    if now.day < 10: fnm += "0"
    fnm += str(now.day) + "_"
    if now.hour < 10: fnm += "0"
    fnm += str(now.hour) + "_"
    if now.minute < 10: fnm += "0"
    fnm += str(now.minute) + "_"
    if now.second < 10: fnm += "0"
    fnm += str(now.second) + "_"
    if now.microsecond < 10: fnm += "0"
    if now.microsecond < 100: fnm += "0"
    if now.microsecond < 100: fnm += "0"
    if now.microsecond < 1000: fnm += "0"
    if now.microsecond < 10000: fnm += "0"
    if now.microsecond < 100000: fnm += "0"
    fnm += str(now.microsecond)
    name = filePrfx + str(fnm) + (".jpg")
    thisfile = grab_a_snap()
    if currentZipTime != (datetime.datetime.now().hour *
6 + datetime.datetime.now().minute / 10):
        #close currently open zipfile
        try:
            z.close()
        finally:
            currentZipTime =
(datetime.datetime.now().hour * 6 +
datetime.datetime.now().minute / 10)
            now = datetime.datetime.now()
            zipname = "images_" + str(now.year) + "_"
            if now.month < 10:zipname += "0"
            zipname += str(now.month) + "_"
            if now.day < 10: zipname += "0"
            zipname += str(now.day) + "_"
            if currentZipTime < 100: zipname += "0"
            if currentZipTime < 10: zipname += "0"
            zipname += str(currentZipTime)
            #create a zip archive for the images
            z = zipfile.ZipFile(localFileLocation +
zipname + ".zip", "w") #Opening an existing zip file in write
mode will erase the zip,

```

```
#did we get an image?
if str(thisfile) != "NO IMAGE FILE":
    try:
        print "Image: " + name
        #add to zip
        z.writestr(name,thisfile)
    except:
        print "problem adding to zip"
else:
    #NOT DAYLIGHT
    print "night"
    currentZipTime = -1
    #close currently open zipfile
    try:
        z.close()
    finally:
        #ftp the day's zip files
        print "call ftp"
        ftpUpload()
        #have a kip before we try again
        time.sleep(60)
```


Appendix 2.8: Picworks Assessment

By setting up sample points one pixel away (to the right, left, above and below) the control points used in the PicWorks calculation we can assess how much variability there is in pixel-metre scaling across the image. Results show that elevation variability is less than 1 meter. Results are below for reference- also look at matlab files dated 5/9/13. An elevation plane was fitted at 31.8m and 35.5m and results from each were interpolated across this plane from left to right to account for elevation differences across the image due to slope of channel downstream.

Control point	Shift direction (1 pixel)	Difference between control point location and 1 pixel shift			Distance from control point (m)
		Eastings difference (m)	Northings difference (m)	Elevation difference (m)	
3	left	3.81664	6.524741	0.509288	7.576171
3	right	3.934906	6.356142	0.514936	7.493276
3	up	4.274339	7.033137	0.512112	8.246044
3	down	3.477252	5.847739	0.512112	6.822726
2	left	-0.58281	-1.14391	0.708143	1.466177
2	right	-0.48199	-1.30093	0.713791	1.5602
2	up	-0.41501	-0.82216	0.710967	1.163467
2	down	-0.60501	-1.62268	0.710967	1.872064
1	left	0.997956	-5.40505	0.344297	5.507178
1	right	1.116214	-5.45661	0.349945	5.580588
1	up	1.117504	-5.06802	0.347121	5.201358
1	down	1.057504	-5.80222	0.347121	5.908009

Results from shifting sample points by 1 pixel around the control points used in the pic works calculation. Control point 1 is closest to the camera, control point 3 is furthest away in the right hand side of the image.

Appendix 3

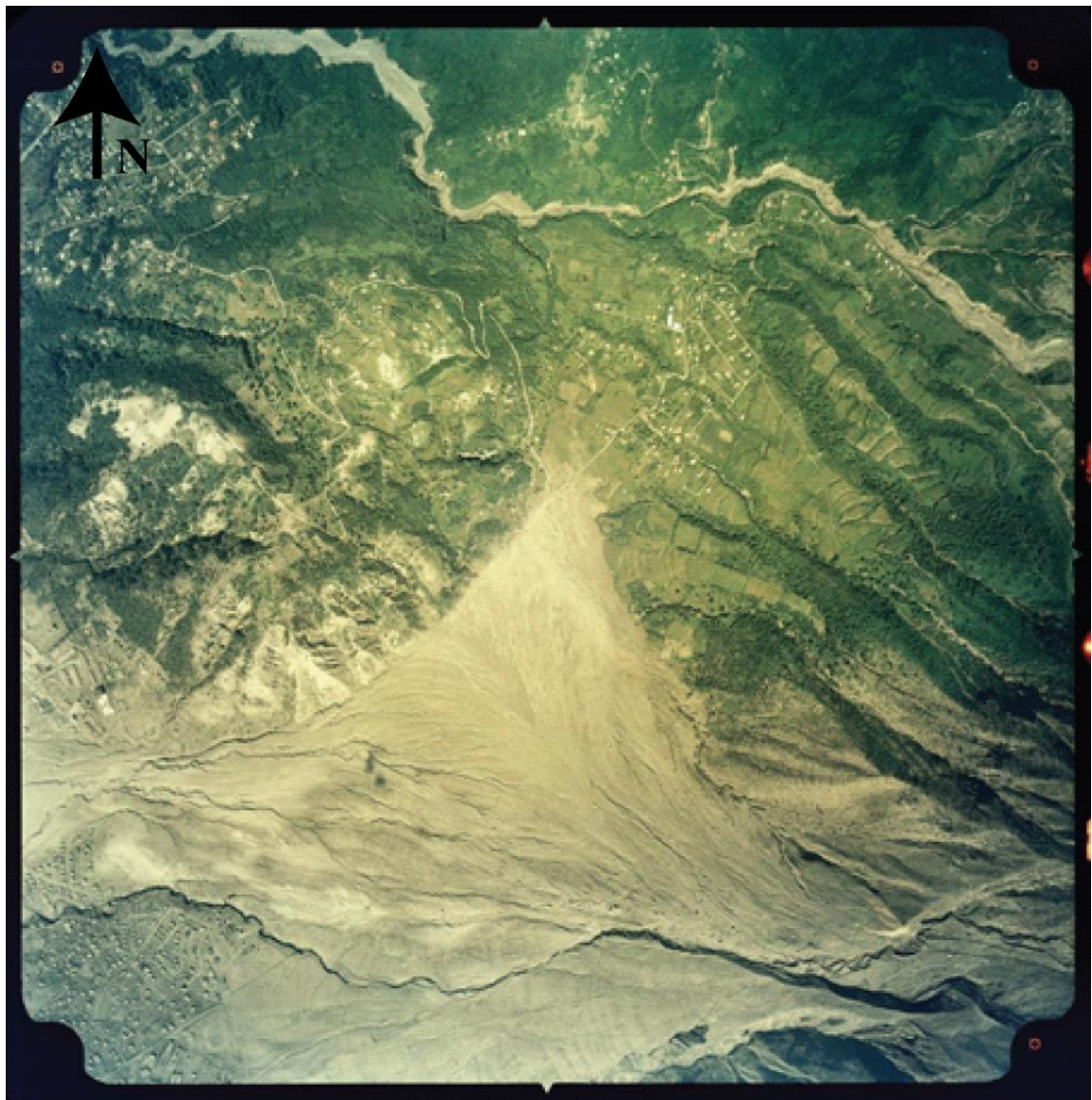
Appendix 3.1: Gages Fan photographs



Appendix 3.1a: Looking south-east to Gages Mountain, 7/8/1997. BGS (2014), P063380



Appendix 3.1b: Looking south-east up Gages Fan, 1/2/1998. BGS (2014), P063974



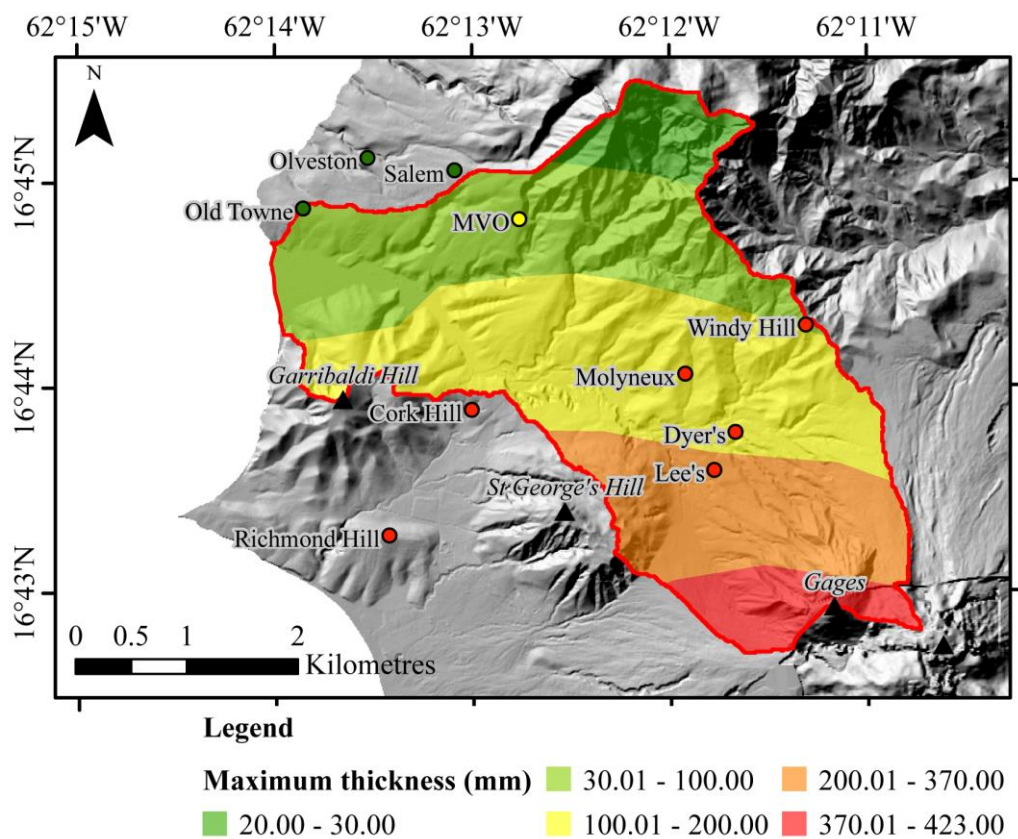
0.6 km

Appendix 3.1c: Photograph of Gages fan looking north from the vertical aerial survey conducted in February 1999. Reproduced with permission from Geoff Wadge, University of Reading

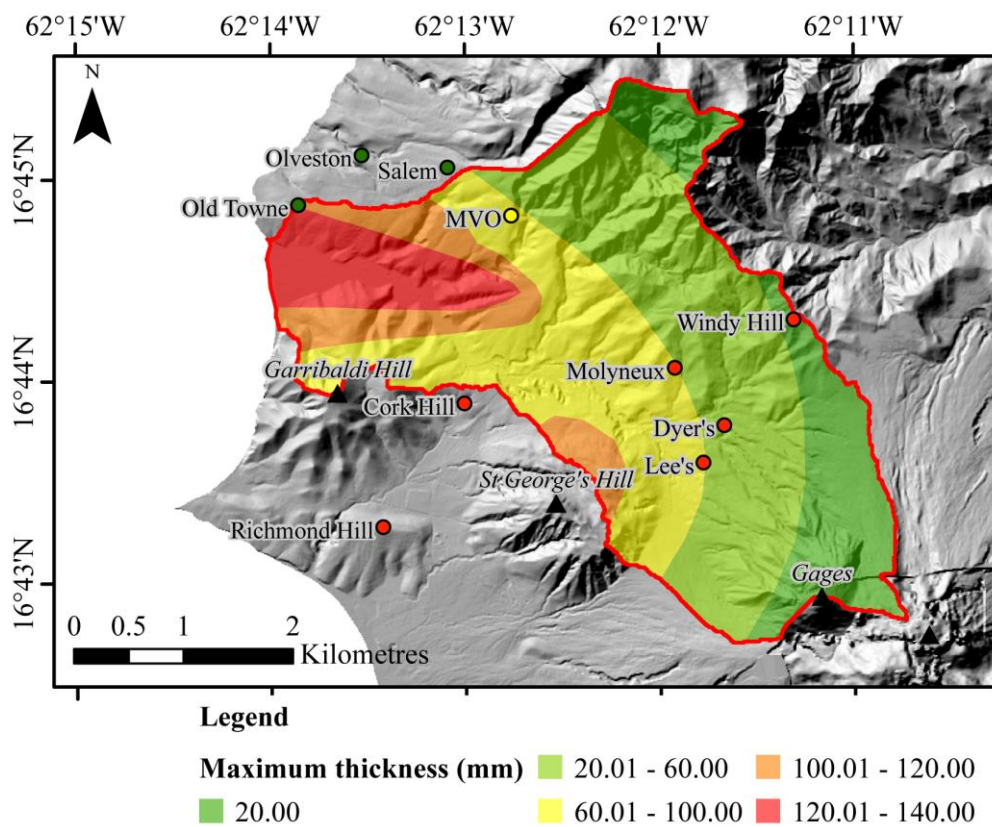


Appendix 3.1d: Looking south across Gages Fan, 26/2/2001. BGS (2014), P556446

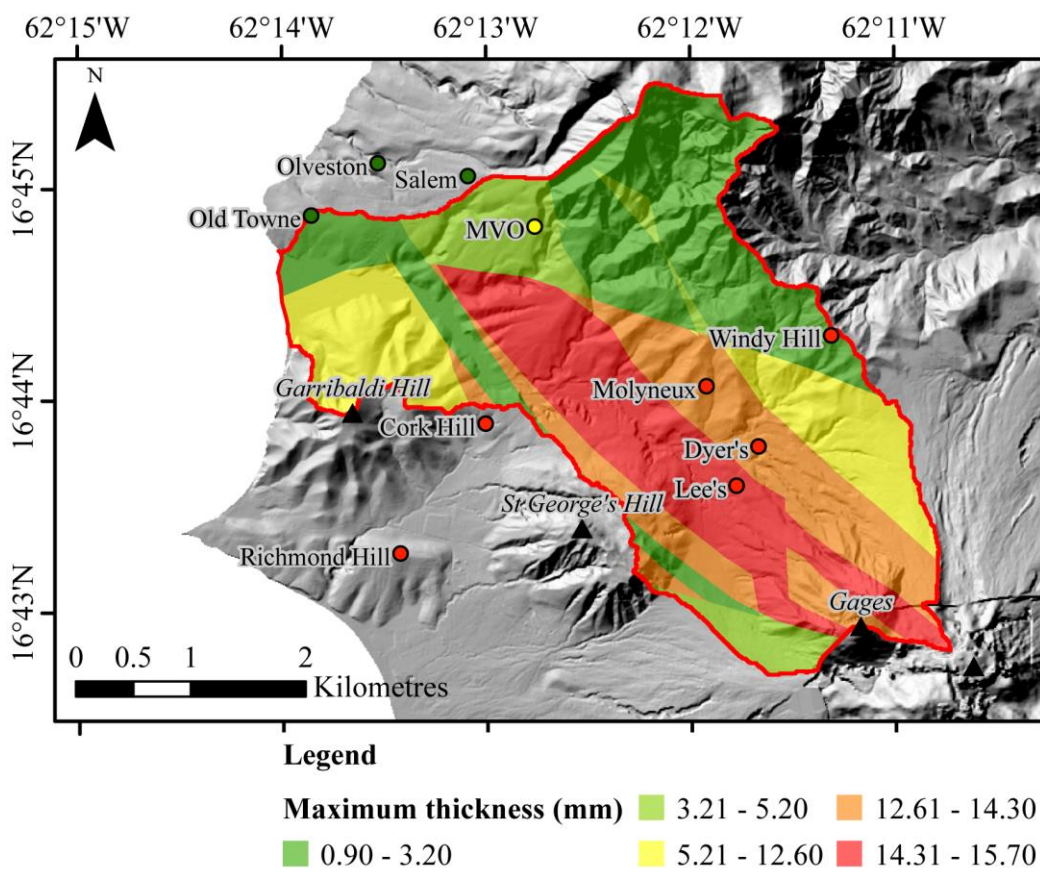
Appendix 3.2. Tephra Fall maps



Appendix 3.2a: Tephra fall from Bonnadonna *et al.* (2002), Phase 1.

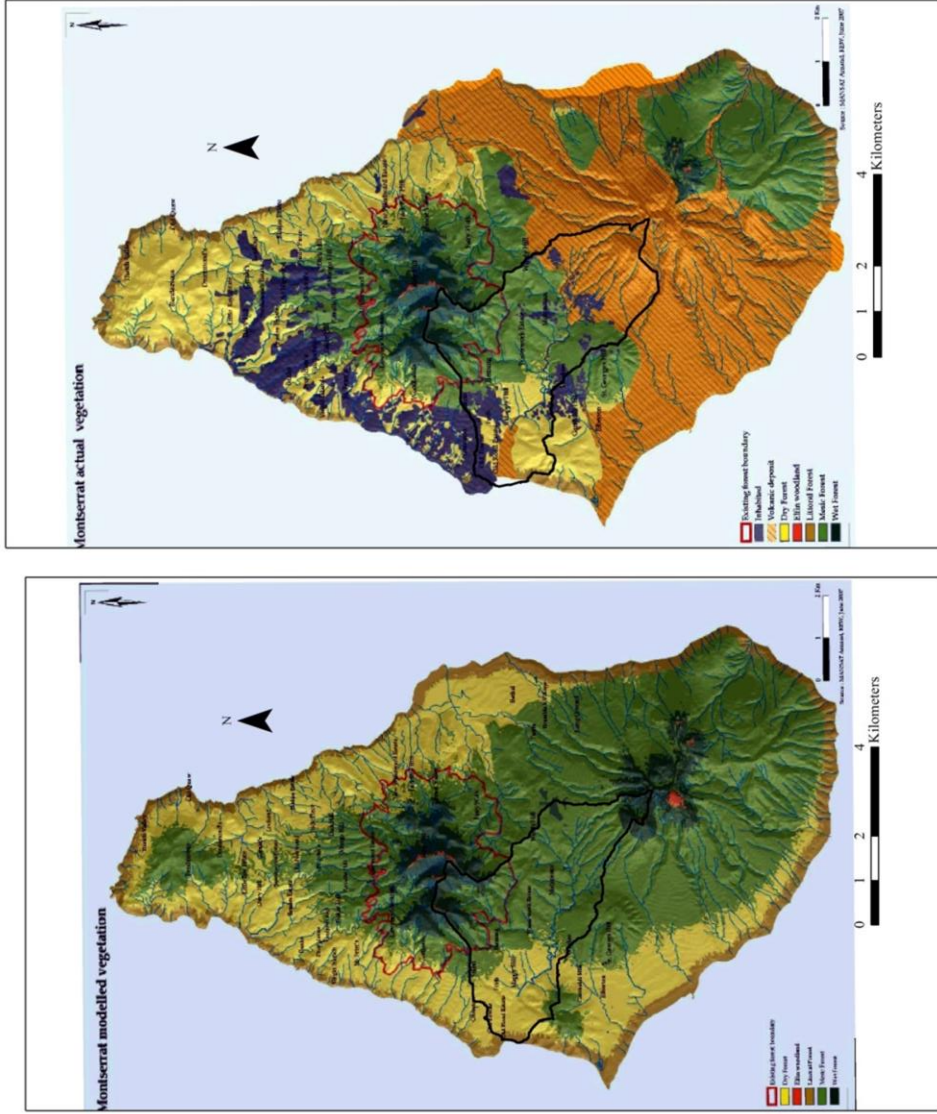


Appendix 3.2b: Tephra fall from Edmonds *et al.* (2006). Deposits emplaced on 12-15 July 2003.



Appendix 3.2c: Tephra fall from MVO (2010), Phase 5.

Appendix 3.3 Vegetation maps, Montserrat



Appendix 3.3a: Pre-eruption vegetation (Reproduced from Young *et al.* 2008) [left]
 Appendix 3.3b: Vegetation present day (Reproduced from Young *et al.* 2008) [right]

Appendix 3.4 Digital Appendix

- **Appendix 3.4a:** Belham Photographic archive= *belhamphoto* folder
Contains sub-folders *B4, B6, Belhambridge, Camerasitearea, Coast, Islesbaycrossing, pdfdisint, sandmining, wind*
- **Appendix 3.4b:** Video from 30/10/2009= *30_10_2009lahar* folder
- **Appendix 3.4c:** Lahar video footage, copyright David Lea, used with permission from David Lea. For reference purposes in examination of thesis only. Not to be reproduced or used in other presentations without permission from David Lea.= *please request, footage too large for digital appendices*
- **Appendix 3.4d:** Youtube clip lahar 13th April 2010=
<https://www.youtube.com/watch?v=AEny25AocYw>
- **Appendix 3.4e:** Lahar flow front video = *remotecamera* folder

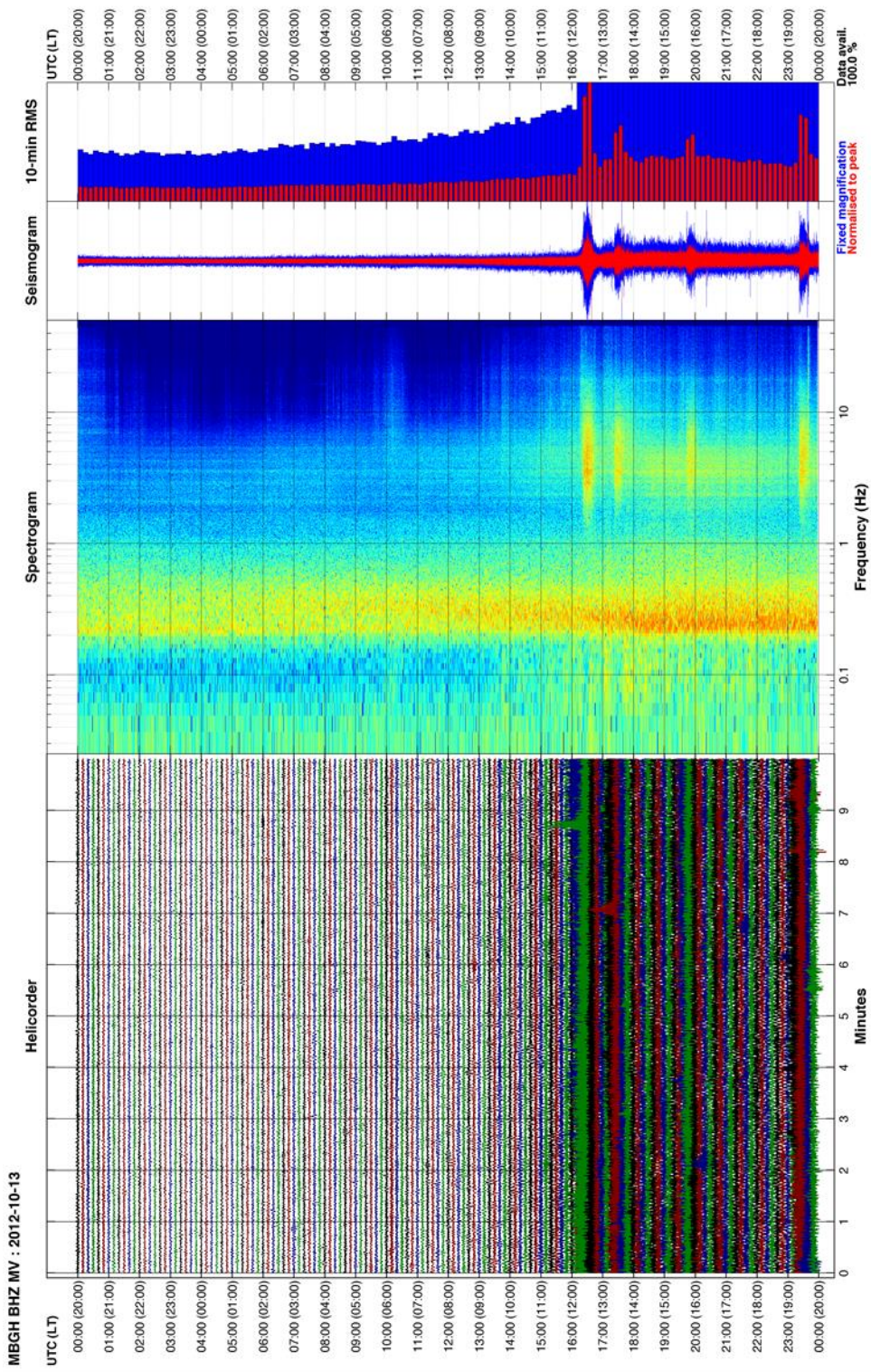
Appendix 4

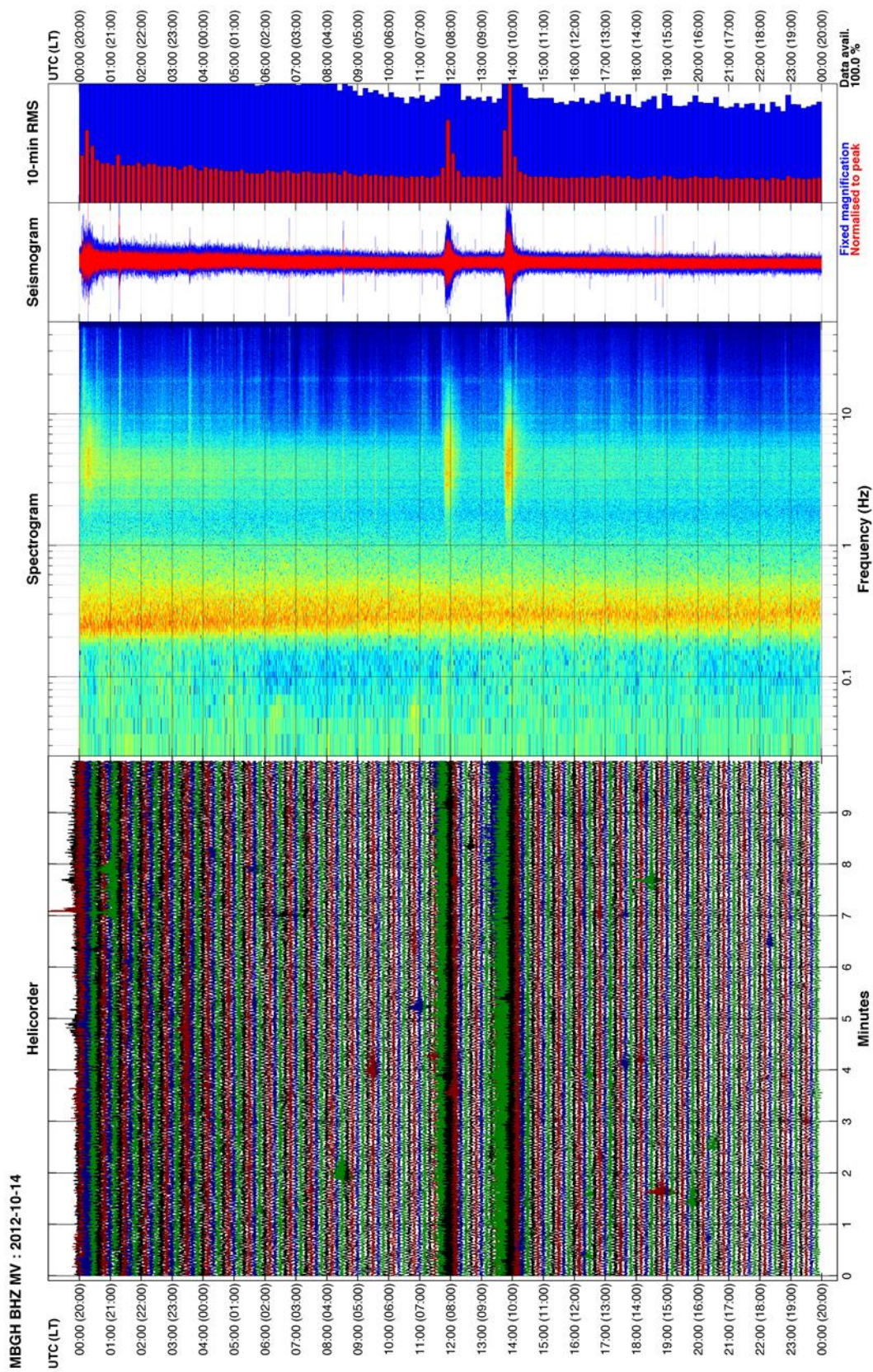
Appendix 4.1: Digital Appendix

- **Appendix 4.1a:** PAP photographs= *bedsurface* folder
- **Appendix 4.1b:** Site A Remote Camera images raw= *remotecamera* folder
- **Appendix 4.1c:** Site A camera video= *2012laharsiteA* folder
- **Appendix 4.1d:** Site B1 2012 ground observations= *2012laharssiteB1* folder
- **Appendix 4.1e:** Site B2 2012 ground observations= *2012laharssiteB2* folder
- **Appendix 4.1f:** Site C 2012 ground observations= *2012laharssiteC* folder
- **Appendix 4.1g:** Suspended sediment concentration= *suspended.xls*

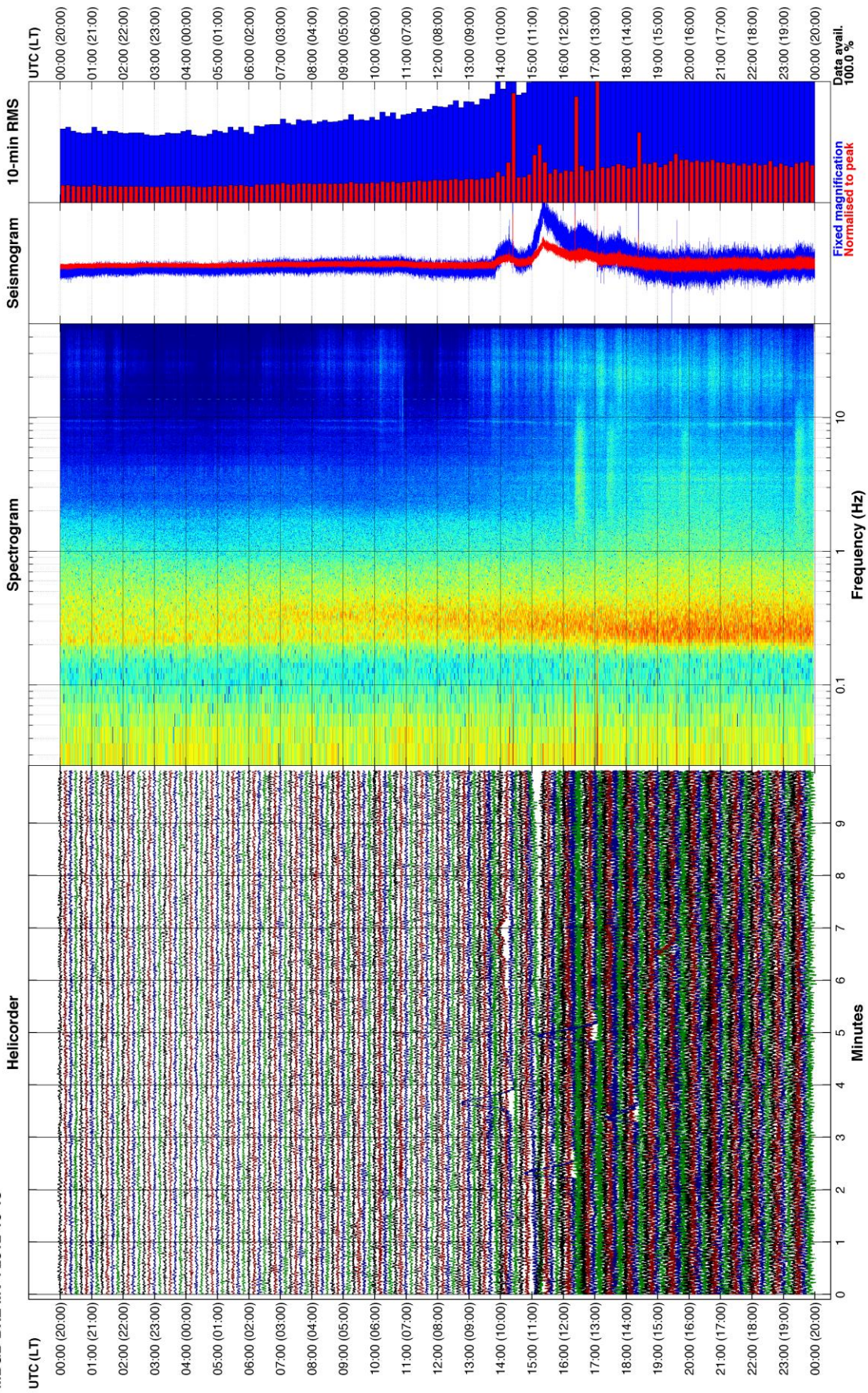
Appendix 4.2: Pan plots (including spectrograms): 13th-14th October 2012, MBGH, MBGB and MBLY.

Generated by Montserrat Volcano Observatory

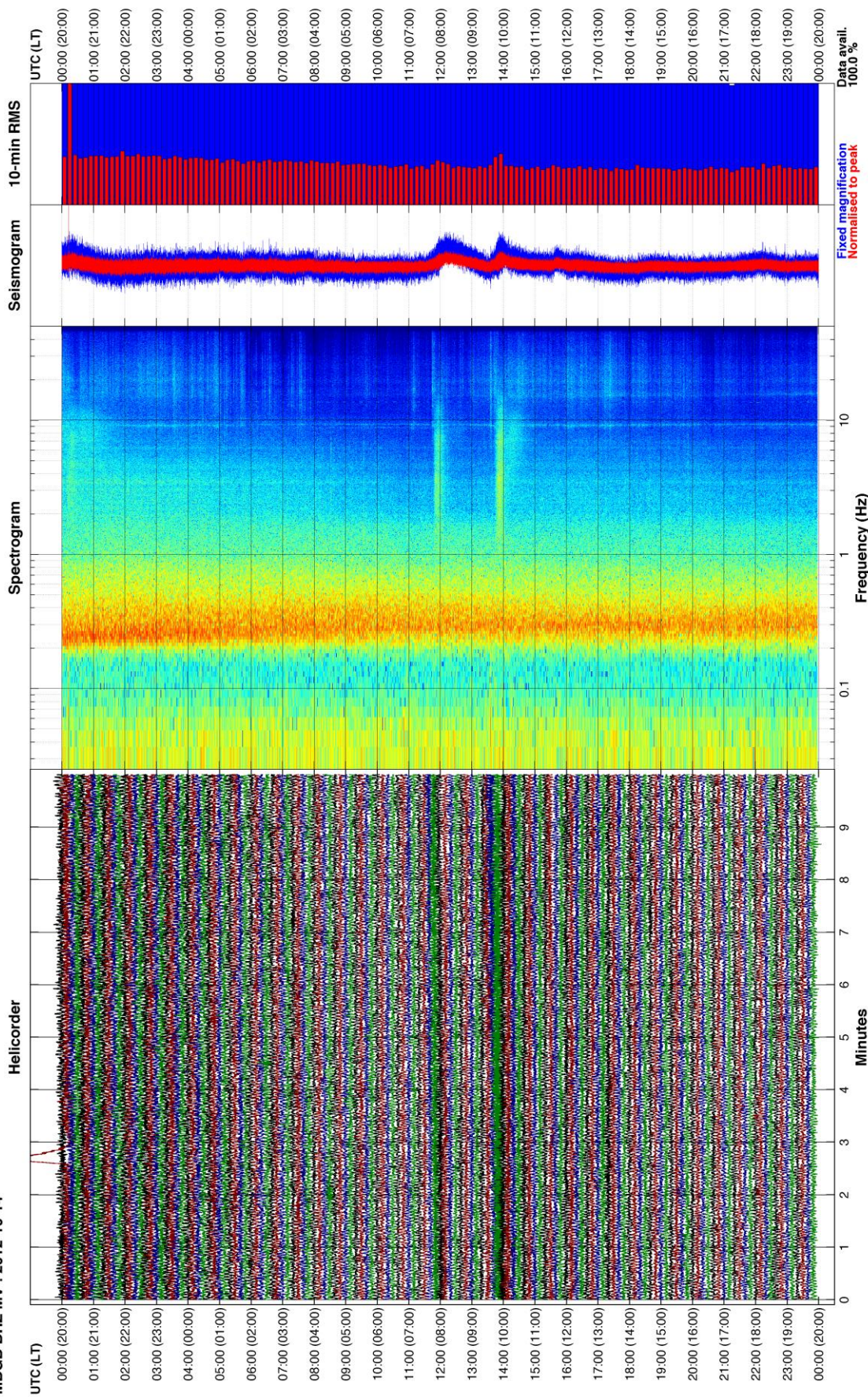




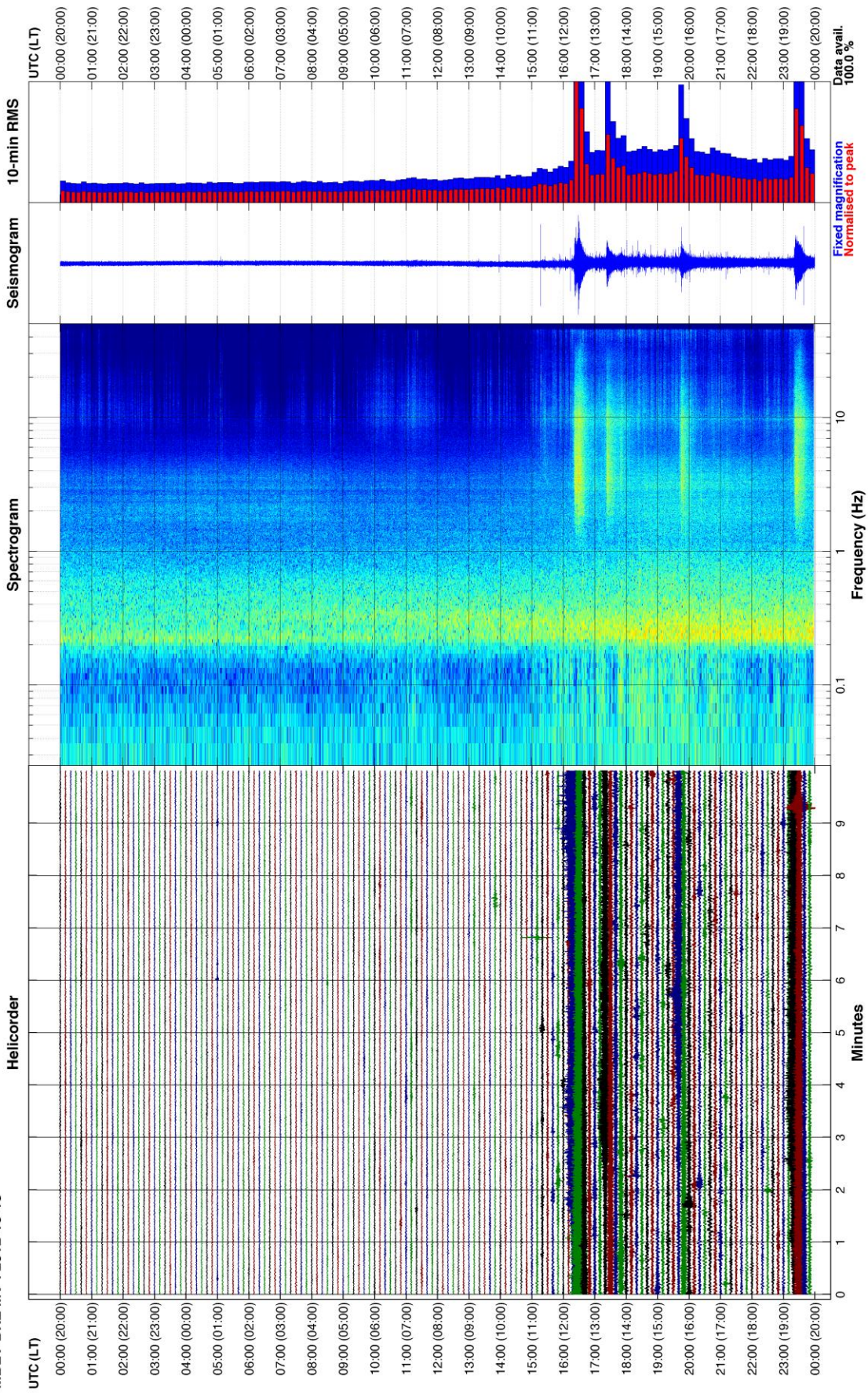
MBGB BHZ MV : 2012-10-13



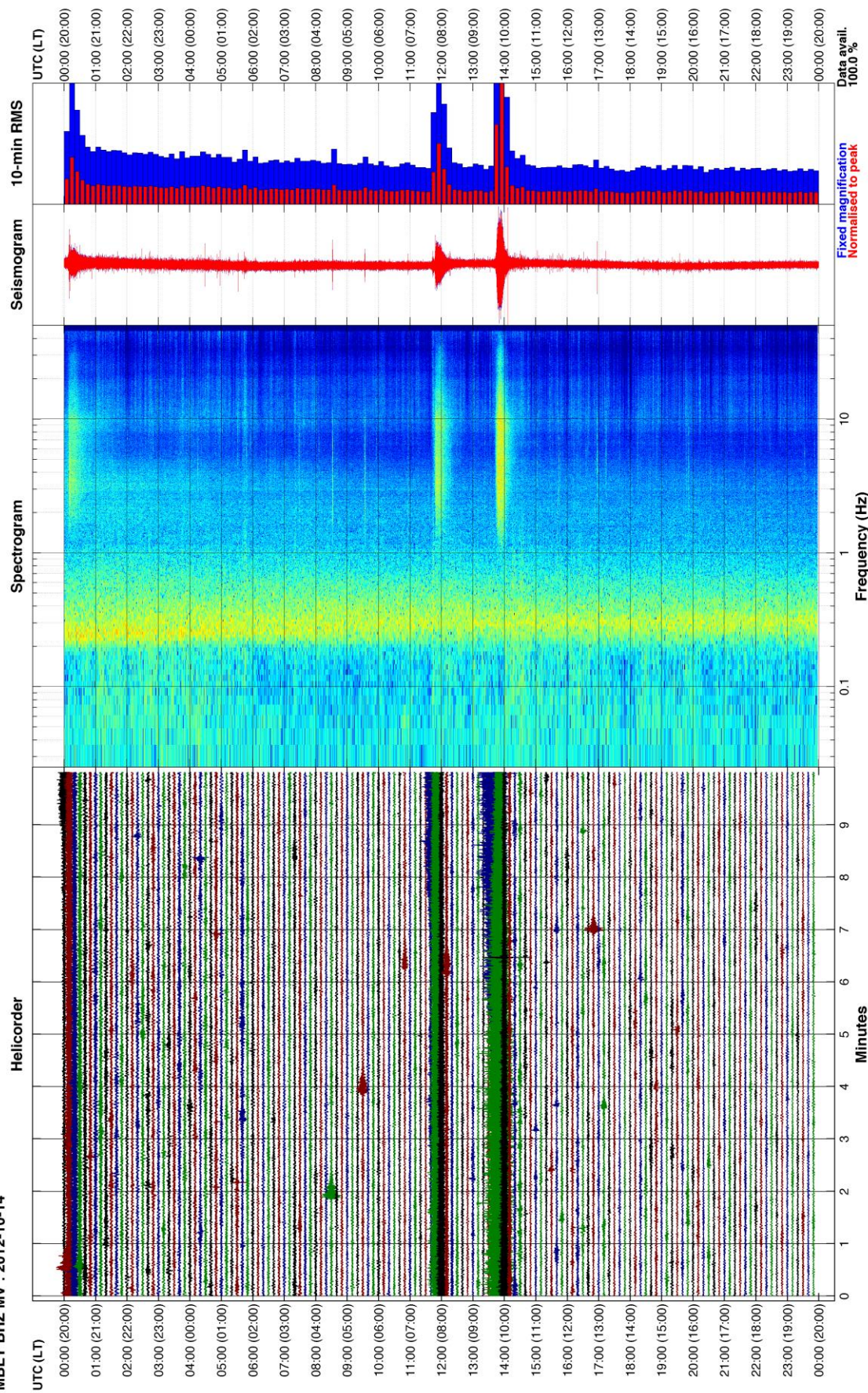
MBGB BHZ MV : 2012-10-14



MBLY BHZ MV : 2012-10-13



MBLY BHZ MV : 2012-10-14



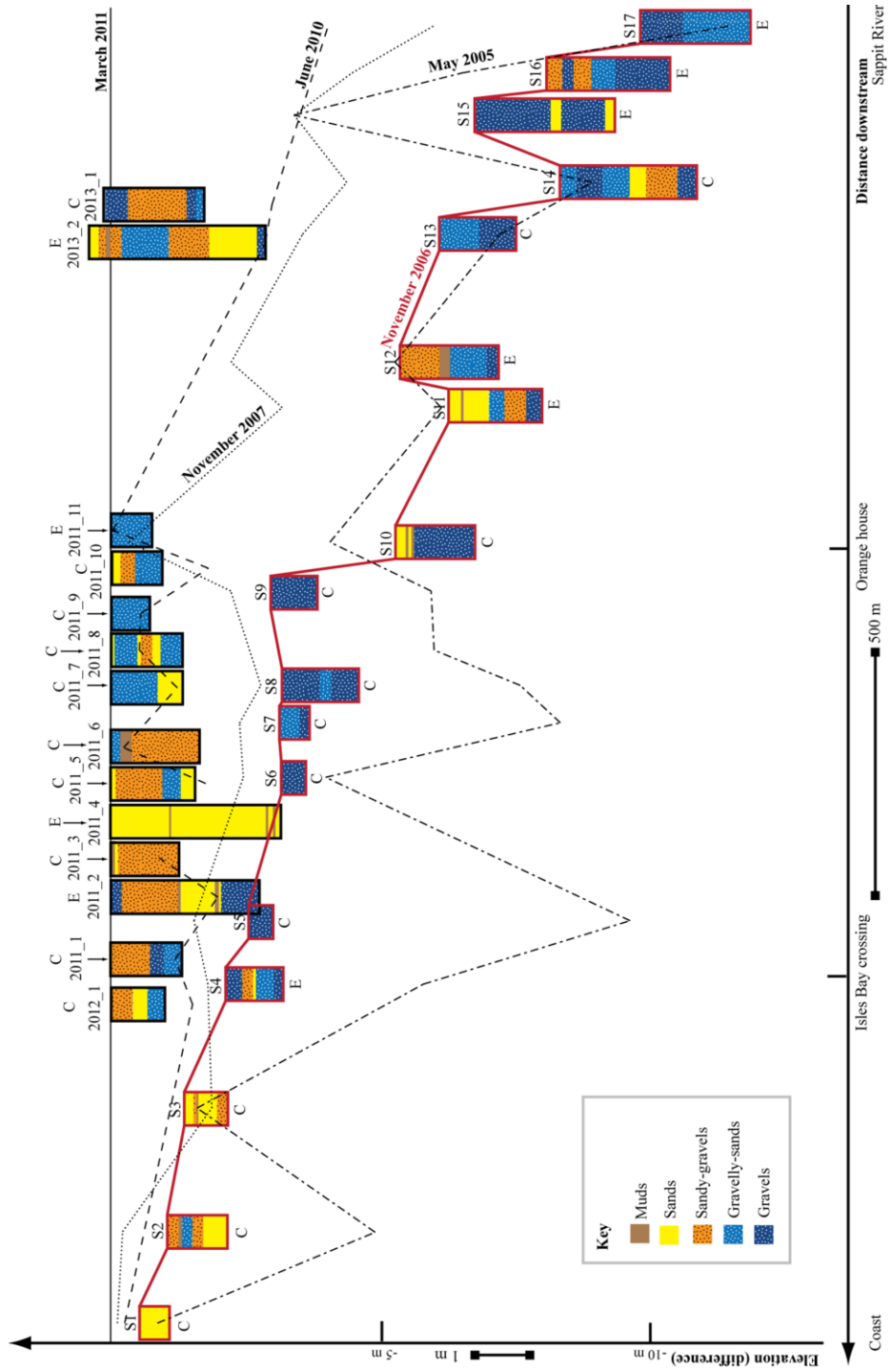
Appendix 5

Appendix 5.1: Digital Appendix

- **Appendix 5.1a:** Deposit photographs March 2011= = *deposit_Mar_2011* folder
- **Appendix 5.1b:** Deposit photographs February 2012= *deposit_Mar_2012* folder
- **Appendix 5.1c:** Deposit photographs October 2012= *deposit_Oct_2012* folder
- **Appendix 5.1d:** Deposit photographs March 2013= *deposit_Mar_2013* folder

Appendix 6

Appendix 6.1: Summary of sediment logs from this study (top) and from Šušnik (2009) and from Šušnik (2009) by bulk grain size characteristics (see Šušnik, 2009 for full logs)



REFERENCES

References

- Alexander, J., and Fielding, C. (1997)** Gravel antidunes in the tropical Burdekin River, Queensland, Australia, *Sedimentology*, 44 (2), 327-337, DOI: 10.1111/j.1365-3091.1997.tb01527.x
- Alexander, J., Bridge, J. S., Cheel, R. J. and LeClair, S. F. (2001)** Bedforms and associated sedimentary structures formed under supercritical water flows over aggrading sand beds, *Sedimentology*, 48, 133-152, DOI: 10.1046/j.1365-3091.2001.00357.x
- Alexander, J., Barclay, J., Sušnik, J., Loughlin, S.C., Herd, R.A., Darnell, A. Crossweller, S. (2010)** Sediment-charged flash floods on Montserrat: the influence of synchronous tephra fall and varying extent of vegetation damage. *Journal of Volcanology and Geothermal Research*, 194 (4), 127-138, DOI: 10.1016/j.jvolgeores.2010.05.002
- Allen, J. R. L. (1982)** *Sedimentary Structures*, Vol 1-2, Elsevier, Amsterdam, Netherlands, 592 p.
- Allen, J. R. L. (1985)** *Principles of Physical Sedimentology*, George Allen & Unwin, London, UK, 272 p.
- Ambeh, W. and Lynch, L. (1996)** Seismicity preceding the current eruption of the Soufrière Hills Volcano, Montserrat, West Indies. In: Ahmad, R., ed., *Science, Hazards and Hazard Management. The Second Caribbean Conference on Natural Hazards and Disasters, 9-12 October 1996, Kingstone, Jamaica*. Unit for Disaster Studies, Department Geography and Geology, The University of West Indies, Jamaica, vol. 1 (30)
- Arnott, R. W. C. and Hand, B. M. (1989)** Bedforms, primary structures and grain fabric in the presence of suspended sediment rain, *Journal of Sedimentary Petrology*, 59 (6), 1062- 1069
- Aspinall, W. P., Miller, A. D., Lynch, L. L., Latchman, J. L., Stewart, R. C., White, R. A. and Power, J.A. (1998)** Soufrière Hills eruption, Montserrat, 1995-1997: volcanic earthquake locations and fault-plane solutions. *Geophysical Research Letters*, 25 (18), 3397-3400, DOI: 10.1029/98GL00858
- Auer, A., White, J. D. L. and Manville, V. (2012)** Cryptic eruption of Mount Ruapehu revealed by deposits of sediment laden streamflow in a steep mountain valley: The 4 ka Kiwikiwi Formation, Whangaehu Valley, NZ. *Journal of Volcanology and Geothermal Research*, 243, 45-58, DOI: 10.1016/j.jvolgeores.2012.07.003
- Auker, M. R., Sparks, R. S. J., Siebert, L., Crossweller, H .S. and Ewert, J. (2013)** A statistical analysis of the global historical volcanic fatalities record. *Journal of Volcanology*, 2 (2), DOI: 10.1186/2191-5040-2-2
- Aulitsky, H. (1980)** Preliminary two-fold classification of torrents. In: Alutizky, H., Grubinger, H. and Nemecek, E. (eds) *Proceedings of the International Praevent Symposium, Vienna, Austria, 8-12 September*, 243-256

- Avila, (2013)** Tropical Cyclone Report, Hurricane Rafael, 12-17 October 2012, *National Hurricane Centre*, http://www.nhc.noaa.gov/data/tcr/AL172012_Rafael.pdf (accessed 30/5/2014)
- Baas, J. H.; Best, J. L. and Peakall, J. (2011)** Depositional processes, bedform development and hybrid bed formation in rapidly decelerated cohesive (mud-sand) sediment flows, *Sedimentology*, 58 (7), 1953- 1987, DOI: 10.1111/j.1365-3091.2011.01247.x
- Baas, J. H., Davies, A. G. and Malarkey, J. (2013)** Bedform development in mixed sand-mud: The contrasting role of cohesive forces in flow and bed, *Geomorphology*, 182, 19-32, DOI: 10.1016/j.geomorph.2012.10.025
- B.A.N.C. (1986)** British Admiralty Nautical Chart 254: Montserrat and Barbuda, United Kingdom Hydrographic Office, published 27 June 1986
- Barclay, J., Johnstone, J. E and Matthews, A. J. (2006)** Meteorological monitoring of an active volcano: Implications for eruption prediction, *Journal of Volcanology and Geothermal Research*, 150 (4), 339–358, DOI: 10.1016/j.jvolgeores.2005.07.020
- Barclay, J., Alexander, J., Sušnik, J. (2007)** Rainfall induced lahars in the Belham Valley, Montserrat, West Indies. *Journal of Geographical Society*, 164, 815-827, DOI: 10.1144/0016-76492006-078
- Barclay, J., Herd, R. A., Edwards, B. R., Christopher, T., Kiddle, E. J., Plail, M. and Donovan, A. (2010)** Caught in the act: Implications for the increasing abundance of mafic enclaves during the recent eruptive episodes of the Soufrière Hills Volcano, Montserrat, *Geophysical Research Letters*, 37 (19), L00E09, DOI: 10.1029/2010GL042509
- Barwis, J. H. and Tankard, A. J. (1983)** Pleistocene shoreline deposition and sea-level history at Swartklip, South-Africa, *Journal of Sedimentary Petrology*, 53 (4), 1281-1294
- Barwis, J. H. and Hayes, M. O. (1985)** Antidunes on modern and ancient washover fans. *Journal of Sedimentary Petrology*, 55 (6), 907-916
- Bennett, S. J. and Bridge, J. (1995)** The geometry and dynamics of low-relief bed forms in heterogeneous material in a laboratory channel and their relationship to water flow and sediment transport, *Sedimentology*, 42, 117- 146
- Benvenuti, M. and Martini, I. P. (2002)** Analysis of terrestrial hyperconcentrated flows and their deposits. In: Martini, I. P., Baker, V. R., and Garzon, G., ed., Flood and megaflood processes and deposits: Recent and ancient examples, *Special Publication. International Association of Sedimentologists*, 32, pp. 167-193
- Berke, P. and Wenger, D. (1991)** Montserrat: emergency planning, response and recovery related to Hurricane Hugo. Report available at: http://hrrc.arch.tamu.edu/media/cms_page_media/558/91-02R.pdf (accessed 22/1/2015)

References

- Best, J., and Bridge, J. (1992)** The morphology and dynamics of low amplitude bedwaves upon upper stage plane beds and the preservation of planar laminae. *Sedimentology*, 39 (5), 737-752, DOI: 10.1111/j.1365-3091.1992.tb02150.x
- Beverage, J. P. and Culbertson, J.K. (1964)** Hyperconcentrations of suspended sediments. *Journal of Hydraulics Division* 90, 117-126
- BGS (2014)** British Geological Survey Geoscenic archive., <http://geoscenic.bgs.ac.uk/asset-bank/action/viewHome> (accessed 24/9/2014)
- Blair, T.C. (1999)** Sedimentary processes and facies of the waterlaid Anvil Spring Canyon fan, Death valley, California. *Sedimentology*, 46 (5), 913-940, DOI: 10.1046/j.1365-3091.1999.00259.x
- Blair, T. C. and McPherson, J. G. (1999)** Grain-size and textural classification of coarse sedimentary particles, *Journal of Sedimentary Research*, 69 (1), 6-19 A
- Blair, T. C. (2000)** Sedimentology and progressive tectonic unconformities of the sheetflood-dominated Hell's Gate alluvial fan, Death Valley, California, *Sedimentary Geology*, 132 (3-4), 233-262, DOI: 10.1016/S0037-0738(00)00010-5
- Bonadonna C., Mayberry, G. C., Calder, E. S., Sparks, R. S. J., Choux, C., Jackson, P., Lejeune, A. M., Loughlin, S. C., Norton, G. E., Rose, W. I., Ryan, G. and Young, S. R. (2002)** Tephra fallout in the eruption of Soufriere Hills Volcano, Montserrat. In: Druitt T. H., and Kokelaar B. P., ed., *The eruption of the Soufriere Hills Volcano, Montserrat, from 1995 to 1999*, Geological Society, London, Memoirs, 21: pp. 483-516
- Bouysse P., Westercamp D. and Andreieff P. (1984)** The Lesser Antilles island arc-structure and geodynamic evolution. In: Moore J. C., and Mascle A., ed., *Proceedings initial reports of the Deep Sea Drilling Project*, 78 (AUG), 83- 103
- Bradley, J. N. and Peterka, A. J. (1957)** The Hydraulic Design of Stilling Basins, Hydraulic Jumps on a Horizontal Apion, *Journal of Hydraulic Division ASCE*, 83, No. HY5, paper 1401, 1402 and 1403
- Bradley, J. B. and McCutcheon, S. C. (1987)** Influence of large suspended sediment concentrations in rivers. In: Thorne C.R., Bathurst, J.C., Hey, R.D., ed., *Sediment transport in gravel-bed rivers*, John Wiley & Sons, Chichester; 645–674
- Brakespear, R. (2008)** Hydrodynamics and Sedimentary Structures of Antidunes in Gravel and Sand Mixtures, Ph.D. thesis, University of Southampton, UK
- Branney, M. J. and Gilbert, J. S. (1995)** Ice-melt collapse pits and associated features in the 1991 lahar deposits of Volcan-Hudson, Chile - criteria to distinguish eruption-induced glacier melt, *Bulletin of Volcanology*, 57 (5), 293-302, DOI: 10.1007/BF00301289

- Brasington, J., Rumsby, B. T. and Mcvey, R. A. (2000)** Monitoring and modelling morphological change in a braided gravel-bed river using high resolution GPS-based survey, *Earth Surface Processes and Landforms*, 25 (9), 973-990, DOI: 10.1002/1096-9837(200008)25:9<973
- Briden J. C., Rex D. C., Faller A. M. and Tomblin J. F. (1979)** K-Ar geochronology and paleomagnetism of volcanic rocks in the Lesser Antilles island arc, *Philosophical Transactions of the Royal Society A-Mathematical Physical and Engineering Sciences*, 291 (1383), 485-528, DOI: 10.1098/rsta.1979.0040
- Bridge, J. S. and Best, J. L. (1988)** Flow, sediment transport and bedform dynamics over the transition from dunes to upper-stage plane beds: implications for the formation of planar laminae, *Sedimentology*, 35 (5), 153-163, DOI: 10.1111/j.1365-3091.1988.tb01249.x
- Bridge, J. S. and Best, J. (1997)** Preservation of planar laminae due to migration of low-relief bed waves over aggrading upper-stage plane beds: comparison of experimental data with theory, *Sedimentology*, 44 (2), 253-262, DOI: 10.1111/j.1365-3091.1997.tb01523.x
- Bridge, J. S (2003)** Rivers and floodplains: forms, processes, and sedimentary record, Blackwell Science, Oxford, UK, 504 p.
- Brierley, G. J. and Fryirs, K. A. (2013)** Geomorphology and River Management: Applications of the River Styles Framework. *John Wiley & Sons*, 416 p.
- Brown, G. M., Holland, J. G., Sigurdsson, H., Tomblin, J. F., and Arculus, R. J. (1977)** Geochemistry of the Lesser Antilles volcanic island arc. *Geochimica et Cosmochimica Acta*, 41 (6), 785-801, DOI: 10.1016/0016-7037(77)90049-7
- Brunori, F., Penzo, M. C. and Torri, D. (1989)** Soil shear strength: its measurement and soil detachability, *Catena*, 16 (1), 59–71, DOI: 10.1016/0341-8162(89)90004-0
- Brush, L. M., Wolman, M. G. and Huang, B. ed. (1989)** Taming the Yellow River: Silt and Floods. Kluwer, Dordrecht, 690 p.
- Bryan, R. B. (2000)** Soil erodibility and processes of water erosion of hillslope, *Geomorphology*, 32 (3-4), 385-415, DOI: 10.1016/S0169-555X(99)00105-1
- Bull, W. B. (2011)** Tectonically Active Landscapes. *John Wiley & Sons*, 320 p.
- Bursik, M. and Reid, J. (2004)** Lahar in Glass Creek and Owens River during the Inyow eruption, Mono-Inyo Craters, California. *Journal of Volcanology and Geothermal Research*, 131 (3-4), 321-331, DOI: 10.1016/S0377-0273(03)00385-8
- Calder, E. S., Cole P. D., Dade, W. B., Druitt, T. H., Hoblitt, R. P., Huppert, H. E., Ritchie, L., Sparks, R. S. J. and Young, S. R. (1999)** Mobility of pyroclastic flows and surges at the Soufrière Hills Volcano, Montserrat, *Geophysical Research Letters*, 26 (5), 537-540, DOI: 10.1029/1999GL900051

References

- Campbell Scientific (2014)** New Zealand: Lahar Observations, Campbell dataloggers and camera key to historic recording of mud flow, <https://www.campbellsci.co.uk/new-zealand-lahar> (Accessed 22/3/2014)
- Canisius, F. Honda, K. and Tokunaga, M. (2009)** Updating geomorphic features of watersheds and their boundaries in hazardous areas using satellite synthetic aperture radar. *International Journal of Remote Sensing*, 30 (22), 5919-5933, DOI: 10.1080/01431160902791879
- Carling, P. A. and Shvidchenko, A. B. (2002)** A consideration of the dune: antidune transition in fine gravel, *Sedimentology*, 49 (6), 1269–1282, DOI: 10.1046/j.1365-3091.2002.00496.x
- Carling, P. A. and Breakspear, R. M. D. (2006)** Placer formation in gravel-bedded rivers: a review, *Ore Geology Reviews*, 28 (4), 377-401, DOI: 10.1016/j.oregeorev.2005.02.002
- Carling, P. A., Burr, D. M, Johnson, T. F. and Brennand, T. A. (2009a)** A review of open-channel megaflood depositional landforms on Earth and Mars, Chapter 3. In: Burr, D. M., Carling, P. A. and Baker, V. R. ed., *Megaflooding on Earth and Mars*. Cambridge University Press, pp. 33–49
- Carling, P. A., Martini, I. P., Herget, J., Borodavko, P. and Parnachov, S. (2009b)** Megaflood sedimentary fill: Altai Mountains, Siberia, Chapter 13. In: Burr, D. M., Carling, P. A. and Baker, V. R., ed., *Megaflooding on Earth & Mars*, Cambridge University Press, pp. 243–264
- Carling, P.A. (2013)** Freshwater megaflood sedimentation: What can we learn about generic processes?, *Earth-Science Reviews*, 125, 87-113, DOI: 10.1016/j.earscirev.2013.06.002
- Carling, P., Jansen, J. and Meshkova, L. (2014)** Multichannel rivers: their definition and classification, *Earth Surface processes and landforms*, 39 (1), 26-37, DOI: 10.1002/esp.3419
- Carn, S.A., Watts, R.B., Thompson, G. and Norton, G.E. (2004)** Anatomy of a lava dome collapse: the 20 March 2000 event at Soufrière Hills Volcano, Montserrat. *Journal of Volcanology and Geothermal Research*, 131 (3-4), 241-264, DOI: 10.1016/S0377-0273(03)00364-0
- Cartigny, M. J. B., Ventra, D., Postma, G. and Van den Berg, J. H. (2014)** Morphodynamics and sedimentary structures of bedforms under supercritical-flow conditions: New insights from flume experiments. *Sedimentology* 61 (3), 712–748, DOI: 10.1111/sed.12076
- Cassidy, M., Taylor, R.N., Palmer, M.R., Cooper, R.J., Stenlake, C. and Trofimovs, J. (2012)** Tracking the magnetic evolution of island arc volcanism: Insights from a high-precision Pb isotope record of Montserrat, Lesser Antilles. *Geochemistry Geophysics Geosystems*, 13(5), DOI: 10.1029/2012GC004064

- Cassidy, M., Trofimovs, J., Palmer, M. R., Palmer, M. R., Talling, P. J., Watt, S. F. L., Moreton, S. G., Taylor, R. N. (2013)** Timing and emplacement dynamics of newly recognised mass flow deposits at similar to 8-12 ka offshore Soufrière Hills volcano, Montserrat: How submarine stratigraphy can complement subaerial eruption histories, *Journal of Volcanology and Geothermal Research*, 253, 1-14, DOI: 10.1016/j.jvolgeores.2012.12.002
- Chanson, H. (2000)** Boundary shear stress measurements in undular flows: Application to standing wave bedforms, *Water Resources Research*, 36 (10), 3063-3076, DOI: 10.1029/2000WR900154
- Chanson, H. (2011)** Current knowledge in tidal bores and their environmental, ecological and cultural impacts, *Environmental Fluid Mechanics*, 11 (1), 77-98, DOI: 10.1007/s10652-009-9160-5
- Chanson, H. and Docherty, N.J. (2012)** Turbulent velocity measurements in open channel bores, *European Journal of Mechanics B-Fluids*, 32, 52-58, DOI: 10.1016/j.euromechflu.2011.10.001
- Chanson, H. (2013)** Propagation of surge waves in channels with large-scale bank roughness, *Journal of Hydraulic Research, IAHR*, 51 (6), 740-742, DOI: 10.1080/00221686.2013.863229
- Cheel, R. J. and Middleton, G. V. (1986)** Horizontal Laminae formed under upper flow regime plane bed conditions, *Journal of Geology*, 94 (4), 489-504
- Cheel, R.J. (1990)** Horizontal lamination and the sequence of bed phases and stratification under upper flow regime conditions, *Sedimentology*, 37 (3), 517-529, DOI: 10.1111/j.1365-3091.1990.tb00151.x
- Chien, N. and Wan, Z.H. (1998)** *Mechanics of Sediment Transport*, Reston VA: ASCE Press, 913 p.
- Chiodini, G., Cioni, R., Frullani, A., Guidi, M., Marini, L., Ptrati, F. and Raco, B. (1996)** Fluid geochemistry of Montserrat Island, West Indies, *Bulletin of Volcanology*, 58 (5), 380-392, DOI: 10.1007/s004450050146
- Chow, V. T. (1959)** *Open-Channel Hydraulics*, New York, Toronto, London: McGraw-Hill Civil Engineering Series, McGraw-Hill Book Company, 680 p.
- Christeson, G. L., P. Mann, A. Escalona, and T. J. Aitken (2008)** Crustal structure of the Caribbean–northeastern South America arc-continent collision zone, *Journal of Geophysics Research- Solid Earth*, 113 (B8), B08104, DOI: 10.1029/2007JB005373
- Cienfuegos, R., Villagran, M., Aguilera, J. C., Catalan, P., Castelle, B. and Almar, R. (2014)** Video monitoring and field measurements of a rapidly evolving coastal system: the river mouth and sand spit of the Mataquito River in Chile, *Journal of Coastal Research*, special issue 70, 639-644, DOI: 10.2112/SI70-108.1

References

- Clifton, T.R. (1990)** Sedimentology of antidune flow; controls on sediment transport and stratification. PhD Thesis, University of California, Santa Cruz, CA, United States.
- Cobenas, G., Thouret, J-C., Bonadonna, C. and Boivin, P. (2012)** The c.2030 yr BP Plinian eruption of El Misti volcano, Peru: Eruption dynamics and hazard implications, *Journal of Volcanology and Geothermal Research*, 241, 105-120, DOI: 10.1016/j.jvolgeores.2012.06.006
- Cole, P. D., Calder, E. S., Druitt, T. H., Hoblitt, R., Robertson, R. A. E. , Sparks, R. S. J. and Young, S. R. (1998)** Pyroclastic flows generated by gravitational instability of the 1996-97 lava dome of the Soufriere Hills volcano, Montserrat, *Geophysical Research Letters*, 25 (18), 3425-3428, DOI: 10.1029/98GL01510
- Cole, P. D., Calder, E. S., Sparks, R. S. J., Clarke, A. B., Druitt, T. H., Young, S. R., Herd, R.A., Harford, C. L. and Norton, G. E. (2002)** Deposits from dome collapse and fountain collapse pyroclastic flows at Soufrière Hills Volcano, Montserrat. In: Druitt T. H., and Kokelaar B. P. ed., *The eruption of the Soufrière Hills Volcano, Montserrat, from 1995 to 1999*, Geological Society, London, Memoirs, 21, pp. 231-262
- Cole, S. E., Cronin, S. J., Sherburn, S. and Manville, V. (2009)** Seismic signals of snow-slurry lahars in motion: 25 September 2007, Mt Ruapehu, New Zealand. *Geophysical Research Letters*, 36, L09405, DOI: 10.1029/2009GL038030
- Cole, P. D., Smith, P. J., Stinton, A. J., Odbert, H. M., Bernstein, M. L., Komorowski, J. C. and Stewart, R. (2014)** Vulcanian explosions at Soufrière Hills Volcano, Montserrat between 2008 and 2010. In: Wadge, G. Robertson, R. E. A. and Voight, B., ed., *The Eruption of Soufrière Hills Volcano, Montserrat from 2000 to 2010*. Geological Society, London, Memoirs, 39, 71-92
- Cole, P. D. (2014)** personal communication, 3/7/2014
- Collins, B. D. and Dunne, T. (1986)** Erosion of tephra from the 1980 eruption of Mount St. Helens, *Geological Society of America Bulletin*, 97 (7), 896-905, DOI: 10.1130/0016-7606(1986)97<896
- Committee on Methodologies for Predicting Mudflow Areas (1982)** Selecting a methodology for delineating mudslide hazard areas for the National Flood Insurance Program: Washington, D.C., National Research Council, National Academy Press, 35 p.
- Comitti, F., Marchi, L., Macconi, P., Arattano, M., Bertoldi, G., Borga, M., Brardinoni, F., Cavalli, M., D'Agostino, V., Penna, D. and Theule, J. (2014)** A new monitoring station for debris flows in the European Alps: first observations in the Gadria basin, *Natural Hazards*, 73 (3), 1175-1198, DOI: 10.1007/s11069-014-1088-5
- Cornwell, K. (1998)** Quaternary break-out flood sediments in the Peshawar basin of northern Pakistan, *Geomorphology*, 25 (3-4), 225-248, DOI: 10.1016/S0169-555X(98)00061-0

- Costa, J. E. (1983)** Paleohydraulic reconstruction of flash-flood peaks from boulder deposits in the Colorado Front Range, *Geological Society of America Bulletin*, 94, 986-1004, DOI: 10.1130/0016-7606(1983)94<986:PROFPF>2.0.CO;2
- Costa, J. E. and Williams, G. P. (1984)** Debris-flow dynamics (videotape): U.S. Geological Survey Open-File Report 84-606, 22 ½ min
- Costa J. E. (1988)** Rheologic, geomorphic and sedimentologic differentiation of water floods, hyperconcentrated flows and debris flows. In: Baker V. R., Kochel R. C. and Patton P. C., ed., *Flood Geomorphology*, Wiley, pp 113-122
- Cotter, E. and Graham, J. R. (1991)** Coastal plain sedimentation in the late Devonian of Southern Ireland; hummocky cross-stratification in fluvial deposits, *Sedimentary Geology*, 72 (3-4), 201-224, DOI: 10.1016/0037-0738(91)90012-3
- Cronin, S. J., Neall, V. E., Lecointre, J. A. and Palmer, A. S. (1997)** Changes in Whangaehu river lahar characteristics during the 1995 eruption sequence, Ruapehu volcano, New Zealand, *Journal of Volcanology and Geothermal Research*, 76 (1-2), 47-61, DOI: 10.1016/S0377-0273(96)00064-9
- Cronin, S. J., Neall, V. E., Lecointre, J. A. and Palmer, A. S. (1999)** Dynamic interactions between lahars and stream flow: A case study from Ruapehu volcano, New Zealand, *Geological Society of America, Bulletin*, 111 (1), 28-38, DOI: 10.1130/0016-7606(1999)111<0028:DIBLAS>2.3.CO;2
- Cronin, S. J., Lecointre, J. A., Palmer, A. S. and Neall, V. E. (2000)** Transformation, internal stratification, and depositional processes within a channelised, multi-peaked lahar flow, *New Zealand Journal of Geology and Geophysics*, 43 (1) 117-128
- Crown Copyright (1983)** Tourist map of Montserrat, Emerald Isle of the Caribbean, published by the British Ministry of Overseas Development, reprinted by Ordnance Survey for Government of Montserrat 1996
- Daag, A. S. (2003)** Modelling the Erosion of Pyroclastic Flow Deposits and the Occurrences of Lahars at Mt. Pinatubo, Philippines, PhD Thesis, International Institute for Geoinformation Science and Earth Observation
- Darnell, A.R. (2010)** Application of geographical information systems to lahar hazard assessment on an active volcanic system, Ph.D. Thesis, University of East Anglia, UK
- Darnell, A. R., Lovett, A. A., Barclay, J. and Herd, R. A. (2010)** An application-driven approach to terrain model construction, *International Journal of Geographical Information Science*, 24 (8), 1171–1191, DOI: 10.1080/13658810903318889
- Darnell, A. R., Barclay, J., Herd, R. A., Phillips, J. C., Lovett, A. A. and Cole, P. D. (2012)** Geographical system mapping of dilute lahars on Montserrat, West Indies. *Bulletin of Volcanology*, 74 (6), 1337-1353, DOI: 10.1007/s00445-012-0596-y

References

- Darnell, A. R., Phillips, J. C., Barclay, J., Herd, R. A., Lovett, A. A. and Cole, P. D. (2013)** Developing a simplified geographical information system approach to dilute lahar modelling for rapid hazard assessment. *Bulletin of Volcanology*, 75 (4), UNSP713, DOI: 10.1007/s00445-013-0713-6
- Davidson, J. and De Silva, S. (2000)** Composite volcanoes. In Sigurdsson, H., Houghton, B., McNutt, S.R., Rymer, H. and Stix, J., ed., *Encyclopedia of Volcanoes*, New York Academic Press, pp. 601-616
- Davis Instruments (2010)** Weather Station Sensor Accuracy, Resolution and Range (Technical Specifications). 3465 Diablo Avenue, Hayward, CA 94545-2778 USA
- De Angelis, S., Bass, V., Hards, V. and Ryan, G. (2007)** Seismic characterization of pyroclastic flow activity at Soufrière Hills Volcano, Montserrat, 8 January 2007, *Natural Hazards and Earth System Sciences*, 7 (4), 467–472
- De Baets, S., Poesen, J., Knapen, A. and Galindo, P. (2007)** Impact of root architecture on the erosion-reducing potential of roots during concentrated flow, *Earth Surface Processes and Landforms*, 32 (9), 1323-1345, DOI: 10.1002/esp.1470
- De Baets, S., Poesen, J., Reubens, B., Wemens, K., De Baerdemaerker, J. and Muys, B. (2008)** Root tensile strength and root distribution of typical Mediterranean plant species and their contribution to soil shear strength, *Plant and Soil*, 305 (1-2), 207-226, DOI: 10.1007/s11104-008-9553-0
- de Bélizal, E., Lavigne, F., Hadmoko, D.S., Degai, J. P., Dipayana, G. A., Mutaqin, B. W., Marfai, M. A., Coquet, M., Le Mauff, B., Robin, A. K., Vidal, C., Cholikh, N. and Aisyah, N. (2013)** Rain triggered lahars following the 2010 eruption of Merapi volcano, Indonesia: A major risk. *Journal of Volcanology*, 261, 330-347, DOI: 10.1016/j.jvolgeoes.2013.01.010
- DeMets, C., Jansma, P.E., Mattioli, G.S., Dixon, T.H., Farina, F., Bilham, R., Calais, E. and Mann, P. (2000)** GPS geodetic constraints on Caribbean-North America plate motion. *Geophysical Research Letters*, 27 (3), 437-440, DOI: 10.1029/1999GL005436
- De Rose, R. C., Oguchi, T., Morishima, W. and Collado, M. (2011)** Land cover change on Mt. Pinatubo, the Philippines, monitored using ASTER VNIR. *International Journal of Remote Sensing*, 32 (24), 9279-9305, DOI: 10.1080/01431161.2011.554452
- Dietrich, W. E., Kirchner, J. W., Ikeda, H. and Iseya, F. (1989)** Sediment supply and the development of the coarse surface layer in gravel-bedded rivers. *Nature*, 340 (6230), 215-217, DOI: 10.1038/340215a0
- DigitizeIt (2014)** Digitizer software, <http://www.digitizeit.de/> (Accessed 26/01/2014)
- Dinehart R. L. (1999)** Sediment transport in the hyperconcentrated phase of the March 19, 1982, lahar. In: Pierson T. C., ed., *Hydrological consequences of hot-rock/snowpack interactions at Mount St. Helens Volcano, Washington, 1982-1984*, USGS Professional Paper 1586, pp 37-52, US Geological Survey, Reston, VA

- Dingman, S.L. (2002)** Physical Hydrology (2nd ed.), Prentice Hall
- Donovan, A., Oppenheimer, C. and Bravo, M. (2014)** Chapter 25: Reflexive volcanology: 15 years of communicating risk and uncertainty in scientific advice on Montserrat. In: Wadge, G., Robertson, R.E.A. and Voight, B. ed. *Eruption of Soufriere Hills Volcano, Montserrat from 2000 to 2010*, Geological Society, London, Memoirs 2014, v.39; pp.1-40, DOI: 10.1144/M39.1
- Doyle, E. E., Cronon, S. J., Cole, S. E., and Thouret, J.-C. (2010)** The coalescence and organization of lahars at Semeru Volcano, Indonesia, *Bulletin of Volcanology*, 72 (8), 961- 970, DOI: 10.1007/s00445-010-0381-8
- Doyle, E. E., Cronin, S. J., Cronin, J. S. and Thouret, J. C. (2011)** Defining condition for bulking and de-bulking in lahars, *Geological Society of America Bulletin*, 123, (7-8), 1234-1246, DOI: 10.1130/B30227.1
- Doyle, E. E. (2012)** personal communication, 17/7/2012
- Dressler, R. F. (1949)** Mathematical solution of the problem of roll waves in inclined channel flows, *Communications Pure Applied Mathematics*, 2 (2-3), 149–194, DOI: 10.1002/cpa.3160020203
- Druitt, T.H., Young, S.R., Baptie, B., Bonadonna, C., Calder, E.S., Clarke, A.B., Cole, P.D., Harford, C.L., Herd, R.A., Lockett, R., Ryan, G. and Voight, B. (2002a)** Episodes of cyclic Vulcanian explosive activity with fountain collapse at Soufrière Hills Volcano, Montserrat. In: Druitt T. H., and Kokelaar B. P. ed., *The Eruption of the Soufrière Hills Volcano, Montserrat, from 1995 to 1999*, Geological Society, London, Memoirs, 21, pp. 281-306
- Druitt, T.H., Calder, E.S., Cole, P.D., Hoblitt, R.P., Loughlin, S.C., Norton, G.E., Ritchie, L.J., Sparks, R.S.J. and Voight, B. (2002b)** Small-volume, highly mobile pyroclastic flows formed by rapid sedimentation from pyroclastic surges at Soufrière Hills Volcano, Montserrat: an important volcanic hazard. In: Druitt T. H., and Kokelaar B. P. ed., *The Eruption of the Soufrière Hills Volcano, Montserrat, from 1995 to 1999*, Geological Society, London, Memoirs, 21, pp. 236-279
- Duller, R. A., Mountney, N. P., Russell, A. J. and Cassidy, N. C. (2008)** Architectural Analysis of a Volcanistic Jökulhlaup Deposit, Southern Iceland: Sedimentary Evidence for Supercritical Flow. *Sedimentology*. 55 (4),939-964, DOI: 10.1111/j.1365-3091.2007.00931.x
- Dunstone, N. J., Smith, D. M., Booth, B. B. B., Hermanson, L., Eade, R. (2013)** Anthropogenic aerosol forcing of Atlantic tropical storms. *Nature Geoscience*, 6, 534-539, DOI: 10.1038/ngeo1854
- Edmonds, M., Herd, R. A. and Strutt, M. H. (2006)** Tephra deposits associated with a large lava dome collapse, Soufrière Hills Volcano, Montserrat, 12–15 July 2003, *Journal of Volcanology and Geothermal Research*, 153 (3-4), 313–330, DOI: 10.1016/j.jvolgeores.2005.12.008

References

- EGS (2010)** Final Report Geothermal Exploration in Montserrat, Caribbean. *Minister of Communications and Works Government of Montserrat, Caribbean*
- Engelund, F. and Fredsøe, J. (1974)** Transition from dunes to plane bed in alluvial channels, Institute of Hydrodynamics and Hydraulic Engineering, Technical University of Denmark, Series Paper 4, Lyngby, Denmark, 46p.
- ESRI (2014)** Fundamentals of georeferencing a raster dataset
<http://resources.arcgis.com/en/help/main/10.1/index.html#//009t000000mn000000>
(Accessed on 25/4/2013)
- Fagents, S. A., Gregg, T. K. P. and Lopes, R. M. C. (2013)** Modeling Volcanic Processes: The Physics and Mathematics of Volcanism, *Cambridge University Press, Nature*, 421 p.
- Fahnestock, R. K. and Haushild, W. L. (1962)** Flume studies of the transport of pebbles and cobbles on a sand bed, *Geological Society of America Bulletin*, 73 (11), 1431-1436, DOI: 10.1130/0016-7606(1962)73[1431:FSOTTO]2.0.CO;2
- Feuillet, N., Manighetti, I., and Tapponnier, P. (2002)** Arc parallel extension and localization of volcanic complexes in Guadeloupe, Lesser Antilles. *Journal of Geophysical Research- Solid Earth*, 107 (B12) no. 2331, DOI: 10.1029/2001JB000308
- Feuillet, N., Manighetti, I. and Tapponnier, P. (2001)** Active arc-transverse normal faulting in Guadeloupe (French Lesser Antilles), *Comptes rendus de l'academie des sciences serie 2 fascicule a-sciences de la terre et des planetes*, 333 (9), 583-590, DOI: 10.1016/S1251-8050(01)01543-9
- Feuillet, N., Beauducel, F. and Tapponnier, P. (2011)** Tectonic context of moderate to large historical earthquakes in the Lesser Antilles and mechanical coupling with volcanoes. *Journal of Geophysical Research- Solid Earth*, 116, B10308, DOI: 10.1029/2011JB008443
- Feuillet, N., Leclerc, F., Tapponnier, P., Beauducel, F., Boudon, G., Le Friant, A., Deplus, C., Lebrun, J.F., Nercessian, A., Saurel, J.M. and Clément, V. (2010)** Active faulting induced by slip partitioning in Montserrat and link with volcanic activity: New insights from the 2009 GWADASEIS marine cruise data. *Geophysical research Letters*, 37, L00E15, DOI: 10.1029/2010GL042556
- Fielding, C. R. (2006)** Upper flow regime sheets, lenses and scour fills: Extending the range of architectural elements for fluvial sediment bodies, *Sedimentary Geology*, 190 (1-4), 227–240, S.I., DOI: 10.1016/j.sedgeo.2006.05.009
- Foley, M. G. (1977)** Gravel-lens formation in antidune-regime flow – a quantitative hydrodynamic indicator, *Journal of Sedimentary Petrology*, 47 (2), 738-746
- Foley, M. G. (1978)** Scour and fill in steep, sand-bed ephemeral streams. *Geological Society of America Bulletin*, 89 (4), 559-570, DOI: 10.1130/0016-7606(1978)89<559:SAFISS>2.0.CO;2

Fralick, P. (1999) Paleohydraulics of chute-and-pool structures in a Paleoproterozoic fluvial sandstone, *Sedimentary Geology*, 125 (3-4), 129-134, DOI: 10.1016/S0037-0738(99)00013-5

Fryirs, K. A. and Brierley, G. J. (2012) Geomorphic Analysis of River Systems: An Approach to Reading the Landscape, 362, p.

Fuchs, S., Heiss, K. and Huebl, J. (2007) Towards an empirical vulnerability function for use in debris flow risk assessment, *Natural Hazards and Earth System Sciences*, 7 (5), 495- 506,

Gagoshidze, M. S. (1969) Mudflows and floods and their control. *Soviet Hydrology*, 4, 410-422

Garcin, M., Poisson, B. and Pouget, R. (2005) High rates of geomorphological processes in a tropical area: the Remparts River case study (Reunion Island, Indian Ocean). *Geomorphology*, 67 (3-4), 335–350, DOI: 10.1016/j.geomorph.2004.11.002

GEBCO (2014) General Bathymetric Chart of the Oceans, data available from http://www.gebco.net/data_and_products/gridded_bathymetry_data/, accessed 15/7/2014

Germain, D. and Ouellet, M.-A. (2013) Subaerial sediment-water flows on hillslopes: Essential research questions and classification challenges. *Progress in Physical Geography*, 37 (6), 813-833, DOI: 10.1177/0309133313507943

Gernon, T. M., Field, M. and Sparks, R. S. J. (2009) Depositional processes in a kimberlite crater: the Upper Cretaceous Orapa South Pipe (Botswana), *Sedimentology*, 56 (2), 623- 643, DOI: 10.1111/j.1365-3091.2008.00989.x

Giannetti, B. and De Casa, G. (2000) Stratigraphy, chronology, and sedimentology of ignimbrites from the white trachytic tuff, Roccamonfina Volcano, Italy, *Journal of Volcanology and Geothermal Research*, 96 (3-4), 243-295, DOI: 10.1016/S0377-0273(99)00144-4

Gomez, C. (2012) Multi-scale topographic analysis of Merbabu and Merapi volcanoes using wavelet decomposition, *Environmental Earth Sciences*, 67 (5), 1423-1430, DOI: 10.1007/s12665-012-1587-1

Gomez, C. (2014) Digital photogrammetry and GIS-based analysis of the bio-geomorphological evolution of Sakurajima Volcano, diachronic analysis from 1947 to 2006, *Journal of Volcanology and Geothermal Research*, 280, 1-13, DOI: 10.1016/j.jvolgeores.2014.04.015

Gourley, J., Hong, Y., Flamig, Z. L., Arthur, A., Clark, R., Calianno, M., Ruin, I., Ortel, T., Wiczorek, M. E., Kirstetter, P. E., Clark, E. and Krajewski, W. F. (2013) A Unified Flash Flood Database across the United States, *Bulletin of the American Meteorological Society*, 94 (6), 799-805, DOI: 10.1175/BAMS-D-12-00198.1

References

- Graettinger, A. H., Manville, V. and Briggs, R. M. (2010)** Depositional record of historic lahars in the upper Whangaehu Valley, Mt. Rupaehu, New Zealand: implications for trigger mechanisms, flow dynamics and lahar hazards, *Bulletin of Volcanology*, 72 (3), 279- 296, DOI: 10.1007/s00445-009-0318-2
- Gran, K. B. and Montgomery, D. R. (2005)** Spatial & temporal patterns in fluvial recovery following volcano eruptions: Channel response to basin sediment loading at Mt Pinatubo, Phillipines, *Geological Society of America Bulletin*, 117 (1-2), 195-211, DOI: 10.1130/B25528.1
- Gran, K. B., Montgomery, D. R. and Halbur, J. C. (2011)** Long-term elevated post-eruption sedimentation at Mount Pinatubo, Philippines, *Geology*, 39 (4), 367-370, DOI: 10.1130/G31682.1
- Grant, G. E. (1997)** Critical flow constrains flow hydraulics in mobile-bed streams: A new hypothesis, *Water Resources Research*, 33 (2), 349-358, DOI: 10.1029/96WR03134
- Gruntfest, E. and Handmer, J. (2001)** Dealing with flash floods: Contemporary issues and future possibilities. In: Gruntfest, E. and Handmer, J. *Coping with flash floods*, NATO science series, partnership sub-series 2: environmental security, 77, pp. 3-10
- Gruntfest, E. and Huber, C. (1991)** Status-report on flood warning systems in the United-States, *Environmental Management*, 13(3), 279-286, DOI: 10.1007/BF01874906
- Guy, H. P., Simons, D. B. and Richardson, E. V. (1966)** Summary of alluvial data from flume experiments 1956-61, *U. S. Geological Survey Professional Paper*, 462-1
- GVP (2014)** Global Volcanism Program hosted by Smithsonian Institution of National Museum of Natural History, <http://www.volcano.si.edu/#> [accessed on 29/7/2014]
- Hand, B., Wessel, J. M. and Hayes, M. O. (1969)** Antidunes in the Mount Toby Conglomerate (Triassic), Massachusetts, *Journal of Sedimentary Petrology*, 39 (4), 1310-1316, DOI: 10.1306/74D71E1A-2B21-11D7-8648000102C1865D
- Hards, V., M., Strutt, S., De Angelis, G., Ryan, T., Christopher, T. C., Syers, T. and Bass, V. (2008)** Report to the scientific advisory committee, April 2008, Open File Rep. 09/01, Montserrat Volcano Obs., Montserrat
- Harford, C. L., Pringle, M. S., Sparks, R. S. J. and Young, S. R. (2002)** The volcanic evolution of Montserrat using Ar/Ar geochronology. In: Druitt, T.H. and Kokelaar, B.P. ed. *The eruption of Soufriere Hills Volcano, Montserrat, from 1995 to 1999*. Geological Society, London, Memoirs, 21, pp. 93-113.
- Harms, J. and Fahnstock, R (1965)** Stratification, bedforms, and flow phenomena (with an example from the Rio Grande). In: *Primary Sedimentary structures and their hydrodynamic interpretation*, Society of Economic Palaeontologists and Mineralogists, Special Publication 12, pp. 84-115

- Harpel, C. J., De Silva, S. and Salas, G. (2013)** Comment on: “Cobeñas, G., Thouret, J.-C., Bonadonna, C., Boivin, P., 2012. The c.2030 yr BP Plinian eruption of El Misti volcano, Peru: Eruption dynamics and hazard implications. *Journal of Volcanology and Geothermal Research* 241, 105-120.” *Journal of Volcanology and Geothermal Research*, 265, 94-101, DOI: 10.1016/j.jvolgeores.2013.08.016
- Harris, A. J. L. and Thornber, C. R., (1999)** Complex effusive events at Kīlauea as documented by the GOES satellite and remote video cameras, *Bulletin of Volcanology*, 61, 382-395
- Harrison, S. and Fritz, W. J. (1982)** Depositional features of march 1982 Mount St-Helens sediment flows, *Nature*, 299 (5885), 720-722, DOI: 10.1038/299720a0
- Hautmann, S., Gottsmann, J., Camacho, A. G., Fournier, N., Sacks, I. S. and Sparks, R. S. J. (2010)** Mass variations in response to magmatic stress changes at Soufrière Hills Volcano, Montserrat (W.I.): Insights from 4-D gravity data. *Earth and Planetary Science letters*, 290 (1-2), 83-89, DOI: 10.1016/j.epsl.2009.12.004
- Hautmann, S., Camacho, A. G., Gottsmann, J., Odbert, H. O. and Syers, R. S. (2013)** The shallow structure beneath Montserrat (West Indies) from new Bouguer gravity data. *Geophysical Research Letters*, 40 (19), 5113-5118, DOI: 10.1002/grl.51003
- Hayes, S., Montgomery, D. and Newhall, C. (2002)** Fluvial sediment transport and deposition following the 1991 eruption of Mount Pinatubo, *Geomorphology*, 45 (3-4), 211-244, DOI: 10.1016/S0169-555X(01)00155-6
- Hemmings, B., Whitaker, F. and Gottsmann, J. (2012)** Initial investigations of the productive perched aquifers on the volcanic island of Montserrat. Proceedings, TOUGH Symposium 2012, Lawrence Berkeley National Laboratory, Berkeley, California
- Henderson, F. M. (1966)** Open Channel Flow. MacMillan Company, New York, USA, 360 p.
- Herd, R. A., Edmonds, M. and Bass, V. (2005)** Catastrophic lava dome failure at Soufrière Hills Volcano, Montserrat, 12-13 July 2003, *Journal of Volcanology and Geothermal Research*, 148 (3-4), 234-252, DOI: 10.1016/j.jvolgeores.2005.05.003
- Hicks, P. D., Matthews, A. J. and Cooker, M. J. (2010)** Triggering of a volcanic dome collapse by rainwater infiltration, *Journal of Geophysical Research*, 115, B09212, DOI: 10.1029/2009JB006831
- Huang, C. J. (2013)** Modeling the Spatial Evolution of Roll Waves, Ph.D. Thesis, University of Southern California
- Hydrosorce (2004)** Groundwater exploration and development of high yield water supply wells for The Montserrat Water Authority, Hydrosorce Associates Inc., Ashland, N.H.

References

- Hjulström, F. (1935).** The Morphological Activity of Rivers as Illustrated by River Fyris, *Bulletin of the Geological Institute*, Uppsala, vol. 25, ch. 3.
- IFRC (2011)** Public awareness and public education for disaster risk reduction: a guide, International Federation of Red Cross and Red Crescent Societies, Geneva, http://www.ifrc.org/Global/Publications/disasters/reducing_risks/302200-Public-awareness-DDR-guide-EN.pdf (Accessed: 3/5/2014)
- International Sabo Centre (2013)** Personal visit to Sakurajima International Volcanic SABO center on Sakurajima, Japan in July 2013
- IPCC (2013)** Climate Change 2013: The Physical Science Basis. *Contribution of Working Group I to the Fifth Assessment Report of the Intergovernmental Panel on Climate Change*. Stocker, T. F., Qin, D., Plattner, G.-K., Tignor, M., Allen, S. K., Boschung, J., Nauels, A., Xia, Y., Bex, V. and Midgley, P. M. (eds.), Cambridge University Press, Cambridge, United Kingdom and New York, NY, USA, 1535 pp.
- Iverson, R. M. (1997)** The physics of debris flow, *Reviews of Geophysics*, 35 (3), 256-296, DOI: 10.1029/97RG00426
- Iverson, R. M., Schilling, S. P. and Vallance, J. W. (1998)** Objective delineation of lahars-inundation hazard zones, *Geological Society of America Bulletin*, 110 (8), 972-984, DOI: 10.1130/0016-7606(1998)110<0972
- Jackson, T. A. (2013)** A review of volcanic island evolution and magma production rate: an example from a Cenozoic island arc in the Caribbean. *Journal of the Geological Society* 2013, 170 (3), 547-556, DOI: 10.1144/jgs2011-166
- Jakob, M. (2005)** Debris-flow hazard analysis. In: Jakob, M. and Hungr, O., ed., *Debris-flow hazards and related phenomena*. Springer-Verlag, Berlin, p. 411-443
- Jeffreys, H. (1925)** The flow of water in an inclined channel of rectangular section. *Philosophical Magazine Series 6*, 49 (293), 793-807, DOI:10.1080/14786442508634662
- Jiyu, C., Cangzi, L., Chongle, Z. and Walker, H. J. (1990)** Geomorphological development and sedimentation in Qiantang estuary and Hangzhou bay, *Journal of Coastal Research*, 6(3), 559-572
- Johnson, N. and Parnell, R. A. (1986)** Composition, distribution and neutralization of “acid rain” derived from Masaya volcano, Nicaragua, *Telhus*, 38 B, 106-107
- Jolivet, M., Barrier, L., Dominguez, S., Guerit, L., Heilbronn, G. and Fu, B. (2014)** Unbalanced sediment budgets in the catchment-alluvial fan system of the Kuitun River (northern Tian Shan, China): Implications for mass-balance estimates, denudation and sedimentation rates in orogenic systems, *Geomorphology*, 214, 168-182
- Jones, I. (2011)** Initial investigation into the revegetation of volcanoclastic deposits on the Soufrière Hills volcano, Montserrat, Montserrat Volcano Observatory report (unpublished)

- Jones, M. T., Hembury, D. J., Palmer, M. R., Tonge, B., Darling, W. G. and Loughlin, S. C. (2011)** The weathering and element fluxes from active volcanoes to the oceans: a Montserrat case study, *Bulletin of Volcanology*, 73 (3), 207–222, DOI 10.1007/s00445-010-0397-0
- Jopling, A. and Richardson, E. V. (1966)** Backset bedding developed in shooting flow in laboratory experiments, *Journal of Sedimentary Petrology*, 36 (3), 821-825
- Julien, P. Y. (1989)** Laboratory analysis of hyperconcentrations. In: Wang, S. S. Y., ed., *Proceedings of the International Symposium on Sediment Transport Modelling*, New Orleans, LA, New York: ASCE; pp. 681–686.
- Kenedi, C. L. (2010)** Fractures, Faults, and Hydrothermal Systems, of Puna, Hawaii, and Montserrat, Lesser Antilles. PhD thesis, Duke University
- Kenedi, C. L., Sparks, R. S. J., Malin, P., Voight, B., Dean, S., Minshull, T., Paulatto, M., Peirce, C. and Shalev, E. (2010)** Contrasts in morphology and deformation offshore Montserrat: new insights from the SEA-CALIPSO marine cruise data. *Geophysical Research Letters*, 37, L00E25, DOI: 10.1029/2010GL043925
- Kennedy, J. F. K. (1960)** Stationary waves and antidunes in alluvial channels, Ph.D. Thesis, California Institute of Technology, W.M. Keck laboratory of Hydraulics and Water, Resources, Pasadena, 146 p.
- Kennedy, J.F. (1963)** The mechanics of dunes and antidunes in erodible-bed channels. *Journal of Fluid Mechanics*, 16 (4), 521-546, DOI: 10.1017/S0022112063000975
- Khezri, N. and Chanson, H. (2012a)** Undular and breaking bores on fixed and movable gravel beds, *Journal of Hydraulic Research*, 50 (4), 353-363, DOI: 10.1080/00221686.2012.686200
- Khezri, N. and Chanson, H. (2012b)** Inception of bed load motion beneath a bore, *Geomorphology*, 153, 39-47, DOI: 10.1016/j.geomorph.2012.02.006
- Khezri, N. and Chanson, H. (2012c)** Sediment inception under breaking tidal bores, *Mechanics Research Communications*, 41, 49-53, DOI: 10.1016/j.mechrescom.2012.02.010
- Kokelaar, B. P. (2002)** Setting, chronology and consequences of the eruption of Soufrière Hills Volcano, Montserrat (1995- 1999). In: Druitt T. H., and Kokelaar B. P. ed., *The Eruption of the Soufrière Hills Volcano, Montserrat, from 1995 to 1999*, Geological Society, London, Memoirs, 21, pp. 1-44
- Kokelaar, B. P., Graham, R. L., Gray, J. M. N. T. and Vallance, J. W. (2014)** Fine-grained linings of leveed channels facilitate runout of granular flows, *Earth and Planetary Science Letters*, 385, 172-180, DOI: 10.1016/j.epsl.2013.10.043
- Komar, P. D. (1987)** Selective grain entrainment by a current from a bed of mixed sizes: A reanalysis, *Journal of sedimentary Petrology*, 57 (2), 203-211

References

- Komorowski, J. -C., Legendre, Y., Christopher, T., Bernstein, M., Stewart, R., Joseph, E., Fournier, N., Chardot, L., Finizola, A., Wadge, G., Syers, R., Williams, C. and Bass, V. (2010)** Insights into processes and deposits of hazardous vulcanian explosions at Soufrière Hills Volcano during 2008 and 2009 (Montserrat, West Indies). *Geophysical Research Letters*, 37, L00E19, DOI:10.1029/2010GL042558
- Kopp, H., Weinzierl, W., Becel, A., Charvis, P., Evain, M., Flueh, E. R., Gailler, A., Galve, A., Hirn, A., Kandilarov, A., Klaeschen, D., Laigle, M., Papenberg, C., Planert, L. and Roux, E. (2011)** Deep structure of the central Lesser Antilles Island Arc: relevance for the formation of continental crust, *Earth and Planetary Science Letters*, 304 (1-2), 121-134, DOI: 10.1016/j.epsl.2011.01.024
- Knutson, T. R., McBride, J. L., Chan, J., Emanuel, K., Holland, G., Landsea, C., Held, I., Kossin, J. P., Srivastava, A. K., Masato, S. (2010)** Tropical cyclones and climate change. *Nature Geoscience*, 3, 157-163, DOI:10.1038/ngeo779
- Krimmel, R. M. and Post, A. (1981)** Oblique aerial photography, March- October 1980. In: U.S. Geological Survey, The 1980 eruptions of Mount St. Helens, Washington, pp.31-52
- Kubo, Y. and Yokokawa, A. (2001)** Theoretical study on breaking of waves on antidunes. In: McCaffrey, W. Kneller, B. and Peakall, J., *Particulate Gravity Currents*, Special Publications of the I.A.S., 31, pp.65-70
- Lahitte, P., Samper, A. and Quidelleur, X. (2012)** DEM-based reconstruction of southern Basse-Terre volcanoes (Guadeloupe archipelago, FWI): Contribution to the Lesser Antilles Arc construction rates and magma production. *Geomorphology*, 136 (1), 148-164, DOI: 10.1016/j.geomorph.2011.04.008
- Lang, J and Winesmann, J (2013)** Lateral and vertical facies relationships of bedforms deposited by aggrading supercritical flows: From cyclic steps to humpback dunes, *Sedimentary Geology*, 296, 36-45, DOI: 10.1016/j.sedgeo.2013.08.005
- Langford, R. and Bracken, B. (1987)** Medano Creek, Colorado, A model for upper-flow-regime fluvial deposition, *Journal of Sedimentary Research*, 57 (5), 863- 870, DOI: 10.1306/212F8C88-2B24-11D7-8648000102C1865D
- Lavigne, F., Thouret, J.C., Voight, B., Suwa, H. and Sumaryono, A (2000)** Lahars at Merapi volcano, Central Java: an overview. *Journal of Volcanology and Geothermal Research*, 100 (1-4), 423-456, DOI: 10.1016/S0377-0273(00)00150-5
- Lavigne, F., Thouretm J.-C., Voight, B., Young, K., LaHusen, R., Marso, J., Suwa, H., Sumaryono, A., Sayudi, D.S., Dejean, M. (2000b)** Instrumental lahar monitoring at Merapi Volcano, Central Java, Indonesia. *Journal of Volcanology and geothermal Research*, 100, 457-478, DOI: 10.1016/S0377-0273(00)00151-7
- Lavigne, F. and Thouret, J.-C. (2003)** Sediment transportation and deposition by rain-triggered lahars at Merapi Volcano, Central Java, Indonesia, *Geomorphology*, 49 (1-2), 45-69, DOI: 10.1016/S0169-555X(02)00160-5

- Lavigne, F. (2004)** Rates of sediment yield following small scale volcanic eruptions: a quantitative assessment at the Merapi and Semeru stratovolcanoes, Java, Indonesia, *Earth Surface Processes and Landforms*, 29 (8), 1045-1058, DOI: 10.1002/esp.1092
- Lawless, M. R., Lane, S. N. and Best, J. L. (2004)** The junction vortex system: time-mean and instantaneous flow fields. In: Jirka, G. H. and Uijtewaal, W. S. G., ed., *Shallow Flows: research presented at the International Symposium on Shallow Flows*, Delft, Netherlands, CRC Press, pp. 117- 126
- Lea, D. (2011)** personal communication, 4/5/2011
- Leavesley, G. H., Lusby, G. C. and Lichty, R. W. (1989)** Infiltration and erosion characteristics of selected tephra deposits from the 1980 eruption of Mount St. Helens, Washington, USA, *Hydrological Sciences Journal*, 34 (3), 339-353, DOI: 10.1080/02626668909491338
- Leclair, S. F. and Roy, A. G. (1997)** Variability of bed morphology and sedimentary structures at a discordant river confluence during low flows, *Geographie Physique et Quaternaire*, 50 (2), 125-139
- Lefriant, A., Harford, C. L., Deplus, C., Boudon, G., Sparks, R. S. J., Herd, R. A. and Komorowski, J. C. (2004)** Geomorphological evolution of Montserrat, West Indies: importance of flank collapse and erosional processes. *Journal of Geological Society*, 161 (1), 171-182, DOI: 10.1144/0016-764903-017
- Lennon, J. M. and Hill, D. F. (2006)** Particle image velocity measurements of undular and hydraulic jumps, *Journal of Hydraulic Engineering ASCE*, 132 (12), 1283-1294, DOI: 10.1061/(ASCE)0733-9429(2006)132:12(1283)
- Li, W. (2014)** Mathematical modelling of morphological changes and hyperconcentrated floods in the Yellow River, PhD Thesis, TUDelft
- Li, W., van Maren, D.S., Wang, Z.B., de Vriend, H.J. and Wu, B.S. (2014)** Peak discharge increase in hyperconcentrated floods, *Advances in water resources*, 67, 65-77, DOI: 10.1016/j.advwatres.2014.02.007
- Liggett, J. A. (1994)** *Fluid Mechanics*, McGraw-Hill, New York, USA, 495 p.
- Lighthill, J. (1978)** *Waves in Fluids*, Cambridge University Press, Cambridge, UK, 504 p.
- Lirer, L., Vinci, A., Alberico, I., Gifuni, T., Bellucci, F., Petrosino, P. and Tinterri, R. (2001)** Occurrence of inter-eruption debris flow and hyperconcentrated flood-flow deposits on Vesubio volcano, Italy, *Sedimentary Geology*, 139 (2), 151- 167, DOI: 10.1016/S0037-0738(00)00162-7

References

- Loughlin, S. C., Baxter, P. J., Aspinall, W. P., Darroux, B., Harford, C. L. and Miller, A. D. (2002)** Eyewitness accounts of the 25 June 1997 pyroclastic flows and surges at Soufriere Hills Volcano, Montserrat, and implications for disaster mitigation. In Druitt, T. H. and Kokelaar, B. P. ed., *The Eruption of Soufrière Hills Volcano, Montserrat from 1995 to 1999*. Geological Society of London, Memoir 21, pp. 211- 230
- Loughlin, S., Baptie B., Christopher, T., Ryan, G., Luckett, R., Hards, V., Jones, L., Fournier, N., Bass, V., Syers, T., Ruzie, L., Higgins, M., Williams, P. and Williams, D., (2006)** Report to the Scientific Advisory Committee, Montserrat, August 2006, MVO Open File Report 06/07, 39pp
- Lowe, D. R., Williams, S. N., Leigh, H., Connort, C. B., Gemmell, J. B. and Stoiber, R. E. (1986)** Lahars initiated by the 13 November 1985 eruption of Nevado del Ruiz, Colombia, *Nature*, 324, 51-53, DOI: 10.1038/324051a0
- Lowe, D. R. (1988)** Suspended-load fallout rate as an independent variable in the analysis of current structures, *Sedimentology*, 35 (5), 765-776, DOI: 10.1111/j.1365-3091.1988.tb01250.x
- Lube, G., Cronin, S. J., Manville, V., Procter, J. N., Cole, S. E. and Freundt, A. (2012)** Energy growth in laharcic mass flows, *Geology*, 40, 475-478, DOI: 10.1130/G32818.1
- MacDonald, R., Hawkesworth, C.J. and Heath, E. (2000)** The Lesser Antilles volcanic chain: a study in arc magmatism, *Earth Science Reviews*, 49 (1-4), 1-76, DOI: 10.1016/S0012-8252(99)00069-0
- Macdonald, R. G., Alexander, J., Bacon, J. C., andCooker, M. J. (2013)** Variations in the architecture of hydraulic-jump bar complexes on non-eroding beds, *Sedimentology*, 60 (5), 1291-1312, DOI: 10.1111/sed.12035
- Macgregor, A. G. (1938)** The Royal Society Expedition to Montserrat, B.W.I. The volcanic history and petrology of Montserrat with observatiosn of Mt. Pele, in Martinique. *Philosophical Transactions of the Royal Society of London*, B229, 1-90
- Mack, G. H., McIntosh, W. C., Leeder, M. R. and Curtis Monger, H. (1996)** Plio-Pleistocene pumice floods in the ancestral Rio Grande, southern Rio Grande rift, USA, *Sedimentary Geology*, 103 (1-2), 1-8, DOI: 10.1016/0037-0738(96)00009-7
- Magill, C. Wilson, T. and Okada, T. (2013)** Observations of tephra fall impacts from the 2011 Shinmoedake eruption, Japan, *Earth Planets Space*, 65, 677-698, DOI: 10.5047/eps.2013.05.010
- Major, J. J. (1984)** Geologic and rheologic characteristics of the May 18, 1980 southwest flank lahars, Mount St. Helens, Washington, M.S. Thesis, The Pennsylvania State University, 225 p.

- Major, J. J and Voight, B. (1986)** Sedimentology and clast orientations of the 18 May 1980 southwest flank lahars, Mount St. Helens, Washington, *Journal of Sedimentary Petrology*, 56 (5), 691-705
- Major, J. J., Pierson, T. C., Dinehart, R. L. and Costa, J. E. (2000)** Sediment yield following severe volcanic disturbance: A two-decade perspective from Mount St. Helens, *Geology*, 28 (9), 819-822, DOI: 10.1130/00917613(2000)28<819:SYFSVD>2.0.CO;2
- Major, J. J and Mark, L. E. (2006)** Peak flow responses to landscape disturbances caused by the cataclysmic 1980 eruption of Mount St. Helens, Washington, *Geological Society of America Bulletin*, 118 (7-8), 938-958, DOI: 10.1130/B25914.1
- Major, J. J., Kingsbury, C. G., Poland, M. P. and LaHusen, R. G. (2009)** Extrusion rate of the Mount St. Helens lava dome estimated from terrestrial imagery—November 2004-December 2005, chap. 12. In: Sherrod, D. R., Scott, W. E., and Stauffer, P. H., ed., *A volcano rekindled; the renewed eruption of Mount St. Helens, 2004–2006*: U.S. Geological Survey Professional Paper 1750
- Manga, M., Hornbach, M. J., Le Friant, A. L., Ishizuka, O., Stroncik, N., Adachi, T., Aljehdali, M., Boudon, G., Breikreux, C., Fraas, A., Fujinawa, A., Hatfield, R., Jutzeler, M., Kataoka, K., Lafuerza, S., Maeno, F., Martinez-Colon, M., McCanta, M., Morgan, S., Palmer, M. R., Saito, T., Slagle, A., Stinton, A. J., Subramayam, K. S. V., Tamura, Y., Talling, P. J., Villemant, B., Wall- Palmer, D. and Wang, F. (2012)** Heat flow in the Lesser Antilles island arc and adjacent back arc Grenada basin, *Geochemistry, Geophysics, Geosystems*, 13, Q08007, DOI: 10.1029/2012GC004260
- Manville, V., Segschneider, B. and White, J. D. L. (2002)** Hydrodynamic behaviour of Taupo 1800a pumice: implications for the sedimentology of remobilized pyroclasts, *Sedimentology*, 49 (5), 955-976, DOI: 10.1046/j.1365-3091.2002.00485.x
- Manville, V. and White, J. D. L. (2003)** Incipient granular mass flows at the base of sediment-laden floods, and the roles of flow competence and flow capacity in the deposition of stratified bouldery sands, *Sedimentary Geology*, 155 (1-2), 157–173, DOI: 10.1016/S0037-0738(02)00294-4
- Manville, V., Hodgson, K. A. and Nairn, I. A. (2007)** A review of break-out floods from volcanogenic lakes in New Zealand, *New Zealand Journal of Geology and Geophysics*, 50 (2), 131-150
- Manville, V., Németh, K. and Kano, K. (2009)** Source to sink: A review of three decades of progress in the understanding of volcanoclastic processes, deposits, and hazards. *Sedimentary Geology*, 220 (3-4), 136–161, DOI: 10.1016/j.sedgeo.2009.04.022
- Martinez, M. L., Ma, Arboleda, R. A., Delos Reyes, P. J., Gabinete, E. and Dolan, M. T. (1996)** Rainfall, acoustic flow monitor records and observed lahars of the Sacobia River in 1992. In: Newhall, C.G. and Punongbayan, R.S., ed., *Fire and mud: eruptions and lahars of Mount Pinatubo, Philippines*, Philippine Institute of Volcanology and Seismology, Quezon City and University of Washington Press, Seattle, pp. 921-950

References

- Mastbergen, D. R. and Winterwerp, J. C (1987)** Het gedrag van zand-watermengselstromingen boven water: Verslag experimentele vervolgstudie, Report Z46-02, Delft Hydraulics, Delft, The Netherlands
- Mather, A. E. and Hartley, A. J. (2005)** Flow events on a hyper-arid alluvial fan: Quebrada Tambores, Salar de Atacama, northern Chile. In: Harvey, A. M., Mather, A. E. and Stokes, M., ed., Alluvial fans: geomorphology, sedimentology, sedimentology, dynamics, *Geological Society special publication 251*. Geological Society, London, pp. 9-24
- McBride, E. F., Shepard, R. G and Crawley, R. A. (1975)** Origin of parallel, near-horizontal laminae by migration of bed forms in a small flume, *Journal of Sedimentary Petrology*, 45 (1), 132-139
- McKee, E. D., Crosby, E. J. and Berryhill, H. L. (1967)** Flood deposits, Bijou Creek, Colorado, *Journal of Sedimentary Petrology*, 37 (3), 829–851
- Meyer, D. F. & Dodge, J. E. (1988)** Post- eruption changes in channel geometry of streams in the Tuttle River drainage basin, 1983-1985, Mount St Helens, Washington: USGS Open file report, 85- 412, 128 p.
- Meyer, D. F. and Martinson, H. A. (1989)** Rates and processes of channel development and recovery following the 1980 eruption of Mount St. Helens, Washington, *Hydrological Sciences - Journal - des Sciences Hydrologiques*, 34 (2), 4/1989
- Middleton, G. (1965)** Antidune cross-bedding in a large flume, *Journal of Sedimentary Petrology*, 35 (4), 922-927
- Miller, V., Voight, B., Ammon, C. J., Shalev, E. and Thompson, G. (2010)** Seismic expression of magma-induced crustal strains and localized fluid pressures during initial eruptive stages, Soufrière Hills Volcano, Montserrat, *Geophysical Research Letters*, 37, L00E21, DOI: 10.1029/2010GL043997
- Milliman, J. D. and Syvitski, J. P. M. (1992)** Geomorphic/ tectonic control on sediment discharge to the ocean: the importance of small mountainous rivers, *Journal of Geology*, 100 (5), 525-544
- Montserrat Reporter (1999)** Rainfall-produced mud flows close Belham River Bridge, 17th September 1999,
http://www.montserratreporter.org/index.php?option=com_wrapper&view=wrapper&Itemid=50 (Accessed 1/11/2012)
- Montserrat Reporter (2010)** Hurricane Earl becomes a major category 3 storm, 30th August 2010,
<http://www.themontserratreporter.com/hurricane-earl-becomes-a-major-category-3-storm/> (Accessed 22/1/2015)
- Mosley M. P. (1974)** Experimental study of rill erosion, *American Society of Agricultural Engineers, Transactions*, 17 (Sep-O), 909-916

- Mulder, T. and Alexander, J. (2001)** The physical character of subaqueous sedimentary density flows and their deposits, *Sedimentology*, 48 (2), 269-299, DOI: 10.1046/j.1365-3091.2001.00360.x
- Muñoz-Salinas, E. Manea, V. C., Palacios, D. and Castillo-Rodriguez, M. (2007)** Estimation of lahar flow velocity on Popocatepetl volcano (Mexico), *Geomorphology*, 92 (1-2), 91-99, DOI: 10.1016/j.geomorph.2007.02.011
- Murata, H. and Okabayashi, T. (1983)** The erosion and failure of the volcanic ash slopes of Sakurajima, Technology reports of the Yamaguchi University, 3 (2), 141–149
- MVO (2010)** Report to SAC15 on activity between 28 February 2010 and 31 October 2010. *Montserrat Volcano Observatory*, Open File Report OFR10-02a/b. Montserrat Volcano Observatory, Flemmings, Montserrat
- MVO (2011)** Camera Monitoring of the Soufrière Hills volcano, MVO website, <http://208.90.113.192/science/monitoring/171-volcano-live> (Accessed: 2/5/2011)
- MVO (2014)** Montserrat Hazard Level System, http://mvo.ms/pub/Hazard_Level_System/HLS-20140801.pdf (Accessed 25/8/2014)
- MVOFlickr (2014)** Flickr: Montserrat Volcano Observatory photo stream, <https://www.flickr.com/photos/mvo> (Accessed 23/8/2014)
- MVOobs (2014)** Montserrat Volcano Observatory, daily-weekly obs (July 1995-September 2014), unpublished. Available by request, Roderick Stewart, MVO director
- Nakatani, K., Wada, T., Satofuka, Y. and Mizuyama, T. (2008)** Development of “Kanako 2D (Ver.2.00),” a user-friendly one- and two-dimensional debris flow simulator equipped with a graphical user interface, *International Journal of Erosion Control Engineering*, 1 (2), 62-72
- Naranjo, J. L., Sigurdsson, H., Carey, S. N. and Fritz, W. (1986)** Eruption of the Nevado del Ruiz volcano, Colombia, on 13 November 1985: tephra fall and lahars, *Science*, 233 (4767), 961- 963
- NERC (2014)** AVTIS: All-weather Volcano Topography Sensor, <http://www.nerc-essc.ac.uk/~gw/AVTIS/Overview/overview.html> (Accessed 25/01/2014)
- Norton, G. E., Watters, R. B, Voight, B., Mattioli, G. S., Herd, R. A., Young, S. R., Devine, G. E., Aspinall, W. P., Bonadonna, C., Baptie, B. J., Edmonds, M., Jolly, A. D., Loughlin, S. C., Lockett, R. and Sparks, S. J. (2002)** Pyroclastic flow and explosive activity at Soufrière Hills Volcano, Montserrat, during a period of virtually no magma extrusion (March 1998 to November 1999). In: Druitt T. H., and Kokelaar B. P. ed., *The Eruption of the Soufrière Hills Volcano, Montserrat, from 1995 to 1999*, Geological Society, London, Memoirs, 21, pp. 236-279
- Núñez-González, F. and Martín-Vide, J. P. (2011)** Analysis of antidune migration direction, *Journal of Geophysical Research*, 116, F02004, DOI: 10.1029/2010JF001761

References

- Ogburn, S. E. (2013)** FlowDat: VHub Mass Flow Database. <https://vhub.org/resources/2076> (Accessed 23/5/2014)
- Ogburn, S. E., Calder, E. S., Cole, P. D. and Stinton, A. J. (2014)** The Eruption of the Soufrière Hills, Montserrat from 2000 to 2010. In: Wadge, G. Robertson, R. E. A. and Voight, B., ed., *The Eruption of Soufrière Hills Volcano, Montserrat from 2000 to 2010*. Geological Society, London, Memoirs, 39, 172-192
- Pathiraja, S., Westra, S. and Sharma, A. (2012)** Why continuous simulation? The role of antecedent moisture in design flood estimation, *Water Resources Research*, 48, W06534, DOI: 10.1029/2011WR010997
- Patrick, M. R., Orr, T., Antolik, L., Lee, L. and Kamibayashi, K. (2014)** Continuous monitoring of Hawaiian volcanoes with thermal cameras, *Journal of Applied Volcanology*, 3 (1), DOI: 10.1186/2191-5040-3-1
- Peaks, Harriet Joan (2010)** Comment on Montserrat Volcano Observatory Facebook page, <https://www.facebook.com/mvoms/posts/105532079488105> (Accessed 15/03/2013)
- Perret, F. A. (1939)** The Volcano-Seismic Crisis at Montserrat 1933-1937, *Carnegie Institution of Washington, Publications*, 512, 76 p.
- Perry, C. and Taylor, K. (2007)** Ch 1: Environmental sedimentology: induction. In: Perry, C. and Taylor, K., ed. *Environmental Sedimentology*, Blackwell Publishing, Oxford, UK, 460 p.
- Petit, F., Gob, F., Houbrechts, G., and Assani, A. A. (2005)** Critical specific stream power in gravel bed rivers, *Geomorphology*, 69, 92-101, DOI: 10.1016/j.geomorph.2004.12.004
- Picard, M. D. and High, L. R. (1973)** Sedimentary structures of ephemeral streams. *Developments in Sedimentology*, vol. 17. Elsevier, Amsterdam. 223 p.
- Picard, M., Schneider, J. L. and Boudon, G. (2006)** Contrasting sedimentary processes along a convergent margin: the Lesser Antilles arc system, *Geo-Marine Letters*, 26 (6), 397- 410, DOI: 10.1007/s00367-006-0046-y
- Pierson, T. C. and Scott, K. M. (1985)** Downstream dilution of a Lahar: Transition from debris flow to a hyperconcentrated streamflow, *Water Resources Research*, 21 (10), 1511-1524, DOI: 10.1029/WR021i010p01511
- Pierson, T. C. and Costa, J. E. (1987)** A rheologic classification of subaerial sediment-water flows. In: Costa, J.E. and Wieczorek, G.F., ed. *Debris flows/avalanches – Process, recognition and mitigation. Reviews in Engineering Geology*, 7, 1-12

- Pierson, T. C., Daag, A. S., Delos Reyes, P. J., Regalado, M. T. M., Solidum, R. U. and Tubianosa, B. S. (1996)** Flow and deposition of posteruption hot lahars on the east side of Mount Pinatubo, July-October 1991. In: Newhall, C.G. and Punongbayan, R.S., ed., *Fire and mud: eruptions and lahars of Mount Pinatubo, Philippines*, Philippine Institute of Volcanology and Seismology, Quezon City and University of Washington Press, Seattle, pp. 921-950
- Pierson, T. C. (1998)** An empirical method for estimating travel times for wet volcanic mass flows, *Bulletin of Volcanology*, 60 (2), 98-109, DOI: 10.1007/s004450050219
- Pierson, T. C. (2005)** Chapter 8 Hyperconcentrated flow transition process between water flow and debris flow. In: Jakob, M. and Hungr, O., ed. *Debris flow hazards and related phenomena*, New York, Springer-Verlag, pp. 159-196
- Postma G., Nemec W. and Kleinspehn K. L. (1988)** Large floating clasts in turbidites: a mechanism for their emplacement, *Sedimentary Geology*, 58 (1), 47-61, DOI: 10.1016/0037-0738(88)90005-X
- Poulidis, A., Renfrew, I. and Matthews, A. (2014)** Orographic Flow over an Active Volcano, EGU General Assembly, 2014, held 27 April- 2 May 2014, Vienna Austria. Poster presentation
- Powell, C. F. (1938)** The Royal Society expedition to Montserrat, BWI: Final Report. *Philosophical Transactions Royal Society, London, A*, 237 (771), 1-34, DOI: 10.1098/rsta.1938.0002
- Power, W. R. (1961)** Backset beds in the coso formation, Inyo County, California. *Journal of Sedimentary Petrology*, 31 (4), 603-607, DOI: 10.1306/74D70BFA-2B21-11D7-8648000102C1865D
- Procter, J. N., Cronin, S. J., Fuller, I.C., Sheridan, M., Neall, V. E. and Keys, H. (2010)** Lahar hazard assessment using Titan2D for an alluvial fan with rapidly changing geomorphology: Whangaehu River, Mt. Ruapehu, *Geomorphology*, 116 (1-2), 162-174, DOI: 10.1016/j.geomorph.2009.10.016
- Qian, Y. Yang, W., Zhao, Q., Cheng, X., Zhang, I., and Xu, W. (1980)** Basic characteristics of flow with hyperconcentrations of sediment. In: *Proceedings of the International Symposium on River Sedimentation: Beijing, Chinese Society of Hydraulic Engineering*, p. 175- 184
- Rathburn, S. L., Rubin, Z. K. and Wohl, E. E. (2013)** Evaluating channel response to an extreme sedimentation event in the context of historical range of variability: Upper Colorado River, Rocky Mountain National Park, Colorado, *Earth Surface Processes and Landforms*, 38 (4), 391-406, DOI:10.1002/esp.3329
- Raudkivi, A. J. (1963)** Study of sediment ripple formation, *ASCE Journal of the Hydraulic Division*, 89 (6), 15- 33
- Raudkivi, A. J. (1966)** Bedforms in alluvial channels, *Journal of Fluid Mechanics*, 26, 507- 514

References

- Rea, W. J. (1974)** The volcanic geology and petrology of Montserrat, West Indies. *Journal of the Geological Society*, 130, 341-366, DOI: 10.1144/gsjgs.130.4.0341
- Reed, R. J., Norquist, J. C., Recker, E. E. (1977)** The structure and properties of African wave disturbances as observed during phase III of GATE. *Monthly Weather Review*, 105, 317-333, DOI: 10.1175/15200493(1977)105<0317:TSAPOA>2.0.CO;2
- Reid, I. and Frostick, L. E. (1987)** Flow dynamics and suspended sediment properties in arid zone flash floods, *Hydrological Processes*, 1 (3), 239- 253, DOI: 10.1002/hyp.3360010303
- Rickenman, D. (1991)** Hyperconcentrated flow and sediment transport at steep slopes, *Journal of Hydraulic Engineering- ASCE*, 117 (11), 1419- 1439, DOI: 10.1061/(ASCE)0733-9429(1991)117:11(1419)
- Robertson, R., Cole, P., Sparks, R. S. J., Harford, C., Lejene, A. M., McGuire, W. J., Miller, A. D., Murphy, M. D., Norton, G., Stevens, N. F. and Young, S. R. (1998)** The explosive eruption of Soufrière Hills Volcano, Montserrat, West Indies, 17 September 1996, *Geophysical research letters*, 25 (18), 3429-3432, DOI: 10.1029/98GL01442
- Robillard, L. and Kennedy, J. F. (1967)** Some experimental observations on free surface flow over a wavy boundary, *Proceedings 12th Conference IAHR*, Vol.1, pp. 41-48. Fort Collins, Colorado, USA
- Rocabado, O. I. (1999)** Modelling highly concentrated turbulent flows with non-cohesive sediments, *PhD thesis*, Civil Eng. Dept., Katholieke Universiteit Leuven
- Rodolfo, K., S. (1989)** Origin and early evolution of a lahar channel at Mabinit, Mayon Volcano, Philippines, *Geological Society of America Bulletin*, 100, 351-370, DOI: 10.1130/0016-7606(1989)101<0414:OAEEO>2.3.CO;2
- Rodolfo, K. S., Arguden, A. T., Solidum, R. U. and Umbal, J. V. (1989)** Anatomy and behaviour of a post-eruptive rain lahar triggered by a typhoon on Mayon volcano, Philippines, *Bulletin of the International Association of Engineering Geologists*, 40 (1), 55-66
- Rodolfo K. S. and Arguden A. T. (1991)** Rain-lahar generation and sediment-delivery systems at Mayon volcano, Philippines. In: Fisher R. V. and Smith G., ed., *Sedimentation in volcanic settings*, SEPM Special Publication, 45, 71-87
- Rodolfo, K. S., Umbal, J. V., Alonso, R. A., Remotigue, C. T., Paladio-Melosantos, M. L., Salvador, J. H. G., Evangelista, D. and Miller, Y. (1996)** Two years of lahars on the western flank of Mount Pinatubo: Initiation, flow processes, deposits and attendant geomorphic and hydraulic processes. In: Newhall C. G. and Punongbayan R. S., ed., *Fire and Mud: Eruptions and lahars of Mount Pinatubo, Philippines*, Quezon City, Philippines Institute of Volcanology and Seismology, Seattle University Wash. Press

- Roman, D. C., De Angelis, S., Latchman, J and White, R. A. (2008)** Patterns of volcanotectonic seismicity and stress during the ongoing eruption of Soufrière Hills Volcano, Montserrat (1995-2007), *Journal of Volcanology and Geothermal Research*, 173 (3-4), 230-244, DOI: 10.1016/j.jvolgeores.2008.01.014
- Roobol, M. J. and Smith, A. L. (1998)** Pyroclastic stratigraphy of the Soufrière Hills volcano, Montserrat- Implications for the present eruption, *Geophysical Research Letters*, 25 (18), 3393- 3396
- Rouse (1938)** Fluid Mechanics for Hydraulic Engineers, Engineering Societies Monographs, 1st ed., New York, McGraw-Hill Book Co., 422 p.
- Rubin, D. M. and Hunter, R. E. (1982)** Bedform climbing in theory and nature, *Sedimentology*, 29, 121- 138
- Rubin, D. M. and Mcculloch, D. S. (1980)** Single and superimposed bedforms- a synthesis of San- Francisco Bay and Flume observations, *Sedimentary Geology*, 26 (1-3), 207-231, DOI: 10.1016/0037-0738(80)90012-3
- Russell, H. A. J. and Arnott, R. W. C. (2003)** Hydraulic-jump and hyperconcentrated-flow deposits of a glacialigenic subaqueous fan: oak ridges moraine, southern ontario, canada, *Journal of Sedimentary Research*, 73 (6), 887- 905, DOI: 10.1306/041103730887
- Rust, B. R. and Gibling, M. R. (1990)** Three-dimensional antidunes as HCS mimics in a fluvial sandstone: The Pennsylvanian South Bar formation near Sydney, Nova Scotia. *Journal of Sedimentary Petrology*, 60 (4), 540-548
- Ryan, G. A., Peacock, J. R., Shalev, E. and Rugis, J. (2013)** Montserrat geothermal system: A 3D conceptual model. *Geophysical Research Letters*, 40 (10), 2038–2043, DOI: 10.1002/grl.50489
- SAC (2011)** Report to the Scientific Advisory Committee on Volcanic Activity at Soufriere Hills Volcano Montserrat. Report between 28 February 2010 and 31 October 2010. Open File Report OFR 10-02a.
- Saint-Venant, A. (1871)** Theorie du mouvement non permanent des eaux, avec application aux crues des rivieres et a l'introduction de marees dans leurs lits. *Comptes rendus des seances de l'Academie des Sciences*.
- Schneider, A., Gerke, H. H. and Maurer, T. (2011)** 3D initial sediment distribution and quantification of mass balances of an artificially-created hydrological catchment based on DEMs from aerial photographs using GOCAD, *Physics and Chemistry of the Earth*, 36 (1-4), 87-100, DOI: 10.1016/j.pce.2010.03.023
- Scott, K. M. (1988)** Origins, behaviour, and sedimentology of lahars and lahar runoff flows in the Toutle-Cowlitz River system, *USGS Professional Paper 14470 A*, 76 p.

References

- Scott, K. M., Janda, R. J., de la Cruz, E. G., Gabinete, E., Eto, I., Sexon, M., and Hadley, K. C. (1996)** Channel and sedimentation responses to large volumes of 1991 volcanic deposits on the east flank of Mount Pinatubo. In: Newhall C. G. and Punongbayan R. S., ed., *Fire and Mud: Eruptions and lahars of Mount Pinatubo, Philippines*, Quezon City, Philippines Institute of Volcanology and Seismology, Seattle University Wash. Press
- Sevruk, B. (1982)** Methods of correction for systematic error in point precipitation measurement for operational use. *Technical Report Operational Hydrology Report 21*, WMO-No. 589, 91 p., World Metrological Organization
- Shalev, E., Kenedi, C. L., Malin, P., Voight, V., Miller, V., Hidayat, D., Sparks, R. S. J., Minshull, T., Paulatto, M., Brown, L. and Mattioli, G. (2010)** Three-dimensional seismic velocity tomography of Montserrat from SEA-CALIPSO offshore / onshore experiment, *Geophysical Research Letters*, 37, L00E17, DOI: 10.1029/2010GL042498
- Shaw, J. and Kellerhals, R. (1977)** Paleohydraulic Interpretation of antidune bedforms with applications to antidunes in gravel, *Journal of Sedimentary Petrology*, 47 (1), 257-266, DOI: 10.1306/212F7149-2B24-11D7-8648000102C1865D
- Shepherd, J. B., Tomblin, J. F. and Woo, D. A. (1971)** Volcano-seismic crisis in Montserrat, West Indies 1966-67. *Bulletin of Volcanology*, 35(1), 143-163, DOI: 10.1007/BF02596813
- Shou, K. J., Fei, L.Y., Lee, J. F., Lee, J. F., Wei, C. Y., Huang, S. T. and Lin, Y. C. (2012)** Landslides and catchment sedimentation in the Ta-Chia River influenced by the 1999 Taiwan Chi-Chi earthquake, *International Journal of Remote Sensing*, 33 (15) Special issue, 4815-4840, DOI: 10.1080/01431161.2011.638338
- Shreve, E. A. and Downs, A. C. (2005)** Quality- assurance plan for the analysis of fluvial sediment by the U.S. Geological Survey, Kentucky Water Science Center Sediment Laboratory: *U.S. Geological Survey Open-File Report 2005-1230*, 28 p.
- Siebert, L., Simkin, T. and Kimberley, P. (2010)** *Volcanoes of the World*, University of California Press, Science, 551 p.
- Simons, D.B. and Richardson, E.V. (1960)** Forms of bed roughness in alluvial channels, U. S. geological Survey, Colorado State University, 62 p.
- Simons, D. B., Richardson, E. V. and Albertson, M. L. (1961)** Flume studies using medium sand (0.45mm): Studies of flow in Alluvial channels: A comprehensive study of fluvial hydraulics, *U.S. Geological Survey Water-Supply paper*, 1498-A.
- Simons, D. B., Richardson, E. V. and Nordin, Jr. C. F. (1965)** Sedimentary structures generated by flow in alluvial channels. In Middleton, G. V., ed., *Primary Sedimentary Structures and their Hydrodynamic Interpretation: SEPM Special Publication 12*, pp. 34-52, DOI: 10.2110/pec.65.08.0034

- Smith, G. A. (1986)** Coarse-grained nonmarine volcanoclastic sediment: Terminology and depositional process, *Geological Society of America, Bulletin*, 97 (1), 1-10, DOI: 10.1130/0016-7606(1986)97<1:CNVSTA>2.0.CO;2
- Smith, G.A. and Fritz, W.J. (1989)** Volcanic influences on terrestrial sedimentation. *Geology*, 17 (4), 375-376, DOI: 10.1130/0091-7613(1989)017<0375
- Smith, G. A. and Lowe D. R. (1991)** Lahars: Volcano-hydrologic events and deposition in the debris flow – hyperconcentrated flow continuum. In: Fisher, R. V. and Smith G., ed., *Sedimentation in volcanic settings, SEPM Special Publication*, 45, pp. 59-70
- Smith, A. L., Roobol, M. J., Schellekens, J. H. and Mattioli, G. S. (2007)** Prehistoric Stratigraphy of the Soufrière Hills–South Soufrière Hills Volcanic Complex, Montserrat, West Indies. *Journal of Geology*, 115 (1), 115- 127, DOI: 10.1086/509271
- Sohn, Y. K. (1997)** On traction carpet sedimentation, *Journal of Sedimentary Research*, 67 (3), 502-509
- Sohn, Y. K., Rhee, C. W. and Kim, B. C. (1999)** Debris flow and hyperconcentrated flood-flow deposits in an alluvial fan, northeastern part of the Cretaceous Yongdong Basin, Central Korea, *Journal of Geology*, 107 (1), 111-132, DOI: 10.1086/314334
- Southard, J. B. and Boguchwal, L. A (1990)** Bed configurations in steady unidirectional water flows. Part 2: synthesis of Flume Data, *Journal of Sedimentary Petrology*, 60 (5), 658-679
- Spampinato, L., Calvari, S., Oppenheimer, C. and Boschi, E. (2011)** Volcano surveillance using infrared camreas, *Earth-Science Reviews*, 106 (1-2), 63-91, DOI: 10.1016/j.earscirev.2011.01.003
- Sparks, R .S. J. and Wilson, L. (1982)** Explosive volcanic-eruptions .5. Observations of plume dynamcis during the 1979 Soufriere eruption, St. Vincent, *Geological Journal of the Royal Astronomical Society*, 69 (2), 551- 570, DOI: 10.1111/j.1365-246X.1982.tb04965.x
- Spinewine, B., Sequeiros, O. E., Garcia, M. H., Beaubouef, R. T., Sun, T., Svoje, B. and Parker, G. (2009)** Experiments on wedge-shaped deep sea sedimentary deposits in minibasins and/or on channel levees emplaced by turbidity currents. Part II. Morphodynamic evolution of the wedge and of the associated bedforms, *Journal of Sedimentary Research*, 9 (8), 608- 628, DOI: 10.2110/jsr.2009.065
- Starheim, C. C. A., Gomez, C., Davies, T., Lavigne, F. and Wassmer, P. (2013)** In-flow evolution of lahar deposits from video-imagery with implications for post-event deposit interpretation, Mount Semeru, Indonesia, *Journal of Volcanology and Geothermal Research*, 256, 96-104, DOI: 10.1016/j.jvolgeores.2013.02.013

References

- Stinton, S., Cole, P.D., Stewart, R.C., Odbert, H.M. and Smith, P. (2014)** Chapter 7: The 11 February 2010 partial dome collapse at Soufrière Hills Volcano, Montserrat. In G. Wadge, R. Robertson, and B. Voight, editors, *The Eruption of Soufrière Hills Volcano, Montserrat from 2000 to 2010*, Geological Society Memoirs, London, 39, pp. 133–152, DOI:10.1144/M39.7
- STREVA (2014)** Strengthening Resilience in Volcanic Areas project website, <http://streva.ac.uk/> [accessed 30/6/2014]
- Sušnik, J. (2009)** Lahars in the Belham River Valley, Montserrat, West Indies. PhD Thesis, University of East Anglia, UK
- Suwa, H. and Sumaryono, A. (1995)** Sediment transportation by storm runoff at the Bebeng River on Mount Merapi. In: Proceedings of Workshop on Erosion Control through Volcanic Hydrological Approach (WECVHA), Sabo Technical Center, Yogyakarta, 10-11 January, pp. 106-137
- Tabary, P. (2006)** The French operational radar network: current state and perspectives inland and overseas. gpm.ipsl.polytechnique.fr/documents/d3-tabary/download.html (Accessed 2/03/2013)
- Takahashi, T. (2014)** Debris Flow: Mechanics, Prediction and Countermeasures, 2nd edition, London: CRC Press, 572 p.
- Tanarro, L. M., Zamarano, J. J. and Palacios, D. (2005)** Glacier degradation and lahar formation on the Popocatepetl volcano (Mexico) during the last eruptive period (1994-2003). In: Thouret, J.-C., Chester, D. K., Ollier, C. and Joyce, B., ed., *Volcanic landforms, Processes and hazards*. Zeitschrift fur Geomorphologie supplement series, 140, pp. 73-92
- Tanarro, L. M., Andrés, N., Zamorano, J. J., Palacios, D. and Renschler, C. S. (2010)** Geomorphological evolution of a fluvial channel after primary lahar deposition: Huiloac Gorge, Popocatepetl volcano (Mexico), *Geomorphology*, 122 (1-2), 178-190, DOI: 10.1016/j.geomorph.2010.06.013
- Taylor, M. A., Enfield, D. B. and Chen, A. A. (2002)** Influence of the tropical Atlantic versus the tropical Pacific on Caribbean rainfall. *Journal of Geophysical Research: Oceans*, 107 (C9), 3127. DOI: 10.1029/2001JC001097
- Terzaghi, K., Peck, R. B. and Mesri, G. (1996)** Soil Mechanics in Engineering Practice, 3rd ed., John Wiley & Sons, New York, 549 pp
- Thomas, R. B. (1985)** Measuring suspended sediment in small mountain streams. *General Technical Report. PSW-83*. Berkeley, C.A: Pacific Southwest Forest and Range Experiment Station, Forest Service, U.S. Department of Agriculture, 9 p.
- Thorncroft, C. D. and Hoskins, B. J. (1994)** An idealised study of African easterly waves: 2. A nonlinear view. *Quarterly Journal of Royal Meteorological Society*, 120, 983-1015. DOI: 10.1002/qj.49712051810

- Thouret, J.-C., Lavigne, F., Suwa, H., Sukatja, B. and Surono (2007)** Volcanic hazards at Mount Semeru, East Java (Indonesia), with emphasis on lahars. *Bulletin of Volcanology*, 70 (2), 221–244, DOI: 10.1007/s00445-007-0133-6
- Todd, S. P. (1989)** Stream-driven, high-density gravely traction carpets: possible deposits in the Trabeg Conglomerate Formation, SW Ireland and some theoretical considerations of their origin, *Sedimentology*, 36 (4), 513-530, DOI: 10.1111/j.1365-3091.1989.tb02083.x
- Toorman, E. A., Bruens, A. W., Kranenburg, C. and Winterwerp, J. C. (2002)** Interaction of suspended cohesive sediment and turbulence. In Winterwerp, J.C. and Kranenburg, C., *Fine Sediment Dynamics in the Marine Environment*. Proceedings in Marine Science, 6th International Conference on Cohesive Sediment Transport (INTERCOH 2000), 5 (155-169)
- Torri, D., Santi, E., Marignani, M., Rossi, M., Borselli, L. and Maccherini, S. (2013)** The recurring cycles of biancana badlands: Erosion, vegetation and human impact, *Catena*, 106 SI, 22-30, DOI: 10.1016/j.catena.2012.07.001
- Torri, D. and Poesen, J. (2014)** A review of topographic threshold conditions for gully head development in different environments, *Earth-Science Reviews*, 130, 73-85, DOI: 10.1016/j.earscirev.2013.12.006
- Tunbridge, I. P. (1981)** Sandy high-energy flood sedimentation – some criteria for recognition, with an example from the Devonian of S.W. England, *Sedimentary Geology*, 28 (2), 79-95, DOI: 10.1016/0037-0738(81)90058-0
- Tuñgol, N. M. and Regalado, T. M. (1996)** Rainfall, Acoustic Flow Monitor Records, and Observed Lahars of the Sacobia River in 1992. In: Newhall, C. G., and Punongbayan R. S., ed. *Fire and Mud: Eruptions and Lahars of Mount Pinatubo, Philippines*, Quezon City, Philippine Institute of Volcanology and Seismology and Seattle, Univ, Washington Press, pp. 951-970
- Umbal, J. V. and Rodolfo, K. S. (1996)** The 1991 lahars of southwester Mount Pinatubo and evolution of the lahar-dammed Mapanuepe Lake. In: Newhall, C. G., and Punongbayan R. S., ed. *Fire and Mud: Eruptions and Lahars of Mount Pinatubo, Philippines*, Quezon City, Philippine Institute of Volcanology and Seismology and Seattle, Univ, Washington Press, pp. 951-970
- U.S.G.S. (2014)** Analysis of Photographs and Other Images for Monitoring Purposes, Mount St. Helens, Volcano Hazards Program, USGS website, http://volcanoes.usgs.gov/volcanoes/st_helens/st_helens_monitoring_101.html (Accessed: 23/4/2014)
- Vallance, J. W. and Scott, K. M. (1997)** The Osceola Mudflow from Mount Rainier: Sedimentology and hazard implications of a huge clay-rich debris flow, *Geological Society of America Bulletin*, 109 (2), 143-163, DOI: 10.1130/0016-7606(1997)109<0143:TOMFMR>2.3.CO;2

References

- Vallance, J.W. and Savage, S. B. (2000)** Lahars. In Sigurdsson, H., Houghton, B., McNutt, S.R., Rymer, H. and Stix, J., ed., *Encyclopedia of Volcanoes*, New York Academic Press, pp. 601-616
- Van den Berg, J. H. and Van Gelder, A. (1993)** A new bedform stability diagram, with emphasis on the transition of ripples to plane bed in flows over fine sands and silt. In: Marzo, M. and Puigdefabregas, C., ed., *Alluvial Sedimentation*, Special Publication 17 of the IAS, pp. 11–21
- Van den Berg, J. H., Van Gelder, A., Kostaschuk, R. and Villard, P. (1998)** Discussion: Flow and sediment transport over large subaqueous dunes: Fraser River, Canada, *Sedimentology*, 45 (1), 217–221, DOI: 10.1046/j.1365-3091.1998.00149.x
- Van den Berg, J. H. and Nio, S. D. (2010)** Sedimentary Structures and their Relation to Bedforms and Flow Conditions, EAGE Publications, Houten, 138 p.
- van Maren, D. S., Winterwerp, J. C., Wu, B. S. and Zhou, J. J. (2009a)** Modelling hyperconcentrated flow in the Yellow River. *Earth Surface Processes and Landforms*, 34 (4), 596–612, DOI: 10.1002/esp.1760
- van Maren, D. S., Winterwerp, J. C., Wang, Z. Y. and Pu, Q. (2009b)** Suspended sediment dynamics and morphodynamics in the Yellow River, China, *Sedimentology*, 56 (3), 785- 806, DOI: 10.1111/j.1365-3091.2008.00997.x
- Vanoni, V. A. (2006)** Sedimentation engineering: Manuals and Reports on Engineering Practice No. 54. In: Vanoni, V.A. (ed). American Society of Civil Engineers Publications: Reston, V.A.
- Vázquez, R., Capra, L., Caballero, L., Arámbula-Mendoza, R. and Reyes-Dávila, G. (2014)** The anatomy of a lahar: Deciphering the 15th September 2012 lahar at Volcán de Colima, Mexico, *Journal of Volcanology and Geothermal Research*, 272, 126-136, DOI: 10.1016/j.jvolgeores.2013.11.013
- Vedernikov, V. V. (1945)** Conditions at the front of a translation wave disturbing a steady motion of a real fluid, *USSR Academy of Sciences*, 48 (4), 239-242
- Vedernikov, V. V. (1946)** Characteristic features of a liquid flow in an open channel, *USSR Academy of Sciences*, 52, 207-210
- Venditti, J. G., Church, M. and Bennett, S. J. (2005)** Morphodynamics of small-scale superimposed sand waves over migrating dune bed forms, *Water Resources Research*, 41 (10), W10423, DOI: 10.1029/2004WR003461
- Venditti, J. G., Best, J. L., Church, M. and Hardy, R. J. (2013)** Coherent Flow Structures at Earth's Surface, John Wiley & Sons, Science, 408 p.
- Vessel, R. K. and Davies, D. K. (1981)** Nonmarine sedimentation in an active fore arc basin, *The Society of Economic Paleontologists and Mineralogists (SEPM)*, 31, 31-45

- Voight, B., Komorowski, J. C., Norton, G. E., Belousov, A. B., Belousova, M., Boudon, G., Francis, P. W., Franz, W., Heinrich, P., Sparks, R. S. J. and Young, S. R. (2002)** The 26 December (Boxing Day) 1997 sector collapse and debris avalanche at Soufriere Hills Volcano, Montserrat. In: Druitt T. H., and Kokelaar B. P., e.d, *The eruption of the Soufrière Hills Volcano, Montserrat, from 1995 to 1999*, Geological Society, London, Memoirs, 21, pp. 483-516
- Wadge, G. (1986)** The dykes and structural setting of the volcanic front in the Lesser Antilles island arc, *Bulletin of Volcanology*, 48 (6), 349-372, DOI: 10.1007/BF01074466
- Wadge, G., Isaacs, M. C. (1988)** Mapping the volcanic hazards from Soufriere Hills Volcano, Montserrat, West Indies using an image processor, *Journal of the Geological Society of London*, 145, 541-551
- Wadge, G. (2000)** A DEM of the volcanic deposits of Soufrière Hills Volcano during 1999, Open File Report 00-07-1999, MVO
- Wadge, G., Ryan, G. and Calder, E.S. (2009)** Clastic and core lava components of a silicic lava dome, *Geology*, 37 (6). 551-554, DOI: 10.1130/G25747A.1
- Wadge, G., Voight, B., Sparks, R.S.J., Cole, P.D., Loughlin, S.C., Robertson, R.E.A. (2014)** Chapter 1 An overview of the eruption of Soufrière Hills Volcano, Montserrat from 2000 to 2010. In: Wadge, G., Robertson, R.E.A. and Voight, B. ed. *Eruption of Soufriere Hills Volcano, Montserrat from 2000 to 2010*, Geological Society, London, Memoirs 2014, v.39; pp.1-40. DOI: 10.1144/M39.1
- Wadge, G., Macfarlane, D. G., Odger, H. M., Stinton, A., Robertson, D. A., James, M. R. and Pinkerton, H. (2014)** AVTIS observations of lava dome growth at Soufrière Hills volcano, Montserrat: 2004-2011. In, Wadge, G., Robertson, R.E.A. and Voight, B: *The eruption of Soufrière Hills Volcano, Montserrat from 2000 to 2010*. Geological Society, London, Memoirs, 39, pp. 229-240
- Wainwright, J. and Mulligan, M. (2005)** Environmental Modelling: Finding simplicity and complexity, John Wiley & Sons, England, 408 p.
- Walder, J. S. and Driedger, C. (1995)** Living with a volcano in your backyard; volcanic hazards at Mount Rainier, U.S. Geological Survey Open-File Report, 95-421
- Walter, T. R., Legrand, D., Granados, H. D., Reyes, G., and Arámbula, R (2013)** Volcanic eruption monitoring by thermal image correlation: pixel offsets show episodic dome growth of the colima volcano, *Journal of Geophysical Research: Solid Earth*, 118 (4), 1408–1419, DOI: 10.1002/jgrb.50066
- Wan Z. and Wang Z. (1994)** Hyperconcentrated Flow, Balkena, Rotterdam, 290pp
- Wang, M., Zhan, Y. Liu, J., Duan, W. and Wu, W. (1983)** As experimental study of turbulence characteristics of flow with hyperconcentrations of sediment. In: *Proceedings of the Second International Symposium on River Sedimentation*, Water Resources and Electrical Power Press, Nanjing, China, p. 45-46

References

Web of Science database (2014) Web of Science, Web of Knowledge, http://apps.webofknowledge.com/UA_GeneralSearch_input.do?product=UA&SID=Q23y19bFpeEjClNYQix&search_mode=GeneralSearch [Accessed on 1/9/2014]

Weber, J. C., Dixon, T. H., DeMets, C., Ambeh, W. B., Jansma, P., Mattioli, G., Saleh, J., Sella, G., Bilham, R. and Perez, O. (2001) GPS estimate of relative motion between the Caribbean and South American plates, and geologic implications for Trinidad and Venezuela. *Geology*, 29 (1), 75-78, DOI: 10.1130/0091-7613(2001)029<0075:GEORMB>2.0.CO;2

Wells, S. G. and Harvey, A. M. (1987) Sedimentologic and geomorphic variations in storm-generated alluvial fans, Howgill Fells, northwest England, *Geological Society of America Bulletin*, 98, 182-198

Whitham, A. G. and Sparks, R. S. J. (1986) Pumice, *Bulletin of Volcanology*, 48, 209-223

Whiting, P. J., Dietrich, W. E., Leopold, L. B., Drake, T. G. and Shreve, R. L. (1988) Bedload sheets in heterogeneous sediment, *Geology*, 16 (2), 105-108, DOI: 10.1130/0091-7613(1988)016<0105:BSIHS>2.3.CO;2

Wieprecht, S. (2000) Development and Behaviour of Bed Forms of Coarse Bed Material, University of Federal Armed Forces, Institute of Hydraulics, Vol. 74. Oldenbourg Verlag, 153 p (in German)

Wilcock, P. R. (1993) Critical shear stress of natural sediments, *Journal of Hydraulic Engineering- ASCE*, 119 (4), 491-505, DOI: 10.1061/(ASCE)0733-9429(1993)119:4(491)

Wolf, P. (1983) Elements of Photogrammetry with air photo interpretation and remote sensing, 2nd ed. Mc Graw Hill book company, NY. 628 p.

World Bank (2014) The World Bank Open data, <http://data.worldbank.org/> [accessed 3/5/2014]

World Meteorological Organisation (2013) Review of the past hurricane season: Reports of hurricanes, tropical storms, tropical disturbances and related flooding during 2012. *RA IV Hurricane Committee, Thirty-fifth session, Willemstad, Curacao. RAIV/HC-35/Doc/ 4/2(6) (1 I.III.2013) Item 4.2*, Report from France (French West Indies), April 2013

WMO (2013) Review of the Past Hurricane Season: Reports of hurricanes, tropical storms, tropical disturbances and related flooding during 2012, Report from France (French West Indies), World Meteorological Organization, RA IV Hurricane Committee, Thirty-fifth session, Willemstadm Curaçao, 8-12 April 2013, https://www.wmo.int/pages/prog/www/tcp/.../d_04.2.6_hc-35_france.doc (Accessed: 23/4/2014)

- Wren, D. G., Barkdoll, B. D., Kuhnle, R. A. and Derrow, R. W. (2000)** Field techniques for suspended sediment measurement. *Journal of Hydraulic Engineering*, 126, 97-104, DOI: 10.1061/(ASCE)0733-9429(2000)126:2(97)
- Wren, D. G., Bennett, S. J., Barkdoll, B. O. and Kuhnle, R. A. (2005)** Distributions of velocity, turbulence, and suspended sediment over low-relief antidunes, *Journal of Hydraulic research*, 43 (1), 3-11
- Xie, P. P. and Arkin, P. A. (1997)** Global Precipitation: A 17-year monthly analysis based on gauge observations, satellite estimates, and numerical model outputs, *Bulletin of the American Meteorological Society*, 78 (11), 2539-2558, DOI: 10.1175/1520-0477(1997)078<2539
- Xu, J.X. (1999)** Erosion caused by hyperconcentrated flow on the loess plateau of China, *Catena*, 36 (1-2), 1-19
- Yagishita, K. and Taira, A. (1989)** Grain fabric of a laboratory antidune. *Sedimentology*, 36 (6), 1001-1005, DOI: 10.1111/j.1365-3091.1989.tb01537.x
- Yalin, M. S. and da Silva, A. M. F. (2001)** "Fluvial Processes", IAHR Monograph, IAHR, Delft, The Netherlands, 197 p.
- Yamakoshi, T., Doi, Y. and Osanai, N. (2005)** Post-eruption hydrology and sediment discharge at the Miyakejima volcano, Japan. In: Thouret, J.-C. and Chester, D. K. ed., *Volcanic Landforms, Processes and Hazards*, Zeitschrift fur Geomorphologie Supplement Series, 1 40, pp.55-72
- Yang, D., Goodison, B. E., Metcalfe, J. R., Golubev, V. S., Elomaa, E., Gunther, T., Bates, R., Pangburn, T., Hanson, C. L., Emerson, D., Copaciu, V. and Milkovic, J. (1995a)** Accuracy of tretyakov precipitation gauge: result of WMO intercompariosn. *Hydrological Processes*, 9(8), 877-895, DOI: 10.1002/hyp.3360090805
- Yang, D. Goodison, B.E. and Ishida, S. (1998)** Adjustment of daily precipitation dat at 10 climate stations in Alaska: application of world meteorological organization intercomparison results. *Water Resources Research*, 34 (2), 241-256, DOI: 10.1029/97WR02681
- Yin, J., Huang, H. F., Wang, S. M. and Xu, F. (2012)** Chapter 4: Remote video surveillance applications in landslide monitoring. In: Wang, L. and Xu, G., *Advances in Industrial and Civil Engineering, Advanced Materials Research*, 594-597, pp. 1086-1092
- Yokokawa, M., Masuda, F., Sakai, T., Endo, N. and Kubo, Y. (2000)** Sedimentary structures and Grain Fabric of antidune cross-stratification in an experimental flume with sediment supply: the origin of HCS mimics, Unpublished Manuscript
- Yokokawa, M. and Naruse, H. (2007)** Features of parallel lamination related to the bed-aggradation rates: An experimental study. In: Dohmen-Janssen, M. and Hulscher, S. J. M. H., ed., *River, coastal and estuarine morphodynamics*, RCEM 2007, Vols 1-2. Proceedings and Monographs in Engineering, Water and Earth Sciences, pp. 457-462

References

- Yokokawa, M., Hasegawa, K., Kanbayashi, S. and Endo, N. (2010)** Formative conditions and sedimentary structures of sandy 3D antidunes: an application of the gravel step-pool model to fine-grained sand in an experimental flume, *Earth Surface Processes and Landforms*, 35 (14), 1720–1729, DOI: 10.1002/esp.2069
- Young, S. R., Hoblitt, R. P., Smith, A. L., Devine, J. D., Wadge, G. and Shepherd, J. B. (1996)** Dating of explosive volcanic eruptions associated with dome growth at the Soufrière Hills volcano, Montserrat, West Indies. In: *Second Caribbean Conference on Natural Hazards and Hazard Management*, MVO Open File Report 96/22, Kingston, Jamaica, 1996.
- Young, S.R., Francis, P.W., Barclay, J., Casadevall, T.J., Gardner, C.A., Daroux, B., Davies, M.A., Delmelle, P., Norton, G.E. and Maciejewski, A.J.H. (1998a)** Monitoring SO₂ emission at the Soufrière Hills volcano: implications for changes in eruptive conditions, *Geophysical Research Letters*, 25 (19), 3681-3684, DOI: 10.1029/98GL01406
- Young, S.R., Steven, R., Sparks, J., Aspinall, W.P., Lynch, L.L., Miller, A.D., Robertson, R.E.A. and Shepherd, J.B. (1998b)** Overview of the eruption of Soufrière Hills volcano, Montserrat, 18 July 1995 to December 1997, *Geophysical Research Letters*, 25 (18), 3389-3392
- Young, R. P., ed. (2008)** A biodiversity assessment of the Centre Hills, Montserrat, Durrell Conservation Monograph No. 1, Durrell Wildlife Conservation Trust, Jersey, Channel Islands
- Zellmer, G. F., Sparks, R. S. J., Hawkesworth, C. J. and Wiedenbeck, M. (2003)** Magma emplacement and remobilization timescales beneath Montserrat: insights from Sr and Ba profiles across plagioclase phenocrysts. *Journal of Petrology*, 44 (8), 1413-1432, DOI: 10.1093/petrology/44.8.1413
- Zobel, D. B. and Antos, J. A. (1997)** A decade of recovery of understory vegetation buried by volcanic tephra from Mount St. Helens. *Ecological Monographs*, 67, 317-344
- Zobin, V. M., Plascencia, I., Reyes, G. and Navarro, C. (2009)** The characteristics of seismic signals produced by lahars and pyroclastic flows: Volcán de Colima, México, *Journal of Volcanology and Geothermal Research*, 179 (1-2), 157–167, DOI: 10.1016/j.jvolgeores.2008.11.001